Title

Tailoring the Mechanical Behavior of Architected Materials through the Strategic Arrangement of Defects and the Tactical Coalescence of Lattice Members

Author

Vangelatos, Zacharias

Publication Date

2021

Peer reviewed|Thesis/dissertation

Tailoring the Mechanical Behavior of Architected Materials through the Strategic Arrangement of Defects and the Tactical Coalescence of Lattice Members

by

Zacharias Vangelatos

A dissertation submitted in partial satisfaction of the

requirements for the degree of

Doctor of Philosophy

in

Engineering - Mechanical Engineering

in the

Graduate Division

of the

University of California, Berkeley

Committee in charge:

Professor Costas P Grigoropoulos, Chair
Professor Kyriakos Komvopoulos
Professor Andrew Minor

Summer 2021

Tailoring the Mechanical Behavior of Architected Materials through the Strategic Arrangement of Defects and the Tactical Coalescence of Lattice Members

Abstract

Tailoring the Mechanical Behavior of Architected Materials through the Strategic Arrangement of Defects and the Tactical Coalescence of Lattice Members

by

Zacharias Vangelatos

Doctor of Philosophy in Engineering - Mechanical Engineering

University of California, Berkeley

Professor Costas P Grigoropoulos, Chair

Architected materials are considered the state of the art of engineering ingenuity. Specifically, mechanical metamaterials have been accentuated due to their unconventional and augmented responses. They have been gingerly investigated under the context of ultralight-ultrastiff structures for aerospace applications, tailored buckling mechanisms for energy storage, soft robotics and controlled wave propagation and designed anisotropy for tissue engineering.

Albeit the plethora of remarkable results promulgating this subject, the analysis of architected materials has many questions that need to be addressed. There is no rigorous explanation for the selection of specific 3D designs that have been thoroughly utilized in the literature (regarding the selection of specific design variables and cost functions). Consequently, in practice specific structures are repeatedly used, without any explanation whether further search of the design space could not provide a substantially improved result. Therefore, the lack of understanding of the design space and the inherent physical phenomena has not elucidated the tools to obtain a globally optimal design. Thus, tailoring mechanical metamaterials is extremely arduous and has led to an obstacle in the progress of this field.

This thesis aims to provide an analysis for the design of architected materials by illuminating the physical mechanisms and how to model and optimize such problems. The structure of this thesis is comprised of two main themes. The first method aims to control the mechanical performance through interconnected beam members that enhance the densification of the structure and impede catastrophic failure. The second method is related to geometrical defects that dictate the localized failure and anisotropic behavior. Furthermore, the optimization of specific design examples will be presented, employing low computational power for large design spaces and demonstrate how such design problems can be addressed, setting the framework for the systematic design and characterization of architected materials.

To my family, the Greek taxpayer who paid for my undergraduate education and the American taxpayer who paid for my graduate education and research at UC Berkeley.

Contents

List of Figures

List of Tables

Acknowledgments

This thesis would have been nothing but Ixion's embrace without the advice and support of many people I encountered in my ephemeral halcyon days at UC Berkeley. I am certain that I have forgotten to acknowledge several colleagues, professors and friends, but regardless of whether or not this is *solem lucerna, quod aunt, ostendere*, they should all know that they will always have my eternal gratitude. The following should not be considered an encomium of *kolakeia* or a panegyric of sycophancy, but rather a scintilla of rotund *Eusebeia*. Verba volant, scripta manent!

First and foremost, I must express my eucharistia to my family, both in Greece and the United States, both tied by blood or perennial allegiance, for their support and sophron advice throughout my studies. Their mere presence was a catalyst in my academic anaptyxis through the years of yore. *Pietas erga parentes* is one of the greatest virtues!

From my alma mater, in the spirit of *Redde Caesari quae sunt Caesaris*, I must provide an eulogy for two professors that had a scintillating impact on my katabasis to the propylaeum of engineering. The first is Prof Dimitrios Manolakos. Albeit *opera olla legit*, Prof Manolakos was the harbinger to the developments of my character from a *table rase* to an Ébauche in mechanics and the mechanical behavior of materials and a düreresque neophyte in engineering. During the parodos and epitasis of my undergraduate studies, his insight and teaching were the sine qûa non of my engineering foundations. The second is Prof Panayota Vassiliou. Although I met Prof Vassiliou at the exodos of my studies, her plenipotent ardor and avidity to teach corrosion had a great influence on me. This is a critical subject which unfortunately is often portrayed as *mal à propos* by the inane novices in engineering. Moreover, her willingness to involve me to a dalliance with the Parthenon precipitated a cardinal vagation to my indefatigable desire to advance the repertoire of my cultural and scientific spirit. My obeisance and reverence for them can only be limned as a cavernous bathos of tantalizing velleity for *aristeia*.

Next, I must thank my advisor, Prof Costas P Grigoropoulos. Prof Grigoropoulos gave me the baptême du feu to join the Laser Thermal Lab and work on a unique and riveting topic, which at that stage seemed *insaisissable*. The avoirdupois of his decorum and plethoric phronesis were instrumental to embrace the nous of a researcher and cultivate a panoply of epistemic mentality. The *eleutheria* that he provided me to pursue my research was ipso facto translunary and proceleusmatic for the development of new scientific findings. He vehemently encompasses the Homeric: «᾽Αιὲν ἀριστεύειν καὶ ὑπείροχον ἔμμεναι ἄλλων, μηδὲ γένος πατέρων αἰσχυνέμεν, οἳ μέγ᾽ ἄριστοι ἔν τ᾽ ᾽Εφύρῃ ἐγένοντο καὶ ἔν Λυκίῃ εὐρείῃ. Ταύτης τοι γενεῆς τε καὶ αἵματος εὔχομαι εἶναι.» (*Ever to excel, to do better than others, and to bring glory to your forebears, who indeed were very great. This is my ancestry; this is the blood I am proud to inherit. Iliad Z 208-211*). I also want to thank him for his munificent and stolid beneficence and equanimity regarding my thersitical use of circumlocution and sesquipedalian lexicon in our scientific publications. This aspect of my idiosyncrasy can become irksome, especially during the reviewing process (Employing an hapax legomenon is the summum bonum for the eloquence of the findings!). He is a true erudite and a prescient!

Furthermore, I want to thank Prof Kyriakos Komvopoulos for our collaboration. His punctilious assiduity and fermentation to discuss and interpret experimental results in a pellucid manner bolstered my scientific analysis and aperçu as a researcher. In retrospect, I realize that I tyrannized him (and a myriad of others...) with my obstinate and intransigent logos, but I truly appreciate his desire for scientific dialogue.

In addition, I want to thank Prof Andrew Minor for being a member of my qualifying exam and dissertation committees. His candid and sagacious insight helped me in my pursuit to attain a more rigid articulation and exegesis of my experimental and theoretical results. I also want to thank him for giving me access to the 950 Triboindenter at his lab, allowing me to initiate my first nascent characterization experiments.

There are also a few more people I feel indebted to acknowledge. I want to thank Prof Peter Hosemann for giving me access to the picoindenter of his lab, providing me the avenue to delineate the micromechanical phenomena of my tailored lattice-creations. I must also thank Prof Ma from Syracuse University and his PhD student, Chenyan Wang, for our collaboration regarding the implementation of architected defects in tissue engineering. Our work illuminated an untrodden vagation for the utility of my designs and ideas.

Moreover, I want to thank Prof David Steigmann, as a member of my qualifying exam committee, and additionally for his deep insight during our discussions regarding the mechanics of architected materials. He is a true luminary and perhaps the fulcrum towards my inculcation into the peregrination of mechanics. I must also thank Prof Philip Marcus for providing me the opportunity to collaborate with him. His tremendous effervescence and alacrity augmented the eloquence of my scientific arguments and elucidated how I must convey and delineate my explanations. His holistic scientific gnosis will always be an inspiration for me. Furthermore, I would like to thank Dr Frances Allen for teaching me how to use the Helium Ion Microscope. Despite the unforeseen challenges of the pandemic, she was always available to help me when her assistance was required. The Helium Ion microscope proved to be an august repertoire in the eidetic conveyance of my results and I employed it in my research with contemplating élan.

I also want to thank Yoonsoo Rho, Minok Park, Matthew Eliceiri and Brian Blankenship for their help and meaningful conversations while we were conducting experiments or working on proposals at Etcheverry Hall. The sometimes monotonous days in the lab are much more vivid when you are surrounded by acute colleagues. From FORTH, I want to thank Dr Maria Farsari and Dr Vasilia Melissinaki. Their help during my first year at UC Berkeley was significant and with their advice I was able to fathom and employ the fabrication process of multiphoton lithography. Bereft of their help, this thesis would have been realized *ad kalendas Graecas*.

For the peroration, I want to thank Haris M. Sheigh. We spent most of our academic life at UC Berkeley struggling to find something novel and have an impact in our respective fields by collating our research subjects and contemplating with scrutiny over the apotheosis of our results. His enthusiasm rendered Berkeley much more compelling and the intriguing tête-à-tête that we had broadened my horizons and made me comprehend a different culture and the mindset of coruscating bel-esprit.

I also aspire that this thesis was a débouché for *docendo discimus* for them. Evidently, *et saepe extrema necessitas in virtutem vertitur* is vain. Despite the fact that *faber est quisque fortunae suae*, I consider this work my personal chef-d'œuvre and without the support of all of these remarkable people this raison d'être would have just been an oneiric path, ebbing in an untenable purpose.

Comme la célèbre Villa des Mystères de Pompéi, que les cendres du Vésuve recouvrirent pendant des siècles, une admirable peinture, mauve sur fond rouge, évoque le dévoilement des mystères au cours d'une cérémonie d'initiation, donc cette thèse suscite aussi l'inaugurement des metamatériaux méchaniques. L'ordonnance est parfaitement dessinée, les géométries esquissées, le voile soulevé; mais, pour le non-initié, les metamatériaux méchaniques restent entier et lourd d'équivoques.

Cette thèse pourrait servir au lecteur de fil d'Ariane, qui le guiderait dans les détours ténébreux du labyrinthe des metamatériaux.

Chapter 1

Prologue

The recent advances in additive manufacturing and FEA modeling have established the interest of the scientific community towards the design of architected materials. Another name for this category of designs is also *metamaterials*, aspiring to possess responses that surpass the physical properties found in nature [20, 105]. This objective might seem unrealistic or ambitious, considering that nature is the very experienced regarding the architecture of tailored designs [17]. Nevertheless, there are a lot of great architectures that can be regarded as state of the art compared to conventional engineering materials. This set spans from the interesting invisibility [107] to the superior structural integrity of auxetics [5].

In the academic and research literature there is a tendency to merge all of the categories of metamaterial structures together. Undeniably, this would render the analysis much more convenient. However, there are distinct differences based on the domain that needs to be addressed, which are remarkably diverse. A major type of metamaterials are thermal metatamaterials, structures with tailored thermal properties such as conductivity [100] or thermal expansion [415]. Furthermore, another prime category is that of electromagnetic metamaterials, structures that aim to control properties such as the electric permittivity and the magnetic permeability [412] for superconductivity and high absorption [50]. While this category must be addressed as the first of metamaterial designs, the one that has been most thoroughly investigated with great effort is the category of acoustic metamaterials [76]. This design approach aims to control of the wave propagation in the medium at the wavelengths of sound and aims to realize structures with controlled band gaps [219, 111], as well as media for the controlled directionality of the wave in space [89]. In addition, this field has led to the creation of non-reciprocal metamaterials, structures that defy the physical laws of action and reaction [321], due to the design principles of the engineers [69]. Finally, at this category the bistable metamaterials should also be included. These are structures with multiple equilibrium positions that are tailored to control mechanical waves through the medium, cause tailored buckling and aim to lead to major energy storage devices [163] and soft robotics [61]. Despite the fact that there are other design examples focused in the control of mechanical waves [27] through origami [441], kirigami [454] or tensegrity structures [123], bistability is still the main way to address such problems. A principal reason for this

tendency is the convenient analysis of 2D Euler buckling in the theory of elastic stability [384], enabling an easy experimental implementation of these designs. However, the analysis of Koiter for 3D buckling [215] still remains unused.

Finally, the category that is closer to conventional structural engineering applications is that of the mechanical metamaterials [371]. These structures have extraordinary properties in the elastic [125, 63], plastic [447, 157] and fracture domains [453, 255, 456]. They are also relevant to the bistable metamaterials due to the fact that buckling is a static structural phenomenon. This field has led to the interesting concepts of auxeticity, e.g. structures with negative Poisson's ratio [238], tailored anisotropy [261] and architected isotropy [254], and most importantly 3D tailored buckling for controlled densification and strengthening of the structure [407, 126]. All of these properties have significant effects in the design of bio implants [168], in tissue engineering [440] in aerospace engineering [373] and even in the properties of lithium-ion batteries [287].

Despite the important character and role of that many applications, the main objective of mechanical metamaterials is to imitate properties that are observed in nature, even at the most extreme states. While ceramic nanolattices have been proved to possess remarkable ductility [264], the same phenomenon has been observed in flash-sintered TiO_2 [229]. Geometries such as the octahedron and tetrakaidecahedron have been presented as metastructures [466], despite the fact that they can be found on sponges [209, 422]. Moreover, auxeticity has been observed in natural tendons [418], despite the attempts to include it in the category of metamaterial properties. In that regard, mechanical metamaterials might need to lose their *meta* character, with a more appropriate title to be *architected*. However, that should not be considered by any means an argument that belittles their significance in the aforementioned engineering fields. Nature has millions of years of experience in design and the inspiration by its lessons can lead to interesting results. Since the vast majority of the literature addresses these structures as metamaterials, this definition will be employed for the rest of this thesis.

This thesis will investigate, model, analyze and test the mechanical performance of mechanical metamaterials, predicated on the definitions that were provided before. Even though mechanical metamaterials have been thoroughly studied during the past decades [146], at lengthscales spanning from nanometers [345, 463] to centimeters [175, 448], there are still many questions that remain unanswered. Specifically, there is limited work on the analysis of the elastoplastic behavior of 3D structures [83, 217]. While the vague concept of densification and failure impedance [140] has been elucidated, there is no systematic way to control it under the context of a design problem (i.e. the definition of design variables and the cost function that needs to be optimized). Despite the fact that optimization techniques such as topology optimization have been employed [306, 428], their utility is convenient either in 2D geometries [416] or 3D structures that are symmetric [57]. Moreover, the design variables are always related to material volume [452], limiting the analysis to convex-gradient based optimization with real, quantitative variables. Hence, reading the literature reveals an extremely limited number of proposed designs, the vast majority of which are related to bistability [45, 234, 90]. In addition, these optimal designs are not even used in the vast majority of the

literature. Besides, most researchers employ standard, thoroughly studied lattice structures such as the octet truss or the Kelvin foam [456, 25, 466, 264, 377, 91, 265, 63, 363, 153, 306, 140, 344, 292, 243, 98, 193, 419, 421, 217, 220, 147, 180, 178, 273, 136, 208, 13, 376, 264, 466, 265, 38, 91, 263, 292]. However, there is no evidence that these structures are indeed optimal based on a very explicit cost function, and assuming that their properties as close to optimum is a disputed argument. Even though new classes of metamaterials, such as the plate lattice structures [433, 73, 377, 289, 355, 125], are employed to resolve this issue and improve the aforementioned designs, they are constrained to a handful of geometries. In addition, in theory it has been proven that they can ideally possess isotropy and they can reach the theoretical Hashin–Shtrikman upper bound [420] of strength [25]. However, isotropy was not reached [377] with precision in the experimental validation. Moreover, very difficult processing techniques must be employed to attain the theoretical limit of strength [73] at the microscale [23]. All of these reasons have alienated the public from this field, limiting the frontier of research to a handful of *noli me tangere* (touch me not) groups around the globe, especially in microscale structures [371, 264, 143, 466, 429]. Since their work is so limited, unfortunately, other researchers face difficulties addressing these problems, continuously using the same geometries. It must be noted that there are some examples of exceptional results related to the optimization of 3D structures [57, 28, 460, 64, 63, 149, 425]. The optimization techniques that are employed though are hard coded for these very specific problems and the complexity is always limited to symmetrical problems. In addition, they require tens or hundreds of thousands of data to perform their methods, limiting their analyses to small problems with just a single unit cell or denigration of the 3D structure to a 2D problem.

All of these remarks can be used to conclude that there are many questions that need to be addressed regarding the analysis of 3D mechanical metamaterials. The primary questions are: i) Which are the inherent physical mechanisms that control the elastic, plastic and fractural behavior, ii) is there any rigorous systematic approach to model such structures and define specific design variables without the limitation of just real quantitative variables, iii) how can these structures be optimized for nonsymmetric arbitrary problems with a small computational budget and iv) what are the conclusions of this optimization analysis? The sole purpose of this thesis is to address the answers to these questions, aspiring to resolve them.

The structure of this thesis will be related to two proposed strategies. The first one refers to the merge of lattice members such that internal and external intersections in the unit cell can control the buckling, the densification, the stiffness and the plasticity of the structure. The second refers to the asymmetrical removal of lattice members in the structure. These defects imitate the defects observed in the crystal structure of lattices [383]. This arrangement of defects can also regulate the same properties. The main difference lies on the fact that one method adds members, while the other removes them. Based on these approaches, specific design variables will be defined and the cost functions that need to be optimized. These methods will be analyzed in both microscale and macroscale, aiming to comprehend the inherent challenges of each fabrication technique and the employed materials. As it

will be shown, several mechanical properties cannot be used based on the constitutive behavior of the bulk material. For the optimization of these designs, a novel implementation of Bayesian optimization will be utilized [458]. This work is related to the PhD thesis of Haris M. Sheikh, Department of Machanical Engineering, UC Berkeley. Therefore, further information about his intellectual creations will be provided there. The main focus of this thesis will be to interpret the results of the optimization algorithm under the context of mechanics and mechanical behavior. In addition, the prowess of architected materials will also be proved to be useful on tissue engineering and tissue formation, which is considered one of the main applications of architected materials. These results are related to the work of Chenyan Wang, Department of Biomedical & Chemical Engineering, Syracuse University and her investigation of the mechanobiology of the cells. Apart from these examples, this thesis will provide an extensive introduction to introduce the work that has already been conducted in the field and its incapacities. The main reason for this summary is that the vast majority of the literature does not connect the different aspects of metamaterial design. A lot of designs seem to emerge out of thin air, while they have been proposed almost half a century ago. That is the case especially for the literature related to the mechanics and the one related to the mechanical behavior, giving the impression that these two fields are two separate subjects. Finally, the vast majority of this work has already been published and it is supported by extensive recordings of the mechanical experiments. It is recommended that the reader should search these publications to observe the mechanical performance *in-situ* [404, 393, 84, 402, 395, 396, 399, 401, 397, 394, 119, 400, 392, 398, 403, 365]. At the stage that this thesis will be published, several more publications will have been available, and thus they were not cited at the moment that this passage was written. But the reader can always find more results at the website of the Laser Thermal Laboratory.

Chapter 2

Introduction

2.1 The Foundations of Mechanical Metamaterials

Reading the latest publications of mechanical metamaterials may lead to the conclusion that several designs emerged out of nowhere. However, the design of mechanical metamaterials took decades to be realized for different structures. The first studies of mechanical metamaterials were initiated on two different fronts. The first one was the design of ultra-light, ultra-strong structures for structural engineering applications such as trusses. This work was promulgated by agencies such as NASA, aspiring to create significantly lighter structures and simoultaneously preserving their strength [225, 223]. At this stage of analysis, the initial first step was the listing of geometrical properties such as the number of vertices and edges for 2D designs. Characteristic geometries are the regular and irregular hexagon and pentagon and their variations. In retrospect, such analysis might belie the importance of such structures and it might be considered simplistic compared to the present. However, as it will be addressed in detail in the next chapters, the geometrical configuration has a major role in the mechanical performance of the structure. This notion became the catalyst for the design and classification of hyperstructures [224]. These structures are generated by the minimum reduction of asymmetrical parts in a 3D solid, and led to the creation of 128 polyhedral geometries. These principal geometries constitute the set that all of the architected materials employed in literature originate from. Characteristic first examples such as the honeycomb [283], the octet truss [91], the tetrakaidekahedron, the cuboctahedron and the Kelvin foam [164] emerged from this classification of 3D polyhedra. Even more futuristic structures such as the Bucklicrystals [16] with tailored buckling and negative Poisson's ratio were defined at that stage. Some of these structures are also defined as stellations of regular polyhedra [424]. A polyhedron is stellated by the extension of either its edges or its face planes until they encounter again to form a new polyhedron or compound. These structures are subject to specific rules that dictate they generation. These are the Miller's rules [272]. The rules are the following: a) The tetrahedron and the cube have no stellations; b) the stella octangula (i.e. the octet truss) is the only stellation of the cuboctahedron; c) the dodecahedron has

three stellations and d) the icosahedron has fifty eight stellations. These rules constrain the design space that can be employed by just adding lattice members in the unit cell apropos of its geometrical center with spherical symmetry. It must be noted that out of all of these combinations, the only one that is the most used in experimental testing is the octet truss. Moreover, The Kelvin foam is a truncated octahedron [382], which is not a stellation. These polyhedral structures can become the framework for two types of geometries. If the edges of the polyherdra are utilized, they constitute lattice structures. However, if the faces of the sides are employed, then they create plate lattice structures [25, 102]. However, it will take almost thirty years for the latter to appear in the literature as 3D structures. Furthermore, other types of structures were also proposed, even though they were still not known for their exceptional properties. A characteristic example is minimal surfaces [48]. These structures possess minimum mean curvature and, as it was proven decades latter, they also possess high stiffness-to-weight ratio, heat dissipation control, and enhanced mechanical energy absorption [207]. Another category was the planar jitterbug [241]. These structures are comprised of cubic blocks connected at their corners but without connection at the edges. This name is not used anymore. The contemporary definition for these structures is rotating squares [152, 27, 15]. These structures furnish auxetic behavior and resilience to failure. Nevertheless, at that stage they could not be employed for aerospace applications and they were only a subject of theoretical analysis.

Based on this analysis of topological configuration of lattice members, the next step was to obtain a methodology that explains the mechanical behavior appropriately. Since there was an incipient analysis of continuum mechanics with respect to lattice continua [104], the first viable conducted that was conducted employed linear elasticity by discretizing the lattice structure into beam or truss members [288]. Therefore, for a structure with linear elastic behavior, the constitutive equation that correlates the components of the Cauchy stress tensor $\tilde{\sigma}$ and the linear strain tensor $\tilde{\epsilon}$ is: $\sigma_{ij} = C_{ijkl}\epsilon_{kl}$, where i, j are the indices of the coordinate system [251]. This correlation between stresses and strains is predicated on the fact that the stiffness properties of the unit cell must be averaged over its respective volume. An alternative way to convey this is the assumption that the unit cell is a fundamental building block with stiffness matrix $\mathbb{K}$, as it is defined in finite elements analysis [374]. It must be noted that $\mathbb{C}$ is a fourth order tensor with four indices. This tensor has eighty one components. However, based on the theory of elasticity (major symmetry) and the (minor) symmetry of the stress and strain tensors, this number can drop to twenty one. In addition, using the so called Voigt notation, it can be represented as a 6x6 matrix. The independent components of this matrix depend on the symmetry of the structure [39]. The symmetry of the structures is directly related with its symmetry group $\Re_K$, which is the set of transformations that do not alter the configuration of the structure for the reference system K. For instance, monoclinic symmetry imposes thirteen independent elastic variables, orthorhombic symmetry nine, tetragonal six and cubic three. Isotropy imposes the minimum number of elastic constants, which are the Lamé parameters λ and μ. While there are certain behaviors, such as auxeticity of Cauchy symmetry [298], that can drop the constant to one, they are related to the structural topology of the design. Thus, they correspond to the

macroscopic response of the structure and not the constitutive behavior of the bulk material. Most of the studied unit cells in the literature (i.e. octet truss, Kelvin foam etc) possess cubic symmetry and thus have three independent elastic moduli. The most interesting finding was that all of the elastic moduli are proportional to $E\rho_c$, where E is the Young's modulus of the bulk material and ρ_c is the relative density of the structure. The relative density is defined as the volume of the unit cell over the volume of a bulk material that encloses all of the unit cell. Hence, ρ_c is an imperative property of the structure, limiting the maximum value that the stiffness can reach and it also controls the anisotropy of the material. In a truss structure, it only depends on the length and cross section of each lattice members. However, in a beam model, it also depends on the nodal intersection between members. Trusses forfeit this trait, due to the low computational cost and easy structural analysis. As it will be discussed in later chapters, the sensitivity of the relative density to nodal intersection can be a powerful arsenal to tailor the anisotropy of the structure. However, it must augured that some of the most thoroughly employed unit cells have anisotropy which is relatively invariant with respect to the relative density [400], rendering this feature research as a design variable in the design of architected materials [1, 2].

Even though this field begun advancing in aerospace engineering, its true progress was shown in the second front, that is the design of metallic foams for ultralight structural members [211]. Undeniably, the main researchers of this progress were Prof Michael F. Ashby from the University of Cambridge and his student, Prof Lorna Gibson, who later became a professor at MIT [140, 141, 139, 142]. The modelling, mechanics and characterization of foams cannot be separated from that of mechanical metamaterials and their analysis will pave the way for the ascent of mechanical metamaterials after the major advances in additive manufacturing. Metal or ceramic foams are cellular solids with extremely high porosity [334]. They can comprise of either struts or plate members [115, 247], with the most basic and ordered being the honeycomb. During this period it was determined that the single most relevant property of a foam is the relative density ρ_c, as it was defined before. It must be noted that foams are structures with relative density less than 0.3, the threshold between isolated pores and sponge-like topology. These structures can be fabricated by either liquid or solid state processing [307]. At this process, metal powder can be heated close to the melting point and with the use of hydrogen in can lead to bubble formation in the material. Foams have low strength but extremely high compressive strain, rendering them potential candidates for energy absorption applications. However, they can also be employed for thermal insulation [461], bone tissue engineering and recuperation [138], filtration [31], sound insulation [161] and even tissue modelling for the study of diseases and detrimental modes of cellular behavior [150]. More specific details about these applications will be provided in the following sections. Foams are divided into *closed* and *open*. In closed foams each cell is separated by its neighbors by membrane faces, whereas open foams encompass interconnected cells. Another major property of such structures is the coordination number of the members at each node and as it will be shown later, it is as quintessential as the relative density in the study of architected materials.

For the calculation of the relative density, the critical parameters are the thickness t of

the struts and the length L of the face of the unit cell. At low relative densities, the open cell foam has $\rho_c \propto (t/L)^2$, while close cell foams have $\rho_c \propto t/L$. Such characteristic relations can be found in the literature [140]. However, as the thickness of the struts increases, the relative density becomes sensitive to higher order terms, such as $(t/L)^3$ and $(t/L)^4$. These higher order terms are a reverberation of the nodal intersection of members. Certainly, dovetailing the struts decreases the actual volume of the material. However, these terms will appear much later in the literature with the advances in computer aided design (CAD) and the effective calculation of intersecting volumes [147]. Having obtained the relative density of the structure, the foam must be juxtaposed with other materials of the same relative density to validate whether its fabrication cost and properties can surmount them. For this comparison, the Ashby charts must be utilized [14]. From the perspective of mechanical analysis, these charts demonstrate the variance of properties (i.e. the Young's modulus or the yield strength) with respect to the relative density for different material families (i.e. engineering alloys, engineering composites, ceramics etc). For instance, alloys and ceramics are on the top right corner of the chart (e.g. strongest but heaviest), whereas polymer foams are on the bottom left (lightest but weakest). The objective of the engineer is to select the best material, depending on the desired application and in most cases the Ashby charts are the guideline to accomplish this. Therefore, it is appropriate to include both random foams and architected lattices in these plots and then evaluate the costs and benefits compared to other materials. Since foams are the lightest, but weakest family of structures with respect to every mechanical property, the next stage of research was to tailor their mechanical properties. For the case of honeycomb structures, the mechanical response demonstrates high sensitivity to the relative density. As ρ_c increases, the plateau in the stress-strain response of the ordered foam decreases due to the transition from elastic buckling or plastic bending to cell wall bending. Hence, the structure has linear elastic behavior for an increased value of ρ_c. This pattern is observed in most random foams as well. The plateau in the stress strain response, similar to a plateau observed in a mechanical test of a rubber material, is precipitated by the densification of the struts and the commencement of post-contact between them. However, hardening is instigated at extremely high strains. At the instigation of nonlinear behavior the main mechanism that is observed is strain-softening. The reason for this phenomenon is the initiation of collapse in the members, heralding the weakening of the structure. Since the failed beam members come in contact with the proximal ones, the densification ceases the stress drop [388, 121, 357]. However, this global failure of the whole structure forebears the incapacity of foam structures for multiple loading cycles of high force amplitude without excessive fracture. As it will be addressed in the next chapters, failure must be regulated at specific locations and be controllable. Moreover, despite the fact that analytical equations for the critical buckling load are provided for simple structures to regulate the rise of instability, it is torrid to attain an analytic equation for 3D complex structures.

From the perspective of other mechanical properties, it is crucial to correlate other quantities, such as the stiffness E, the effective Poisson's ratio ν or the yield strength σ_y with the relative density of the structure. In most cases such equations can be derived analytically for

2D geometries in the linear elastic domain. To accomplish this, the deformation field must be estimated. Hence, the strains can be calculated through kinematics and 3D Hooke's law can be implemented for either plane stress or plane strain [423, 327, 173]. For the case of plastic collapse, similar arguments can be utilized through the lower bound theorem of the limit analysis [62]. This theorem dictates the lower bound in the critical load that can lead to plastic collapse. Again, this value can be evaluated by an assumption of the deformation field and the plastic flow velocity through the methodology of hodographs [101, 174]. It must be noted though that the verity of the calculated value is predicated on whether the deformation filed is either shipshape or folly. Hence, it is evident that this calculation is dependent on the expertise and experience of the engineer in the study for plastic deformation and might be subject to a big difference from the experimental results. Furthermore, it is important to investigate the mechanical performance of foam structures from the perspective of fracture mechanics [133]. For this analysis, the structure must possess a flaw of a characteristic length and investigate under which conditions the flaw will begin growing. For the case of a brittle material, the limit load that leads to fracture can be calculated through the methodology that was provided before. Based on that, a quantity proportional to the applied stress and the square root of the crack length, namely the stress intensity factor can be evaluated and compared with the critical fracture toughness. However, this theory furnishes major incapacities. The stress intensity factor is a quantity related to linear elastic fracture mechanics. Linear elastic fracture mechanics is predicated on the assumption that the continuum is uniform and the only region of discontinuity is the edge of the crack. In addition, the stress intensity factor is the integration constant of the solution of linear momentum balance. The validity of this solutions lays only in the K-dominant region, whereas in the plastic zone and the zone of higher order terms it is not valid [154]. If the foam is comprised of voids or pores that are disproportionally inordinate, then the material is not uniform and this specific solution of the linear momentum balance is not correct. In that case, comparing a quantity defined as stress intensity factor with a hypothetical material property called critical fracture toughness provides a weak safety criterion which imitates of the equivalent continuum model. For the utility of this criterion , the voids in the structure must be extremely small compared to the whole material, such that the localized theorem is experimentally valid in the highest degree [301] and a continuum model can be used [258]. These models will appear much later in the literature for microscale structures [137]. Nevertheless, this analysis is still employed for the study of fracture in mechanical metamaterials. However, it is case-sensitive to the specific structure that is investigated. In addition, the stress intensity factor K_I has no mathematical interpretation, but it is the stress applied in a loading mode similar to mode I, multiplied by $\sqrt{\pi a}$, where a is the crack length. The critical fracture toughness K_{IC} is not a material property, but the limit value of the stress intensity factor that results in crack propagation. Based on these definitions, mechanical testing has been conducted in various geometries with different geometrical parameters and crack lengths and a geometry dependent critical fracture toughness has been obtained. Nevertheless, a purely mechanistic and catholic model, independent of structure or pore size for every design, is an intriguing subject of research even to the day this thesis

was written [317, 318]. The strain energy density W is always calculated as a function of the transient relative density ρ^*, which is the value of the relative density as a function of the deformation. In addition, the peak stress σ_p is also calculated as a function of the ρ^*. These equations are usually curve-fitted third order polynomials, since in most cases both W and σ_p are calculated in the nonlinear domain. For the selection of foam structures with respect to energy absorption, it is required to employ the curves that convey the relationship between W and σ_p. By varying ρ^*, parametric families of curves can be attained that have an upper bound [140]. These curves, defined as energy absorption diagrams, are the primary tool to select foams along with Ashby charts. The upper bound, defined as an envelope, is characteristic of this specific foam independent of material and fabrication technique. Since the inherent mechanical mechanisms such as nonlinear buckling, post contact and plasticity are computationally expensive to be calculated, these curves provide a fast way to select a foam without the holistic analysis of mechanics. For random foams fabricated with specific fabrications techniques, changing the relative density and then conducting experiments is an expedient compromise and has been acquiesced even in contemporary scientific literature. However, for a 3D structure with a specific arrangement of members, there is an exorbitant number of potential combinations that can provide a totally different design, either symmetric or asymmetric. Therefore, it is computationally and experimentally extremely expensive to obtain an envelope for every type of geometry and every type of modification. Therefore, these curves are not widely used in any other design apart from foams and have are not employed in the literature for architected materials.

Regarding the initital analysis of architected structures, another subject that was addressed was the analysis of defects. It was reported that the arrangement of members at specific locations of a 2D structure can cause abrupt decrease in the mechanical properties such as the stiffness and the compressive strength [156]. This weakening in the structural integrity also causes shifts in the failure modes [358]. In addition, introducing members with different thickness can lead to band formation near their proximity, impelling the failure to specific locations [325]. This deformation resembles shear bands observed in the failure mode of the crystal lattice [383]. While this deformation mode can cause densification in the lattice and strain hardening, the inevitable commencement of fracture at the defected regions, combined with the weakened mechanical properties, had rendered this strategy nonviable to design high energy absorption materials with structural rigidity [140]. For this reason, this detail in the design of mechanical metamaterials was considered as detrimental and egregious and was not inoculated as a design paradigm. As it be described later, it took almost three decades for the scientific community to resurface this very old problem again [153, 393].

All of these information lay the framework for the advance of mechanical metamaterials. It is ostensible that their analysis was interlaced with that of foam structures, limiting the mechanistic analysis over the purely experimental one. Another reason of the limited designs was the limited number of fabrication options. As it will be presented later, the advances in additive manufacturing enabled the design of complex structures and expanded the ambit of more complex models. However, at this stage it would be instructive to provide a brief review of the second front. That is the mechanics of architected materials, as long as they

remained independent of fabrication validation.

From the perspective of mechanics, the design of architected materials was primarily focused on plate structures. Plate structures were the only structural members that could be fabricated with the available fabrication techniques [257]. Despite the fact that the present study of plate architected materials has primarily focused in the linear elastic domain of 3D structures, before the rise of 3D printing, the principal subject of focus was the analysis of 2D structures. 2D plate theory is convenient since it provides analytical expressions to obtain the stress distribution and the buckling load [385, 366] even at the plastic domain [191]. Nevertheless, several preternatural concepts such as architected arrangement and tailored buckling originate from this subject [33, 284]. Specifically, such designs were thoroughly employed for aircraft design [32]. The arrangement of fibers in specific patterns results in the substantial increase of the buckling load up to 700% [35]. In addition, the nonlinear post-buckling behavior can be tailored such that specific buckling modes can be attained and the stiffness of the plate can embrace controlled values [34, 196]. All of these ideas will be bequeathed in the design of architected materials through both FEA modelling and continuum modelling. In addition, there was no connection with architected materials regarding a pure continuum theory. However, a very specific model that will play a much more important role later is second gradient elasticity. This model is predicated on the fact that the strain energy of the material does depend explicitly on the strain tensor (i.e. the deformation gradient), but also the spatial variation of the deformation gradient [213, 275, 256]. However, this model is applicable to materials and structures that have an ordered structural arrangement that is orders of magnitude lower than the length scale of the structure. Characteristic examples are fibers of micrometer thickness that can possess extremely high curvatures as the bulk material deforms. Hence, these continuum models faced a barrier despite demonstrating responses that were intriguing for their time. Such structures will be resurfaced much later in the literature [106] and will be discussed in the following chapters.

All of the above constitute the foundations of the design and modelling of architected materials. Nevertheless, the limitations of fabrications and consequently the lack of applicability in aerospace engineering did not support further research of these designs. With the advances in additive manufacturing and 3D printing, architected materials will be reinvigorated, ceasing the inactivity to exclusively 2D honeycombs. The next chapter will focus on the numerous fabrication techniques that will set the framework for the fabrication of architected materials at a range of lengthscales. In this thesis the main focus will be on the description of laser printing techniques, since they were the main arsenal for the study of mechanical metamaterials in this work. Techniques such as 3D and 4D printing will be briefly mentioned as the tools to fabricate and test macroscale structures. But to avoid any tautology, the analysis will be secluded to the mechanical behavior.

2.2 Fabrication Techniques

Section Synopsis

The inexorable advance in printing technologies through the past decades is a consequence of the establishment of the laser on this field. Utilizing a beam instead of a deposition tip or nozzle to modify the shape of a material provides an auspicious advantage to create complex structures and devices with extremely high resolution. Laser printing techniques are defined as all of the technologies that modify the material to create a new structure in an additive manner with a laser source. Even though technologies such as digital light processing or Dynamic Optical Projection Stereolithography utilize the same physical principles for fabrication, they employ light sources or projectors, which will not be discussed in this introduction apart from a brief summary of characteristic fabricated specimens. Among the plethora of various techniques encompassing both high resolution and malleability, some of the most remarkable ones are the multi-photon polymerization techniques for fabrication and the Laser-Induced Forward Transfer for controlled deposition. This chapter will focus on the fundamental mechanisms dictating these techniques. Since the primary fabrication technique that was employed in this thesis was multiphonon lithography, a succinct description of this technique and its juxtaposition with other fabrication techniques of the same lengthscale is considered pertinent to set a coherent framework in the development of mechanical metamaterials. Moreover, the corollary of increasing the resolution with stimulated emission depletion will be addressed and its contemporary scientific challenges. All of these techniques are considered direct laser writing techniques, because they do not require pre-existing patterns, such as lithographic masking or stamping. Even though the aforementioned techniques are imperative due to their low cost in mass production, direct laser writing techniques can provide significant advantages, such as resource footprint for device fabrication, allowing rapid prototyping, simple modifications and MEMS device fabrication and repair. Other fabrication techniques such as 3D and 4D printing will be briefly addressed regarding how they have been employed in applications in the next sections. But since they were not employed directly in the realization of this thesis, their analysis will remain laconic.

Multi photon polymerization

3D fabrication utilising photoresists was initially developed as a form of stereolithography [214]. In conventional stereolithography, thin layers of photoresist are irradiated by ultraviolet (UV) light, depending on the specific geometry splitting it into subsequent layers and utilizing projecting miromirror devices [418], converting a monomer material into a polymer. Utilizing this technique, 2D lines of 1 μm thickness can be fabricated [253]. However, the depth resolution of this technique is still restricted to several micrometers due to the layer-by-layer nature of the technique. To overcome the limitations of single photon polymerization (1PP), two photon-absorption polymerization (2PP) was employed for producing 3D microstructures [299, 252]. An alternative name for the commercialized apparatuses uti-

lizing 2PP is Direct Laser Writing (DLW). The physical mechanism of 2PP is delineated in Fig. 2.1(A-B).During this procedure, a photoresist absorbs two near-infrared photons concurrently in a single quantum event. The coalesced energy of these photons must correspond to the UV region of the spectrum. The rate of two-photon absorption is proportional to the square of the light intensity, such that the near-infrared light is primarily absorbed only at the focal point within the photoresist. This quadratic intensity dependence enables to confine the writing to submicron dimensions, even beyond the diffraction limit of light as it will be discussed later. The above effect of the multiphoton polymerization provides the fabrication of 3D microstructures by scanning the laser focus inside a photoresist [99]. Fig. 2.1(C) juxtaposes the excitation regions in the case of 1PP and 2PP.

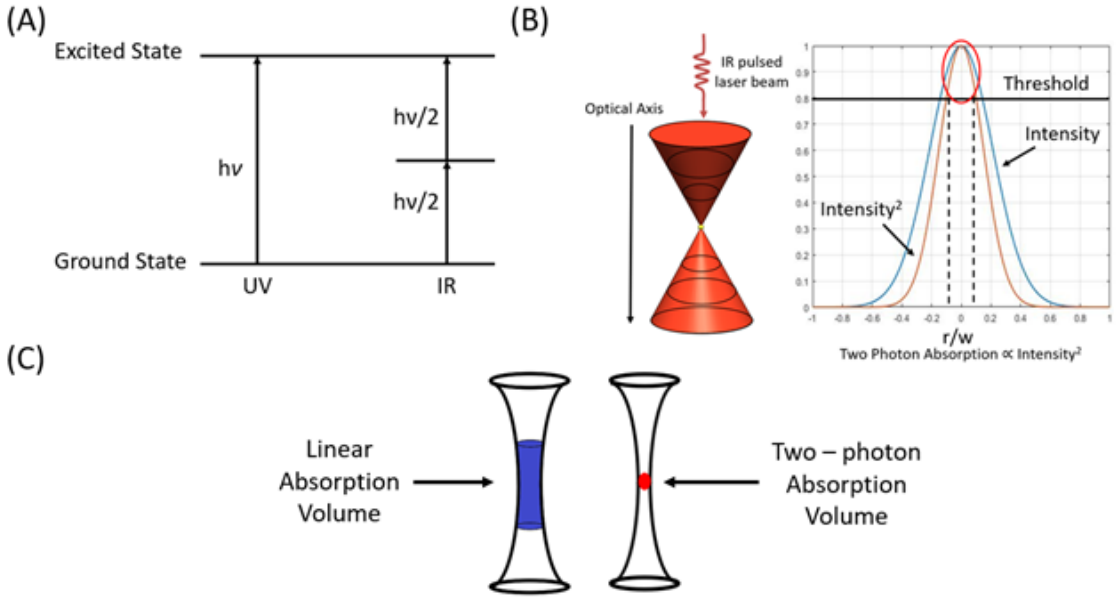

Figure 2.1: Fundamentals of multiphoton polymerization generated by a focused laser beam. (A) The excitation process for single photon and two photon absorption. (B) Comparison of the intensity and the squared intensity (which is proportional to the two-photon absorption, as a function of the beam radius. (C) Comparison of the polymerized volume for the case of the single photon absorption and the two – photon absorption.

The probability of 2PP is extremely low, as its cross section is approximately 31 orders of magnitude lower than the cross section of the single-photon process [99]. Hence, 2PP requires a substantial high density of photons to be effective, by spatially and temporally restraining the photons. This can be accomplished by coupling high numerical aperture objectives to ultra-short pulsed lasers such as titanium-sapphire lasers emitting in the near-IR region [66]. Approaching the focal point of the objective lens, the photon density will sharply increase, as it was depicted in Fig. 2.1. Therefore, the low probability of the 2PP

process will be automatically confined around this focal point in an area defined in literature as "voxel". If the sample is transparent to the IR radiation of the laser and absorptive to the UV irradiation, the voxel around the focal point will be excited, while the adjacent regions of the sample will remain transparent and unaffected by the incident radiation. A characteristic experimental setup for the 2PP is demonstrated in Fig. 2.2(A). The system includes a FemtoFiber pro NIR laser with a wavelength of 780 nm, pulse width of 100 fs, and repetition rate of 80 MHz. At this repetition rate and wavelength the desired localized polymerization can be achieved. The system includes a FemtoFiber pro NIR laser with a wavelength of 780 nm, pulse width of 100 fs, and repetition rate of 80 MHz. At this repetition rate and wavelength the desired localized polymerization can be achieved. The beam is focused by a 100× microscope objective lens (Plan-ApoChromat 100×/1.40 Oil M27, Zeiss). By tightly focusing the laser in the photosensitive material, the material was locally polymerized. The stage is then translated so that the focused beam can "write" inside the material and fabricate the desired 3D structure. In this fabrication method, the beams of the structure were designed as lines in a 3D space. This geometry was then converted to a g-code, whose coordinates defined the edges of the structure to be fabricated [402, 393]. Utilizing this setup, highly complex architected geometries can be fabricated in microscale, as the ones presented in Fig. 2.2(B). For the case of 1PP, the same setup can be utilized, but instead of a Ti:sapphire laser, a UV wavelength laser must be utilized, such as an Argon Ion (Ar+) laser with a wavelength of 365 nm.

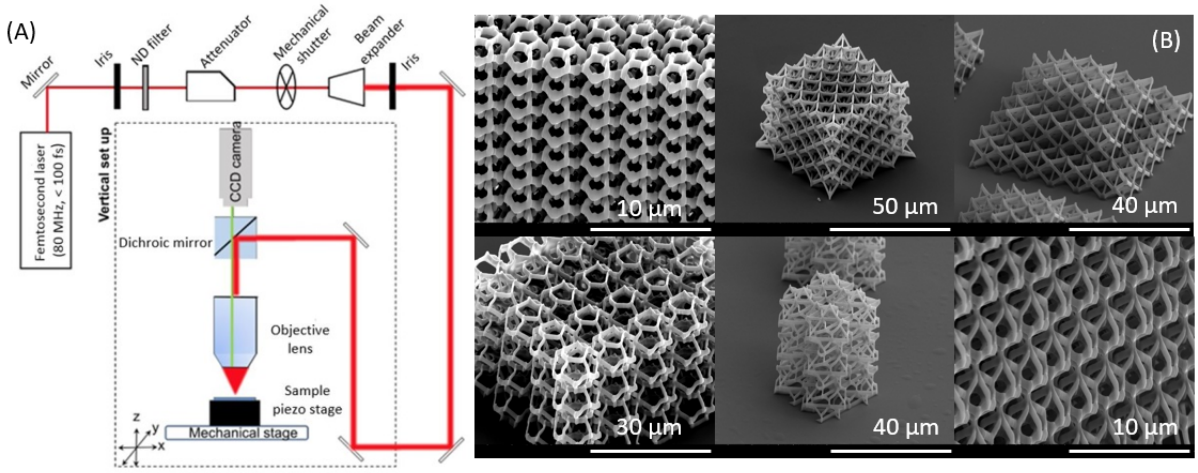

Figure 2.2: (A) Schematic of the 2PP experimental setup. (B) Fabricated structures by 2PP.

Even though these polymerization techniques enable the fabrication in the regime of a few micrometers, they are still substantially inadequate to reach the nm length scale. To overcome this barrier, there are two main techniques. One is the surpassing of Abbe's diffrac-

tion limit with multi-wavelength mechanisms that will be addressed later. The other one is to tailor the photochemistry of the photoresist to mitigate the effective area of the voxels via the so-called Diffusion-Assisted High-Resolution Direct Femtosecond Laser Writing [343]. This method utilizes an inhibiting molecule, such as a quencher, into the photoresist [304]. Regarding the photochemical procedure during the 2PP, the photoresist consists of three main components, (1) the monomer chains that will crosslink creating the polymer hybrid, (2) the ceramic core that provides stability to the crosslinked network and (3) the photoinitiator that initiates the photon excitation process. As the photoinitiator becomes excited, it starts producing radicals that "attack" the monomer molecules to create the macroradicals of the polymer. Finally, the radicals are terminated to provide the final polymer. Radical termination can also be substantiated by oxygen and various other molecules into the system, defined as scavengers. The quenching is competitive with the photopolymerization and is initially detrimental to the process. Nevertheless, in multiphoton photopolymerization, it can be utilized to fabricate structures of very high resolution. This can be accomplished by modulating the light intensity at the focal point such that the produced radicals, whose spatial concentration is proportional to the square of the light intensity, supersede the quenchers and initiate polymerization in the region where the exposure energy is larger than the upper threshold. This is determined by the nexus between a mobile quenching molecule and a slow laser scanning speed, enabling the diffusion of the quencher in the polymerized area, the depletion of the radicals, and the regeneration of the consumed quencher. This technique has enabled the fabrication of woodpile structures, used as photonic crystals, with approximately 100 nm thickness, illustrated in Fig. 2.3 [343]. However, there are also other means to improve the resolution of these laser printing processes, by introducing multiple laser sources hitting the sample and will be presented next.

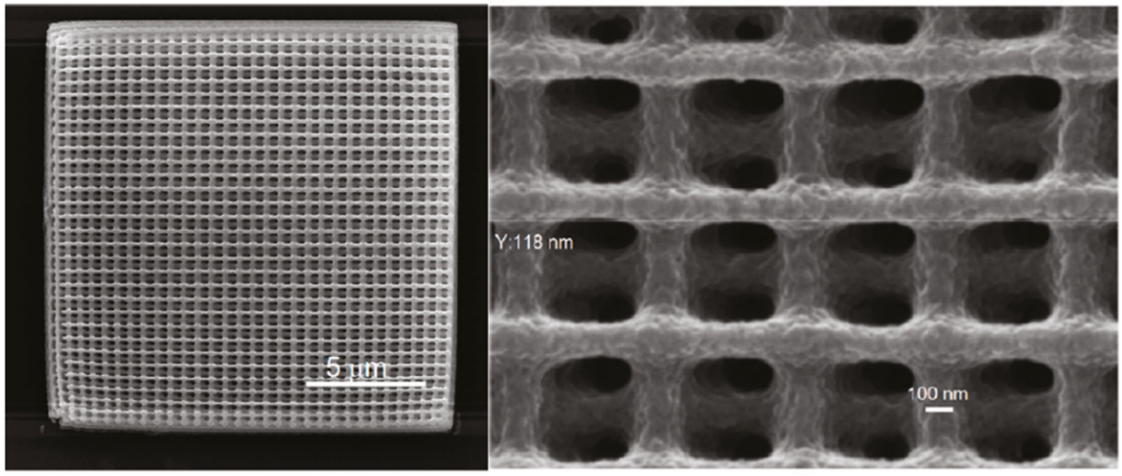

Figure 2.3: 3D woodpile structure with 600 nm interlayer periodicity fabricated utilizing Diffusion-Assisted High-Resolution Direct Femtosecond Laser Writing [343].

Stimulated Emission Depletion for multiphoton lithography (STED)

One of the major reasons that limit the resolution of the fabrication process is the diffraction limit. Diffraction prohibits light to be focused to a volume smaller than approximately one and a half of the light wavelength along the lateral directions and three times larger along the optical axis (around 200 nm and 600 nm, for the case of visible light respectively) based on the following equations [406].

$$Abbe\ Resolution_{x,y} = \frac{\lambda}{2NA} \tag{2.1}$$

$$Abbe\ Resolution_{z} = \frac{\lambda}{NA^2} \tag{2.2}$$

Where λ is the wavelength of the source and NA is the numerical aperture of the lens. STED microscopy surpasses this diffraction limit by reversibly depleting fluorophores at predetermined locations of the diffraction-limited excitation regions [359]. Therefore, only the nondepleted fluorophores in the complementary areas emit light, providing the threshold for features indistinguishable by the diffraction limit to be separated. In the most typical STED microscopy implementation, the fluorescent confinement is accomplished by aligning the Gaussian excitation beam of a scanning microscope with a second beam, defined as the STED beam, whose wavelength is tailored to de-excite fluorophores by stimulated emission and is modulated in phase and polarization to form a doughnut-shaped focal intensity distribution without any intensity at the center. Even though the distribution of the STED beam focal intensity is also limited by Abbe's criterion, high intensities saturate the stimulated emission transition and preserve the fluorophores in the ground state, except those positioned in a region with no intensity, whose size reaches sub diffraction values and diminishes with the rise of the STED beam intensity. Theoretically, the resolution of STED microscopy can reach the size of a molecule, which is the absolute limit of a fluorescent microscope. In practice, it is hindered by the signal-to-noise ratio. To obtain the desired resolution enhancement, it is imperative to synergistically generate sub diffraction fluorescent regions across the whole specimen (according to the Nyquist sampling condition) and to attain, from all these regions, ample fluorescent photons to facilitate an adequate signal-to-noise ratio. With the profound advance in STED microscopy, the direct consequence was to transfer this technology to a field that required high resolution as well, that of microstereolithography [118]. For the coupled multiphoton polymerization and STED the schematic of the electron states and how the physical mechanism is manifested is delineated in Figure 2.4.

Two photons mediate the optical transition from the ground state into an electronically excited state. Rapid non-radiative relaxation occurs afterwards. Under normal circumstances, the "virtual" intermediate state should be occupied for a very short period of time such that the photo-induced excitation is efficiently transcended into a chemical reaction resulting in cross-linking. Spontaneous emission of light (fluorescence) from the intermediate

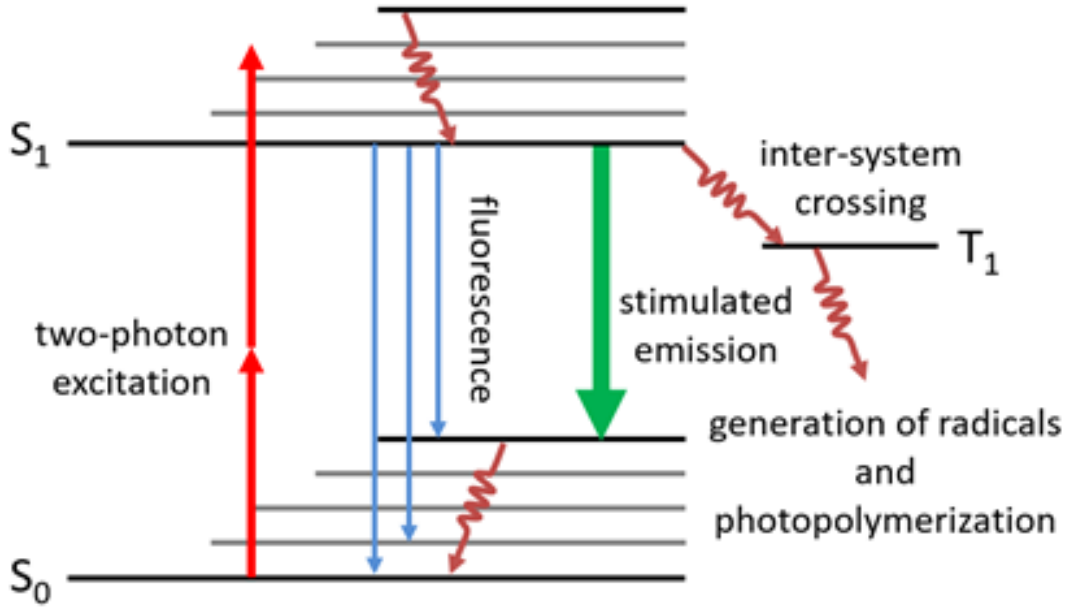

Figure 2.4: Schematic Jablonski diagram of a photoinitiator molecule and illustration of the relevant optical transitions and processes.

S1 state is not desired, as the fluorescence quantum efficiency is low and the inter-system crossing efficiency is substantial. Nevertheless, without spontaneous emission, the required stimulated emission would not be efficient. In particular, the STED rate is unlikely to overcome the inter-system crossing rate. Efficient stimulated emission demands an electric-dipole-allowed optical S0 –S1 transition. A large oscillation strength requires a sufficient spatial overlap of the involved orbitals. Hence, a $\pi - \pi^*$ transition is preferred instead of a $n - \pi^*$ transition. In addition, the inter-system crossing rate must not be too large. The setup required to perform coupled MPL with STED is depicted in Figure 2.5 [427].

The two-photon polymerization initiator is excited with 780 nm ultra-short laser pulses and are locally depleted in the outer volume of the voxel with a depletion beam (532 nm, continuous wave). The depletion beam is shaped into a donut shape function for 2D structuring utilizing a 2π spiral phase mask and a $\frac{\lambda}{4}$ wave plate [427]. For 3D fabrication, an annular phase mask combined with a $\frac{\lambda}{4}$ wave plate can be used to create a bottle beam shape function. Both beams have to be focused through an oil immersion objective lens, with the same NA as the photoresist. Excitation and depletion powers are measured in front of the objective lens. Nevertheless, even though STED seems a promising technique to improve the resolution of the fabricated geometries, understanding and optimizing of the photochemistry

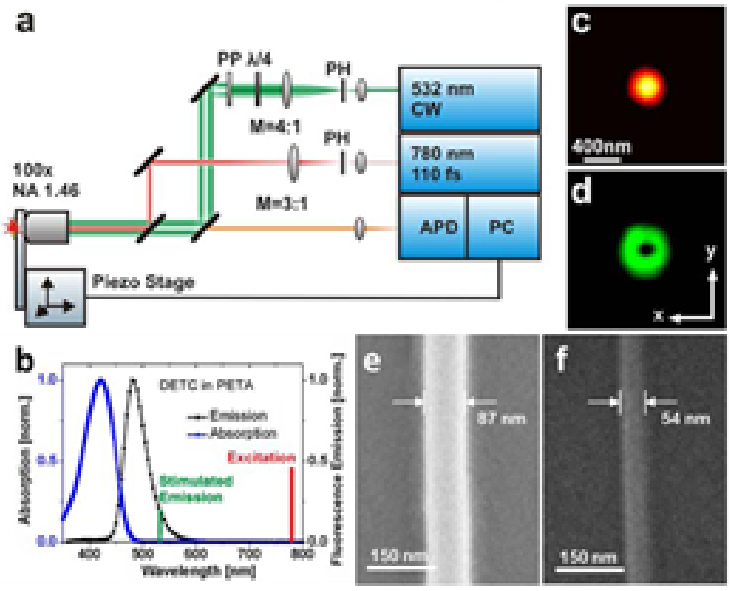

Figure 2.5: a) Scheme of a characteristic 2PP/STED lithography setup. Red depicts the excitation beam for 2PP (780 nm, 100 fs pulse duration) and green depicts the optional depletion beam (532 nm continuous wave CW). The depletion beam is shaped into a donut using a 2π spiral phase plate (PP) or into a 3D STED beam using an annular phase plate rotating the center by π, b) Measured spectra of the photoinitiator used, c,d) measured cross sections at the focal plane of the 2PP and the depletion beams, respectively, upon back-reflection from a 50 nm gold nanoparticle. e) polymerized line by 2PP, f) polymerized line by STED+2PP manifesting the higher resolution. [427]

is likely the key factor for further resolution improvement. Under this scope, it can be stated that photochemistry and polymer-chemistry are limiting the attainable resolution in STED-DLW and not the optics of the system. This is evidenced by the fact that the field has not advanced in the fabrication of highly complex structures such as plasmonic or mechanical metamaterials. The main challenge lies on creating a material that utilizes the monomer, the ceramic the photoinitiator (for multiphoton absorption) and for STED the coinitiator (for depletion) to create a stable and rigid hybrid material. Therefore, this is the objective that must be accomplished for the STED MPL to be utilized efficiently in the fabrication procedure.

Laser-Induced Forward Transfer (LIFT)

The laser-induced forward transfer (LIFT) technique can be utilized for direct writing for a vast range of materials with a resolution that can reach 300 nm [19]. It has gained the interest

of the research community due to its ability to pattern materials in ambient conditions onto any substrate [302]. Typical materials that can be deposited include metals, oxides, superconductors, DNA, proteins, fungal spores and polycrystalline Si [315]. To employ LIFT, a pulsed laser beam is focused on a thin film of the donor material (i.e. the material that will be deposited) through its supporting substrate. The substrate must be transparent to the laser irradiation. Because of the laser pulse, a miniscule portion of the donor material is ejected towards the receiving substrate. However, this mechanism occurs for thicker films and high laser fluence; for thin films and fluence above the threshold for material transfer, LIFT can occur by melting through of the source film [19, 302, 315]. The process is illustrated in Fig. 2.6. Through this process a voxel is formed on the substrate. Repeating this process for multiple voxels can lead to the fabrication of a patterned surface [451]. For the case of depositing liquids, the deposition process begins with the absorption of the laser irradiation that initiates a swift vaporization of the absorbing agent. Hence, a vapor bubble is generated, expanding against the surrounding fluid. The dynamic response of both bubble and displaced fluid has been unravelled utilizing time-resolved imaging for different fluids and irradiation conditions [315]. The extreme pressure inside the bubble promotes its rapid propagation during the first microseconds after the laser pulse. Simultaneously with the expansion of the bubble, a protrusion is formed in the fluid layer as the vapor pressure pushes the liquid surrounding the bubble. When the bubble starts collapsing, it creates a thin needle-like jet. During the bubble collapse, the jet continues advancing in the axial direction towards the receiving substrate. The contact of the jet, with the receiving substrate results in the deposition of the droplet, even for high aspect ratios (width of a few micrometres over a length of few millimeters).

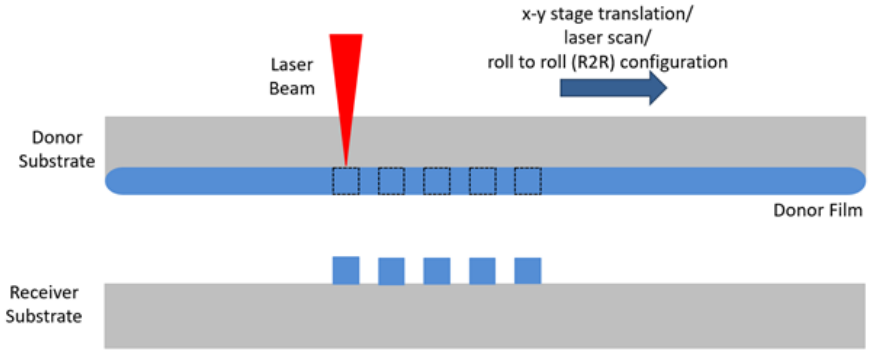

Figure 2.6: The principle of operation of the LIFT technique for solid films.

LIFT has been conducted utilizing short pulses (ns) or ultrashort pulses (ps or fs). Nevertheless, there are some LIFT variants using long pulses (from μs to cw) [282]. Shorter pulses are preferred as the thermal effects are diminished and smaller voxels can be obtained [19]. The wavelength is selected based on the intermediate layer or the transferred material but the most common is UV. The Pulse energy and the laser beam size are the key parameters

for LIFT to be efficient. However, laser fluence is actually another major factor [68]. Typical deposited droplets are shown in Fig. 2.7 using a Ti:sapphire laser (800 nm, 110 fs) [19]. The center of the 4 mm diameter full width at half maximum Gaussian laser output illuminated a 120 μm diameter circular aperture to give an approximately uniform profile. The aperture was transferred onto the carrier-film interface using a 100× microscope objective lens with NA equal to 0.8, resulting in a spot diameter of approximately 4 μm at the film surface.

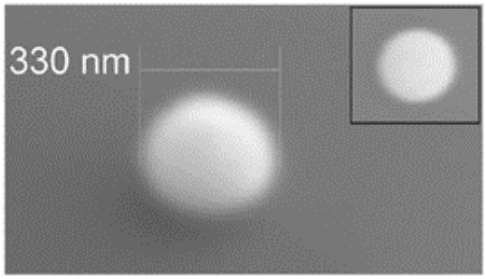

Figure 2.7: SEM image of a deposit produced using fluence equal to 325 mJ/cm^2. The image was taken at an angle of 45^o to the receiver surface normal. Inset: same deposit from directly above [19].

Regarding the alignment of the donor and the receiver, a minimum gap between the donor film and the receiving substrate must be preserved to avoid any contact between them, which might cause the volatile massive transfer of fluid. Since jets generated in LIFT are stable during several millimeters of travel, transfer in the jetting regime allows some tolerance between the donor film and the receiver substrate. Thus, it can vary from a few tens of micrometers up to a few millimetres. This degree of tolerance is beneficial taking into account the potential industrial implementation of the technique in a production line. However, in the case of small gaps and under certain operating conditions, the jet when impacting the receiving substrate can be faster compared to large gaps, thus leading to the modification of the contact angle [42, 337], resulting in different droplet diameters. In that case, even though the deposition mechanism is manifested differently, the transferred volume is like that for larger gaps. However, the final diameter of the droplets is different due to the different contact angles. Consequently, the gap between the donor and the receiver can affect the wetting of the fluid on the receiving surface [42]. There are many instantiations of the LIFT mechanism, with the main difference laying on how the laser power is absorbed and converted into the mechanical energy required for ejection [282]. Characteristic examples include the (1) indirect interaction – LIFT [205], (2) The Matrix – Assisted Pulsed Laser Evaporation – Direct Write (MAPLE-DW) [314], (3) the Laser Molecular Implantation [151], (4) the Long – Pulsed Lift (LP-LIFT) [201] and (5) the Blast Lift [202]. Indirect interaction – LIFT involves the implementation of an intermediate layer, which absorbs the laser radiation and protects the donor material from direct laser irradiation. This obstructs photolytic and

pyrolytic damage to the transferred material and enables the use of sensitive materials as receiver substrates. MAPLE-DW is an alternative process to the standard Pulsed Laser Deposition (PLD), in which the material to be deposited is dissolved into a solvent matrix material with a lower evaporation point. The laser pulse evaporates the matrix and the material is released with ample energy to be deposited in the receiver substrate without an egregious result, allowing the deposition of complex undamaged molecules. In the Laser Molecular Implantation, the molecules are deposited into a thin polymer film applied to a glass substrate. For this case, the receiver substrate, which can be another polymer film, and the donor are kept in contact. The laser pulse heats the polymer, expanding it, and subsequently increasing the contact between the films. The molecules are then transferred and deposited into the receiver film through diffusion process. As both the donor and the receiver are polymers, backward-transfer is also possible. LP-LIFT conducted using laser pulses in the order of μs or longer. The LP-LIFT experimental apparatus is similar to the common LIFT, but the donor and the receiver are preserved in close contact. The donor is heated, resulting in its thermal expansion overcoming the small gap. The donor is annealed to the acceptor without melting and is bounded to the receiver. The physical mechanism of this process is different from the conventional LIFT. Ballistic Laser-Assisted Solid Transfer (BLAST) is utilized for solid materials. With multiple, subthreshold energy femtosecond laser pulses, the adhesion of the solid film to the transparent substrate is reduced until a solid block of material is ejected towards the receiver substrate. As BLAST-LIFT is functional for low fluences, it can be utilized to deposit more delicate materials than with the other variations of LIFT. The major advantage of LIFT as a laser printing technique is the potential of depositing a vast range of materials, both inorganic and organic, solid or liquid [316], rendering LIFT a versatile tool to be employed in various crucial fields. For example, time-resolved imaging of LFT of copper nanoparticle (NP) inks in conjunction with computational imaging revealed the dynamics of the jetting process, whose understanding is crucial towards optimizing the deposition process [199]. First, a potential application is the electronics industry, to print the circuit itself and various active and passive elements such as diodes, transistors and sensors. Second, LIFT can be utilized as an additive manufacturing technique for microfabrication of arbitrary 3D structures. Finally, the third major area of LIFT is the bioprinting [282, 54].

Section Conclusions

Direct Laser Writing processes have rapidly expanded. The extremely high resolution of new materials that can be incorporated has mediated into industrial applications, paving the way to design and fabricate structures for a plethora of applications. Characteristic examples are electromagnetic, acoustical and mechanical metamaterial, scaffolds for tissue engineering and bioprinting. Even though this vast and imperative range of applications has advanced these techniques, there are still scientific challenges regarding the photochemistry of the utilized materials and the physical mechanism dictating these phenomena. Nevertheless, the utility and perpetual advance and research of these processes facilitate them as the

spearhead of additive manufacturing and laser printing. The next section will focus on the advances of architected materials from the perspective of the mechanical behavior, for structures fabricated by either direct laser writing or 3D and 4D printing, since they are also instrumental in the fabrication of architected materials.

2.3 Illuminating the Mechanical Metamaterials from the Lens of Mechanical Behavior

Beginning from the Fundamental Structures

The remarkable advance in the study the mechanical behavior of mechanical metamaterials was the result of the development in 3D printing technologies, mentioned in the previous section, and the interminable improvement in the employed models. The mechanical characterization of architected materials was radically advanced during 2010 with the research at Lawrence Livermore [466] and Caltech [264], rendering these institutions the epicenter of mechanical metamaterial research. However, the progenitor to this advancement was the work on the modeling and characterization on macrostructures of Prof Vikram Deshpande at University of Cambridge, Prof Stelios Kyriakides at the The University of Texas at Austin and Prof Nicolas Triantafyllidis from LMS, Ecole Polytechnique. While Deshpande's work primarily focused on the octet truss, Kyrakides' and Triantafyllidis' work was focused on Kelvin foams. Their work revealed a rather challenging field, providing a way for the future researchers to investigate it. Therefore, it would appropriate to present their findings before progressing to microscale structures and their characterization. Their results in printing, modeling and testing and scientific approach elicited the end of the doldrums, for many more groups to study these phenomena. Therefore, relevant publications of this and following period will also be provided. In this section it is important to distinguish that the mechanical behavior will be analyzed using beam or truss models. A purely mechanistic analysis from the perspective of continuum mechanics will be presented in the next section. While Triantafyllidis employed fundamental concepts from continuum mechanics, the major part of the results was edified by Bloch wave theory [326], which is more germane to acoustic metamaterials than mechanical metamaterials. Therefore, the primary questions about continuum mechanics will be addressed in the next section, while the main results of Bloch wave theory will be presented in the section.

Beginning with the octet truss structure, it was crucial to define how the assumed elastic field, and consequently the stiffness tensor can be evaluated. For this case, it is critical to determine the principal deformation mode of the structure. To accomplish this, Maxwell's criterion was employed [93]. More specifically, lattice geometries can be bifurcated into bending dominated and stretching dominated, depending on which is the dominant deformation mode of the members. To evaluate whether a structure is stretching dominated, the following equation must hold true:

$$b - 3j + 6 \geq 0 \tag{2.3}$$

where b is the number of the members and j is the number of the nodes. To quantify this criterion with a single numeric, the average connectivity Z is defined. Z is approximately equal to $2b/j$. If Z is greater or equal to 12, then the structure is stretching dominated. An innate feature that might be considered cause célèbre is that an array of periodic bending dominated elements may lead to a stretching dominating response at specific regions of the structure, which is an acute way to tailor the localized properties of the lattice. Bending dominated structures may sustain larger deformation, which can lead to densification as in the case of foams and candidate designs for energy absorption. Countervailing, stretching dominated structures aim to possess higher stiffness and strength. Which factor will be the most important for the design while forfeiting the other will depend on the application of the lattice. It must be noted that there have been attempts to unify both requirements [410, 7, 400], but they will be unveiled later. This understanding of the deformation mode can also lead to the assumed deformation field that can be utilised to obtain the effective stiffness tensor under different loading conditions [91]. As in the dingy designs almost 30 years earlier, the stiffness components of the octet truss are related to the relative density ρ_c. Interestingly, the maximum normalized stiffness of the lattice is proportional to the square of the relative density. Nevertheless, as it will be addressed later, the verisimilitude of this relation also depends on the fabrication method that is employed. Regarding the yielding of the structure, FEA simulations can provide projections of the yield surface for various loading directions. These curves can be provide a generalized formula for the yielding equation of the structure using Hill's theory of plasticity [167]. The yield surface possesses a rhomboid shape compared to the elliptical of the von Mises failure criterion. The yield strength of the structure is proportional to $\rho_c^{1.5}$. Nevertheless, collapse and subsequent failure is also relevant to buckling, which significantly diminishes the area of the failure envelope. Regarding this topic, it was haplessly still established that imperfections and defects diminish the failure surface and lead to egregious débâcle. Therefore, further research from the perspective of mechanical enhancement was considered ineffective. These remarks will perpetuate the quiescence of architected defects even more.

Conducting experiments on aluminum alloys revealed a small divergence between experiments and simulations. This must be attributed to the casting process that did not increase the nodal intersection of the beam members. But as it will be discussed later, the validity of the theoretical model is associated with the fabrication process and the resemblance of the fabricated specimen with the CAD file used in the simulations. Regardless, it was proven that the octet truss lattice possesses one order of magnitude higher stiffness and strength than metal foams for the same relative density, which is a remarkable improvement. Similar characterizations were later conducted on Ti–6Al–4V octet-truss lattice structures fabricated by water jet cutting [97]. This fabrication technique leads to significantly higher volume at the nodes, necessitating the modification of the model by adding higher order terms in the relative density. However, even for this case the power dependence on the Ashby charts

remained the same as before. It was also proven that the transition from linear buckling to yielding is dependant of the the thickness of the structure, a trait conferred by the mechanical performance of foams that was described before.

Regarding the mechanical performance of Kelvin foams that followed, the methodology was similar but with distinct improvements [130, 179, 178, 148, 129]. The investigation of the mechanisms of collapse and instability were systematically addressed by calculating the respective buckling modes of long chains of arrays. These modes will be defined as long wavelength instability modes and will also be discussed in the following chapters regarding interconnectivity. All of the phenomena lead to a plateau in the stress strain response due to the combined effect of collapse and contact. This response is also accommodated by shearing effects due to the anisotropy of the structure leading to tilted densification of the layers. Even though these effects were also observed in random foams, it was blatant that now these phenomena can be tailored by the localised arrangement of members in the unit cell. The improved models of the CAD files provided more precise calculations in the merging areas of the beam members. Hence, the effect of nodal intersection was found to have an abrupt influence on the relative density of the structure. This leads to consequent variations in the Ashby relations for strength and stiffness. This result is also amplified due to the amplification of the geometrical anisotropy of the unit cell. Regarding the instability that occurs, the analysis is related with the work of Triantafyllidis [352, 351, 135, 386]. This analysis related to scale effects and instabilities was the best utility of continuum mechanics that was related to architected structures up to this point and should still be considered relevant despite the proclivity of contemporary researchers to consider it hoary.

Specifically, in a lattice structure two instability mechanisms may occur. One is called global buckling instability, which occurs at wevelengths comparable to the length of the structure (thus the metonymy long wavelength buckling). However, nonuniformities in the lattice can lead to a secondary instability mode, defined as localized (short-wave) buckling instability. While these two mechanisms may be competing, transition from global instability to local instability may also occur [192]. While global buckling is related to collapse mechanism observed in structural members and is egregious for the structure, localized buckling can transmogrify the structure to possess burgeoning nonlinear properties, such as negative Poisson's ratio. Therefore, it hampers the development of uncontrollable catastrophic collapse. It must be noted that instabilities are conventionally addressed under the context of Euler Bucking. However, regarding localized instabilities, there are other buckling modes, namely alternating modes that are associated with the superior mechanical properties. For instance, in holey materials with pores shaped as circles the alternating buckling modes lead to elliptical shapes, enhancing both the structural mechanical performance [378] and the vibrational response [181].

In addition, several researchers also hunkered how to employ these localized instability patterns for tailored densification [158]. The basic building blocks that were analyzed were the square grid, the triangular grid and the regular hexagonal grid. The square grid possesses three distinct buckling modes, defined as swaying, non-swaying and longwave, whereas the triangular possesses two and the hexagonal possesses three, the uniaxial, biaxial and chiral.

Based on these modes, the instability surfaces can be constructed, illuminating when buckling will occur and multiaxial loading. It must be noted that for these results the beam model that was employed was the Euler-Bernoulli model, which is only valid for long and thin structural members. Moreover, all of this analysis can be addressed for 2D problems or sandwitch panels [189]. where the balance equations and the assumed deformation fields can be expediently obtained. However, it is extremely herculean to accomplish the same for 3D structures, especially including the effect of nodal intersection. The only 3D structure that has analytical expressions without the use of FEA tools is the cubic lattice [295], since it can be degraded to a symmetric 2D problem.

From the perspective of a mechanistic analysis, instability commences due to the loss of the ellipticity in the homogenized incremental equilibrium equations of the material [386]. To validate this, a potential function is defined, similar to the Airy stress function in linear elasticity [251]. Substituting this function into the compatibility equation can lead to a 4th order partial differential equation. The ellipticity of this equation varies with the stretch of the material, and at a specific stretch buckling will commence. To investigate the influence of global or localized instabilities, the Fourier transform is applied in the compatibility equation. Hence, the stretching can be calculated as a function of the frequency ω, for both long wavelengths ($\omega \to 0$) and short wavelengths ($\omega \to \infty$). While these results may tersely harbinger the commencement of buckling in 2D materials, an intriguing result was the commencement of buckling even without loss of ellipticity, depending on the constituent material employed (such as the Mooney-Rivlin for instance). These more advanced models can also be employed to provide the macrofailure surfaces of the structure. In addition, demonstrating remarkable engineering ingenuity, the effect of nonuniformities can be incorporated, requiring higher order terms in the macroscopic strain energy density of the model. However, these models did not advance any further than the cubic lattice and they were vaguely explored as onus probandi for the study of the Kelvin foam. Even though they constitute a lode of brimful design notions, the vast majority of the scientific community has abnegated these results, focusing exclusively on experimental validation that will be addressed next. Moreover, higher gradient models will not be employed for complex 3D structures, with only one exception that will be presented later.

The Riveting Reverberations in Nano/Microscale

The aforementioned analysis in microscale printing led to the design of microscale mechanical metamaterials. Specifically, there was an urgent demand and desire to fabricate structures using the resolution capabilities of MPL, but extricated by the limitations of the photopolymers, employing stronger and more versatile materials, such as ceramics. There are two main approaches for this. For the first one, ceramic materials are deposited onto the polymerized structure. A characteristic example is nickel-boron electroless deposition [271]. It has been proven that the layer thickness is apposite on the mechanical performance of the structure. Samples deposited with 10 nm layer thickness can demonstrate ductile performance, while layer thickness equal to 100 nm can lead to brittle behavior of the lattice geometry. Hence,

the deposition thickness can pervert the overall mechanical performance. Even though it might seem inscrutable, this phenomenon is associated with the critical layer thickness that dictates the buckling load of the structure. Precocious or early development of buckling can lead to contact of members to betide, with the fracture impedance in the internally photoresist geometry. This mechanism ekes out the fracture impedance, resembling ductile fracture. However, it was more appealing to elucidate strategies for an exclusively ceramic structure. An extremely useful technique that was utilized is plasma etching [264]. After the ceramic deposition, the specimen is treated with plasma and the photoresist evaporates, leaving only the ceramic coating. This enables the fabrication of 3D structures comprised of ceramic tubes of nanoscale thickness. It was experimentally proven that such structures can possess large deformations, despite the fact that the material is ceramic. This is a interesting result, considering the future implications of such microscale structures in bio mimicry and highly durable materials. Nevertheless, there is still no coherent explanation from a material science perspective that could provide a pragmatic analysis of this mechanism. While arguments about defect density in the ceramic tube have not provided a strong explanation, the manifestation of shell buckling, leading to large but reversible deformations, has been used to address the reversible and nonlinear nature of this phenomenon. This beleaguered challenge restricts the mechanism to purely structural mechanics. Regardless, this technique enables the fabrication of extremely complex geometrical features, such as woven geometries [278]. Woven geometries can deftly combine the high stiffness of a spring-like geometry, the postcontact of the turns and the densification in the domain of large deformations and the large wall deformations caused by shell buckling.

Another technique that was employed was pyrolysis [23, 128]. With pyrolysis the polymeric constituent of the photoresist gets evaporated, leaving only the ceramic part. One of the advantages of this technique is that it diminishes the feature size even more. It has been reported that MPL samples can have 80% volume reduction after the process [23]. These structures, albeit they are ultralight and forfeit their size, they can have extremely high strength. Despite the fact that this technique has been surfeited in lattice structures, it's true application is the design of plate lattices [73]. As it was addressed in the previous sections, plate structures are comprised of plate elements instead of struts or beams. The substantial decrease in porosity and pass-through voids in the structure leads to isotropic mechanical behavior in every direction. Nevertheless, this application has a major weakness that may render it unfeasible. While such structures have been fabricated in microscale, the experimental results do not prove this theoretical finding [377]. The primary reason for this is related to the ideas delineated in the description of MPL. The laser beam has to fabricate members in such an order that there is not overlapping of the beams with polymerized material. during the "growth" of the structure. For the case of plate structures, the laser beam polymerizes whole planes, while the material between two plates is not polymerized. To create an ultralight geometry with vacant space between the plate elements, holes need to be included in the structure to enable the non-polymerized material to be dissolved during the development process. However, in an ultralight plate, these voids diminish the overall effective stiffness of the element, leading to an anisotropic behavior. In addition, it has not been

shown whether the nonpolymerized material is actually removed, affecting the efficacy of this technique. However, there is a way to circumvent this beleaguered state. Combined with pyrolysis, isotropic ultra strong metamaterial structures have been successfully fabricated and tested. Hence, these structures can be lifted in the Ashby chart close to the theoretical upper bound. During the pyrolysis, the size of the pores also diminishes drastically, rendering them innocuous and perfunctory for the overall mechanical performance.

Another riveting area that has progressed indefatigably in microscale mechanical metamaterials is that of mechanical cloaking designs [46]. These structures enshrine the notion of invisibility in optics [389], but now the objective is to make a specific location of the body "unfeelable" (i.e. it does not deform locally). Therefore, the task of the engineer is to pastiche the principles of optics to mechanics. This has been accomplished using another category of metamaterials, the pentamode mechanical metamaterials [350]. These designs were proposed by Graeme Milton and Andrej Cherkaev in 1995 [274] as a way to design 4th order stiffness tensors with tailored properties, but were first fabricated in 2012 [197]. They have a bulk modulus close to infinity, but the shear modulus is approximately zero. Therefore, while they can deform due to shear, it is extremely hard to compress them. In this way, they can posses zero deformation while the rest of the structure away from the pentamode geometry has a specific deformation field, rendering them "invisible" from the perspective of deformation. Being cognizant of this riveting property, the primary impetus to design such structures is protection from mechanical waves [122, 109]. A variation of this design has been applied for 2D structures by putting elements of controlled stiffness around the location that needs to have zero deformation [305, 464]. This concept has also been employed for wave mechanics to isolate a specific region from the effect of the wave, but has not been implemented in lattice metamaterials yet.

Moreover, another class of designs that has been studied is that of nanolabyrinth structures [322, 465]. These structures are comprised of triply periodic minimal surfaces, first introduced by Gauss in *Theorema Egregium* [328], published in 1827. These surfaces possess the symmetries of a crystallographic group. The most rudimentary design is the Schwarz P ("Primitive") [259], which in algebraic form is given by the following formula:

$$cos(x) + cos(y) + cos(z) = 0 \tag{2.4}$$

Other characteristic examples are the Schwarz D ("Diamond"):

$$sin(x)sin(y)sin(z)+sin(x)cos(y)cos(z)+cos(x)sin(y)cos(z)+cos(x)cos(y)sin(z) = 0 \tag{2.5}$$

or the Schwarz G ("Gyroid"):

$$cos(x)sin(y) + cos(y) + sin(z) + cos(z)sin(x) = 0 \tag{2.6}$$

They have been observed as biological membranes, as block copolymers, and equipotential surfaces in crystals. They locally minimize the surface area for a given boundary such that

the mean curvature at each point on the surface is zero. These surfaces have fascinating and distinctive geometrical characteristics, for instance, a minimal surface is smooth in nature, has no sharp edges or corners, and splits the space into two or more nonintersecting, intertwined, and infinite domains that can be repeated periodically in three perpendicular directions. In comparison to the lattice geometries, the smooth surfaces mitigate stress concentration and hinder catastrophic collapse in the structure [208]. In addition, they have been employed to tailor the anisotropic behavior of the structure, rendering them compliant in specific directions and extremely stiff at others [322]. This feature, combined with the shift towards the upper bound of the Ashby charts, has rendered them feasible candidates for bioimplants and ultralight structures. They also possess interesting nonlinear properties. Since there are comprised of shell elements they can easily buckle in the elastic domain, capable to posses large deformations that are reversible. While this response is related to shell buckling similar to a deformation sustained by a piece of paper, the inherent complexity of this structures has not allowed for further investigation of the mechanics from an analytical perspective. However, they constitute better candidates compared to nanotubes since they encompass higher reversibility during the buckling deformation.

At this point it is important to exude a category of structures that resembles architected materials, which is block copolymers [160]. Block copolymers comprise of two or more homopolymer subunits linked by covalent bonds. The union of the homopolymer subunits may require an intermediate non-repeating subunit, known as a junction block. By merging the block copolymer into architected lattice materials, complex nanoscale features, imbricating with each other, can be realized [66]. These features have complex morphology, spanning from membrane like honeycombs to nanolabyrinth spirals inside the embrasures of the structure. While their utility in the mechanical performance has not been investigated, it can be averred that such features could provide controlled post contact and energy dissipation through the contact of the features due to the occupation of the sample's lacunae. In addition, these features are purely impromptu. Therefore, it has been demurred which is the best approach to tailored such designs and control their shapes experimentally. It must be noted though that such attempts have been successfully conducted on a theoretical framework [162].

Another topic of interest is the effect of crack propagation in the lattice structures [381]. Since the structures are comprised of beam members, a precise continuum model cannot be employed to quantify measures such us the stress intensity factor or the plastic zone size. To accomplish this, a continuum model needs to be devised considering that the feature size of the beam members is significantly smaller than the size of the specimen or the crack itself. Some initial attempts for such models have been presented [279, 255, 249], with the main focus of this work being on the ways to impede crack propagation. To accomplish this, the usual technique is to use beam members of different materials or thickness or include voids in the structure. When the crack encounters these features it changes direction to follow a path that requires less energy for the beam members to break. However, there is still no general rule for the ways to universally apply these strategies, as most of them depend on the employed materials, the 3D printing process and the specific types of unit cells used.

Despite the fact that all of these results have interlarded the field of mechanical metamaterials and most of the research community is investigating on this domain, the complexity of these structures has limited their analysis in the elastic domain and only experimental observation of the nonlinear one. Moreover, most of these designs are inimitable, affecting the paucity of novel designs. However, there are specific types of structures that possess nonlinear behavior and have been studied analytically using continuum mechanics. The next section will present these endeavors.

2.4 The Mechanics of Mechanical Metamaterials

Despite the remarkable advances in micro/nanoscale mechanical behavior or metamaterials, the study of mechanics has been primarily focused in macroscale structures. More specifically, the requirement for a constitutive model that describes the mechanical performance of the structure as a continuum must be addressed. To accomplish this, it is desired to obtain a strain energy function W that can be employed to calculate the total potential energy I using a variational setting:

$$I[\bar{\phi}] = \int_{\Omega} W(\bar{\phi}, \bar{F})\, dV - \int_{\vartheta\Omega_N} \bar{T} \cdot \bar{\phi}\, dS \tag{2.7}$$

where $\bar{\phi}$ is the map from the initial configuration to the deformed structure, $\bar{T}$ are the tractions on the boundary and $\bar{F}$ is the deformation gradient:

$$\bar{F} = Grad(\bar{\phi}) \tag{2.8}$$

and the stress field can be calculated by:

$$\bar{P} = \frac{\partial W}{\partial \bar{F}} \tag{2.9}$$

For the definition of the constitutive model, it is crucial to obtain the map $\bar{\phi}$. As it has been reported [145], $\bar{\phi}$ can be calculated by the average displacement of all the n nodes in the structure, defined as:

$$\langle x \rangle = \frac{1}{n} \sum_{a-1}^{n} x_a = \bar{\phi} \tag{2.10}$$

Thus, the deformation gradient can be calculated by:

$$F = \sum_{a-1}^{n} x_a \otimes X_a (\sum_{a-1}^{n} X_a \otimes X_a)^{-1} \tag{2.11}$$

where X is the coordinate of node a in the initial configuration.

By applying the variational principle on eqn 2.7 the minimum of the strain energy density W can be obtained. It must be noted that such an expression will describe the mechanical behavior in the linear elastic domain. The components of the elastic tensor $\mathbb{C}$ can be calculated by the following equation:

$$\mathbb{C}_{ijkl} = \frac{\partial^2 W}{\partial \varepsilon_{ij} \varepsilon_{kl}} \tag{2.12}$$

Comparison of this model with the conventional FEA methods showed close matching between the two methods, validating it's feasibility. The inherent challenge of this approach is to obtain the strain energy W for every different type of unit cells. Taking into account the myriads of combinations for even the slightest alterations on the geometrical parameters, this can become extremely strenuous.

In the study of dynamic phenomena, another method has been proposed which is relevant to phonon vibrations [210]. Specifically, the lattice structure is modelled as a system of springs and masses. Therefore, the total kinetic and potential energy of the lattice can be calculated and through them the effective strain energy density of the system. To obtain a model that can depict the mechanical behavior, the constitutive parameters that are related to the stiffness of the springs can be calculated by curve fitting the simulations with the experimental results. This approach is convenient with compliant metamaterials or mechanisms. However, it possesses the same incapacities as the previous method.

In macroscale, it has been shown that relevant structures can be modelled with a second gradient continuum, rendering the strain energy a function of the second gradient of the displacement [364, 443]. In the strain-gradient theory of linear elasticity, the constitutive law gives the symmetric Cauchy stress tensor σ and the hyper-stress (double stress) tensor σ^s. Apart for the strain tensor ε, the stress tensors also depend on the second gradient of the displacement field, tensor K, which is equal to $grad(grad(u))$, where u is the displacement field. Hence, the stress fields are given by the following formulae [26]:

$$\sigma_{ij} = \mathbb{C}_{ijlm} \epsilon_{lm} + M_{ijlmn} K_{lmn} \tag{2.13}$$

$$\sigma^s_{ij} = M_{ijklm} \epsilon_{lm} + D_{ijklmn} K_{lmn} \tag{2.14}$$

where D_{ijklmn} is the sixth order elastic tensor and M_{ijlmn} the fifth-order coupling tensor between the first and second order elasticity.

The total energy of the system is given by the following equation:

$$U_{strain-gradient} = \frac{V}{2} [\epsilon_{ij} \mathbb{C}_{ijkl} \epsilon_{kl} + K_{ijk} D_{ijklmn} K_{lmn}] \tag{2.15}$$

where V is the material volume. This problem is significantly more challenging that first gradient elasticity since the are many more elastic components that must be calculated.

From a theoretical standpoint, this sublime result reveals that the ideas initiated by different mechanical models regarding higher gradient elasticity since the late 19th century

are conceivable and realizable [134] with advanced additive manufacturing fabrication techniques. Accordingly, different higher gradient models have been developed to investigate the mechanical behavior of pantographs [86]. Furthermore, simple first gradient models (i.e. models that the strain energy is only dependent on the first gradient of displacement) cannot depict the mechanical response of the material, since second gradient elasticity becomes more predominant in materials with a specific tactical ordonnance of "fiber" constituents. Hence, the nonlinear mechanical response of the pantograph has been conveyed even when the employed 3D printing materials are highly brittle. Thus, the pantographic structures are compelling due to the fact that they constitute a synthesis for second gradient 2D continua. To attain the required macroscopic deformation energy, a specific rescaling of micro-stiffnesses is required. Therefore, there are constraints on the feasible variations for obtain any desired macro-behavior. While large elongations in the elastic regime have been explored [85], optimization is crucial to control the range of elastic deformations under specific imposed constraints. To accommodate this, optimization procedures have been employed in the context of pantographic micro-structures, showing that the geometry of the considered structure can be optimized using as control parameters some of the sizes of the constituent elements [94]. To design microstructures realized by additive manufacturing, the construction specifications of involved structural members have to be determined. In particular, it is critical to define the elastic pivots having small torsional stiffness. To accomplish this, an expedient procedure of structural optimization would be the use of beams with variable thickness with an alternation of very stiff parts and very compliant ones [405]. The softest parts of the beams can be regarded as elastic hinges, and design schemes like those can be efficiently implemented with meagre computational cost. In addition, it has been demonstrated that they also incur more complex responses, such as the Poynting effect, out-of-plane or 3D buckling modes and coupling deformation modes [144]. To comprehend this behavior, a panoply of other analytical [106] and numerical approaches has been proposed, such as the Hencky-type discrete model or the nonlinear Euler-Bernouilli beam modelling [10]. These models have also been employed to ameliorate the inordinate computational cost of the FEA simulations that is required to solve the various boundary value problems substantiated in these structures. Consequently, these computational tools, embracing higher order terms, have successfully diminished the computational cost that is needed to solve complex structural problems even beyond pantographic structures. This extensive investigation of the mechanical behavior of pantographic structures has rendered them a celebrated paradigm of designed, modelled and experimentally validated hyperelastic architected geometries. Hence, their intriguing behavior should also beget a viable candidate for large deformations in microscale.

2.5 Aspects of Structural Optimization in Mechanical Metamaterials

The aforementioned advances inevitably elicited the desire to optimize the designed structures. The basic techniques that have been unremittingly employed are topology optimization, genetic algorithms, neural networks and machine learning. During the last decade there is great zeal to employ these optimization tools.

Regarding topology optimization, this is a gradient based method. The design variables of this problem are the material density of the structure at specific locations. The initial structure is a square block of bulk material and steadily material is "removed" until the desired structure is attained [431]. For the case of bistable structures, the cost function is the energy dissipation during the commencement of snap through buckling [59]. In other cases the elastic behavior is tailored through the strain energy density before plasticity evinces [467]. Another case is the design of auxetic structures [428] or multiobjective optimization for auxeticity and thermal expansion [416]. Since it is a gradient based, the partial derivatives of the cost function with respect to the design variables need to be calculated and through iterations reach 0. This technique has been primarily employed for 2D structures, but there are also examples of 3D symmetric problems [57]. A major constraint on published research using topology optimization is the scarcity of results regarding nonlinear behavior. The reason for this is that there is not explicit formula for the cost function to calculate the derivatives. In addition, it is computationally expensive to solve problems that are not symmetric or solve for problems that are not comprised of single unit cells. Finally, the requirement for the calculation of derivatives restricts the design space to problems which exclusively have continuous quantitative variable.

Another optimization technique is genetic algorithms. This technique requires a sample of initial data and through selection, crossover and mutation, it can explore the design space and find the optimum. This technique has been explored for 3D structures to optimize quantities such as the stiffness [363], the stress field during large deformations [414] and even wave propagation insulation [430]. The advantage of genetic algorithms is that they can remedy any kind of design variable. The major challenge is the extremely high computational cost, requiring thousands of data. In addition, genetic algorithms cannot reassure whether the global optimum has been reached or whether the design space region that is highlighted is not a local optimum region. Therefore, without any insight or premonition for the global optimum, the validity of a global optimum is vitiated.

However, the techniques that have been most thoroughly used are neural networks and machine learning. There techniques are predicated on the fact that the problem that needs to be resolved is a "black box" problem. This indicates that the cost function cannot be given by a closed expression and it can be obtained by either simulations or experiments. Both approaches use a network with different gains that aims to correlate the input and the output of the blackbox. Through training and validation this "curve fit" can be utilized to find the optimum of the design space. These techniques can also employ various types

of design variables and have been successfully employed for nonlinear deformation profiles [434], resilience to failure [44], bistability [236], auxeticity [237] merged with isotropy [64] and bandgaps [429]. These techniques have also been automated using topology optimization as the "black box", enabling the more efficient exploration of the design space [216]. Again, as in the previous case, these techniques require a large number of data points to find the optimum. Thus, they are primarily restricted to problems that the FEA simulations are extremely fast and can be automated through the optimization loop. Thus, they have not been employed for complex 3D problems with nonlinear properties and mixed types of design variables.

To resolve this issue, another Bayesian Optimization has started emerging as a potential solution. Bayesian optimization is a sequential design strategy for global optimization of black-box functions that does not assume any functional forms. It is usually employed to optimize expensive-to-evaluate functions. Thus far, it has been employed for single unit cell problems [149, 28] and has successfully resulted in optimized structures with nonlinear properties. Up to the point that this section was written, it has not been utilized for hybrid design variable or quantities discrete design variable. Under the general field of materials, some results have been published towards this goal [458], but nothing related to mechanical metamaterials. As it will be shown in the next chapters, this was one of the main topics of this thesis in collaboration with Haris M. Sheikh.

2.6 Applications of Mechanical Metamaterials in Tissue Engineering

Section Summary

The deeper comprehension of biological phenomena has led to the pursuit of designing and architecting complex biological systems. This has been incorporated through the advances in bioprinting of artificial organs and implants. In addition, tissue modeling has been employed to understand and prevent malfunctional and detrimental mechanisms that lead to fatal diseases. This section aims to provide a brief review on the design, modelling and characterization of conventional and architected structures employed in bioengineering. While these research domains are vast and provide a lot of space for innovation, they are steadily aligning to create "metamaterial" biological systems with superior properties. Even though several applications of mechanical metamaterials were addressed in the previous sections, this domain diverges from the conventional notions. Specifically, the interaction between cell and scaffold provide substantially more riveting results. Hence, their repercussions in tissue modeling and the study of cellular response render it a subject that should be illuminated separately.

Establishing the framework for meta-implants and architected tissue engineering

During the last decades there has been a significant progress in the design and modeling of artificial tissue engineering. That is a repercussion of our assiduity to deeper comprehend both the cellular and extracellular matrix behavior of such systems [230]. However, their mechanical response is evinced substantially differently for a variety of different mechanisms, such as shear stresses in blood vessels [320, 360] for blood flow or tensional and compressive forces in muscles1 for instance. In addition, the environment wherein the cells reside has an imperative role in their response [185].

Different external stimuli can affect the development and growth of the extracellular matrix and the cells in remarkably different ways [127, 409]. To this end, tissue modeling has been exponentially contemplated to provide an answer on how the combination of applied forces and the structural environment affects the cellular behavior [346]. Based on either fundamental mechanics [347] or in-vitro testing [172], the mechanical behavior of the cells can be illuminated depending on the applied external stimuli. Characteristic examples of such phenomena are the dynamic reorganization of the cytoskeleton [369], tension-dependent assembly of the actin and myosin into stress fibers, the cross-bridge cycling between the actin and myosin filaments [47] or even the triggering of specific internalization pathways, such as endocytosis and macropinocytosis [230].

Furthermore, from the perspective of the design variables that can be tailored, the properties of the extracellular matrix or the scaffold, such as the rigidity [96, 442] and configuration of the structural members [311] can control a plethora of different phenomena, such as stem cell intracellular signaling, membrane rearrangement, proliferation, differentiation, migration, actuation and cell adhesion [47, 462]. All of these properties can be efficiently monitored and controlled through either an extracellular matrix or a two-dimensional environment [127, 346, 29]. These various properties, that are critical for the operation of the cells as a constituent component or a part of a tissue or organoid, span a vast category of different cells. Characteristic examples that their response has been controlled are neurons [114, 203, 390], U87 cells [311, 171] (i.e. glioblastoma cell line) or even human induced pluripotent stem cell-derived cardiomyocytes (hiPSC-CMs) [245]. All of these different cells and their respective responses expand our understanding of mechanobiological phenomena from neurological to cardiac systems. While the mechanical response of such systems is comprised of mechanisms occurring in the highly nonlinear domain (e.g. viscoelasticity, plasticity and nonlinear elasticity) [230, 369], fundamental constitutive models have been proposed, effectively characterizing the manifested stress and displacement fields distribution of either the cell, the tissue or the scaffold [308, 92, 379].

These advances have also been accomplished by progress in multiphoton lithography (MPL) [343]. MPL enables the fabrication of complex architected matrices, imitating the features of the environment that the cells can interact with each other [245]. Moreover, it can be utilized to even emulate environments that will lead to malfunctional behaviors of the tissue, such as cardiomyopathy [413] and explicate them. The realization of these effects

has been steadily employed for the design of 3D tissues and organoids with the objective to design bioimplants [361]. While these architected organs will provide an avenue for implants and experimentation without living specimens, a new trend aims to create implants that surpass the conventional behavior of living organisms, scilicet meta-implants [449].

Employing properties found in architected materials [444], novel designs such as kirigami or origami [37] can be used as scaffolds to create implants or may lead to organs with unprecedented properties. More specifically, bistability through large deformations induced by buckling can lead to malleability and actuation of the structure [36]. In addition, auxeticity, leading to negative Poisson's ratio, provides resilience of the scaffold, impeding localized failure that inevitably leads to malfunction [250].

All of these aspects of tissue engineering at the design level of the extracellular matrix or the cellular response are steadily convening to provide novel techniques and methodologies in artificial organ design. In this brief review we will address the major aspects of these domains and explore the common links between them. First, we will address the modeling and design in tissue engineering, leading to efficient ways to tailor the cellular behavior at the constitutive level or with in-vitro testing. Next, we will address the progress in scaffold bioengineering, how it is utilized to imitate a healthy or a malfunctional environment and how it affects different cellular mechanisms. The control parameters that will be reported are both the cell types and the architected matrix architecture. Finally, we will explore how the design paradigm of metamaterials can be employed to improve and tailor the response of the organs. This review aims to illuminate the landscape of tissue engineering from the perspective of mechanical behavior and to set to framework for further advancement of these domains, some of which are still nascent.

Tissue Design and Modelling

In the literature there are two main approaches to depict the mechanical behavior of tissues and cells under the influence of the external environment. The first is through a bio-chemo-mechanical model that provides the constitutive relation between forces and displacements during the deformation of the cell [308, 92, 379]. The second requires a patterned surface, either 2D or 3D, that living cells can be attached, enabling the observation and characterization of their behavior [186]. While the first method is predicated on simple mechanical systems to elucidate whether the constitutive relation is consonant, the second method enables the depiction of much more complex phenomena, providing more information related to the physiological response of the cells or the developed tissue.

At this point it is instructive to provide further details regarding the mechanical response of the cells and the materials of their environment from a purely experimental perspective. The primary materials that were employed to study the impact of the extracellular matrix mechanics on the cellular function have been the hydrogels [372]. Nevertheless, in the hydrogel environment, the fibrous structural features and the compositionally constrained biological ligands are often interconnected, rendering the contribution to the cell behavior of each individual material property obscure to capture, such as the binding affinity for cells,

the mechanical stiffness, the fibrous arrangement, the porosity, and viscoelasticity [230]. Therefore, novel techniques were employed to investigate the effect of stiffness, degradability and viscoelasticity. The polyacrylamide (PAAm) gels and polydimethylsiloxane (PDMS) were utilized to study the mechanics of cell adhesion and migration [319]. The different surface chemistry of such gels enabled the control of the density of conjugated biological ligands. Regarding the stiffness of the substrate, it can be controlled by directly varying the ratio of polymer and crosslink solution, the curing temperature and the duration of curing. Since these gels possess linear elastic behavior, decoupling biomechanical signals from the substrate stiffness can be achieved. Utilizing this finding, it was observed that the matrix rigidity can regulate the cell morphology. Cells that adhere to stiff substrates demonstrate larger contact area and display higher proliferation in comparison to adhesion on softer substrates [108]. When the cell interacts with the extracellular matrix protein (fibronectin), a class of molecules called integrins engage with this protein, leading to morphological variations, enabling clustering and adhesion of integrins. Therefore, the cell is stable on the substrate, providing actin strands that are polymerized in the lamellipodia of the cell to migrate at the centre of the cell. This mechanism is called retrograde flow [230]. This mechanism causes an increasing tension that is transferred to the fibronectin fibres. When the cell is on soft substrates, this force will lead to displacement of the extracellular matrix, without any resilience. However, on stiff substrates, the extracellular matrix fibers will resist against the probing force, generating traction and resulting in stretching and unfolding of adaptor proteins, such as talin and vinculin located. This event triggers the formation and expansion of filament actin stress fibers that permeate through the cell. This phenomenon leads to a mechanism called durotaxis, a propensity of the cells to migrate from soft to stiffer substrates. Despite the insight provided by such mechanisms, these phenomena are predicated on linear elasticity. However, as it will be shown next in the constitutive modelling, more complex phenomena must also be considered, such as plasticity and viscoelasticity. These mechanisms have significant repercussions on increased focal adhesion ligand density, enhanced adhesion signaling, cell spreading and proliferation signaling. Therefore, these effects must also be included in the modelling of the system that will be presented next.

Regarding the bio-chemo-mechanical modelling, a constitutive model for the contractility of cells has been proposed that takes into account the dynamic reorganization of the cytoskeleton of the cell [92]. While previously employed models consider the cytoskeleton as an interlinked structure of passive filaments [347], the biochemical effects that lead to resultant forces are neglected. This significantly constrains the realistic depiction of the mechanical behavior of the cells and the model is bereft experimental validation. However, the aforementioned suggested model employs the activation signals that inhibit actin polymerization and myosin Phosphorylation, as well as the tension-dependent agglomeration of the actin and myosin into stress fibers, and the cross-bridge cycling between the actin and myosin filaments that precipitate the tensile load. This information can be utilized such that the generalized model must be able to characterize the fundamental interactions among the forces, the convening and dissolution of stress fibers, and also the compliance of the substrate. Even though a lot of imperative details regarding the biochemical processes that

occur during the deformation of the cell have yet to be unravelled with veracity [47], basic assumptions have been made to provide an explanation on several aspects of such a model. More specifically, when the cell is either suspended or at rest, the binding proteins or integrins are rearranged over the interface between the cell and the surface [369]. Furthermore, the short actin filaments inside the cytoplasm are encompassed by actin monomers which are bound to profilin. Myosin II is bent, and the tail domain interacts with the motor head. Moreover, the stress fibers are formed through either a nervous impulse or an external signal [280]. When there is no applied tension, the actin filaments are free of rein by the bipolar-myosin filaments, leading to the disassembly of the stress fibers. These mechanisms lead to the conclusion that tensile forces are critical for the formation of stress fibers and that the cells can respond to any restraining forces through a greater tensile load on the integrins.

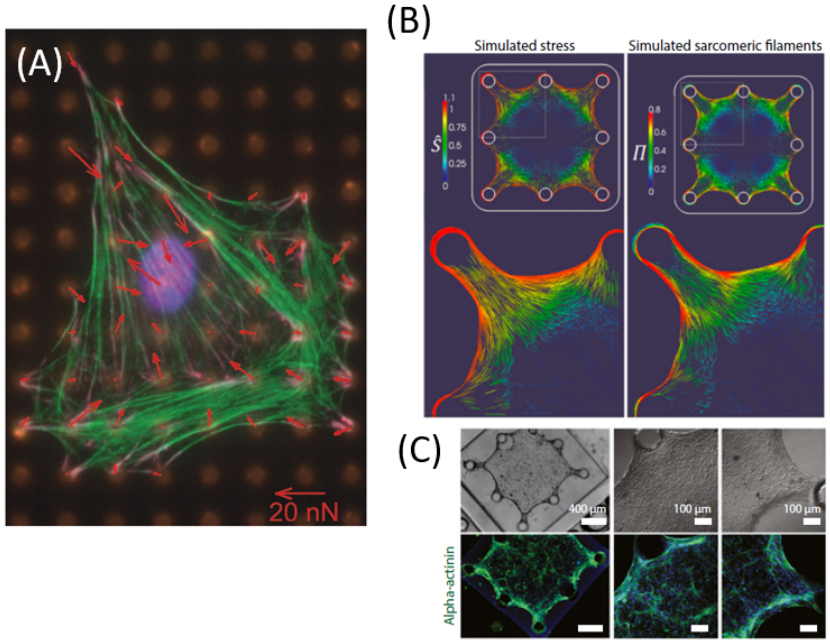

Figure 2.8: Evaluation of the constitutive modelling in individual cells and tissue. (A) Estimation of the contractile forces in a fibroblast cell, layed on a bed of microneedles. The actin fibers are stained in green. The arrows point the deflection of the posts. The lengths of the arrows are proportional to the magnitude of the force exerted by the cell on the posts [92]. (B) Simulation results of cardiac tissue showing the normalized stress distribution $\hat{S}$ and the expression of sarcomeres Π. (C) The fluorescent imaging of the stained sarcomeric α-actinin (green) confirms the estimated expression by the FEA analysis [379].

In addition, the following assumption must be considered [92]. The stress fibers can be uniformly activated and formed in each direction. Hence, the signal of the triggering event can be modelled as an exponential function of time. This triggering affects the activation level

of the stress fibers. When there is full activation, then the maximum stress is applied and can be related with the strain rate of the tissue. Utilizing a version of the Hill equation [166] and taking into account the fiber lengthening, we can attain the hyperplastic constitutive law of the system. Experiments on cells placed on a bed of microneedles and compared with the computational model show that there is a decrease in the forces that the cell generates as the substrate becomes less stiff [92]. In addition, there are strong anisotropic effects that depend on the boundary conditions of the cells and there is high concentration of the stress fibers at the focal adhesions. Characteristic examples of such cells and are presented in Fig. 2.8(A). It must be noted that this model has been employed to tailor the design of aligned and functional 3D cardiac tissues from human pluripotent stem cells [379]. Fig. 2.8(B) shows how heart cells in the extracellular matrix can introduce stress alignment and a patterned expression of sarcomeric filaments Π in both simulations and in fluorescent imaging (Fig. 2.8(C)). Interestingly, this model correlated regions exhibiting highly aligned sarcomeres with areas of high stresses. Formed sarcomeres are predicted in regions where the local stress state is uniaxial, whereas sarcomeres are not observed in regions where the stresses are biaxial. Hence, uniaxial loading causes highly aligned tissues that express spatially homogeneous contractile proteins. This is a riveting finding since these proteins can be employed for in-vitro imitation of cardiac muscle fibers. Nevertheless, it must be noted that this model has been employed for 2D structural systems only, since the full 3D mechanical response is much more challenging to be conveyed from the perspective of both modelling assumptions and numerical evaluation.

However, even without complex models for a facile mechanical prediction, there is significant progress in 3D tissue modelling for in-vitro testing. Through MPL, complex microscale structures [311] and arrays [311] can be fabricated such that they can be seeded with cells. More specifically, patterned surfaces are considered to be a powerful arsenal for affecting cellular functions [187]. Cell-trapping well arrays can control the cell shape and behavior. For example, fibroblast cells (NIH-3T3) align more effectively when cells are nested in deeper grooves and narrower ridges [187]. In addition, various cell morphologies can be observed, depending on both the height and the type of the arrays with a threshold of obstacle height equal to 1 μm to permit cell alignment. A characteristic pattern like this is presented in Fig. 2.9(A). The different cellular morphology depending on the pattern dimensions is presented in Fig. 2.9(B). Even though this work was still incipient at that point, it elucidated how geometrical parameters of the environment that the cells are positioned can affect them. It must also be remarked that the cell morphology is imperative to design biomaterials for tissue engineering. A more realistic observation of the cellular behavior can be reported using complex patterns such as pillars [165]. In particular, a primary objective of such in vitro tissue models is to measure the contractile forces that are generated by the cells [184]. For instance, tractional and contractile forces generated by fibroblastic cells have a significant impact in wound contraction and closure during the healing of an injury. Due to the migration of the fibroblasts, the tractional forces reorganize the cells along stress lines to mechanically precipitate generation of collagen and acquisition of proto-myofibroblast phenotype. Moreover, tractional forces caused by migrating cells can initiate wound contraction. Therefore,

it is crucial to measure such forces. An expedient experimental approach is to fabricate cantilever beams through MPL and observe their deformation due to the attachment of cells [165, 184]. When a cell has grown on the fiber, an axial compressive force is generated due to the cell contraction. This leads to large deformations on the fiber that can be measured through fluorescent imaging and correlated with the applied load from the cells. Fig. 2.9(C) demonstrates the imaging of such cells on a fiber. Through this process, it is easy to fathom how the contractile forces that are generated by the cells can affect the deformation of the fibers, leading to a better understanding of the edifice mechanisms of wound healing. Fig. 2.9(D) shows the deformation of the whole fiber due to the loading of the cells. From the perspective of 2D tissue samples as the ones that were reported in the FEA modelling, 2D microtissues were attached to columns, again investigating tissue healing properties [40]. A characteristic image of such a scheme is presented in Fig. 2.9(E). These microtissues loaded under tension possess tissue contractions and matrix remodelling, leading to wound closure when the microtissue has a cut. A similar structural paradigm was utilized to investigate the behavior of cardiac microtissues. Nevertheless, the tissue exhibits 3D structural features, leading to effects that a 2D model cannot convey effectively.

To expand this concept one step further, an array of columns can be fabricated to attach a conglomeration of cells on them. Microtissues, with or without the utility of the extracellular matrix, are generated through the cessation of cells' merging before they can compact. This occurs when cells adhere to one another and to their proximal extracellular matrix. Thus, the density of the microtissue increases. Under this principle, it proved to be enticing to study the behavior of the cardiac tissues in-vitro. Human inducing pluripotent stem cells (hiPSCs) and genome-editing tools enables the investigation of physiological phenotypes and the recapitulation of disease pathologies using these the pillar scaffolds [245]. Moreover, hiPSCs can be utilized to model human heart diseases in the cell culture. Mechanical factors such as the applied stresses exhibit a significantly crucial role in the normal operation of the heart and the pathogenesis of diseases such as cardiomyopathy [3]. Hence, introducing mechanical stresses based on the scaffold morphology into the engineered hiPSC-based tissue models can set the framework to precisely model disease phenotypes. Cardiomyopathies are often related to mutations of myosin-binding protein C cardiac isoform (MYBPC3), a thick-filament accessory protein of the striated muscle sarcomere A-band. To provide an explanation whether tissue mechanical resistance to contraction can regulate cardiomyocyte sensitivity and disease phenotypes due to the loss of function mutation of MYBPC3, highly ordered 3D fibres have been fabricated and seeded. Due to the mechanical properties of these fibers, cardiac tissue self-assembly and dynamic remodeling can be promoted and observed. Although these fibers have constant mechanical properties, thicker fibers have a higher mechanical resistance to cellular contraction than thinner fibers. Hence, cardiac microtissues produce higher forces when they are developed on the matrices with stiffer fibers. This leads to the manifestation of contractile deficits where the tissue is devoid of the MYBPC3 protein. Characteristic fluorescent images of such tissue models are shown in Fig. 2.10(A). These results reveal how 3D scaffolds can be employed for in vitro modelling of the external mechanical load to cardiac tissues, either by passive stretch of cardiac tissues

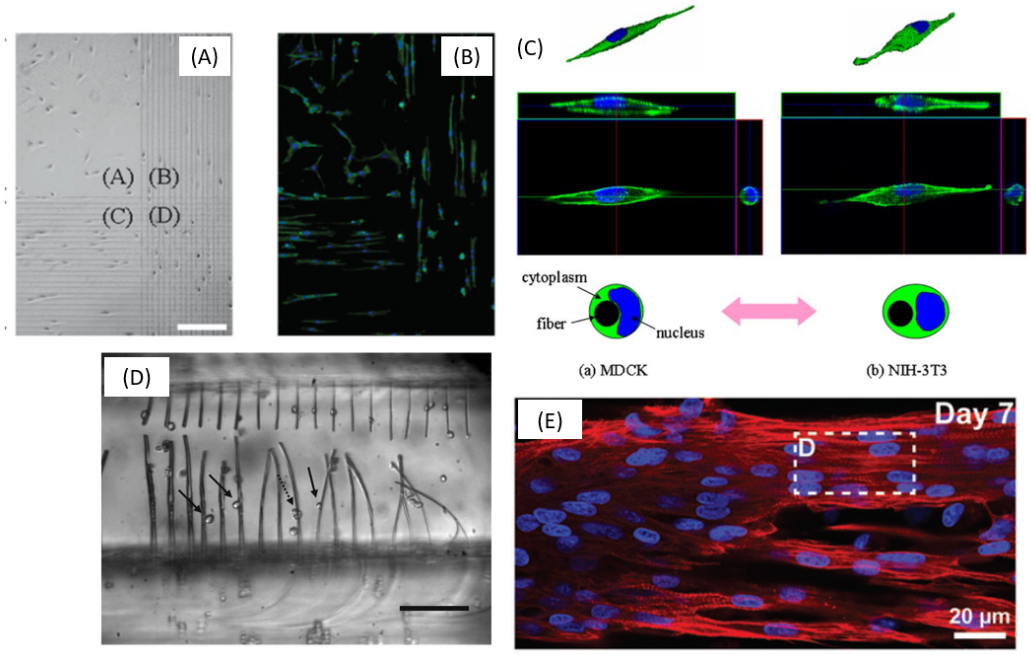

Figure 2.9: Effect of the patterned surface in the cellular response. (A) Patterned surface observed through Scanning Electron Microscopy. (B) Fluorescent imaging of the cellular alignment on the patterned surface [187]. (C). Images of three dimensional cell morphology, cross-sectional images, and cross-sectional schematics for the individual cells attached on a fiber [165]. (D) Deformed fibers due to the forces applied by the attached cells [184]. Reprinted with permission from Springer. (E) Immunostaining of troponin-T (red) and nuclei (blue) of a cardiac tissue attached on two pillars [40].

mimicking the increase of preload or by stiffening the flexible cantilevers to cardiac tissues mimicking the increase of afterload. These findings can unveil the nuance of abnormalities due to genetic deficiencies in the heart.

Furthermore, nonuniformity of the mechanical properties of the tissue also affects the development of heart dysfunctions. To inquire how this effect manifests itself, 3D cardiac microtissue models with engineered mechanical nonuniformity were also developed. Nonuniformity of the tissue's mechanical environment has been established as one of the essential constituents that regulate cardiac pathophysiology [342]. For instance, it affects the heart's pumping efficiency, inevitably causing heart failure by propagating local cardiac dysfunction spreading through the whole heart. To architect a nonuniform mechanical environment and evaluate the function of hiPSC-based cardiac microtissues, a "pathological" 3D cardiac microtissue model was designed [413]. Different mechanical loads could be accomplished by fabricating the matrices with different fiber thickness. More specifically, fibers with either 5

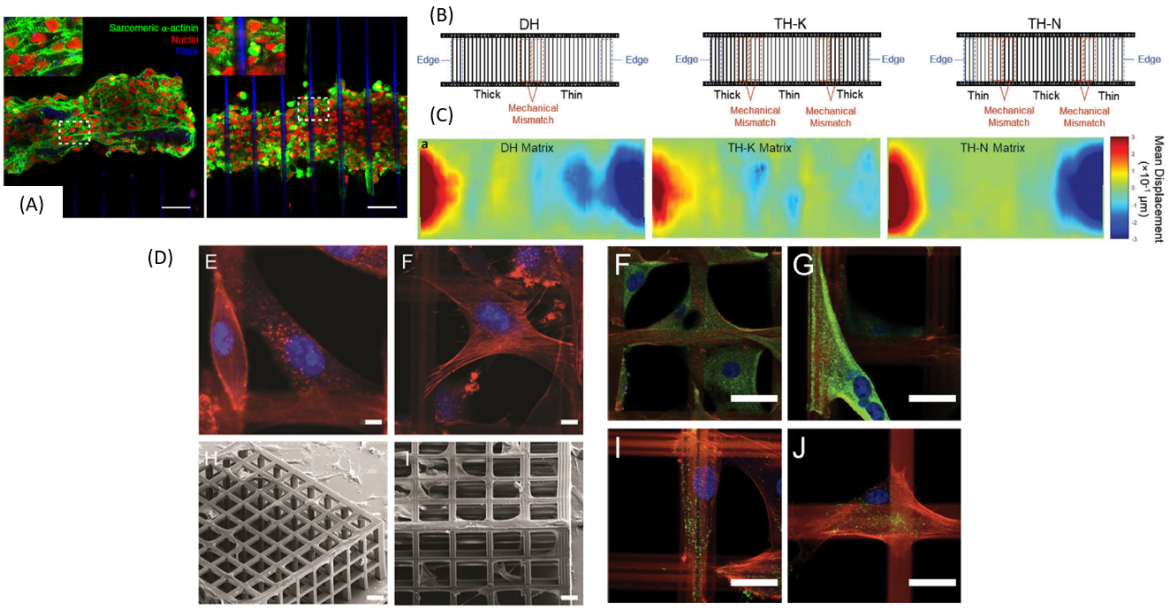

Figure 2.10: Cellular behavior of cardiac tissue at an either uniform or nonuniform environment. (A) Confocal microscopy images of the MYBPC3-/- cardiac microtissues [245]. (B) Schematic representation of the nonuniform scaffolds. (C) Displacement heatmaps of entire cardiac microtissues for the different nonuniform environments [413]. (D) Adhered cells in either 3D (Label E) or flat structures Label (F), showing significant morphological variation. The SEM images of the 3D structures are shown in Label H, I. The other set of Labels (F, G, I, J) shows fluorescence images on either flat (F, I) or 3D structures (G, J) [311].

μm or 10 μm thickness were in the same designed matrix, in comparison with the uniform thickness of the previously presented case. In addition, the configuration of the nonuniformity was investigated by varying the location of fibers with different thickness. Fig. 2.10(B) shows the different scaffolds that were tested. Fig. 2.10(C) shows the mean displacement of the tissue for the different designs. Through the characterization of the tissue morphology, contractile motion velocity, motion synchronicity, force generation and kinetics, power output and energy of contraction, it was revealed that cardiac microtissues possessed a high proclivity to adaptation in a double-hybrid mechanical environment, while adjusting in contraction was limited and exhibited pathological phenotypes in a triple-hybrid mechanical environment. In this particular case the double hybrid scaffold possesses only one mismatch boundary (e.g. fibers of different thickness), whereas the triple-hybrid scaffold exhibits two mismatch zone. The configuration of the beam members for these environments is illustrated in Fig. 2.10(C). These results illuminated how engineering a nonuniform mechanical environment can provide a new avenue to examine in vivo pathological conditions and comprehend cardiac disease progression.

It should be pointed out that the effect of 3D environment has been investigated for more general biomechanical phenomena, such as cytoskeleton structuration and nucleus deformation. It has been reported that by designing three-dimensional (3D) cagelike scaffolds with a variety of topographical features, the effects of induced membrane curvature can be evaluated even at the nanoscale. More specifically, the 3D cage structures with pitch equal to 4.5 μm, and height equal to 500 nm were seeded with U87 cells [311], shown in Fig. 2.10(D). Using confocal and electron microscopy enables the close observation of both cytoskeleton structuration and membrane rearrangement at the material interface. It is reported that cells that adhered on the 3D surfaces have substantially different behavior than those normally found on 2D substrates. On 2D structures, cells tend to match the profile of the surface maximizing the contact with the surface, while the cells attached on the 3D surfaces demonstrated a remarkable membrane deformation encompassing the topographical design. This is a major mechanistic trait, since modulation of the shape of mesenchymal stem cells can lead to specific molecular pathways through the rearrangement of the cellular membrane connected to the plasma membrane activity. In addition, a dilly of cellular functions can be regulated, such as in the tissue homeostasis mechanisms. Despite the fact that this work deviates from results exclusively focused on specific aspects of a healthy tissue, it still demonstrated that the mechanical design of 3D scaffolds can provide compelling findings regarding the cellular behavior.

Architected Biological Scaffolds

Even though the aforementioned simple structures have provided great insight in the mechanics of the cellular response, in most cases the physical tissue has a much more complex 3D architecture. Therefore, different designs inspired by the extraordinary properties of metamaterials have also been employed to investigate the mechanical performance of the tissue.

The mechanical properties of the architected bioscaffolds can be controlled either by the architecture or their innate material properties. Regarding the mechanical properties, this is significant progress in the development of heterogeneous micro-mechano-environments through the control of the material. As it was discussed in the previous section, nonuniformity is a major factor for cardiovascular diseases, but also morphogenesis, regeneration and breast tumorigenesis. A primary technique that can lead to a stiffness gradient in the extracellular matrix is oxygen inhibition [88]. Oxygen inhibition can forestall the curing thickness since it obstructs the free radical photopolymerization of the scaffold. Modulating the oxygen inhibition in the layer by layer fabrication process modulates the local crosslinking of the polymerized photoresist, consequently controlling the local stiffness of the scaffold. This fabrication technique has been reported to monitor the cellular organization and in vitro tissue reconstruction [445]. It has been demonstrated on oxygen-permeable polydimethylsiloxane (PDMS). Utilizing atomic force microscopy, it was shown that the materials possess localized stiffness varying between 2-15 kPa. Seeding such scaffolds with bovine pulmonary artery smooth muscle cells (bPASMCs) showed a directionality in cellular attachment and

morphology. These observations are cogent with the principles that were presented regarding the adherence of cells in either soft or stiff substrates. While this is a major breakthrough in the design of architected bioscaffolds, creating bioscaffolds through architected structural configurations is the primary approach to tune the mechanical properties.

A major category that has been studied is that of zero Poisson ratio scaffolds. When these scaffolds are axially strained, there is no traverse deformation. While this effect has been reported in nature in tendons or skin [250], it is also expedient to imitate the tissue response during wound healing or tissue ingrowth. Therefore, these scaffolds are auspicious for tissue engineering of the ligament, the cartilage or the corneal. Zero Poisson ratio can be realized through the design of semi-re-entrant honeycomb structures, which have been thoroughly investigated from the perspective of tissue engineering [418]. More specifically, polyethylene glycol (PEG) materials with controllable Poisson ratio have been fabricated through projection printing. These materials were selected since PEG hydrogels can be successfully incorporated in three-dimensional cell cultures. It was observed that the cells could successfully get attached to the scaffold, revealing that these designs can be potentially utilized for tissue ingrowth. In addition, seeding these scaffolds with 10T1/2 fibroblast cells and C2C12 myoblast cells showed the aggregation of cell growth. From the mechanical perspective, the dimensions of the structure are critical to obstruct non-specific autopolymerization, since this causes large deformations and ineffective aggregation of the cells. Utilizing a Stabilized-Rounded' Hinge, stiffening of the neighboring regions can be embraced, prohibiting non-specific autopolymerization. Furthermore, structures with negative Poisson ratio have been employed to create 3D artificial scaffolds [119]. Utilizing the photoresist SZ2080, 3D bowtie structures possessing negative Poisson ratio were fabricated. Structures with negative Poisson ratio have the same type of deformation in all directions, prohibiting barrel shape formation for the case of compression or necking for the case of tension. Hence, the structure can sustain significantly larger deformations without failure. By performing in-situ micromechanical testing incorporated in the scanning electron microscope, it was shown that the unseeded scaffolds can sustain even 60% deformation without fracture. Characteristic deformation regimes are shown in Fig. 2.11(A). Even though the structure is resilient to fracture, seeding it with fibroblast cells revealed high compliance, as it is presented in Fig. 2.11(B). This enables the proliferation and migration of cells in the scaffold, rendering it a suitable candidate for tissue engineering. Moreover, the effect of the scaffold's 3D geometry has also been addressed from the perspective of bone tissue growth [246]. Seeding tetrakaidekahedral structures with Osteoblast-like cells (SAOS-2) showed increase of intracellular f-actin for those structures with higher compliance. This elucidated that osteoblasts are highly sensitive to substrate elasticity at low stiffness. Again, it was proved that the distribution of actin filaments depends on the substrate stiffness, which is consistent with the rest of the reported results. In addition, the activation of f-actin concentration was calculated utilizing linear elasticity, providing close match between the experimental results and a simple phenomenological model. In addition, the scaffold architecture has also been investigated with respect to its effect on neuronal networks. The brain can be considered as a 3D structure [248], requiring a complex 3D architected to imitate the mechanical envi-

ronments of the neurons. By designing hollow tower structures by MPL, a complex network of neurites can be led to predefined pathways in 3D space [114]. This enables the neurites to be rearranged inside the cavities of the scaffold. In addition, the electrophysiology of the tissue was evaluated through patch clamp measurements. These experiments revealed that the neuronal function of nerve cells is not hampered even in the reclusive environment of hollow architectures. All of these complex structures, applied at a plethora of different cells, elucidate the importance of architectural complexity to design bioimplants that would be feasible to living organisms. Nevertheless, more complex design principles have also to be taken into account for the design of implants and will be presented next.

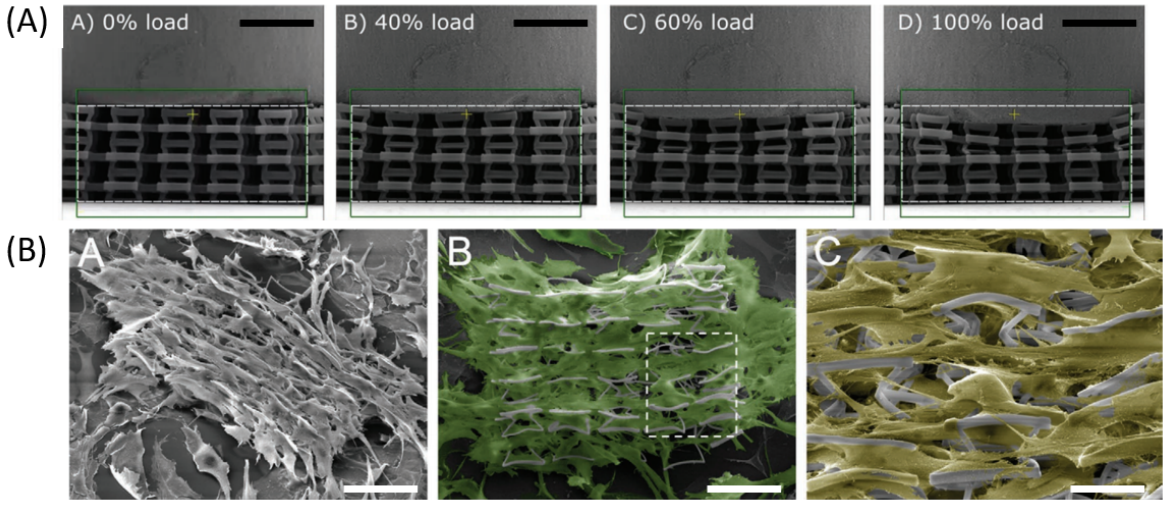

Figure 2.11: 3D auxetic scaffolds for tissue engineering. (A) Mechanical testing on the unseeded specimens reveals resilience to fracture due to the auxetic behavior. (B) Seeding the scaffolds with cells reveals high compliance, rendering them efficient for tissue engineering [119].

Design of Meta-Implants

In the previous analysis, regarding the correlation between scaffold topology and cellular mechanical behavior, all of the related phenomena were investigated at the microscale. While this is critical to comprehend how cells behave at different environments and provide and explanation of the constitutive behavior of mechanobiological systems, it is also critical to improve the mechanical performance of constituent parts at a larger scale. Hence, there is inexorable advance in the design of implants that embrace design principles from mechanical metamaterials [36] (e.g. metaimplants). The principal objective is to improve bone tissue growth, diminish infections, as well as provide enhanced mechanical performance [367].

Properties such as negative Poisson's ratio or high stiffness for low weight are also observed in nature [22]. Therefore, properties, which from a conventional perspective would be considered "meta", have evolved in nature through natural selection and must be imitated by the architected design. Nevertheless, even though nature is the paragon of efficient design, there are ways to improve the mechanical performance even more. This is due to the fact that there are states where the performance of the tissue is not the desired one. A characteristic example is tissue regeneration's spatial and temporal limitations. A trademark of an implant must be to match the anatomy of the part that it will replace. Therefore, functionalities such as deployability and shape-morphing have been developed to assist in that endeavor. Deployable metaimplants can be used for minimum surgical invasiveness [449]. Before they are placed in the patient, they possess a state of minimum surface area, which is reconfigured to obtain its full size and its full loading capacity. This notion is inspired by stents, which change their geometrical configuration when placed inside a blood vessel [290]. However, orthopaedic implants need to withstand much larger compressive forces to sustain the body weight compared to the small tensile forces introduced by the blood flow. This is a major design constraint that must be taken into account when designing deployable metaimplants. An expedient way for the design to be deployable is through multistability [36, 37]. Multistable mechanisms have more than one stable configurations that they can remain at rest. Each equilibrium point is associated with a specific geometrical configuration and it requires a specific amount of energy to be reached. Characteristic designs are presented in Fig. 2.12(A).

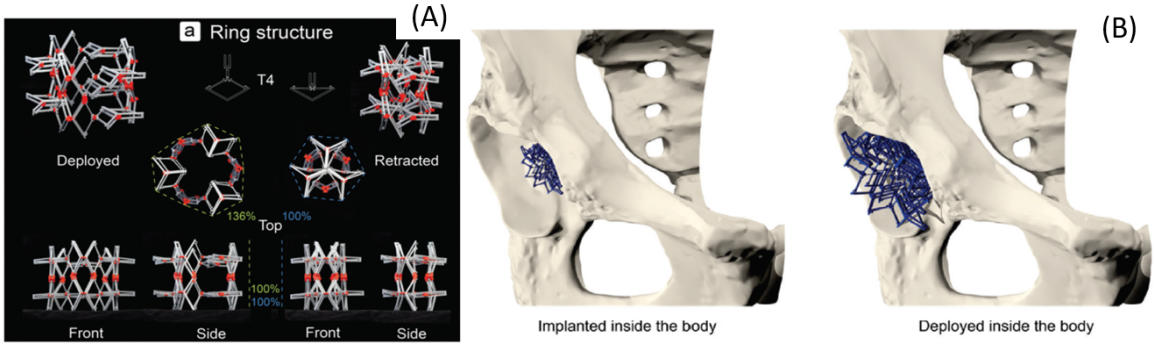

Figure 2.12: Design and implementation of Bioimplants. (A) Snap-through designs for bioimplants. (B) Arrangement of the implant in the human body, at the two distinct equilibrium states [36].

For such designs, bistability was accomplished through a snap-through mechanism, which is a form of buckling [395]. The new state that the implant will have with respect to the initial one is shown in Fig. 2.12(B). Another way to accomplish different equilibrium positions is through origami, kirigami and mulitlayered designs. These designs have superior mechanical performance from the perspective of both strength and surface area. Another

concept that has been suggested is that of shape-morphing and shape-locking [227]. These implants will possess a shape that's characteristic for the specific patient (i.e. shape morphing) and then will remain at this equilibrium position (i.e. shape locking). However, this design required many kinematic mechanisms such that it can alter its shape and then be constrained at a specific position, rendering it significantly more complex than deployable implants. However, bone tissue has multiple different aspects that are essential for it to be functional. Characteristic examples are mass transport or biological properties such as the porosity. Therefore, the architected designs utilized for metal implants must also possess properties from different domains to become truly functional. These properties are achieved by microscale design of the morphology of the implant. While there are not many cases that have been demonstrated experimentally, as it was addressed in the previous section, several concepts are also suggested for potential utility. Structures comprised of beam members or thin walled structures have been thoroughly investigated regarding multi-physics properties. From the mechanical perspective, they can possess extreme densification when loaded, due to the post contact of their members during buckling. This ushers enhanced strain energy density and stiffness [402]. Moreover, another category of structures, called triply periodic minimal surfaces [207], possess elastic modulus similar to that of the bone, very high yield strength, extremely long fatigue lives, and transport imitating the bone structure. In addition, pentamode structures can be utilised for bone tissue regeneration since their mechanical properties are affected by specific regions of their geometry. This provides the control of their porosity, such that regeneration can be realized. Furthermore, larger scale structures with negative Poisson ratio can also be utilized. PCL nanofiber membranes have been fabricated and have been proved to possess an almost tenfold elongation capacity. Thus, they can affect the lineage differentiation of the cells [30]. However, such designs have only been tested under mechanical distraction (e.g. a specific loading condition and not a complex mechanical environment). Therefore, this concept has not been proved as a promising solution for tissue growth yet. While all of these designs bear great potential for advanced implants, their commercial utility is still incipient. The reason for this is that conventional implants are competent and clinically safe to be utilized. Thus, future work must also be focused on actual trials of such systems to investigate whether they are indeed efficient. It must also be pointed out that the vast majority of the metamaterial properties have only been addressed in macroscale. Since there is deep understanding of mechanobiology, incorporation of novel designs such as reconfiguration and bistability in the extracellular matrix or scaffold has not been realized. This provides a new avenue to design in-vitro microscale tissue models inspired by the concepts of metal implants, which have been thoroughly investigated in the macroscale.

Section Conclusions

In conclusion, the mechanical modeling of the cellular behavior and the engineering design and scaffolds were summarized. There are many physiological mechanisms associated with the interaction between cells attached to the substrate that affect their mechanical perfor-

mance. These affects occur in both the linear elastic and nonlinear domain and have been efficiently captured for 2D structural models. In addition, the mechanisms of proliferation, migration and differentiation can also be associated with mechanical phenomena, providing a deeper understanding in ways to improve the established models. Moreover, the architecture of scaffolds, with properties such as stiffness and geometrical configuration have significant implications in the normal or malfunctional operation of the cells. While this principle has been efficiently utilised to study cardiac diseases, more complex environments inspired by architected materials will also pave the way to observe more complex functions of the cells in a 3D environment. Perplexed architectures have been efficiently utilized from the perspective of tissue growth and penetration of the scaffold, revealing a potential convergence of the two fields. In addition, larger scale structures, used as implant for potential surgical operations, namely metaimplants, have demonstrated how the concepts of architected materials can be utilized for the improved behavior of the part of the human body that needs to be replaced. While all of these domains orbit around the concepts of fundamental mechanics, mechanobiology and metamaterial design, they are still not integrated together. However, this fact elucidates that there are plenty of complex environments, embosoming bistability or tailored buckling, that could potentially lead to different patterns in the cellular behavior. Since MPL has been successfully utilized for the design of complex structures, it will be a vital tool to achieve this goal. Therefore, merging the additive manufacturing technology of MPL with tissue modelling and architected scaffold design can potentially merge all of these fields to realize complex cellular responses, create bio implants and study malfunctions of the human body simultaneously. This will elevate the tissue engineering design and advance our understanding of enhanced physical performance.

2.7 Contemporary Challenges of the Field and Overview of the Thesis

The main challenges in the field of mechanical materials can be summarized into the different schools of thought. Based on the analysis provided in the previous sections, a lot of groups mainly employ ad hockery to interpret their findings, limiting the investigation to a specific type of unit cell. This is a repercussion of the scarcity of insight regarding the post yielding response of the structure and its exorbitant computational cost. The other approach is to employ optimization tools. However, this analysis is also constrained by the demand for thousands of experimental or simulation data, rendering the analysis to either computationally difficult or expensive for big problems. All of this aspects can also be attributed to the lack of short termed applications of this field.

The cardinal objective of the thesis is to address some of these challenges. The main focus will be in the design principles, the characterization, the mechanical behavior and an avenue for applications. The challenge of optimization will also be addressed, but this endeavor is a consequence of the collaboration with Haris M. Sheikh. Therefore, first, the basic principles

of mechanical matamaterials design will be demonstrated through designs that have been reported before in the literature. These are auxetic, pantographic and tensegrity structures. Fundamental ideas regarding the arrangement of beam members, the solid mechanics, the simulation tools and characterization and fabrication techniques will be analysed for each case. These results will set the prodrome for interconnected structures. In these structures, elastic, plastic and fracture properties are controlled through the arrangement of the polyhedral blocks that are used to construct them. Next, the same notions will be addressed using geometrical defects. Now, instead of arranging beam members, a strategic removal of beam members is utilised such that the mechanical performance can be augmented in lieu of an execrable behavior due to weakening. These themes will be explored primarily from the standpoint of mechanical behavior and FEA simulations. Next, the Bayesian optimization technique will be demonstrated in a test case problem. As it will be shown, a solution thousands of times better than the well established geometry can be found with a minuscule number of simulations. Finally, the thesis will end with the utility of architected materials in tissue engineering and it's implications in biocomposites.

Chapter 3

The Fundamentals to Microscale Design through Fundamental Analysis on Established Structures

3.1 Design and Testing of Bistable Lattices with Tensegrity Architecture and Nanoscale Features Fabricated by Multiphoton Lithography

Section Summary

In this work, mechanical tests were performed on different modular assemblies to verify whether the fabrication technique, the length scale, and the employed material response can preserve the bistable nature of tensegrity designs. The presented experiments are focused on uniaxial compression loading-unloading tests. The obtained force-displacement plots show a softening type of response initiating from the primary stable configuration, leading to snapping into the secondary stable configuration, illuminating the existence of bistable mechanisms in the fabricated structures. Thus, it can be concluded that the fabrication of multistable metamaterials using MPL is feasible. Hence, it can be extended in future studies on different types of bistable unit cells with tensegrity architectures, such as static and dynamic experiments and applications.

Materials and Methods

Microfabrication

As it was previously elucidated, simple bistable frameworks based on monostable tensegrity structures can be obtained through recourse to the benchmark system shown in Figure 3.1(a-b). This system is defined as a first-order infinitesimal mechanism or prestress-stable

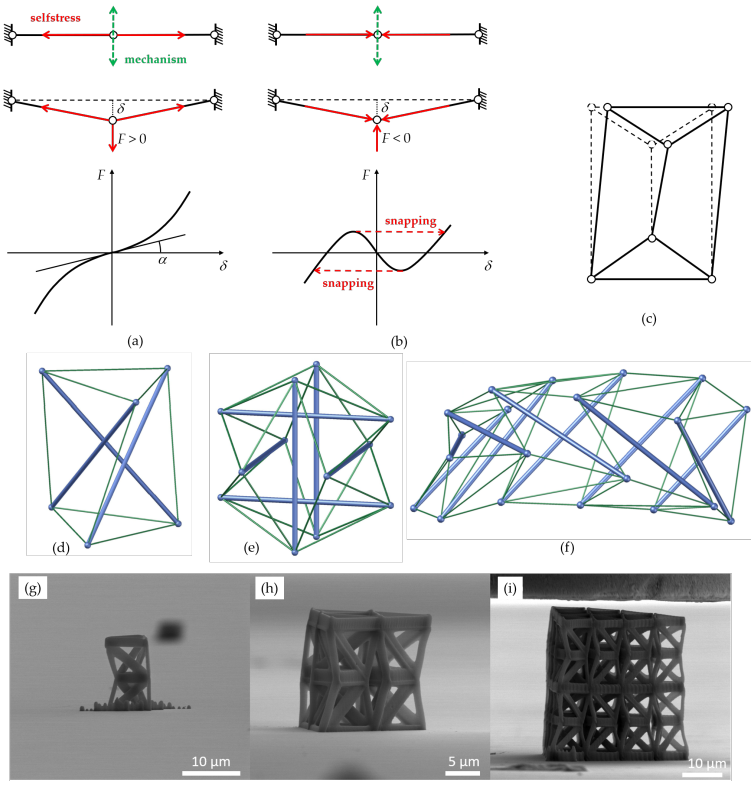

Figure 3.1: Illustration of the analyzed behaviors and fabricated structures. (a) Selfstress and mechanism in the prestress-stable two-element system (top). Deformed configuration under a vertical load and corresponding response (center and bottom). (b) Corresponding bistable system and bistable snapping response under the same vertical load. (c,d,e,f) Examples of prestress-stable systems with one seflstress state and one mechanism: (c) A two-dimensional system displaced along its mechanism; (d) triangular ten (e) expanded octahedron or tensegrity icosahedron; (f) an irregular x-tower. Fabricated geometries of structures: (g) individual unit cells, (h) arrays of three unit cells in one layer, (i) arrays of two layers with ten unit cells at each layer.

mechanism. It can possess a selfstress state, in which the two elements are in tension, imparting first-order stiffness to the internal mechanism [49]. If the two elements are linearly elastic, the load-displacement relationship for a load acting along the mechanism can be approximated by a cubic polynomial. The slope in the origin ($tan(\alpha)$ in Figure 3.1(a)) is directly proportional to the axial selfstressing forces in the elements. By reversing the sign of selfstress, leading to the compression of two elements in the aligned configuration, it becomes unstable. Moreover, moving along the mechanism, two more stable configurations can be found wherein the two elements are unstressed. The load displacement relationship in this case is the standard bistable snapping curve shown in Figure 3.1(b).

A prestress-stable tensegrity structure with just one independent selfstress state and one independent infinitesimal mechanism embosoms the exact same behavior. Several examples in two dimensions have been presented (e.g., the one in Figure 3.1(c)). Typical three-dimensional examples include: the classical triangular tensegrity prism (Figure 3.1(d)) [49]; tensegrity prisms with rigid polygonal bases [268]; the expanded octahedron (aka tensegrity icosahedron) [267] (Figure 3.1(e)); the x-towers and the needle towers built by Kenneth Snelson (Hirshhorn Museum & Sculpture Garden, Washington D.C., United States) [268] (Figure 3.1(f)). As the (monostable) tensegrity structure is displaced along the mechanism away from the equilibrium configuration, its bars get compressed while its cables get tensioned. Furthermore, as the corresponding lattice structure is displaced along the mechanism from the unstable equilibrium configuration, the compression of the compressed elements is decreased, whereas elements in tension sustain less tension, until an unstressed stable equilibrium is reached.

The procedure for designing a bistable structure can be provided as follows: (i) find a prestress-stable tensegrity structure with just one independent selfstress state and one internal mechanism; (ii) consider a configuration slightly displaced along the mechanism and realize it as a conventional framed unstressed structure; (iii) adopt a reduced-order model or a finite element model to simulate its bistable response under static loads; (iv) adjust its geometric and material properties to adapt it to fabrication methods and experimental conditions; and (v) perform experiments on fabricated structures to confirm the designed behavior. It must be noted that for the step (i) it is necessary to consider only tensegrities where the number of elements e and the number of nodes n satisfy Maxwell's relation for isostatic systems: $n = e+3$ for two-dimensional systems, and $n = e+6$ for three-dimensional ones.

Double Tensegrity Prism to Design a Bistable Unit and Corresponding Assemblies

The standard triangular tensegrity prism shown in Figures 3.1(b) and 3.2 is employed in the present work to design a bistable unit cell. This tensegrity structure can be obtained from a bar framework with the shape of a regular triangular prism and elements on the diagonals of the lateral faces of the prism (Figure 3.2(a)), such that the system possesses a three-fold symmetry axis passing through the centers of base triangles. The diagonal elements correspond to the bars, while all the others correspond to the cables of the tensegrity system, as shown in Figure 3.2(b). The bottom nodes have been pinned to the ground and the bottom cables are removed, while the top triangle has been highlighted. Figure 3.2(c) shows the unique prestress-stable equilibrium configuration for a regular triangular prism, corresponding to a fixed value of its *twist angle* φ, which is the relative rotation between the two bases. For a tensegrity prism with triangular base, the twist angle is equal to $\varphi = \pi/6$. The internal mechanism of this system is a twisting motion, which is the combination of a vertical translation accompanied by a rotation of the top base with respect to the bottom base (Figure 3.2(d)). We define the *relative twist* $\theta = \varphi - \pi/6$to be the twist angle

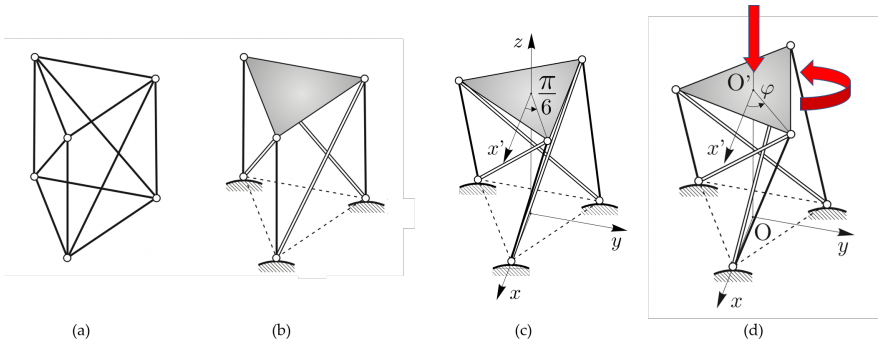

Figure 3.2: Design process of a tensegrity structure. (a) A bar framework in the shape of a regular right prism. (b) A corresponding right-handed tensegrity prism with cables (single line) and bars (double line). (c) Prestress-stable equilibrium configuration of the tensegrity prism. (d) When the internal mechanism is activated, the top triangle rotates about and translates along the vertical three-fold symmetry axis.

measured clockwise starting from the equilibrium configuration. For a tensegrity prism to be prestress-stable, it is only necessary to have $\varphi = \pi/6$, while the height of the prism and the sizes of each of the two equilateral polygonal bases have free rein. In addition, it can be observed that tensegrity prisms have a chiral geometry. The system shown in Figure 3.2 has a right-handed orientation, while its mirror image would have a left-handed orientation.

If a tensegrity prism is realized as a bar framework, and with a slightly smaller or larger twist angle, then it incurs a bistable behavior. Hence, it can snap from a primary stable configuration to a secondary stable configuration through a relative roto-translation between bases. Such motion is similar to the twisting mechanism of the parent tensegrity framework and will be referred to as a *bistable mechanism*. Each of the two stable configurations of such a bar framework is stress-free. During the activation of the bistable mechanisms, the diagonal elements are in tension, while the rest are in compression.

The relative roto-translational motion between bases in a tensegrity prism is too perplexed to be used in practical bistable lattices. A simpler translational motion between bases can be obtained by superposing two tensegrity prisms with opposite orientations on top of each other, obtaining a *double tensegrity prism*. Figure 3.3(a) conveys the bar-framework corresponding to such a system, where each prism has height h; a small initial relative twist θ_0; and different sizes a and b of base triangles. The doubled structure possesses two independent bistable mechanisms, which can be amalgamated together by composition to negate the relative rotation between end bases. When the top base is displaced vertically while keeping its rotation blocked, the bistable mechanisms of the two prisms are activated simultaneously, resulting in the rotation of the middle triangle only, as illustrated in Figure 3.3(a). Figure 3.3(b) depicts the system in the corresponding stable equilibrium configurations before and after such process, which are addressed here as *primary* (in blue) and *secondary* (in grey).

This system is the individual *bistable unit cell* which serves as a building block of the larger modular assemblies shown in Figure 3.3(e,g). The size of the middle triangle in the bistable unit is selected such that there is enough clearance, circumventing collisions between adjacent units during activation of the bistable mechanism. While the single unit has two independent bistable mechanisms, assembling three unit cells side-by-side shown in Figure 3.3(e) leads to a single bistable mechanism. Correspondingly, a multi-layer assembly such as the one in Figure 3.3(g) has one bistable mechanism per layer.

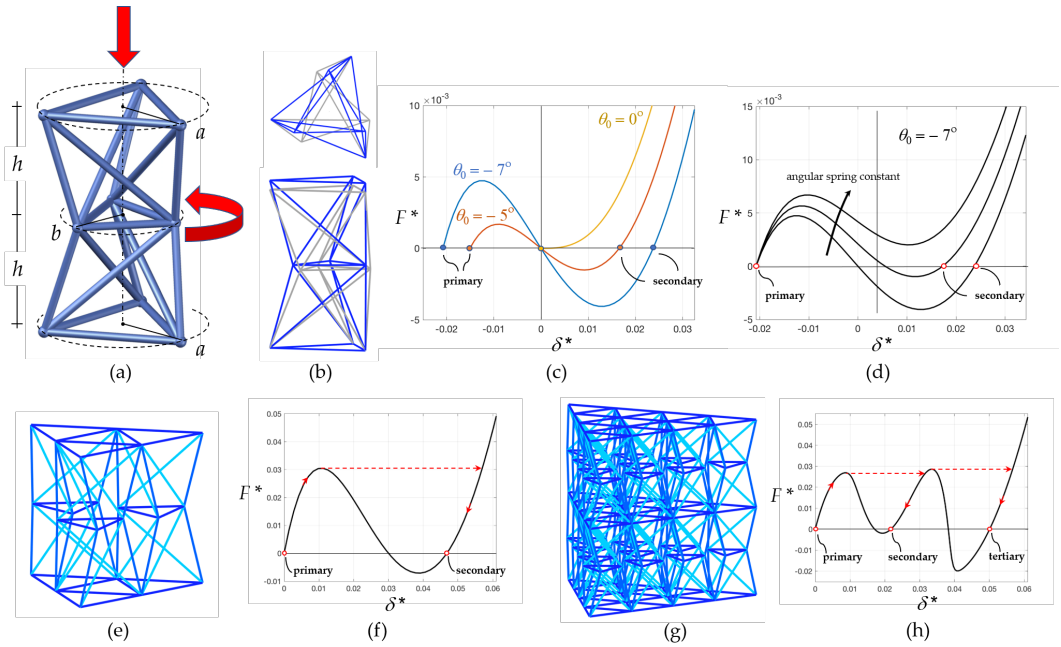

Figure 3.3: Mechanical modeling of the analyzed structures. (a) Geometry of the individual unit cell based on a double tensegrity prism. (b) Top view and side view of the primary (in blue) and secondary (in grey) stable configurations when the bistable mechanisms of the two prisms are activated simultaneously. (c) Static response of an individual unit cell with no angular springs under a vertical load for different values of the relative twist. (d) Static response of an individual unit cell with angular springs for different values of their spring constant. (e) Three-unit array. (f) Static response of a threeunit array. (g) Twenty-unit two-layer array. (h) Static response of a twenty-unit two-layer array.

A *Stick and Spring* reduced-order elastic model [112, 9, 113] is employed in this study to perform the numerical simulations of the structures. The nodal coordinates are selected as Lagrangian parameters. The bars are considered rigid with respect to bending and shearing deformations, and linearly elastic with respect to axial deformations. Linearly elastic angular springs are associated with variations in angle between the pairs of adjacent bars which are not part of a triangle of elements. These elements take into consideration the bending energy

of an actual fabricated structure, assumed to be localized at the ends of the bars. Numerical calculations are performed in a regime of large displacements, taking into account geometric nonlinearities, following the approach provided in [112, 9].

In a preliminary analysis of this unit cell, the circular cross section of bars has a radius of 375 nm, whereas the height of each prism is $h = 0.7\mu m$, for a total height of the unit equal to $14\mu m$. The top and bottom base triangles are inscribed in a circle of radius $a = 5\mu m$ and the radius of the circle circumscribing the middle base triangle is $b = 3.5\mu m$. The initial relative twist is $\theta_0 = -7$ degrees, corresponding to an initial twist angle $\varphi_0 = 23$ degrees. The Young's modulus is taken as equal to 1.2 Gpa (the methodology to obtain it is provided in the next subsection) and the stiffness constant of the angular springs has been assigned to be $k_s = 1.24\mu N\mu m$.

Each of the structures in Figure 3.3(a,e,f) have been subjected to a controlled-displacement uniaxial compression test, where the bottom nodes are kept fixed, while vertical downward displacements are imposed on the top nodes, without constraining horizontal displacements. Figure 3.3(c) displays the dimensionless force–displacement plot for the single unit (a) realized with no angular springs and different values of the initial relative twist angle θ_0. The dimensionless force parameter F^* is the resultant compressive force F divided by the axial spring constant of the shortest bar, k_a, and by the bars' diameter. The dimensionless displacement δ^* is the actual vertical displacement divided by the unit's height. The null value of δ^* corresponds to the unstable equilibrium configuration.

When $\theta_0 = 0$, the response is qualitatively the same as the one of the parent tensegrity system. For negative values of θ_0, the plot embosoms the form of typical bistable systems, with the snapping load increasing with the magnitude of the relative twist. Positive values of θ_0 are impractical from an experimental viewpoint and are not considered in this work, as they correspond to an upward bistable mechanism which can be activated from the primary stable configuration by an upward displacement imposed on the top nodes. Figure 3.3(d) depicts the force-displacement plot for the single unit cell (a) realized with angular springs and for different values of the angular stiffness constant, keeping $\theta_0 = -7$degrees. As the angular stiffness constant increases, the slope of the curve increases. In addition, if the force is never negative, the bistable behavior diminishes. Figure 3.3(f) elucidates the force-displacement relationship for a three-unit assembly (e): loading the primary configuration cause the structure to snap on the other equilibrium path; then the structure reaches the secondary equilibrium configuration upon unloading. Figure 3.3(h) presents the force-displacement relationship for a twenty-unit-two-layer assembly (g), where one of the two layers has slightly different spring constants. For this structure, two snapping events commence, one for each layer of the structure, and there can be three stable configurations.

Fabrication by Multiphoton Lithography and Mechanical Testing

All of the metamaterial structures analyzed in the present work were fabricated by multiphoton lithography [299] using the experimental setup shown in Figure 3.4(a) [393]. The structures were fabricated with a hybrid organic-inorganic material Zr-DMAEMA (FORTH, Her-

aklion, Greece) consisting of 70 wt% zirconium propoxide, 10 wt% (2-dimethylaminoethyl) methacrylate (DMAEMA) (Sigma-Aldrich, St. Louis, MO, United States) and 20 wt% ASTM type II deionized, distilled water. In total, $1.4mL$ of 3-(trimethoxysilyl)propyl methacrylate (MAPTMS) (Sigma-Aldrich) was first mixed with $0.14gr$ of hydrochloric acid in a vial. Afterwards, $137.7\mu L$ of DMAEMA was mixed with $0.66mL$ of zirconium (IV) propoxide solution containing 70 wt% 1-propanol in another vial. After adding the two mixtures together, they were diluted with $0.2mL$ of distilled water and $0.016gr$ of photoinitiator consisting of 4,40'-bis(diethylamino)benzophenone (Sigma-Aldrich). Before the fabrication, the experimental material was placed on glass substrates and remained for 24 h in vacuum. Further details regarding the material synthesis and experimental setup have been provided in the Introduction section. It should be noted that multiphoton lithography is the only fabrication technique capable of constructing the minuscule structures examined in this study. All of the metamaterial structures were fabricated several times to ensure repeatability during both the fabrication and the mechanical testing.

In situ indentation tests were performed with a nanoindentation apparatus (PI 88SEMPicoIndenter, Hysitron, Bruker, Billerica MA, United States) placed inside a scanning electron microscope ((Field Electron and Ion) FEI Quanta 3D (Field Emission Gun) FEG, FEI Company, Hillsboro OR, United States), thereby enabling high precision nanomechanical testing and real-time recording of the deformation. The molybdenum tip (model number 72SC-D3/035 (407A-M)) (Probing Solutions, Inc., Carson City NV, United States) was cut to a diameter of $70\mu m$ by a femtosecond laser and then flattened using a focused ion beam. The maximum tip displacement was set at $10\mu m$. A triangular force function was triangular force function was used in all the tests. To ensure repeatability of the measurements, each experiment was repeated.

To obtain the mechanical properties of the photoresist employed for the fabrication of the structures, three-point bending was performed on single double-clamped beam members with square cross section. A characteristic structure is presented in Figure 3.4(b), whereas the exact dimensions of the beam and the indenter are presented in Figure 3.4(c). The side anchoring walls have dimensions 50 by $50\mu m^2$ and thickness $20\mu m^2$.

For the uniaxial compression testing of the lattices, three different types of structures were fabricated, shown in Figure 3.1(g-i). These are individual unit cells (Figure 3.1(g)), arrays of 3 unit cells in one layer (Figure 3.1(h))) and arrays of two layers with ten unit cells at each layer (Figure 3.1(i))).

Initially, individual unit cells were fabricated. The beams have an oval cross section with $250nm$ and $500nm$ minimum and maximum radii respectively. The dimensions of the individual unit cell are $h = 7\mu m$, $a = 5\mu m$ and $b = 3.5\mu m$, with an initial relative twist of $\theta_0 = -7$ degrees. After calibrating the fabricating conditions, the following geometric parameters were decided to be suitable for an effcient fabrications of the unit cell used in the arrays: $h = 9\mu m$, $a = 6\mu m$ and $b = 4.5\mu m$, and the initial relative twist $\theta_0 = -9$degrees. All structures were fabricated with constant cross sections, since tapering of the cross section at the nodes resulted in inept photopolymerization of the structure. Figure 3.5 shows two SEM images of a fabricated three-unit array.

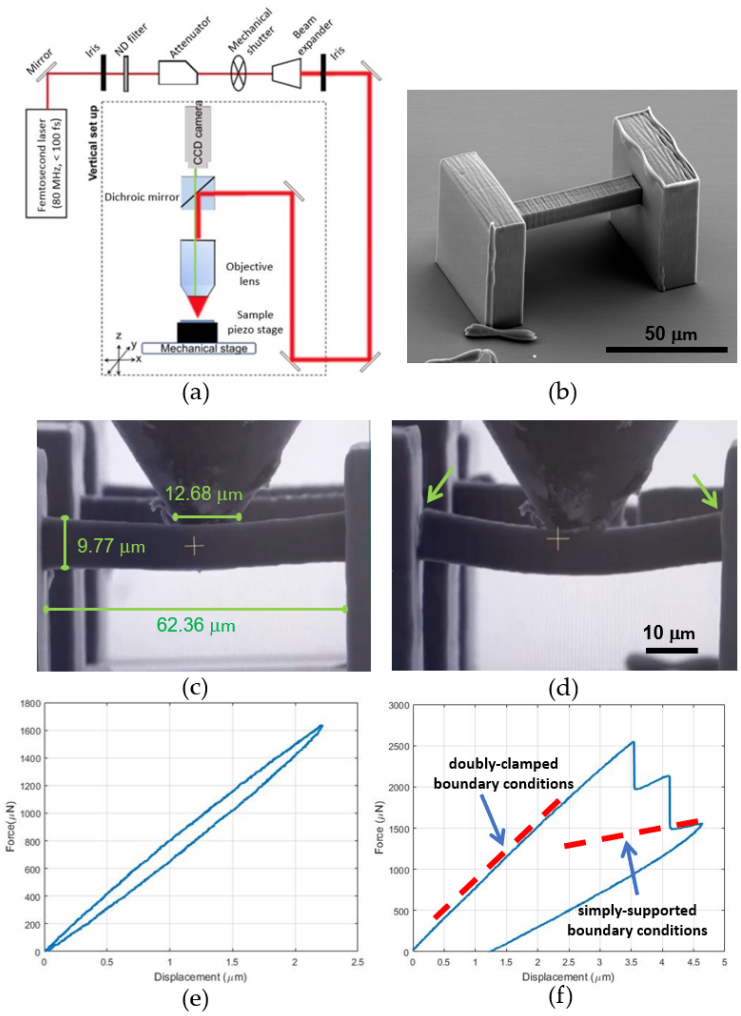

Figure 3.4: Experimental setup and testing to obtain the mechanical properties. (a) Schematic of the multiphoton lithography experimental setup [393]. (b) Beam structure employed for three-point bending measurements. (c) Beam structure at the beginning of the testing and dimensions. (d) Beam structure after cracking at the end sections. (e) A characteristic force-displacement curve obtained by three-point bending. (f) The force-displacement curve of a beam reaching the failure strength (cf. Video S1: Three-point bending [401]).

Results

Three-Point Bending of Double-Clamped Beams

It is observed that that the initial slope of the curve is $800\mu N/\mu m$, while the material failed at $2596\mu N$ at deflection of the center of the beam at $3.545\mu m$. Given that the dimensions of the

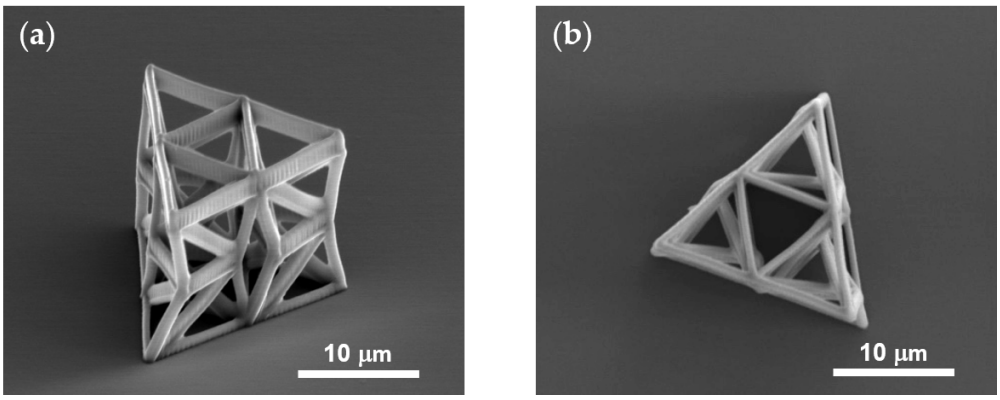

Figure 3.5: SEM images of a three-unit array. (a) axonometric and (b) top view.

side anchoring walls are much larger than those of the beam cross section, such measurements are conducted under the assumption of a double-clamped beam. Consequently, the Young's modulus was estimated using the Euler-Bernoulli theory equal to $E = 1.281 \pm 0.036 GPa$ and the breaking strength of the material equal to $\sigma_B = 131.99 \pm 0.17 MPa$. From the loading-unloading force-displacement plot in Figure 3.4(e), a slight viscoelastic behavior of the material can be observed, characterized by hysteresis, energy dissipation and loading-rate dependency. In addition, from the plot in Figure 3.4(f), two cracking events can be distinguished, highlighted by the two vertical drops in the plot. These are also confirmed by visual inspection of the images (Figure 3.4(d)) and the movie of the testing (see Video S1: Three-point bending [401]). The cracking commences at the end sections of the beam, where the bending moment is maximum. This result is consistent with the assumption of clamped boundary conditions. After cracking, the beam can still sustain some loading, and the corresponding slope in the subsequent branch of the plot decreases to about one-fifth of the initial slope, a value which is consistent with simply supported boundary conditions.

Individual Unit Compression Testing

Figure 3.6(a) shows the force-displacement plot obtained for the unit cell of the analyzed structures. The three snapshots of the unit cell in Figure 3.6(b) correspond to the three points highlighted in Figure 3.6(a). Upon a visual inspection of the images and the movie of the testing (Video S2: Individual unit [401]), it can be observed that the response of this structure is uneven, with the middle base of the unit moving out of the horizontal plane. This insinuates that the two prisms composing it may have different responses in the actual fabricated structure, and such a difference may be accentuated by the fact that an individual unit cell possesses two bistable mechanisms. However, despite this unsymmetrical behavior, twisting of the middle base during testing can still be observed. Furthermore, the loading branch of the force-displacement plot shows a softening tendency, while it is evident that

there is a residual deformation after unloading. Both of these traits embrace the theoretical response of the elastic structural model. The force-displacement plot also reveals an initial slope during loading which is lower than the slope during unloading, consonant with the viscoelastic response and the polymeric nature of the bulk photoresist material.

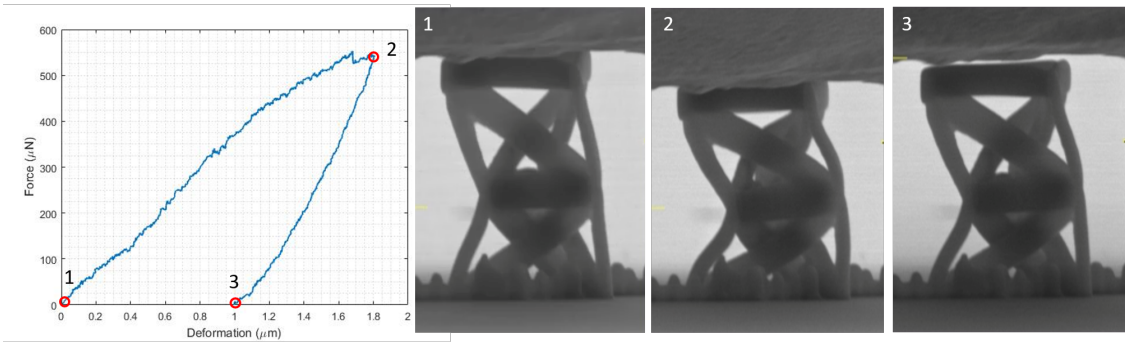

Figure 3.6: Mechanical testing on a single unit cell. (a) The force-displacement plot for an individual unit. (b) Snapshots of the structure at different times during testing (cf. Video S2: Individual unit [401]). The white scale bar for each SEM figure is $5\mu m$.

Three-Unit Array Compression Testing

Figure 3.7(a,b) shows the imposed displacement vs. time and the force vs. displacement plots for the array composed by three unit cells, while the snapshots shown in Figure 3.7(c) correspond to the points highlighted in Figure 3.7(b). As a result of the adjustment and calibration of the fabrication process, and the utility of a different set of values for the geometric parameters of the unit cell, a smooth softening curve from point 1 to point 2 can be irrefutably observed. The curve starts with constant slope; then the slope increases slightly before decreasing smoothly until it becomes almost horizontal when it reaches point 2. At the first unloading, the slope of the curve is higher than the initial one, decreasing slightly until the force returns to a null level at point 3, when a new stable configuration is encountered. Inspection of the images and the movie of the testing (see Video S3: Three-unit array [401]), reveals the discernible rotation of the middle triangles. In particular, the three middle triangles are free to rotate without interfering with each other and the twisting angle at the end of the first loading-unloading cycle differs from that of the initial configuration. Correspondingly, the height of the array at point 3 differs from the height at point 1 by approximately $1.2\mu m$. During the subsequent loading-unloading cycles, the response highlights a moderate preconditioning effect and a typical viscoelastic effect, while the twisting mechanism is preserved in the three units during each cycle.

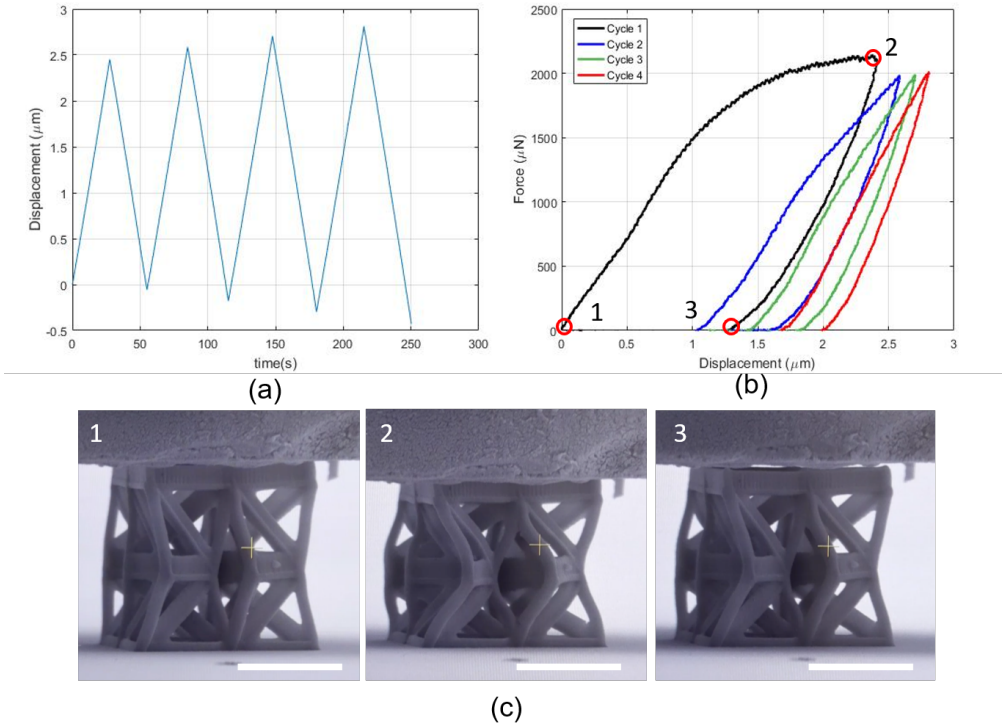

Figure 3.7: Mechanical testing on a three-unit array. (a) Imposed displacement vs. time and (b) force vs. displacement plots. (c) Snapshots of the sample during testing (cf. Video S3: Three-unit array). The white scale bar for each SEM figure is $8\mu m$). The white scale bar for each SEM figure is $5\mu m$.

Two-Layer Twenty-Unit Array Compression Testing

Figure 3.8(a,b) shows the imposed displacement–time and the force-displacement plots for the array composed by two layers of ten units each, while the snapshots shown in Figure 3.7(c) correspond to the points highlighted in Figure 3.7(b). The response of the structure is not as smooth as in the preceding case, with several irregularities in the plot which are likely to be related to microcracking events. Regardless, the softening response is still present, along with the residual deformation corresponding to the secondary stable configuration. Upon a visual inspection of the images and the movie of the testing (see Video S4: Twenty-unit two-layer array [401]), the middle bases in the top layer are categorically rotating, while the rotation of those in the bottom layer is ensconced. This may be related to a higher stiffness of the bottom layer, which subsequently can be associated with the fact that the bottom layer is attached to the fabrication floor, and/or that there are undesired polymerized regions in the bottom layer.

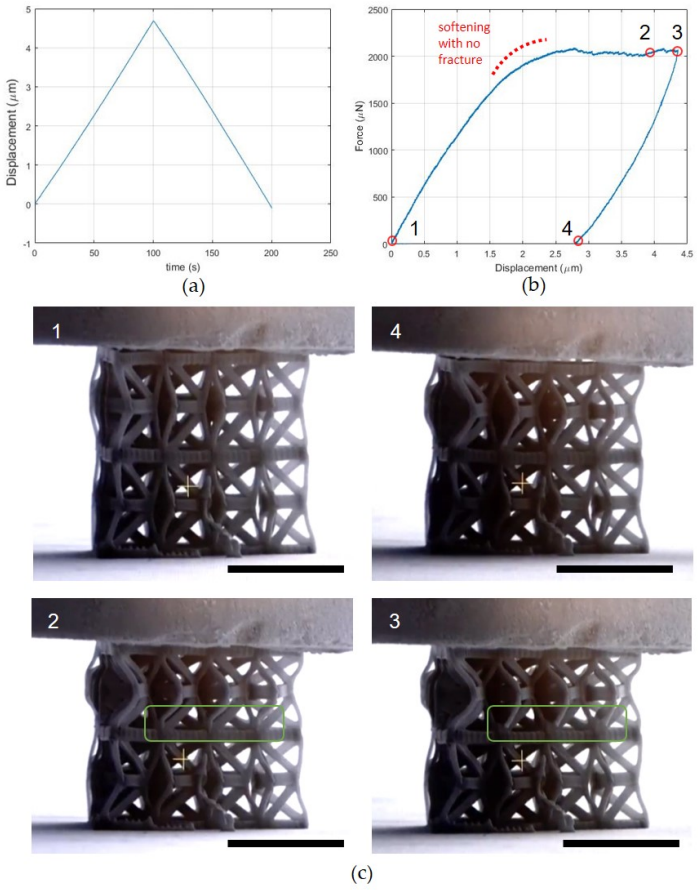

Figure 3.8: Mechanical testing on a twenty-unit two-layer array. (a) Imposed displacement–time and (b) force-displacement plots. (c) Snapshots of the sample during testing (cf. Video S4: Twenty-unit two-layer array). Some fracturing beams are enclosed in the green rectangle The black scale bar for each SEM figure is $10\mu m$.

Cracking and Fracture during the Testings

We observed fracture of the struts during several experiments. Figure 3.9 shows representative force-displacement plots and the corresponding images where fracture events can be observed (pointed at by the arrows in Figure 3.9). Upon a visual inspection, it is fairly clear that fracture occurred in beams because of excessive bending deformation. The breaking strength of the material is approximately $128MPa$. Considering for the sake of argument, a rectangular cross section with thickness $0.5\mu m$ and width $1.0\mu m$, the radius of curvature of a beam at the onset of fracture, computed according to linear elasticity theory, is about $2.22\mu m$. This value seems to be consonant with the observed beam deformations. Figure 3.10 shows helium ion microscopy (HIM) images of the samples. HIM enables extremely

high resolution ($\sim 20nm$ features) avoiding sputtering of the samples, distorting their morphologies. Figure 3.10(c,d) shows the fractography. The dominant fracture mechanism is river markings, tacitly leading to brittle fracture.

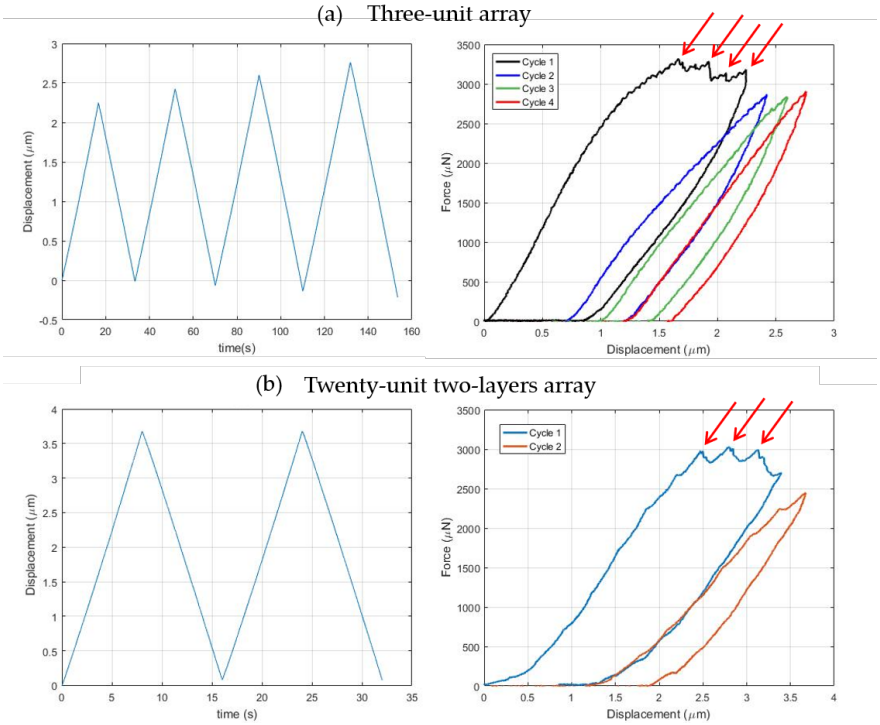

Figure 3.9: Mechanical responses revealing microcrack and fracture. (a) Imposed displacement-time and force-displacement plots for a three-unit array (cf. Video S5: Three-unit cracking). (b) Imposed displacement-time and force-displacement plots for a twenty-unit two-layer array (cf. Video S6: Twenty-unit two-layer cracking [401]). The red arrows indicate fracture events during the deformation.

Discussion

The main goal of this work was to address the question of whether lattice structures with nanoscale features and a bistable response can be efficiently fabricated through AM technologies. The experimental results given in the previous sections allow us to conclude that this objective can be satisfactorily accomplished utilizing the multiphoton lithography technique [299, 343]. The design of functional models of 3D bistable tensegrities with nanoscale features required several iterative adjustments and modifications, as shown by the results presented in the previous sections. A bistable-type response has been clearly observed in the two types of structures considered in this work, although in the two-layer system such a re-

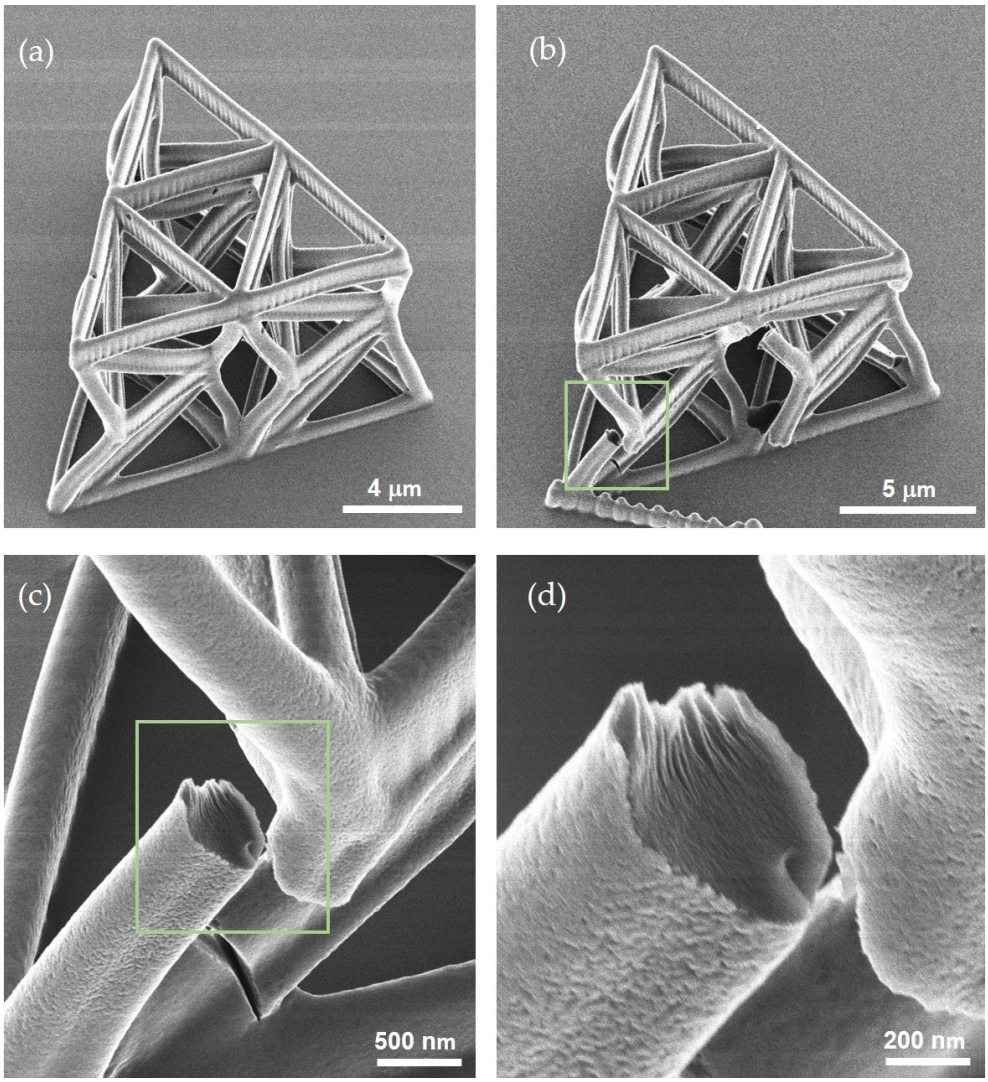

Figure 3.10: Helium ion microscopy (HIM) images of a three-unit array after testing. (a) HIM imaging of a structure that fracture did not commence. (b,c,d) HIM images of a fractured sample.

sponse was confined in space. Possible explanations of this behavior might be the following: (i) the bottom layer of such a system has a different stiffness with respect to the top layer; (ii) the bottom layer is contiguous with the fabrication substrate; (iii) there are undesired polymerized regions in the bottom layer.

Cracking and fracture of the tested samples often occurred during the execution of compression tests, when the imposed displacement caused excessive bending deformation in the beams/struts. The results presented in the previous sections highlight that such a drawback

can be mitigated by taking the estimated value of the maximum curvature of the beams before failure as an input variable of the design procedure. The HIM images presented in that section show nanoscale river markings as fractography features, which indicate the occurrence of brittle fracture. These nanoscale features have never been reported before in the literature dealing with the fracture of nanolattice structures.

One important feature observed in the presented experiments was an appreciable viscoelastic behavior of the material composing the analyzed tensegrities, which was reflected in their experimental response under compression loading. Bistability is essentially a consequence of the geometrically nonlinear response of the examined tensegrity lattices. The force-displacement curves obtained under compression tests highlight that bistable deformation mechanisms are combined with viscoelastic response in all of the structures examined in the present work. Such an observation calls for the formulation of mechanical models accounting for viscoelastic response of tensegrity structures, which we address to future work.

Regarding the optimal design of novel bistable lattices with tensegrity architecture, it must be noted that the present work has established the theoretical basis of such a study. The required constraint of having just one independent state of selfstress and just one independent mechanism can be easily implemented in available tensegrity form-finding procedures. This will accomplish bistable tensegrities with desired geometries [270, 200, 313]. While it is plausible to inquire for tensegrities with a target geometry, it must be observed that the problem of obtaining a desired snapping mechanism between two stable configurations is substantially challenging. Hence, it requires iterative design procedures that make use of accurate prediction models in the large displacement regime. A key feature revealed by the numerical results and the experimental tests presented in this work is that the analyzed structures exhibit large static indeterminacy. Consequently, despite the fact that each individual unit is actually an isostatic structure, the tested structures did not collapse even after the fracture of multiple struts.

Another peculiar property of a tensegrity system exhibiting a single soft mode is that the deformation process associated with the internal mechanism can be regarded as a "breathing," or pumping motion, which can be efficiently employed to design novel types of bistable pumps at multiple scales [103]. Such a feature of bistable structures can also be exploited to design systems that support the transport of mechanical energy through compact solitary waves, which is a subject receiving growing interest in the area of nonlinear mechanical metamaterials [78, 123, 124, 79, 269]. Figure 3.11 conveys this characteristic quiddity of ten bistable prisms clamped at one end. Numerical results on the wave dynamics of such a system, which have been obtained through the procedures diffusely illustrated in [123, 124, 79, 269, 112, 9], show that they support the formation of compression waves with compact support when subjected to an impulsive load at the free end.

Figure 3.11 shows some snapshots of the motion of the examined tensegrity column, which is impacted with initial vertical speed v0 and initial angular speed !0 of the top base, so as to activate the bistable mechanism of the first unit. The simulations shown in Figure 3.11 correspond to assuming $a/h = 0.5$, $\theta_0 = -3$ deg, $v_0(E/\rho)^{-0.5} = 0.3609$, $v_0/\omega_0 = a^2/h$, $k_s/(a^2 k_a) = 0.0041$, with ρ denoting the mass density of the material. One observes

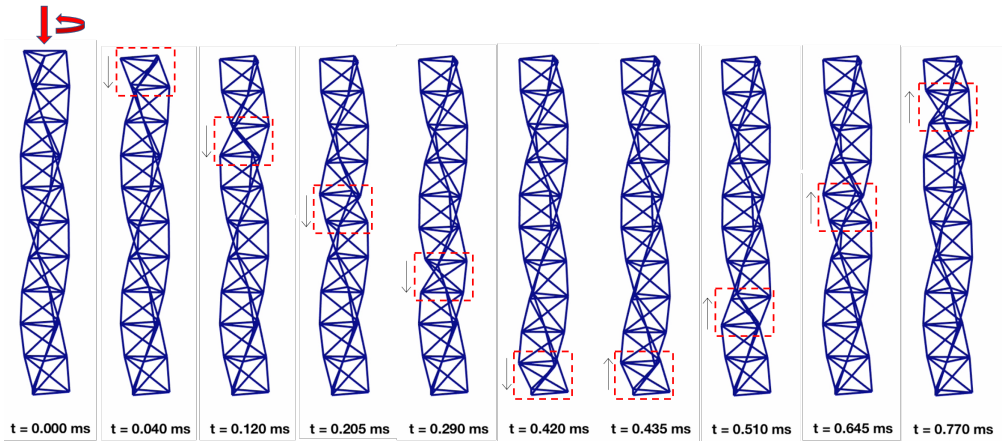

Figure 3.11: Snapshots extracted from the video of the motion of a column of ten bistable prisms impacted with initial vertical and angular speeds at the top base (see also Video S7 [401]).

the propagation of a compression wave localized on a single prism (enclosed by the red dashed rectangle in Figure 3.11), with negligible motion of the rest of the column, under the examined loading condition. The reader is referred to the Video S7 [401] of Supplementary Materials for an animation of the motion of the structure illustrated in Figure 3.11. The response of the benchmark bistable structure under examination highlights that the use of highly nonlinear tensegrity systems with nanoscale features may allow the creation of revolutionary types of acoustic lenses, to be used as a noninvasive scalpel to accurately target defects in engineering and biological materials. Micro- and nano-scale tensegrity lattices with bistable responses (acting as phononic crystals) can indeed be employed to generate compact-support waves within tensegrity acoustic lenses [269, 82], which may travel and coalesce at a focal point in an adjacent medium (i.e., a material defect or a tumor mass in a host medium). A comprehensive study on this exciting, novel application of micro- and nano-scale tensegrites with a bistable response is addressed to future work. Furthermore, the structures analyzed in this paper utilize marked tunability (due to geometry and prestress) and scalability (size-independent properties) to go beyond conventional systems. The scalability property derives from the geometric nature of the bistable response, and the material nature of the viscous behaviors observed in the experiments. The mechanical modeling presented in this study can be applied down to the scale at which Van derWaals forces can be neglected, (several angstroms, see, e.g., [233], where tensegrity structures with strut length of 65 nm have been studied) A bistable viscous response can also observed in the macro-scale tensegrity structure shown in Video S8 of Supplementary Materials, which shows $20cm$ timber struts connected with flexible polyvinyl chloride (PVC) tubes. In addition, it must be noted that this work paves the way for the fabrication of tensegrity systems comprised of different polymeric materials. Even though this process requires specific photochemical properties to achieve

such a high resolution [299], new materials must be employed that encompass hyperelastic behavior. Consequently, structures sustaining large deformations and repeatability of the loading under multiple cycles without failure could be realized.

Section Conclusions

The bistable response of tensegrity structures made of three-dimensional assembles of tensegrity prisms was investigated in microscale structures equipped with nanoscale features. The modeling of the mechanical behavior of such structures provided guidelines for the fabrication of multi-cell systems featuring bistable responses under compression loading. MPL combined with diffusion-assisted high-resolution direct femtosecond laser writing enabled the efficient fabrication of unit cells and arrays comprised of struts with $250nm$ radius. Microindentation experiments assisted by scanning electron microscopy imaging provided the in situ observation of nanoscale deformation phenomena and how they are reflected in the macroscopic force-displacement curves. Overall, the results presented in this work showed that the analyzed structures, which are comprised of all bar members, combine a bistable response; viscoelastic behavior; and softening and stiffening deformation mechanisms. In addition, helium ion microscopy elucidated the unblemished fractured morphology of the structures in nanoscale, insinuating brittle fracture as the primary fracture mechanism, regardless of the macroscopic ductile behavior. These findings set the framework for the design and characterization of nanolattice structures governed by bistability for a variety of applications, with a particular focus on pioneering approaches to sound focusing through compact solitary waves [123, 269, 78].

3.2 Investigating the Mechanical Response of Microscale Pantographic Structures Fabricated by Multiphoton Lithography

Section Summary

In section we aim to expand the study of microscale pantographic structures and investigate their utility as a hyperelastic structure in microscale. More specifically, through MPL, we fabricate a push to pull out mechanism to achieve tensile tests by applying compression to the structure [24]. MPL enables the fabrication of pantographic unit cells, with fixed beams and pivots. Through in situ SEM – microindentation experiments we are able to observe deformations in the nanoscale regime. In addition, we can juxtapose the mechanical performance with the macroscopic force displacement response and the dominating deformation modes in the structure. Furthermore, we perform finite element analysis (FEA) simulations to evaluate the sensitivity of the mechanical response to the geometrical parameters of the unit cell. We prove that the experimental response of up to 25% deformations of panto-

graphic unit cells can be modelled through hyperelasticity, even though the base material is not hyperelastic. These findings aim to accentuate the characterization and modeling of pantographs in microscale for applications that necessitate nonlinear elastic deformations and pave the way to incorporate specimens fabricated by MPL in this endeavor.

FEA Modelling of Microscale Pantographs

The design of the pantographic unit cells is delineated in Fig. 3.12(a). The unit cells are comprised of beam members of width w_b and height h_b oriented at 45^o with respect to each other. Each beam is connected with the proximal one through three pivots at the edges and its center. The pivots have radius r_p and height h_p. While in macroscale pantographs the pivots can enable the rotation of the beams through angular sliding [86], this mechanism cannot be realized in microscale with MPL. The reason for this constraint is that the material is polymerized through subsequent laser beam scans and the respective components are not assembled together. Hence, in our design, the specimen is fabricated with fixed beam supports. Nevertheless, as we will show later, the pivots still dominate the mechanical response. Since the in-situ microindentation testing can only be conducted for compression measurements, to realize tensile tests an expedient mechanism needs to be utilized. To accomplish this, we employed a push to pull out mechanism that has been previously employed for tensile specimens in microscale [24]. Specifically, the unit cell is attached at one end on a base that is fixed to the substrate and at the other end on a rectangular base that can be translated under compression, thus enabling the manifestation of tensile deformation on the tested structure. Fig. 3.12(b) demonstrates the FEA simulation of the mechanism under compression of the upper base. It is shown that the deformation field has a constant and uniform distribution on the mechanism. Therefore, the mechanical response of the unit cell is impervious of localised deformation effects that would be caused by the tensile mechanism. Therefore, conducting such measurements will not distort the actual behavior of the pantographic structure.

In order to numerically investigate the mechanical behavior of the microscale pantograph in this study, FEA simulations were performed using the commerical FEA software COMSOL Multiphysics®. A characteristic 3-D FEA model of the microscale pantograph with pivot radius $r_p = 1.35\,\mu$m, pivot height $h_p = 0.6\,\mu$m, beam width $w_b = 1.25\,\mu$m and beam height $h_b = 0.5\,\mu$m was generated and is precented in Fig. 3.12(c). A hyperelastic model available in COMSOL Multiphysics®, namely the Yeoh model, was adopted in the simulations. In this model, the strain energy density is defined as follows

$$W = c_1(I_1 - 3) + c_2(I_1 - 3)^2 + c_3(I_1 - 3)^3 \tag{3.1}$$

where c_1, c_2 and c_3 are the material parameters of the constitutive equation and I_1 is the first invariant of the Cauchy-Green deformation tensor $\mathbf{C}$. The main reason that the Yeoh model was selected is that the mechanical behavior of pantographic structures seems to be described fairly well compared to other hyperelastic models, as it has been highlighted in

previously reported work [437]. Accordingly, the 2nd Piola-Kirchhoff stress tensor can be calculated by the following equation

$$\mathbf{S} = 2\frac{\partial W}{\partial \mathbf{C}} \tag{3.2}$$

Hence, the stress field and the displacement field in the structure can be calculated by solving the corresponding boundary value problem of the linear momentum balance. As it will be discussed later, even though the Yeoh's model has been employed for macroscale specimens, it can also capture the convex behavior of the microscale results, while other tested models such as the Neo-Hookean or Mooney–Rivlin hyperelastic constitutive models could not capture the experimental results. The numerical computations were conducted with a mesh of 90,235 tetrahedral elements and 351,255 degrees of freedom. To simulate the tensile test of the specimen, a 2.5 μm displacement was applied in a stepwise manner, and the material parameters were taken as follows: $c_1 = 3.29 \times 10^9$, $c_2 = 2.02 \times 10^{10}$, and $c_3 = 6.10 \times 10^{10}$. As it will be explained in the next section, the numerical values of these parameters were selected based on a parametric analysis to match the experimental results. An iterative process was addressed to obtain the material parameters. Hence, the presented values were found to closely match the experimental results. As it will be described next, these paprameters were also employed to conduct a sensitivity analysis in the specimen by varying the dimensions of the characteristic geometric parameters of the unit cell. The force-displacement behavior was obtained through the integration of the reaction forces at the fixed end of the specimen for each corresponding displacement. In Fig. 3.12(c), the calculated von Mises stresses are presented when the displacement is equal to 2.5 μm.

Fabrication and Testing

To evaluate the designed tensile response of the modelled pantograph, benchmark test structures were fabricated by MPL, presented in Fig. 3.13. The experimental apparatus utilized for this process has been reported in previous work with respect to the fabrication of microscale metamaterial structures [395]. It has also been demonstrated in the previous section. More specifically, the fabrication conditions for the preparation of the samples were 2 mW output laser power of a Ti:Sapphire femtosecond laser (FemtoFiber pro NIR) and 10 μm/s scanning speed for the stages that translate the sample such that the laser beam can "write" the geometry into the photoresist. Since each laser pulse creates a voxel of polymerized material, the laser beam was passing through the same direction at least four times to increase the rigidity of the structures. The material that was used is the commercial photoresist SZ2080TM, originated from FORTH. The fabrication conditions were selected such that the viscous effects of the material are diminished based on material characterization that has been reported elsewhere [119]. Further details about the preparation of the material can be found elsewhere [299]. Fig. 3.13(a) shows multiple specimens fabricated in the push to pull out mechanism (Fig. 3.13(b)). The dimensions of the unit cells match the ones of the simulations that were provided in the previous section to calculate the material parameters. Fig.

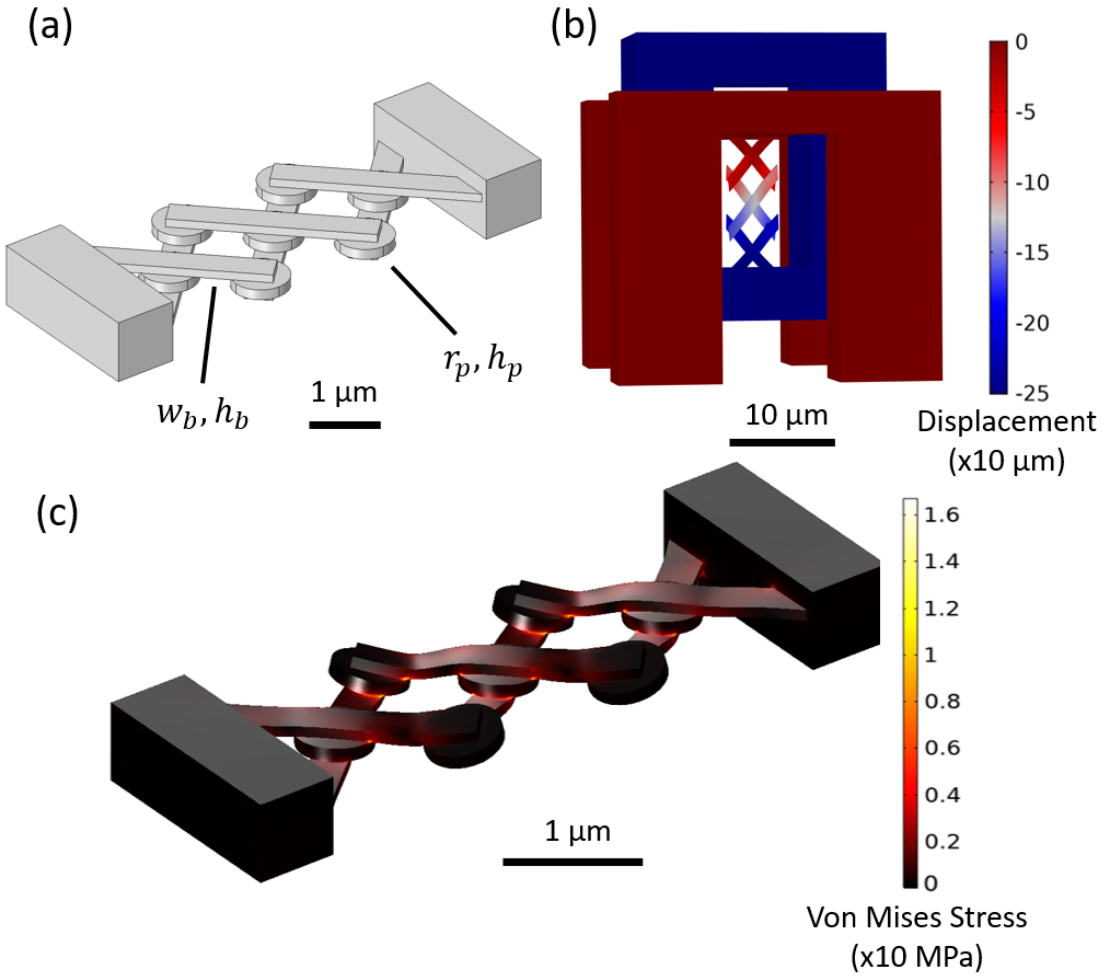

Figure 3.12: Modelling of microscale pantographic structures. (a) The pantographic unit cell, comprised of beam members with width w_b and height h_b, arranged on two planes and with relative angle 45^o. The beam members on the two planes are connected with a pivot of radius r_p and height h_p at the center and the edges of the beams. (b) FEA simulation of the pantographic unit cell on the tensile mechanism. The two parts of the mechanism have a uniform displacement, ensuring that they do not affect the mechanical response of the unit cell. (c) FEA simulations of the panotgraphic unit cell under tension. It is observed that the maximum stress of the specimen is localized in the pivots, dominating the mechanical response of the material through torsion.

3.13(c) shows the side of one of the specimens demonstrating the pivot dimensions (Fig. 3.13(d)). Fig. 3.13(e) shows the pantographic unit cell detached from the tension mechanism, illuminating that all of the beam members and pivots have the same dimensions,

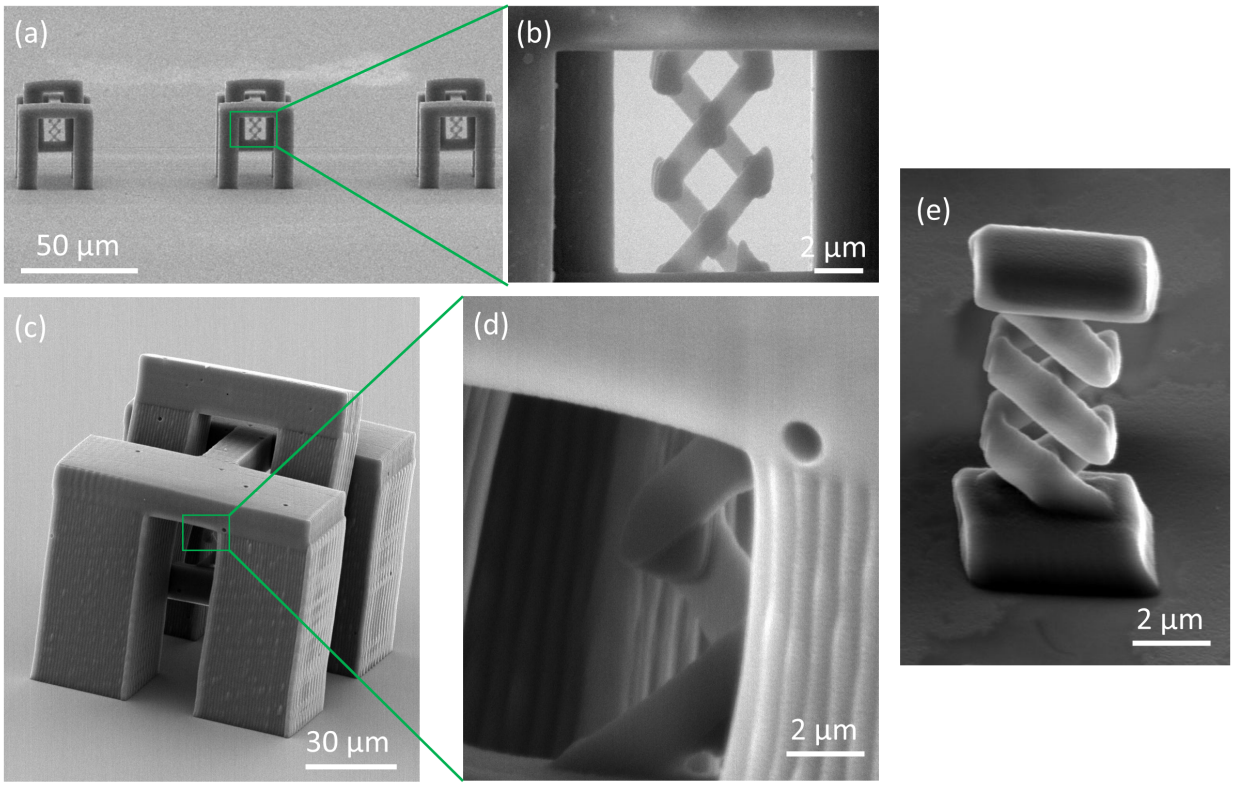

Figure 3.13: Fabricated micropantographic specimens through MPL. (a) Front view of frabricated unit cells in the tensile mechanism. (b) High magnification image of the unit cell. (c) Side view of the specimen, showing the thickness of the pivot and the two parts of the tensile mechanism. (d) High magnification image of the pivot to verify that the dimensions are in agreement with the fabrication parameters and the simulations. (e) The pantographic unit cell without the tensile mechanism, showing the connection of the beam members on the two different planes through pivots at the edges and the center.

respectively.

To conduct the mechanical experiments, nanoindentation experiments were performed. The nanoindenter (Hysitron P188 SEM PicoIndenter, Bruker), which is mounted inside an SEM, was applying a compressive force to the top base of the structure, pulling it downwards and applying a tensile deformation to the unit cell. The specimens are positioned such as the front view is visible from as in Fig. 2b to enable the in situ observation of the deformation of the unit cell. To avert any strain rate effects during the deformation of the material, the specimens were loaded with a constant rate of 10nm/s until 25% uniaxial strain. The range of the deformation was selected to be congruous with the dimensions of the tensile mechanism. Higher tolerance in the translation of the upper base would precipitate tilting

and out of plane deformation, tottering the unit cell and providing egregious experimental results. To ensure that the experimental results are repeatable, eight specimens were tested five times each, and the average curve of all the results was obtained. The strain rate was selected to obstruct the development of any instantaneous viscoelastic effects in the material and reassure the feasibility of the theoretical model. The loading and unloading stages of the specimen revealed extremely small close loops, which were on the verge of statistical error that the indenter can capture. In addition, close observation of the recorded videos showed that the specimens were returning to the initial equilibrium position before loading was applied.

Results and Discussion

To evaluate the mechanical response of the tested specimens, it is critical to comprehend the mechanical response that was observed in the FEA simulations. Figure 3.12(c) shows that the highest stress distribution is emerged at the pivots, while the von Mises stress at the other members of the specimen is minuscule. This result alludes that the geometric properties of the pivots must have an imperative role to comprehend the mechanical behavior of pantographic structures and they must be the dominating constituents in the mechanical response. Consequently, to obtain a better understanding regarding the mechanical behavior of the structure, a sensitivity analysis was performed with respect to the four main geometric properties, namely the pivot radius (r_p), the pivot height (h_p), the beam height (h_b), and the beam width (w_b). This analysis may also be useful to provide an exegesis regarding discrepancies that may occur due to the printing and testing processes regarding variations in the dimensions of the printed specimens. In each case, the targeted parameter was varied while the other parameters were preserved fixed, and using the same material parameters given in the previous section in all of the simulations. The obtained results for the sensitivity analysis are presented in Fig. 3.14. In Figs. 3.14(a) and 3.14(b), the obtained force-displacement curves are presented with variation in the pivot radius and the pivot height, respectively. The stiffness of the pantographic structure decreases significantly with decreasing the pivot radii, and ostensibly, the concavity of force-displacement curves changes with lower values of the pivot radius.

Especially for $r_p = 0.6$ and 0.4 μm, the force-displacement curves are concave up as opposed to the concave down curves obtained for higher values of pivot radius. To show this, each curve was curve fitted by a second polynomial and its linear part is plotted by dashed lines in Fig. 3.14(a). This conveys that the curves diverge from linearity and the value of the second derivative shifts the convexity of the curve from one verge of the line to the other. Even though the R^2 is close to 1 for all of the curves, a second degree polynomial curve fitting should only be employed to convey the variance of the convexity and not for any other physical interpretation of the simulation result. As it is expected, a decrease in the height of the pivot will lead to a stiffer behavior for the pantographic structure, as it is observed in Fig. 3.14(b). Even though the variance of the pivot height is ranging between 1.2 μm and 0.4 μm, the differences in the computed reaction forces are not as significant as

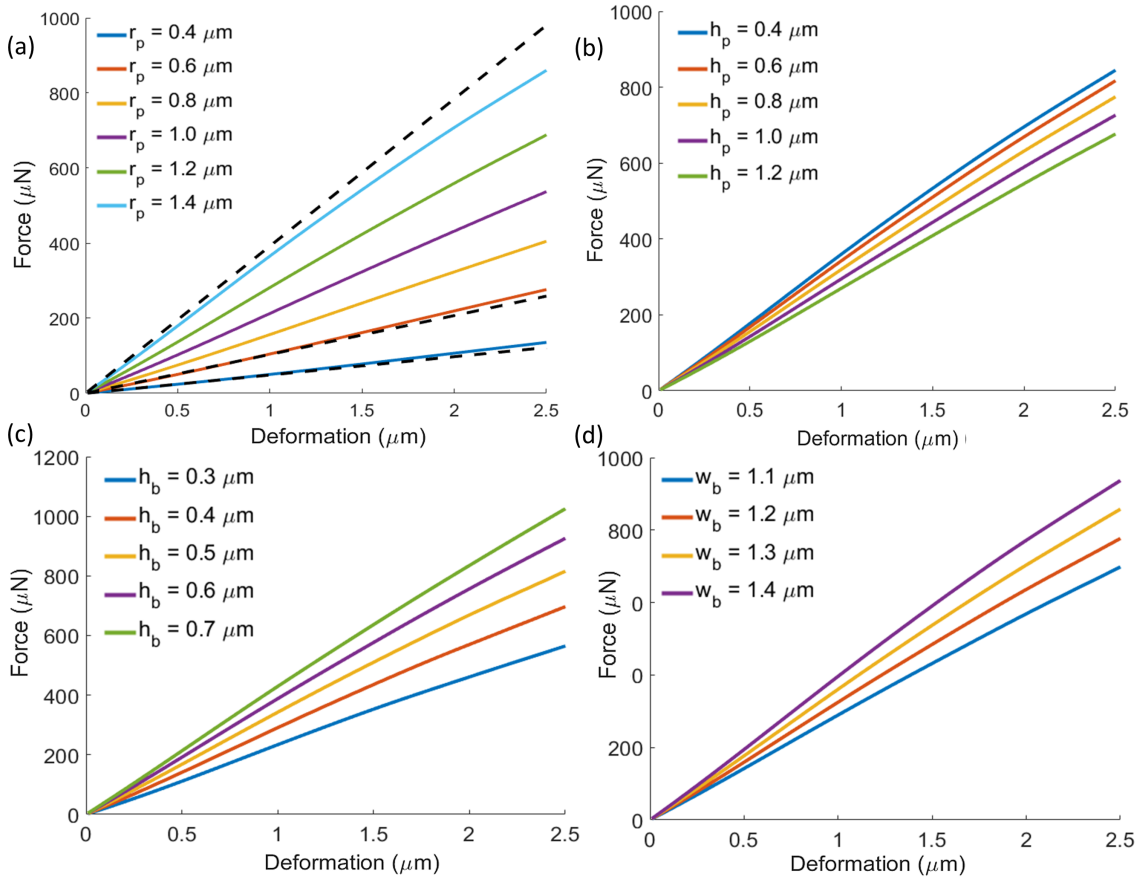

Figure 3.14: Sensitivity analysis of the mechanical performance based on the geometric parameters. (a) Variation of the mechanical response due to different pivot radii. It is observed that the response is highly sensitive to the radius, with substantial variation in both the magnitude and convexity of the force-displacement curve, since the torsion of the pivots dictates the mechanical response. The dashed lines are the linear part (i.e. the second derivative) of a second degree polynomial that was used to curve fit the simulation results. For $r_p = 0.4$ the second derivative is 2.38, while for $r_p = 1.4$ the second derivative is -17.30. (b) Variation of the mechanical response due to different pivot thicknesses. The response is not highly sensitive to the thickness, since significant variation will be discernible for longer pivots. (c) Variation of the mechanical response due to different beam heights. There not commensurate sensitivity with the pivot radius. since the beams rotate due to the pivot deformation. (d) Variation of the mechanical response due to the beam length. Again, since bending of the beam members is not the dominant mechanism, the response is not highly sensitive to the variation of the length.

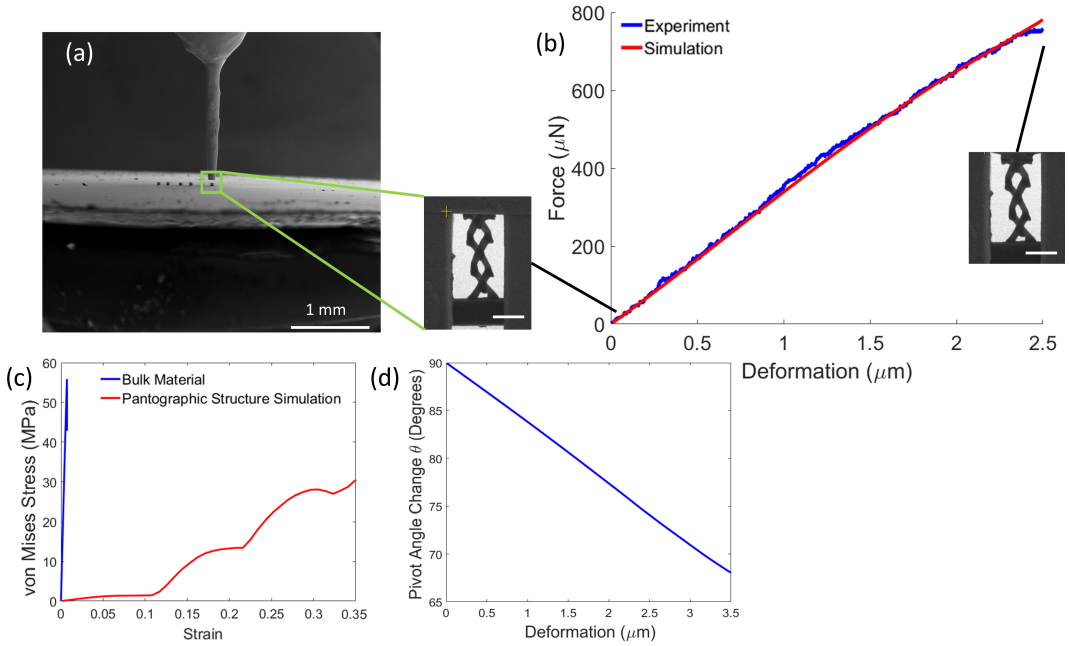

Figure 3.15: In-situ microindentation testing on the fabricated specimens. (a) Far front view of the specimens next to the indenter right before the testing inside the SEM. (b) Comparison of the average experimental curve with the FEA simulations until 25% deformation. There is close match between experiments and simulations, elucidating that the Yeoh hyperelastic model can delineate the mechanical response of the microscale pantograph. (c) Comparison of the von Mises of the bulk material in juxtaposition with the FEA simulation of the pantographic structure for 35% deformation. The bulk material demonstrates brittle behavior and linear elastic response, whereas the pantographic structure can sustain stresses below the strength of the material at a significantly larger regime of deformations. (d) The angle variation between two perpendicular material lines at the pivot. The manifestation of large deformation is caused by the large rate of angle change of the pivot which is ~ 32 degrees at 35% deformation.

the variance in the behavior that is observed for the variation in the pivot radius. Moreover, in Figs. 3.14(c) and 3.14(d), the results are given for variation in beam height and beam width, respectively. It is evident that the variation of the geometric parameters associated with bending do not lead to substantial changes in the resulted force-displacement curves, corroborating the dominance of the pivots in the resulted mechanical response. Hence, as in macroscale pantographs, bending is not the driving mechanism, but instead the torsion of the pivots.

Figure 3.15 shows the tested specimens and the resulted force-displacement curve. As it is shown in Fig. 3.15(a), a compressive load is applied by the indenter to the tensile mechanism and the SEM is focused on the pantographic unit cell. A representative video recording of the testing is provided in the the published version of this chapter [403]. The specimen is loaded under 25% uniaxial deformation and then it goes back to the reference configuration. Figure 3.15(b) shows the comparison between the experimental result and the numerical simulation employing Yeoh's hyperelastic model.

Our results show a close match between the experiments and simulations, validating the hyperelastic behavior of microscale pantographic structures for this range of deformation. A careful observation of the experiments also illuminated that the dominant mechanism is torsion in lieu of the bending of the beams, a result that is consonant with the FEA simulations. Hence, based on both the numerical and the experimental results, bending is not the dominant mechanism for the examined microscale pantographic structure. Therefore, the control of the mechanical behavior for these types of structures should solely focus on the geometry of the pivot. This result shows that even though the pivots are fixed in MPL fabrication, the capability of the pantographic structure to possess hyperelastic behavior is also feasible at the microscale. To put this mechanical performance into perspective, the behavior of the bulk material was also evaluated. The experimental result of the von Mises stress as a function of the strain for the bulk material, along with the deformation of the structure that was simulated up to 35%, are presented in Figure 3.15(c). It is evident that the bulk material possesses brittle linear behavior that can sustain stress equal 55.89 $\pm$2.95 MPa at strain 0.7% when fracture commences. This response is consistent with the fabrication conditions we employed in our previous work and the fractographies that revealed brittle fracture [392]. However, the simulation of the pantographic structure shows that the von Mises stress reaches 30.5 MPa, enabling the structure to possess irreversible deformations without failure. Thus, despite the fact that the material used in MPL is not hyperelastic, the response of the pantographs can be modelled with Yeoh's hyperelastic model.Furthermore, the deformation of the pivot was evaluated to assess the effect of the rotation on the deformation of the structure. The simulation result is demonstrated in Figure 3.15(d). The angle θ is the angle between two material lines on the pivot that are perpendicular (90^o) in the undeformed configuration. It is shown that the angle variation is linear throughout the deformation of the structure, rising to 32 degrees at the maximum deformation. Hence, larger dimensions on the pivot can result in an abrupt change of the deformation, a result which is consistent with the effect of r_p conveyed in Figure 3.14(a) and the initial assumption of the physical mechanism. Nevertheless, pantogaphic structures can be deformed at even higher

deformations as it has been presented in previous work [364, 443], reaching 85% reversible deformation. To experimentally realize these remarkable results, larger specimens comprised of hundreds of beam members must be fabricated. Hence, more advanced techniques in MPL microfabrication should be employed [195], providing a new avenue to study the hyperleastic behavior of architected metamaterials. However, the analysis of the mechanical performance at even smaller length scales would be of cardinal significance. More specifically, techniques such as pyrolysis, as it was addressed before [23], and stimulated emission depletion MPL [427] enables the fabrication of members at a few tens of nm. It must be pointed out that the pantographic behavior of the examined structure is based on the particular arrangement of the constituent elements that allow, in the ideal case, a relative motion between them without any expense of energy. This instance is also known as a floppy mode. This peculiarity can be described at a proper observation level with a second gradient continuum model if many unit cells of such a pantographic mechanism are assembled to create an array. Nonetheless, a first gradient model can be employed at the constituent elements level. The asymptotic homogenization procedure illuminates how the constitutive parameters at the macroscopic level are to be determined in terms of the constitutive parameters at the micro-level [86]. The rescaling laws of micro-constitutive parameters, depending on the size of the homogenization cell, are determined to provide the onset of second gradient effects at the macro level. Specifically, for pantographic sheets, and if ϵ denotes the distance between the closest pivots, the rescaling that characterizes 2D continuum models requires that the beam bending stiffness, the beam extensional stiffness, and the torsional stiffness of the pivots must rescale respectively with ϵ^0, ϵ^0, and ϵ^2. Hence, the torsional stiffness of the pivots must be very weak compared to the bending stiffness, and the bending stiffness must vary with epsilon along with the extensional stiffness. Therefore, when the aforementioned rescaling laws are followed and until classical mechanics is applicable such that nanoscale effects do not play a relevant role, then the presented modeling can be used regardless of the size. When the overall scale of the structure is dramatically decreased to scales close to nm, second gradient continuum models are still valid in principle. However, the scale reduction may have another important consequence even when the theory of classical mechanics remains applicable: the inner substructure of the bulk material constituting the pantographic micro-structure, depending on the particular technological process used for constructing it, could have a characteristic length comparable with one of the constituents. Then, the model required for the micro-constituents could be dependent on nanoscale mechanics or, if classical mechanics applies, to second or higher gradient continuum mechanics. Experimental results [226] at the nanoscale have revealed that higher gradient continuum models can be utilized. Albeit there are no general homogenization results producing second gradient continua from complex micro-structures, some nascent results have been demonstrated [41]. These findings provide us the threshold to reach the following conjectures: 1) Higher-order continua can be obtained at macro-level only when periodical cells are interacting in such a way that any periodic boundary condition for each cell countervails potential higher gradient effects; 2) macro-boundary conditions at the current boundary of the structure must regard the interaction between the external environment and some cells that are not on the boundary

but at a distance of several cells inside, depending on the higher gradient appearing in the deformation energy; 3) to employ higher gradient continua, at the macro level, it is necessary to have high contrast in micro-stiffnesses. Rigorous Gamma-convergence results have been obtained [6], proving that the three listed conjectures are reasonable in the particular case of linear pantographic beams. Moreover, assembling many cells produces a structure described at the overall observation scale as a complete second gradient 1D continuum model [21]. From this perspective, the implemented boundary conditions can be interpreted as the imposition of a displacement on the ends of the structure, to which a constraint on the strain must be added at the same locations. At the scale of the constituent elements, the particular geometry produces a triple-hinged arch at the ends of the structure that is rather stiff. Therefore, the points in correspondence of the triangle wedge have a minimal displacement, and consequently, the overall elongation in these extreme zones is negligible.

In addition, other designs that require large but recoverable deformations, such as bistability [332] should be investigated with respect to the utility of pantographic structures in complex 3D deformations [348]. In the literature such designs are defined as deployable scissor grids [340]. These structures are comprised of the same geometrical constituents as the pantographs of this study and they can possess complex and multiple equilibrium positions even with 3D deformation modes. Characteristic designs have been incorporated in cellular graphene for energy storage and polymer composites for highly wear resistant devices [235]. Despite the fact that a certain degree of stability can be accomplished with fixed pivots, future work should also focus on the improvement of the MPL process such that rotation-free pivots can be accomplished. In addition, since the MPL encompasses a directionality in the fabrication of polymerized structures through subsequent laser scans, this leads to an inherent "fiber-like" pattern in the microstructure of the material. Hence, for specimens comprised of multiple unit cells, higher gradient elasticity could also be realized, as in the macroscale [86]. Therefore, higher gradient elasticity could be employed as a design tool to model MEMS devices and soft microrobotic mechanisms. Specifically, force-sensitive 3D microgrippers have been fabricated by MPL, enabling the precise grasping of minuscule objects through the deformation of helical microsprings [324]. In micro surgical operations that require substantially higher elongation of the instruments, the hyperelastic behavior of the pantographs would prove to be an instrumental repertoire to design such devices. Finally, light-controlled soft microrobots fabricated by MPL can be employed for cell regulation of transfer of microscale specimens [300] at different locations of a large device or even an organ. Encompassing hyperelasticity in such devices will render them more versatile without the constraint of small strains or high material volume to accommodate the required stresses to perform complex tasks.

Section Conclusions

In summary, the hyperelastic behavior of microscale pantographic structures was investigated. FEA simulations along with performed in situ SEM - microindentation tensile tests provided insight into the mechanical behavior of pantographic unit cells. Even though the

MPL enables the fabrication of fixed pivots, their torsional response is the dominant mechanism and can still embrace the mechanical response of pantographs observed in macroscale. In addition, it was elucidated that the deformed structures can obtain large reversible deformations, leading to 25% reversible deformation. This hyperelastic behavior can be modelled through Yeoh's hyperelastic model, even though the photoresist material is not hyperelastic. Our findings promulgate the utility of pantographs for microscale applications requiring hyperlastic behavior and just through the utility of the the MPL process without any additional fabrication process or materials.

3.3 Design and Characterization of Microscale Auxetic and Anisotropic Structures Fabricated by Multiphoton Lithography

Section Summary

In this work, the nascent results towards the construction of functional mechanical metamaterials microstructures are presented. First, we investigate the mechanical properties of the bulk material used in MPL. Using these data, we conduct finite element analysis (FEA) simulations to evaluate the designs and control the fabrication parameters. Then, we fabricate a series of auxetic devices based on the re-entrant triangular design and characterize their composite material. Finally, we propose a new geometry which can act as a vertical displacement spring. Through in-situ scanning electron microscopy (SEM) nanoindentation experiments, we test and validate the response of the tested specimens. Our results and methodology present a design strategy that can be utilized in the modeling, fabrication and testing or microscale auxetic and anisotropic metamaterials for biomedical applications.

Materials and Methods

Nano-Dynamic Mechanical Measurement and Analysis (Nano-DMA)

The mechanical properties of the employed resin after photopolymerization were characterised using a TI 950 TriboIndenter (Bruker, Eden Prairie, MN, USA) to conduct nano-DMA experiments, a dynamic testing technique equipped with continuous measurement of X (CMX) control algorithms that provide a continuous measurement of mechanical properties as a function of indentation depth, where X can be hardness H, storage modulus E', loss modulus E'', complex modulus E^* and the mechanical damping $tan\delta$. The technique can be applied from ultra-soft hydrogels to hard coatings, with a greatly improved signal to noise ratio. Dynamic testing can be performed in a range of frequencies between 0.1–300 Hz. A quasi-static force, up to 10 mN, is applied to the indentation probe while superimposing a small oscillatory force of 5 mN maximum. A lock-in amplifier measures phase and amplitudes changes in the resulting force-displacement signal. To obtain the viscoelastic properties the

material is modeled as two Kelvin -Voigt systems in parallel, with one end fixed and applying the indenters force to the other. This model requires four viscoelastic parameters to calculate the moduli of the material, providing highly accurate results compared to the simple Maxwell model or even the Standard Linear Solid [117]. More specifically, a Berkovich 142.3^o 50 nm tip radius nanomechanical probe was utilized to apply a 5 Hz periodic load on cubic $40 \times 50 \times 50 \times \mu m^3$ samples of DMAEMA 10% with 10 nm amplitude to calculate the hardness, the loss modulus and the storage modulus of the viscoelastic response. Each measurement was conducted on specimens fabricated with different fluence to investigate the effect of the laser on the mechanical properties of the photoresist. For repeatability of the measurements, each specimen was tested at least 10 times on locations at least $0.5\mu m$ away from the previously indented location to avoid the distortion of the results due to stress localization.

In-Situ SEM -Microindentation Experiments

To evaluate the mechanical performance of the fabricated architected structures, micromechanical measurements we conducted utilizing the nanoindentation apparatus (PI 85 SEM PicoIndenter, Hysitron, Bruker, Eden Prairie, MN, USA), positioned inside the chamber of a scanning electron microscope (Quanta 3D FEG, FEI, Hilsboro, OR, USA) for high precision measurements with extremely low noise to amplitude ratio. The mechanical measurement was recorded using the Hysitron Triboindenter software that is used to control the indenter. A flat tip (model 72SC-D3/035 (407A-M)) of $120\mu m$ diameter was used in all the compression tests. The glass substrates on which the specimens were fabricated were fixed onto an SEM pin stub mount (TED PELLA, Redding, CA, USA) with PELCO® Pro C100 Cyanoacrylat te Glue, (TED PELLA, Redding, CA, USA). Each structure was deformed at a rate of 250 nm/s to a maximum compressive strain of $10\mu m$ and immediate unloading such that the development of viscoelastic phenomena is hampered. To validate the repeatability of the tests, at least 8 measurements were conducted on each different design. To evaluate the mechanical performance, the measured force-displacement curves were compared with the recorded deformation to distinguish any blatant variation in the mechanical performance that is reflected in the measured curves. To evaluate the Poisson ratio of the bulk material, cylinders of $70\mu m$ height and $8\mu m$ diameter were compressed and the transverse to axial strain ratio was measured by capturing the SEM image of the deformation.

Results

Nanomechanical Characterisation of the Photoresist

The mechanical properties of the photopolymerized composite were evaluated using the mechanical characterization procedures presented in the methods section to quantify its hardness H, storage modulus E', loss modulus E'' and Poisson's ratio ν, as a function of the fabrication laser fluence. Arrays of cubes and cylinders were fabricated with laser fluence

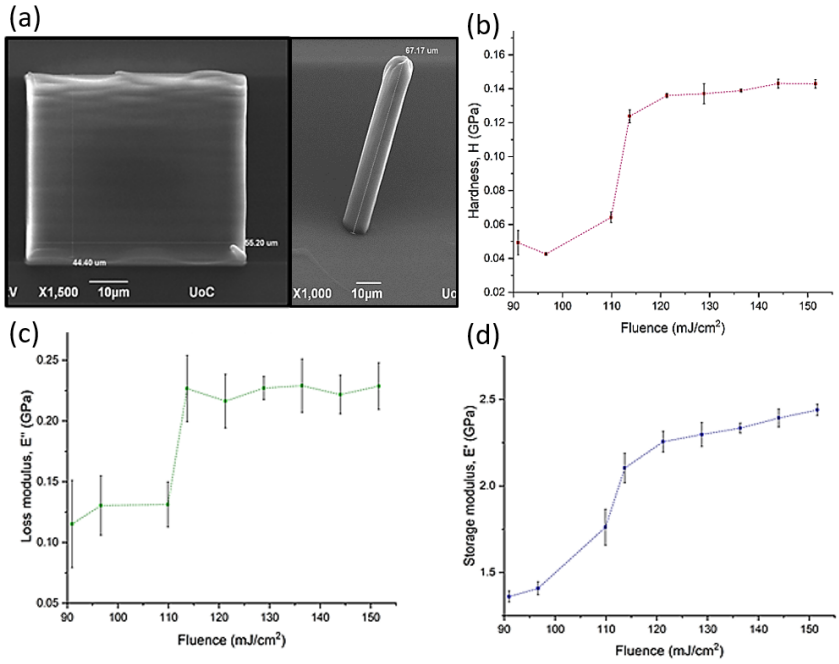

Figure 3.16: SEM images of the cubes and the cylinders used for the evaluation of the mechanical properties, (b) Hardness(red line) vs. fluence, (c) Loss modulus (green line) vs. fluence, and (d) Storage modulus (blue line) vs. fluence. The abrupt change at $\sim 110(mJ/cm^2)$ is attributed to the printing strategy followed.

ranging from $90-150(mJ/cm^2)$ to evaluate the properties of the material, as it was analyzed in the previous section. All structures were fabricated with a scanning speed of $10\mu m/s$ at the Galvo-scanner system. The measurements were conducted and analyzed utilizing nano-DMA, as it was described earlier. The cubes were used for the measurement of H, E' and E'', while the cylinders were used for the measurement of Poisson's ratio, by using an additional high-speed camera to accurately capture the structures' deformation. The plots of H, E' and E'' with respect to laser fluence are shown in Figure 3.16.

It is evident that a transition takes place at the vicinity of $110(mJ/cm^2)$. As it has been discussed previously [119], this material behaviour is attributed to the polymerization threshold and the fabrication strategy which was followed. A line-by-line hatching strategy was used for each structure, with a $\sim 200nm$ distance between the centers of parallel lines. As the laser's pulses have a repetition rate of 80 MHz and the laser beam is scanned at a $10\mu m/s$ speed, the duration between consecutive laser pulses in the order of $1pm$. Thus, the test samples consist of densely cross-linked plates and the less dense non-polymerized material between them, which has a cross-link density dependent on the photon flux of the laser beam. Above a certain laser fluence, approximately at $\sim 110(mJ/cm^2)$ in this case,

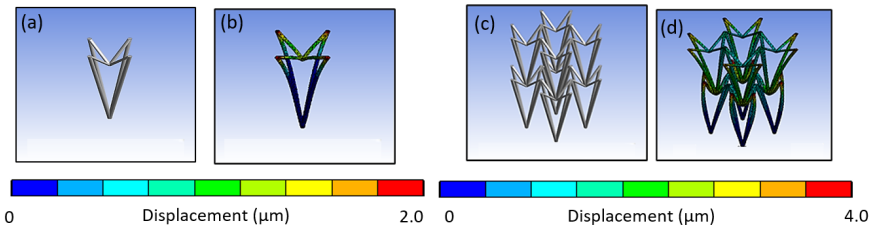

Figure 3.17: FEA simulations of the re-entrant triangular unit cell. (a) The undeformed unit cell, (b) A compression in the lateral direction causes compression of the beam members in the transverse direction, (c) An undeformed $2 \times 2 \times 2$ lattice, and (d) Compression along the lateral direction causes a clearly more visible compression of the beam members in the transverse direction. Thus, the possession of auxetic behavior is scalable to an array of unit cells.

the cross-linking density saturates and can no longer increase.

In addition, the Poisson's ratio was found to be independent of the laser fluence and have a constant value of 0.490 ± 0.002. This finding can be adduced to expound that DMAEMA 10% behaves like an incompressible material.

Auxetics Metamaterials

In this study, the re-entrant triangular unit cell, a thoroughly studied auxetic geometry [438], was investigated. The behaviour of the unit cell and a $2 \times 2 \times 2$ lattice can be seen in the FEA simulations of Figure 3.17. All of the simulations were performed with Ansys R18 and conducted in the linear elastic domain, using 3D–10–node tetrahedral solid elements. Specifically, the single re-entrant triangular unit cell is comprised of 5529 nodes and 2428 elements. The array is comprised of 13532 nodes and 4536 elements. To match the loading conditions of the experimental setup, the bottom intersection of the unit cells was fixed, while the top intersections were set to a displacement of $2.0\mu m$ and $4.0\mu m$, respectively. Under axial compression, lateral compression also occurs, resulting in a negative Poisson's ratio. By measuring the maximum strain in the lateral and transverse dimensions, the ratio is close to -1 for both cases. However, it is observed that in the array there is more excessive deformation on the middle node, resulting in a more abrupt effect at the intersection of the layers. Under axial compression, lateral compression also occurs, resulting in a negative Poisson's ratio. Fabricated structures based on this geometry could be used as tunable filters (Figure 3.18) and auxetic stents (Figure 3.19). Both structures were realised using the Nano-Cube setup with a laser fluence of $90(mJ/cm^2)$ and $100\mu m/s$ scanning speed. The unit cell of the filter is $\sim 10\mu m$ and the stent is $\sim 5\mu m$. The diameter of the entire stent is $\sim 50\mu m$.

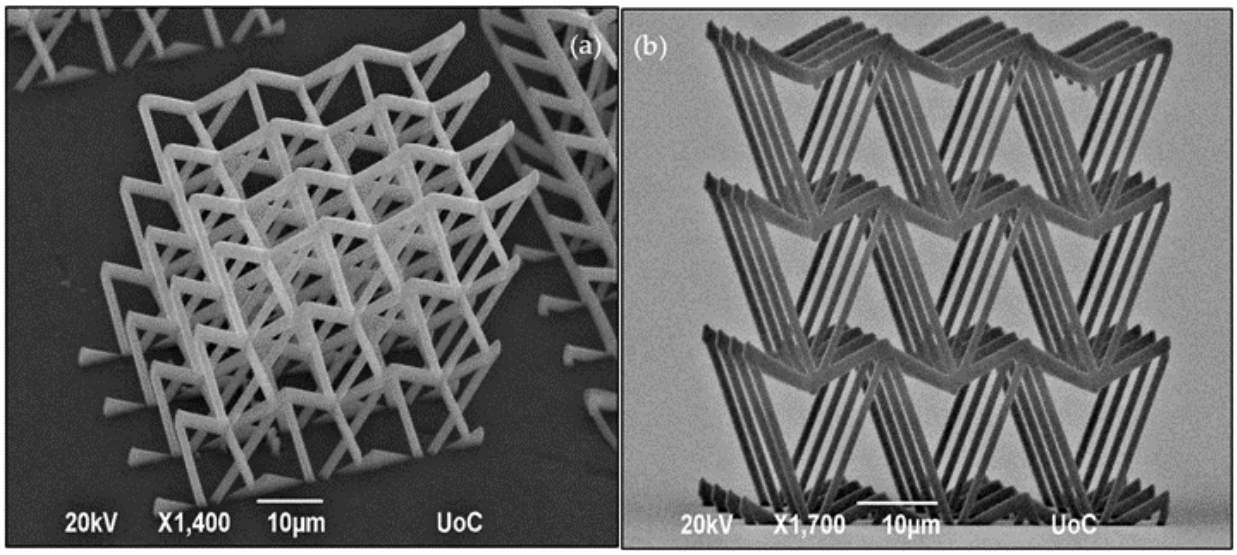

Figure 3.18: SEM images of the 2D tunable filter comprised of the re-entrant triangular fabricated using Nano-cube at $90(mJ/cm^2)$ laser fluence and $100\mu m/s$ scan speed. (a) Perspective view, and (b) Side view.

Chiral Mechanical Metamaterials

Chiral mechanical metamaterials exhibit a rotational response, perpendicular to their main axis, when an axial force is applied along it [125, 338]. Properties such as this, of described as "mechanical activity" (corresponding to optical activity in optics), are the result of geometrical optimization, arising from intense and aimed computations in continuum mechanics. This degree of freedom has become accessible only in the recent years and could give rise to advanced metamaterial devices in the future. Applications could potentially include mode conversion, force filed steering or dynamic mechanical cloacking citemilton2006cloaking.

Numerous approaches to mechanical chirality have been presented [183]. In this work, a novel geometry with no sharp corners was fabricated. It consists of three rods that spiral around the center of the unit cell as the height changes for a total turn of 180^o. In Figure 3.20(a), a qualitative mechanical simulation of the structure is shown. Two-unit cells stacked on top of each other were modelled, so the rotation will be clearly visible at the middle cap rotates. To perform this simulation, the structure was discretized using the same element type and with 24638 nodes and 9360 elements. The bottom base was fixed, and the top plate was subject to a $0.5\mu m$ vertical compression. It is shown that the compression of the structure results in rotation of the unit cell. During the actual indentation measurement, the top and bottom of the structure are not free to move. The structure twists clockwise when pushed downwards. The fabricated specimens are shown in Figure 3.20(b,c). The were made using the Nano-Cube setup at $90(mJ/cm^2)$ laser fluence and $100\mu m/s$ scan speed.

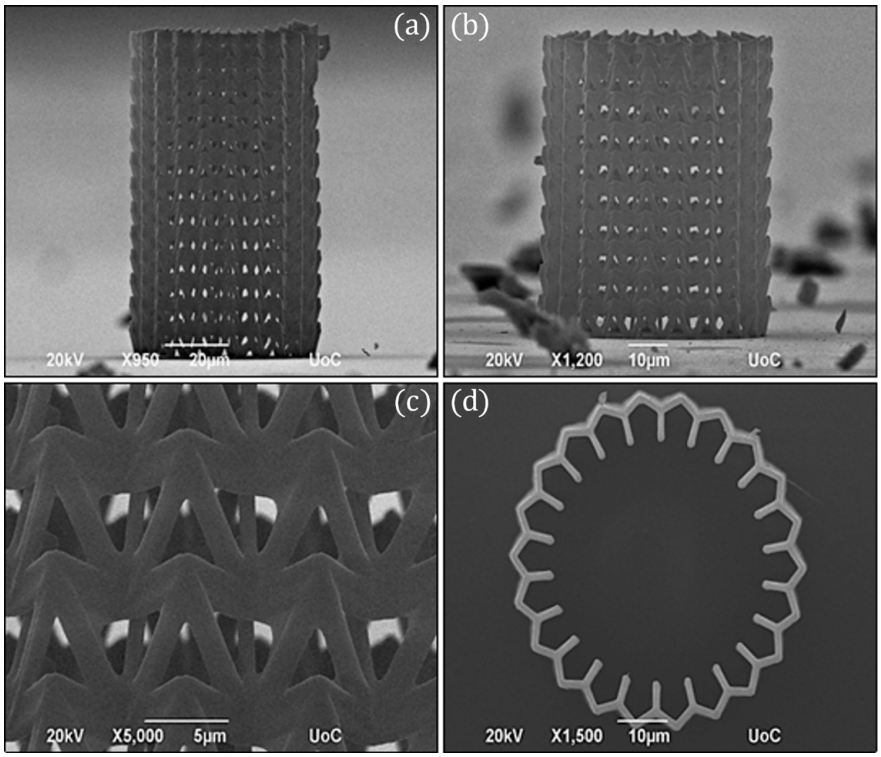

Figure 3.19: SEM images of the auxetic stent comprised of the re-entrant triangular fabricated using Nano-cub at $90(mJ/cm^2)$ laser fluence and $100\mu m/s$ scan speed. (a) Side view of $\sim 90\mu m$ in height stent, (b) Side view of $\sim 60\mu m$ in height stent, (c) Close view of the lattice, and (d) Top view.

Micromechanical Testing

To assess the mechancial performance of the fabricated speciemns, in-situ SEM microindentation experiments were conducted. A characteristic stress-strain response of re-entrant triangular in Figure 3.21. As the structure deforms, the beam members traverse to the interior of the structure, leading to a plateau in the force displacement curve. This deformation mode provides densification of the specimen and obstructs egregious features such as barrel shape formation, verifying the feasibility of the auxetic design. The compression of the stent-like array is presented in Figure 3.22. In this design, the auxetic behavior precipitates instability similar to non-linear shell buckling, as it was validated by the FEA simulations shown in Figure 7. For this simulation, a third of the structure was simulated by applying periodic boundary conditions. The structure was comprised of 53800 nodes and 276988 elements. To match the experiments, the bottom nodes were fixed and the top nodes were subject to a unit load. This loading condition leads to a buckling mode that demonstrates large deformation on the middle of the array, as it was also observed in the experiment.

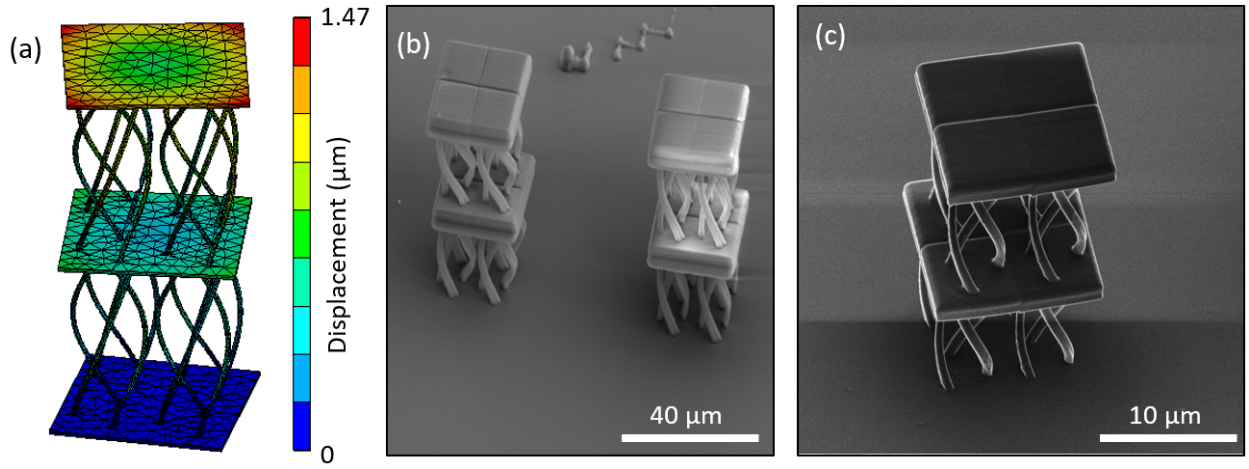

Figure 3.20: Design and fabrication of the twisting mechanical metamaterial fabricated using Nano-cube at $90(mJ/cm^2)$ fluence and $100\mu m/s$ scan speed. (a) FEA simulation of the structure under loading, revealing the anisotropic response of rotation due to uniaxial loading, (b) Isometric view of SEM imaging of such unit cells, and (c) Close view of the anisotropic structure using the Helium Ion Microscope.

This instability lead to a drop in the force displacement curve, and contraction of the structure. For a stent mechanism that is subject to a uniform axial load on its surface, such a deformation mode must be taken into consideration, in order to obtain the correct fabrication parameters before applying it to the patient. This is an extra parameter that must be accounted for in the design of auxetic specimens and has not been highlighted before. Nevertheless, the resilience of the auxetic design to cyclic loading can countervail this additional design constraint.

Furthermore, to validate the FEA simulations of the proposed anisotropic design, the fabricated twisting mechanical metamaterial was also tested (Figure 3.23). Again the twist of the unit cell leads to entanglement of the undulated members, that causes the plateau in the fore displacement curve for large deformations. This mechanism, apart from deformation modes similar to chirality, can improve the mechanical performance through densification, augmenting the mechanical performance beyond the elastic domain.

Section Conclusions

In summary, the modelling, fabrication and testing of auxetic and anisotropic lattice structures was investigated. Utilizing FEA simulations, their intrinsic behavior was validated and modulated. Fabrication of such structures through MPL and in-situ micromechanical testing provided insight into their mechanical behavior. While auxeticity can improve the mechanical performance, specific topologies can possess additional design constraints that

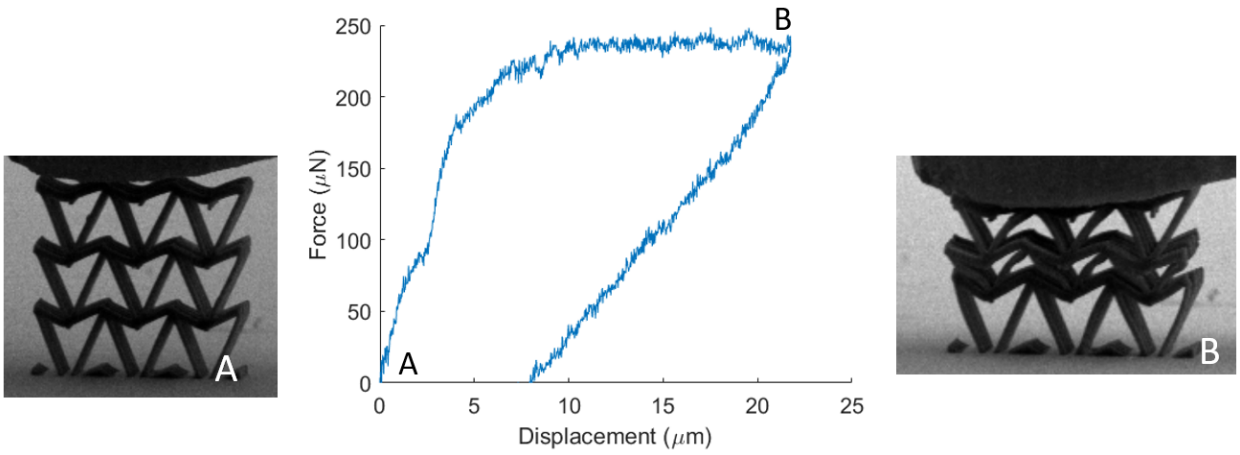

Figure 3.21: Mechanical testing of the re-entrant triangular filter. From stage A (undeformed configuration), the structure gets compressed, leading to the emergence of the auxetic behavior and the densification of the structure (stage B). A video of this mechanical testing is included in the published version [365].

need to be evaluated before the structure is utilized. In addition, anisotropy converts uniaxial compression to shear due to torque can provide densification mechanisms and lead to an improved mechanical performance. These results provide a strategic approach to implement architected structures with tailored elastic properties in microscale and validate their feasibility before they are employed in bioengineering applications, such as tissue engineering or stent technologies and percolation.

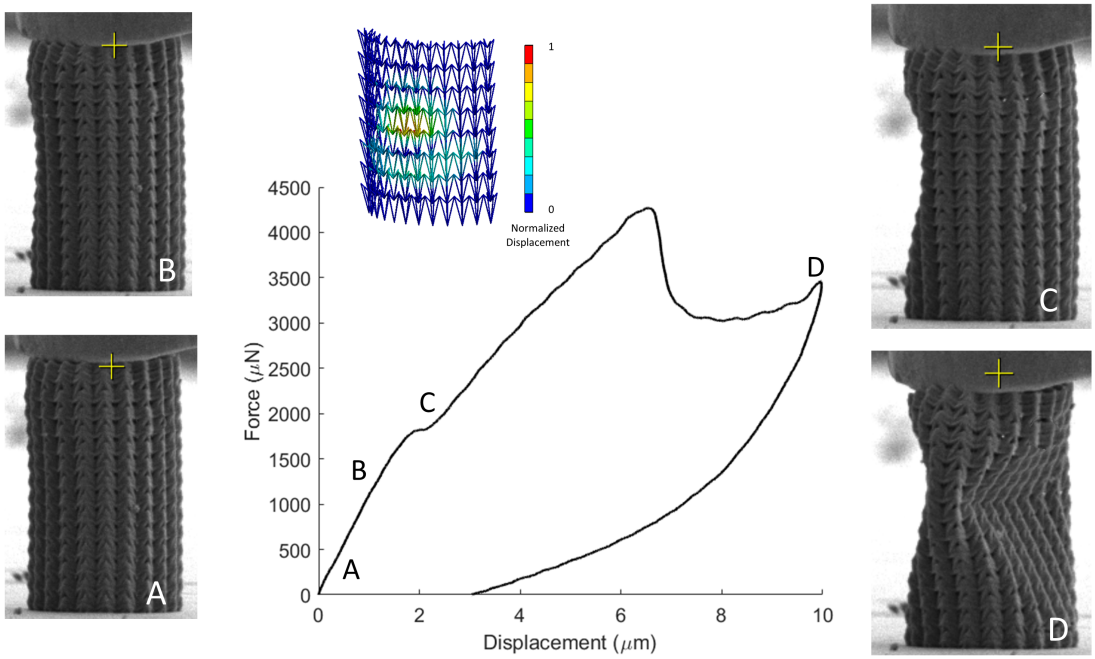

Figure 3.22: Mechanical testing of the re-entrant triangular stent. While the auxetic effect suppresses barrel shape formation, it leads to the formation of a nonlinear buckling mode which needs to be included in the design methodology. A video of this mechanical testing is included in the published version [365].

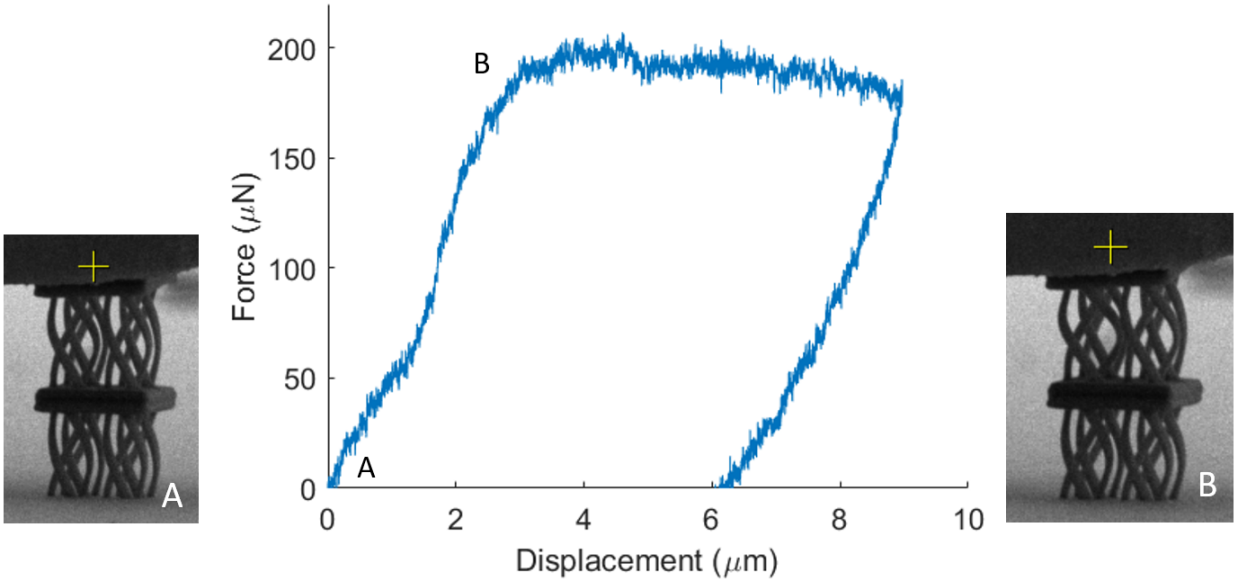

Figure 3.23: 8. Mechanical testing of the twisting mechanical metamaterial. During the compression of the structure, the unit cell cell rotates leading to densification through contact of the curved members and a plateau in the response of the structure.

Chapter 4

Interconnected Members in Lattice Structures

4.1 Intertwined microlattices greatly enhance the performance of mechanical metamaterials

Section Summary

The objective of this study was to investigate and compare the mechanical performance of macroscopic and microscopic intertwined lattice structures. Using the first stellation (FS) of the rhombic dodecahedron [402], it was investigated whether controlled intersection of neighboring unit cells can also enhance the mechanical performance at the macroscale.Because in these geometries the extensions of the faces of unit cells overlap with those of other unit cells, the structure is equipped with an artificial lattice in-growth mechanism. Structures that can be used for this design process are the stellations. These geometries belong to a set of myriad different designs corresponding to various platonic solids. The octahedron has one stellation, while the dodecahedron has three and the icosahedron has fifty-nine. The potential design space can be vastly expanded, including the stellations of Archimedean solids. For a valid evaluation, the FS structure was compared to one of the most thoroughly investigated lattice structures, i.e., the octet truss (OT), and its respective bulk material. Finite element analysis (FEA) provided insight into the effects of intersection and densification on the directional stiffness and material isotropy. Mechanical testing of structures fabricated by 3D printing and multiphoton lithography (MPL) at the macroscale and microscale, respectively, and FEA simulations were used to evaluate the mechanical properties of the aforementioned 3D lattice structures relative to those of their bulk material. To obtain insight into scale effects on the mechanical performance of architected structures with intertwined lattices, the findings of this study are also compared with microscale lattice structures.

The design concept of the metamaterial structure

The design process of the present metamaterial structure is depicted in Fig. 4.1. The unit cell structure is the first stellation of a rhombic dodecahedron. Each individual unit cell is formed by the primary geometry of regular octahedra with a height-to-base ratio of 1 : 2. To utilize lattice in-growth such that to tailor the buckling behavior, the spatial orientation of the unit cells is arranged so that the edges of the regular octahedra to penetrate the neighboring octahedra. Figures 4.1(A) and 4.1(B) show that the first stellation unit cell consists of three octahedra rotated clockwise or counterclockwise by $90o$ with respect to each other. The second design step is to connect two unit cells by inserting the edge of one cell into the other cell in order to create a two-unit-cell structure (Fig. 4.1(C)). The same process step is then repeated to construct a four-unit-cell structure, hereafter termed the hyper unit cell (Fig. 4.1(D)). The last design step involves the use of the hyper unit cell as a building block to form a multi-level structure (Fig. 4.1(E)) of in-grown lattice members inside the hyper unit cell produced by the repetitive intertwining of the hyper unit cells. SEM images of the first stellation hyper unit cells having (with each octahedron distinguished by a different color) are shown in Fig. 4.1(F), whereas SEM images of a three-layer first stellation structure (Fig. 4.1) are shown in Fig. 4.1(G). It will be proven later, that lattice member in-growth is particularly effective not only in increasing the strength, but also the energy dissipation capacity of the structure.

For the comparison to macroscale strucutres, the number of unit cells in the array was different. Figure 4.2 shows the design and relative density of the FS and OT macroscopic structures examined in this study. The OT architected geometry [450, 281, 188] is shown in Fig. 4.2(A). The intertwined geometry used in this study was inspired by the FS of the rhombic dodecahedron. The FS unit cell of the structure consists of three octahedra – two of the octahedra are rotated by 90^o in the clockwise and counterclockwise directions with respect to the central axis of the stationary third octahedron (Fig. 4.2(B)). In contrast to the OT unit cell, which does not have any fastigiated beam members on its faces, the beams of the hyper unit cell formed by the assembly of 9 (i.e., 3×3 array) FS unit cells produce a bulk core in the interior of the lattice structure (Fig. 4.2(C)). Hereafter, this structure will be referred as the FS hyper unit cell. The relative densities of both structures are compared in Fig. 4.2(D). By measuring the volume of each structure in the CAD files using the ANSYS 18.0 Design Modeler and then curve fitting the obtained data, the following equations of the relative density $\bar{\rho}$, of the FS and OT macroscopic structures were obtained,

$$\bar{\rho}_{FS} = 139.4(\frac{r}{L})^2 - 7.678(\frac{r}{L})^3 \tag{4.1}$$

and

$$\bar{\rho}_{OT} = 71.38(\frac{r}{L})^2 - 4.099(\frac{r}{L})^3 \tag{4.2}$$

where r is the radius and L is the length of the lattice beam members. Equations 4.1 and 4.2 indicate that the relative density is a cubic polynomial of r/L that takes into

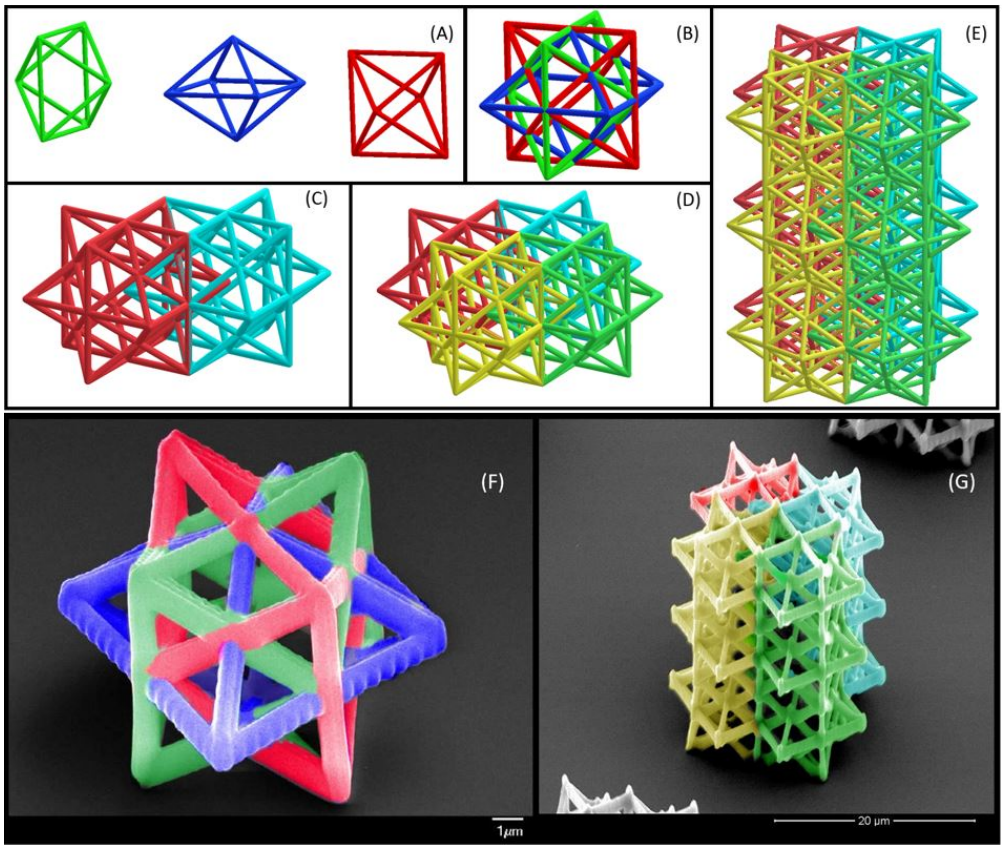

Figure 4.1: Conceptual design of a new mechanical metamaterial. (A) Three octahedra are used to form the first stellation by rotating the left and right octahedra clockwise and counterclockwise by 90^o with respect to the middle octahedron, respectively. (B) The three octahedra are assembled to form the first stellation of a rhombic dodecahedron (unit cell). (C) The formation of a two-unit cell assembly, with the rhombic pyramid at the edge of one cell inside the other cell. (D) The formation of a four-unit cell assembly, with the rhombic pyramids of the unit cells inside neighboring cells. (E) The designed metamaterial structure consisting of three layers of four-unit cell assemblies. (F) SEM micrograph of a fabricated unit cell. For improved legibility, each octahedron is distinguished by a different color in the whole assembly. (G) SEM micrograph of a fabricated three-layer hyper unit cell. Each subunit cell of the hyper unit cell is distinguished by a different color. The novelty of the design is the increase in strength of each unit cell through the mutual sharing of truss members between neighboring unit cells and the enhancement of strain hardening by introducing a deformation mechanism in the interior of each hyper unit cell to tailor the buckling behavior of the whole structure.

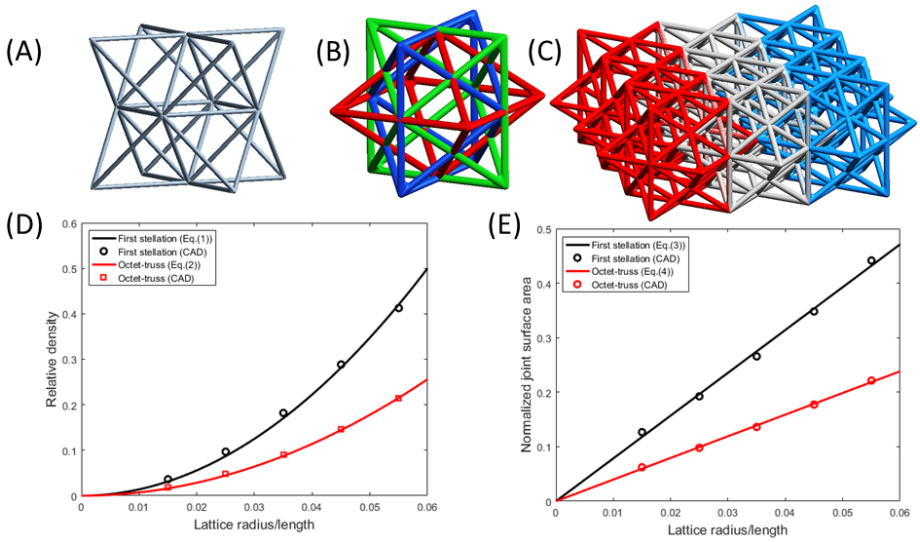

Figure 4.2: Design and relative density of the first stellation (FS) and octet truss (OT) macroscopic structures. Side views of (A) the OT unit cell, (B) the FS unit cell consisting of three octahedra offset by 90^o from each other, and (C) the FS hyper unit cell constructed by merging three FS unit cells distinguished by different colors. (D) Relative density of the OT and FS structures versus lattice radius/length ratio. The intertwined lattice members of the FS structure lead to a faster increase of the relative density with the lattice radius/lattice length ratio compared to the OT structure.

account the effect of nodal intersection on the relative density, which becomes significant for $\bar{\rho} \geq 0.05$. Although there are other intertwined geometries demonstrating significantly higher densification, such as the three-compound octahedron, the spatial orientation of the regular polyhedra of such structures reduces the gaps at their faces, rendering the removal of supporting material in macroscale 3D printing considerably more challenging. The same challenge can be encountered with microstructures fabricated with the MPL process because overlapping of sections of the structure can enclose unpolymerized material that cannot be dissolved during fabrication [402]. However, the orientation of the three octahedra in the FS unit cell offsets this design constraint, as seen in Fig. 4.2(C)).

The average coordination number was used to determine whether the mechanical response of the structures was bending or stretching dominated. The calculated coordination number of the FS hyper unit cell was found equal to 8, rendering it a bending dominated structure [265]. This implies that the stiffness of the FS structure should be significantly lower than that of the stretching dominated OT structure. However, the densification caused by the lattice intertwining compensates for this effect. This was proven by FEA simulations of the directional stiffness of each structure. Because the OT structure exhibits cubic symmetry, its elastic behavior can be fully described by three elastic constants (C_{11}, C_{12}, and C_{44}), whereas the elastic behavior of the FS structure that demonstrates tetragonal symmetry depends on six elastic constants (C_{11}, C_{12}, C_{13}, C_{44}, and C_{66}). The indices of the elastic constants are compatible with the Voigt notation of the stiffness tensor. To calculate the elastic constants, FEA simulations were performed with the ANSYS Workbench 18.0 code, using a numerical technique that provides close matching between theoretical and experimental results of anisotropic structures [432]. Both structures were meshed with 10-node tetrahedral elements. The OT unit cell consisted of 21974 elements and 9963 nodes, whereas the FS hyper unit cell consisted of 76513 elements and 35902 nodes. To ensure elastic deformation, both structures were subjected to very small strains ($\leq 10^{-5}$). As discussed in the next section, the experimentally determined elastic modulus of the bulk material used in 3D printing is equal to 160 MPa. Since this material is incompressible, the Poison's ratio was set equal to 0.499. Because the desired direction of enhanced stiffness is perpendicular to the top face of the OT unit cell and FS hyper unit cell (Figs. 4.2(A) and 4.2(C)), this study was focused on enhancing the mechanical performance in the [001] direction. The stiffness of the OT unit cell and FS hyper unit cell in this direction was calculated from the following equations (Voigt notation):

$$E_{[001]_{OT}} = \frac{C_{11}(C_{11} + C_{12}) - 2C_{12}^2}{C_{11} + C_{12}} \tag{4.3}$$

and

$$E_{[001]_{FS}} = \frac{C_{33}(C_{11} + C_{12}) - 2C_{13}^2}{C_{11} + C_{12}} \tag{4.4}$$

Calculating the elastic constants for different relative densities yielded Ashby charts of the FS hyper unit cell (Fig. 4.2(D) and the OT unit cell (Fig. 4.2(A) in the form of the normalized stiffness E/E_b, where E_b is the stiffness of the bulk material, shown in Fig. 4.3. The FS stiffness in the [001] direction is significantly higher than that of the OT, even though the FS is a bending dominated structure. The relation between the OT stiffness and relative density reported elsewhere [265] was validated by the present FEA for different relative densities. The normalized stiffness of the FS hyper unit cell, obtained by curve fitting the FEA data, is given by

$$\bar{E}_{[001]_{FS}} = 14.485\bar{\rho}_{FS}^{1.31} \tag{4.5}$$

Furthermore, because lattice intertwining affects significantly the anisotropy of the FS hyper unit cell at different relative densities, it is necessary to examine its directional stiffness, which in a direction n is given by

$$E(n) = \frac{1}{(n \otimes n) : C^{-1}(n \otimes n)} \tag{4.6}$$

where C^{-1} is the compliance tensor of the lattice structure and n is the normal vector of the loading direction. For structures without intertwined lattices, such as the OT, the stiffness map increases in size with the relative density, while its shape remains the same [1]. The calculated stiffness map of the OT unit cell is the same with that obtained from analytical expressions reported elsewhere [1], supporting the validity of the present FEA. Alternatively, the FS stiffness map shows a dependence on relative density. Specifically, for $\bar{\rho}_{FS} = 0.02$, the stiffness map has a star-like shape, whereas for $\bar{\rho}_{FS} = 0.2$ the stiffness map is more uniform. The variation of the anisotropy of the FS hyper unit cell and the invariance of the anisotropy of the OT unit cell can be quantified in terms of the anisotropy Zenner ratio A [432], which for cubic symmetry is defined by

$$A_{[OT]} = \frac{2C_{44}}{C_{11} - C_{12}} \tag{4.7}$$

A structure exhibits isotropic behavior when A=1. Nevertheless, Eq. 4.7 is only valid for structures that demonstrate cubic symmetry. The variation of the stiffness map of the FS hyper unit cell implies that its anisotropy also varies. To quantify the anisotropy of a structure exhibiting arbitrary symmetry, it is necessary to use the universal elastic anisotropy index [336]. Because the FS hyper unit cell demonstrates tetragonal symmetry, its universal elastic anisotropy index A^u is given by [336]

$$A^u_{[FS]} = \langle C \rangle : \langle S \rangle - 6 \tag{4.8}$$

where $\langle C \rangle$ is the average stiffness tensor and $\langle S \rangle$ is the average compliance tensor. For an isotropic structure, $A^u = 0$. Each average tensor was obtained by calculating the average of each component using the transformation tensor in spherical coordinates,

$$Q = \begin{bmatrix} cos\theta & sin\theta & 0 \\ -sin\theta & cos\theta & 0 \\ 0 & 0 & 1 \end{bmatrix} \begin{bmatrix} 1 & 0 & 0 \\ 0 & cos\phi & sin\phi \\ 0 & -sin\phi & cos\phi \end{bmatrix} \tag{4.9}$$

where ϕ is the polar angle and θ is the azimuthal angle. The average $\langle C_{ijkl} \rangle$ component of the C tensor can be calculated from the following formula by applying the summation rule,

$$\langle C_{ijkl} \rangle = \frac{1}{4\pi} \int_0^{\pi} \int_0^{2\pi} Q_{ip} Q_{jq} Q_{kr} Q_{ls} C_{pqrs} sin\theta \, d\theta \, d\phi \tag{4.10}$$

where the indices range from 1 to 3. The $sin\theta$ is included in Eq. 4.10 because all directions are assumed to have a uniform distribution (i.e., probability density $=sin\theta d\theta d\phi/4\pi$). Equation 4.10 gives the average tensor component as the summation of the transformed tensor in every direction in the 3D space. The use of Eq. 4.10 to calculate the components of the average tensors in Eq. 4.8 provides the universal elastic anisotropy index. To render it comparable to the anisotropy index for cubic symmetry (Zenner index), the following equation can be used [336]

$$A_{FS}^{eq} = (1 + \frac{5}{12}A_{FS}^{u}) + \sqrt{(1 + \frac{5}{12}A_{FS}^{u}) - 1} \tag{4.11}$$

While $A_{OT} = 6.35$ (i.e., independent of $\bar{\rho}_{OT}$), $A_{FS}^{eq} = 14.96$ and 8.54 for $\bar{\rho}_{FS} = 0.02$ and 0.2, respectively. This is indicative of the anisotropy variance of intertwined geometries with different relative densities, a characteristic not observed with unit cells that are not intertwined with neighboring unit cells [194]. The reason for the anisotropy variance is that the increase of the beam member radius leads to localized "bulk" spots in the unit cell. As the relative density increases, these spots begin to merge, creating a bulk core in the structure. This property is apparent in non-intertwined geometries at very high relative densities. However, at a very high relative density the unit cell becomes almost the same as the bulk material; consequently, its mechanical behavior is governed by the properties of the bulk material, not those of the architected design. Nevertheless, the FS hyper unit cell exhibits anisotropy variance at a much lower relative density ($\bar{\rho}_{FS} = 0.2$).

A more succinct comparison of the directional stiffness of the FS hyper unit cell and the OT unit cell at a relative density of 0.2 is shown in Fig. 4.4(A). This figure was created by projecting the directional stiffness map on a plane with [110] normal direction. It can be seen that despite the significant enhancement of the stiffness of the FS hyper unit cell (179% higher than that of the OT unit cell in the [001] direction), this effect occurs between $\pm 45^o$ and -45^o with respect to the [001] direction. Nevertheless, it is noted that in the vast majority of the literature, the OT structure has been tested in the [001] direction [448, 281, 188, 444], presumably due to the high stress developing at the corners of the unit cell when loaded in the [111] direction, which coincides with the maximum stiffness of the structure.

A buckling analysis was also performed to determine the critical buckling load of the FS and OT structures in the [001] direction of the stiffness enhancement. Specifically, the instability of infinitely large structures consisting of periodic arrays of the FS and OT unit cells was examined by fixing one plane of the structure and applying a unit load to the mirror plane of the structure. The critical buckling load of each structure was obtained by solving the eigenvalue relation 4.13 that will be presented in the next section.

For consistency with the directional E/E_b map (Fig. 4.4(A)), the directional normalized critical buckling load $\frac{\lambda}{\lambda_{FS_{[001]}}}$ was also mapped onto the (110) plane (Fig. 4.4(B)). The significantly higher critical buckling load in the [001] direction of the FS structure than that of the OT structure is attributed to the higher stiffness of the FS structure in that direction and the different directional dependence of the inertia matrix of each structure.

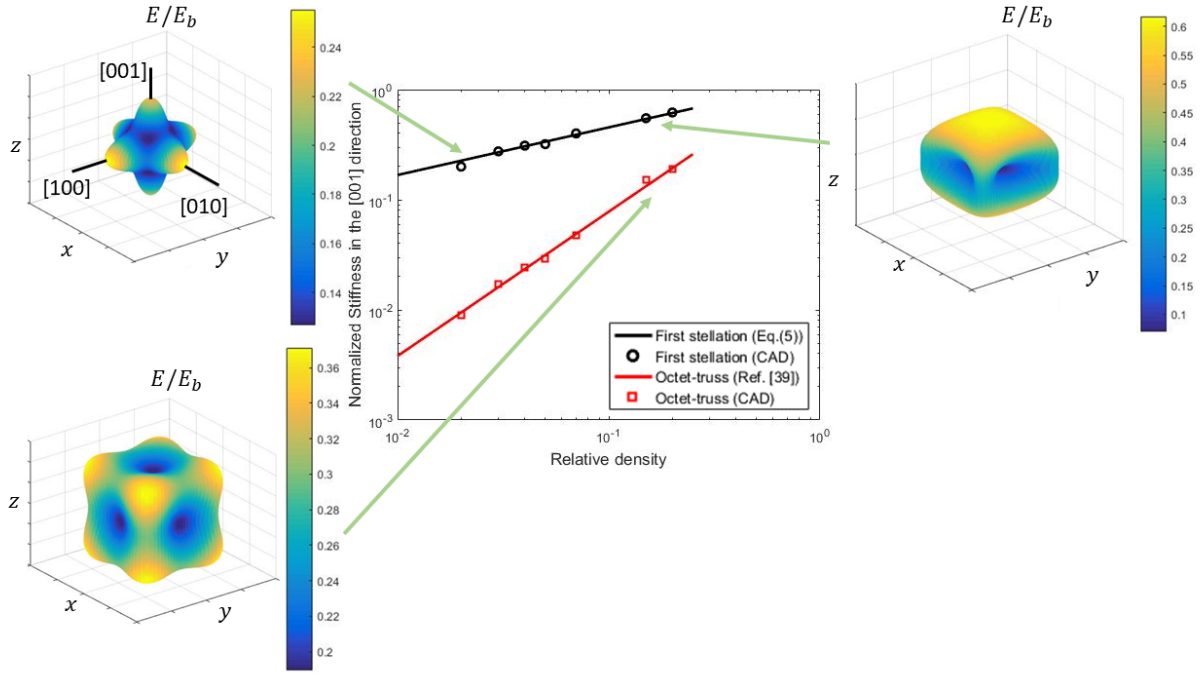

Figure 4.3: Numerical results of the normalized stiffness E/E_b of the first stellation (FS) and octet truss (OT) macroscopic structures. Despite the fact that the FS is a bending dominated structure, its normalized stiffness is significantly higher than that of the OT structure due to the significant number of intersecting beam members in this structure. In addition, although the shape of the 3D stiffness map of the OT structure does not change with the increase of relative density [1], the intertwined beam members in the FS structure alter both the shape of the stiffness map and the anisotropic behavior.

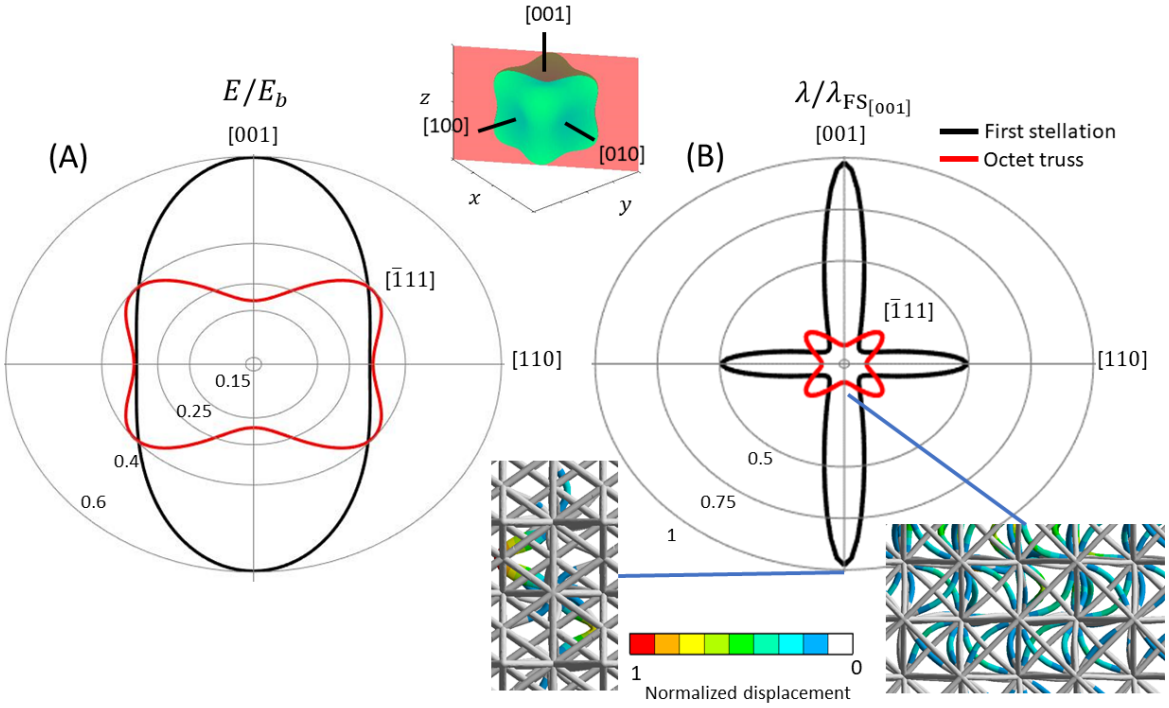

Figure 4.4: Maps of (A) normalized directional stiffness E/E_b and (B) critical buckling load $\frac{\lambda}{\lambda_{FS_{[001]}}}$ of the first stellation (FS) and octet truss (OT) macrostructures for fixed relative density ($\bar{\rho}_{FS} = 0.02$) plotted on the (110) plane. The stiffness of the FS macrostructure is significantly higher than that of the OT macrostructure in the [001] direction. The intertwined unit cells at this specific alignment enhance the stiffness of the FS macrostructure between the $\pm 45\circ$ directions and the [001] direction. Although the desired direction of stiffness enhancement is the [001] direction, different spatial orientations of the intertwined unit cells may increase the stiffness in different orientations. The critical buckling load of the FS macrostructure is significantly higher than that of the OT macrostructure in all directions except in the domain defined by the $\pm 30^o$ directions and the [111] direction, a consequence of the lower FS stiffness in these directions and the differences in the inertia of the structures in various directions. The buckling mode in the [001] direction is characterized by the twisting of beam members at the center of both structures, although beam buckling is significantly more pronounced in the OT structure.

It is noted that the OT structure displays a higher critical buckling load between the $\pm 30^o$ directions and the [111] direction, in accord with the higher stiffness of the OT structure in this range (Fig. 4.4(A). Interestingly, the buckling mode of both structures comprises twisting of internal beam members (normal displacement distributions are shown as insets in Fig. 4.4(B)). However, the significantly larger number of beam members in the OT structure undergoing buckling indicates a higher likelihood for the simultaneous collapse of more beam members compared to the FS structure.

Results

Simulations

Simulations for Microscale Comparisons

Before the fabrication of the structures microscale structures, a series of finite element analysis (FEA) simulations were performed in order to obtain insight into the efficacy of our conceptual design by comparing the mechanical responses due to compressive loading of both the first stellation and the octet truss structures and identifying the most likely locations of failure in each structure. All of the FEA simulations were performed with the multi-physics finite element software ANSYS (Workbench 18.0). The selected material properties are in agreement with those of polymeric materials used in multi-photon lithography (MPL). The octet truss structure was modeled with 660,960 elements having 1,234,133 nodes, the single-layer first stellation structure was modeled with 92,171 elements having 168,117 nodes, whereas the three-layer first stellation structure was modeled with 652,961 elements having 1,108,141 nodes. In all the FEA models, the smallest element size is $\sim 0.24\mu m$. The boundary conditions were chosen to closely much those in the experiments. Because of the slightly thicker hinges connecting the beams. Contact between the nanoindenter tip and the top face of each structure occurred at the elevated hinge points. Thus, the compressive load of the nanoindenter was transmitted to the structure through these hinge points. For this reason, concentrated forces were applied to the mesh nodes corresponding to the top-face hinges. Since the bottom face of each structure was firmly attached to the substrate, all of the degrees of freedom of the bottom nodes were fully constrained. The ANSYS Design Modeler was used to design the structure geometries. Figure 4.5 shows simulation results of elastically deformed structures. In these simulations, the octet truss structure consists of 3 layers each having 16 unit cells, whereas the first stellation structure consists of 3 layers each having 4 unit cells, i.e., 4×4 and 2×2 unit cell array per layer, respectively. While both structures have the same scaling relationship with an overall height of $30\mu m$ and a beam diameter of $0.5\mu m$, the first stellation structure has an apparent base area of $14.5 \times 14.5\mu m^2$, whereas the octet truss structure has a much larger apparent base area of $40 \times 40\mu m^2$. The relative density of the octet truss is ~ 0.05, while the relative density of the intertwined stellated geometry is ~ 0.13. Hence, despite the fact that the octet truss array has more unit cells than the hyper unit cell array, the intertwining of the lattice members in the latter

structure greatly enhances the relative density for much less volume and same dimensions of lattice members. The height of the octahedra comprising the first stellation structure is $10\mu m$ and the apparent base area is $10 \times 10\mu m^2$. Potential failure points (i.e., maximum displacement points) are red-colored in the deformed structure configurations. This simulation also revealed a significantly higher elastic strain energy density for the first stellation structure than the octet truss structure, despite the $\sim 30\%$ higher volume and 4 times more unit cells of the latter structure.

To identify the mechanisms responsible for the different deformation behaviors, a buckling analysis was performed to determine the effect of beam buckling on the deformation behavior of each structure. Buckling commences upon the occurrence of a displacement x that is not parallel to the applied compressive force. For this deformation mode, the overall stiffness of the structure is the sum of the elastic stiffness K_e and the initial stiffness K_σ. From the theory of elastic stability [218], buckling initiates when $x \neq 0$, even though the force f that is parallel to x is equal to zero, as only a compressive force is applied. Mathematically, this occurs when the total stiffness becomes positive semidefinite. Therefore, the following equation holds

$$[\lambda[K_\sigma[\sigma_o]] + [K_\epsilon]]x = f = 0 \tag{4.12}$$

Since the vector x cannot be zero, Eq. 4.12 represents an eigenvalue-eigenvector problem. This Therefore, the was accomplished by solving the following eigenvalue equation must be solved

$$det[[K_\sigma^{-1}[\sigma_o]][K_\epsilon] + \lambda I] = 0 \tag{4.13}$$

The physical meaning of λ is that buckling occurs when a load of magnitude equal to λ times a unit compressive load is applied to the structure. The ratio of the load multiplier corresponding to the octet truss (OT) structure λ_{OT} to that of the first stellation (FS) structure λ_{FS}, obtained from an eigenvalue buckling FEA, was found to be $\frac{\lambda_{OT}}{\lambda_{FS}} = -0.55$. The negative sign is because of the negative load multiplier of the octet truss, implying that buckling in this structure occurs under tensile loading. This result indicates that buckling commences in the first stellation structure at a much lower load compared to the octet truss structure, suggesting that strain hardening, manifested by buckling events at relatively high loads, is more favorable in the first stellation structure.

An elastic-plastic (large deformation) FEA was also performed to provide further insight into the occurrence of buckling in the first stellation structure. Figure 4.6 shows plastic buckling of beams in two of the three octahedra of a single-layer first stellation structure compressed by a total vertical distance of $4\mu m$ (i.e., 40% height decrease). Plastic beam bending may increase the structure stiffness, a mechanism not fully explored with octet truss structures [376]. Although the elastic behavior of the octet truss structures has been thoroughly examined, plastic deformation of these structures and its effect on the structural stiffness have not been considered in previous studies [466, 38, 218, 446]. In addition, two more factors must be considered for the selected size of the structures. First, the inherent complexity of

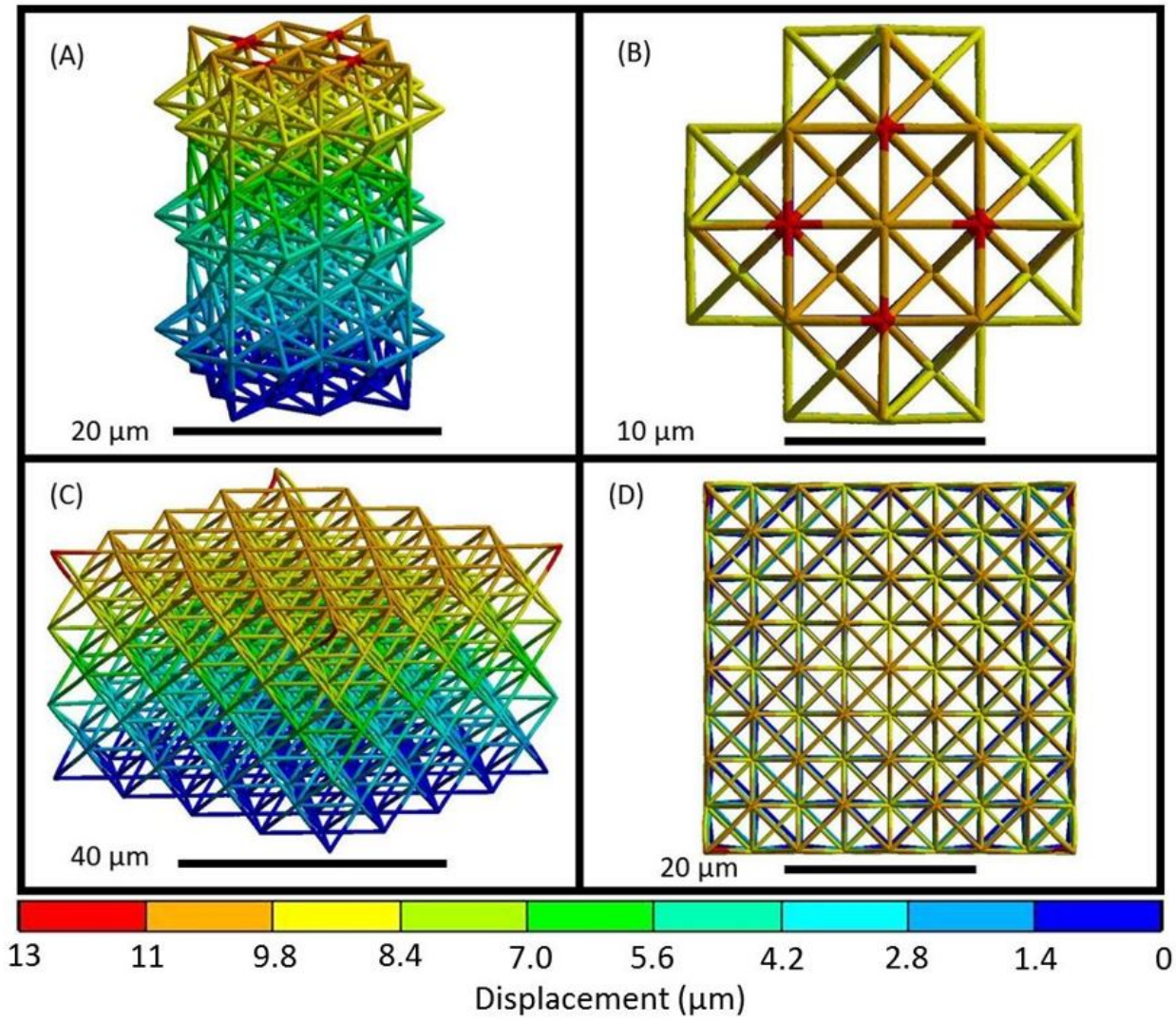

Figure 4.5: FEA results of elastically compressed metamaterial structures. (A) Deformed structure designed based on the first stellation concept consisting of 12 unit cells. (B) Top view of the same deformed first stellation structure. The simulation shows that the most likely failure locations are the surface hinges (red colored points). (C) Deformed octet truss structure consisting of 48 unit cells. (D) Top view of the same deformed octet truss structure. The simulation shows that the most likely failure locations are the corners of the upper layer (red colored points). Both structures have a nominal height of $30\mu m$ and consist of three layers of $10\mu m$ tall unit cells. All simulation results are for compression by a total distance of $13\mu m$.

the in-grown lattice members is reflected in the requirement of a high-resolution fabrication printing process. Hence, a printing technique that can fabricate 3D structures with very high resolution is required. Second, as the length scale decreases, the defects dominating the mechanical behavior of the structure are mitigated [264] and the architected mechanisms of controlled buckling and plastic deformation can be clearly observed. Therefore, it was deduced that the first stellation structures should be designed and compared in this scale, rendering the MPL method as most suitable to fabricate these structures. Unequivocally, MPL is presently the only method capable of fabricating such complex 3D structures.

Simulations for Micro/Macroscale Comparisons

To compare the micro/macroscale designs, it is instructive to examine the stress distribution in both macrostructures and juxtapose the origin of failure with that observed in the macroscale experiments. Figs. 4.7(A) and 4.7(B) show von Mises equivalent stress distributions in the FS and OT macrostructures, respectively, obtained from a linear elastic FEA. While the stress is uniformly distributed across the OT beam members (Fig. 4.7(B)), only the vertical beam members of the FS macrostructure sustained high stress, while the stress in the rest of the beams is almost zero (Fig. 4.7(A)). This result is in agreement with the failure mechanisms observed at both length scales, where failure was found to commence in the vertical beam members. In addition, the results shown in Figs. 4.7(A) and 4.7(B) explain why the FS macrostructure maintained its structural integrity, with only a small number of beam members exhibiting failure. The uniform stress distribution in all of the unit cells of the OT macrostructure is also consistent with the failure of this structure at both length scales, where a group of unit cells failed simultaneously as opposed to only a few beam members failing in the FS structure. This is further evidence of the superior mechanical behavior of the FS structure compared to the OT structure.

Fabrication and Testing

Microscale Experiments

The first stellation and octet truss structures and the bulk material were fabricated by the MPL method [299]. The dimensions of the lattice members, which are approximately the same as in the simulation model, were selected so that to preserve the structural stability of the unloaded structure, while enhancing controlled buckling. Structures with higher slenderness ratios were unstable and collapsed under their own weight. Therefore, the critical diameter-to-maximum length ration was determined to be equal to 0.05. The fabrication process used to mimic lattice member in-growth is illustrated in Fig. 4.8. The order in which each lattice member is fabricated as the intertwined unit cells are forming is crucial to avoid the overlapping of lattice members; otherwise parts of the geometry will be rendered inaccessible by the focal point of the laser beam, preventing the fabrication of respective lattice members.

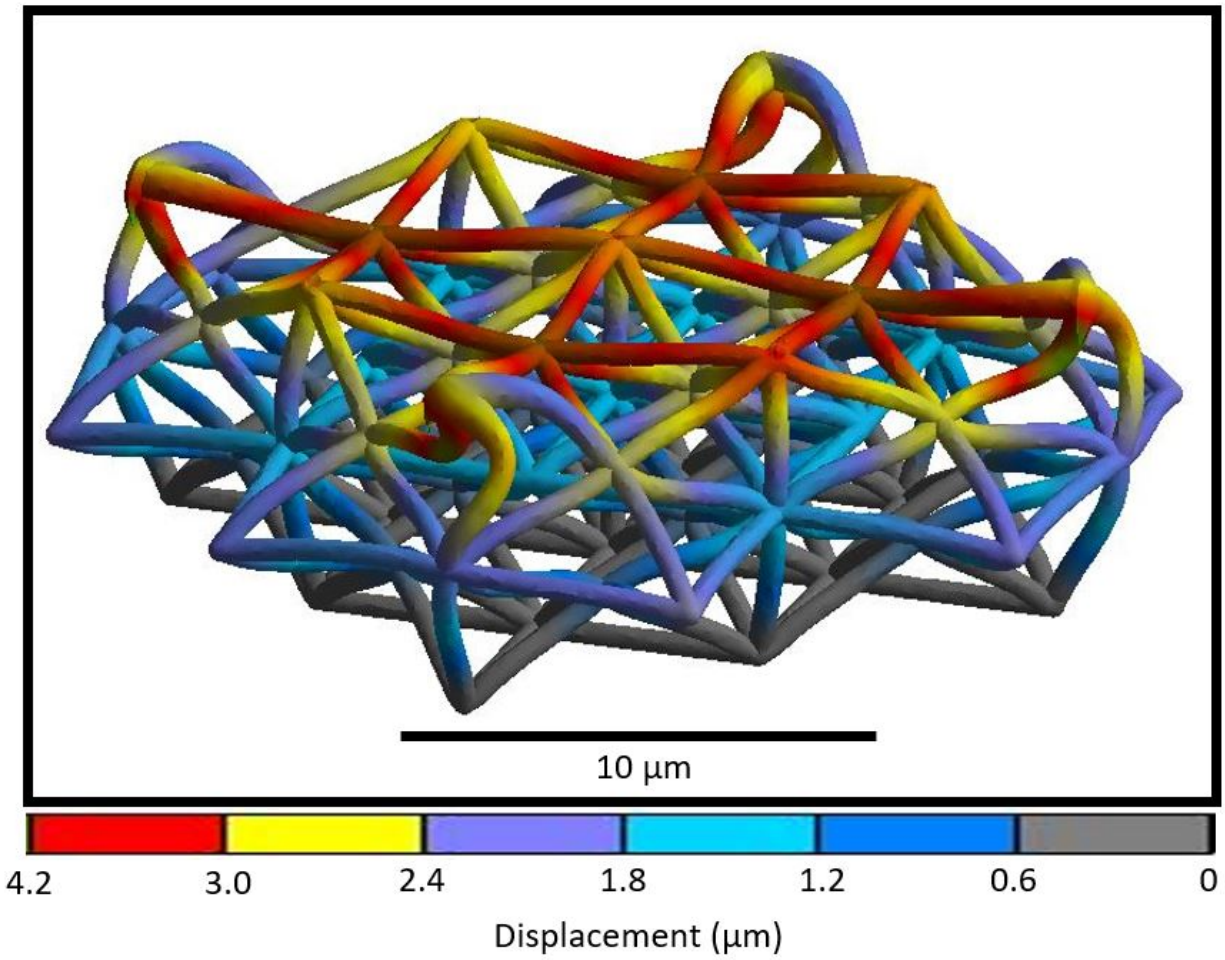

Figure 4.6: FEA results of an elastic-plastically compressed single-layer structure consisting of four first stellation unit cells. Compression by a distance of $4\mu m$ promoted beam buckling in two of the three octahedra of the unit cells, a mechanism observed with octet truss structures at much larger deformations. The first stellation structure together with the specific arrangement of the unit cells are responsible for the significant enhancement of the mechanical behavior compared to the octet truss structure.

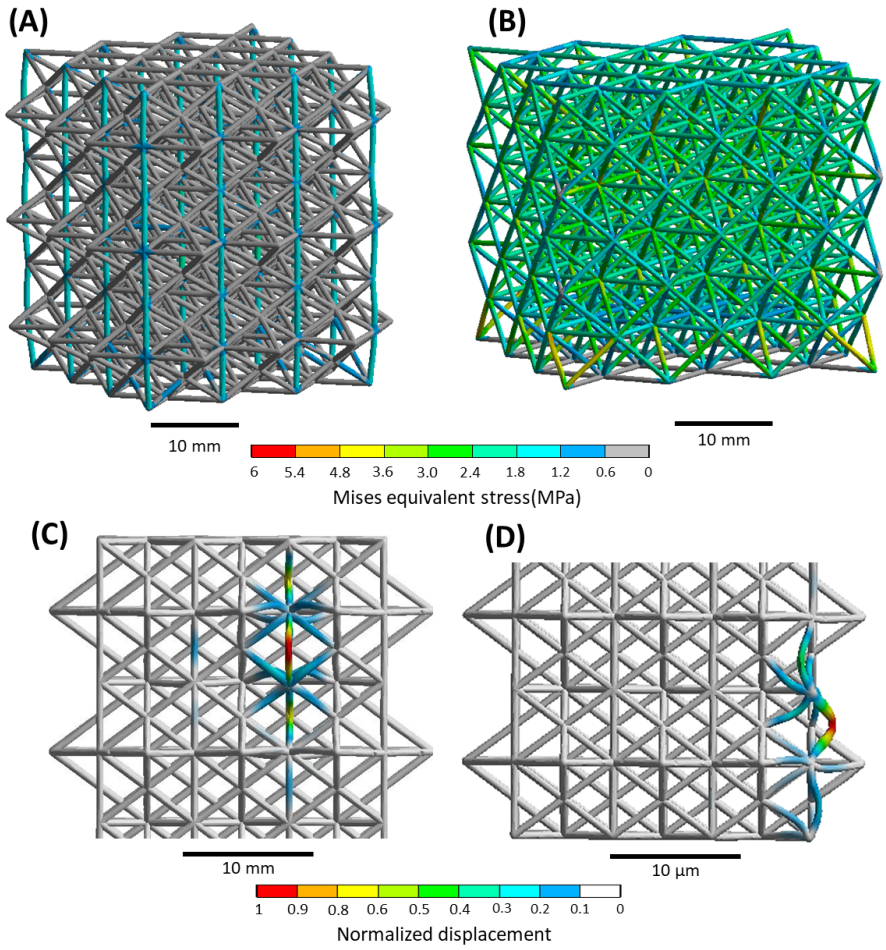

Figure 4.7: Distribution of the von Mises equivalent stress in the (A) FS and (B) OT macrostructures revealing the development of high stresses only in the vertical beams of the FS macrostructure, with the rest of the beams showing almost zero stress, and a uniform distribution of higher stress in the beams of all the unit cells of the OT macrostructure. Eigenvalue buckling mode of the FS hyper unit cell for loading applied to (C) the cusps of top beam members of the FS macrostructure and (D) the joints of top beam members of the FS microstructure. In the former case, the first mode encompasses twisting of a joint at the top of the hyper unit cell, presumed to be responsible for the subsequent fracture of the FS macrostructure observed in the macroscale experiments, whereas in the latter case, the first mode shows excessive beam bending at the bottom of the microstructure, consistent with the FS microstructure behavior observed in the microscale experiments.

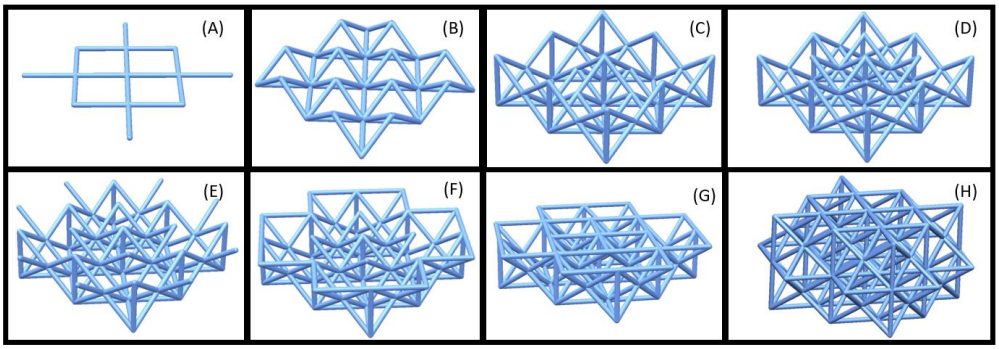

Figure 4.8: Fabrication procedure of hyper unit cell with in-grown lattice members. (A) Initial base of the hyper unit cell structure. (B) Interior of the lower quarter of the hyper unit cell with in-grown lattice members. (C) Internal lattice member fabrication without overlapping with lower laying lattice members. (D) Fabrication of all internal lattice members. (E) Fabrication of external lattice members sustained by the previously fabricated lower half of the structure. (F) Fabrication of the boundaries connecting the edges of unit cells. (G) Last fabrication step of the lower half of hyper unit cell involving the connection of the internal edges of the in-grown lattice members. (H) Fully fabricated hyper unit cell obtained by applying the same procedure as in (A)–(G) to the upper half of the hyper unit cell.

SEM images of the octet truss structure (Fig. 4.9) and the first stellation structure (Fig. 4.10) obtained before and after testing reveal different deformation characteristics. Each structure was compressed by a distance of $4.5\mu m$ (15% height decrease) three consecutive times (the displacement history of each cycle is shown in Fig. 4.12) and the corresponding force-displacement responses are shown in Fig. 4.11. The indentation results of the bulk material are shown in Fig. 4.12 Fracture in the octet truss structure occurred close to beam joints (Figs. 4.9(D)), while fracture in the first stellation structure commenced at the internal hinge of the cross-shaped top face (Figs. 4.10(D)–4.10(F)). These findings are in agreement with the FEA predictions of the possible failure locations in each structure (Fig. 4.6). The fact that failure is not symmetric is attributed to structural defects at failure points and the possible offset of the indenter tip from the center point of contact.

A comparison of characteristic force-displacement responses of the first stellation and octet truss structures shown in Fig. 4.11 shows that, although both structures exhibited strain hardening after each loading cycle, the first stellation structure demonstrated superior energy dissipation and more pronounced strain hardening. For a legitimate comparison, the strain energy density of each structure was calculated by dividing the strain energy dissipated per cycle (represented by the force hysteresis area) by the corresponding true volume of the structure. Table 4.1 gives the change in height δh, residual nominal strain after full unloading ϵ_r, and strain energy density u of both structures versus load/unload cycles N.

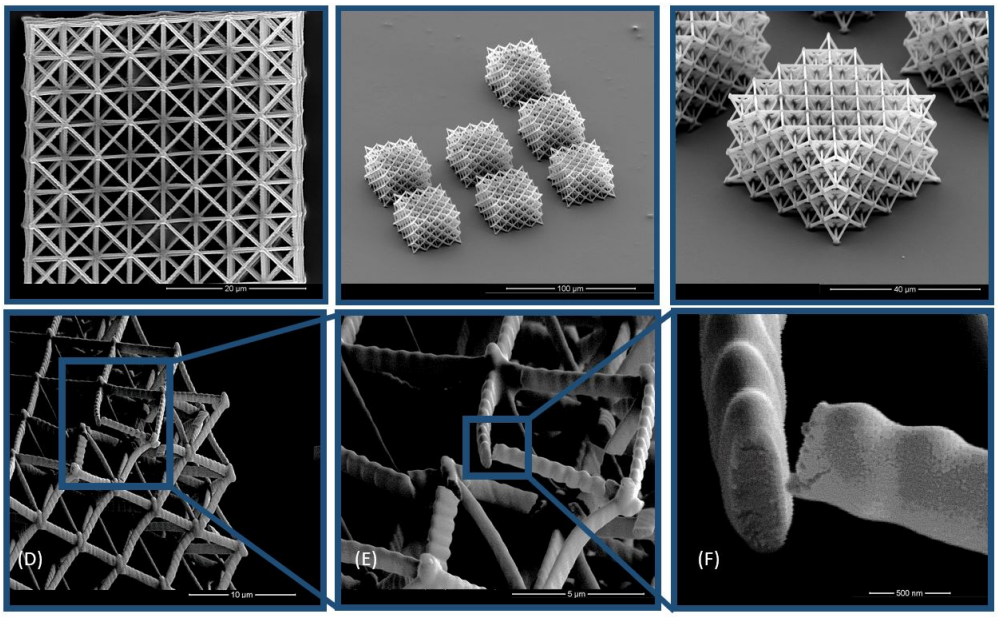

Figure 4.9: SEM micrographs of octet truss structures obtained before and after testing. (A) Top view of a structure fabricated by the MPL process. (B) Isometric view of an array of structures elucidating the repeatability of the fabrication process. (C) Isometric view of an undeformed structure. (D) Close-up view of a fractured structure. (E) High-magnification image of the region where most of the deformation and fracture occurred. (F) High-magnification image of a fracture cross section. Fracture occurred only at the top layers near the two corners of the structure, as predicted by the FEA results. The failure of this unit cell (instead of the neighboring corner cell) is attributed to a small offset of the nanoindenter tip from the center point of the upper face. The fairly rough fracture cross section suggests the occurrence of ductile fracture. In all images, the unit cell height is $10\mu m$ and the beam diameter is $\sim 0.5\mu m$.

For the same maximum compression, the first stellation structure demonstrated significantly higher deformation resistance and energy dissipation more than an order of magnitude higher than the octet truss structure in all loading cycles. In addition, the higher maximum force sustained by the first stellation structure without causing severe damage and the steeper slope of the unloading response indicate a much higher load carrying capacity and stiffness compared to the octet truss structure, despite the $\sim 30\%$ higher volume and 4 times more unit cells of the octet truss structure. The results of the structural stiffness S at each loading cycle, also given in Table 4.1, reveal a consistently stiffer first stellation structure than the octet truss structure by a factor of 3. Furthermore, the residual strain (permanent height decrease) of the first stellation structure did not change significantly after the second loading cycle compared to the octet truss structure, indicating more pronounced strain hardening

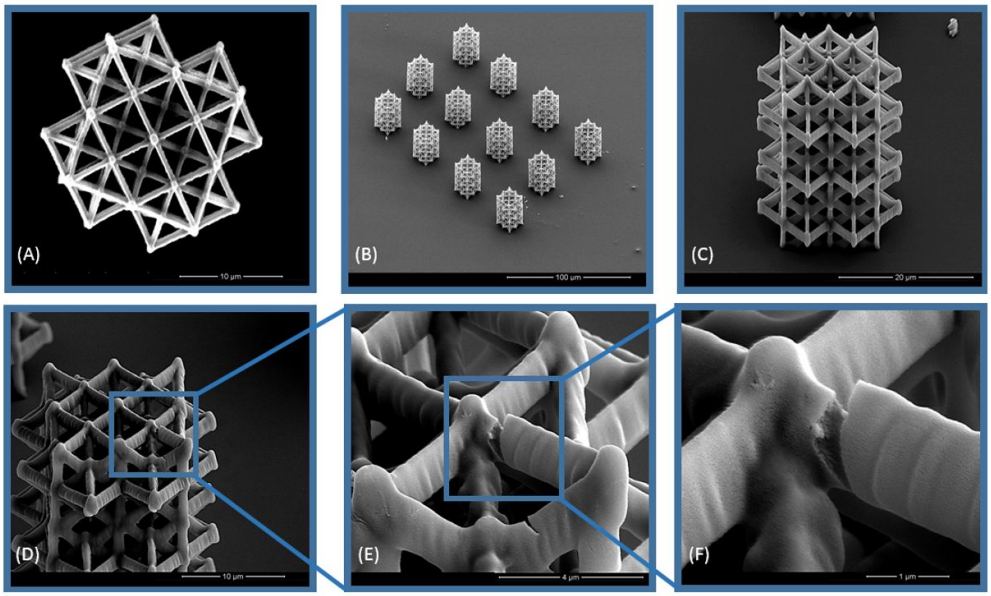

Figure 4.10: SEM micrographs of first stellation structures obtained before and after testing. (A) Top view of a structure fabricated by the MPL process. (B) Isometric view of an array of structures fabricated for multiple mechanical tests. (C) Isometric view of an undeformed structure. (D) Close-up view of a deformed structure. (E) High-magnification image of the only region with a fractured hinge, in agreement with predictions based on the FEA results. (F) High-magnification image of a fracture cross section. The fairly rough fracture cross section suggests the occurrence of ductile fracture. In all images, the unit cell height is $10\mu m$ and the beam diameter is $\sim 0.5\mu m$.

of the former structure. The fairly rough cross-sectional surface topographies of fractured beams (Figs. 4.9(F) and 4.10(F)) reveal the dominance of ductile fracture, which is a desirable fracture mode for the enhancement of energy dissipation. The first stellation structure and the bulk material demonstrate an increase in energy dissipation by $\sim 95\%$ and $\sim 33\%$, respectively. Therefore, it may be inferred that controlled buckling and plastic deformation of select lattice members both contributed to the increase of strain hardening of the first stellation structure by a factor of ~ 3 compared to the bulk material.

Macro/Microscale Experiments

For the micro/macroscale comparison, To validate the enhancement of the mechanical performance in the [001] direction owing to lattice intertwining, mechanical testing was performed with macrostructures fabricated by 3D printing using a Stratasys Objet260 Connex3 multi-material printer. The structural material was PolyJet VeroWhitePlus RGD835 photopolymer resin, whereas the soluble support material for 3D printing was PolyJet FullCure

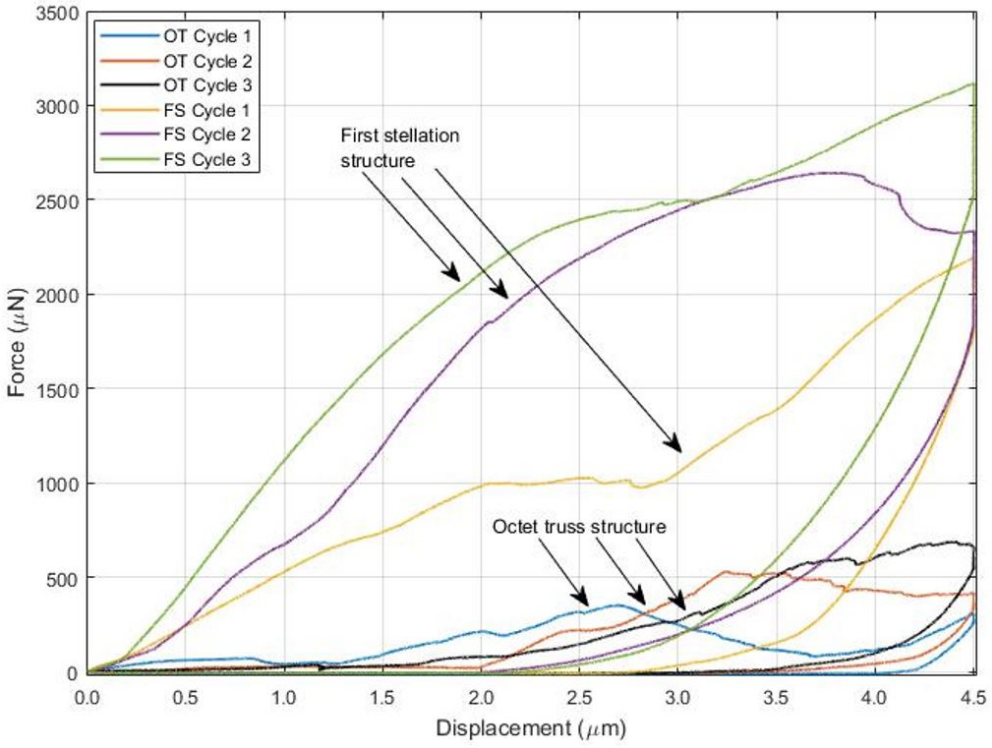

Figure 4.11: Force-displacement responses of first stellation and octet truss structures. The three sequential load/unload cycles of each structure reveal a more significant increase in stiffness, strength, and strain hardening of the first stellation (FS) structure than the octet truss (OT) structure, despite the $\sim 30\%$ higher volume and 4 times more unit cells of the octet truss structure.

Load/unload cycle	Octet Truss Structure				First stellation structure				Bulk Material			
Metrics	$\delta h_{OT}(\mu m)$	$\varepsilon_{r_{OT}}$	$u_{OT}(\frac{J}{m^3})$	$S(\frac{kN}{m})$	$\delta h_{FS}(\mu m)$	$\varepsilon_{r_{FS}}$	$u_{FS}(\frac{J}{m^3})$	$S(\frac{kN}{m})$	$\delta h_B(\mu m)$	ε_{r_B}	$u_B(\frac{J}{m^3})$	$S(\frac{kN}{m})$
1	4.14	0.138	0.263	1.582	2.78	0.093	2.870	3.161	0.705	0.045	5.870	9.219
2	3.38	0.113	0.395 (+50%)	1.622	2.18	0.073	4.706 (+64%)	3.195	0.576	0.029	6.308 (+7.5%)	9.351
3	3.14	0.105	0.462 (+17%)	1.625	2.05	0.068	5.620 (+20%)	3.226	0.521	0.026	7.818 (+24%)	9.528

Table 4.1: Mechanical performance of octet truss structure, first stellation structure and bulk material versus load cycles.

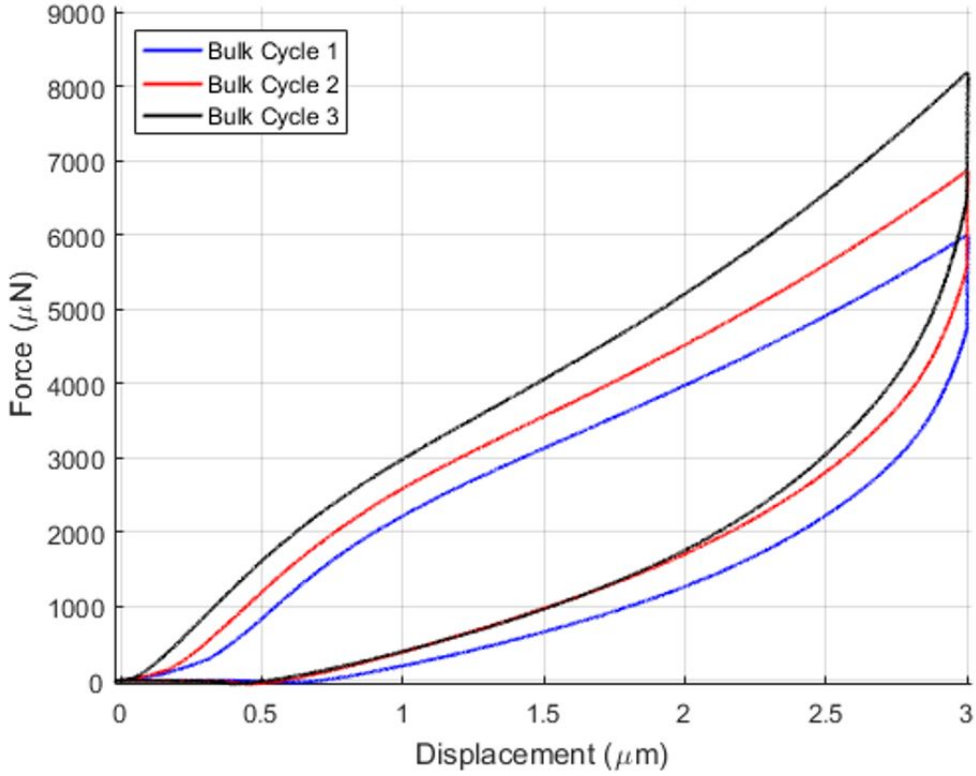

Figure 4.12: Force-displacement responses of the bulk material. The bulk material was subjected to three sequential loading cycles. To avoid reaching the transducers force limit, the maximum vertical displacement was set at $3\mu m$.

706. After 3D fabrication, the support material was removed with a water jet. To validate the mechanical properties of the bulk material, $30 \times 30 \times 30mm^3$ blocks were also fabricated by 3D printing. The OT and FS macrostructures were fabricated to have a surface area of $30 \times 30mm^2$ and a relative density of 0.2. At lower relative densities, the beam members were damaged and fractured during the removal of the support material. The FS macrostructure consisted of $1 \times 1 \times 3$ hyper unit cells, each having 9 FS unit cells, whereas the OT macrostructure consisted of $3 \times 3 \times 3$ unit cells. Mechanical tests were performed with an Instron-5500 apparatus, using a compression rate fixed at 2 mm/min. For statistical analysis, 5 macrostructures of each design were tested under identical conditions. All of the lattice macrostructures were tested up to the instigation of fracture. The experiments were recorded with a high-speed camera (i-SPEED 3, ix Cameras). Characteristic recordings of the tested OT and FS macrostructures can be seen in Videos A and B, respectively, presented on [400].

Furthermore, to compare with the mechanical performance at the microscale, the same

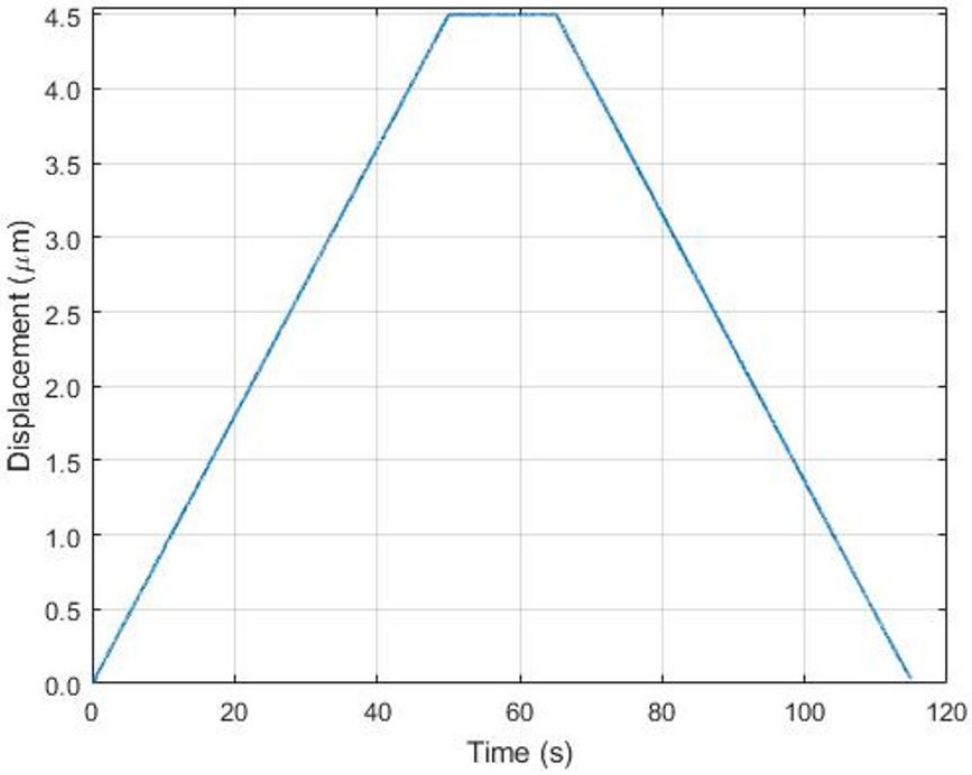

Figure 4.13: The displacement profile used in the mechanical tests of the metamaterial structures. Both loading and unloading rates were set equal to $90nm/s$, while a maximum vertical displacement of $4.5\mu m$ was maintained for $15s$ before initiating the unloading.

structure geometries were fabricated with the MPL process, a highly efficient process for fabricating complex 3D microstructures, using the photoresist ZS2080 as structural material. Fig. 4.14 shows characteristic helium ion microscopy (HIM) images of microstructures fabricated by MPL. An isometric and a close-up view showing the joints of intersecting beam members of the OT microstructure are shown in Figs. 4.14(A) and 4.14(B), respectively. Similarly, an isomeric view and a close-up view of the joints of significantly more intersecting beam members of the FS microstructure are shown in Figs. 4.14(C) and 4.14(D), respectively. Figs. 4.14(E) and 4.14(F) show top views of the OT and FS microstructureswhere the loading was applied during mechanical testing. To examine the mechanical performance at the microscale, in situ compression tests were performed with a picoindenter (PI 85 SEM PicoIndenter, Hysitron) placed inside a scanning electron microscope (FEI Quanta 3D FEG). This setup enables high-precision nanomechanical testing and real-time recording of the deformation process. The compression tests were conducted with a flat cylindrical molybdenum tip (model #72SC-D3/035 (407AM)) with a diameter equal to $130\mu m$. The maximum tip displacement was set at $5\mu m$, whereas the deformation rate was fixed at 800

nm/s. While the macrostructures were tested up to fracture, the mechanical performance of the microstructures was evaluated only in the plastic deformation range because of the limited maximum force applied by the picoindenter. Characteristic recordings of the tested FS and OT microstructures can be seen in Videos C and D of [400], respectively.

Results and Discussion

Microscale Experiments

The high strain hardening and significant energy dissipation capacity demonstrated by the first stellation structure are due to the design inspired by lattice in-growth. The uniqueness of the designed structure is that its high strength and strain hardening are a consequence of the spatial arrangement of unit cells, which is characterized by the mutual sharing of beam members. Among the 3D geometries that can utilize this structural effect are the stellations of polyhedra, such as the first stellation structure in our study. Simulation results revealed a superior mechanical performance of this structure, including stiffness, strain hardening, and energy dissipation, compared to the bulkier octet truss structure. Experimental results showed that the physical mechanisms responsible for the enhancement of the mechanical performance at large deformations is beam buckling resulting in plastic deformation, strain hardening, and ductile fracture. These mechanisms contributed to the increase of the strength and energy dissipation capacity of the first stellation metamaterial. The different deformation behaviors demonstrated by the two structures in the first loading cycle are interesting. At a compressive displacement of $\sim 2.8\mu m$ (i.e., engineering strain of 0.093), the octet truss structure exhibited softening, as opposed to the first stellation structure that showed an increase in strain hardening (Fig.4.11). This trend is attributed to the design intricacies of each structure. Because there are several beams in close proximity in the core of the first stellation structure, as the deformation progressed these beams begun to bend and buckle, eventually coming into contact with each other, thus providing an intrinsic stiffening mechanism. On the other hand, the unit cells of the octet truss structure do not have intertwined beams and the internal free volume is larger. As a result, beam plastic bending and buckling are less restricted and fracture commences in the octet truss structure in the first loading cycle. On the contrary, fracture in the first stellation structure does not occur until the final stage of the second loading cycle, as evidenced by the sharp slope decrease of the loading curve at a downward displacement of $\sim 4.2\mu m$ (i.e., much higher engineering strain of ~ 0.14). Importantly, the fractured first stellation structure maintained its remarkable strain hardening and energy dissipation characteristics in the subsequent loading cycle (Fig. 4.11, Table 4.1), surpassing the performance of the bulk material. The impressively higher strain hardening and energy dissipation capacity of the first stellation structure compared to the octet truss structure and significant enhancement compared to the bulk material not only illustrate the importance of the unit cell structure but also the spatial arrangement of the unit cells in the design of high-performance mechanical metamaterials. To this end, several lattice-based deformation mechanisms can be considered. For example, simple platonic

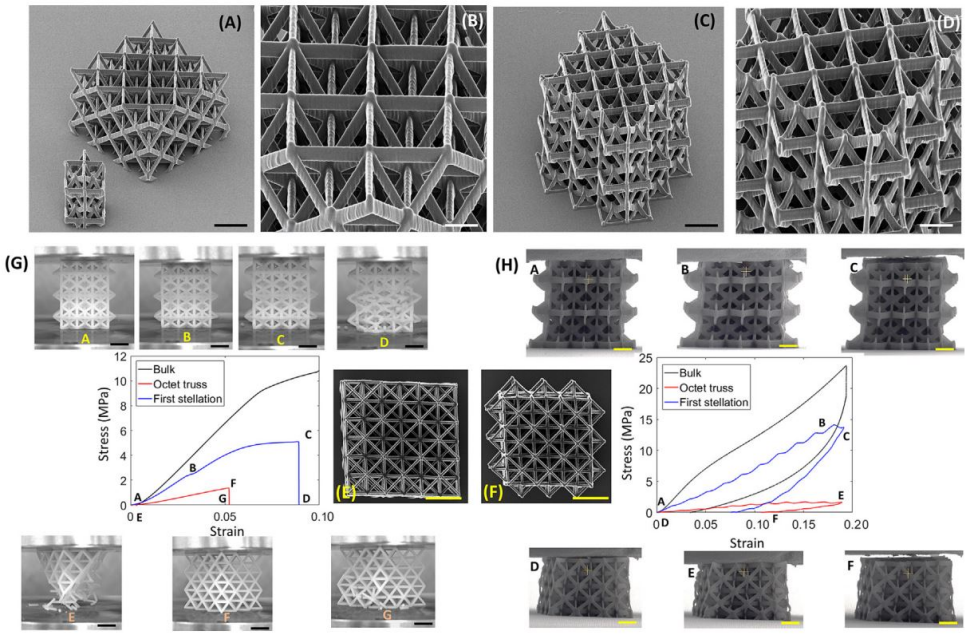

Figure 4.14: (A–F) HIM images of microstructures fabricated by MPL and (G, H) representative stress–strain responses with SEM images of deformed structures obtained at characteristic loading stages. The stress–strain response of the respective bulk structure is also shown for comparison. (A) Isomeric view of the OT microstructure (scale bar = 5 µm). (B) Close-up view of the OT microstructure showing the uniform beam intersection at all joints of the structure (scale bar = $2\mu m$). (C) Isomeric view of the FS structure (scale bar = $5\mu m$). (D) Close-up view the FS microstructure showing more beams intersecting at the joints compared to the OT microstructure (scale bar = $2\mu m$). (E) Top view of the OT microstructure (scale bar = $10\mu m$). (F) Top view of the FS microstructure (scale bar = $10\mu m$). (G) The mechanical response of the FS and OT macrostructures. The FS macrostructure shows a transition from elastic deformation (AB range) to a stress plateau terminated by the instigation of buckling (point C) and the subsequent instantaneous collapse of the structure (point D). Alternatively, the OT macrostructure demonstrates a linear elastic behavior (EF range), exhibiting fracture at significantly lower stress and strain that activates the spontaneous collapse of the structure (point G) (scale bars = $10mm$). (H) The mechanical response of the FS and OT microstructures. The FS microstructure demonstrates an elastic response (AB range) until the instigation of buckling in some bottom beam members (point B), resulting in the drop of the stress–strain curve (BC range). Unloading reveals that buckling resulted in irreversible deformation. The OT microstructure also exhibits a linear elastic behavior (DE range) until the beam members that sustained large deformation as a result of bending begin to deform plastically (point F) (scale bars = $5\mu m$).

solids with different orientations can be used to design unit cells possessing high strength and small volume. A mechanism that merits further study is the controlled development of plasticity in select structural members of metamaterials, which can be used to optimize strain hardening and energy dissipation. The present study shows how structural design can be tailored to yield mechanical behaviors superior to that of the bulk material. The design space for intertwined microlattice structures is vast, considering all of the potential stellated geometries that can be utilized. However, the present study has shown that another critical factor is the spatial arrangement of unit cells. The design of our metamaterial structures can be further extended and improved by using topology optimization, a technique to design augmented materials [428, 59] by utilizing buckling modes for high energy absorption. Moreover, since these structures are anisotropic, specific orientations may further enhance the mechanical performance. Thus far, microscale anisotropic effects on the behavior of mechanical metamaterials have not been examined, presumably due to the lack of advanced nanomechanical experimental techniques and standardized testing protocols. Thus, mechanical tests for additional deformation modes must be devised [24]. Integrating computational design methodology with contemporary fabrication and experimental approaches to guide the development of new metamaterial structures may unravel more details about deformation mechanisms similar to those encountered in natural materials, providing effective means for tailoring the mechanical response. Our study provides a basis for implementing microlattice-deformation-driven design of metamaterials with unique mechanical behaviors. In view of the significant enhancement of the mechanical performance of the metamaterials developed in this study, which is attributed to the hyper unit cell exhibiting lattice member in-growth and the scale effect, it is essential to extent the applicability of the MPL process to larger overall structure dimensions. Rapid fabrication of such structures on surfaces spanning several centimeters would facilitate applications including structural materials and bio-implants. This goal can be achieved by various methods currently under study, such as widening the working area of the process [293] or using holographic lithography [51, 408, 294], a technique that not only increases the effective fabrication area, but also reduces the fabrication time significantly. Clearly, the construction of metamaterials with superior mechanical characteristics at engineering scales can be achieved by utilizing the advantages of fabricating metamaterial structures at larger scales, while preserving the unit cell resolution.

Macro/Microscale Experiments

Fig. 4.14 shows representative stress–strain responses of the macroscopic and microscopic FS and OT structures and respective bulk structures. The stress in the macroscale tests was calculated by dividing the load with the contact area of the rigid plate with the macrostructure, determined from the FEA contact simulations. This was accomplished by assigning 8-node surface elements to the beam members of the contacting surfaces of the macrostructure and the plate. While at the instigation of deformation the contact area was very small, it increased with the applied load, eventually reaching a constant value of $738.63mm^2$ for the FS macrostructure and $1477.25mm^2$ for the OT macrostructure for a downward displace-

ment of the rigid plate by $0.1mm$. These values of the contact area were used to compute the stress during the entire loading cycle of each macrostructure. In the MPL fabrication, the beam members were fabricated by scanning the laser beam multiple times over the same path, which resulted in the formation of small joint protrusions. While this suggested that contact of the tip would be confined at the joints of the beam members at the contact face of the microstructures, after a very small downward displacement of a few nm the tip came into contact with the cusps of the beam members as with the macroscopic structures. Therefore, considering the similarity in structure and contact area at both scales, the stress in the microscale experiments was calculated by dividing the load with the contact area computed in the macroscale experiments expressed in units of nm^2 , i.e., contact area of 738.63 and $1477.254nm^2$ for the FS and OT microscale structures, respectively. The strain was obtained as the ratio of the vertical displacement of the rigid plate (or tip) to the height of the undeformed structure. The bulk material was compressed up to the available maximum force of the Instron machine or the picoindenter apparatus. A significantly greater capacity for ductile deformation was observed at the microscale. While the OT and FS macrostructures fractured at a strain of 0.05 and 0.09, respectively, both the OT and FS microstructures exhibited plastic deformation without fracturing up to a strain of 0.19. This result reveals a different effect of the structure geometry on the mechanical behavior at each scale. Because the FS structure demonstrated a brittle-like behavior at the macroscale, the mechanical behavior was controlled by the initial configuration of the lattice members. At the microscale, however, when the FS microstructure experienced post-yield deformation, contact of the beam members that sustained large deformation inhibited fracture, resulting in ductile-like behavior. While this was one of the principal design objectives of the intertwined lattice structures, , this study shows that the design principle of post-contact behavior is redundant at the macroscale. Therefore, the elastic analysis presented in the previous section is cogent at the macroscale.

The differences in the mechanical behavior of the structures at the two length scales can be further interpreted in terms of their respective stiffness, strain energy density, and critical buckling load. The elastic stiffness E and strain energy density u of each structure at both length scales are given in Table 4.2.

The stiffness was measured as the slope of the stress–strain curve at the beginning of loading, whereas the strain energy density was obtained as the area under the stress–strain curve at a fixed strain. To compare the mechanical performance of the FS macrostructure with that of its respective bulk structure and the OT macrostructure, the corresponding strain energy densities were calculated for a strain equal to 0.05, which is the fracture strain of the OT macrostructure (Fig. 4.14(A)). As mentioned in the previous section, the mean value of the measured bulk stiffness (160 MPa) was used in all the FEA simulations. Because the microstructures did not fracture, their strain energy density was computed for a strain equal to 0.19 (Fig. 4.14(B)) corresponding to the maximum load applied to the microscale structures.

A comparison of the stress–strain responses shown in Fig. 4.14 and the data given in Table 4.2 reveals a superior mechanical performance of the FS structure compared to the OT

Structure	Numerical Elastic Stiffness E (MPa)		Experimental Elastic Stiffness E (MPa)		Strain energy density u (kJ/m^3)	
Scale	Macro	Micro	Macro	Micro	Macro	Micro
Bulk	160	95	160 ± 5.0	95.38 ± 3.22	76.02 ± 1.52	2285.3 ± 100.5
First Stellation (FS)	89.8	68	86.5 ± 1.4	65.13 ± 5.81	28.12 ± 3.15	1324.0 ± 58.3
Octet Truss (OT)	30.4	15	29.03 ± 0.08	16.69 ± 1.57	3.28 ± 0.83	196.4 ± 15.7

Table 4.2: Numerical and experimental results of the elastic stiffness and strain energy density of bulk, FS, and OT macroscopic and microscopic structures. For an objective comparison, the stain energy density of the bulk and FS macrostructures was obtained at a strain equal to the fracture strain (0.05) of the OT macrostructure. The strain energy density of all microstructures was computed at the maximum strain (0.19) achieved in these tests.

structure at both scales. Specifically, the FS macrostructure demonstrated a monotonically increasing stress–strain response, reaching a stress plateau before the instigation of fracture (point C in Fig. 4.14(A)). However, the OT macrostructure exhibited a linear stress–strain response and failed at a much lower stress and strain (point F in (Fig. 4.14(A)) compared to the FS macrostructure. This result indicates a significantly higher (by a factor of $\sim$ 5.4) strain energy density at fracture for the FS structure than the OT structure at the macroscale. Moreover, at a strain equal to 0.05, the FS macrostructure demonstrated a strain energy density equal to $\sim$ 37% of its bulk material (Table 4.2), showing that the FS macrostructure can absorb a high amount of strain energy despite having 80% less material than the respective bulk structure. In addition, the FS macrostructure showed $\sim$ 8.6 times higher strain energy density (at a strain of 0.05) compared to the OT macrostructure (Table 4.2). This finding is important for ultralight structure applications that can potentially utilize beam structures, such as those used in aerospace engineering [71]. In addition, as shown in Table 4.2, the stiffness of the FS macrostructure is $\sim$ 3 times higher than the OT stiffness and $\sim$ 54% of the bulk stiffness. Importantly, even though the FS macrostructure possesses a bending dominated geometry, it is about three times stiffer than the OT macrostructure, which is a stretching dominated structure, a finding consistent with the FEA simulation results.

At the microscale (Fig. 4.14(B)), the FS structure demonstrated an increasing stress response up to a strain of 0.19, at which instant some beam members at the bottom of the microstructure buckled. The larger stress–strain hysteresis area of the FS microstructure compared to that of the OT microstructure reveals a significantly higher strain energy density for this microstructure. More specifically, the strain energy density of the FS microstructure is $\sim$ 6.7 times higher than that of the OT microstructure and $\sim$ 58% that of the bulk structure (Table 4.2). Likewise with the macroscale, the FS structure demonstrates significant strain energy capacity at the microscale. In addition, its elastic stiffness is $\sim$ 4.5 times higher than that of the OT microstructure and $\sim$ 71% of the respective bulk structure

(Table 4.2). These results indicate that the FS structure exhibits a superior mechanical performance than the OT structure at both length scales, while it reserves a significant portion of the mechanical capacity of the bulk material, despite having only 20% of the volume of the bulk structure.

The critical buckling load and buckling modes of the FS structure were also examined at both length scales. The critical buckling load was computed by solving Eq. 4.13. The loading area used in the eigenvalue buckling analysis matched that in the experiments. To apply the initial loading conditions in the experiments in the buckling analysis of the macrostructures, the load was applied at the cusps of the top beams that initially came into contact with the rigid plate, whereas in the buckling analysis of the microstructures, the load was applied to the joints of the top beam members. At both scales, the bottom nodes of the structures were fixed to prevent any movement during loading.

The critical buckling load of the FS macrostructure ($1 \times 1 \times 3$ hyper unit cells) was found to be equal to $3706.4N$, which is in close agreement with the experimentally measured buckling load of $3735 \pm 30N$. In addition, a close inspection of the deformation response shown in Video B [400] shows localized twisting of the beam members at the top of the FS macrostructure before the instigation of fracture. This failure mode is the same as the buckling eigenvector mode obtained from the FEA simulations (Fig. 4.7(C)). However, the critical buckling load of the OT macrostructure ($3 \times 3 \times 3$ unit cells) was found to be equal to $6926.4N$, which is ~ 1.87 times that of the FS macrostructure, implying premature failure of the OT macrostructure before buckling, which for a material demonstrating limited plasticity, such as the resin material used to fabricate the macrostructures, will lead to brittle fracture. The foregoing scenario is validated by the absence of any buckling events during testing of the OT macrostructure, as seen in Video A [400]. Another potential reason for the premature failure of the OT macrostructure is that the FS hyper unit cells have disproportionally more beam members connected to their joints compared to the OT unit cells, implying a greater enhancement of the FS structural integrity. Specifically, while there are 4 beams projecting outwardly from each face of the FS unit cell (Fig. 4.2(B)), such beams do not exist in the OT unit cell (Fig. 4.2(A)). This is because non-intertwined geometries, such as the OT, are not augmented with this critical feature. Hence, the OT is negatively affected by higher stress concentration effects leading to premature collapse. The critical buckling load of the FS microstructure was found to be equal to $10.3mN$, which is close to the experimental value of $10.27 \pm 0.055mN$. As seen in Video C [400], the buckling instability in the FS microstructure commenced at the end of loading upon the collapse of bottom beam members. This deformation mode is consistent with the eigenvalue buckling mode (Fig. 4.7(D)) for the respective loading conditions. However, the critical buckling load of the OT microstructure was found to be equal to $18.73m$N, which is ~ 1.82 times that of the FS microstructure. Although the deformation of the OT microstructure, seen in Video D [400], demonstrated excessively large deformation of some beam members, the absence of a discernible abrupt drop in the respective stress–strain response (Fig. 4.14(B)) suggests that these beam members bent but did not buckle. Therefore, plastic deformation developed in the OT microstructure at a much lower load than the critical buckling load. It should be

noted that the critical buckling load of the infinitely large structure consisting of FS hyper unit cells was found to be higher than that of the infinitely large structure consisting of OT unit cells, evidently because of the different sizes of the structures and boundary conditions used in the two buckling analyses.

The obtained results elucidate the specific mechanical attributes of intertwined structures at different length scales. Because the fabrication material of the microscopic lattices exhibits significant ductility, these structures demonstrated high energy dissipation in plastic deformation mode. Hence, geometric effects of lattice intertwining become more important from the perspective of tactical densification and post contact. Alternatively, the fairly rigid structural material used to fabricate the macroscopic lattices necessitates architecting the structures such that to enhance their mechanical behavior in the elastic deformation mode. Therefore, the initial configuration of the lattice structure is critical at the macroscale. This is important consideration for optimizing the design strategy depends on the length scale and intertwining geometry.

The present analysis shows that intertwined structures are characterized by high stiffness and high strain energy density at both microscale and macroscale, using either brittle or ductile materials for their fabrication. In addition, the intriguing concept of variable anisotropy [432] enables the relative density to be used as a design parameter to control the directional stiffness of the structure. However, this was accomplished by merging different unit cells [432], not by intertwining select beam members. Therefore, different orientations of intertwined geometries must be explored to obtain lattice structures demonstrating isotropic behavior at low relative densities. Although this may increase the complexity of the design, optimization techniques, such as machine learning, can be used to identify such structures for a wide range of orientations [429]. Additionally, tailoring the directional stiffness may lead to novel dynamic behaviors, such as tailored bandgaps in dispersion curves of resonant metamaterials for controlling wave propagation [391]. The foregoing effects observed with intertwined structures provide impetus for developing new design strategies for metamaterials with architected lattices demonstrating unprecedented mechanical performance.

Section Conclusions

Experimental and numerical studies were undertaken to investigate the mechanical behavior of macroscopic and microscopic structures possessing intertwined lattices fabricated by 3D printing and MPL, respectively. FEA simulations showed that the elastic stiffness can be tailored and enhanced even for a bending dominated structure and that the anisotropic behavior of the structure can be altered by intertwining the lattice members. Mechanical testing of the FS structure revealed both high stiffness and strain energy density despite having only 20% of the volume of the respective bulk structure. The obtained results indicate that the superior stiffness and strain energy density of intertwined geometries can be realized either under purely elastic deformation conditions at the macroscale or in the presence of excessive plasticity at the microscale. This study paves the way for the investigation and utility of intertwined structures for controlling the anisotropy of ultralight/ultrastiff

geometries at micro/macroscales, which is of particular importance in largescale engineering applications and microstructural engineering of structures. In addition, it promulgates how different mechanical effects manifest themselves at different length scales, depending on the fabrication material and deformation regime.

4.2 Anisotropic and Curved Lattice Members Enhance the Structural Integrity and Mechanical Performance of Architected Metamaterials

Section Summary

The objective of this investigation was to introduce a comprehensive design methodology for highly complex structures using geometrically simple elements. To this end, a novel mechanical metamaterial inspired by the isotropy groups in crystals undergoing phase change [368] was designed, fabricated, and tested. The geometry of the fabricated structures is based on the three-compound octahedron, a variation of the first stellation of the rhombic dodecahedron. The stellations of regular polyhedra provide basic geometries for an expanded and continuous design space [70]. This is mainly due to the fact that the intertwining nature of multiple lattice members can be used to tailor buckling and stiffening. Two different paradigms of hierarchical assembly were considered in this study. As a design concept in nature, hierarchy depends on structural features existing at different scales of the same geometry [266, 110]. However, hierarchical patterns of the same length scale can simplify the fabrication process, hence significantly mitigating the complexity of the design process. Another principal objective of this study was to demonstrate how the structural integrity may be improved by modifying the lattice members of the metamaterial structure. Results from finite element simulations and in situ scanning electron microscopy-nanoindentation experiments are presented to elucidate the characteristic deformation stages of the fabricated metamaterial structures.

Design of anisotropic intertwined structures

Intertwined Structures

The conceptual design process for assembling the architected metamaterial structures of this study is depicted in Fig. 4.15. The building blocks of the unit cell are three equilateral octahedra Fig. 4.15(a) with their edges connected in such a way that the intersection points divide each edge according to the $1 : \sqrt{2}$ ratio (Fig. 4.15(b)). To obtain this geometrical arrangement, known as the three-compound octahedron [72], each octahedron is rotated by 45^o with respect to the other two octahedra. It will be shown that such intertwining and positioning of lattice members in a confined space enables tailored buckling, which, in turn, enhances energy dissipation and contact of the buckled lattice members that causes

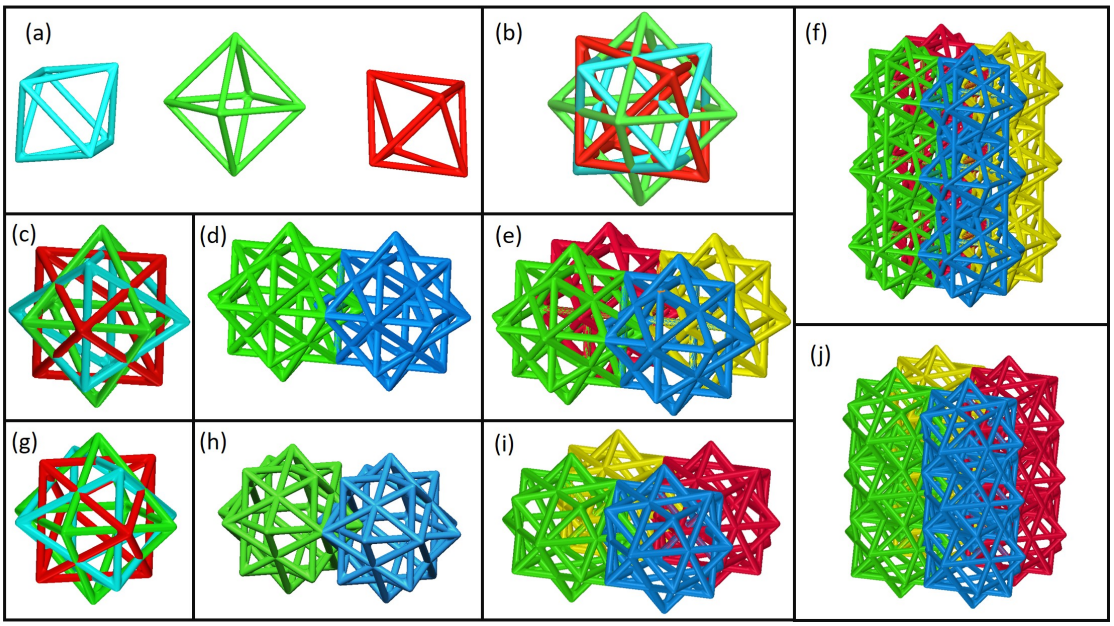

Figure 4.15: The design process of anisotropic intertwined lattice structures with straight members. (a) Three regular octahedra are rotated clockwise and counter clockwise by 45^o with respect to each other. (b) and (c) The three octahedra are assembled to form a three-compound octahedron unit cell. (d) Two unit cells are connected at their neighboring edges. (e) The same process is repeated in the normal direction to form a hyper unit cell (design A). (f) The final structure is assembled by connecting hyper unit cells in the vertical direction, creating a three-layer structure. (g) The unit cell shown in (b) rotated by 90^o either clockwise or counter clockwise. (h)–(j) The process shown in (d)–(f) is used to create a three-layer structure by connecting hyper unit cells consisting of unit cells connected at their vertices (design B). The intertwining of lattice members enables tailored buckling and stiffening during deformation.

structure stiffening. The reason for selecting this relative orientation of octahedra from a myriad of potential configurations is that this geometry has one symmetry group, i.e., octahedral symmetry [356]. Hence, the effect of the unit cell orientation on the deformation mode is drastically decreased. Nevertheless, it is not a uniform polyhedron compound, that is, transformations do not map every vertex to every other vertex; therefore, further intervention on the design process may alter the topology of the structure, e.g., the relative density or even the coordination number and, consequently, the mechanical properties [356].

The potential design space is vast, considering there are 36 more isohedral deltahedra and many more stellations of regular polyhedra, such as the 59 stellations of the regular icosahedron [70]. To further improve the mechanical performance, a second-level assembly was used in which neighboring unit cells were connected with each other; however, the

symmetry of the formed hyper unit cell depends on the orientation of unit cells. Hence, different connections of unit cells may significantly affect the mechanical performance. In this study, the three-compound octahedron (Fig. 4.15(c)) was connected to the horizontal edges of neighboring unit cells in the horizontal plane (Figs. 4.15(d) and 4.15(e)) and the resulting hyper unit cell was used to assemble a three-layer structure (Figs. 4.15(f)). This design will be hereafter referred to as the design A. Alternatively, the three-compound octahedron was rotated by 45^o (Fig. 1(g)), and the same process was used to form a hyper unit cell consisting of two three-compound octahedra connected to their vertices (Figs. 4.15(h) and Figs. 4.15(i)). The final structure was assembled by connecting the vertices of neighboring hyper unit cells (Figs. 4.15(j)). This design will be hereafter referred to as the design B. The reason for selecting these designs is that they represent two extreme cases from the connectivity perspective. In design A, each unit cell is connected to the edges of neighboring unit cells, whereas in design B, the unit cells are connected at their vertices. Therefore, the investigation of these two extreme designs may elucidate the effect of the present design process on the overall mechanical response [43, 368]. Another reason for studying these designs is to unravel the effect of connectivity on the mechanical response. The particular design principle was inspired by the distortion of crystal symmetry during phase change in solids, which causes a variation in the mechanical response [43].

At this juncture, it is instructive to categorize the structure as either bending or stretching dominating and compare its performance with characteristic architected materials from these families [291, 450]. For this purpose, the average connectivity Z of the two designs was obtained by computing the number of beam elements and joints in each hyper unit cell [93]. The average connectivity for designs A and B was found to be equal to 7 and 5, respectively. As both structures are 3D, a necessary and sufficient condition for the structures to be stretching dominated is $Z \geq 12$ [291]. Therefore, these structures exhibit bending dominated behavior and belong to the same category of structures as the BCC, cube, diamond, Kelvin, and rhombic dodecahedron structures [450].

According to the classical theory of the mechanical properties of foams and ultralight structures, the elastic stiffness, E, yield strength, σ_Y, and energy dissipation, u, depend on the relative density, $\bar{\rho}$, of the structure [140, 13, 264, 265]. This property can be used to compare the mechanical properties of the unit cells. For the three-compound octahedron hyper unit cells with designs A and B, the relative density is given by

$$\bar{\rho}_A = 134.16(\frac{d}{L})^2 - 699.12(\frac{d}{L})^3 \tag{4.14}$$

and

$$\bar{\rho}_B = 121.96(\frac{d}{L})^2 - 431.29(\frac{d}{L})^3 \tag{4.15}$$

respectively, where d and L are the diameter and length of lattice members, respectively. The relative density of the structures for various values of the diameter/length ratio, d/L was obtained with the 3D CAD design software (Solidworks 2016 $\times$ 64). To discount the effect of

the excessive overlapping of the lattice members at the nodes from the relations of the relative density, the ends of the beams were cut with appropriately chosen cut surfaces in the CAD files and the results were then curve fitted to obtain Eqs. 4.14 and 4.15. The intertwining employed in design A may affect the relative density of the final structure compared to design B. The relative density corresponding to designs A and B is $\bar{\rho}_A \approx 0.248$ and $\bar{\rho}_B \approx 0.251$, respectively. These values were obtained from Eqs. 4.14 and 4.15 for $d = 0.5\mu m$ and $L = 10\mu m$, which are the dimensions of the lattice members in the fabricated test structures. Although the difference in relative density is only 0.003, it will be shown that the strength and energy dissipation of the structures with designs A and B differ significantly. It is noted that the present 3D intertwining of only 12 unit cells yields very large relative densities. This can be ascertained by comparing the relative densities of the structures with designs A and B (Eqs. 4.14 and 4.14, respectively) with those of other thoroughly studied mechanical metamaterials (e.g., octet truss, cube, rhombic dodecahedron, diamond, Kelvin, and Weaire-Phelan) that have lattice members with circular cross sections [164, 450]. In the equations of the relative density from the literature used for comparison, the overlapping of the lattice members at the nodes was also excluded from the calculated volume of these structures.

Figure 4.16(a) shows the relative density of different unit cells as a function of the lattice diameter/length ratio. The significantly higher relative densities of the unit cells with designs A and B than those of other unit cells are attributed to their intrinsic intertwining, which becomes especially pronounced as d/L increases above 0.01. According to a previous study [148], the estimated relative density of the Kelvin unit cell is also significantly lower than that of designs A and B in this range of d/L. To obtain the same relative density as in designs A and B, the diameter of each lattice member of the rhombic dodecahedron, for example, would have to be increased to $4\mu m$ [164]. However, this would greatly increase the fabrication time and the volume of the structure, making the mechanical performance mainly dependent on the bulk behavior, which is contrary to the main objective of this study to develop a design strategy effective in promoting localized buckling and overall stiffening. Importantly, the present design provides a means of enhancing the mechanical performance of structures in Ashby's charts [264, 265] with a limited number of unit cells relative to conventional ultralight structures that do not utilize intertwining. A solid evidence of this effect can be obtained in the light of the results shown in Fig. 4.16(b). The effective stiffness ($\bar{E}$) of the octet truss was plotted to follow the scaling law reported elsewhere [265], while the effective stiffness of the structures with designs A and B was plotted by curve fitting the data of FEA simulations performed for various d/L values and small normal displacements. The effective stiffness of bending dominated structures scales with the square of the relative density, whereas that of stretching dominated structures shows a linear scaling proclivity [265]. While these power laws differ at high relative densities, the mechanical properties of bending and stretching dominating structures with $\bar{\rho} \leq 0.05$ can be accurately modeled by quadratic and linear scale laws, respectively. Although $\bar{\rho}_A$ and $\bar{\rho}_B$ are significantly larger than 0.05 (Fig. 4.16(a)), the quadratic scaling law fits closely the FEA data in the 0–0.06 range of d/L (Fig. 4.16(b)). Even though the octet truss is stiffer in the range of $d/L \leq 0.055$, the remarkably higher relative density of the intertwined structures yields a stiffness of

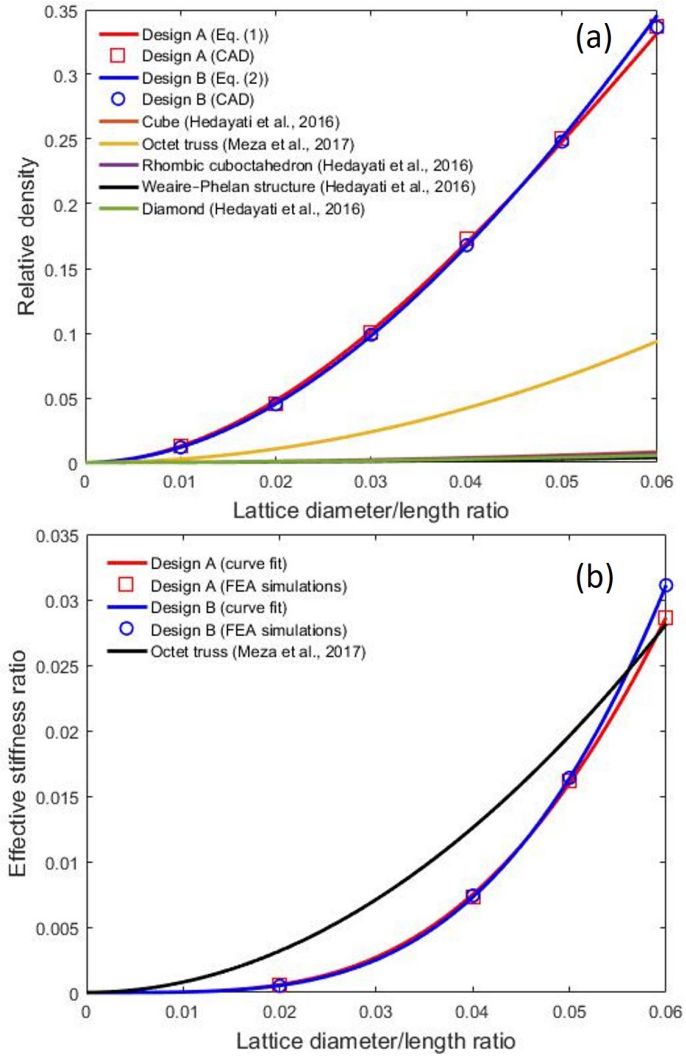

Figure 4.16: Variation of the (a) relative density and (b) relative stiffness with the diameter/length ratio of lattice members in various unit cells. The 0–0.1 range of the diameter/length ratio is typical of the dimensions of structures fabricated by micro/nanolithography techniques. For this realm of dimensions, the structures with designs A and B show remarkably higher relative density compared to other bending dominated structures and higher relative stiffness than that of the octet truss structure for diameter/length ratios greater than 0.055.

approximately the same order of magnitude as the octet truss for $d/L = 0.05$. At higher relative densities, even higher order terms (e.g., $(d/L)^4$) may have an additional contribution [265]. However, since the present test structures are at the threshold of $d/L = 0.05$, their stiffness is comparable to that of stretching dominated structures. It is also noted that at

higher d/L values, $\bar{\rho}_B$ begins to diverge from $\bar{\rho}_A$ significantly. Nevertheless, it will be shown that contact of beam members with neighboring members due to deformation is also critical to the mechanical behavior of the structure.

Curved Lattice Members

Another way to tailor the mechanical behavior of metamaterials is to use curved lattice members in certain locations of the structure. Introducing curvature in some lattice members can forestall deformation in specific directions [53], hindering deformation in other members as the stiffness will vary depending on whether the curved lattice members are convex or concave in the direction of loading. This design will be hereafter referred to as the design C (Fig. 4.17(a)). The curved red and blue lattice members were selected such that the structure to exhibit softening during loading, accordingly becoming more susceptible to large deformations. The curved members were placed where a unit cell was connected to neighbouring unit cells (Figs. 4.17(b) and 4.17(c)), providing a union of connections for both edges and vertices. The assembled structure consisting of three layers of hyper unit cells is shown in Fig. 4.17(d). The coordination number of this structure is equal to 4, rendering it a bending dominated metamaterial structure as well. To enhance the deformability, the diameter of the lattice members was reduced to $0.25\mu m$, thereby increasing the slenderness ratio and, in turn, decreasing the critical load for buckling. The increase of the distance between the unit cells in the vertical direction yielded $\bar{\rho}_C = 0.023$, i.e., an order of magnitude less than $\bar{\rho}_A$ and $\bar{\rho}_B$. Despite the significantly reduced stiffness, it will be shown that this structure can sustain recoverable large deformations. Since this design is an alteration of design B, the curvature r of the curved lattice members leads to the following modification of Eq. 4.15, i.e.,

$$\bar{\rho}_C = f(r)\bar{\rho}_B \tag{4.16}$$

For the specific configuration of design C, curve fitting of the relative densities corresponding to designs A and B obtained from the CAD models yielded $f(r) = 0.331$.

Modeling and experimental methods

Finite Element Analysis

A quasistatic finite element analysis (FEA) was performed to evaluate the mechanical response of the architected structures and to obtain preliminary insight into the anisotropy effect of the hyper unit cells on buckling and post-contact behavior. The FEA simulations were performed with the multi-physics code ANSYS (Workbench 18.0). The ANSYS Design Modeler was used to design the structure geometries. All of the beam members were discretized by 10-node, tetrahedral, finite elements. Surface contact was detected by 8-node surface elements assigned to the beam members of the top layer of the structure. The selected contact condition of the flat tip with the structures was no separation of the elements

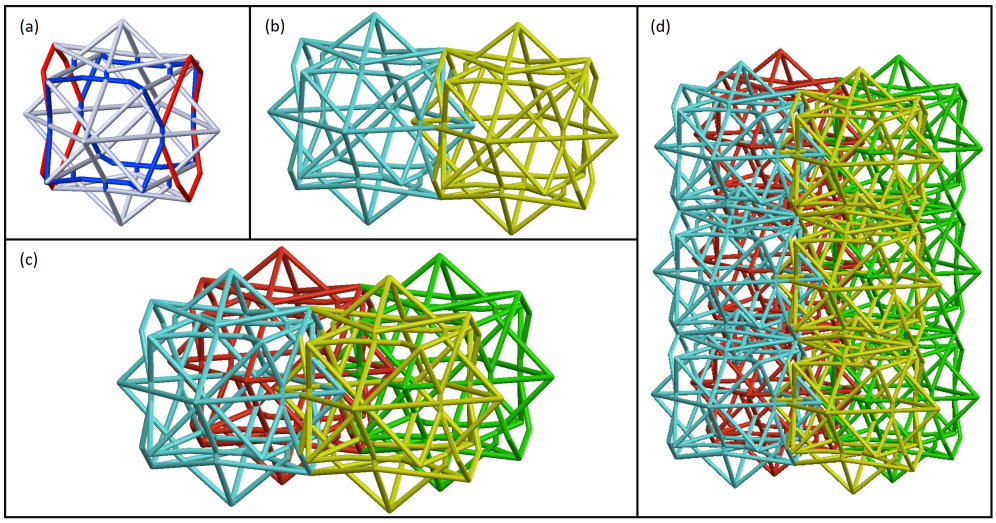

Figure 4.17: The design process of anisotropic intertwined lattice structures with curved members. (a) The initial three-compound octahedron with curved lattice members coloured blue and red. (b) The assembly of two unit cells connected at their edges. (c) Two of the foregoing unit cells connected to two more unit cells at their vertices in the direction perpendicular to the direction the former unit cells were connected to their edges to allow larger deformation in a specific direction and to form a hyper unit cell. (d) The assembled final structure consisting of three layers of hyper unit cells (design C). The use of curved lattice members combined with strategic positioning of unit cells preserves the structural integrity even at large deformations.

at the tip/structure contact interface. The structure with design A comprised 791,913 elements with 1,283,397 nodes, the structure with design B had 937,285 elements with 1,511,432 nodes, while the structure with design C was modelled with 332,721 elements having 635,257 nodes. Since the bottom face of each structure was firmly attached to a substrate, all the degrees of freedom of the bottom nodes were fully constrained. The base solid was modelled to have 0.5 GPa elastic modulus, 0.45 Poisson's ratio, and 18 MPa yield strength. These material properties are similar to those of the polymers used in MPL fabrication. The tip was modeled to have 330 GPa elastic modulus, 0.29 Poisson's ratio, and 324 MPa ultimate tensile strength.

An eigenvalue buckling analysis was performed to investigate the buckling behavior of the structures. This was accomplished by solving the eigenvalue equation 4.13. The details of the derivation of Eq. 4.13 for 3D problems have been reported elsewhere [218]. Buckling commenced when the load applied to the structure reached a value equal to λ times a unit compressive load.

To extract engineering stress-strain responses from the experimental force-displacement

curves, the tip-structure contact area was calculated as a function of tip displacement. The obtained numerical data were used to derive expressions of the contact area, which was then used to divide the measured force and compute the engineering stress. The engineering strain was calculated by dividing the tip displacement by the initial height of the structure. Any abrupt changes in contact of the beam members during the simulation were recorded by the FEA solver, enabling the post-contact events during the deformation to be enumerated. This result was also verified by visualizing the deformed configuration in the simulations.

Microfabrication

All of the test structures were fabricate by the MPL process, which uses multiphoton absorption to induce photoresist photopolymerization. The high spatial resolution provided by the MPL enables precise 3D fabrication [343]. The MPL is particularly efficient for fabricating arbitrary 3D geometries compared to other techniques, such as fused deposition modelling or microstereolithography [75] requiring a very high resolution to fabricate complex structures. The test structures were fabricated with an MPL apparatus equipped with a NIR laser (FemtoFiber pro, Toptica) of $780nm$ wavelength, 100 fs pulse width, and 80 MHz repetition rate. The laser beam was focused by a $100\times$ microscope objective lens (Plan-ApoChromat $100\times/1.40$ Oil M27, Zeiss). Localized polymerization of the structure material was achieved by tightly focusing the laser into the photosensitive material. The stage was translated so that the focused beam could 'write' inside the material and fabricate the desired structure. The structure beams were designed as lines oriented in a 3D space. This geometry was then converted to a g-code, whose coordinates defined the edges of the desired structure. Because the fabrication occurred from top to bottom, depending on the design of the structure, the geometry was designed to prevent line overlapping; otherwise the beam would interact with polymerized material. Further details about the experimental setup and materials used in the present study can be found elsewhere [66]. The high resolution provided by MPL enables complex arbitrary structures to be produced by fabricating each individual lattice member in 3D space.

Mechanical Testing

In situ indentation tests were performed with a nanoindentation apparatus (PI 85 SEM PicoIndenter, Hysitron) placed inside a scanning electron microscope (FEI Quanta 3D FEG), thus enabling high-precision nanomechanical testing and real-time recording of deformation. The molybdenum tip (Model # 72SC-D3/035 (407A-M)) was cut to a diameter of $130\mu m$ with a femtosecond laser. The maximum tip displacement was set at $10\mu m$. A triangular force function with loading and unloading rates both set at $0.2\mu m/s$ was used in all the tests. To ensure the repeatability of the measurements, each experiment was repeated at least three times.

Results and discussion

Finite Element Simulations of Metamaterial Structures

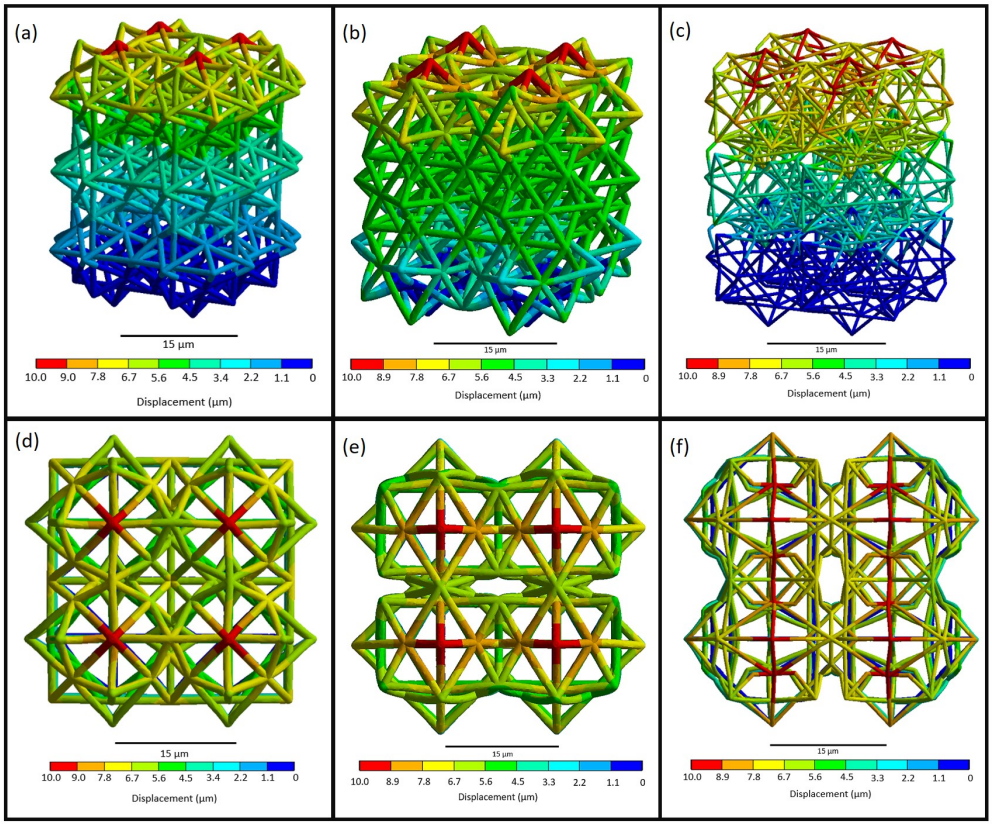

Figure 4.18: FEA results of anisotropic intertwined lattice structures deformed in compression. Deformed structures with (a) design A, (b) design B, and (c) design C. Top-view of deformed structures with (d) design A, (e) design B, and (f) design C. Each structure consists of 12 unit cells with a height equal to 20 μm. The structure height in designs A, B, and C is 23, 20, and 48 μm, respectively. The simulations indicate that the lattice members of the upper layer (red colored) are most likely to fail first. The orientation of lattice members in design A lessens the deformation in the upper layer compared to the structure with design B. Because the structure with design C shares structural features common to both structures with designs A and B, deformation of the lower layers is minimal, while the largest deformation is sustained by the less supported lattice members of the upper layer.

Figure 4 shows FEA simulation results of structures with designs A–C compressed by a flat tip. Each structure comprises three layers consisting of a 2 × 2 hyper unit cell (i.e., 12 unit cells). As expected, the largest deformation was sustained by the lattice members of the

top layer of each structure (red colored). However, a comparison of Figs. 4.18(a) and 4.18(b) indicates that lattice intertwining in design A was significantly more effective in reducing deformation compared to design B, especially in the lattice members of the upper layer. This is attributed to the positioning of lattice members in the second stage of the assembly process of design A (Figs. 4.15(b)–1(e)). Because the lattice members in design A that sustained most of the compressive deformation were much closer to each other, they contacted each other during deformation, increasing the structure's stiffness and strength. This result can be validated by considering the number of contacting beams (calculated at each of 1-μm-displacement steps) versus the tip displacement shown in Fig. 4.19. Design A shows a significantly larger number of beams in contact, with these post-contact events commencing at a smaller displacement (4 μm) compared to designs B and C (8 μm). As shown in the next section, the onset of post-contact at this early stage of deformation is critical to impeding microcracking through this intrinsic stiffening effect. Because the intertwined unit cells in design B (Figs. 4.15(g)–1(i)) are connected with neighboring unit cells at their vertices rather than their edges, post-contact behavior was greatly mitigated. The lattice intertwining in design A also inhibited deformation of the lower layers (blue colored), whereas in design B all of the layers under the top layer exhibit fairly similar and relatively higher deformation (green colored). This intertwining also provides an energy dissipation mechanism in a multilayer structure. Interestingly, although the relative densities of designs A and B are approximately the same, the spatial orientation of the unit cells plays a critical role on the mechanical performance. The deformation encountered with design B was also observed with design C (4.18(c)). This is attributed to the increased distance between lattice members. However, the connection of each unit cell to the edges mitigated the deformation in the lower layer, similar to what was observed with design A. The upper layers of each structure accrued most of the deformation, relaxing the rest of the structure. In particular, only eight of the top lattice members of the structure with design A sustained the largest deformation (Fig. 4.18(d)) as opposed to more lattice members in the structures with designs B and C (Figs. 4.18(e) and 4.18(f), respectively).

From the eigenvalue buckling analysis, the load multiplier ratio of designs A and B, $\frac{\lambda_A}{\lambda_B}$, was found to be equal to 1.08, implying essentially the same buckling load for both designs. Hence, structure anisotropy did not show a significant effect on buckling behavior. However, the load multiplier ratio of designs A and C, $\frac{\lambda_A}{\lambda_C}$, was found to be equal to 7.71, i.e., higher than $\frac{\lambda_A}{\lambda_B}$ by a factor greater than 7. This indicates that curved lattice members can enhance buckling, provided they are positioned appropriately within the metamaterial structure.

Although the computed critical buckling loads provide insight into the overall instability of each structure, the experimental results presented below indicate that this buckling phenomenon is not associated with microscopic buckling instigated at the edges and walls of the unit cells [158] and associated with the bifurcation instability of the beam members [386]. This localized buckling behavior is manifested at specific wavelengths that can be potentially larger than the dimensions of the unit cells [158]. These modes of the buckled structure, termed the representative volume element, demonstrate significant variance

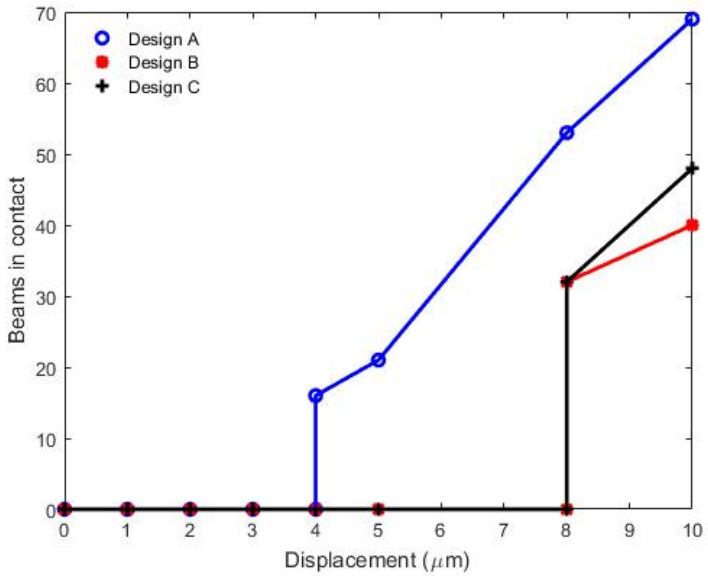

Figure 4.19: Number of beam members coming into contact during deformation as a function of normal displacement. Post-contact of lattice elements in the structure with design A commences at a displacement of $4\mu m$ as opposed to a much larger displacement of $8\mu m$ for the structures with designs B and C.

with each other, depending on the macroscopic loading conditions applied to the structure. These different modes can be obtained by methods like the Bloch wave theory [135, 189]). Moreover, metamaterial structures may also be subjected to macroscopic buckling or overall buckling, as reported for large wavelengths [141, 148, 147, 295, 192]. This behavior has been attributed to the loss of ellipticity of the homogenized incremental equilibrium equations of the material [135]. Nevertheless, both of these effects are investigated and demonstrated under the assumption that the cellular structure extents infinitely in 3D space or for a specific number of unit cells that the solutions converge. Because the MPL can fabricate a small number of unit cells efficiently, the present study does not focus on these effects. Therefore, the critical buckling load and its corresponding mode may not be associated with long-wavelength instability of a large 3D structure and can only be interpreted in terms of the effect of instantaneous localized structural changes on the mechanical response observed in the experimental results of this study.

Fabricated Metamaterial Structures

Figure 4.20 shows SEM images of three-layer metamaterial structures with designs A–C. The length and diameter of the lattice members of design A (Figs. 4.20(a) and 4.20(b)) and design B (Figs. 4.20(d) and 4.20(e)) is 10 and $0.5\mu m$, respectively, while the lattice members

of design C (Figs. 4.20(c) and 4.20(f)) have a length of $10\mu m$ and a diameter of $0.25\mu m$, which is the minimum diameter needed to preserve the structural integrity and prevent the collapse of the structure under its own weight. The dimensions of the unit cells shown in Fig. 4.20 are the same as those in the FEA simulations.

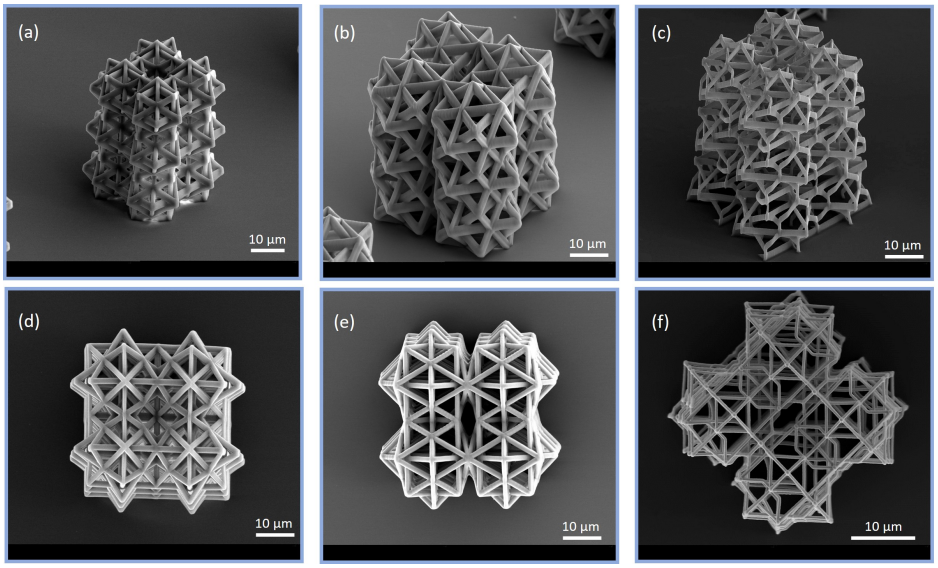

Figure 4.20: SEM micrographs of anisotropic intertwined lattice structures with straight and curved members. Side view of structures with (a) design A, (b) design B, and (c) design C. Top view of structures with (d) design A, (e) design B, and (f) design C. The diameter of the lattice members in the structures with designs A and B is equal to $0.5\mu m$, while that of lattice members in the structure with design C is equal to $0.25\mu m$. The dimensions of unit cells are the same as those in the FEA simulations.

Mechanical Behavior of Metamaterial Structures with Straight Lattice Members

Figure 4.21 shows a representative force versus displacement curve of the metamaterial structure with design A. The response comprises characteristic deformation stages labelled by A–E and shown in representative SEM images. The abrupt change in slope of the force-displacement response at a force of $1640\mu N$ (point B) and $7060\mu N$ (point C) is due to internal buckling of some lattice members, not fracture. The deformation behavior of this structure in the first load/unload cycle can be viewed in the video A of the published version of this chapter [394]. The spontaneous decrease of the force slope at point B was instantly followed by a notable slope increase, attributed to structure stiffening due to the contact of buckled lattice members with other members. A similar buckling and post-contact sequence

of events occurred at point C, i.e., before the maximum load was reached (point D). Importantly, the structure demonstrated significant recovery of its original configuration upon full unloading (point E), revealing a high resilience to large deformations and a unique capacity to dissipate strain energy by its intrinsic nonlinear deformation behavior.

Figure 4.22 shows a typical force-displacement curve of the metamaterial structure with design B. The deformation behavior of this structure in the first load/unload cycle can be viewed in video B [394]. Although the characteristic deformation stages of the mechanical response are similar to those shown in Fig. 4.21, there is an important difference; that is, in addition to the two buckling events encountered at a load of $1401\mu N$ (point B) and $5684\mu N$ (point D), internal beam fracture occurred at a load of $\sim 2000\mu N$ (point C). The ratio of the loads corresponding to the first and second buckling events of designs A and B is equal to 1.17 and 1.24, respectively, which is in good agreement with the load multiplier ratio ($\frac{\lambda_A}{\lambda_B} = 1.08$) obtained from the eigenvalue buckling analysis. The inadequate support of the buckled lattice members due to limited post-contact with neighboring members led to fracture (point C), which continued to concurrently occur with further buckling (point D) as this structure lacked a crack arrest mechanism (video B). Hence, design B does not meet the design objectives, despite having the same unit cell as design A.

To examine the evolution of the mechanical response due to cyclic loading, structures with designs A and B were subjected to three sequential load/unload cycles. The engineering stress-strain responses obtained from these experiments are shown in Fig. 4.23. For design A, energy dissipation (i.e., the force hysteresis area) increased initially and stabilized in the third cycle. Cyclic loading increased the slope of the loading curves of both structures, a consequence of contact between deformed and buckled lattice members. The stress drops in the loading response of the structure with design B in the first and second cycle are manifestations of multiple buckling and fracture events. In addition, the stress-strain response for design B reveals a brittle-like behavior that is devoid of the stress plateau observed with ductile materials and perpetual fracturing.

To further evaluate the mechanical performance of the foregoing structures, the residual strain, ε_r (obtained after full unloading), the energy dissipation per unit volume, u (i.e., the area under the stress-strain curve), and the elastic stiffness, S (i.e., the initial slope of the unloading curve), are compared in Table 4.3. The table includes statistical results obtained from all the cyclic loading tests. These results show that the structure with design A exhibits greater deformation resilience, significantly higher energy dissipation capacity, and much higher stiffness at each cycle compared to the structure with design B. In fact, the third-cycle results show $\sim$2 times higher energy dissipation capacity and $\sim$1.36 times higher stiffness for the structure with design A than that with design B. In addition, the rate of increase in energy dissipation is $\sim 40\%$ for the structure with design A and $\sim 11.5\%$ for the structure with design B, implying more significant strain hardening for the structure with design A, with the energy dissipation for the structure with design B also showing a decrease in the third cycle.

Another important difference is that the stress-strain responses corresponding to design A are fairly smooth, while those corresponding to design B show significant fluctuations during

Load/unload cycle	Design A			Design B			Design C	
Metrics	ε_r	$u(\frac{kJ}{m^3})$	$S(MPa)$	ε_r	$u(\frac{kJ}{m^3})$	$S(MPa)$	ε_r	$S(MPa)$
1	0.210 ± 0.015	731.2 ± 15.5	41.21 ± 3.25	0.295 ± 0.055	446.6 ± 30.8	29.54 ± 5.83	0.153 ± 0.13	6.75 ± 0.25
2	0.150 ± 0.020	1022.3 ± 30.1	47.18 ± 3.91	0.277 ± 0.067	577.4 ± 45.9	36.82 ± 4.23	0.140 ± 0.13	9.45 ± 1.47
3	0.126 ± 0.030	1025.5 ± 45.2 (+40.2%)	49.72 ± 2.14 (+20.6%)	0.258 ± 0.075	497.8 ± 5.3 (+11.5%)	36.58 ± 1.09 (+23.8%)	0.134 ± 0.15	20.16 ± 4.91 (+198.7%)

Table 4.3: Statistical data of the mechanical performance of anisotropic intertwined lattice structures with different designs versus load/unload cycle. Numbers in parentheses indicate differences between the third and first cycle.

loading, indicative of perpetual fracture events. The mechanical responses shown in Fig. 4.23 reveal ductile-like deformation behavior for the structure with design A and brittle-like deformation behavior for the structure with design B. In the context of the developed stresses and deformations, the locations of the fractured lattice members (Figs. 4.24(a) and 4.24(b)) are consistent with the FEA simulation results, considering the maximum bending moments arise at the clamped ends of all beam members. Nevertheless, a comprehensive analysis of the fracture mechanisms requires a different FEA model, which is beyond the scope of the present study. The high-magnification micrographs of the highly damaged areas of metamaterial structures with designs A and B (Figs. 4.24(c)–4.24(f)) provide further insight into the fracture of highly deformed lattice members. The areas containing the fractured lattice members (Figs. 4.24(c) and 4.24(d)) are the highly deformed areas predicted from the FEA simulations (Fig. 4.18). Because fewer buckled lattice members came into contact with other members in the structure with design B, this structure exhibited less deformation resistance compared to that with design A. In addition, Fig. 4.24(f) reveals a three-stage fracture process of the lattice members of the structure with design B, characterized by a transition from ductile-like to brittle-like fracture.

Mechanical Behavior of Metamaterial Structures with Curved Lattice Members

Figure 4.25 shows a force-displacement curve characteristic of the structure with design C, and video C [394] shows the deformation of this structure in the first load/unload cycle. Similar to the structure with design B (Fig. 8), this structure also exhibited two main buckling events at a load of $263\mu N$ (point B) and $643\mu N$ (point C). The load ratio corresponding to the first and third buckling events of designs A and C is equal to 6.23 and ∼11, respectively. The difference between both of these values and the load multiplier ratio ($\frac{\lambda_A}{\lambda_C}$= 7.71) obtained from the eigenvalue buckling analysis is attributed to structural imperfections and the possible misalignment of the structure relative to the tip. Despite the large deformation sustained by this structure after each buckling event, its original configuration was fully

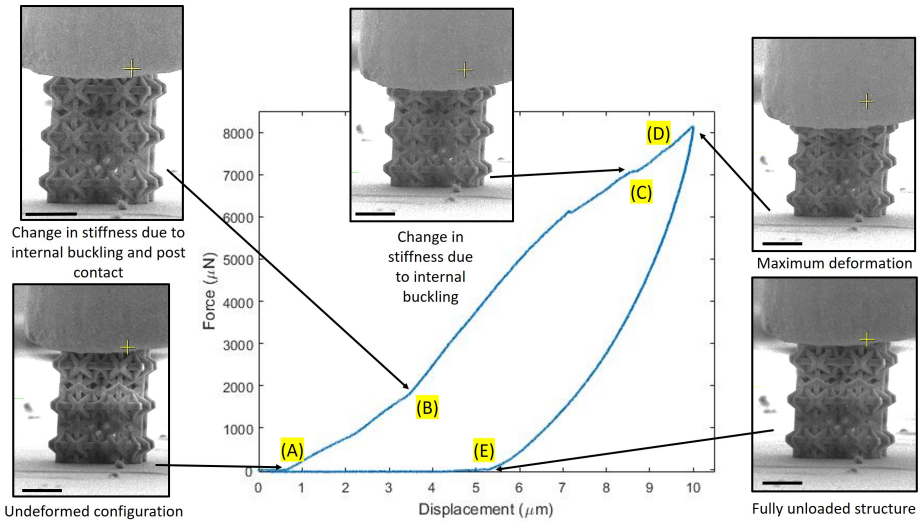

Figure 4.21: In situ characterization of the mechanical performance of an anisotropic intertwined lattice structure with straight members (design A). The mechanical response comprises five distinct deformation states labelled by (A)–(E) and determined from the force versus displacement curve and the video A (SI) of the first load/unload cycle. The flat tip was first brought into contact with the structure (point A). A sudden change in the force slope occurred at a critical load (point B) due to internal buckling. However, the merely instantaneous increase of the slope indicates stiffening due to contact of lattice members with neighboring members. A second similar sudden change in slope occurred at a higher load (point C), suggesting further buckling and contact of lattice members before the maximum load was reached (point D). The original shape of the structure was fully recovered upon full unloading (point E) with only a minor damage accumulated in the lattice members of the top layer, indicative of the structure's resilience to large deformations and high strain energy absorption capacity. In all the SEM images, the bar scale is equal to $20\mu m$.

recovered upon unloading (point D), also seen in video C [394].

To study the evolution of the stress-strain response of this metamaterial structure, the deformation response after each of three consecutive load/unload cycles was examined with the SEM. Figure 4.26 shows undeformed, highly deformed (maximum deformation), and fully unloaded configurations of the structure with design C for each loading cycle, whereas Fig. 4.27 shows the corresponding stress-strain responses. Cyclic loading produced similar buckling events in each cycle (videos C–E in [394]), and the original configuration of the structure was fully recovered after each unloading. Although differences in macroscopic deformation were not detected with the SEM, the loading history differed significantly from those of the structures with designs A and B. Instead of the distinct stress fluctuations that characterized each buckling event in the first cycle, the responses of the second and

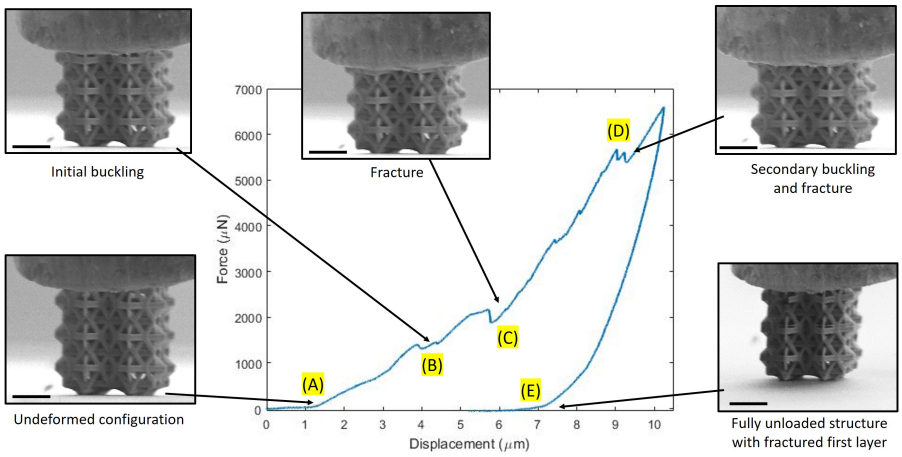

Figure 4.22: In situ characterization of the mechanical performance of an anisotropic intertwined lattice structure with straight members (design B). The mechanical response comprises five distinct deformation states labelled by (A)–(E) and determined from the force versus displacement curve and the video B (SI) of the first load/unload cycle. After the engagement of the flat tip with the structure (point A), a sudden change in the force slope was encountered due to buckling of some lattice members (point B). However, in the absence of proximity lattice members to support the buckled members, fracture of buckled members was instigated with the further increase of the load (point C), and microfracture continued to evolve until the commencement of a second buckling event (point D) before the onset of unloading. The fully unloaded structure (point E) sustained extensive fracture of the lattice members in the top hyper unit cell. In all the SEM images, the bar scale is equal to $20\mu m$.

third cycles were affected by a strain localization mechanism, resembling a strain hardening behavior similar to that caused by shear band formation [176]. This is indicated by the increase of both the stress and the unloading slope between the second and third cycle. While buckling may induce localized strain softening in bulk materials [277], it is possible that this mechanism was triggered by localized fracture in the first cycle of this structure, considering that fracture did not occur in anyone of the following cycles. Hence, the structure with design C demonstrated a macroscopic buckling mechanism that entrenched the fluctuating loading response in the first cycle. In traditional softening, a steady plastic flow is reached and the stress remains constant [58]. However, the stiffness of this metamaterial structure increased after cyclic loading due to post-contact of some lattice members of the unit cells in the upper and intermediate layers, as evidenced from the stress-strain responses of the second and third cycle (Fig. 13), and this effect was conducive to preserving the structural integrity of this structure at all cycles.

The recoverability of this structure compared to those of other designs can be interpreted in the context of the results given in Table 4.3. Although the structure with design C ex-

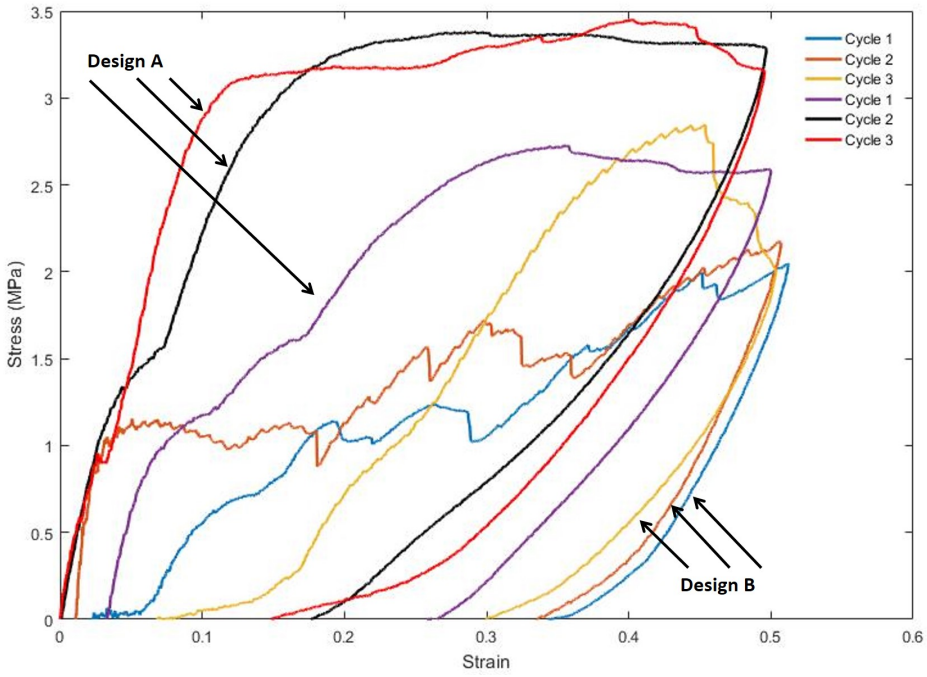

Figure 4.23: Stress-strain responses of cyclically loaded anisotropic intertwined lattice structures with straight members (designs A and B). Three sequential load/unload cycles were applied to examine the dependence of the mechanical performance on the orientation of the unit cells. The results indicate commensurate augmentation of the stiffness, strength, strain hardening, and energy dissipation capacity of the structure with design A compared to that with design B, despite the similar relative densities and identical unit cells. The orientation of the unit cells in design A allowed post-contact of buckled lattice members, resulting in a more ductile-like behavior, whereas continuous fracturing of unsupported lattice members in the structure with design B produced a softening behavior.

hibited the lowest residual strain in the first two cycles, its intrinsic softening mechanism mitigated the higher energy dissipation in the first cycle propelled by buckling (Fig. 4.27); however, the structural integrity was not affected and further fracture of lattice members did not occur. Interestingly, in the third cycle the stiffness increased by ∼200% from the first cycle, a result attributed to the large deformation of lattice members connecting the intermediate layer with the top layer, causing a variance in stiffness due to non-linear geometric effects [53, 87]. The highly deformed regions of this structure (Fig. 4.28) show that the cross-sectional fracture areas of lattice members comprise two regions – an external region at the perimeter of the member and an internal rough region. This morphology indicates that, despite the initial occurrence of instantaneous brittle fracture, the energy dissipation due to buckling transcended into ductile fracture at the later stage of crack growth.

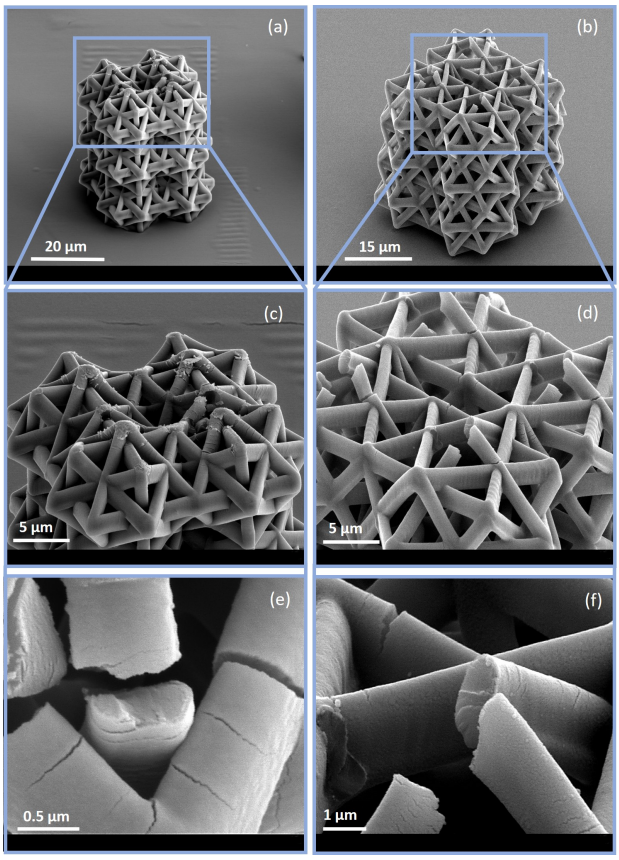

Figure 4.24: SEM micrographs of anisotropic intertwined lattice structures with straight members obtained after three load/unload cycles. Side view of a damaged structure with (a) design A and (b) design B. High-magnification images showing fractured lattice members in the structures with (c) design A and (f) design B. The fractured lattice members correspond to the highly deformed lattice members shown in the FEA simulations. Post-contact of lattice members in design A halted crack growth, enhancing strain hardening and ductility. On the contrary, fracture was not inhibited in the structures with design B during loading in the first cycle due to the lack of post-contact of the buckled lattice members, resulting in a softening behavior. Highly deformed regions of structures with (e) design A and (f) design B. The relatively rough cross-sectional fracture areas of the lattice members of the structure with design A reveal ductile-like fracture, whereas the lines passing through the entire cross-sectional fracture area of the lattice members of the structure with design B reveal a multistage fracture process, demonstrating a transition from ductile-like to brittle-like fracture.

The present study shows that the design of mechanical metamaterials with 3D intertwined lattice structures greatly enhances the stiffness, strain hardening/stiffening, and energy dis-

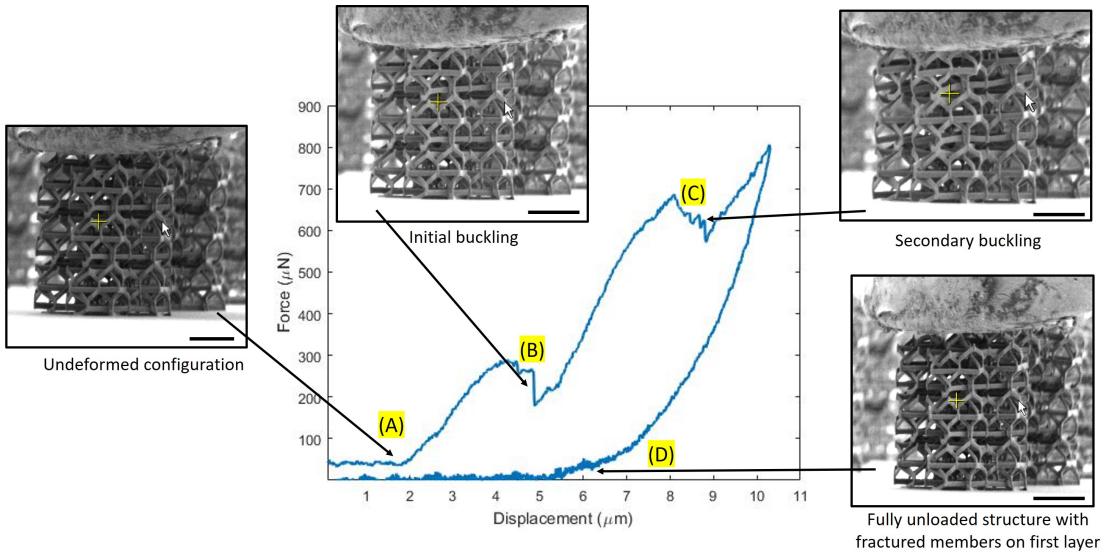

Figure 4.25: In situ characterization of the mechanical performance of an anisotropic intertwined lattice structure with curved members (design C). The mechanical response comprises four distinct deformation states labelled by (A)–(D) and determined from the force versus displacement curve and the video C [394] of the first load/unload cycle. During the loading of the original structure (point A), buckling of the lattice members of the top layer commenced (point B), followed by a second buckling event encompassing lattice members connecting the upper layer with the intermediate layer that resulted in tilting of the structure by $\sim 30^o$. However, due to the capacity of the curved lattice members to sustain large deformations, the structure recovered its initial configuration upon full unloading (point D), despite fracturing of some lattice members of the top layer, consistent with the predictions of the FEA. In all the SEM images, the bar scale is equal to $20\mu m$.

sipation capacity. The employed design owes its effectiveness to the alignment of regular polyhedra in the 3D space and the use of a multilayer assembly method that not only increases the relative density of the structure, but also enhances buckling and post-contact of some lattice members. Importantly, it was confirmed that controlled buckling and post-contact, even for a small number of unit cells, do not exclusively depend on the relative density of the structure, but also on the strategic orientation of the unit cells and their connectivity with neighboring cells in the 3D space. Despite having identical unit cells, the hyper unit cells of the tested metamaterial structures differed in the connectivity of their unit cells. In design A, the unit cells were connected at their edges, while in design B the unit cells were connected at their vertices. Although post-contact of deformed lattice members was possible in both designs, this mechanism was not as effective in the structure with design B because the space between lattice members was not adequately utilized, leaving

large areas unoccupied, hence resulting in post-contact of the deformed lattice members at much higher deformation. As a consequence, the buckled lattice members fractured because they lacked the contact support of neighboring members, resulting in softening and brittle behavior. Alternatively, design A comprised a stable core of intertwined lattice members that exhibited post-contact upon buckling, which was validated by FEA eigenvalue buckling analysis. This design principle is critical to the feasibility of intertwined lattice structures. The post-contact behavior was instrumental in yielding a ductile-like deformation behavior and enhancing the strain hardening and stiffness of the structure. Modifying the original unit cell by introducing curved lattice members (design C) enabled the metamaterial structure to sustain large reversible deformations. Despite the occurrence of softening that ameliorated the mechanical response by preventing buckling, this type of metamaterial structure fully recovered its undeformed configuration upon unloading. Using frame-by-frame visual examination and the force-displacement responses, buckling and fracture events were identified in all structures and the critical failure locations of lattice members were confirmed by FEA simulations.

The fact that the same relative density is not the only factor affecting the mechanical performance was demonstrated by the significant effects of the orientation and connectivity of the unit cells in the structures with designs A and B, despite the identical unit cells of these structures. Therefore, even slight changes in the configuration of the unit cell may result in a completely different geometry that must be addressed separately from all others. The direct consequence is the isolation of structures in the design space as independent entities and the means to efficiently navigate through the design space. In addition, because intertwined lattice structures combine both stretching and bending to enhance stiffening and energy dissipation, the classification of structures dominated explicitly by the former deformation modes is ambiguous. To address this issue, it is necessary to introduce a methodology that can identify isotropy subgroups in crystals. Furthermore, optimization tools, such as topology optimization [380] and deep learning [244], can be used to obtain an optimum configuration of intertwined unit cells. To this end, more advanced experimental techniques must be developed to effectively study anisotropy effects on metamaterial structures [24]. In addition, the MPL process must be advanced to facilitate the fabrication of novel and efficient structures for large-scale applications. Therefore, more systematic research is needed to integrate the MPL process with other techniques, such as holographic lithography [51] or mesoscale fabrication [195], and expediting the design of versatile metamaterial structures for large-scale applications. Additionally, further investigation of both microscopic and macroscopic buckling phenomena is needed to reveal the effect of these mechanisms on large arrays of unit cells and the critical scale for convergence of the obtained modes. Because these structures are 3D and highly complex, optimization techniques, such as deep learning, may be effective in delineating these responses and finding the representative volume element.

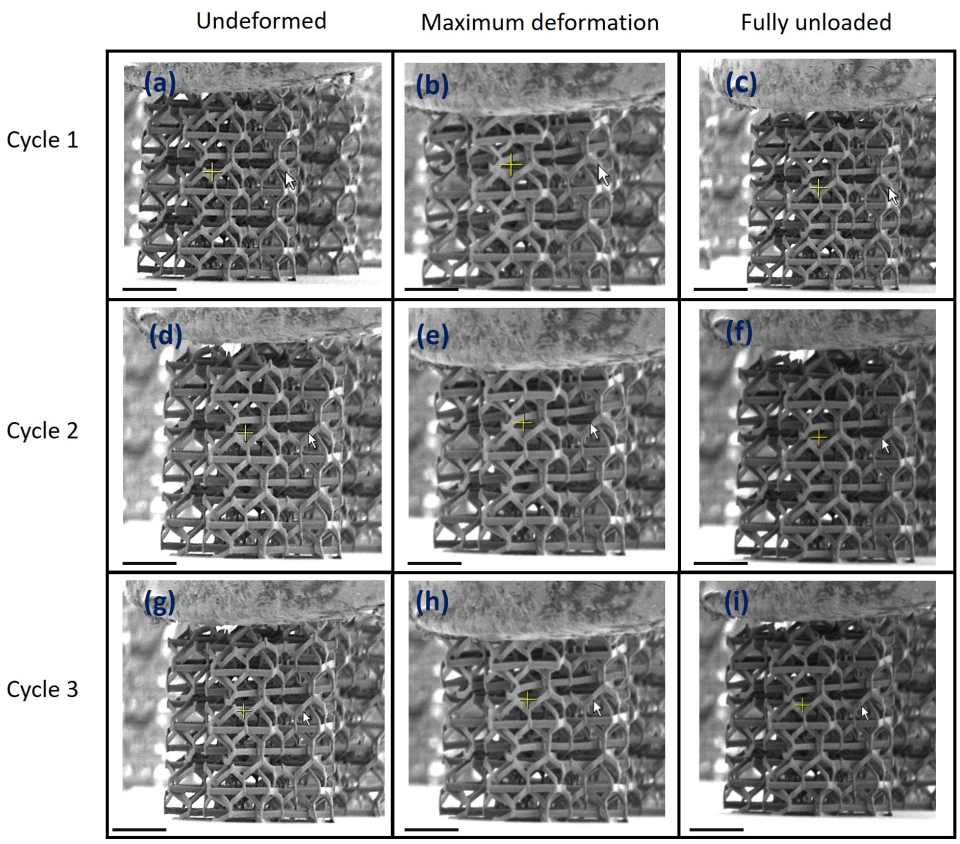

Figure 4.26: SEM micrographs of an anisotropic intertwined lattice structure with curved members (design C) obtained after 1, 2, and 3 sequential load/unload cycles. (a) Undeformed, (b) highly deformed (maximum load), and (c) fully unloaded structure after the first cycle. (d) Undeformed, (e) highly deformed, and (f) fully unloaded structure after the second cycle. (g) Undeformed, (h) highly deformed, and (j) fully unloaded structure after the third cycle. Similar buckling events occurred in each loading cycle enabling the structures to fully recover their original configurations without fracture of any lattice member apart from a few lattice members of the top layer that fractured in the first cycle. In all the SEM images, the bar scale is equal $20\mu m$.

Section Conclusions

A new design approach for mechanical metamaterials that provides significantly enhanced mechanical performance through tailored buckling and post-contact of some lattice members was introduced in this study. The basic geometry is the three-compound octahedron, a variation of the first stellation of the rhombic dodecahedron. The stellated geometries represent a vast source for the design space because they provide an abundance of different complex structures that can be systematically arranged to assemble hierarchical structures

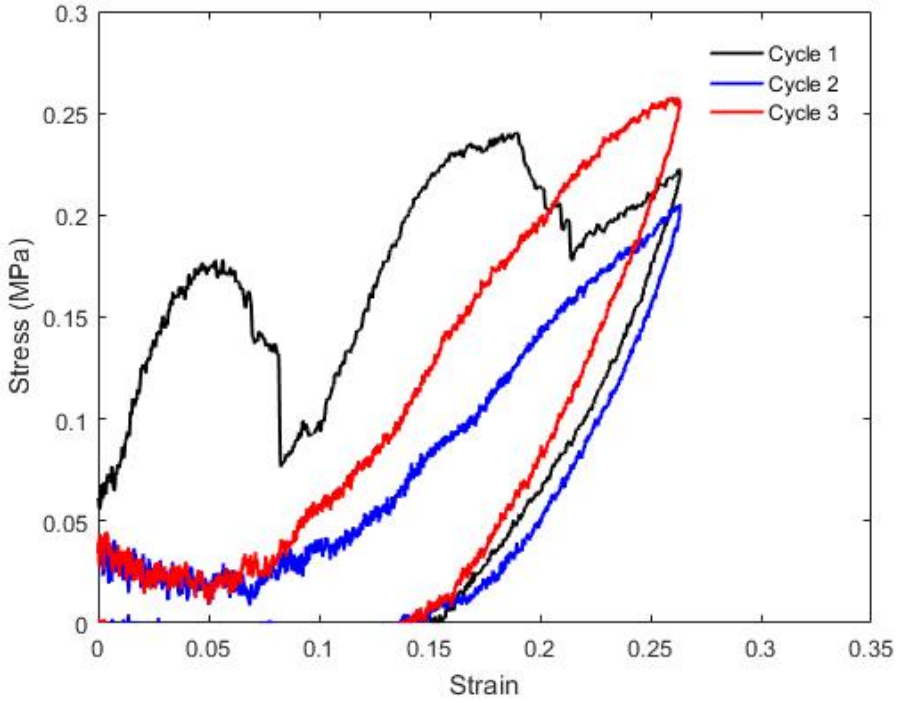

Figure 4.27: Stress-strain responses of cyclically loaded anisotropic intertwined lattice structure with curved members (design C). Three sequential loading cycles were applied to examine the structural integrity of the structure. Despite the similar mechanical responses seen in videos C–E (SI) of the three cycles, localized buckling in the first cycle resulted in contact of lattice members of the top and intermediate layers, causing a significant stiffness increase in the second and third cycles.

with each hierarchy level being at the same length scale. This is advantageous for overcoming the complexities introduced by the length scales needed to resemble the structural characteristics of biomimetic structures. Tailoring the unit cell orientation and shape can be accomplished through the effective integration of design principles, microfabrication, in situ mechanical characterization, and simulations, leading to either unprecedented or inconsistent mechanical behaviors. This study shows that tuning only the relative density and using standard design principles are inept for designing novel ultralight/ultrastiff architected structures. Localized buckling and post-contact of lattice members provided a metamaterial structure with intertwined thick and straight members (design A) that showed increased resilience to large deformations, enhanced stiffness, and high energy dissipation capacity. However, keeping the same unit cell but changing the orientation of the unit cells in the structure degraded the mechanical performance due to fracture of the buckled lattice members (design B). Alternatively, the specific orientation and connectivity of the lattice

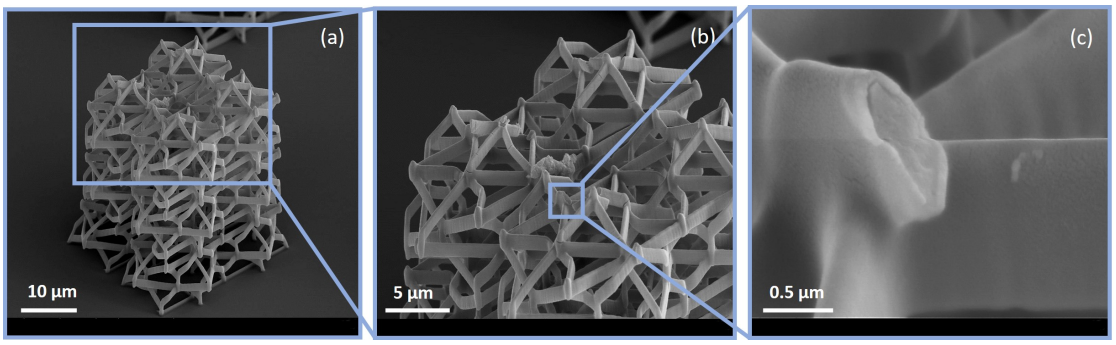

Figure 4.28: SEM micrographs of fractured lattice members of an anisotropic intertwined lattice structure with curved members (design C) obtained after three sequential load/unload cycles. (a) Overall view of the highly deformed structure. (b) A fractured region of the top layer. (c) High-magnification image showing that the cross-sectional fracture area of lattice members comprises an external peripheral zone indicative of brittle-like fracture and an internal rough zone revealing ductile-like fracture.

members in the intermediate and top layers of the metamaterial structure with thin and curved members (design C) provided remarkable recoverability and high stiffness. The unprecedented mechanical responses of structures with designs A–C were achieved by utilizing the connectivity and geometric effects of simple polyhedral structures. The present study establishes an important design foundation for architected metamaterials tuned to exhibit large reversible deformations, significant strain hardening/stiffening, and high energy dissipation capacity. This can be accomplished by controlling localized buckling of the lattice members and inducing ductile and strain localization responses that resemble those of bulk materials.

4.3 Laser Pyrolysis for Controlled Morphing and Chemical Modification on 3D Microlattices

Section Summary

In this study it is demonstrated the localized laser pyrolysis of polymer microlattices. First, localized modification is presented on one single beam with chemical composition mapping. Next, it is shown that localized shrinking can generate collective mechanical deformation and form new geometries on 3D unit cells such as the octet truss (OT) and the first stellation of rhombic dodecahedron (FS) [402]. Highly curved and twisted structures are fabricated, which are a conundrum with conventional MPL. Finally, with controlled CW laser irradiation at specific positions and directions, gradient deformation can be introduced on periodic microlattices. Through heat transfer simulations, we elucidate the underlying mechanisms and

provide a design approach to architect the modified structures. The mechanical performance of deformed structures is also predicted through finite element analysis (FEA). Finally, by performing in-situ SEM on microindentation analysis, we delineate how a 3D hybrid, partly ceramic, partly polymeric hybrid structure [353] can have enhanced mechanical performance due to the combination of structural features and its composite nature.

Results and Discussion

The experimental procedure of the laser selective morphing of the polymer structure is depicted in Fig. 4.29. The femtosecond pulsed laser is used to induce MPL inside a photosensitive resin, whereas the photoexcited structure is developed to form a polymerized microstructure. To convey this, a simple FS structure unit cell is schematically shown as the sample. Then the polymerized structure is sputtered with gold to enhance the absorbance of the micro lattices, which is recommended for the CW laser processing. If no sputtering is applied, the shrinking requires either wavelength below $300nm$ [303] or short pulses ($\leq 1ms$) and the power threshold is much smaller. Preliminary tests conducted using a nanosecond laser showed that the controllability of the shape of the structure is substantially mitigated and the power threshold is limited. Since these methods increase the complexity of the process to obtain the optimum parameters, the CW laser processing was selected. When the CW laser is focused on the prepared sample, the polymer is subject to high temperature heating and localized carbonization. The decomposition of the material and the evaporation of the gaseous phase introduces shrinkage of the structure, encompassed by deformation. When the laser heating is spatially distributed in a controlled fashion, then the tailored deformation is evinced (Fig. 4.29(d)).

More specifically, to increase the absorbance of the material and increase the realm of the laser processing power, we gold sputtered the samples for $100s$. For the designated time, the thickness of the coating is 15 nm. Then, a CW laser (Lighthouse Sprout-C $4W$, $532nm$) is used to process the sample. A Mitutoyo APO 10X objective lens is utilized to focus the laser beam into a 6um FWHM diameter. The in-situ video recording of the process is captured with a CCD camera from AmScope MD1000. The laser power for effective deformation was calibrated to be $5 - 10mW$ depending on the heat dissipation of the processed target. For point irradiation, the laser dwell time is set to be 200ms and for scanning, the speed is set to be $0.1mm/s$. For the heating or the individual beam members, the same apparatus was employed with laser power equal to $10mW$. Higher laser powers lead to the ablation of the beam members. The laser beam was focused on the top of the beam member. By scanning the laser beam along the length of the beam member, uniform shrinkage of the cross section along the whole length was accomplished. In order to accomplish multiple locally heated spots in the structure, the laser beam was splitted using a beam splitter and utilizing a Mitutoyo APO 20X objective lens, two distinct laser beams with distance $10\mu m$ could simultaneously heat the structure.

Detailed geometry and chemical composition changes are characterized on simple structures (Fig. 4.30(a)-(d)) to fathom the associated mechanisms. The length of the triangular

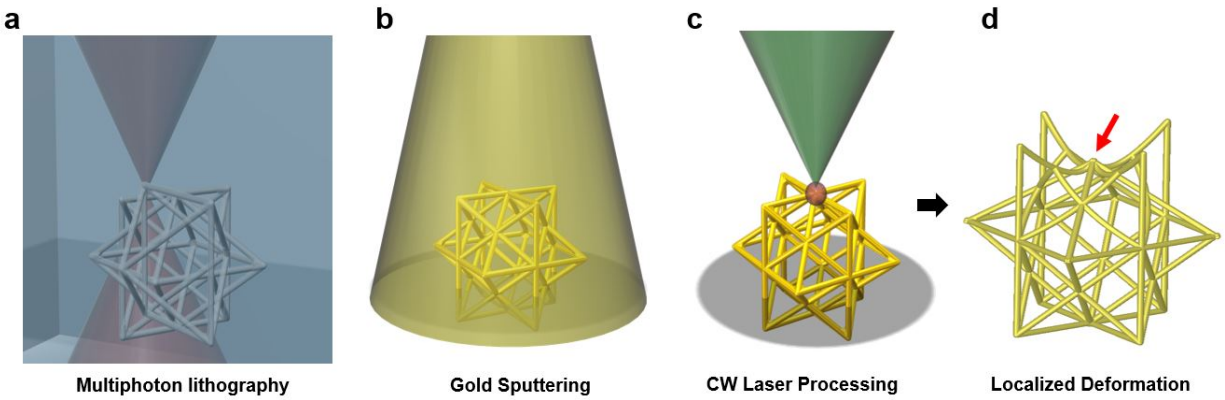

Figure 4.29: The proposed process of the laser site selective modification of MPL fabricated 3D structure. (a). Multiphoton lithography (b). Gold sputtering to enhance absorption, a step which is optional depending on the employed laser power and pulse regimes. (c) The focused laser beam heating at the top of the 3D structure, which is labelled with a red sphere. (d) Laser heating induced gradient volume reduction and the resulted gradient structure. The upper half of the structure is shrank and the upper beam members are curved.

beams is $20\mu m$ and their thickness is approximately $500nm$. Laser irradiation on a single member of the structure leads to the local shrinking of this individual member, whose deformation can be observed from both side view and top view. EDS analysis on heated and unheated structures reveals that the laser heating causes changes in the chemical composition of the material (Fig. 4.30(d)). We observe a significant decrease of carbon content from 41% to 23% on the heated member compared to the non-heated ones. Even though the content of all the other elements is increased in the heated area, their relative ratio remained constant. It is proposed that the conventional carbonization occurs, decomposing the long polymer chains into small volatile hydrocarbon, which evaporated into the ambient air, subsequently reducing the carbon content. Excessive heating on the structures can lead to significant melting and material removal of the polymer. To forestall melting in the structures, the power of the laser beam was optimized to be $5mW$.

On microlattice unit cells, local size reduction can usher collective mechanical deformation and the formation of new geometries. Both individual OT and FS unit cells are processed and the modified unit cells are presented in Fig. 4.30(e)-(i). The height of the unit cells is designed to be $10\mu m$ with slight deviations caused by the alignment of the MPL during the fabrication process. First, it is elucidated in Fig 4.30(i)-(g) through both top view (i) and side view (ii) that the deformation is controllable for different laser powers. In the case of Fig. 4.30(f) and 4.30(g), the laser beam is focused on the top plane and at the center of the unit cell. Hence, a larger deformation is observed on the top plane combined with an overall contraction towards the center. This caused the shape formation of an "octopus

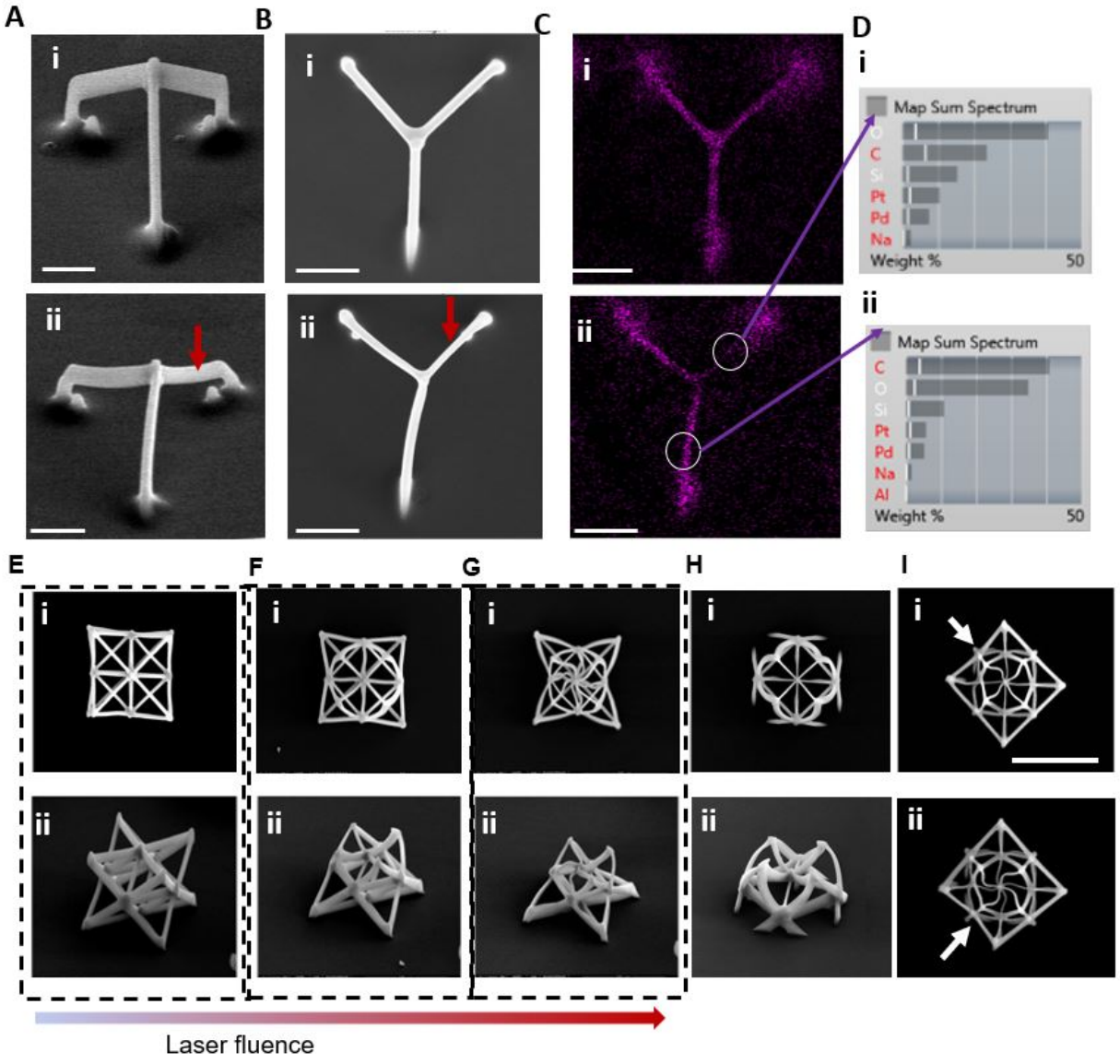

Figure 4.30: Geometry and chemical composition analysis of laser pyrolyzed simple unit cell structures. (a-b) Tilted (a) and top view (b) of simple tetrahedral structures before (i) and after (ii) receiving selective laser heating on the arrow pointed location. (c) EDS composition mapping of the carbon concentration over the microstructure. (d) point composition analysis on structures with (i) and without (ii) laser processing. (e-g) Top (i) and tilted view (ii) Laser processed OT structure with increasing laser power from $0mW$ to $5mW$ and $8mW$. (h) Laser heated OT with the bottom part of the structure not printed due to alignment of the height. (i) Top view of the laser point heated FS structure at different locations labelled with arrows. For all of the figures the white scale bar is $10\mu m$.

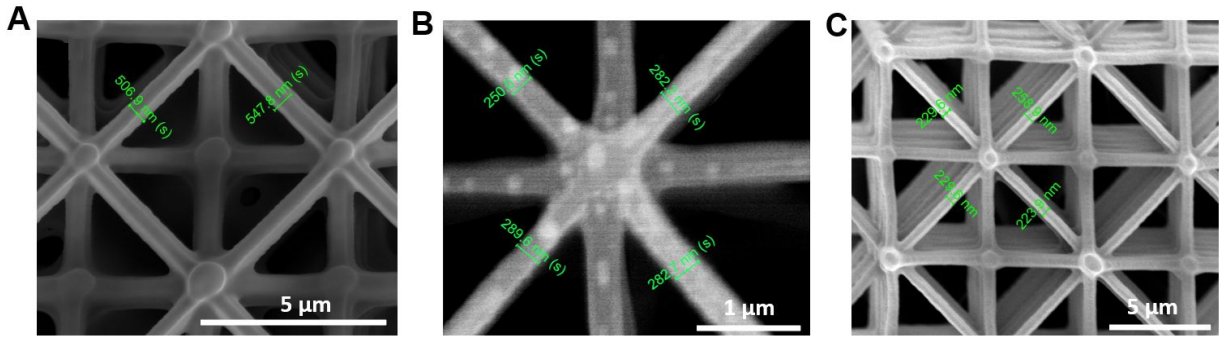

Figure 4.31: SEM micrographs of the lattice thickness for (A) unblemished structures, (B) the laser heated structures and (C) the furnace heated structures.

jaw" like structure, which can be potentially utilized for material grasping and collection of particles on a surface [439]. As for the FS, it is observed that the location of the laser heating with respect to the geometry of the unit cell has a significant affect to the overall geometry deformation. In addition, it created a heating induced undulated morphology. All these convoluted designs with both minuscule diameter and intrinsic curvatures in close proximity are too challenging to be fabricated with conventional MPL only, such as Fig. 4.30(f-ii) and Fig 4.30(f-iv). Beams this thin in such a close proximity cannot be distinguished as separate voxels, and their fabrication cannot be successfully realized by the MPL.

Furnace pyrolysis is compared to the laser extreme pyrolysis on periodic microlattices. The fabricated FS and OT arrays are presented in Fig. 4.31(a). The FS array contains three layers in total with 4 (2×2) unit cells on each layer. The OT array consists of four layers, with 4×4 unit cells on each layer. The initial diameter of the beam members is approximately $550nm$ (Fig. 4.31(A)). The diameter of the beam members due to laser heating drop to $250nm$ (Fig. 4.31(B)), a result congruous to the reported values of the pyrolysis technique [128]. Putting these values into perspective, furnace heating causes shrinking on the same order of magnitude ($\sim 230nm$in diameter) (Fig 4.31(C)). Longer and more uniform heating introduces more volume reduction in the furnace. Tests on polymer structures under different furnace temperatures indicated that the shrinking temperature threshold is approximately 375^oC. Nevertheless, it leads to a uniform isotropic deformation in both OT and FS. Most notably, for the OT array, except for the stepwise transition at the bottom part of the structure, the overall size reduction is uniform. Therefore, the desired localization of induced defects cannot be embraced by furnace heating.

Furthermore, we show that controlled laser carbonization can generate gradient deformation and form functional periodic microlattices. More specifically, the FS structure is converted to a "ziggurat" array, whereas each layer has different height and width caused by the different degree of shrinkage in the beams. This deformation leads to a completely new design. As it will be shown later, this design embosoms significantly enhanced mechanical

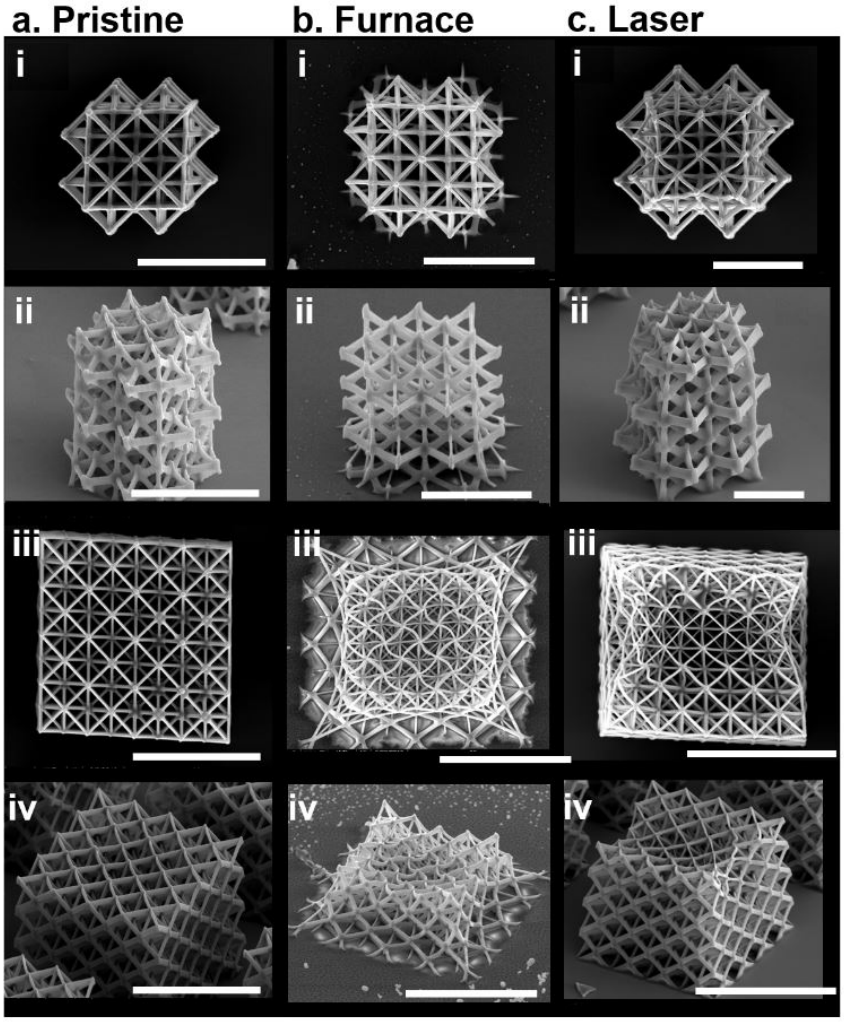

Figure 4.32: Comparison of the laser extreme pyrolyzed polymer microstructures with pristine and furnace pyrolyzed ones. (a) Pristine fabricated FS (i-ii) and OT (iii-iv) microstructure with top view and perspective isometric view. (b) Furnace processed FS and OT structure with uniform deformation. (c) Laser extreme pyrolyzed FS and OT structure. FS structure is processed by a fixed laser beam (labelled with dashed lines) heating and formed forming a ziggurat structure. OT structures are heated by a scanning laser beam (in the direction of arrow) and formed a concave surface. The minimum thickness of the lattices for this case is $223nm$. The white scale bars for all of the top and side views are $10\mu m$.

properties compared to the initial one. To put this result into perspective, long dwell time ascertains that gradient heating with Gaussian planar distribution is established at each vertical layer, thus leading to the vertical gradient deformation. For the case of the OT, as the laser is scanning through the structure, a nonuniform heating and subsequent gradient deformation is formed in the same layer. As the OT is established as one of the best ultralight-ultrathin microlattice mechanical metamaterials, this design can be employed as protection layers for micro-optical devices, where smooth alignment in an undulated profile might be design requirement [387].

The correlation between the laser parameters and the deformation can be constructed and can provide the guidelines to design the desired geometries. To investigate the thermal effects, heat transfer simulations were conducted on an FS array using COMSOL. The simulated temperature distribution is presented in [397]. Further details regarding the simulation parameters and results are provided in [397]. The temperature distribution reveals that the heat flux is constant across the entire beam and no additional heat is accumulated. Nevertheless, geometrical transitions on proximal lattice members lead to a change of slope (i.e. change of the heat flux), which is partially diverted to the new neighboring lattice member. These results show that the effect of the laser is diminished through subsequent layers of lattice members in the structure, elucidating the reason for the localized deformation. The current laser input simulates the case where only initial deformation exist on the top layer of FS, where temperature is higher than 375^oC Based on the steady state equilibrium, when the laser fluence increases, the normalized temperature distribution will still follow the simulated distribution. Therefore, when the laser fluence is increased, the deformed regions will proliferate from the top to the entire domain following the simulated temperature gradient. This phenomenon elucidates the formation of the "ziggurat" FS microlattice. Once the temperature distribution over each lattice member is attained, we can obtain the spatial distribution of the deformation, and predict the resulted geometry. Thus, a physical model connecting the laser input and the resulted geometry is constructed. It is then possible to generate optimization algorithms to do the inverse problem, calculating the required laser heating spot and power to generate the targeted geometry. It must be noted that in the above arguments, we have verified that the pyrolysis is completed on the heated layers, in a time scale much shorter than the laser dwell time, as it is presented in the supplementary information. For more complex deformation control, temperature dependent shrinking speed can be investigated from refined furnace or laser heating experiments.

FEA simulations are further employed to predict the mechanical performance. To be consonant with the laser processing, the stiffness of the laser heated structure has a gradient, based on the measured mechanical properties that will be presented next. The selected material properties are in agreement with those the mechanical testing of the individual beam members. Specifically, the following beam properties were used in the FEA analysis: $2.57GPa$ elastic modulus, 0.45 Poisson's ratio, and 18 MPa yield strength. To compromise with the variation of the stiffness and strength due to the laser heating, these values were modelled to vary linearly with respect to the height of the geometry, up to the modulus equal to $4.92GPa$ and strength equal to $70MPa$, by measuring the force displacement curves of

three point bending. Since the heat transfer simulations revealed that the heat flux varies only when the beam changes, it was modelled that individual beams would have a constant Young's Modulus and Yield Strength along their length, whereas variation in these properties would occur when there is another beam along the height of the structure. Based on the SEM images and the altered geometry of the beam members it was selected that the stiffness step would be 0.26 GPa. The structures were discretized by 10-node, tetrahedral finite elements. The unheated structure was modeled with 394275 elements having 223200 nodes, whereas the heated structure was modeled with 385250 elements having 221250 nodes. The boundary conditions were chosen to closely much those of the experiments. Because of the slightly thicker hinges connecting the beams, the indenter load was initially applied on the hinges. Thus, the compressive load of the microindenter was transmitted to the structure through these hinge points. For this reason, point – displacement boundary conditions were applied to the mesh nodes corresponding to the top face hinges. Since the bottom face of each structure is attached to the substrate, all the degrees of freedom of the bottom nodes were fully constrained. The ANSYS Design Modeler was used to design the structure geometries. The CAD model of the heated structure was based on the SEM imaging of the and the measured dimensions of the individual beam members. The force-displacement responses of the unheated and heated specimens are compared in Fig. 4.33. It is observed that the heated specimen is much more resilient to large deformations. The reason is that the maximum deformation field distribution (colored red) is substantially secluded on the top face of the heated structure. A potential reason for this phenomenon is that the top beams are closer to each other leading to a stiffer structure. This mechanism has been reported before for the case of pyrolysis [132], as the uniform shrinking reconfigures the beams to closer proximity to each other. This mechanism is manifested on the laser heated specimen as well. Nevertheless, the bottom layers are not affected, as the deformation field for both structures is the same at this location. This insinuates that the heated structure is comprised of two parts. A stiff, non-polymeric part at the top and a polymeric backbone on the bottom that can facilitate buckling and larger deformations with plasticity before fracture [271, 353]. This will be verified by both the mechanical testing that will be presented next and EDS analysis on the cross sections of heated and unheated lattices. Therefore, this process can be employed to create materials encompassing both strength and ductility. These results, synergistically coupled with simulation of the mechanical behavior, can be employed to design the laser processing towards the desired mechanical performance.

To experimentally validate the mechanical response, in situ SEM on microindentation tests were performed on single beam members to measure the mechanical properties and on the FS structure. By performing three point bending on the heated and unheated beam structures (Fig. 4.34(a)), the force displacement curves were obtained (Fig. 4.34(b)). Using static analysis of the bending moment diagram for the uniformly distributed load of the indenter, the Young's Modulus can be estimated to be $2.57GPa$ and $4.92GPa$ for the unheated and heated beams respectively. Therefore, the laser heating leads to 91% increase of the stiffness of the material. This result is congruous with the resilience obtained by the FEA, since the top layer is significantly stiffer. By performing uniaxial compression (Fig.

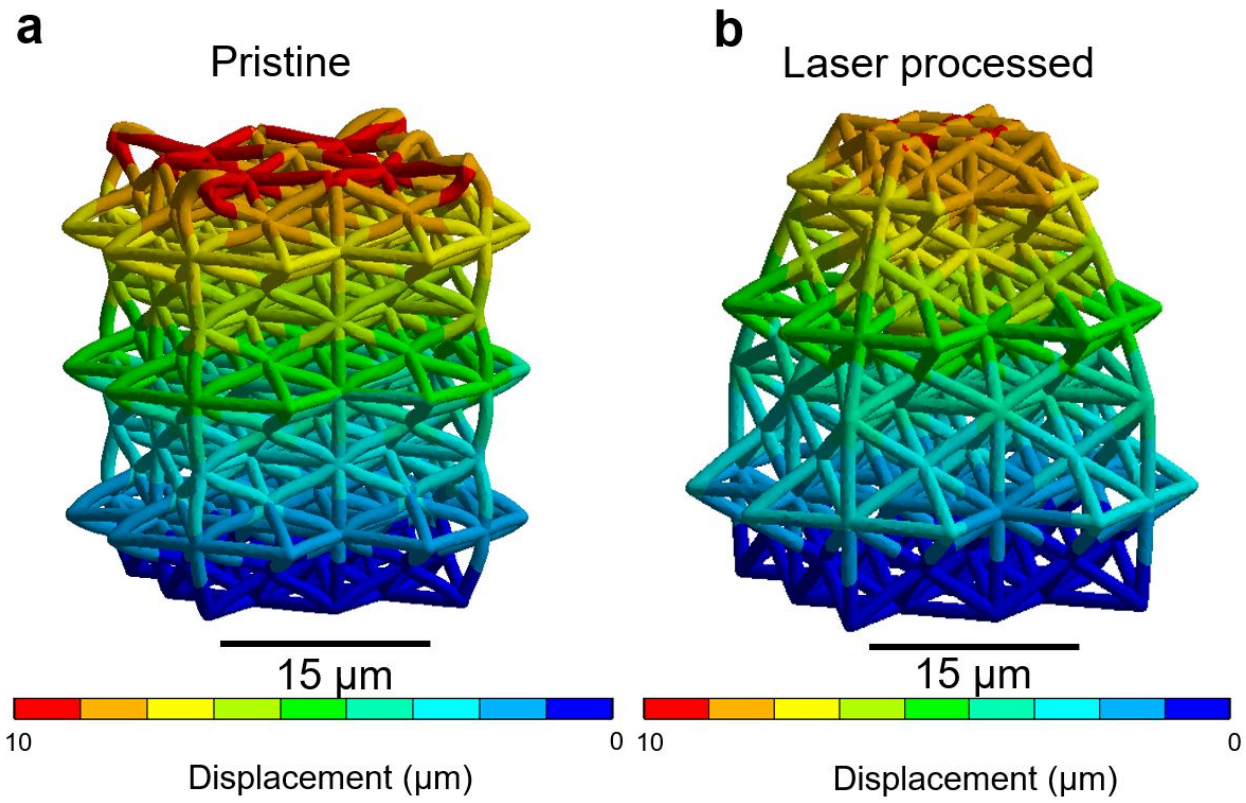

Figure 4.33: Mechanical simulations of the FS structure. The mechanical deformation profile for the pristine(a) and the laser processed(b) structures, demonstrating the resilience of the second over the first to large compression.

4.34(c)) on both heated and unheated samples, the obtained characteristic mechanical responses are presented in Fig. 4.34(d) (engineering stress-strain curves). The recordings of the deformations are presented in VI-Recoding 1 and VI-Recording 2 [397]. It is evident that the energy dissipation of the heated structure, which is attained by calculating the area of the stress - strain curve, is substantially larger than the unheated one. More specifically, for the same amount of deformation, the heated sample has approximately two times higher energy dissipation. One reason for this is that to accomplish uniform shrinking of the upper layers, the internal beam members of the intertwined structure must also either bend or pre-buckle. As these beam members have sustained permanent deformation due to curvature, they are prestressed and therefore hardened. Consequently, they will require more mechanical energy to deform for the same amount of deformation as the straight ones. In addition, they are also in closer proximity to each other compared to the unheated ones. Hence, the increase of post contact events during large deformations will stiffen the structure. This result is consistent with the finite element analysis that was performed. These physical mechanisms

that are employed for this architectural design have been reported before [402]. However, the aforementioned repercussions of the heating enhanced these mechanisms even more. Furthermore, the local evaporation of the polymeric part of the beams increased the contribution of the ceramic part [455]. To validate this, EDS analysis was performed on the fractured cross sections of the tested unheated (Fig. 4.35) and heated structures (Fig. 4.36). The reason that EDS was performed after the mechanical testing was to avoid a potential chemical and structural alteration ushered by the focused ion beam (FIB). Again, we observe a decrease of carbon content from 42% to 27% on the heated member compared to the non-heated one and the relative ratio of all the other elements remained constant. This verifies that the laser heating renders of the whole cross section ceramic and it does not cause a surface effect only. In addition, the conglomeration of the coating particles is also evident in Figs. 4.36 and 4.37. To inspect these morphological features in extremely high resolution, Helium Ion Microscopy (HIM) was employed. HIM enables extremely high resolution of even nonconductive samples and imaging and characterization of nanometer features. Fig. 4.37(a) reveals the unsputtered structure, showing that the initial polymerized material has no nanoscale surface features at intersecting lattice members (Fig. 4.37(b)). Nevertheless, laser heating on the top layer precipitates a convex inverse dome on the structure Fig. 4.37(c)). Higher magnification on the heated region elucidates a highly twisted structure with golden particles of $30 - 40nm$ diameter penetrates inside the lattices, creating a hierarchical material (Figs. 4.37(d)-(e)). In addition, this effect is constrained only in the regions that the laser beam heats, since there is no change in the morphology of the gold layer in the unheated regions. These findings bolster the argument of a hybrid structure.

In addition, the effect of multiple locally heated spots was investigated. To accomplish this, the laser beam was splitted utilizing a beam splitter and the two beams were focused on two different locations of the structure. Characteristic deformed morphologies are presented in Fig. 4.38. This process substantially narrows the threshold of the optimum laser parameters. Low laser power at $0.02W$ does not accomplish large deformations, since the laser power is divided in the two spots (Fig. 4.38(a)). Hence, the blatant distortion and twist observed in the case of single laser heating is not significant. In addition, higher laser power at $0.05W$ significantly damages the structure, since the gold layers melts (Fig. 4.38(b)), leading to even fracture of the beam members. Nevertheless, these is no large and uniform conglomeration of particles from the locations that the laser beam surmounts (Figs. 4.38(c)-(d)). To further investigate this effect, heat transfer simulations with two laser beams at different locations were performed [397]. While the temperature distribution is higher through the depth of the structure, it is also more uniform along the lattice members of each layer. This indicated that while there will be large deformations through the whole structure, as observed in Fig. 4.38(b), the spatial temperature gradient on the horizontal plane is not large enough to cause large deformations as with a single laser beam (Fig. 4.38(a)). While this technique is significantly more challenging to realize complex morphologies like the ones of Fig. 4.32, it is imperative for the efficient design of large-scale structures. Hence, future work should aim on the optimization of the experimental parameters to accomplish complex but controllable topologies.

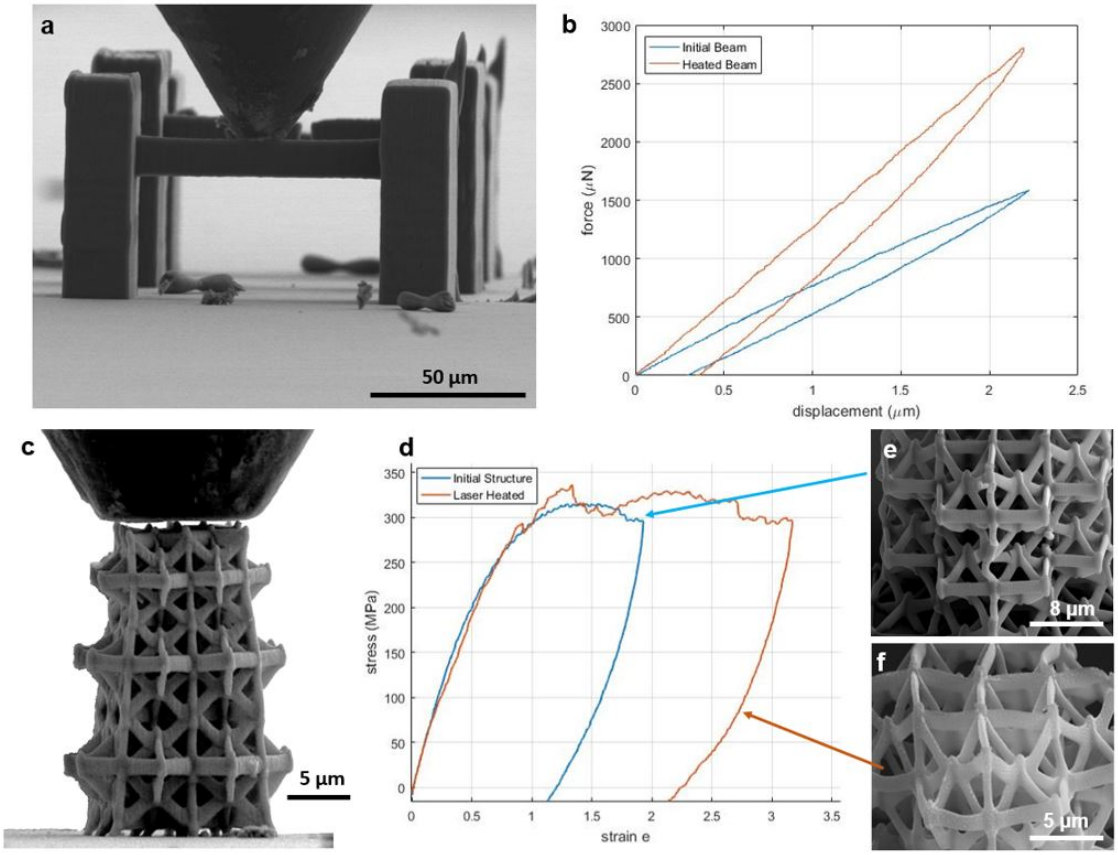

Figure 4.34: Micro-indentation testing of the initial and laser carbonized structures. (a) Front view of characteristic thee point bending beams to measure the mechanical performance (b) Representative force -displacement curves on unheated and laser heated beams to measure the stiffness of the material. It is observed that there is significant increase in the strength of the heated beam, since the ceramic component dominates the composition. (c) Front view of the configuration between the specimen and the indenter. (d) Characteristic stress-strain curves for the two samples for the same deformation length ($5\mu m$). The ductile regime of the curve is significantly larger than the initial design. The reason is the increase of the post contact events in the proximal beams of the heated structure and the induced curvature of the internal beam members, which enhances the resilience of the structure to larger deformations. (e) SEM imaging of the initial FS structure after the indentation experiment. Buckled and fractured members can be observed, resulting in the subsequent instability (softening) of the structure during the plastic portion of the deformation. (f) SEM imaging of the heated FS structure after the indentation experiment. Fracture members are observed, as well as the curved members that contributed to the resilience of the structure to large deformations, manifested through the higher energy dissipation.

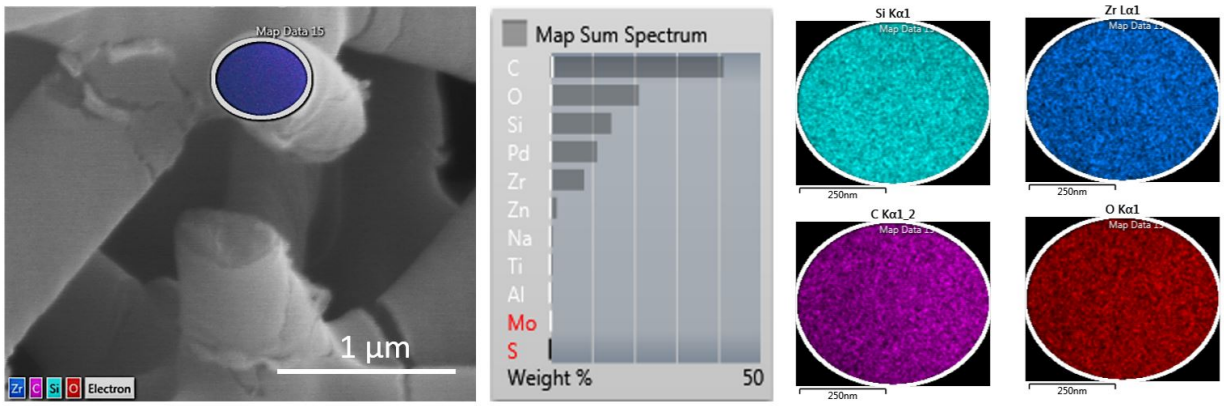

Figure 4.35: EDS Mapping on the fractured cross section of the unheated structure.

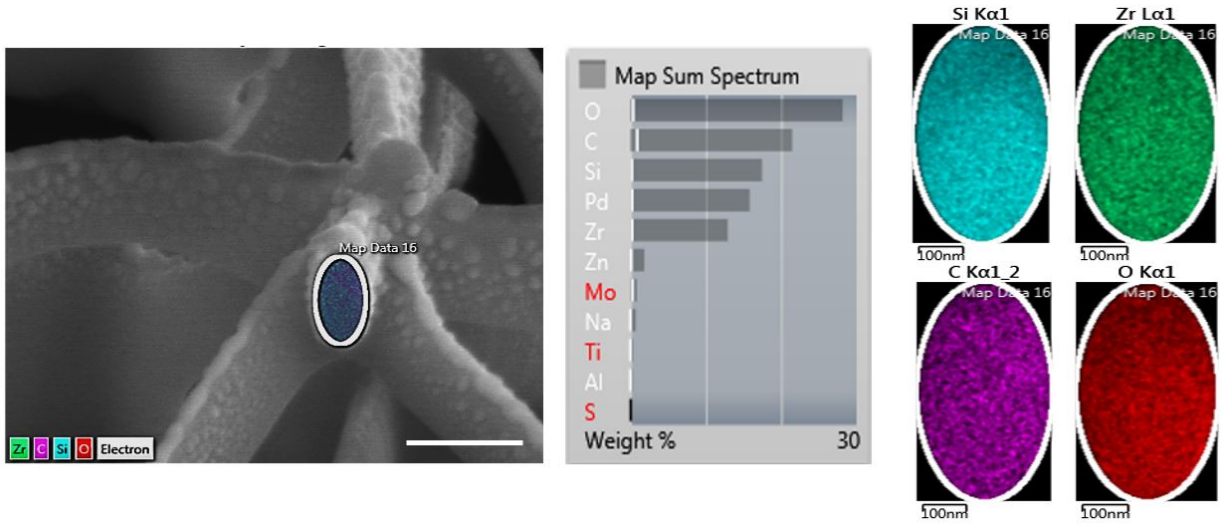

Figure 4.36: EDS Mapping on the fractured cross section of the laser heated structure.

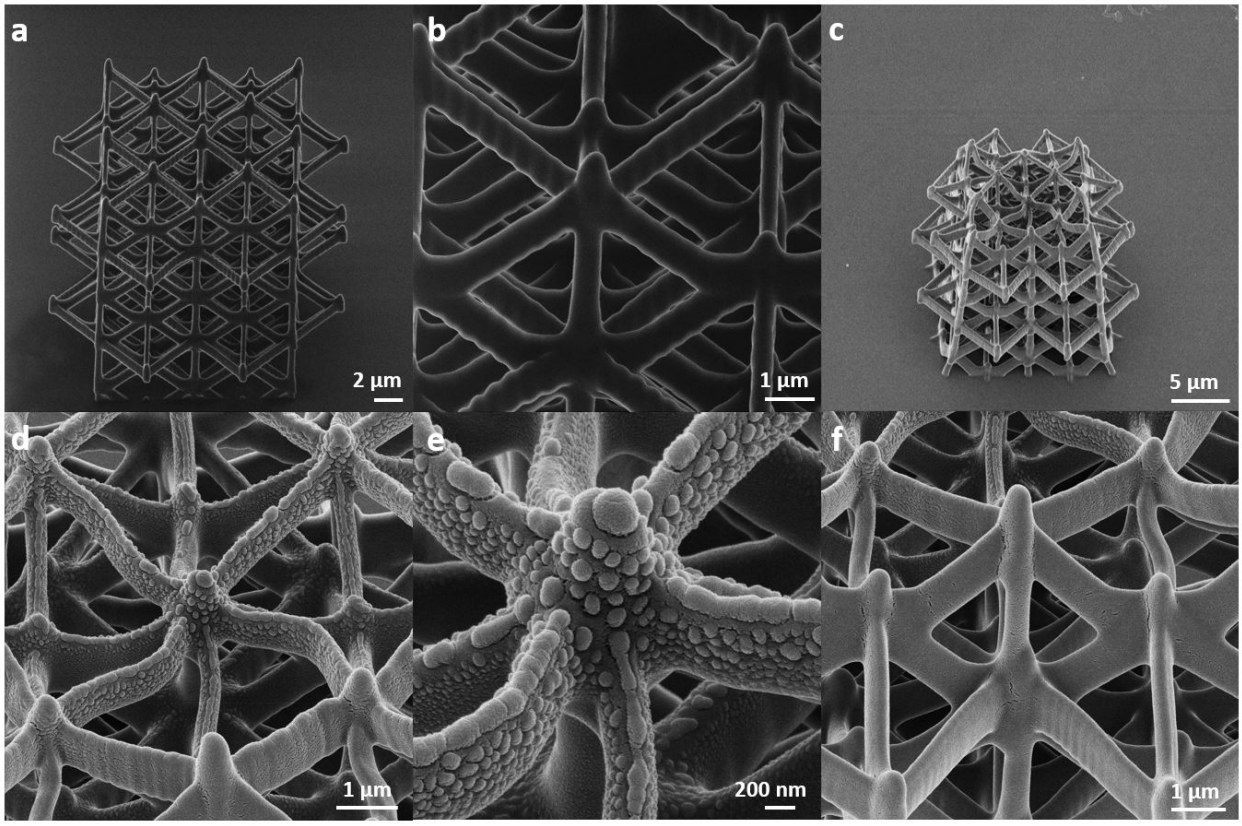

Figure 4.37: Helium Ion Microscopy characterization of unsputtered and laser heated samples. (a) Unspattered FS structure (b) Magnification on intersecting lattice members, revealing no nanoscale morphology of the surface of the lattices. (c) Isometric view of a laser heated structure at the center of the top layer. (d) Magnification in the center of the top layer, revealing a twist of the structure. (e) Higher Magnification on the lattices, revealing the conglomeration and penetration of golden particles in the nanolattices. (f) The undistorted neighboring region that the laser beam has not affected.

Based on the mechanical testing, there is an increase in the strength of material. Ductility and strength are competing mechanisms. Therefore, the trade-off is microscopic fracture of beam members, without the substantiation of buckling events as in the unheated sample (Figs. 4.34(e) and 4.34(f) VI 1 Recording 1 and VI2 Recording 2 [397]). Thus, from the standpoint of mechanical performance, this structure macroscopically combines both strength and ductility, ushering the potential utility of this technique for complex high energy dissipation nanocomposite materials with nanoscale features [431].

As the potential of this process was demonstrated, further research must be conducted to comprehend the laser selective carbonization under the scope of the desired mechanical performance. Detailed characterization of correlations between laser parameters and resulted geometries should also be pursued. Then thorough chemical composition details of heated specimen could be investigated by micro Raman spectroscopy [222] apart from EDS. A shrewd scheme of controlling the laser power, dwell time and scan path is required to implement the observed correlation. For a rarefied design challenge as this one, optimization techniques [57] and even data-driven methods like deep learning [286, 244] can be utilized to design the attainable structure as well as to attain the required laser paths to fabricate them. Moreover, this laser processing causing a distortion in the symmetry of the structures by the introduction of irregularities. These alterations constitute a major challenge in the analytical behavior of such structures. Nevertheless, stochastic methodologies have been demonstrated taking into account the several constituent representative unit cell elements and utilizing probabilistic descriptions of asymmetrical structures [285]. These models should be expanded in the 3D elasto-plastic mechanical behavior of metamaterial structures, providing a coherent framework to model and predict their mechanical response. These irregularities should also take into account the modified localized mechanical properties precipitated by the laser heating.

Section Conclusions

In summary, a novel post-processing procedure for the modification of the geometry and chemical composition of fabricated microstructures was presented. Laser-induced local extreme pyrolysis on polymeric structures introduced localized shrinking and ceramic-polymer hybrid composites. Through furnace annealing, we estimate that the local temperature will reach 375^oC to provide the observed volume reduction in laser processing. With controlled fixed irradiation or laser scanning, complex curved and gradient geometries can be generated. Detailed mechanical simulations illuminate the deformation and predict the resulted mechanical performance. SEM micro-indentation analysis elucidated how the microscopic mechanical response was reflected on the stress-strain curve. The laser carbonized hybrid material combines enhanced macroscopic ductility and strength. Therefore, the present study provides the framework for using the laser to create hybrid structures with complex geometry and enhanced mechanical properties. Their utility could be employed for a plethora of applications, such as tailored scaffolds with stiffness gradient for artificial tissue modeling and stress distribution [245, 311] and 3D patterning of local hierarchical nanofeatures for 3D

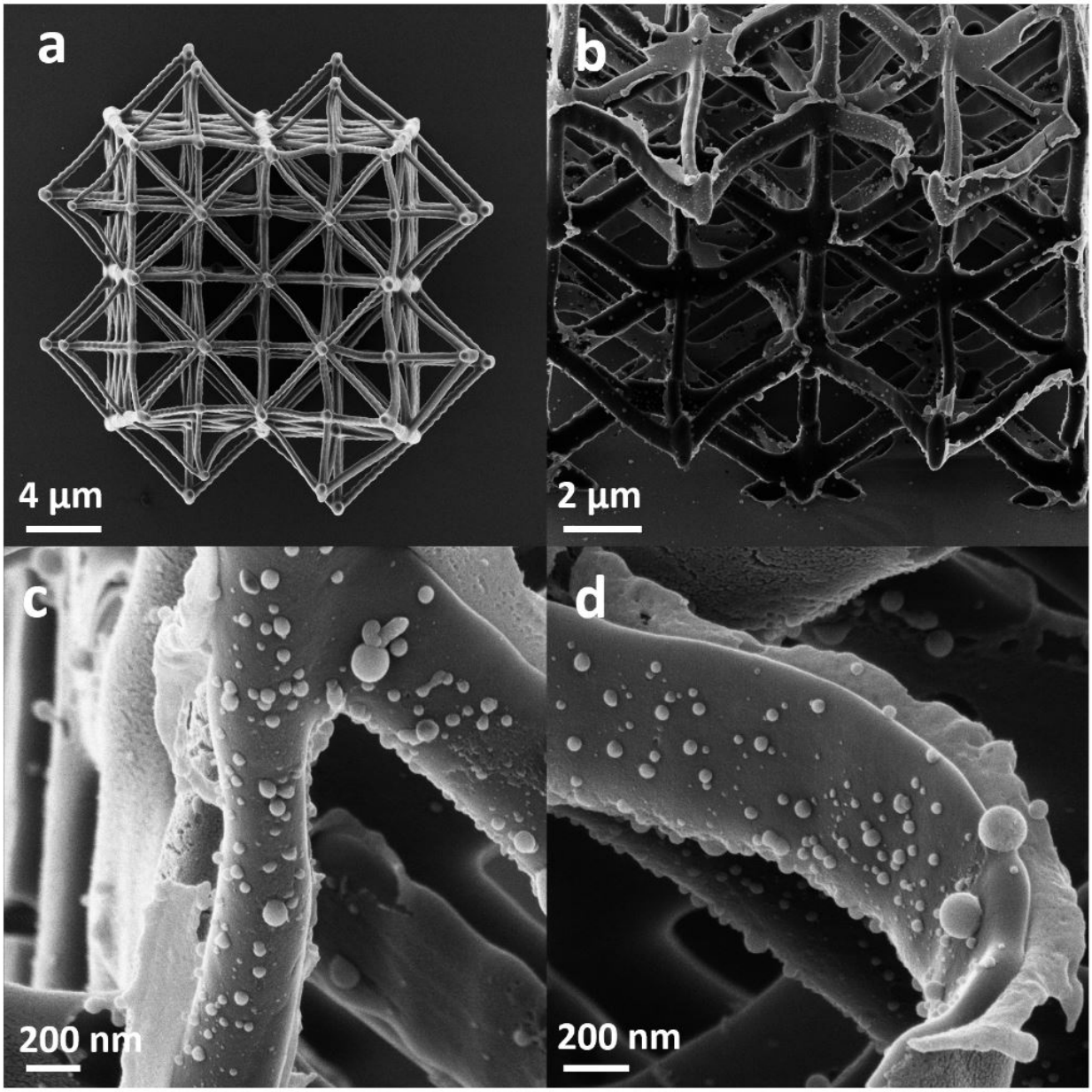

Figure 4.38: Laser heated structure on two spots simultaneously. (a) Top view of the heated structure with laser power equal to $0.02W$. (b). Side view of the laser heated bottom layers with power $0.05W$. (c-d) Partial conglomeration of the gold on the lattice members, without penetration inside the lattice members.

complex biomimetic materials and structures [131, 370, 239, 242]. In addition, this process can provide more complex micro optical components fabricated by MPL [132]. Finally, it sets the framework for new post-processing techniques that can be employed to accompany MPL for hybrid 3D nanoscale structures.

4.4 Architected Metamaterials with Tailored 3D Buckling Mechanisms at the Microscale

Section Summary

The primary objective or this work is the realization of the efficient design to forestall out of plane buckling in the structure, which for the case of multi-layered structures results in "sliding" of some layers with respect to the others. Alternatively, internal buckling of the lattice members of the layer without out of plane deformation of the whole layer can lead to a functional mechanical response. These distinct buckling responses will be examined. The desired buckling behavior for high energy dissipation and reversible large deformations must institute a bistable mechanism in the structure. Bistability provides multiple local equilibrium states due to snap through buckling, which enables mechanical energy absorption and release without the requirement of perpetual actuation [27, 170, 309, 436, 435, 159]. This structural principle has been utilized for a plethora of applications, such as controlled wave propagation [335], soft robotics [61] and malleable structures [354]. The objective of this study is to investigate how out of plane buckling can be prevented and instead utilize a bistable mechanism and internal buckling of beam members of each layer. To instantiate this principle, a specially architected structure was designed, and its scale and size effects were investigated with respect to the buckling performance. The simplicity of this design aims to elucidate how complex 3D structures must be architected and which buckling modes, functional or egregious, can occur. These structures were fabricated by multiphoton lithography (MPL). Multiphoton lithography is the predominant fabrication technique to design complex geometries in nanoscale and microscale [343]. Structural features in these length scales have proved to be critical for the enhanced performance of patterns observed in nature, like seashells and bones [131]. Nature is the most articulated paradigm of design efficiency and hierarchical convoluted structures manifesting the mechanical principles of tailored buckling [262]. In addition, nanolattices with tens of nanometres thickness have proved to provide intriguing scale effects. More specifically, different sizes on the nanoscale regime can provide brittle to ductile transitions and preserve the high strength of the initial bulk material. These effects are a corollary of Euler buckling and shell buckling that emerge when the nanolattices deform [232, 349, 457]. Thus far, snap through buckling and bistability are controlled utilizing slender members and elastomer materials [330]. Hence, the mechanical response is substantiated by the properties of the material for a very specific geometric design. Our proposed design renders the geometric features paramount, as elastomeric polymers are feeble

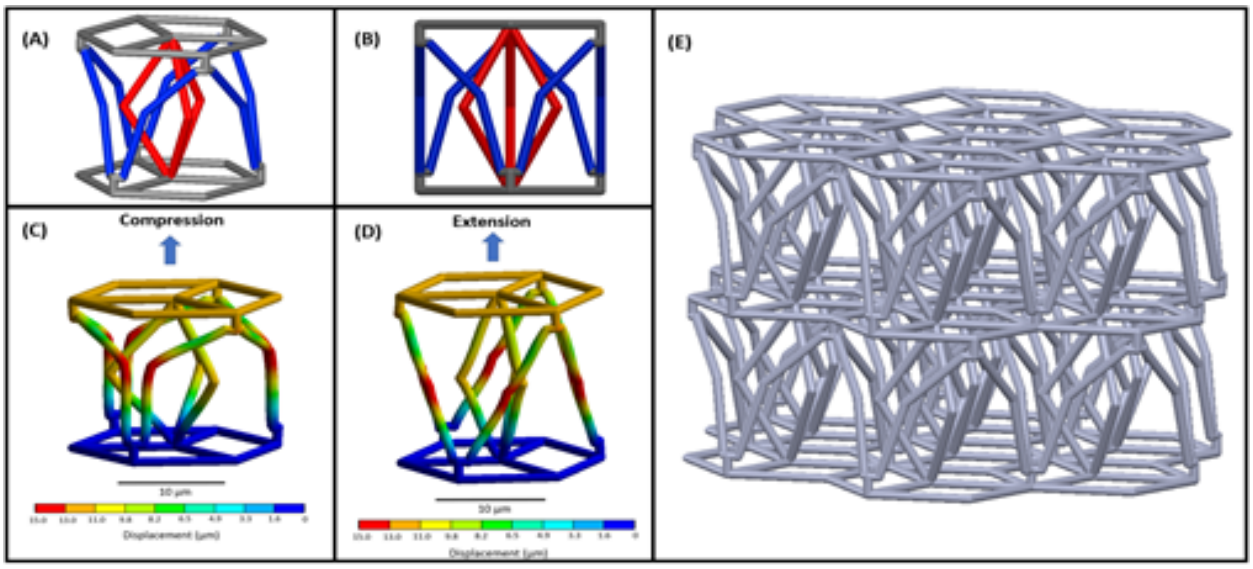

Figure 4.39: The proposed designed structure. (A) Isometric view of the designed structure. (B) Side view of the unit cell. The external beam members (colored blue) provide the primary buckling members, while the main purpose of the internal ones (colored red) is to provide structural integrity for the unit cell. (C-D) The mechanical response of the unit cell under compression and extension by FEA analysis. (E) Assembly of unit cells to form a periodic structure.

to be utilized for very small length scales that require different materials for the fabrication process [182, 61].

Design of controlled buckling structures

The design of the unit cell is delineated in Fig. 4.39(A-B). The unit cell is bifurcated into two main beam members (colored red and blue). The blue members under compression or extension, as it is illustrated in Figs. 4.39(C-D), will facilitate a snap through buckling mechanism due to a pre-existing bent angle of 150^o.

During compression, these beam members will come in contact [330], increasing the stiffness of the structure and reemerging from the local minimum at the force displacement curve which was reached during the snap through mechanism [4]. Fig. 4.40 conveys the developed stresses on the unit cell under compression. The simulations indicate that the maximum stress distribution is located at the pre-bent nodes, but the design strategy of the post contact will increase the resistivity of the structure to catastrophic collapse. Nevertheless, as it will be shown later, these members cannot hinder out of plane buckling, which will be proved to depend on scale effects. Hence, another set of members was included in the unit cell to enhance the structural stability and provide an extra snap through mechanism (col-

ored red). The assembly of the unit cells for the design of a complex structure is depicted in Fig. 4.39(E). The secondary members were positioned such that they will not encounter the primary members during the deformation, thereby maligning the final performance of the structure. All members are connected with a hexagonal base (colored grey) to assemble the unit cells at different layers (Fig. 4.39(E)). Moreover, they will also buckle during the deformation, enhancing the energy dissipation of the structure. This 3D structure has hexagonal symmetry, where each node has six proximal nodes. The reason for this design choice is that this symmetrical configuration will allow beam members at symmetric locations to buckle simultaneously. Otherwise the structure will tilt at a specific direction, and out of plane deformation will commence. In addition, the lattice members at symmetric positions must be on the same plane as the applied load (Figs. 4.39(C-D)). This orientation will lead to compression and at the stage of instability to buckling. Other potential orientations with respect to the applied load can lead to bending, which is not a state of instability and will not be a desired deformation mode. Preliminary experimental results showed that this 3D configuration of beam members can provide a stable structure, that does not collapse during the fabrication process under its own weight and therefore it can be mechanically tested. Unit cell arrays, especially without the red beam members, were susceptible to face this type of collapse.

To validate the feasibility of the designed structure, finite element analysis (FEA) simulations were performed. Further details about the simulations are provided in the supplementary information. The buckling mechanism of the structure is determined by the equation 4.13, provided in the previous section. For the case of one-dimensional problems, buckling occurs when the structure deforms in a direction that there is no loading and the stiffness becomes negative, leading to a state of structural instability. For the three-dimensional case this mechanism is manifested when du is not equal to zero, while there is no external load dq. Then, the stiffness becomes positive semidefinite and the structure will teeter. At this state, NB is the value of the load that will initiate buckling, and du_B is the characteristic buckling deformation, which corresponds to the eigenvector of N_B. The objective is to tailor the value of du_B, prohibiting out of plane buckling and instead enabling a mechanism that transfers the deformation to subsequent unit cells in a manner similar to stable wave propagation [335], one of the primary applications of tailored buckling. To analyse how the dimensions and the number of unit cells affect the characteristic buckling deformation, the FEA was performed for four different cases. The classical theory of structural buckling addresses how the dimensions of beam members affect the buckling load by the following relation $N_B \sim \frac{EI}{L_{eff}^3}$, where E is the Young's modulus, I is the inertia of the structure, which is a function of the cross section dimensions and L_{eff} is the effective length of the beam based on its boundary conditions [13]. Therefore, as the slenderness ratio (effective length over effective radius of cross section) increases, the structure will buckle at lower loads. Nevertheless, there is no formulation how the characteristic buckling deformation is affected by the dimensions of the structures. Therefore, the design principle must focus on how du_B can be tailored as a function of the height and thickness of the members, considering the fabrication capabilities

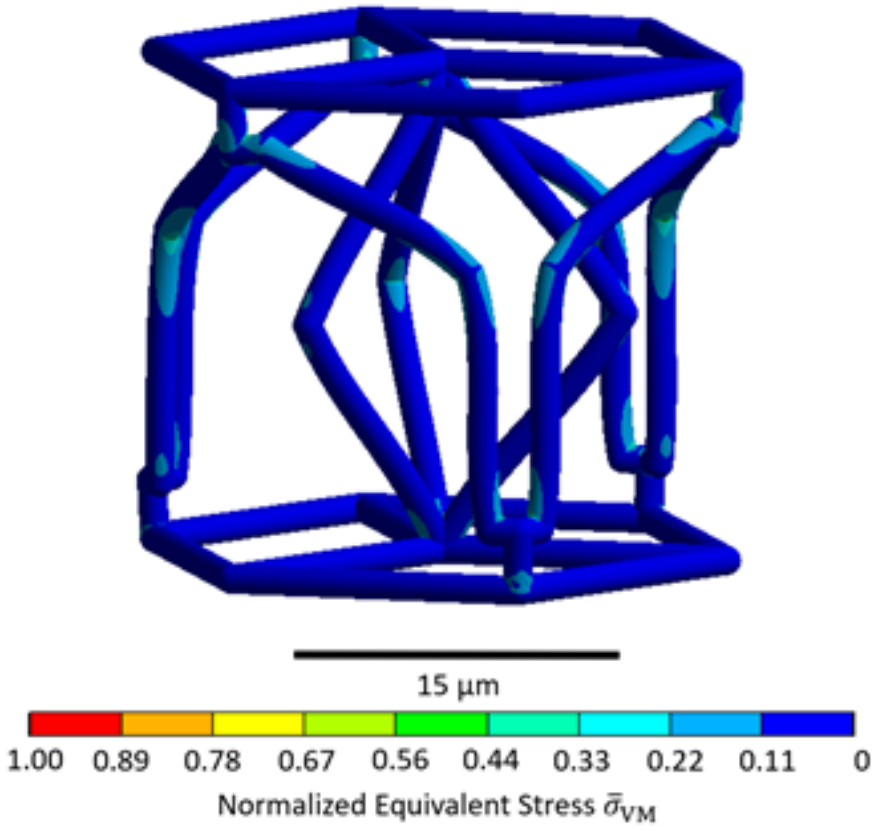

Figure 4.40: FEA Analysis on the distribution of the equivalent stresses over the unit cell under compression.

that are required.

Results

Finite element simulations of the architected structures

All of the FEA simulations were performed with the multi-purpose finite element software ANSYS (Workbench 18.0). The selected material properties are in agreement with those of polymeric materials used in multi-photon lithography [365]. The structures were discretized by 10-node, tetrahedral finite elements. Design 1 was modeled with 898399 elements having 531828 nodes, Design 2 was modeled with 136392 elements having 65763 nodes, Design 3 was modeled with 91680 elements having 45192 nodes whereas Design 4 structure was modeled with 96456 elements having 51166 nodes. The boundary conditions were chosen to closely much those of the experiments. Because of the slightly thicker hinges connecting

the beams (e.g., see Fig. 3, contact between the microindenter tip and the top face of each structure initially occurred at the elevated hinge points. Thus, the compressive load of the nanoindenter was transmitted to the structure through these hinge points. For this reason, concentrated forces were applied to the mesh nodes corresponding to the top face hinges. Since the bottom face of each structure was firmly attached to the substrate, all the degrees of freedom of the bottom nodes were fully constrained. To evaluate the correct eigenvalues and eigenvectors for eigenvalue buckling a compressive load of magnitude $-1\mu N$ was applied instead of the displacement boundary condition. The ANSYS Design Modeler was used to design the structure geometries.

Characteristic examined structures demonstrating the distinct mechanical responses that can be attained are presented in Fig. 4.41(A-D). The unit cell height h over the beam member diameter d for every case is $h/d = 12, 36, 12$ and 14.4 for ten, seven, seven and three unit cells on each layer respectively. These dimensions were selected such that the structures with the slenderest members can preserve their structural integrity under their own weight and not collapse during the fabrication process. The number and orientation of the unit cells were selected to provide symmetry in the 2D space, halting tendency for out of plane buckling. It must be noted that the mechanical response will be affected by the number of the unit cells on the structure until a specific number of unit cells, for which it will be uniform. For the presented designs, we assembled the minimum number of unit cells required to observe the behavior of a uniform material without early fracture of the individual unit cells. Furthermore, functional structures require more than one unit cell, taking into account the provided manufacturing techniques to fabricate them. The static deformations under compression for each design are illustrated in Fig. 4.41(E-H).

For every design, the primary members come to close proximity, enabling post contact that reverses the negative stiffness of the structure due to buckling. The members positioned at the centre mitigate the total compression, providing a threshold for structural integrity and hindering catastrophic failure. However, the height of the first structure is low relative to the deformation that can be applied, resulting the members that deform to come in contact for the case of large deformations, mitigating the buckling instability mechanism and increasing the intrinsic stiffness of the structure. The eigenvalue buckling analysis characteristic deformations are presented in Fig. 4.41(I-L). For the ratios equal to 12 (Fig. 4.41(I) and 4.41(K)), the desired eigenvectors du_B are achieved, providing the buckling of the internal members and preventing out of plane buckling, which occurs for the ratios 36 and 14.4 (Fig. 4.41(J) and 4.41(L)). For these designs, the internal buckling of the beam members is not obtained and instead the whole structure deforms in a direction different from that of the load (i.e. in the lateral direction of the geometry).

Fabrication and mechanical response of the architected structures

To validate the simulations results, the structures were fabricated by MPL. Further details about the experimental apparatus (Fig. 3.4(a)) and the materials are provided in the previous sections. The fabricated structures with the same dimensions as in the simulations

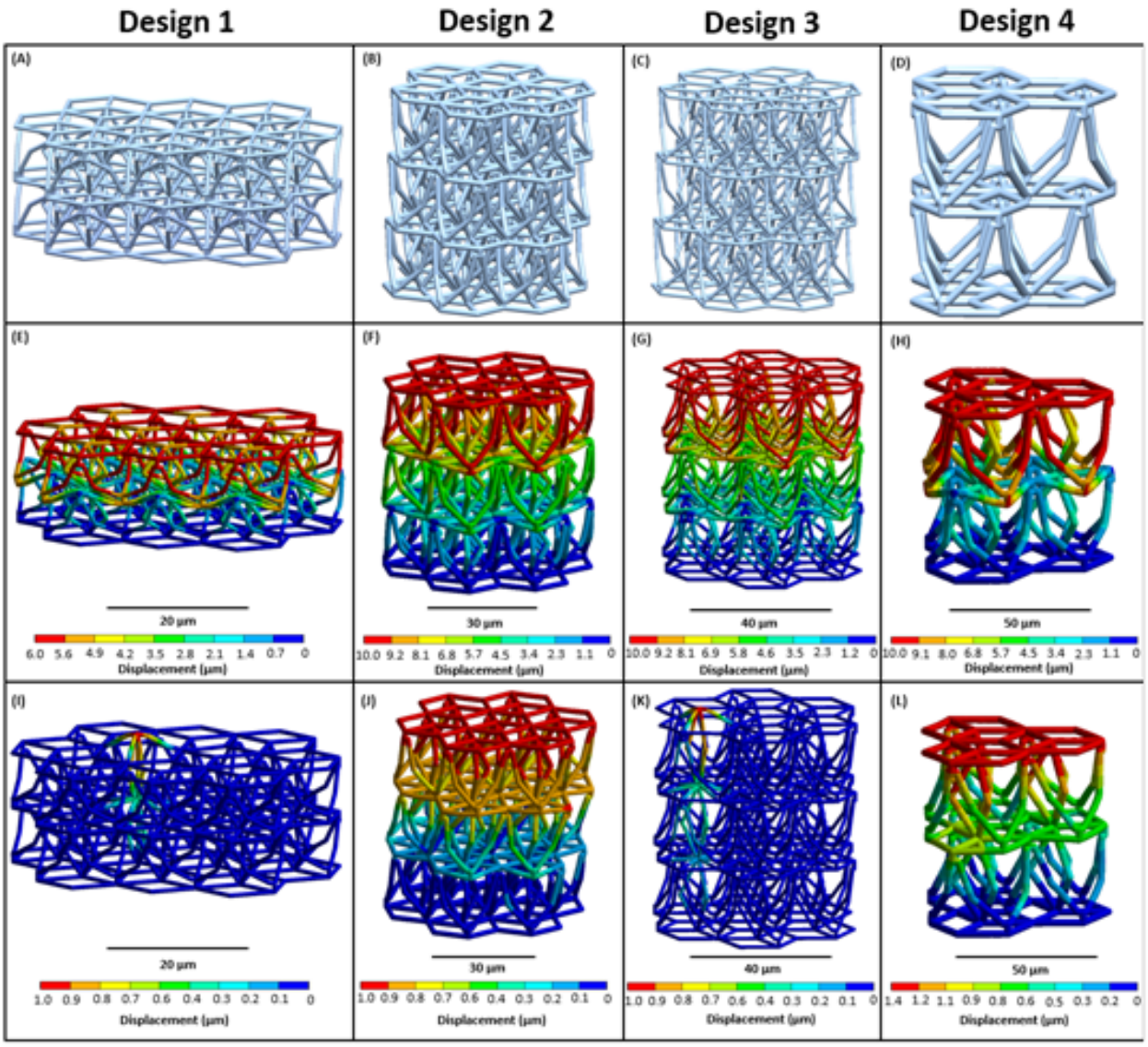

Figure 4.41: FEA analysis for the structural behavior and eigenvalue buckling analysis of the designed structures. (A-D) Final structures for different height/diameter ratios. (E-H) FEA static analysis for every structure illustrating the points of potential failure under compression and how post contact will occur. (I-L) The characteristic buckling deformation du_B for all structures, indicating how buckling will commence when the critical load **NB** is reached.

are presented in Fig. 4.42. The high spatial resolution of MPL enables a truly 3D fabrication process, unbound or layer-by-layer constraints of other fabrication processes such as microstereolithography [1]. The mechanical behavior of the fabricated metamaterial structures was examined with a nanoindentation apparatus, assembled inside a Scanning Electron Microscope for in-situ recording of the deformation. The shape of the indenter and its orientation with respect to the samples are presented in Fig. 4.43.

Characteristic force displacement curves for each structure are presented in Fig. 4.44 and Fig. 4.45. Each curve is collated with the in-situ imaging of the deformed structure to interpret the mechanical response. The first structure has a response that can be distinguished in three stages (Movie1 [395]). From the undeformed configuration (stage A in Fig. 4.44(A)) the structure is loaded until the slope becomes negative (stage B), indicating the initiation of buckling, which occurs at $251.1\mu N$. As the buckled members have sustained large deformations, they encounter the neighboring ones (as it is observed from the SEM imaging on stage B of Fig. 4.44(A)). This post contact causes an immediate intrinsic stiffening mechanism, making the slope positive again until the structure is unloaded (stage C). For this length scale the result is consistent with the FEA, as instability occurs without out of plane buckling. Nonetheless, the distance between the members is small for a large compression, causing the members to encounter the structure instantaneously after buckling, mitigating instability. Regarding the second design (Fig. 4.44(B)) there is a tripartite mechanical response as well (Movie2 [395]). However, as the structure deforms (stage A), out of plane buckling commences at $209.6\mu N$, a result consonant with the FEA analysis. The corollary is the denigration of the structure's performance, as after unloading the structure has collapsed irreversibly (stage C of Fig. 4.44(B)). The third design's response (Fig. 5A) has five stages (Movie3 [395]). The scale factor for this design is the same as the first structure, and the buckling mechanism is evinced at $551.5\mu N$ (stage B on Fig. 4.45(A)). In addition, the higher height of the unit cell enables the secondary members and the base to buckle as well before approaching each other, inaugurating two more buckling mechanisms at $565.7\mu N$ and $571.8\mu N$ (stages C and D), until it is unloaded (stage E). The fourth structure (Movie4 [395]) proved to be the most volatile (Fig. 4.45(B)) as the increased height of the unit cells combined with the slender members resulted in bending of the members and a barrel shape deformed configuration, as it is depicted on stage B. Nevertheless, buckling did not occur, and the mechanical response was not the desired one.

Discussion and Conclusions

Juxtaposing the FEA with the indentation experiments, the buckling mechanism was efficiently demonstrated for the ratio equal to 12, while for the 36 out of plane buckling occurred, and for 14.4 structural failure commenced. Tacitly, tuning the member slenderness will cause structural instability at lower loads. Nevertheless, the structure does not have the proclivity to buckle towards the lower layer of the structure, as it was presented in Fig. 4.44(B) and 4.45(B). Even though members with larger cross sections are less unstable, the inherent higher volume and larger surface area of the material provides the heterodox advantage of

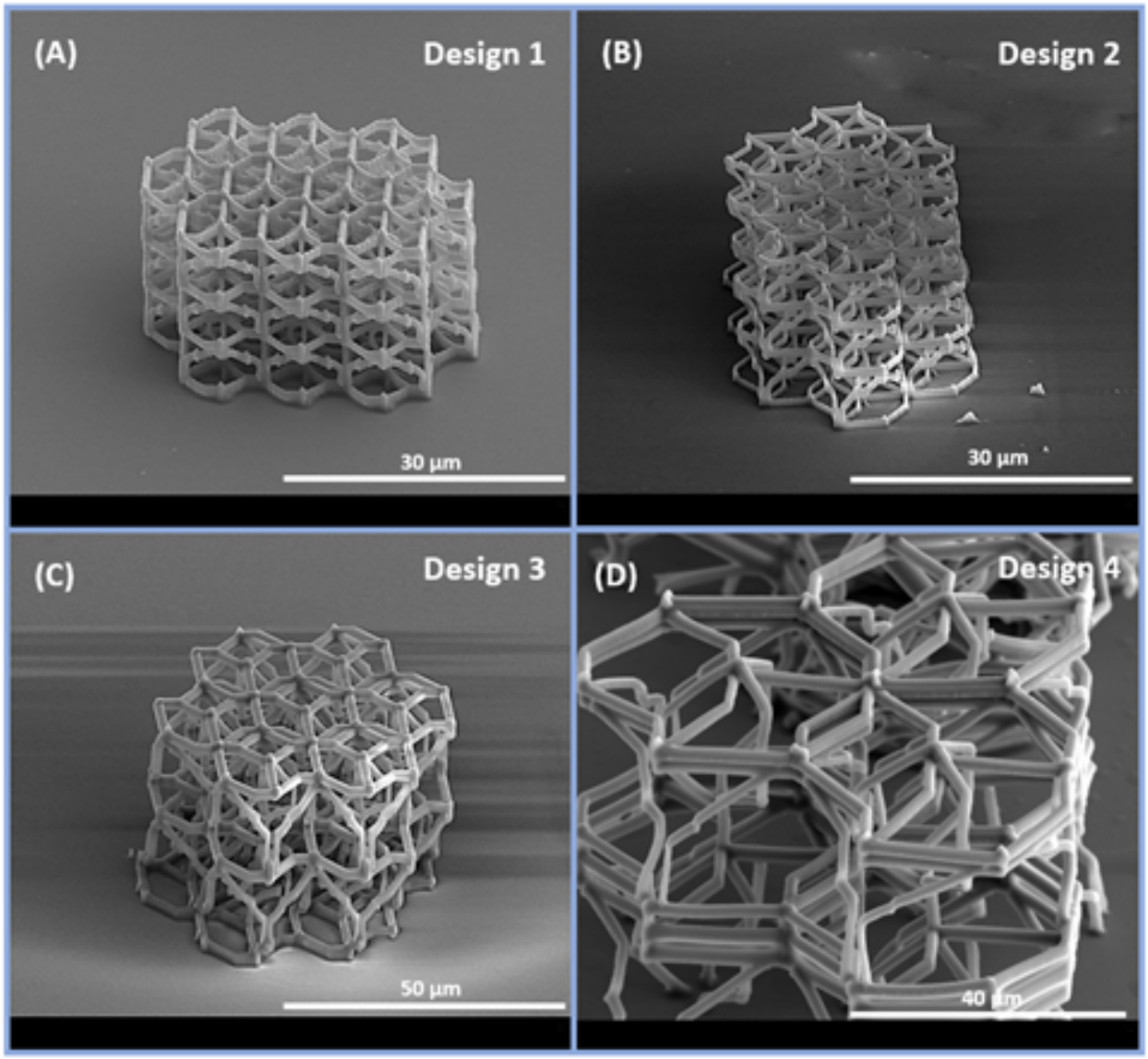

Figure 4.42: The fabricated structures. (A) Design 1 with unit cell height $6\mu m$ and beam diameter $0.5\mu m$. (B) Design 2 with unit cell height $18\mu m$ and beam diameter $1.5\mu m$. (C) Design 3 with unit cell height $18\mu m$ and beam diameter $0.5\mu m$. (D) Design 4 with unit cell height $36\mu m$ and beam diameter $2.5\mu m$. The maximum number of unit cells of each design was utilized to fabricate the largest periodic structure, based on the workspace of the setup.

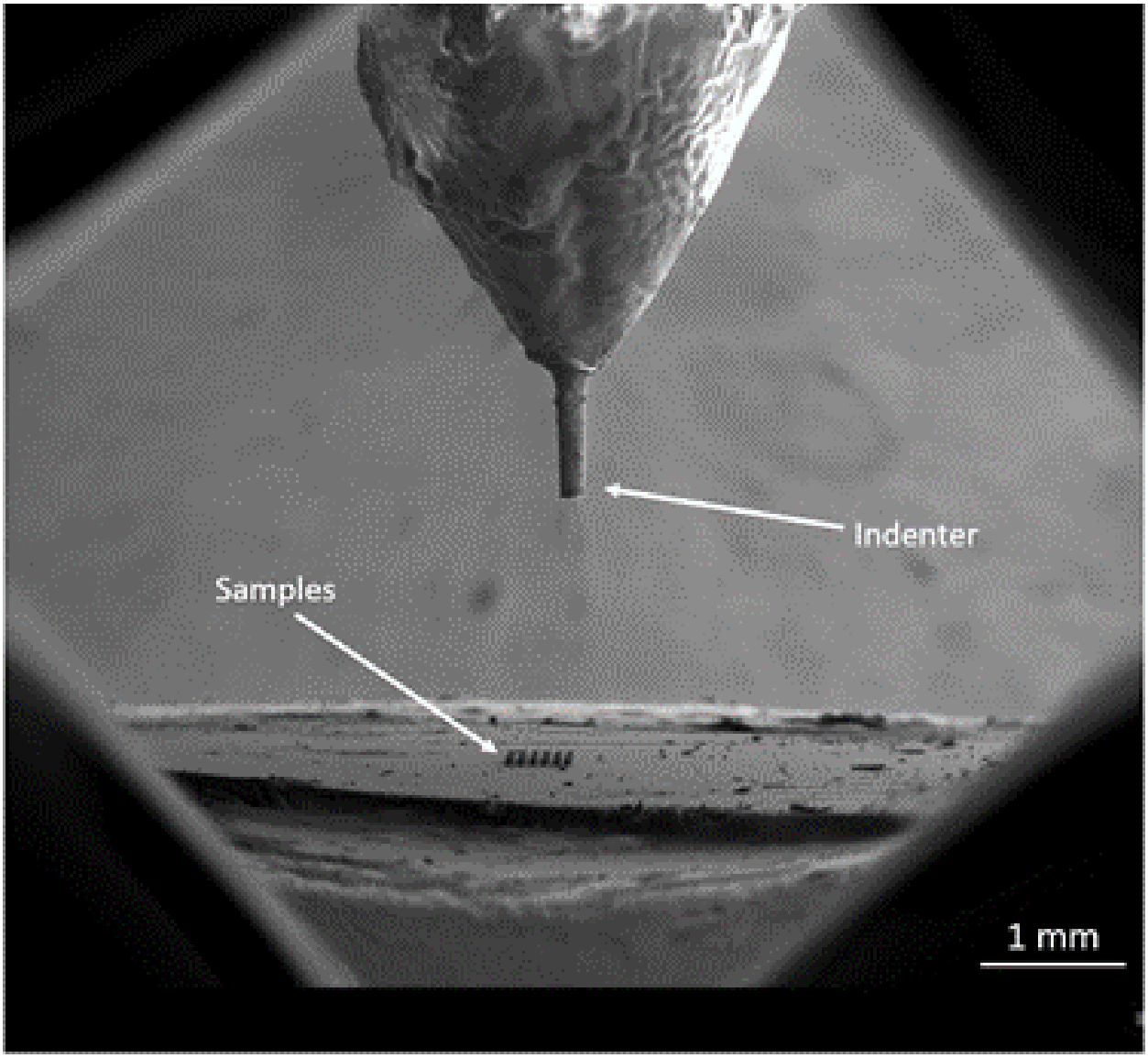

Figure 4.43: Configuration of the flat-punch indenter and a characteristic array of arbitrary samples to be tested.

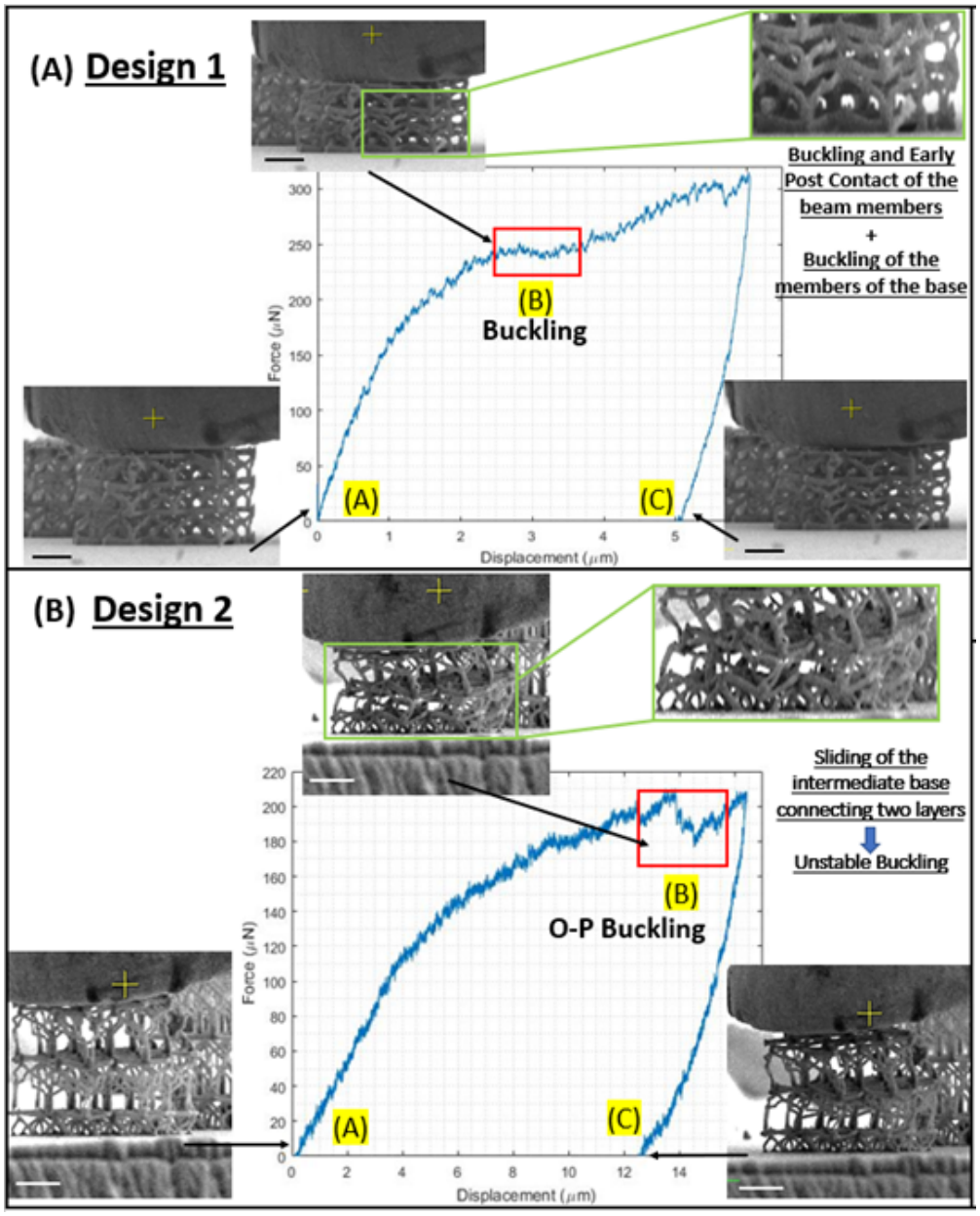

Figure 4.44: In situ SEM – Microindentation tests for designs 1 and 2. (A) Force displacement curve for Design 1. Buckling commences on the designated stage, but the post contact of the beam members due to small height of the unit cells decrease its effect. (B) Force displacement curve for Design 2. For this case out of plane (O-P) buckling occurs, as the slender lattice members cannot provide the required stability to prevent the intermediate base from out of plane buckling. Black length scale bar = $10\mu m$ and white length scale bar = $20\mu m$.

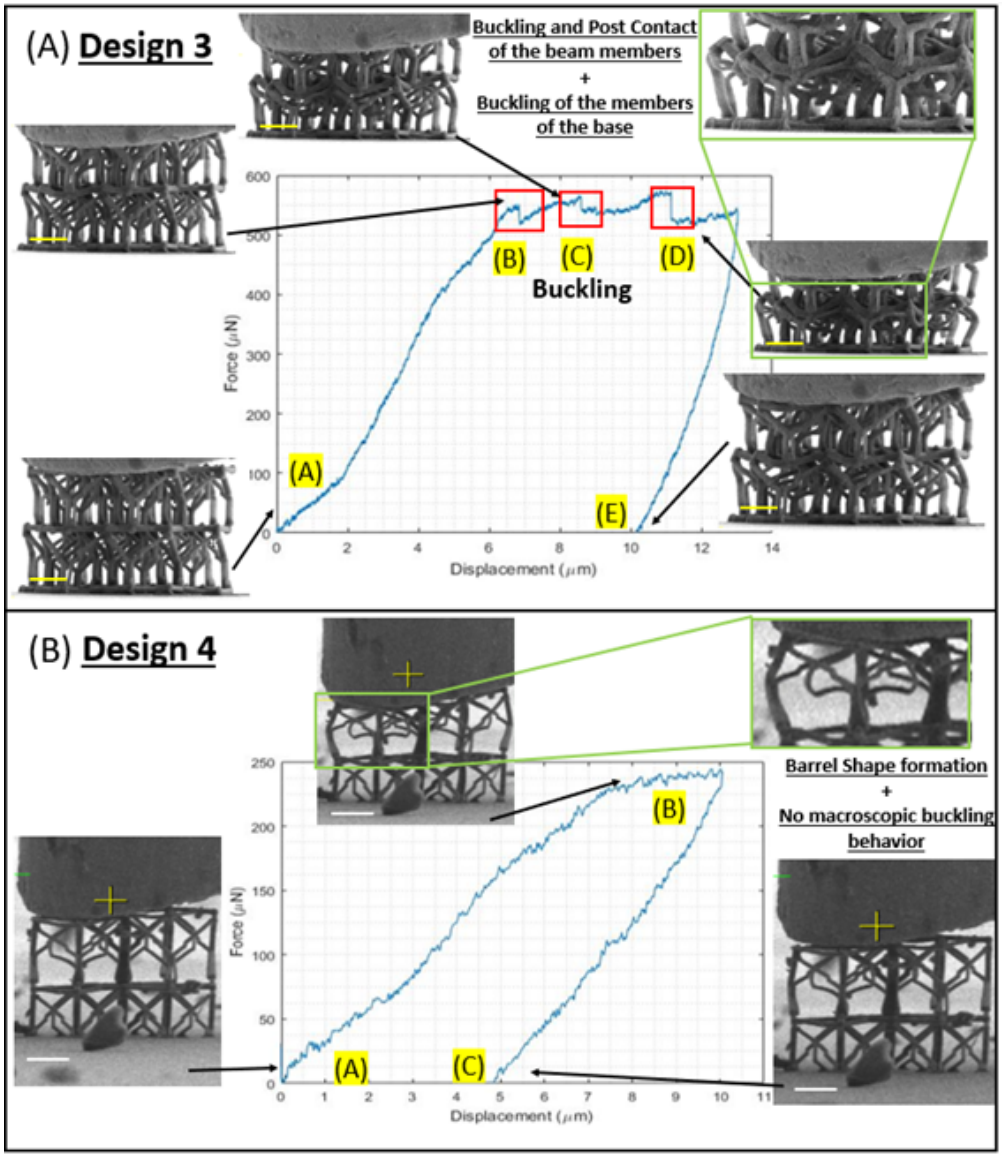

Figure 4.45: In situ SEM – Microindentation tests for designs 2 and 3. (A) Force displacement curve for Design 3. For these dimensions the structure exhibits the desired behavior. The structure is subject to internal buckling and the larger distance between the lattice members provides a multistable response. (B) Force displacement curve for Design 4. The increased height and slender lattice members render the structure non-functional, due to the barrel shape formation during compression. Yellow length scale bar = $15\mu m$ and white length scale bar = $35\mu m$.

the enhanced resilience of the structure to out of plane buckling, while enabling the desired large deformation propagation to subsequent layers. Furthermore, the relative orientation of the beam is crucial for efficient designs. As the surface are of the unit cells increases, to preserve the 150^o pre-bent angle, the unit cell must increase in height as well. Post contact of the buckled members will provide the positive slope to be rejuvenated again, returning the structure to its stable state. However, for short unit cells, the buckled elements come into contact too fast and the buckling behavior cannot be utilized efficiently. The third structure proved to have the correct combination of height and thickness such that the snap through buckling mechanism is observed and the post contact does not occur instantly after buckling. This design provides the perforation for the materialization of buckling on different sections of the unit cells. Hence, at this scaling factor, the designed structure conflates the multistability and the structural integrity that is required for a functional design. From the scope of stiffness, the first design was the most effective, as buckling commenced and the instantaneous post contact of the beam members provided an augmented bulkiness and therefore a stiffer structure. This result can be juxtaposed by the higher slope on the stress-strain curve of Fig. S4A. As both the first and third design have the same height to thickness ratio, for this dimensionless number the mechanisms of stiffness and buckling proved to be the most efficient compared to the other designs. For the barrel shape formation (fourth design), the negative transition of the stiffness is not observed and for the case of out of plane buckling (second design), the structure collapses in a different direction than that of the loading. The front view of the structures after the indentation experiments at the final deformation stage is presented in Figs 4.44(A), 4.44(B) and 4.45(A), 4.45(B). As all of the structures are comprised of a small number of unit cells, the strain energy that is distributed to them surpasses the elastic regime. To encompass both buckling and nonlinear elastic deformations, hyperplastic photoresists can be utilized.

Section Conclusions

In summary, we demonstrated a novel architected structure tailoring the buckling mechanism in three dimensional space for a functional multistable material. The objective was to comprehend how different buckling modes and mechanical responses can commence at the same 3D structure for different length-scales. The structural principle governing the system was based on a buckling mechanism coalesced with the post contact of the structural members, providing the undulated profile on the force displacement curves during snap through buckling. Utilizing simple lattice elements, we accomplished designing a structure that can facilitate buckling based on its geometric configuration. Both the FEA analysis and the microindentation experiments for different length scales provided an insight for the dimensions that manifest internal buckling on the structure rather than out of plane buckling. The simplicity of the design enables the scalability of the structure for applications including robotic actuation [61]. Nevertheless, microscale buckling structures are also imperative for tissue engineering [36]. To facilitate the geometric effects of controlled buckling with reversible large deformations, photoresist that have hyperplastic behavior must be utilized

[228]. Furthermore, the numerical models that can be employed to study large deformations and instability must advance. Models such as Kirchhoff's rods theory [80] must be employed to provide the numerical and analytical tools to simulate the various mechanical responses in microscale structures. Finally, a systematic approach must be addressed to formulate the vector space of the buckling eigenvectors as a function of the unit cell geometric parameters. For this purpose, optimization techniques such as machine learning [55, 56] could be utilized to relate these quantities. This approach will pave the way for the expansion of the design space with more three-dimensional structures that can utilize tailored buckling.

4.5 Tailoring the Dynamic Actuation of 3D-Printed Mechanical Metamaterials through Inherent and Extrinsic Instabilities

Section Summary

In this study, novel 3D metamaterial structures possessing large deformations, hyper elastic behavior and mitigated viscosity at vibrations of different frequencies are designed. These structures incur innate and extrinsic instabilities that cause buckling. These effects combined can enhance the malleability and enable the actuation propagation through the whole structure circumventing the dependence on multiple equilibrium positions. It is also observed that there are significant changes in the creep compliance of the structure, and subsequently to its relaxation modulus. The consequence is a substantial effect on the dissipation losses and the stiffness of the material. To instantiate this principle, a 3D metamaterial unit cell is architected such that buckling commences at the early stages of the deformation, facilitating large deflections. The mechanical response is examined using nonlinear finite element analysis (FEA). In addition, by prebuckling the undeformed structures, we elicit how the viscoelastic effects diminish, leading to the actuation of the whole assembly. Prebuckling makes the whole system highly nonlinear, and it greatly enhances the deformation in the resonant frequency [296]. By studying the dynamic response of the structure through experiments and simulations, we reveal intriguing effects regarding the augmented amplitude of the structure at the resonant frequency and activation of more resonant frequencies. In addition, it is investigated how these effects are evinced for different spatial configurations of unit cells. Our findings establish how controlled instabilities bequeathed by design and boundary conditions can surmount the limitations that materials employed in 3D printing bear. In addition, soft robotic systems are primarily designed from the perspective of the innate properties of the material, e.g. electrical or chemical actuation. Therefore, from the scope of structural design, 2D structures [276, 354] have been thoroughly utilized, since their analysis is easier, while the analysis of perplexed 3D designs has been fairly limited [459, 60, 331, 411]. Therefore, we aim to present how 3D printing can be utilized to its full potential, designing complex 3D structures with tailored dynamic properties. Furthermore, 3D design

can be employed for the control of mechanical signals in multiple directions and for the design of flexible systems with anisotropic 3D mechanical properties, depending on the loading conditions and the desired direction of the output [89]. The modelling of the dynamic behavior will also pave the way to efficiently design control systems that will be utilized for the closed loop control of soft robotic systems. This will mitigate the error to move the system to the desired position or to apply the correct amount of force, which demands an in-depth analysis of the dynamic properties of the controlled system.

Design of architected structures

The candidate designed unit cells are delineated in Fig. 4.46(A). As the objective is to create a 3D structure, the unit cells are designed such that they have hexagonal symmetry, enabling the 3D spatial configuration of the beam members and the 3D assembly of neighboring unit cells. The beam members are connected on two hexagonal bases at the top and bottom of the unit cell. In addition, the hexagonal base provides easy connectivity with all of the unit cells aligned in one orientation. Since each unit cell can be connected with six neighboring ones, the structure can be resilient to out of plane buckling. However, as it will be show later, this is also affected by the number of beam members in the structure. There are two main categories of beam members in the unit cells. The first are the ones connecting the upper and lower base and lie on the faces of the unit cell. The second ones connect the center of each base with the vertices of the other. The number of members of the second category diversify the two unit cells. For the first unit cell (UC1), only one base is connected to the vertices of the other, rendering it nonsymmetric in the lateral direction, whereas both bases are connected to the vertices of the other in the second unit cell (UC2). This asymmetry in the loading direction is critical for out of plane buckling to commence as it will be demonstrated in the next section. To facilitate large deformations for actuation, buckling must commence at early stages of the deformation. 3D structures can have multiple different buckling responses, varying from sliding of the unit cells with respect to the others (out of plane buckling) to internal buckling and propagation of the deformation through subsequent layers [395]. While cubic structures can be considered 3D, they are symmetric with respect to a specific plane, rendering their analysis 2D. These structures have very specific buckling modes that depend on the macroscopic loading conditions [291]. For 3D structures the buckling modes are associated with the dimensions of the geometry, providing multiple design choices for the same structures depending on the design constraints. In previous work we instantiated these principles utilizing unit cells designed with curved beams instead of straight [395]. This effect can lead to post contact and it will stiffen the unit cell. Post contact is imperative to make the stiffness of the structure positive after buckling commences, which leads to negative stiffness. This design paradigm will imitate a snap through mechanism that can lead to a local equilibrium of the potential energy in static loading. Nevertheless, this design will be egregious for our current objective, as it will prohibit larger deformations due to densification of the unit cell. Establishing large deformations as the inherent characteristic of the structure is the main goal of this study. Therefore, the stiffening due to post contact

is diminished by using straight beam members instead of curved ones. As it will be shown later, the effect of stiffening can be manifested in viscoelastic materials through frequency control, which is based on material property instead of a designing tactic [117]. Furthermore, functional architected materials need to be employed in periodic 3D arrays in the structure. Since the unit cells are 3D, they can be assembled either by connecting the edges of each base (Assembly 1) or by intertwining them, connecting the central plates of the bases (Assembly 2) [402]. Both assemblies are illustrated Fig. 4.46(B). To validate their dynamic behavior, each geometry was fabricated by 3D printing. The material of the base is selected to be stiffer than that of the beams to forestall excessive deformation of the base, because this mechanism will obstruct the buckling of the beams. The reason is that if the base has the same stiffness as the material, then they cannot be considered fixed supports, but torsional and bending springs. Then the structure will have the predilection to bending and shear deformation, purloining a portion of the strain energy that accounts to compression. Compression is the only deformation mode that transcends into buckling. Even though bending and buckling have similar macroscopic features, buckling as an instability mechanism can facilitate large deformations for the whole structure [395].

The tested structures were fabricated employing Stratasys Objet 350 Connex 2 printer, using similar materials as shown in previous work [155]. This 3D printer enables the fabrication of complex 3D structures with beam members of thickness reaching $0.5mm$. In addition, different materials can be simultaneously utilized to provide stiffness and strength gradients in the structure. The hybrid structures will have stiffer base than the beam members, mitigating undesired nonsymmetric deformation of the bases.

The periodic arrays that utilize Assembly 1 with unit cell 1 (DS2) and unit cell 2 (DS3) and Assembly 2 with unit cell 1 (DS1) and unit cell 2 (DS4), are presented in Fig. 4.46(C). A characteristic configuration of a fabricated sample on the vibration apparatus with respect to the imaging system is shown in Fig. 4.46(D).

The experimental apparatus that was used to characterize the vibrational response of the structures consists of a high-speed imaging system and the vibration actuation system. Regarding the high-speed imaging, the high-speed camera FASTCAM Mini AX was assembled with a ZOOM 7000 Navitar TV lens for high resolution recording and frame rate up to 6,400 fps, capturing the deformation of the structures, shown in the Recordings [396]. The camera was attached to a gear ruler to translate it to different layers of the structure. The vibration of the structures was accomplished with the 3B SCIENTIFIC® PHYSICS Vibration Generator 1000701. This vibration generator can be utilized for vibrations ranging from 0 to 20 kHz frequency. The vibrator is controlled by the 3B Scientific ® Power Function Generator, 115V, 50/60Hz, that features an external sweep function with a power amplifier for experiments on simple harmonic oscillation, alternating current and induction. For all the experiments the system input was force controlled, with the magnitude of the force being controlled by the voltage of the vibrator using a sine wave actuation. The bottom layer of the structure was attached to the vibration generator, whereas the top layer was fixed supported. The deformation was recorded using the Photron FASTCAM Viewer to modify the frame rate and the quality of the imaging. The deformation was recorded for the six

different structures from 1 Hz to 60 Hz, with step equal to 1Hz. Each video was processed to measure the maximum lateral deformation of the recorded layer and plot it as a function of the frequency, obtaining the experimental curves shown in Figs. 4.48, 4.49 and 4.50. Before the recorded started, 1-2 minutes had already passed vibrating the geometry to reach the steady state of the deformation, since this response is calculated in the transfer function. In all of the curves, the amplitude was normalized with the respect to the amplitude of the prebuckled structure at the resonant frequency to designate the percentage differences in the amplitude for both experiments and simulations. When the region of resonance was reached, the experiments were repeated with 0.2 Hz step to find the precise value of the resonant frequency.

Numerical Modeling and FEA analysis

To validate the intrinsic instability that the structures must embrace, nonlinear FEA analysis was employed to investigate whether any of the unit cells will reach a cauldron, teetering. To obtain the characteristic deformation of the structures under static and dynamic loading, the multi-purpose finite element software ANSYS (Workbench 18.0) was employed. The properties of the geometries were selected such that they match the materials used in the 3D printing. To obtain the nonlinear elastic response of the unit cells, the Static Structural module was used under nonlinear large deformations. In this setting the structure is discretized by 10-node, tetrahedral finite elements. Nevertheless, as the material has hyper elastic nonlinear behavior, the stiffness matrix is also a function of the deformation and the applied stresses at the given deformation, based on the equation 4.13 provided in the previous section [218]. For the nonlinear analysis, one base of the unit cells was fixed, while the other the other base had a step wise displacement to obtain the stress strain curves until buckling commences.

Regarding the dynamic response, as the sample was actuated in the lateral direction, the modal analysis module was utilized to obtain the characteristic frequency which will lead to lateral actuation of the structure. Starting from the differential equation dictating the system [206]

$$[M]\ddot{x} + [C]\dot{x} + [K_o]x = F(t)] \tag{4.17}$$

the following eigenvalue – eigenvector equation must be solved

$$[[M]s^2 + [C]s + [K_o]]x(s) = 0 \tag{4.18}$$

where $[M]$ is the inertia matrix of the structure, $[C]$ is the damping matrix of the structure, s is the eigenvalue of the characteristic polynomial of the system (i.e. the natural frequency), and x is the eigenvector of eigenvalue s corresponding to the deformation of the system for this specific eigenvalue. $F(t)$ is the external force applied to the system. This eigenvalue-eigenvector problem will give multiple eigenvectors, but the purpose of the simulations is to obtain the one related to lateral deformation, presented in Fig. 4.48(C). This

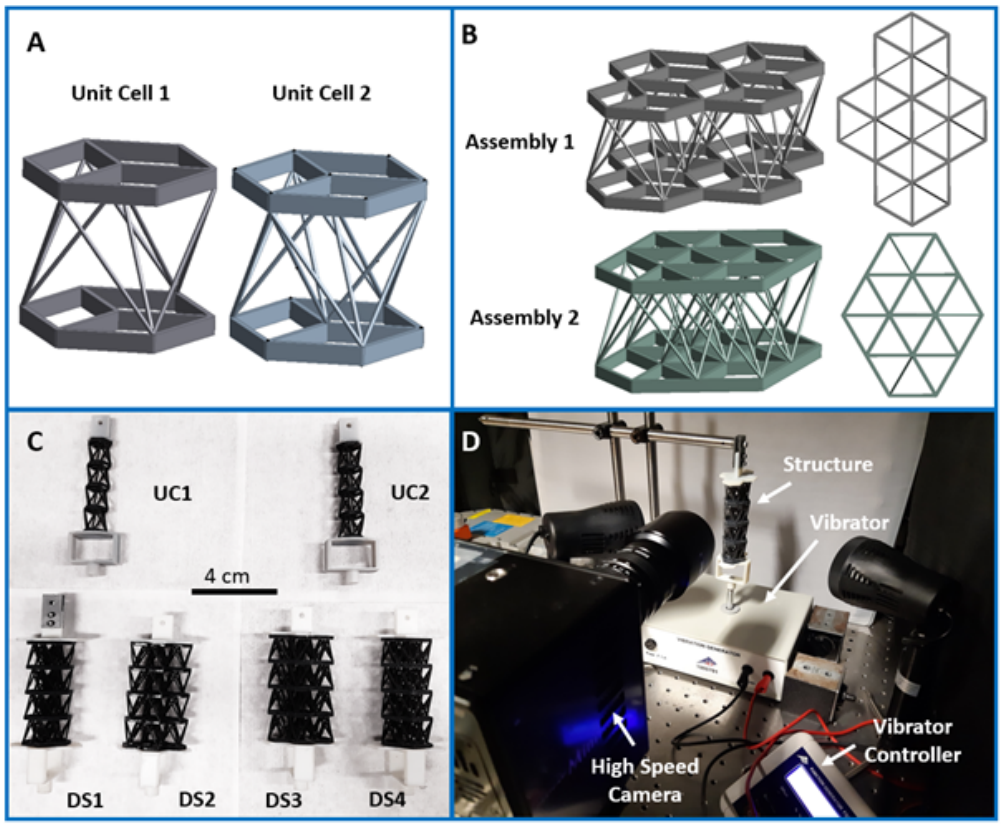

Figure 4.46: Design and Fabrication of the Architected Structures (A) The two basic unit cells, having nonsymmetry in the lateral direction (Unit Cell 1) or being symmetric in the lateral direction as well (Unit Cell 2). (B) Potential assemblies of the unit cells, if there is no intersection of the neighbouring unit cells (Assembly 1) or the proximal unit cells are intertwined (Assembly 2). (C) Characteristic 3D Printed samples for each design and each assembly. (D) Side view of the experimental apparatus employed for the characterization of the dynamic response as a function of the frequency. A high-speed camera is focused on specific layers of the structure, enabling high spatial and temporal resolution of the deformation.

deformation will be substantiated in the experiment apparatus. For the case of prebuckling, the system depends on the nonlinear terms $[K_u]$ and $[K_\sigma]$, increasing the complexity of the problem. The inertia matrix and the stiffness matrix depend on the properties of the materials employed. Nevertheless, the damping matrix is a function of the viscosity of the material. As these properties are not provided for the materials, Rayleigh's Classical Damping methodology was utilized. This analysis expresses the damping matrix as a linear combination of the mass and stiffness matrices, given by the following equation [206]

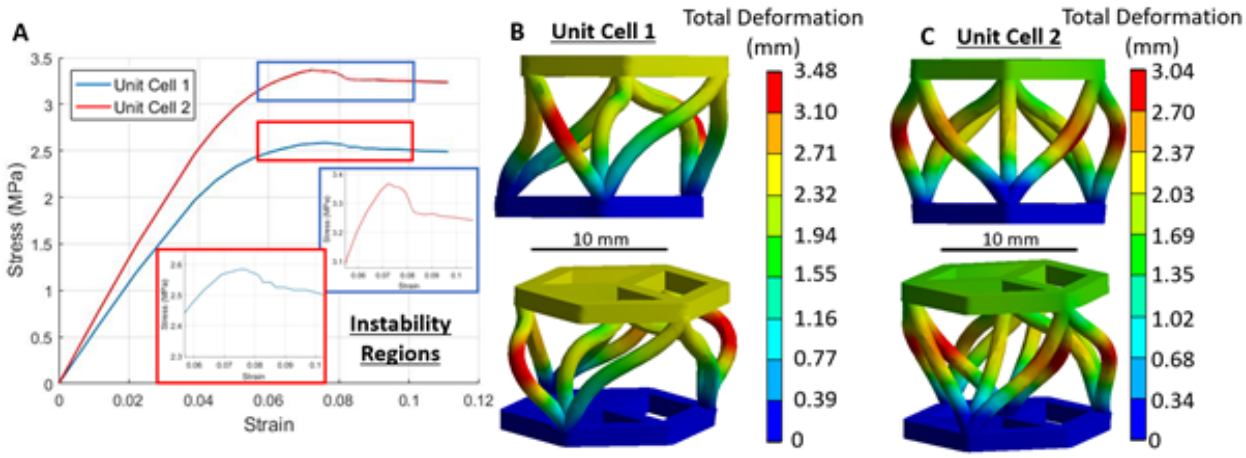

Figure 4.47: Nonlinear FEA analysis for UC1 and UC2. (A) Stress - Strain response of the two unit cells. For the unit cell 1 buckling commences at 7.7% lateral compression, whereas for unit cell 2 it occurs at 7.2%. (B) The deformation field on the unit cell 1. Since this unit cell is not symmetric in the lateral direction, out of plane buckling commences, creating a non-desired deformation mode. (C) The deformation field on the unit cell 2. The buckling leads to external opening of the structure, avoiding in-plane buckling and subsequent post contact that will stiffen the structure and apprehend the deformation propagation.

$$[C] = \alpha_1[M] + \alpha_2[K_o] \tag{4.19}$$

where α_1 and α_2 are constants depending on the material. These values were fine-tuned, such that the number of eigenvectors and eigenvalues corresponding to resonant frequencies matched the experimental results. The values that provided close matching to both experimental and theoretical results were $\alpha_1 = 10^{-2}s^{-1}$ and $\alpha_2 = 0.5 * 10^{-2}s$. These parameters were used for all the assemblies and unit cells. Again, for the case of prebuckling, the terms $[K_u]$ and $[K_\sigma]$ must be included, rendering the problem more difficult to be numerically solved.

Having obtained the resonant frequency, the amplitude – frequency curve (i.e. Bode Plot) can be obtained. From the theory of dynamical systems, for a system characterized by eqn. 4.17, we can measure a desired output as a function of the deformation of all the nodes x. This output y, which in our case is the lateral deformation of the nodes to attain the deformation propagation u, can be obtained as follows

$$u = [C_d]x + [D]F \tag{4.20}$$

where $[C_d]$ is a linear operator with 1 and 0 elements that calculates the lateral deformation based on all the nodes of the system. $[D]$ is a linear operator that correlates the output to the input, which is the applied force F. Using Laplace transform we can obtain the

transfer function matrix of the system that provides the deformation amplitude-frequency response based on the following equation.

$$u(\omega) = [[C_d][M](j\omega)^2 + [C](j\omega) + [D]]F(\omega) \tag{4.21}$$

$$u(\omega) = H(\omega)F(\omega) \tag{4.22}$$

where ω is the frequency of the applied force (r/s). The FEA harmonic response module solves for the transfer function $H(\omega)$ numerically and the bode plots of the function are obtained. To obtain the lateral deformation u_L or the lateral force FL applied by the vibrator, we have to plot the $H_{F_L \to u_L}(\omega)$ component of $H(\omega)$. As it will be presented on the next section, this is actually related to the complex creep compliance of the system. For all of the structures, one base is fixed and on the other a unit load is applied in the lateral direction, to match the experimental conditions of the tested specimens. To match the sampling rate of the experiments (i.e. 1 Hz), but preventing divergence of the algorithm, the sampling rate was set equal to 0.1 Hz. Then the points at each 1 Hz were selected and plotted alongside the experimental curves. The ANSYS Design Modeler was used to design the CADs of the structure geometries.

Fig. 4.47 conveys the simulated behavior for both unit cells. Fig. 4.47(A) shows that both unit cells become unstable during the early stage of the deformation ($\epsilon_{total} = 7.7\%$ and 7.2% at $\sigma_{lateral} = 2.5$ MPa and 3.367 MPa for UC1 and UC2, respectively). UC1 has less members than UC2, therefore it's resilience is lower, leading to instability at a lower load. The reason is that the critical buckling load is proportional to $\sim EI_{eff}/L_{eff}$, where E is the Young's modulus, I_{eff} is the effective bending inertia of the structure and L_{eff} is the effective length of the beam based on its boundary conditions. As both structures have the same boundary conditions, they have the same effective length. Nevertheless, the effective inertia depends on the effective cross section of all the beams. Hence, less beam members will lead to decrease of I_{eff}, as validated by the simulation results. After the buckling event, the slope remains negative, since the unit cells are designed such that there is no post contact of the proximal beams [395]. However, they have two distinct buckling mechanisms, presented in Figs. 4.47(B) and 4.47(C). UC1, since it is asymmetric with respect to the loading direction, is subject to out of plane buckling. This leads the top base to "slide" with respect to the other. This mechanism is not observed in UC2, where the symmetry enables the unit cell to expand uniformly in the radial direction. Furthermore, it must be noted that the asymmetric loading will lead to higher stress distribution at some nodes, leading to failure at the resonant frequency for a small number of cycles. Thus, UC1 is inadequate to provide a steady propagation of the deformation that is required for soft robotic applications for instance. As it will be shown later, a periodic assembly can alleviate this effect, but it will still be observed as it is inherited by the unit cell encompassing this behavior. This result will foreshadow that assemblies with UC2 will likely be better design choices. With the mechanical response of the unit cells delineated, the mechanical response of the unit cells during the vibration can be interpreted.

Results and Discussion

Dynamic Response of Unblemished and Prebuckled Unit Cell Structures

Utilizing the experimental apparatus presented in Fig. 4.46(D), arrays of fabricated individual unit cell structures were tested in vibrations as a function of the frequency. Each array consists of four layers. The unit cells have height 18 mm and beam diameter $1mm$. These dimensions were selected such that the maximum resolution of the 3D printer can be employed. Smaller unit cells can be utilized for smaller scale applications that require small but complex structural features that embrace metamaterial behavior. In addition, a large number of unit cells can be utilized for applications requiring large scale but stable mechanisms [335]. Tacitly, based on previous investigation of scale effects [395], increasing the thickness of the beams will lead to non-desired post contact at early stages of the deformation. Since one of the common repercussions of 3D printing is nonuniform material properties, larger unit cells will also be more susceptible to material inhomogeneity, ushering nonsymmetric deformation due to material properties rather than a rigorous design approach. While scale effects are not pertinent for this study, future work should also focus on their consequences on the 3D printing structures and how material inhomogeneity affects the frequency response. To monitor the experimental results, harmonic response simulations were conducted to attain the Bode plot of the amplitude as a function of the frequency.

By assuming that there are no memory effects (i.e. each measurement has been preformed long after the previous one), the response of the system can express by the following and ordinary differential equation. Since we apply a sinusoid force to the system, the stress has the form $\sigma = \sigma_o e^{j\omega t}$, with σ_o the amplitude of the stress. Hence, by applying Laplace Transform, the strain, and subsequently the displacement can be expressed as follows [117]

$$\epsilon(t) = J^*(\omega)\sigma_o e^{j\omega t} \tag{4.23}$$

Where J^* is the complex compliance of the system. Since it is a complex number, it can be expressed as a function of its real and imaginary parts, as follows

$$J^*(\omega) = J^{'}(\omega) - j * J^{"}(\omega) \tag{4.24}$$

where $J^{'}$ and $J^{"}$ are the storage and the loss compliance respectively. Since the output is the displacement and the force is the input, the normalized deformations $u(t)$ and $F(t)$ are also linked by the loss compliance

$$u(L) \sim J^*(\omega)F_o e^{j\omega t} \tag{4.25}$$

where F_o is the amplitude of the force. Hence, the bode plots can be used to estimate the complex compliance of the metamaterial structures $|J^*(\omega)|$. The energy that is dissipated by the system due to damping for one period is defined as

$$W = \int_0^{2\pi/\omega} Re(\sigma)Re(\dot{\epsilon})\, dx \tag{4.26}$$

It can be proved that

$$W = \pi\sigma_o^2 J^{"}(\omega) \sim J^{"}(\omega)F_o \tag{4.27}$$

Therefore, the loss compliance determines the energy dissipation of the system. In addition, the damping capacity of the material is defined as $\Delta W/W$ is equal to

$$\Delta W/W = \pi/2(J^{"}(\omega)/J^{'}(\omega)) \tag{4.28}$$

By observation of the responses of the assemblies, their behavior has either one or two peaks, a response observed only in coupled quadratic systems. Therefore [206]

$$J^*(\omega) = \prod_{i=1}^{2} \frac{\omega_{ni}^2}{2\omega_{ni}\omega\zeta_i + \omega_{ni}^2 - \omega^2} \tag{4.29}$$

where ω_{ni} is the ith natural frequency (r/s) of the system and ζ_i is the ith damping coefficient of the system. For bode plots the ith resonant peak at the ith resonant frequency are given by

$$Peak = 1/\zeta_i \tag{4.30}$$

$$\omega_{ri} = \omega_{ni}\sqrt{1 - 2\zeta_i^2} \tag{4.31}$$

Hence, increase of the height of the peak indicates drop of the damping. Correlating the damping constant with the damping capacity, the storage and the loss compliance need to be calculated. Focusing on one peak only (i = 1)

$$J^*(\omega) = \frac{\omega_{n1}^2(\omega_{n1}^2 - \omega^2)}{(\omega_{n1}^2 - \omega^2)^2 + (2\zeta_1\omega_{n1}\omega)^2} - j\frac{2\omega_{n1}^3\omega\zeta_1}{(\omega_{n1}^2 - \omega^2)^2 + (2\zeta_1\omega_{n1}\omega)^2} \tag{4.32}$$

Therefore, we can get

$$J^{"}(\omega)/J^{'}(\omega) = \frac{2\omega_{n1}\omega\zeta_1}{(\omega_{n1}^2 - \omega^2)} \tag{4.33}$$

It can be easily shown that

$$\Delta W/W \sim \sum_{n=1}^{2} \frac{2\omega_{ni}\omega\zeta_i}{(\omega_{ni}^2 - \omega^2)} \tag{4.34}$$

This result facilitates that the drop of the damping capacity of the structure is related to the higher height of the peaks observed in the prebuckled configuration. Since the damping capacity drops, the mechanical energy provided to the system can be employed for the actuation of the structure, impeding the energy dissipation of the structure. The measured values, based in the bode plots, are given in table 4.4.

Structure	DS1	DS2	DS3	DS4
Undeformed f_n [Hz]	29	32	9 and 32	11 and 31
Prebuckled f_n [Hz]	32	32	10 and 32	9 and 30
Undeformed $z\bar{e}ta$	1.42	1.25	3.57 and 1.48	2.5 and 1.25
Prebuckled $z\bar{e}ta$	1	1	2.85 and 1	1.25 and 1

Table 4.4: Components of the stiffness tensor (Eq. and 5.8 5.9).

Since the bode plots corresponds to normalized amplitude, these damping coefficients must be addresses as effective as well. Furthermore, the complex creep compliance can be related to the complex relaxation modulus E^* of the material by the celebrated equation [117]

$$J^*(\omega) * E^*(\omega) = 1 \tag{4.35}$$

At high frequencies, we observe from the experiments that the magnitude of J^* drops to zero since there is no deformation. Then from eqn 4.35 the $|E^*|$ will increase. Since the magnitude of the complex relaxation modulus is related to the stiffness and the rigidity of the material, the structure can be tuned to become rigid, by shifting the frequency of the applied force to a high value.

Representative curves of the normalized amplitude as a function of the frequency for both unit cells are presented in Fig. 4.48(A)-4.48(B). For both structures there is close match between the experiments and the simulations, indicating that the modeling employed by the FEA solver can depict the realistic behavior of the structures. The variance may be associated with inhomogeneities in the material, that would be significantly more predominant for larger and thicker members and should be investigated in future work. Characteristic deformations obtained for the resonant frequency are presented in Fig. 4.48(C), revealing partial bending of the bases and radial expansion of the structure, as in the experiments. The captured deformation at the resonant frequency is also presented (Fig. 3A-3B). Both samples we tested in the initially undeformed and prebuckled configurations (with $2mm$ compression). The fact that this state is associated with buckling can be verified by Fig. 4.47(A), since at this deformation regime the structure is unstable. In addition, for $2mm$, only buckling at the beams was observed, whereas for higher deformations overall buckling of the whole structure commences. This causes sliding of the layers, causing out of plane buckling for the whole structure. At the resonant frequency, which is equal to $30Hz$ for the UC1 and 35 Hz for UC2 the amplitude increase compared to low and high frequency actuation is 80% and 70% respectively. Nevertheless, prebuckling renders the individual unit cells highly unstable, as they begin having out of plane deformation and not uniform lateral propagation of the deformation into subsequent layers. Therefore, prebuckling does not have a significant effect in the amplitude increase, which becomes significantly large due to the out

of plane deformation. In addition, it must be noted that the UC1, having less beam members, exhibiting non-symmetric deformation. Consequently, fracture occurs at some beam members (Fig. 4.48(A)), as indicated by the nonlinear structural analysis. Moreover, there is a shift of the resonant frequency of the two unit cells. That is a considerable change as the frequency range that dynamic phenomena are observed is only $60Hz$. This implies that the architected design can be employed as a tool to switch the resonant frequency of functional materials. Moreover, for the case of UC2, prebuckling leads to the creation of two more resonant frequencies, at $12.19Hz$ and at $52.19Hz$ (by interpolation of the experimental curves). This means that more modal shapes in the structures are activated for lateral loading, a result consonant with the simulations. The harmonic response estimated the values of these resonant frequencies at $12Hz$ and $53Hz$ respectively. The variance of the modal shapes and the shifting of the natural frequencies due to prestressing has been reported before [137, 296], and it is consonant with our experimental results. At higher frequencies the amplitude of the deformation tends to 0, as the inertia of the unit cells cannot follow up the high frequency actuation, a result consistent with the dynamic behavior of mechanical systems [206, 333].

Control of the Response of 3D Periodic Assemblies

Next the four different periodic arrays were tested. The results are presented such that the two different combinations for each assembly are compared. Therefore, the designs associated with Assembly 1 (DS1 and DS4) are presented in Fig. 4.49, whereas the designs related to Assembly 2 (DS2 and DS3) are presented in Fig. 4.50. For DS1, prebuckling precipitates 71% increase of the resonant amplitude compared to low frequency actuation, while an initially undeformed structure has 62% increase. It is observed by the captured frames (Fig. 4.49(A)) that the out of plane deformation commences at the assembly as well, as all of the beam members have the proclivity to buckle to the right side of the structure. This is the same mechanism shown for the individual unit cell (Fig. 4.47(B)). While this effect is manifested in the initially undeformed assembly as well, it is significantly mitigated as the viscoelasticity causes energy dissipation which is removed by the strain energy caused by the buckling. Moreover, there is a shift of the resonant frequency. From $29Hz$ for the initially undeformed configuration, it is shifted to $32Hz$ due to prebuckling. Recordings of the deformation of the initially undeformed and prebuckled DS1 are provided in the published version of this work [396]. For DS4, radial expansion is observed (Fig. 4.49(B)), which is the same deformation mode shown in Fig. 4.47(C). Therefore, from a functional standpoint, this design is more efficient as it does not have a detrimental buckling mode [395]. The characteristic responses at the resonant frequencies are provided in the published version of this work [396]. In addition, this assembly has more beam members, leading to 49% increase of amplitude at the resonant frequency (at $31Hz$). This result is reasonable, taking into account that more beam members increase the rigidity of the structure. However, prebuckling increases the amplitude to 61%, while there is also a small shift of the resonant frequency (at $30Hz$). It must be remarked that there is also a new resonant frequency at $9Hz$, which is comparable to the amplitude of the initially undeformed structure.

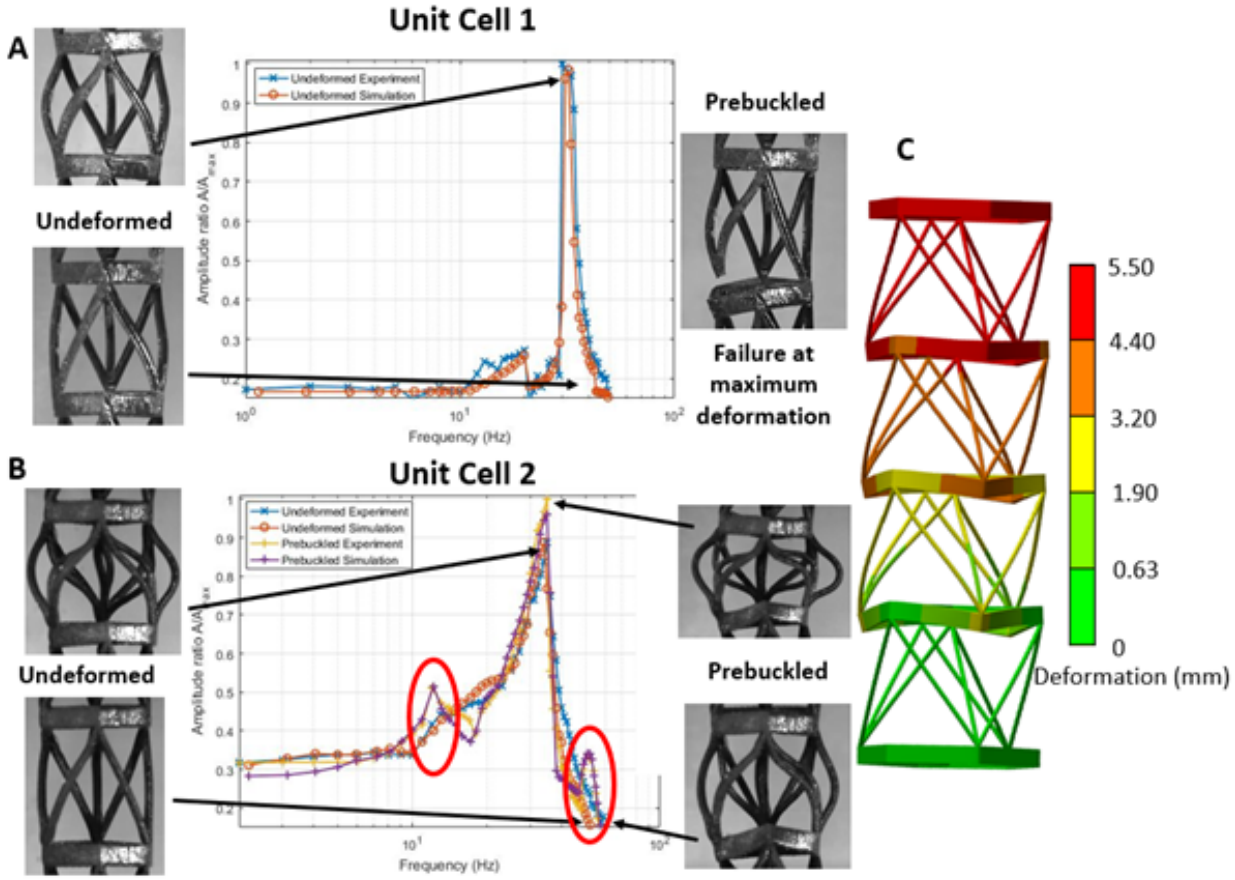

Figure 4.48: Comparison of the harmonic response and the experimental response for UC1 and UC2. (A) Normalized deformation amplitude – frequency curves for UC1. The resonant frequency is at 32 Hz but the small number of beam members renders it susceptible to failure due the dynamic loading at prestressing. (B) Normalized deformation amplitude – frequency curves for UC2. The individual unit cells do not have the structural integrity to have stable vibration propagation through subsequent layers. This out of plane instability renders the maximum amplitude the same for both the undeformed and prebuckled configuration. However, apart from the main resonant frequency at 32 Hz, two more are observed at 12.19 Hz and 52.19 Hz (marked in the red circles). (C) Characteristic deformation distribution obtained by the harmonic response for the unstressed configuration to obtain the amplitude-frequency curve. The deformed state for both unstressed and prestressed configuration of the tested structures are demonstrated at maximum and minimum deformation.

Examining the response of the Assembly two structures, similar instability mechanisms occur even at the intertwined beam members (Fig. 4.50). In DS2, the layers face out of plane deformation for both undeformed and prebuckled configurations (Fig. 4.50(A)) and

DS3 faces radial expansion due to buckling (Fig. 4.50(B)). The resonant frequency of DS2 does not have a remarkable change, shifting from $32.16Hz$ to $32Hz$. Moreover, the amplitude increase at the resonant frequency rises from 60% to 68%. This result is a repercussion of the design of Assembly 2. The beam members are intertwined in comparison to Assembly 1, leading to significant increase of the rigidity. DS3 proved to be a much more efficient design, as the amplitude increase from low frequency to resonant frequency rose from 35% to 77%, at $37Hz$ and $35Hz$, respectively.

Regardless of the amplitude increase, it is imperative to create a design that vanishes the viscoelastic effects and promote uniform deformation propagation through the whole structures. To capture this, the deformation at the layer which is farthest from the vibrator was observed for all the samples. The reason why the bode plots of the amplitude were measured at the initial layers was that there is minuscule deformation of the undeformed structures. Therefore, the variance of the amplitude as a function of the frequency could be distinguished using image processing on the captured deformations. Representative recordings for DS3 and DS1 are given in the published version of this work [396]. As indicated by the measured deformation presented in Fig. 4.51, all the designs have remarkably larger deformation at the final layer in the prebuckled state. This leads to 5 times amplitude increase at the final layer (DS1). DS2 has 2.22 times larger deformation, while DS3 and DS4 have 3.5 and 3.36 times larger deformation, respectively. To fathom this effect, the amplitude increase must be correlated with the energy dissipation of the viscoelastic material. Since for all of the experiments either one or two peaks were observed, the system behaves like a second order system or two convoluted second order systems (i.e. fourth order). These systems can be characterized by their natural frequency ω_n and their damping coefficient ζ. Using the analysis presented on the previous section, the damping capacity of the material, which is the ratio of the energy dissipated over the energy stored, is given by 4.34. Since the peaks of the resonant frequencies are proportional to $1/\zeta$, the increase of the amplitude of the deformation leads to mitigation of the energy dissipation of the whole structure, a conclusion congruous with the experimental results. Based on the experimental values provided in the previous section, the damping capacity of the material drops in the prebuckled configuration. However, since viscoelastic materials have fading memory effects, they can behave nonlinearly. This means that the damping coefficient ζ depends on the loading history of the structure. Nevertheless, by conducting all of the experiments multiple times, the same resonant frequencies were observed and the amplitude of the prebuckled structures was always higher than that of the initially undeformed structures. Hence, even though the results will vary depending on the time the measurements are performed with respect to previous measurements, it can still provide a quantitative argument why prebuckling precipitates the mitigation of viscoelastic effects. Nonetheless, for this analysis to be valid, it is imperative that the mechanical response leads to a closed loop hysteresis curve in the force-displacement curve. Otherwise, the system has a chaotic behavior that cannot be addressed by the presented analysis [260]. Using image processing on the recording deformations, the deformation of selected layers can be measured as a function of time and be compared with the applied force.

Since there is no system to measure the forces, both forces and displacements were attained by image processing. The structures are actuated with a sinusoid force $F = F_o sin(\omega t)$. Since the base of the structure is connected directly to the vibrator, the applied force will be on the same phase as the displacement of the base. My tracking the deformation of the base with image processing, the normalized force time curve can be obtained.However, since the structure is viscoelastic, there will be a phase difference between the applied force and the displacement of the structure [117]. This phase difference depends on the position that the displacement is measured. Since the changes in deformation are more abrupt in the base of the unit cells, their respective positions were tracked.

Characteristic curves for DS4 at the resonant frequency are presented in Fig. 4.52. It is evident that in the steady state there is a phase difference between the applied force and deformation, since the materials is viscoelastic. Plotting the force as a function of the displacement (Fig. 4.53) reveals that there is indeed a closed hysteresis loop, and the system does not have a chaotic nonlinear behavior [260]. Therefore, the harmonic response analysis can be employed.

Despite of this intriguing finding, the mechanical responses that were presented must also be put into perspective. The assemblies with UC2 are much more efficient than UC1, since out of plane buckling is hindered. In addition, this design leads to the activation of more resonant frequencies, modifying the frequencies that can be used to actuate the structure. This effect can be rather expedient for mechanisms that need a stepwise actuation, with large but steady increase of the deformation. There is also a remark that must be addressed regarding the versatility of these materials coupled with architected structures. At higher frequencies, it is observed that all of the structures have miniscule deformations. However, there is another mechanism that is evident at high frequencies. From the theory of mechanical behavior of polymers [117, 417] at high frequencies (above 60 Hz for the fabricated structures) the viscosity of the material tends to become 0, and the material behaves as a rigid structure. This effect, accompanied by the tailored malleability of the prebuckled structures, can lead to adaptive devices that show significant versatility in transitory environments requiring either high strength and rigidity or large deformations and flexibility by frequency modulation.

Nevertheless, it must be noted that based on the recorded deformation of the fabricated structures, coupling of multiple loading modes such as torsion is insinuated. This coupling has significant effects on the modal response of dynamic systems as it has been delineated [260]. While the modal analysis that was conducted revealed rotational modal modes as well, these responses should have a drastic effect depending on the applied loading of the structure. Future work should focus on the modelling of such coupling in the dynamic response of 3D viscoelastic materials. Furthermore, experimental techniques utilizing forces of higher magnitude should be utilized to excite higher buckling modes in the structure. While in this study the deformed profiles that were observed correspond to the first buckling mode, higher buckling modes may rejuvenate more resonant frequencies and therefore lead to even more significant mitigation of the viscoelastic behavior. Since modifying the dimensions of the unit cells may also provide similar effects, scaling analysis should also be investigated under the scope of different buckling modes.

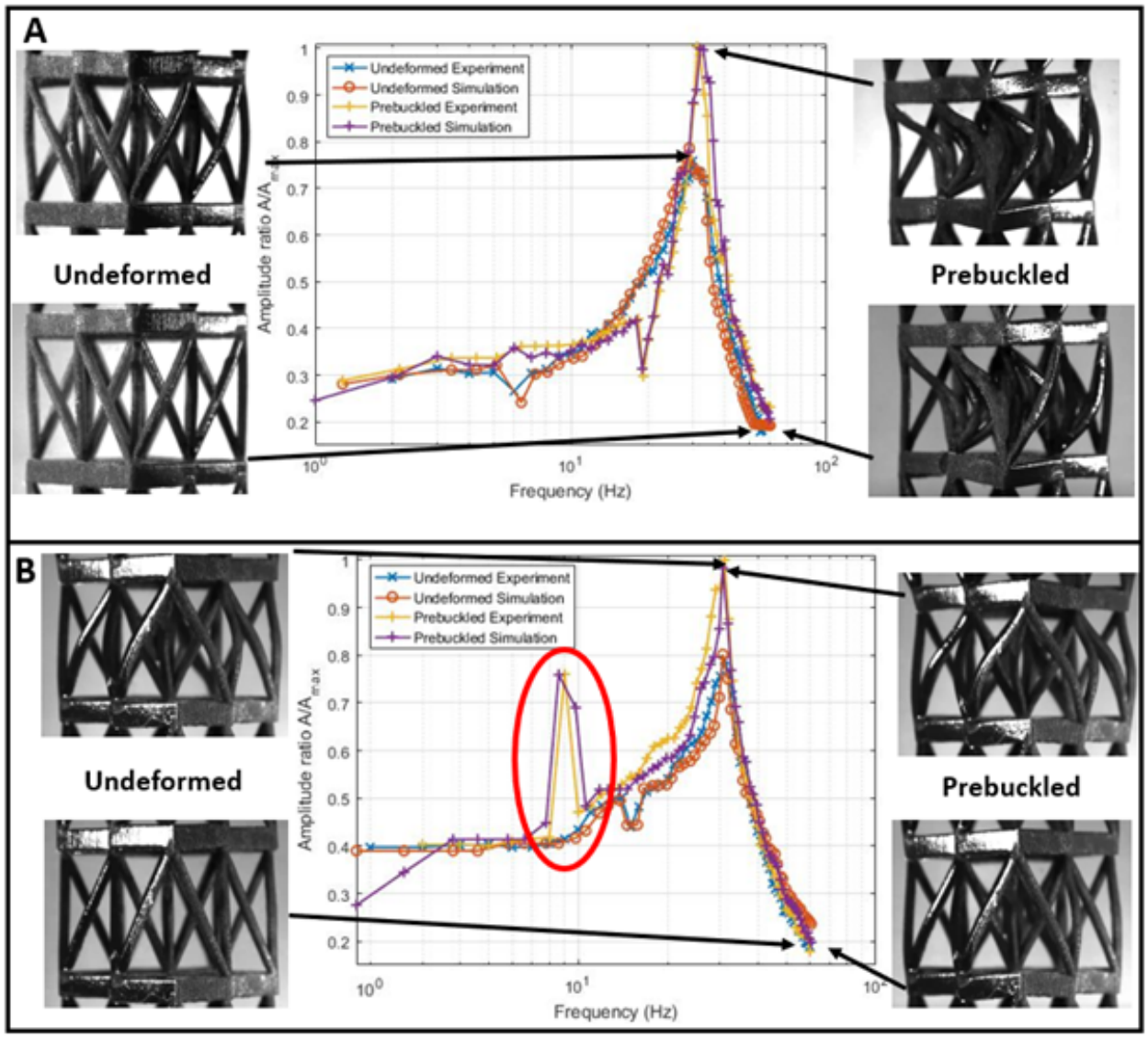

Figure 4.49: Comparison of the Harmonic Response and the experimental response for the Assembly 1 with unit cells 1 and 2 (DS1 and DS4). (A) Normalized deformation amplitude – frequency curves for DS1. The resonant frequency for the prebuckled structure is at 32 Hz, whereas for the undeformed design it occurs at 29 Hz. (B) Normalized deformation amplitude – frequency curves for DS4. While the main resonant frequency is at 30 Hz for the prebuckled (31 for the undeformed), the amplitude at 9 Hz is also significantly enhanced for the prebuckled configuration (marked in the red circle). The deformed state for both unstressed and prestressed configuration of the tested structures are demonstrated at maximum and minimum deformation.

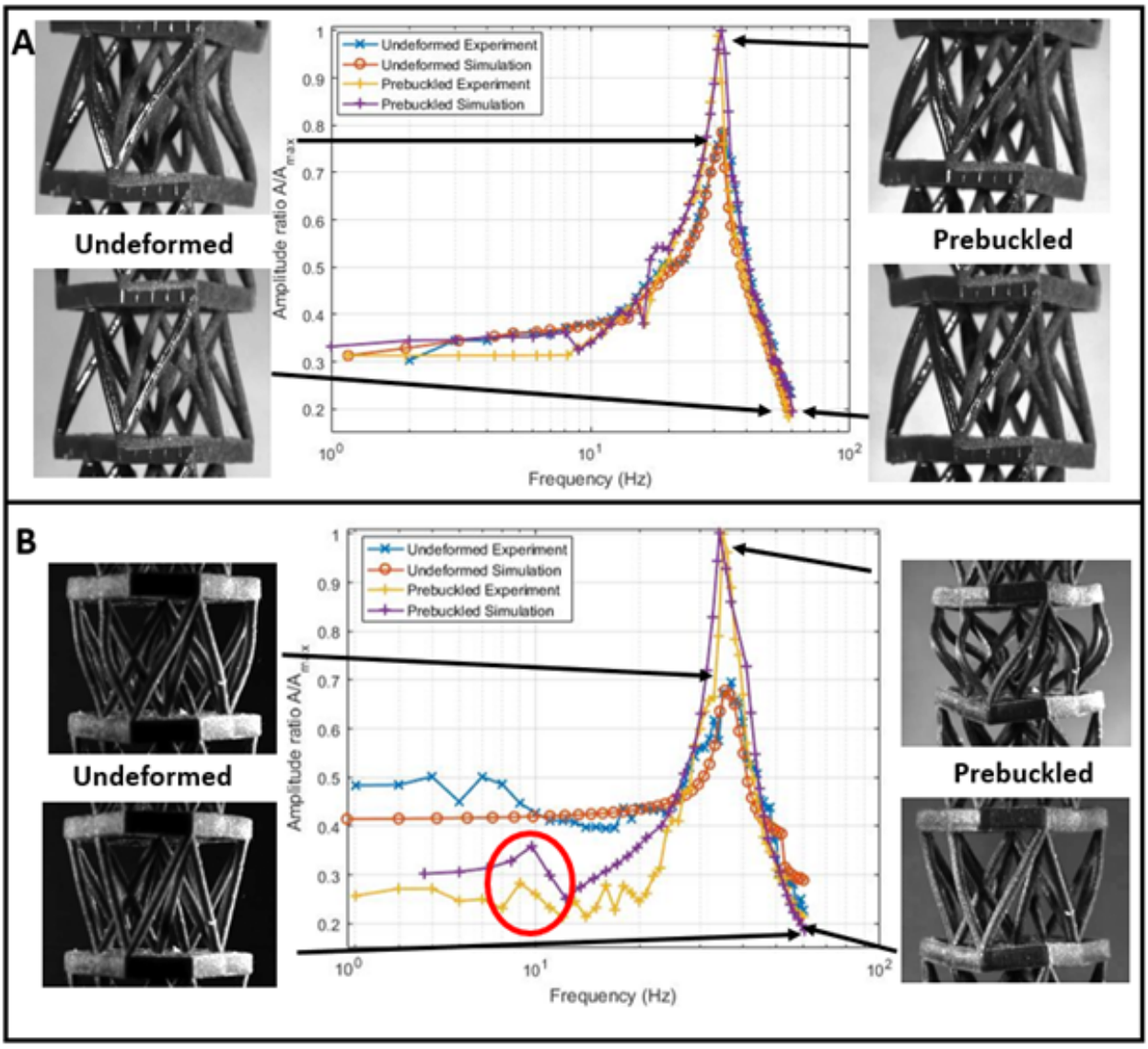

Figure 4.50: Comparison of the Harmonic Response and the vibrational response for the Assembly 2 with unit cells 1 and 2 (DS2 and DS3). (A) Normalized deformation amplitude – frequency curves for DS2. The resonant frequency is at 32 Hz and there is a significant variation of the amplitudes for the unstressed and prestressed configuration. (B) Normalized deformation amplitude – frequency curves for DS3. The main resonant frequency is still at 32 Hz and again there is another resonant frequency at 10 Hz (marked in the red circle). The deformed state for both unstressed and prestressed configuration of the tested structures are demonstrated at maximum and minimum deformation.

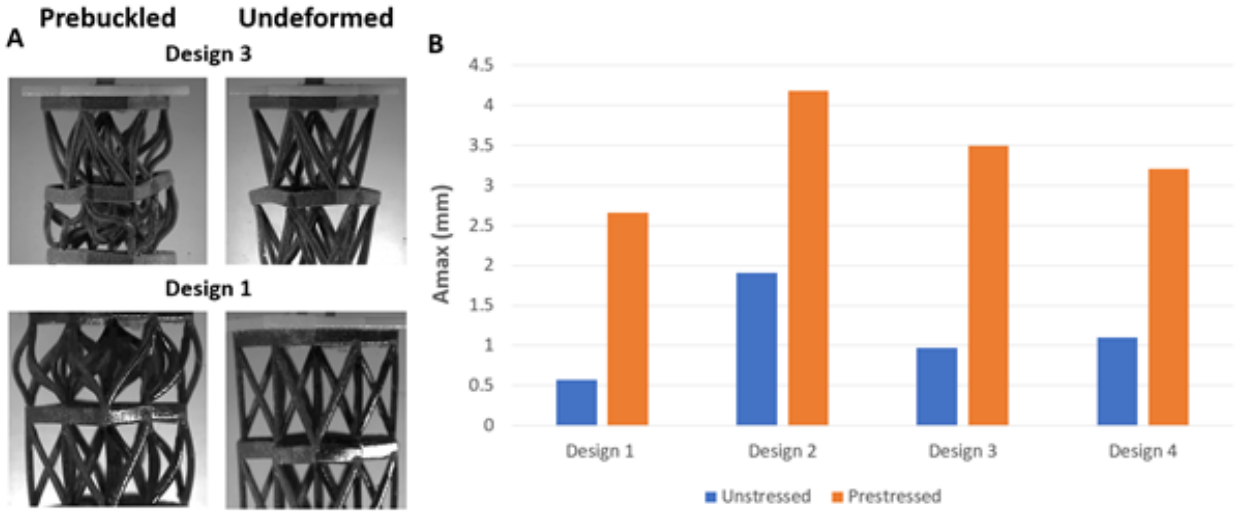

Figure 4.51: The deformation amplitude for each structure at the last layer in the pre-stressed and unstressed configuration. (A) Characteristic response at the final layer for the pre-stressed and unstressed configuration. It is observed that the prebuckled configuration has significantly larger deformation on the final layer providing the actuation propagation through the whole structure. (B) Deformation comparison for both configurations at the last layer, accomplishing increase of the amplitude at 500% for DS1 or 222% for DS2, 350% for DS3 and 336% for DS4.

Section Conclusions

In summary, in this study we demonstrated the design of 3D structures encompassing intrinsic and external instabilities, leading to remarkable enhanced dynamic behavior. The investigated unit cells and their respective assemblies were investigated under the scope of a functional behavior that facilitates large deformations due to vibrations, instead of static loading or wave mechanics that had been reported before. Prebuckling of the beam members of the structures provided augmented flexibility, mitigating the viscoelastic effects of the employed rubber materials. Designing smart structures that furnish prebuckling before loading provides a new design parameter that can be tailored to improve the structural performance of such systems. Simulations and experiments on 3D printed samples revealed that by connecting the unit cells next to each other, more resonant frequencies are rejuvenated. These results provide the guidelines to control the dynamic effects of 3D printed elastomer materials. Nevertheless, it is evident that the design of these systems is highly complex. Optimization techniques such as machine learning can be a useful arsenal to accomplish the objective to find the best design of the desired behavior. In addition, these effects may be incorporated even smaller scales, for the design of microscale metamaterials. This study aims to provide the experimental and numerical approaches that need to be employed for the

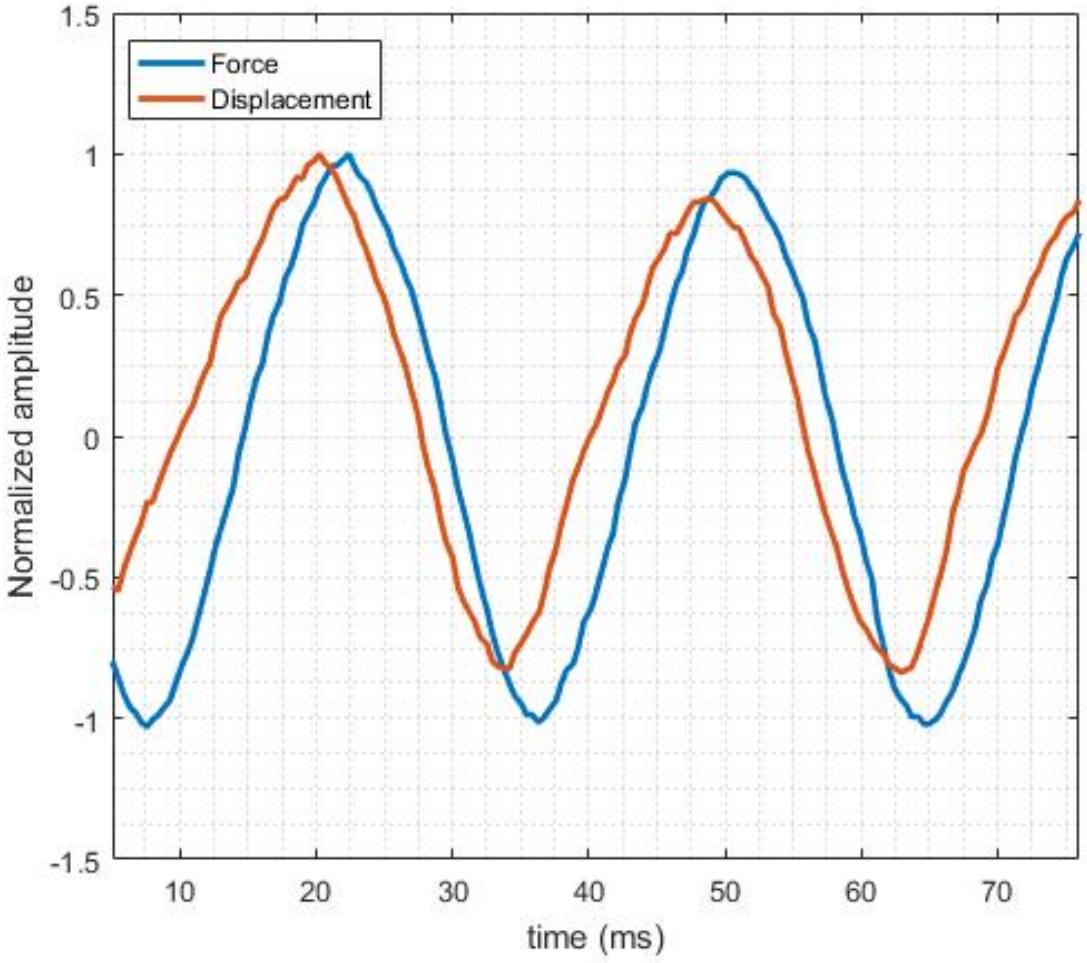

Figure 4.52: Measured force-time curves and displacement-time curves by image processing for DS4 at 30 Hz.

modeling of the dynamic behavior of flexible structures. Finally, our findings pave the way to design smart materials, synergistically coupling rigidity and flexibility on demand, that are also expedient to the caducity of the working environment, such as mechanical signal transport or artificial muscles.

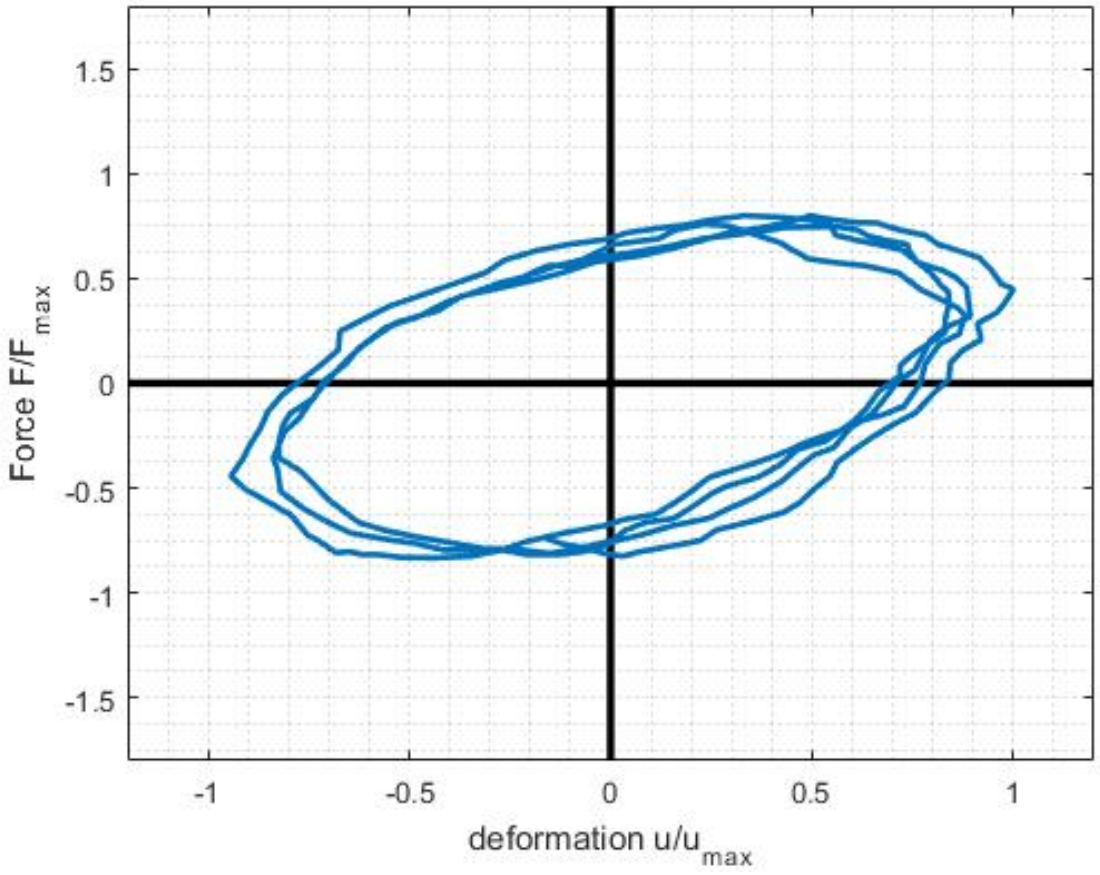

Figure 4.53: Hysteresis Loop of the force-displacement curve at 30 Hz.

Chapter 5

The Arrangement of Defects in Architected Materials

5.1 Vacancies for controlling the behavior of microstructured three-dimensional mechanical metamaterials

Section Summary

The main objective of this study was to design three-dimensional (3D) metamaterial architectures containing vacancies in their lattice structures, using as a geometry of reference the octet-truss structure, a primordial mechanical metamaterial [120] that has been thoroughly studied [208, 13, 376, 264, 466, 265, 38, 91, 263, 292]. Localized buckling was induced by reducing the number of lattice members in specific unit cells of different structure architectures. Nanoindentation experiments and simulations were performed to elucidate the overall deformation behavior, localized buckling, and energy adsorption capacity of metamaterial structures fabricated by multi-photon lithography. In addition, the effects of designed vacancies on the dynamic response were examined in the light of modal analysis simulations. This study shows how the incorporation of vacancies in specific unit cells of metamaterial structures can mitigate the total deformation of the lattice structure and isolate deformation mainly in specific regions of the structure.

Design of lattice vacancies

Various configurations of vacancies were introduced in octet-truss arrays of $5 \times 5 \times 4$ unit cells. The length and diameter of each lattice member was fixed at 10 and $0.5\mu m$, respectively. The octet truss was selected as the base structure in this study because it represents one of the most thoroughly investigated mechanical metamaterials. Changes in the design of unit cells included the elimination of specific lattice members either from the original unit cell or

a group of unit cells. The objective of disrupting the symmetry of the whole structure was to tailor the mechanical behavior of the structure by introducing structural defects. Less lattice members in specific unit cells rendered them more unstable and susceptible to buckling. Because of the 3D structure, the arrays of vacancies were designed as 3D substructures. The octet-truss unit cell is shown in Fig. 5.1(A) and octet-truss unit cells with vacancies are shown in Figs. 5.1(B) and 5.1(C).

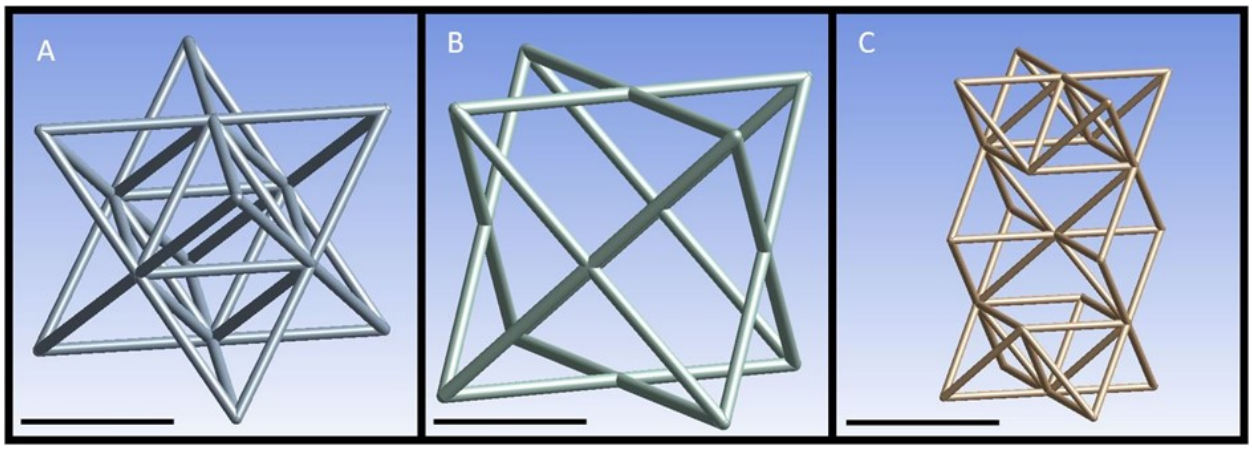

Figure 5.1: The unit cells used to design the metamaterial structures of this study. (A) The original octet-truss unit cell (scale bar = $10\mu m$). (B) A design consisting of two octet-truss unit cells where the lattice members of the top and bottom half of the two unit cells have been removed to increase the instability of the whole assembly (scale bar = $10\mu m$). (C) A design in which the internal octahedron of the octet-truss structure has been removed (scale bar = $5\mu m$).

The assembled designs with vacancies in the unit cells examined in this study, hereafter referred to as V1, V2, V3, and V4 structures, are shown in Fig. 5.2. Inspired by the development of structural defects, such as dislocations, in the direction of the maximum resolved shear stress, the modified unit cells were arranged as a sloped array within the metamaterial structure. The "defected area" was placed in a non-orthonormal planar orientation where shearing is expected to dominate during compressive loading. The modified unit cell shown in Fig. 1B was used to design the V1, V3, and V4 designs, whereas the modified unit cell shown in Fig. 5.1(C) was used to design the V2 structure. Only the V4 structure has unit cells with vacancies that do not reach the top and bottom surfaces of the structure. In the V1 structure, the neighbouring unit cells with vacancies contact each other at one edge, while in the V3 and V4 structures, one-half of a side is in contact with one-half of the side of another unit cell.

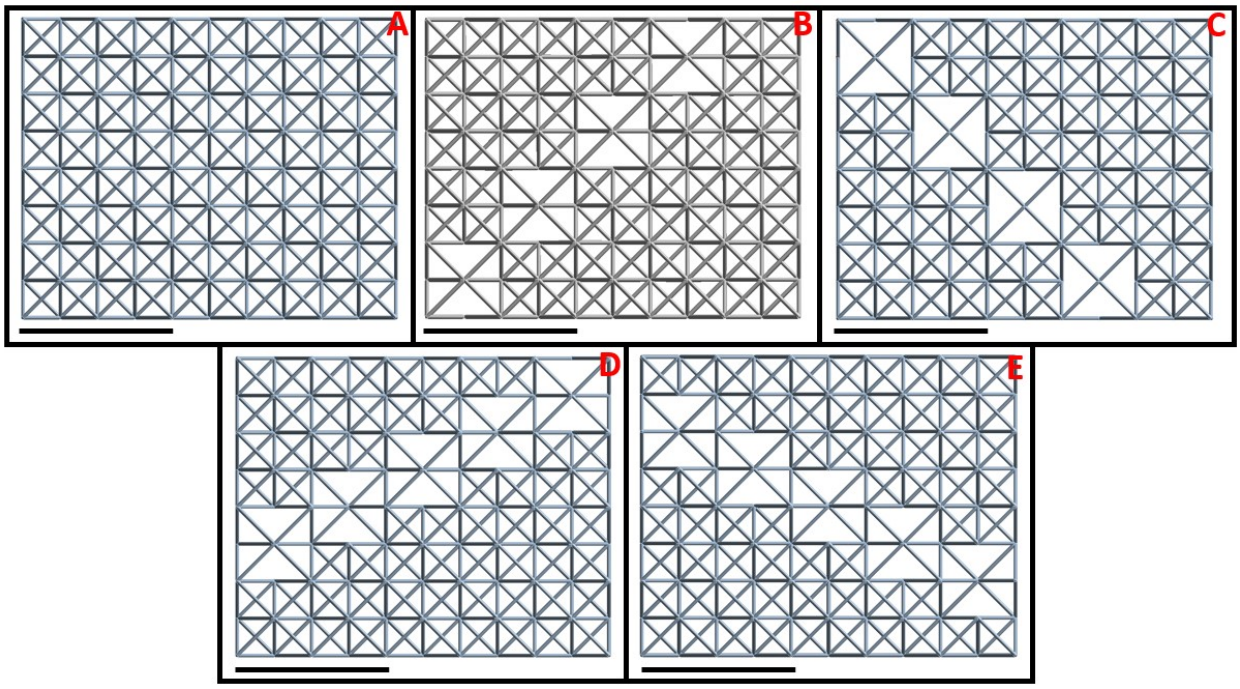

Figure 5.2: The $5 \times 5 \times 4$ assembly of unit cells used in each mechanical metamaterial design: (A) octet-truss structure, (B) V1 structure, (C) V2 structure, (D) V3 structure, and (E) V4 structure. Although the V1, V3, and V4 structures have the same unit cell, the edges in contact with neighbouring unit cells are aligned differently. The scale bar in each figure is $30\mu m$.

Experimental and modelling procedures

Fabrication of the three-dimensional metamaterial structures

All of the metamaterial structures were fabricated by multiphoton lithography using the experimental setup shown in Fig. 2.2(A). Isometric views of the fabricated octet-truss structure without and with defects are shown in Figs. 4A and 4B, respectively. All of the metamaterial structures were fabricated several times to ensure repeatability.

Mechanical testing

The mechanical behavior of the fabricated structures was examined with a nanoindentation apparatus (TI 950 TriboIndenter, Hysitron), which enables high-precision nanomechanical testing. Quasistatic, displacement-control nanoindentation tests were performed using the displacement versus time transducer response shown in Fig. 5.4. Both loading and unloading rates were set at $90nm/s$, while the maximum displacement of $4.8\mu m$ was maintained for

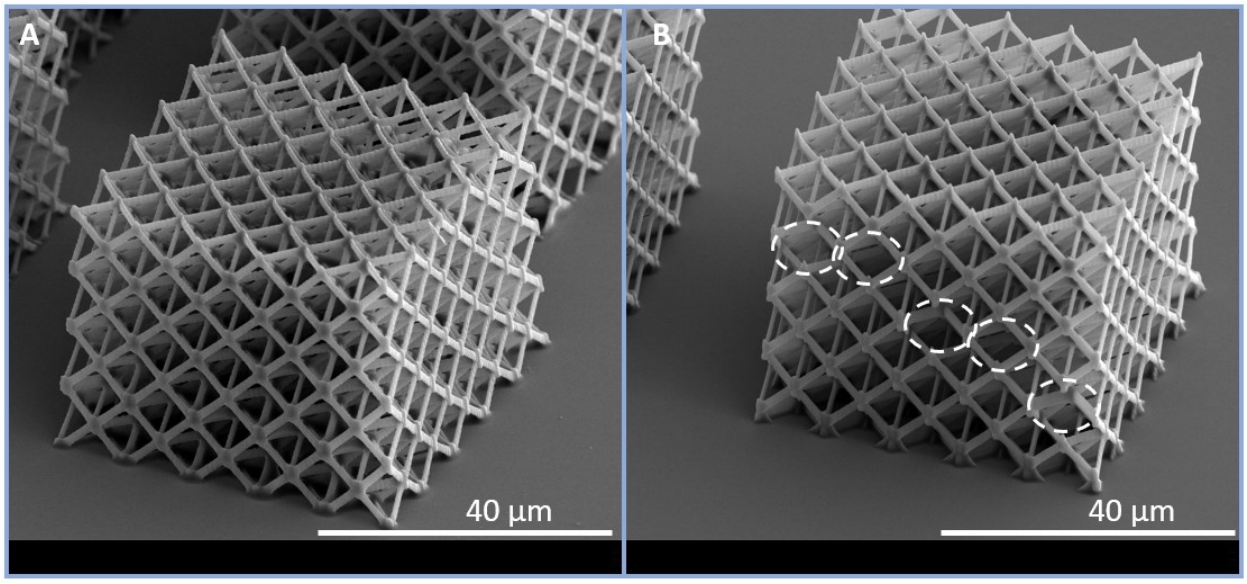

Figure 5.3: Isometric view of an octet-truss structure with $5 \times 5 \times 4$ unit cells and (B) isometric view the structure D4, comprised of the same number of unit cells.

$15s$ before the onset of unloading. All of the nanoindentation experiments were performed with a spherical diamond tip having a radius of curvature equal to $50\mu m$.

Simulations

To evaluate the mechanical performance of each metamaterial structure, quasistatic finite element analysis (FEA) simulations were performed with the multi-physics software ANSYS (version 18.0). The structures were discretized with 10-node, quadratic, tetrahedral finite elements. Specifically, the octet-truss structure was modeled with 509718 elements having 1022297 nodes, the V1 structure was modeled with 454335 elements having 914686 nodes, the V2 structure was modeled with 444384 elements having 894754 nodes, the V3 structure was modeled with 441217 elements having 890063 nodes, and the V4 structure was modeled with 446004 elements having 898350 nodes. In all the finite element meshes, the smallest element size was $\sim 0.24\mu m$. All structures were modelled as elastic-perfectly plastic materials with an elastic modulus of $0.5GPa$, a Poisson's ratio of 0.45, and a yield strength of $18MPa$ [55]. Compression of the structures was simulated by uniformly displacing the nodes of the top surface of each structure by a total distance of $10\mu m$, while keeping the nodes of the bottom surface fully constrained.

An eigenvalue buckling analysis was performed to examine whether buckling of the designed structures occurred at lower loads compared to the octet-truss structure. This was accomplished by solving the equation 4.13

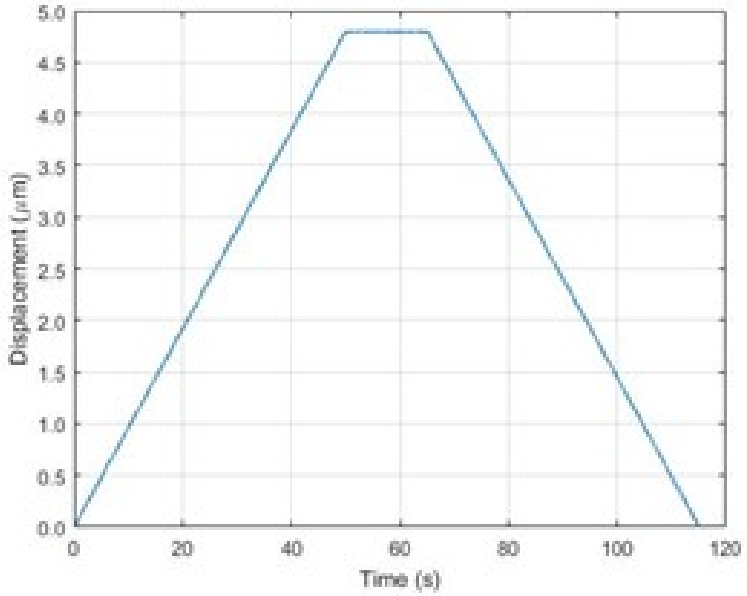

Figure 5.4: The displacement versus time transducer response used in the nanoindentation experiments.

A modal analysis was performed with ANSYS to examine the effect of the designed vacancies on the dynamic behavior of each structure. Eigenvalues of all structures were computed by solving the eigenvalue-eigenvector relation 4.18.

Results

Experiments

Typical force versus displacement responses of the original and modified (V1–V4) octet-truss structures are shown in Fig. 5.5. The larger force hysteresis areas of the structures containing vacancies reveal a larger energy dissipation capacity than the original octet-truss structure. This is attributed to the larger deformations encountered in these structures due to localized buckling of the lattice members in the unit cells with vacancies. Changes in the slope of the loading curves of the structures with vacancies are attributed to localized fracture of some lattice members.

Table 5.1 shows a comparison of the strain energy density u_V of metamaterial structures containing vacancies with the strain energy density u_{ot} of the octet-truss structure. It can be seen that the V1 structure demonstrates the highest energy adsorption capacity for that it can absorb ~ 2.4 more strain energy compared to the octet-truss structure. A plausible explanation for this result is the spatial arrangement of the unit cells with vacancies in the 3D material structure and the type and number of vacancies. As evidenced from Fig.

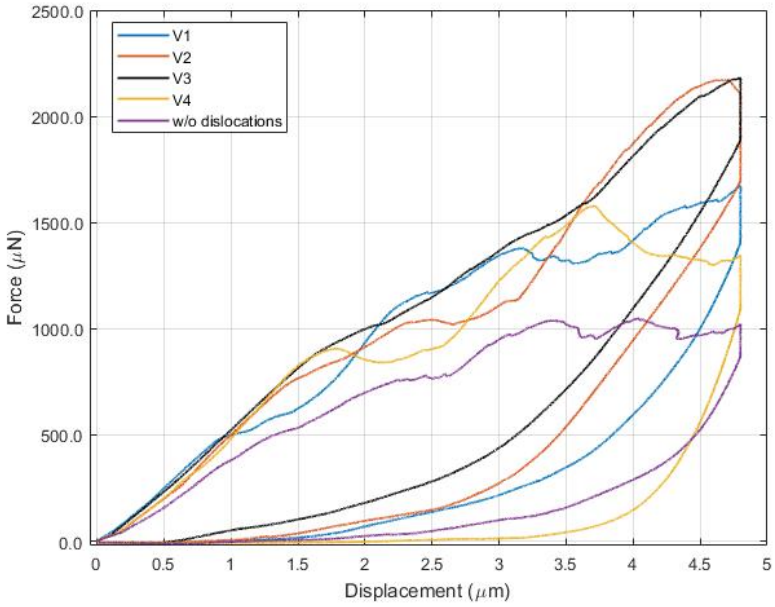

Figure 5.5: Indentation force versus displacement response of various metamaterial structures.

Parameter	OT	V1	V2	V3	V4
$u(J/mm^3)$	0.7800	1.8332	1.0507	0.9662	1.2582
u_V/u_{ot}	1.00	2.3503	1.3471	1.2388	1.6131

Table 5.1: Strain energy density of various metamaterial structures.

5.2, the V1 structure has fewer vacancies than the V2 and V3 structures and the unit cell array with the vacancies is oriented closer to the maximum shearing direction encountered in compressive loading than any other unit cell array with vacancies and also extends from the bottom to the top of the structure. In contrast, the V3 and V4 structures are confined by vacancy-free unit cells at the bottom surface and both the top and bottom surfaces of the structure, respectively. Therefore, the unit cell array with vacancies in the V1 structure can sustain larger deformation, a factor rendering the performance of this structure superior to those of other structures.

Figure 5.6 shows scanning electron microscope images of fractured structures. Some of the images indicate that fracture of some lattice members in the V1–V4 structures resulted from torsional deformation. This type of deformation was not observed in the FEA simulations

and requires further investigation. A plausible explanation is that the instability introduced in these structures a higher deformation gradient behavior [52], making the unit cells with less truss members susceptible to torsion. In the case of the octet-truss structure, part of the first layer collapsed as a result of fracturing of several lattice members, a failure mechanism also reported in previous studies of the octet-truss structure [264, 292]. The greater slope of the unloading curves of the V1–V4 structures than that of the octet-truss structure (Fig. 5.5) indicates a higher stiffness for these structures, despite the fracture of several lattice members in the unit cell arrays with vacancies during loading.

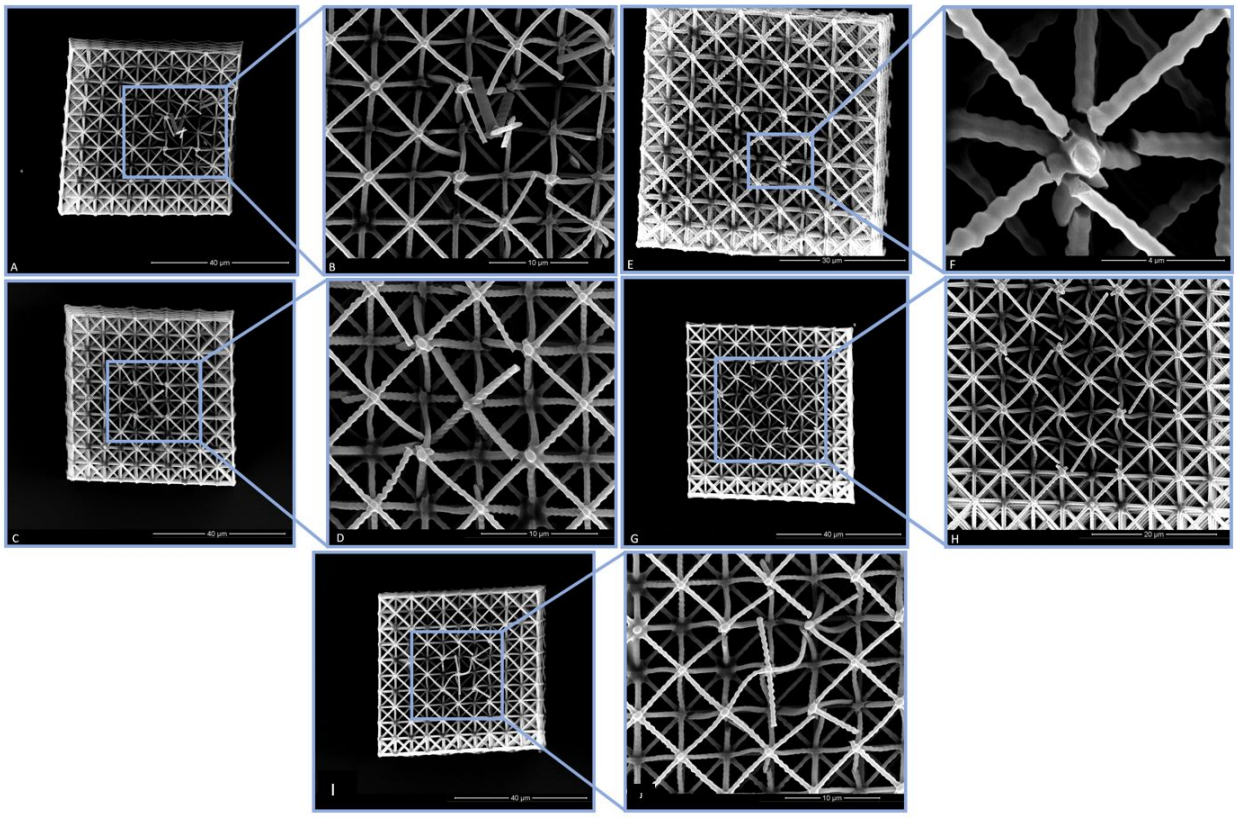

Figure 5.6: Top view (left column) and close-up view of fractured area (right column) of tested (A, B) octet-truss, (C, D) V1, (E, F) V2, (G, H) V3, and (I, J) V4 metamaterial structures.

Simulations-Quasistatic response

Figure 5.7 shows deformed side views of the octet-truss structure and the V1–V4 structures. The FEA simulation results reveal larger deformations in the V1–V4 structures than the octet-truss structure, which are attributed to buckling of truss members in the unit cell

arrays with vacancies. The largest deformation is observed in the unit cells with vacancies that are located at the edges of the structure, evidently due to less support by neighboring unit cells.

Table 5.2 gives the load multiplier λ a of each structure and its ratio to the load multiplier λ_{ot} of the octet-truss structure. The significantly smaller load multipliers of the V1–V4 structures than that of the octet-truss structure indicate that buckling of the defected structures commenced at much lower loads than the octet-truss structure. This is proof that the objective of controlling localized buckling in the designed structures was accomplished. A possible reason for the lowest load multiplier of the V2 structure is that its unit cell at the edge of the structure has the least number of lattice members. Since this unit cell is not supported by any neighbouring unit cells, it is more susceptible to buckling.

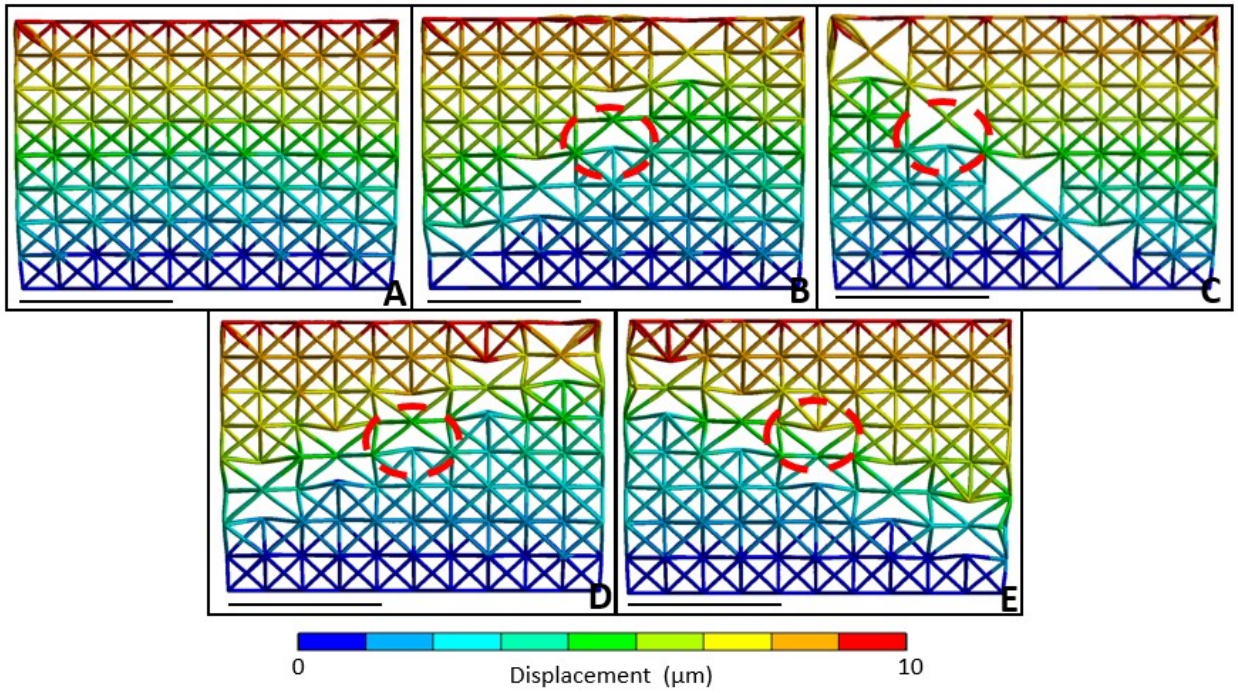

Figure 5.7: Quasistatic FEA simulation results of compressed structures. Side view of (A) octet-truss, (B) V1, (C) V2, (D) V3, and (E) V4 metamaterial structures. The scale bar is $30\mu m$.

Simulations-Dynamic response

Table 5.3 shows the first three eigenvalues of each metamaterial structure. Although there are no significant differences among the eigenvalues, depending on the architecture of the

Parameter	OT	V1	V2	V3	V4
$\lambda(\times 10^{-2})$	6.3316	4.9402	2.3869	4.4179	4.9506
λ/λ_{ot}	1.00	0.780	0.377	0.698	0.782

Table 5.2: Buckling analysis results of various metamaterial structures.

Eigenvalue (MHz)	OT	V1	V2	V3	V4
s_1	6.306	5.849	6.038	5.990	5.482
s_2	6.307	6.007	6.160	6.002	5.507
s_3	9.639	9.218	9.270	9.142	8.727

Table 5.3: First three eigenvalues of various metamaterial structures.

geometry, the deformation varies significantly. The deformation depends on the components of the eigenvector x, which presumably depend on the value of s.

Figures 5.8 and 5.9 show isomeric and front views of the dynamically deformed octet-truss structure and the V1–V4 structures, respectively, corresponding to the third eigenvalue. The dynamic FEA simulations show that, while the octet-truss structure and the V4 structure sustained large deformations throughout, the deformation in the V1–V3 structures is mostly confined within the unit cell arrays with less truss members, while the rest of the body structure is essentially undeformed, a behaviour not encountered with the octet-truss structure. The same result was found for all eigenvalues above the third eigenvalue. The dynamic deformation of the V4 structure differs from that of the V1–V3 structures, resembling more the dynamic deformation of the octet-truss structure. It is noted that the V4 structure is the only structure without unit cells with vacancies extending to the top and bottom surfaces of the structure, suggesting that this feature is critical to the performance of the architectured metamaterial structures.

Discussion

High-energy dissipation mechanical metamaterials were obtained by designing architectures exhibiting buckling and fracture in specific unit cells of octet-truss structures with less lattice members. Simulation results supported by experimental findings revealed that metamaterial structures having unit cells with vacancies can greatly increase the dissipation of strain energy by enhancing localized plastic deformation and fracture of buckled lattice members, while sustaining relative insignificant damage to the rest of the structure body. Modal analysis demonstrated that under dynamic loading, the 3D vacancies tend to "attract" the deformation of the whole structure, insulating the vast majority of the structure from deformation.

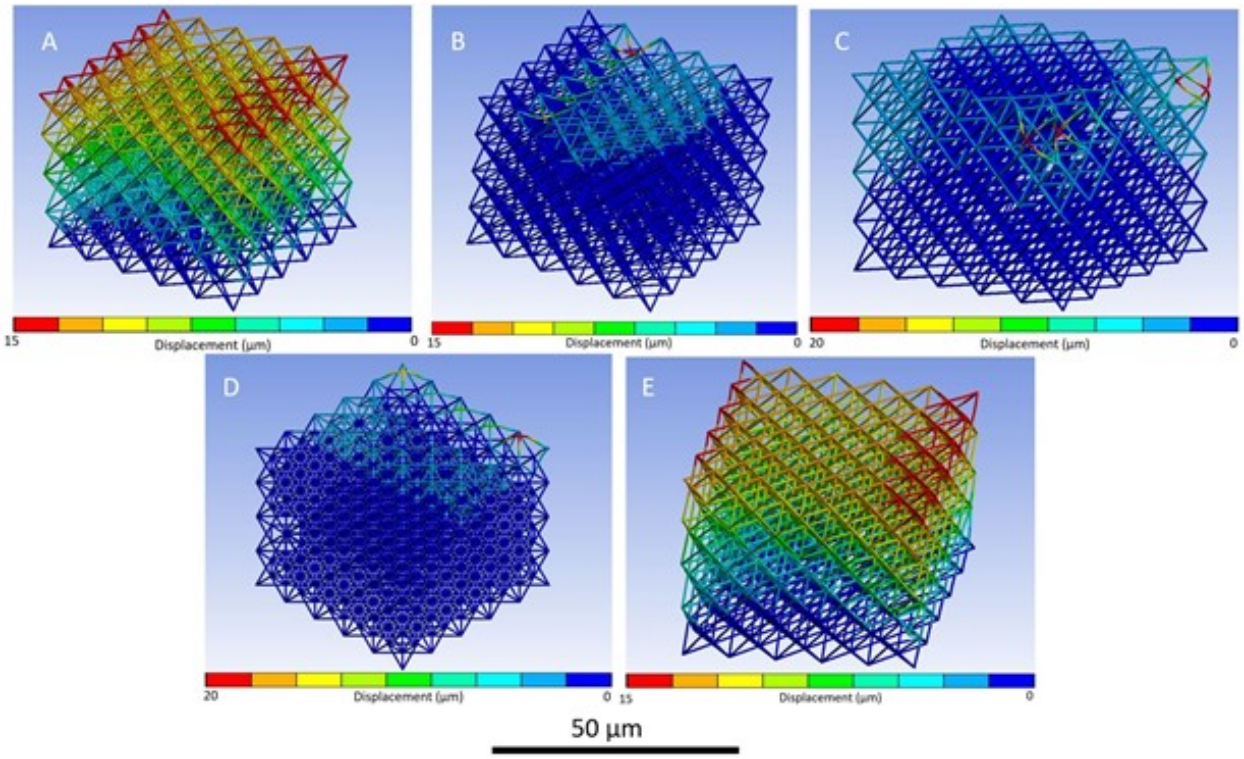

Figure 5.8: Dynamic FEA simulation results of various metamaterials (third eigenvalue). Isomeric views of (A) octet-truss, (B) V1, (C) V2, (D) V3, and (E) V4 structures. All figures have the same scale bar.

Controlled buckling of lattice members was achieved by reducing the number of lattice members in select unit cells, thereby causing specific parts of the structure to become unstable and, hence, localized buckling to commence at lighter loads. The feasibility of this approach was validated by both an eigenvalue analysis and experimental results. The significantly lower load factor of the V2 structure than all other structures is attributed to the least number of unit lattice members in the designed unit cells (Fig. 5.1) positioned at the edge of the structure. Since this unit cell array has less lattice members and is not restricted as much as the rest of the structure, buckling of lattice members occurs at much lighter loads. Because the unit cells with vacancies are at the edge of the V2 structure, their contribution to the overall deformation of the structure when the compressive load is applied at the center of the top surface is limited.

The strain energy density of the V1 structure was found to be ~ 2.4 times higher than that of the octet-truss structure, while that of structures V2, V3, and V4 was found to be $\sim 24 - 35\%$ higher than the octet-truss structure. This remarkable enhancement in energy dissipation capacity is a consequence of the vacancies incorporated in these structures,

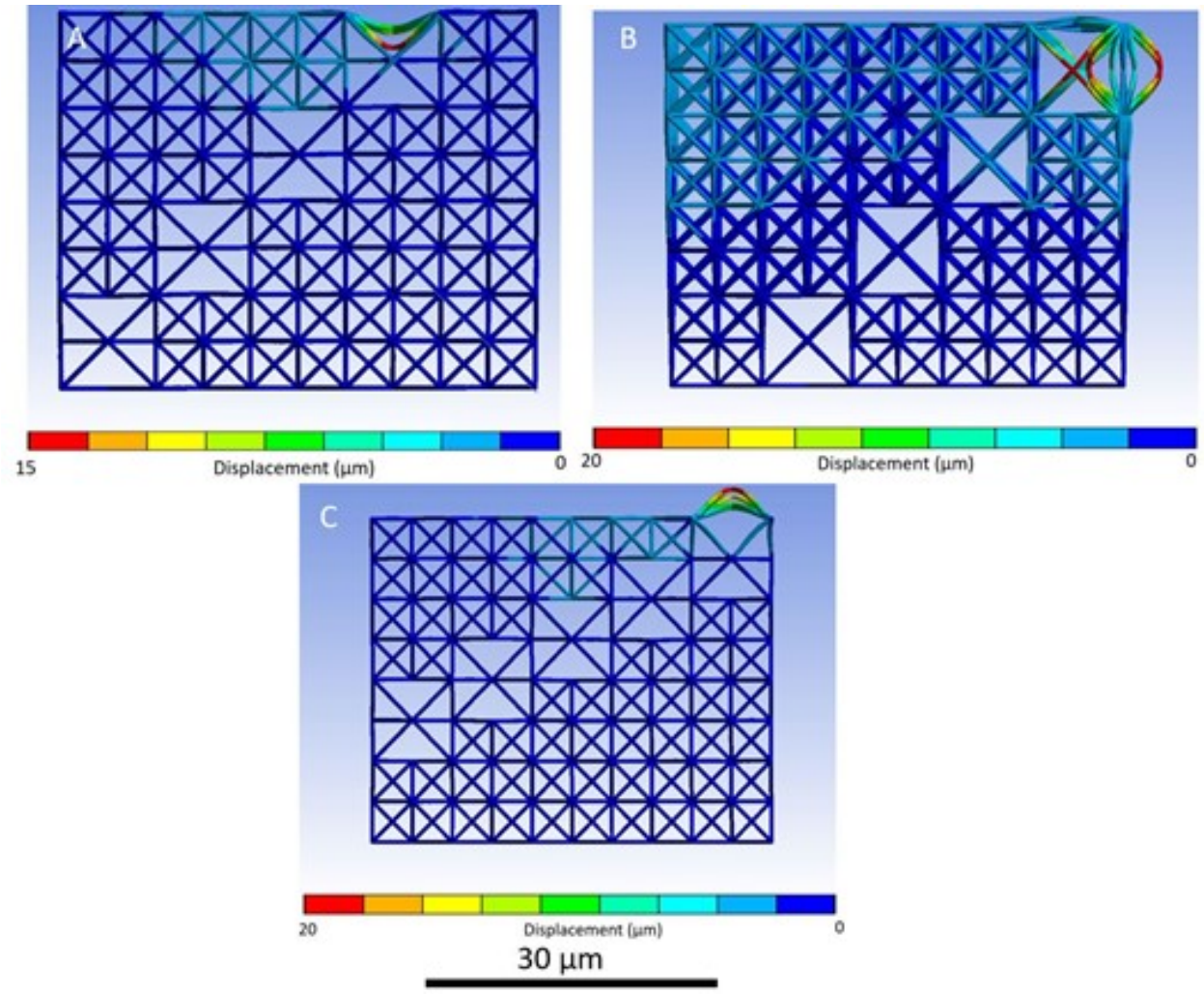

Figure 5.9: Dynamic FEA simulation results of various metamaterials (third eigenvalue). Front views of (A) V1, (B) V2, and (C) V3 structures shown in Fig. 5.8 with isolated deformation. All figures have the same scale bar.

inducing the same effect as the topological states, which are architected structures used to control the softening and hardening behavior of the material as well as the porosity. It has been reported that the porosity may affect the control of the vibrations in the material and can isolate deformation [231, 181]. The results of the modal analysis showed that the architected vacancies can utilize the vibration isolation as the topological states. The nanoindentation tests revealed failure due to torsional deformation, a finding that requires further investigation as it diverges from the simulation results of classical beam theory at larger scales and is linked with the modelling of structures with higher gradient methods

[52].

The vibration isolations observed with the V1–V3 structures (i.e., insignificant change in eigenvalues) indicate a mechanism of decoupling the eigenvalue from the eigenvector. Decoupling of quantities that share a bidirectional relation is observed in a family of mechanical metamaterials known as the pentamode metamaterials [67] where the bulk modulus is independent of density [198]. However, this result occurred only for the designs with unit cells containing vacancies extending to the surface of the structure, indicating that the functionality of unit cells with vacancies depends on the relative positioning within the 3D structure.

The experimental results revealed that vacancies introduced in metamaterial structures may induce higher order gradient behavior, which cannot be captured with commercial software. Hence, it is necessary to develop analytical models for predicting the higher order behavior of 3D mechanical metamaterials in conjunction with models accounting for viscoelastic material behavior [8]. Nevertheless, the dynamic response of the modified structures must be experimentally studied and confirmed. Laser interferometric methods used to study vibrations in such small scales [297, 204, 95, 18] could be applied to the modified metamaterial structures to verify the simulation results of the dynamic response. The present study illustrates the significance of fabricating mechanical metamaterials by preserving the microscale resolution. However, extending the present methodology to engineering length scales requires further innovation. Specifically, techniques to expand the fabrication area, such as holographic lithography [408, 51], must be further developed to enable the incorporation of micro-architected structures in the design of engineering components.

Section Conclusions

The novelty of the structural designs presented in this article is the incorporation of unit cells with vacancies in 3D mechanical metamaterials to control buckling and topological states. While this concept has been previously explored [40], it was applied to an arbitrary geometry, not a deliberately constructed mechanical metamaterial. Notably, designing and fabricating structures with controlled buckling at the microscale has not been reported yet. The present work paves the way toward a design methodology for inserting vacancies in metamaterial structures in order to enhance the mechanical performance by increasing energy absorption and isolating vibrations. Clearly, the insertion of unit cells with vacancies in a 3D metamaterial structure is of critical importance and requires further systematic study to determine the optimum orientation (for a given structure) because of the infinite number of architectures with unit cells containing vacancies that can be designed. Therefore, new optimization schemes should be developed to identify the spatial arrangement(s) of the modified unit cells, which can maximize energy absorption and confine deformation to specific domains of the metamaterial structure.

5.2 Regulating the mechanical behavior of metamaterial microlattices by tactical structure modification

Section Summary

The principal objective of this study was to investigate how the mechanical properties of monolithic microlattices can be tailored by using designs inspired by crystal microstructures [323, 12, 312]. A finite element analysis (FEA) was performed to study how the directional stiffness of the material can be tailored on demand in specific directions. Results from in situ scanning electron microscopy (SEM)-nanoindentation investigations on fabricated specimens elucidate the effects of localized buckling and structure collapse on the stress-strain response. The OT structure, one of the most thoroughly studied mechanical metamaterials [93], was used to demonstrate how these principles can be manifested in the present design paradigm. Features causing localized failure at predetermined planes during large deformation that resemble slip-plane failure were introduced by changing the shape of select microlattice members. It is shown that further modification of these features can also lead to stiffening and enhanced resistance to failure. For example, it is proved that polycrystalline-like structures can be created by substituting the OT with modified structures inspired by the regular isohedron (IE) [72]. Profoundly different deformation and failure mechanisms manifest themselves in the stress-strain response of each design. A dramatic increase of the mechanical integrity and strain energy density of the structure was observed even for fixed relative density, despite the removal of a significant number of microlattice members. High-depth focus imaging of the deformed structures performed by helium ion microscopy (HIM) provided insight into the deformation mode of internal unit cells. Results from fractography studies of the tested structures enabled by the extremely high resolution of HIM, even for nonconductive materials, further elucidated the mechanical behavior of the designed metamaterial structures.

Design principles and modeling of architected microlattice structures

Figure 5.10 shows the design strategy scheme used to control mechanical failure and stiffening in a specific structure direction. Two design approaches were utilized to study the effects of architected defects and substitutional unit cells. In the first approach, an array of OT unit cells was altered either by the selective removal or alteration of specific microlattice beam members, whereas in the second approach, several OT unit cells were replaced by different unit cells, resulting in so-called different states. With both approaches, the objective was to control the directional stiffness of the structure and promote failure in predetermined regions of the structure (design cost functions). This was validated by stress analysis that revealed the existence of excess stress concentrations in the desired locations. Since perform-

ing multiple fabrications and mechanical testing is cumbersome and expensive, the former cost functions were studied by FEA. Consequently, the best structures were tested to validate the credibility of the design and FEA predictions. Nevertheless, it is instructive to provide a methodology of the design variables of the problem, i.e., the design inputs. A convenient method to analyze such a design problem is to use discrete qualitative variables [458], which do not express a physical quantity, such as length or angle, but different states of a variable, such as different surface treatments for enhancing the damage resistance of a material, for instance. Utilizing a similar methodology for the first design approach, each microlattice beam member was unchanged, altered in various ways, or removed. The OT unit cell comprises 36 beam members. However, proximal unit cells of an array share the beam members at their common faces. Thus, the total number of microlattice beam members in an n×n array of OT unit cells is equal to $36n^2 - 8(n-1)$. This equation is different for other types of unit cells, such as the Kelvin unit cell [265], because it depends on the number of beam members at the common faces of the unit cells. To reduce the complexity of the problem, the structures were made symmetric with respect to the horizontal and vertical middle planes, thus reducing the number of design variables to $9n^2 - 2(n-1)$. Consequently, the number of beam elements is represented by a vector x in which each beam element has a state designated by S, R, or V depending on the geometrical configuration of the structure. State S indicates unchanged beam members, state R corresponds to beam members rotated to form a bowtie structure, and state V refers to beam members removed from the unit cell. Characteristic beam members with S or R state are shown in Fig. 5.10 in blue and red color, respectively. These different states are also exemplified in the structures shown in Fig. 5.11. For the second design approach, a unit cell in the array was left unchanged or substituted by a different unit cell structure, i.e., states A, B, C, etc., depending on the number of different states. Therefore, for this design paradigm, an $n \times n$ matrix M with unit cell elements at different states was used to mathematically depict the structure. This type of formulation has been utilized to represent discrete states of a system in a qualitative way [458] and is further interpreted in the discussion section. As mentioned earlier, 5×5 arrays were designed to be symmetric with respect to the horizontal and vertical middle planes, reducing the design space to 25 design variables. Each design variable represents five potential different unit cells (i.e., five states) that are labeled by A, B, C, D, and E in Fig. 5.10. These states are also discernible in the structures shown in Fig. 5.12. More details about the origin of different states are given below.

To examine the effect of different states on the mechanical performance of the structure, different test structures were modeled and fabricated. Figure 2 shows the designs of the metamaterial structures examined in this study. The unit cell of the original structure is the OT (Fig. 5.13(A)). The first design category includes structures SP1 (Fig. 5.13(B)), SP2 (Fig. 5.13(C)), and SP3 (Fig. 5.13(D)) with modified unit cells integrated as bowtie two-dimensional (2D) structures at the $\pm 45^o$ diagonal planes of the structures. The microlattice members of the bowties change the symmetry of the internal octahedron of each OT that they surmount. The difference between the SP1 and the SP2 structure is that the bowtie in the latter structure has an internal microlattice member connecting its central nodes. The

purpose of the SP1 design was to facilitate larger deformations of the bowtie microlattice members causing contact of the beam members during deformation, which is known to increase the stiffness and energy density of the structure [140, 63, 393]. The SP3 structure has the same bowtie design as the SP1 structure; however, several beam members were removed from the $\pm 45^o$ planes containing the bowtie microlattices to promote buckling in these planes. Several microlattice beam members of the SP3 structure were also removed from locations proximal to the diagonal planes to enable the structure to sustain its own weight during the fabrication, while still demonstrating the desired deformation.

The designs SP1, SP2, and SP3 structures are shown in Fig. 5.11. The altered microlattice members of the SP1 structure are red colored (Fig. 5.11(A)). The difference in the modification of the SP2 structure is that the internal hinges of the bowties are connected with an additional microlattice member (blue colored in Fig. 5.11(B)). This design compensates the lack of post contact between neighboring microlattice members during the deformation of the structure, which has been proven to enhance the structural stiffness, through the inherent resilience to large deformation provided by these internal microlattice members. While the bowtie design used in the SP1 structure was also used in the SP3 structure (cyan colored in Fig. 5.11(C)), several microlattice members in the $\pm 45^o$ diagonal planes of the SP3 structure were removed. A representative modified OT unit cell at the bottom edge of the SP3 structure (yellow colored) is shown in Fig. 5.11(C). Because the desired localized failure was selected to be in the $\pm 45^o$ planes of the structures, the number of microlattice members that were removed from these planes was chosen such that to preserve the structural integrity of the structure during fabrication. The foregoing designs imitate the distortion of symmetry in crystal microstructures by slip planes or twin boundaries. Their x vectors are the following

$$x_{SP1} = [\underbrace{S...S}_{33}\underbrace{RRV}_{3}\underbrace{S...S}_{28}\underbrace{R}_{1}\underbrace{S...S}_{42}\underbrace{R}_{1}\underbrace{S...S}_{22}\underbrace{RRV}_{3}\underbrace{S...S}_{11}\underbrace{R}_{1}\underbrace{S...S}_{58}\underbrace{RR}_{2}\underbrace{S...S}_{11}] \tag{5.1}$$

$$x_{SP2} = [\underbrace{S...S}_{34}\underbrace{RR}_{2}\underbrace{S...S}_{28}\underbrace{R}_{1}\underbrace{S...S}_{42}\underbrace{R}_{1}\underbrace{S...S}_{23}\underbrace{RR}_{2}\underbrace{S...S}_{11}\underbrace{R}_{1}\underbrace{S...S}_{58}\underbrace{R}_{1}\underbrace{S...S}_{11}] \tag{5.2}$$

$$x_{SP3} = [\underbrace{S...S}_{21}\underbrace{V...V}_{13}\underbrace{RR}_{2}\underbrace{S...S}_{24}\underbrace{V...V}_{7}\underbrace{R}_{1}\underbrace{S...S}_{42}\underbrace{VVVR}_{4}\underbrace{S...S}_{21}\underbrace{V...V}_{5}\underbrace{RR}_{2}\underbrace{S...S}_{20}\underbrace{VR}_{2}\underbrace{S...S}_{40}\underbrace{RR}_{2}\underbrace{V...V}_{6}] \tag{5.3}$$

It is noted that the numbering of the beam members starts from those beams in the unit cell at the top right corner, continues on to the unit cells in the right direction and starts again at the next layer also moving from right to left.

Another major objective of this study was to develop designs that increase the stiffness of the structure in predetermined directions. Thus, the second design category includes structures SB1 (Fig. 5.13(E)), SB2 (Fig. 5.13(F)), and SB3 (Fig. 5.13(G)). For these structures, instead of modifying the beam members of the unit cells, the OT structure was

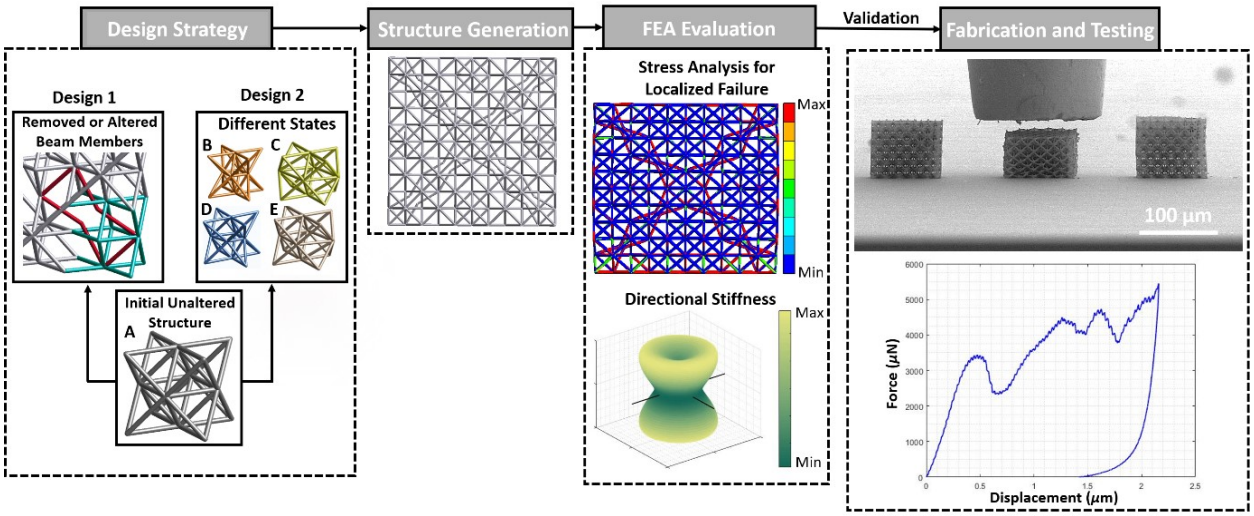

Figure 5.10: Design strategy of metamaterial structures with architected microlattices. The design approach relies on introducing defects and substitutional unit cells in the structure by removing or altering beam members and by modifying unit cells in the array, respectively.

substituted by variations of the regular IE [72] and the unit cells were positioned at the same positions of the modified OT unit cells in the first design category. The reason for selecting the IE is that the size and shape of each of its faces matches those of the OT, thus alleviating the design process. Besides the convenient incorporation of the IE in the unit cell array, the IE is also characterized by a much higher critical buckling load than the OT. Indeed, an eigenvalue buckling analysis showed that the critical buckling load of the IE is 38.8% higher than that of the OT. As shown in the next section, this structural enhancement can be augmented by positioning the IE at specific locations of the OT array. The unit cells in the SB1, SB2, and SB3 structures mimic lattice voids, which, as shown later, enable contact of the microlattice members in the OT array during the deformation of the structure. All of the structure architectures in the second design category imitate the distortion of a crystal lattice by substitutional atoms of various atomic radii [12, 323]. While the SB1 structure has the OT and one variation of the IE only, the SB2 structure has the OT and two different unit cells. The difference between the SB2 and the SB3 structure is that the faces of the modified unit cells in the SB3 structure are connected to neighboring unit cells, as opposed to the substitutional unit cells in the SB2 structure that are not connected with the faces of neighboring unit cells.

The main alteration in these unit cells is the change of the dimensions of the internal octahedron of the OT unit cell. The unit cell (1) was compressed in two vertices, forming a geometry known as the isohedron. In the unit cell (2), the former design was changed by reducing the distance between the two vertices by a factor of 2 compared to the OT unit cell. The unit cells (3) and (4) have only one vertex translated to compress the octahedron,

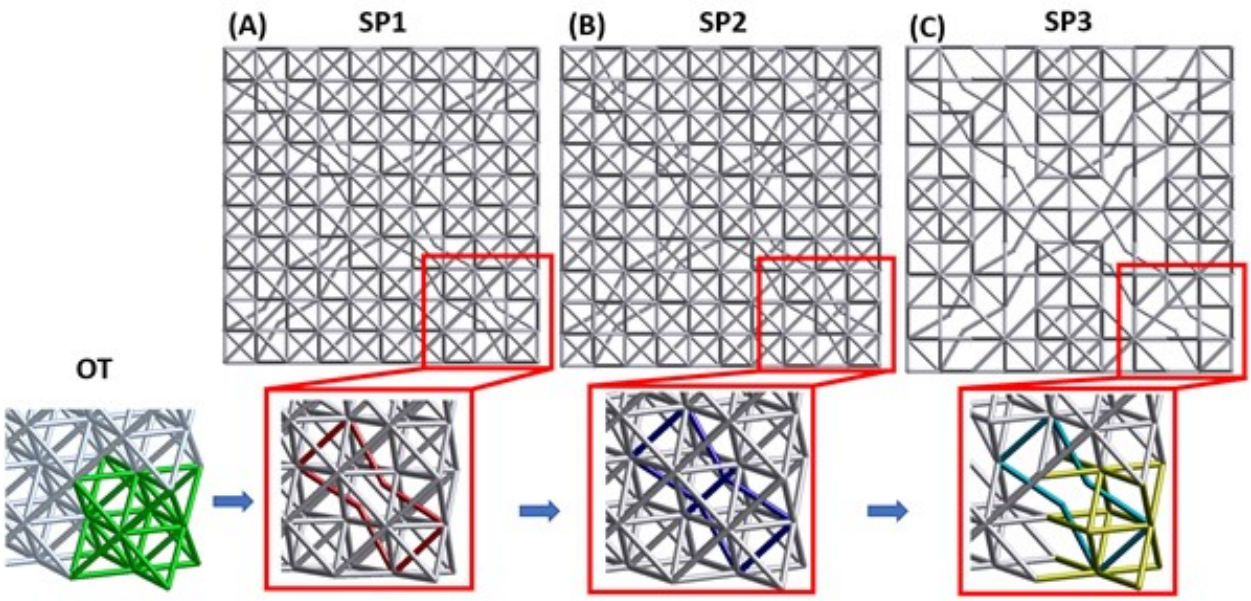

Figure 5.11: Front view of the SP1, SP2, and SP3 metamaterial structures. Each structure has an alteration of a bowtie unit cell inside the octahedron of the OT. (A) The design modification of the SP1 structure with the central nodes of the bowtie unit cell not connected (colored red). The bowties are positioned at the 45^o diagonal plane, substituting the microlattice members of the octahedra that were nested inside the OT unit cells of this plane. (B) The SP2 structure has a similar configuration with the SP1 structure but the central nodes of the bowtie unit cell are connected with a microlattice member (colored blue). (C) The SP3 structure has the same bowtie modification as the SP1 structure (coloured cyan) but several microlattice members of the OT unit cells along the 45^o diagonal plane have been removed (colored yellow) to promote microlattice collapse in that direction, while preserving the effective stiffness in the [001] direction.

whereas the unit cells (5) and (6) have a stretched octahedron at one side and the unit cell (7) has both vertices stretched. The position of different unit cells in the structure array is shown in Figs. 5.12(A)–5.12(C). The purpose for changing the unit cell dimensions is to imitate the distortion of a crystal microlattice caused by substitutional atoms. Based on the labeling used in Fig. 5.10, the matrix M depicting the configuration of different states in the SB1, SB2, and SB3 designs is given by

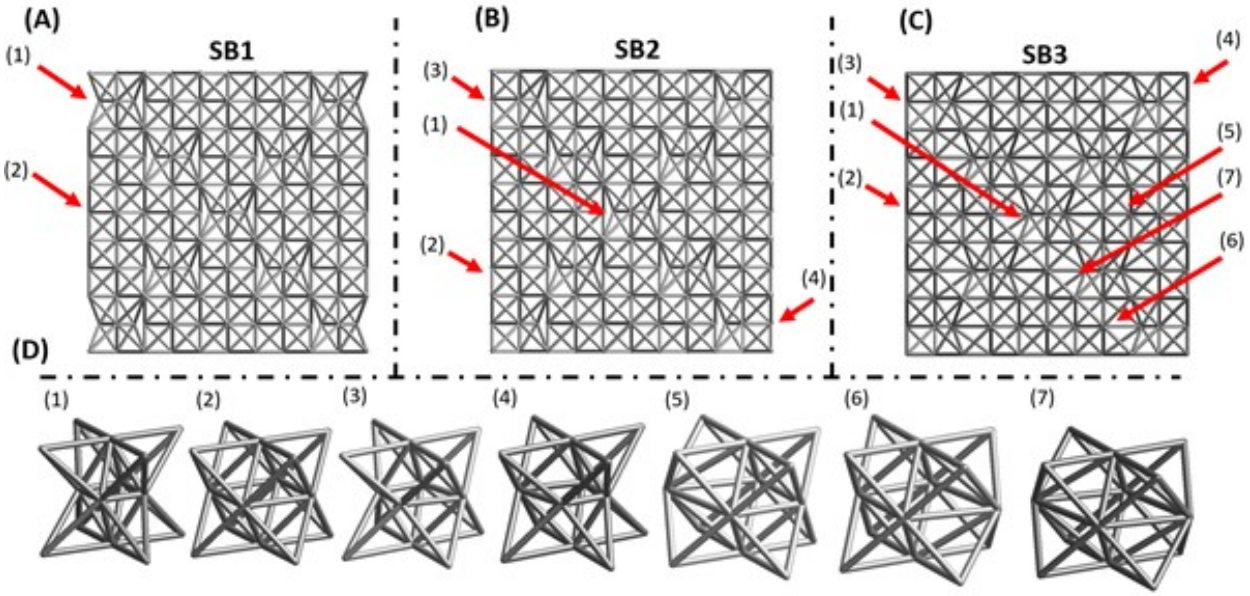

Figure 5.12: Front view of the SB1, SB2, and SB3 metamaterial structures. The schematics show the arrangement of the OT unit cell (1) and the modified unit cells (2–7) in each structure. The orientation of the modified unit cells was selected to enhance the structural integrity of the structure in every layer, while preserving tetragonal symmetry.

$$M_{SB1} = \begin{bmatrix} B & A & A & A & B \\ A & B & A & B & A \\ A & A & B & A & A \\ A & B & A & B & A \\ B & A & A & A & B \end{bmatrix} \tag{5.4}$$

$$M_{SB2} = \begin{bmatrix} D & A & A & A & D \\ A & B & A & B & A \\ A & A & B & A & A \\ A & B & A & B & A \\ D & A & A & A & D \end{bmatrix} \tag{5.5}$$

$$M_{SB3} = \begin{bmatrix} D & E & A & E & D \\ E & B & C & B & E \\ A & E & B & E & A \\ E & B & C & B & E \\ D & E & A & E & D \end{bmatrix} \tag{5.6}$$

The exact location of each modified unit cell can be seen in Fig. 5.12. Although other potential locations of either defect or substitutional unit cells can be considered, in this study

we demonstrate the improved mechanical performance in the planes of maximum shear stress of the compressed bulk material [323]. As shown below, for some of the designs this leads to a profound increase in localized buckling and plastic deformation at the $\pm 45^o$ planes, leading to failure mechanisms that resemble shear band formation [312, 329, 362].

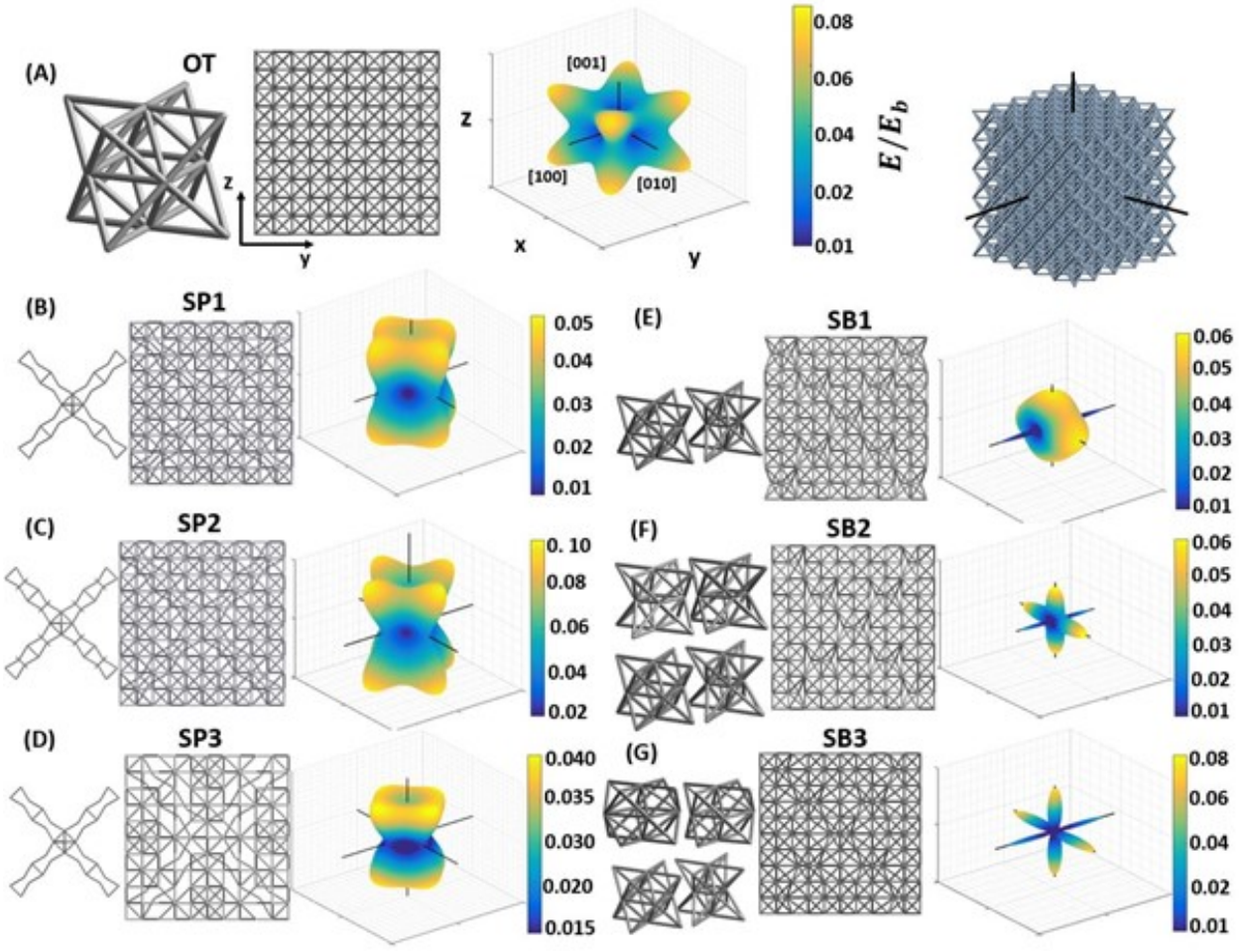

Figure 5.13: Design and effective stiffness of metamaterial structures. (A) The OT structure (unit cell, front view, effective stiffness map, and 3D configuration). (The Cartesian directions shown in the stiffness map and the 3D schematic of the OT are the same for all structures.) Front views of (B–D) SP1, SP2, and SP3 structures and (E–G) SB1, SB2, and SB3 structures illuminating structural modification details and corresponding effective stiffness maps. The unit cells of the former structures are shown on the left of their front views. All the design modifications yield significant changes in directional stiffness, particularly a profound stiffness increase in the [001] direction of all structures compared to the OT structure.

Structure	c_1	c_2
SP1	54.85	–112.8
SP2	54.89	–112.5
SP3	46.7	–110.8
SB1	64.64	–198.7
SB2	64.27	–195.3
SB3	56.16	–28.93
OT	54.8	–112.1

Table 5.4: Fitting parameters of Eq. 5.7

In the present study, it was selected to increase the stiffness of the structure in the [001] direction, as confirmed by the effective stiffness maps shown in Fig. 5.13. Although there are other directions of higher stiffness, such as the [111] direction, for the vast majority of previous studies, the [001] orientation was used to fabricate OT structures [466, 24, 264, 265, 456, 457, 153, 208, 221]. In addition, experimental results do not show a significant improvement of the stiffness in the [111] direction compared to the [001] direction [466].

To obtain the effective stiffness map of each structure, the directional stiffness of the material $E(n)$ was computed by eqn. 4.6.

For a valid comparison of the mechanical performance of the architected structures, it was necessary to fix the relative density. To accomplish this, the CADs of each structure were designed with the FEA code ANSYS and their relative density $\bar{\rho}$ was curve fitted using the relation [265]

$$\bar{\rho} = c_1(\frac{r}{L})^2 + c_2(\frac{r}{L})^3 \tag{5.7}$$

where r and L are the radius and the length of each microlattice beam member, respectively, and c_1 and c_2 are constants determined by curve fitting. The quadratic term represents the summation of the volume of each individual beam over the volume of the bulk material; however, this term does not take into account the overlapping of the beams at the nodes and, therefore, tends to overestimate the relative density. Thus, the cubic term is used to correct the calculation of the relative density for this additional volume. In the CAD designs, the overlap beam volume was not included in the calculation of the total volume. The fitting parameters of each structure are given in Table 5.4.

Using the obtained equations of the relative density, all of the samples were designed to have a relative density $\bar{\rho} = 0.025$, which is also the lowest relative density for preventing structure collapse during fabrication. The relative density was controlled by either modulating the laser power or the velocity of the fabrication stage. For $\bar{\rho} \approx 0.0255$, the beam radius was not found to vary significantly, which increased the fabrication robustness. In all of the designs examined in this study, the beam length was set at $8\mu m$.

To obtain the stiffness tensor of each structure, $5 \times 5 \times 4$ unit cell arrays subjected to different loading conditions were analysed with the ANSYS code (select simulation results are shown in Fig. 5.14). The material properties were obtained from three-point bending tests performed with solid beams fabricated with the MPL process. Specifically, the following beam properties were used in the FEA analysis: $2.76 \pm 0.11 GPa$ elastic modulus, 0.49 ± 0.001 Poisson's ratio (obtained from compression experiments with solid beams of the bulk material), and $34.37 \pm 0.03 MPa$ yield strength. To obtain statistical data, three-point bending tests were repeated five times. The structures were discretized by 10-node, tetrahedral finite elements. In all the FEA models, the smallest element size is equal to $\sim 0.24 \mu m$. The SP1, SP2, SP3, SB1, SB2, SB3, and OT structures consisted of 453077, 464690, 336815, 484117, 477229, 451480, 487995 elements, respectively, with a total of had 903026, 922884, 683389, 957070, 946392, 901057, and 960229 nodes, respectively. Figure 5.14 shows FEA simulation results illustrative of the stress analysis on each structure. High stresses can be especially observed in the $\pm 45^o$ diagonal planes of the SP3 and SB2 structures, suggesting the premature evolution of localized irreversible deformation in these directions of these structures. Using the analytical expression of the relative density (Eq. 5.7), the effective stiffness of each structure was obtained as a function of the relative density (Eq. 5.10). Each design was modeled to have 5 different relative densities and the stiffness in the [001] direction was obtained by simulating uniform compression of the top face of each structure by a vertical distance of $0.2 \mu m$. To match the experiments, the displacement was specified at the hinges of the top face of the structure, while the beams of the bottom layer of the structure were fully constrained. The fitting parameters of the normalized stiffness (Eq. 5.10) of each structure are given in Table S3. These parameters were used to plot the effective stiffness in the [001] direction as a function of the relative density (Fig. 5.14). The stiffness tensor C of the OT unit cell that exhibits cubic symmetry is of the form

$$C = \begin{bmatrix} C_{11} & C_{12} & C_{12} & 0 & 0 & 0 \\ C_{12} & C_{11} & C_{12} & 0 & 0 & 0 \\ C_{12} & C_{12} & C_{11} & 0 & 0 & 0 \\ 0 & 0 & 0 & C_{44} & 0 & 0 \\ 0 & 0 & 0 & 0 & C_{44} & 0 \\ 0 & 0 & 0 & 0 & 0 & C_{44} \end{bmatrix} \tag{5.8}$$

The 3 components of the OT stiffness tensor were obtained by simulating compression and shear loading of the structure and then using the measured average stress and strain components to solve a 3×3 linear system of equations to find the components of the stiffness tensor.

Because all other structures exhibit tetragonal symmetry, their stiffness tensor is of the form

Structure	$\bar{C_{11}}$	$\bar{C_{12}}$	$\bar{C_{44}}$	$\bar{C_{13}}$	$\bar{C_{33}}$	$\bar{C_{66}}$
SP1	301.7	220.7	97.5	241.4	397.2	19.3
SP2	186.6	10.75	83.2	157.8	389.9	19.3
SP3	145.7	85.0	93.5	125.2	280.2	19.3
SB1	811.7	474.2	19.3	8.2	148.8	143.7
SB2	2257.9	659.6	19.3	1389.4	1726	140.0
SB3	2468.9	120.0	19.3	1285.3	1800	19.3
OT	10.1	4.5	19.3	-	-	-

Table 5.5: Components of the stiffness tensor (Eq. 5.8 and 5.9).

$$C = \begin{bmatrix} C_{11} & C_{12} & C_{13} & 0 & 0 & 0 \\ C_{12} & C_{11} & C_{13} & 0 & 0 & 0 \\ C_{13} & C_{13} & C_{33} & 0 & 0 & 0 \\ 0 & 0 & 0 & C_{44} & 0 & 0 \\ 0 & 0 & 0 & 0 & C_{44} & 0 \\ 0 & 0 & 0 & 0 & 0 & C_{66} \end{bmatrix} \tag{5.9}$$

An approach that provides highly accurate results of the macroscopic stiffness of the structure [375, 432] was used in the FEA. Nevertheless, in the present study the stiffness tensor does not refer to the tensor of an equivalent continuum but the stiffness of discrete microlattice structures, as reported previously [466, 432]. Obtaining the equivalent continuum stiffness tensor requires variational approaches [444], which can greatly increase the modeling complexity of the structures. Because of its cubic symmetry, the stiffness tensor of the OT includes three independent constants; however, the distortion promulgated by the modified and substitutional unit cells leads to symmetry loss at one orthogonal plane, elevating the symmetry to tetragonal and increasing the number of independent constants to six. While the cubic symmetry could have been preserved by applying the same 2D modification to other orthogonal planes of the structure, it was decided to keep the modification at planes easily viewed during testing. The calculated components of the stiffness tensor C_{ij} of each structure are given in Table 5.5.

A 3D polar plot of the normalized stiffness $\bar{E} = E/E_b$ (where E_b is the bulk stiffness) of each structure is also shown in Fig. 5.13. All of the modified structures possess stiffness maps profoundly different from that of the OT structure. In particular, while the maximum stiffness of the OT structure is in the [111] direction, the stiffness maps of the SP1, SP2, and SP3 structures are rotated with respect to the [001] direction and are more uniform in the plane normal to the [001] direction, whereas the maximum stiffness of the SB1, SB2, and SB3 structures has been transcended to the [001] and [010] directions.

Figure 5.15 shows the normalized stiffness $\bar{E}$ in the [001] direction of all tested structures

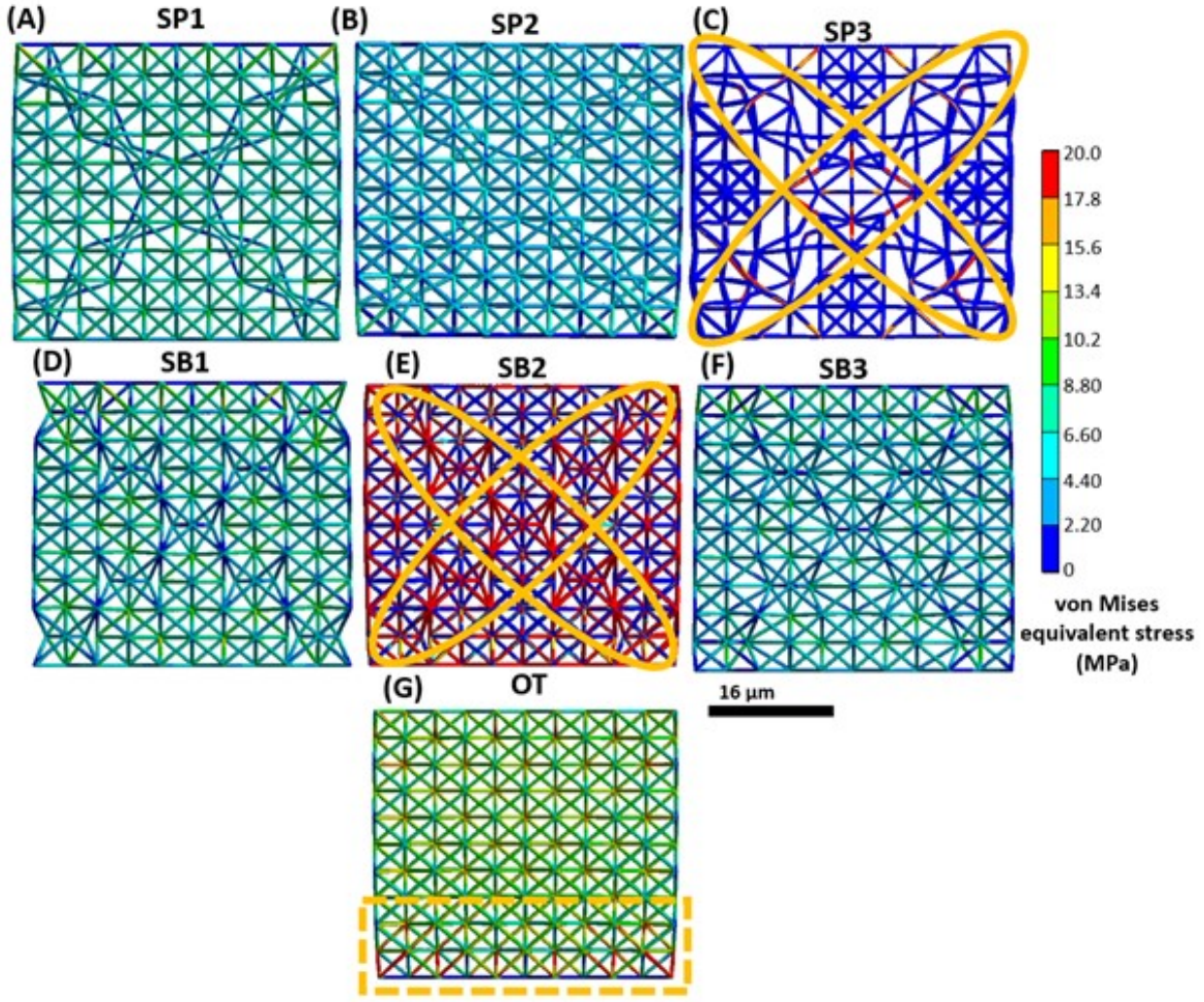

Figure 5.14: FEA stress distributions in various metamaterial structures. While the SP3 structure demonstrates stress localization at specific locations of the beam members in the $\pm 45^o$ diagonal planes, in the SB2 structure all of the unit cells in the $\pm 45^o$ diagonal planes are under maximum stress, which is in agreement with the total collapse of the $\pm 45^o$diagonal planes. All other structures show small variation in stress distribution in each layer. The maximum stress in the OT structure is located at the bottom layers, where collapse commenced first in the experiments.

versus the relative density. Because some structures show an increase in stiffness slope with relative density due to several beams coming into contact, the normalized stiffness is expressed as

Structure	α	β	p	q
SP1	0.01621	1.003	-0.1244	0.5417
SP2	0.09449	-	0.1411	-
SP3	0.7669	-0.6062	0.3233	0.3179
SB1	0.08269	-	0.1689	-
SB2	0.1137	-	0.1769	-
SB3	-1.28	0.2084	6.791	0.3224
OT	0.07626	-	0.2312	-

Table 5.6: Stiffness, critical buckling load, and elastic strain energy density of metamaterial microlattices.

$$\bar{E} = \alpha\bar{\rho}^{p} + \beta\bar{\rho}^{q} \tag{5.10}$$

where α, β, p and q are fitting parameters. While similar models have been used in fatigue to distinguish plastic from elastic behavior, the power p and q parameters in Eq. 5.10 distinguish proximal from intersecting microlattice members. Figure 5.16 illustrates how this geometrical change arises as the radius-to-length ratio is changed. The fitting parameters in Eq. 5.10 were obtained from an FEA of all the structures for various relative densities and are given in Table 5.6.

As shown in Fig. 5.15, except of the SP3 structure, the stiffness of all other structures having $\rho \geq 0.03$ is higher than that of the OT structure, even by a factor as high as 2.12 (SB3 structure). The noticeably higher relative stiffness of the SP2, SB2, and SB3 structures than the other structures is attributed to the highest connectivity of microlattice members in the former designs. The result that the SP3 structure is stiffer than the OT structure for $\rho \leq 0.03$ is consonant with reported results showing that the selective removal of beam members from predefined locations can improve the mechanical properties of lattice structures [153, 393]. Inevitably, the mechanical response of the bulk material becomes prevalent with the significant increase of the relative density [140].

Experimental procedures

Each structure was fabricated by a modified MPL process, known as diffusion-assisted high-resolution direct femtosecond laser writing [343], as it was described in the previous chapters. The dimensions of the architected structures were selected so that all of them to have the same relative density as in the simulations (i.e., $\bar{\rho} = 0.025$), the only exception being the SP3 structure, which had a slightly lower relative density (i.e., $\bar{\rho} = 0.022$) because it comprised fewer microlattice members. The average beam radius in each structure was modulated by changing the laser power to achieve the desired relative density. However,

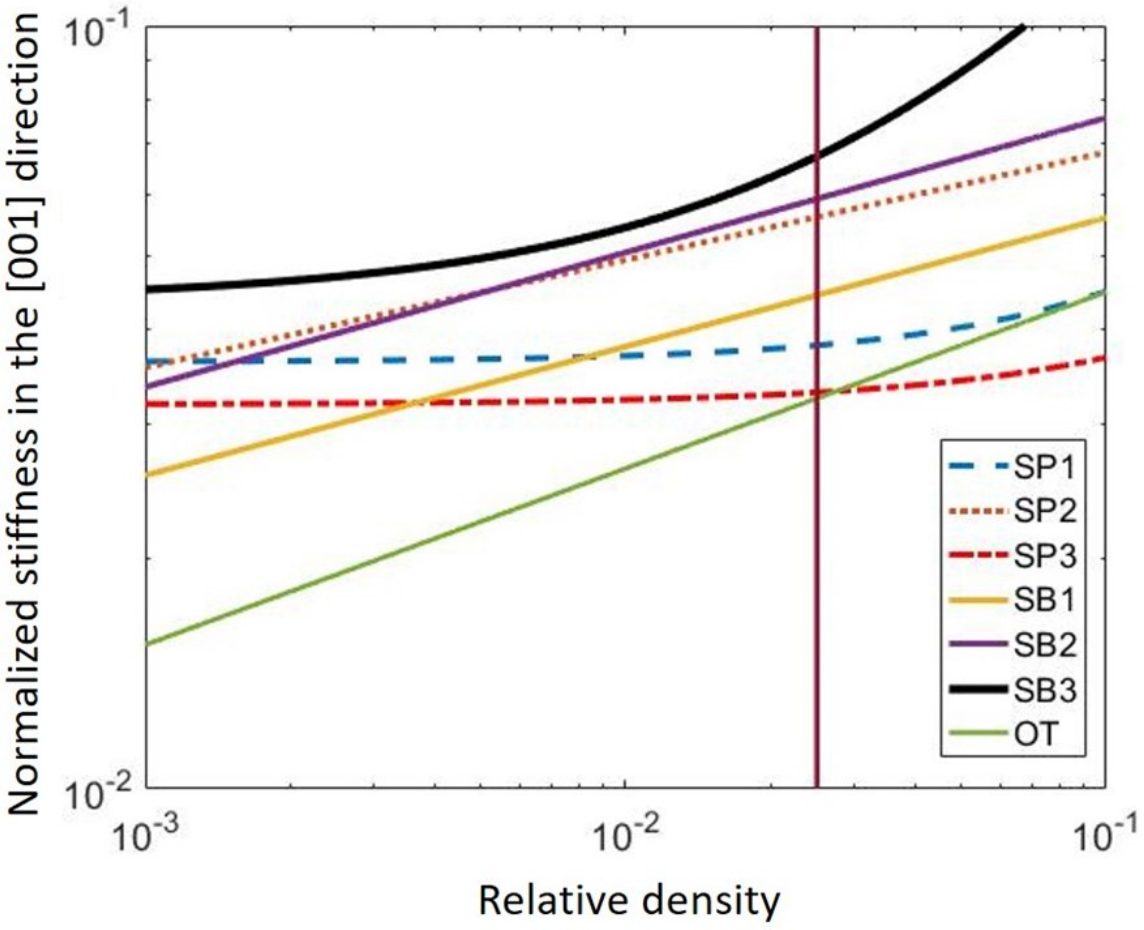

Figure 5.15: Normalized stiffness in the [001] direction versus relative density of metamaterial structures. With the only exception of the SP3 structure, the stiffness of all other structures is significantly higher than that of the OT structure. The vertical line indicates the relative density ($\bar{\rho} = 0.025$) of the tested structures.

at this length scale the MPL produces polymerized ellipsoid voxels that are not perfectly orbicular. To mitigate this effect, the laser beam was scanned four times along the same path to increase the thickness of the voxel in the radial direction. In addition, to ensure that the fabricated structures were bereft of this fabrication constraint, apart from SEM imaging, experimental and simulation results were contrasted and the differences were found

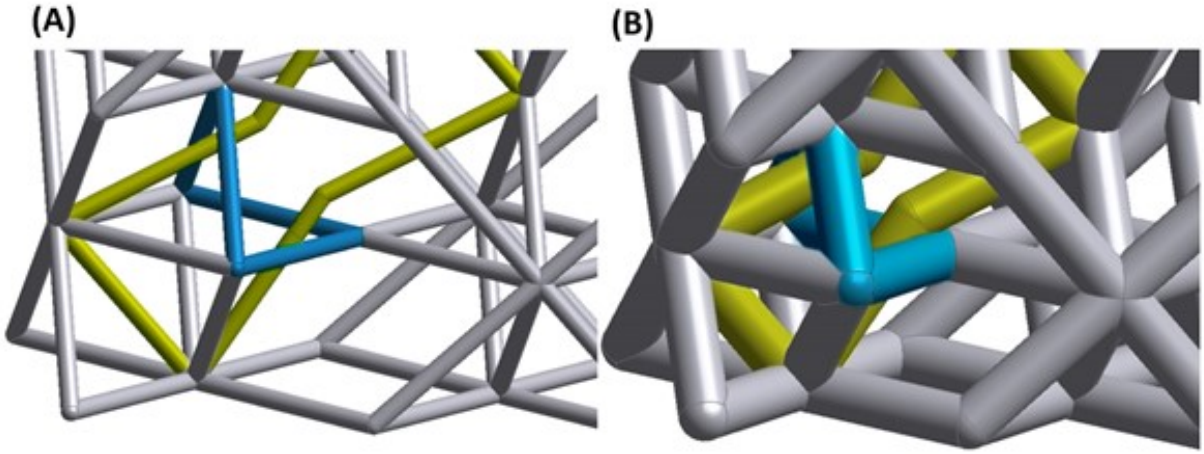

Figure 5.16: Effect of relative density on intersection of microlattice members of the SP3 metamaterial structure ($\bar{\rho} = 0.022$). (A) Proximal microlattice members. (B) Contacting microlattice members ($\bar{\rho} = 0.155$).

to be insignificant. Figure 5.17 shows characteristic SEM images of the fabricated structures. All of the structures consist of $5 \times 5 \times 4$ arrays of unit cells, matching the geometry of the structures used in the FEA. Structure modification is indicated by the different morphologies of neighboring unit cells, such as those for the SB1 structure seen in Fig. 5.17(A). The voids created by the IE can be observed in Fig. 5.17(B), with the magnified view shown in Fig. 5.17(C) revealing that proximal unit cells do not share the same face. Figure 5.17(D) shows a 3D image of the SP3 structure, which is the only structure with some of its microlattice members removed, while Fig. 5.17(E) shows a region from where a few microlattice members were removed (shown by red dot lines). Figure 5.17(F) shows a front view of the SP3 structure, which allowed viewing the evolution of various deformation modes during mechanical testing.

The mechanical tests were performed with a nanoindenter mounted inside an SEM (Hysitron P188 SEM PicoIndenter, Bruker). All of the structures were positioned such that their frontal faces to be observable, similar to the front views of the structures shown in Figs. 5.13 and 5.17. This allowed a frame-by-frame analysis of the video recordings [392] to provide the location and instant of localized deformation events. All of the structures were deformed in compression to 50% of their undeformed height. At least 8 specimens of each structure were tested to ensure the repeatability of the experimental results.

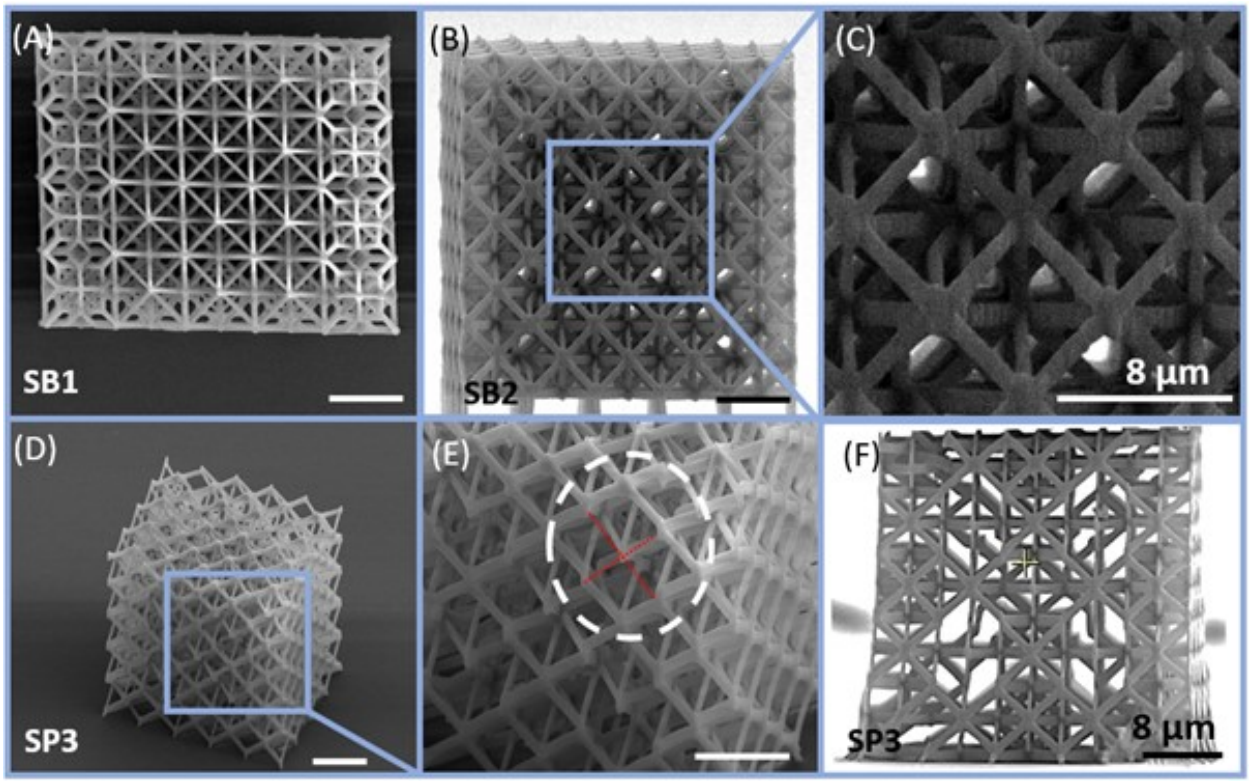

Figure 5.17: Characteristic SEM micrographs of the SB1, SB2, and SP3 metamaterial structures. (A) Top view of the SB1 structure showing the modified unit cells at the edges. (B) Front view of the SB2 structure. (C) High-magnification image of an individual unit cell of the SB2 structure showing the orientation of neighboring microlattice members. (D) Side view of the SP3 structure. (E) High-magnification image of a side array of the SP3 structure showing the locations where a few microlattice members (red dot lines) were removed. (F) Front view of the SP3 structure. All structures have a relative density equal to ~ 0.025, except the SP3 structure that has a relative density of 0.022. The scale bar in all the SEM images is equal to $8\mu m$.

Results

Figure 5 shows a representative force versus displacement response of the SP3 structure. The flat block seen at the top of the structure (also in similar SEM images of following force-displacement plots) is the rigid flat tip. These SEM images and Video S1 [392] showing a full load/unload cycle of the SP3 structure reveal several characteristic deformation stages. Subsequently to the engagement of the flat tip with the structure (Fig. 5.18(A)), a fairly linear force response emerged with the gradual increase of the load, indicative of the overall elastic behavior of the structure, until the occurrence of a noticeable change in force slope

at a load of $\sim 2500\mu N$ (Fig. 5.18(B)) that was prompted by localized buckling of a few microlattice members (shown in red enclosures). This occurrence produced intense force fluctuations, attributed to the collapse of the $+45^o$ diagonal plane of the structure, shown by the large red enclosure (Figs. 5.18(C) and 5.18(D)), involving twisting of the central unit cell (the red circle in Fig. 5C). The maximum stress drop due to the collapse of the $+45^o$ plane of the structure is $\sim 1.88MPa$. After a small increase of the deformation, the mirrored (-45^o) diagonal plane of the structure also collapsed (Fig. 5.18(E)). Unloading of the SP3 structure revealed that localized deformation at the $\pm 45^o$ planes of the structure also deformed slightly the unit cells at the center of plane edges (Fig. 5.18(F)). The marginally asynchronous collapse of the diagonal planes of the structure is attributed to the imperfect alignment of the flat tip with the top face of the structure. The initiation of microlattice beam collapse at the diagonal planes activated the rapid failure of additional beam members at these planes, similar to the generation of localized failures generated by a dislocation avalanche [169, 74]. The foregoing phenomenon differs significantly from the collapse of a whole layer of the structure and the proliferation of damage to the underlying layers encountered with other designs. The localized failure in the diagonal plane of the SP3 structure is also supported by the FEA results shown in Fig. 5.14(C).

Figure 5.19 shows a representative force versus displacement response of the SB2 structure. Again, SEM imaging and Video S2 [392] of a full load/unload cycle of the SB2 structure reveal several characteristic deformation stages. After the tip was brought into contact with the top face of this structure (Fig. 5.19(A)) and the load was gradually increased, buckling of the beams in several unit cells at the -45^o diagonal plane (enclosed by red dashed lines) was instigated at a load of $\sim 3500\mu N$ (Fig. 5.19(B)), which is much higher than that of structure SP3 (Fig. 5.18). However, collapse failure commenced at the $+45^o$ diagonal plane (Figs. 5.19(C) and 5.19(D)). For this structure, the collapse did not propagate to the lower half of the structure as for the SP3 structure; instead, the bottom layers of the structure exhibited fairly uniform deformation (Figs. 5.19(E) and 5.19(F)). Again, stress fluctuations occurred in the post yield regime of the stress-strain curve, with average stress drops just before the instigation of buckling being equal to $\sim 0.29MPa$. At the top of the first stress peak (Fig. 5.19(B)) the stress drop is equal to $0.46MPa$ and demonstrates fluctuations of high repetition rate. However, when the whole -45^o diagonal layer collapsed, the stress fluctuation repetition decreased and the stress drop decreased back to $0.29MPa$ (Fig. 5.19(C)). Another difference is that failure at the diagonal plane of the SP3 structure was not uniform. Instead, it comprised localized buckling and collapse leading to the failure of proximal beam members. Conversely, uniform failure of each diagonal plane as a whole occurred in the SB2 structure. This explains the relatively less intense force fluctuations in the mechanical response of the SB2 structure (Fig. 5.19). The FEA results of the SB2 structure shown in Fig. 5.14(E) reveal high stresses along the $\pm 45^o$ diagonal planes for the vast majority of the beam members comprising these unit cells.

Figure 5.20 shows a representative force versus displacement response of the OT structure. Several characteristic deformation stages were identified by SEM imaging and by observing the deformation of the structure during a full load/unload cycle recorded in Video S3 [392].

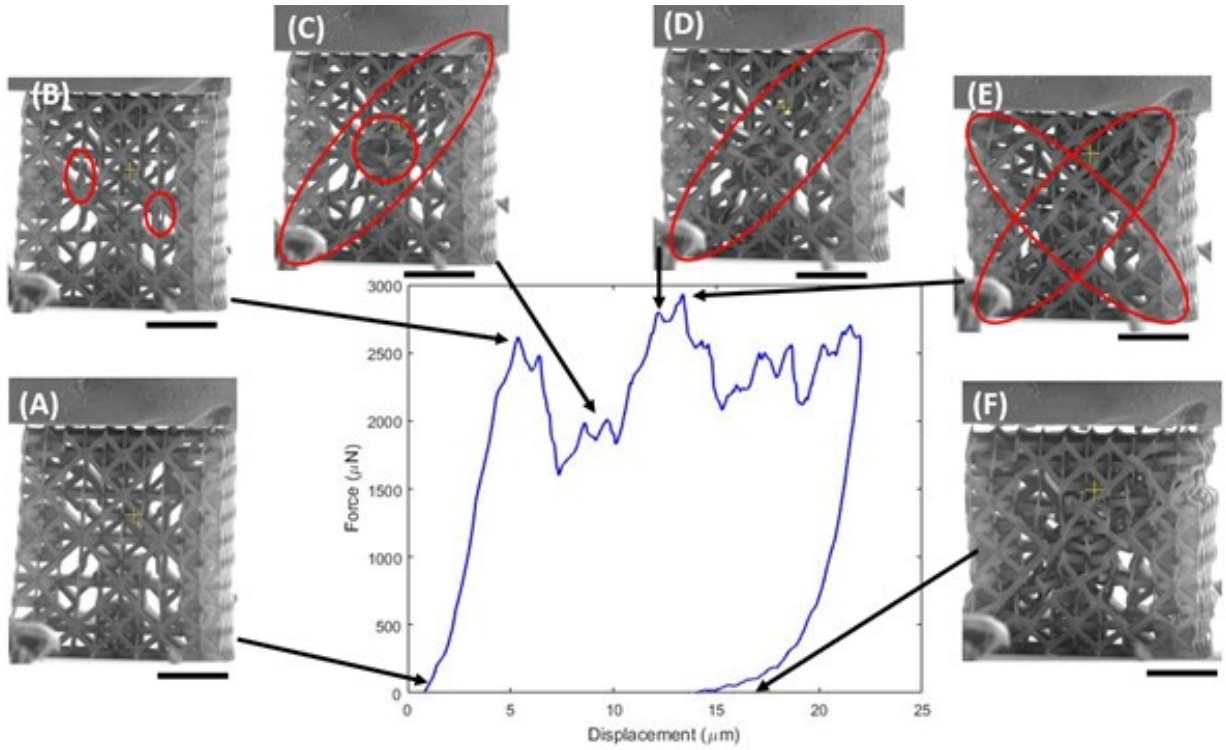

Figure 5.18: Force versus displacement response of the SP3 metamaterial structure. Characteristic deformation stages (A–F) were determined from SEM images and Video S1 of the full load/unload cycle. After the flat tip was brought into contact with the top face of the structure (A), a notable change in force slope was observed as the load was gradually increased due to localized buckling of some microlattice members (enclosed by red circles) (B). This was followed by excessive deformation of the microlattice members at the $+45^o$ diagonal plane (enclosed by an ellipsoid) with the central unit cells (enclosed by red circles) exhibiting torsional deformation (C), resulting in structure densification and stiffening. With the further increase of the load, localized fracture was instigated on the $+45^o$ diagonal plane (D) and soon after on the -45^o diagonal plane (E). Unloading revealed excessive deformation of the microlattice members at both diagonal planes, especially the unit cells at the plane edges (F). The scale bar in all the SEM images is equal to $10\mu m$.

Ensuing the engagement of the tip with the OT structure (Fig. 5.20(A)) and after the gradual increase of the load, a profound change in force slope occurred at a load of $\sim 1600\mu N$ due to localized buckling of the beam members comprising the octahedra of the OT unit cells at the bottom layers (enclosed by red dashed lines in Fig. 5.20(B)). This was succeeded by the uniform collapse of other layers of the structure, consistent with the findings of previous studies [264, 266, 466, 457, 271, 177]. Similar to the previous structures, the OT structure also exhibited a serrated stress-strain response in the post yield regime. The commencement

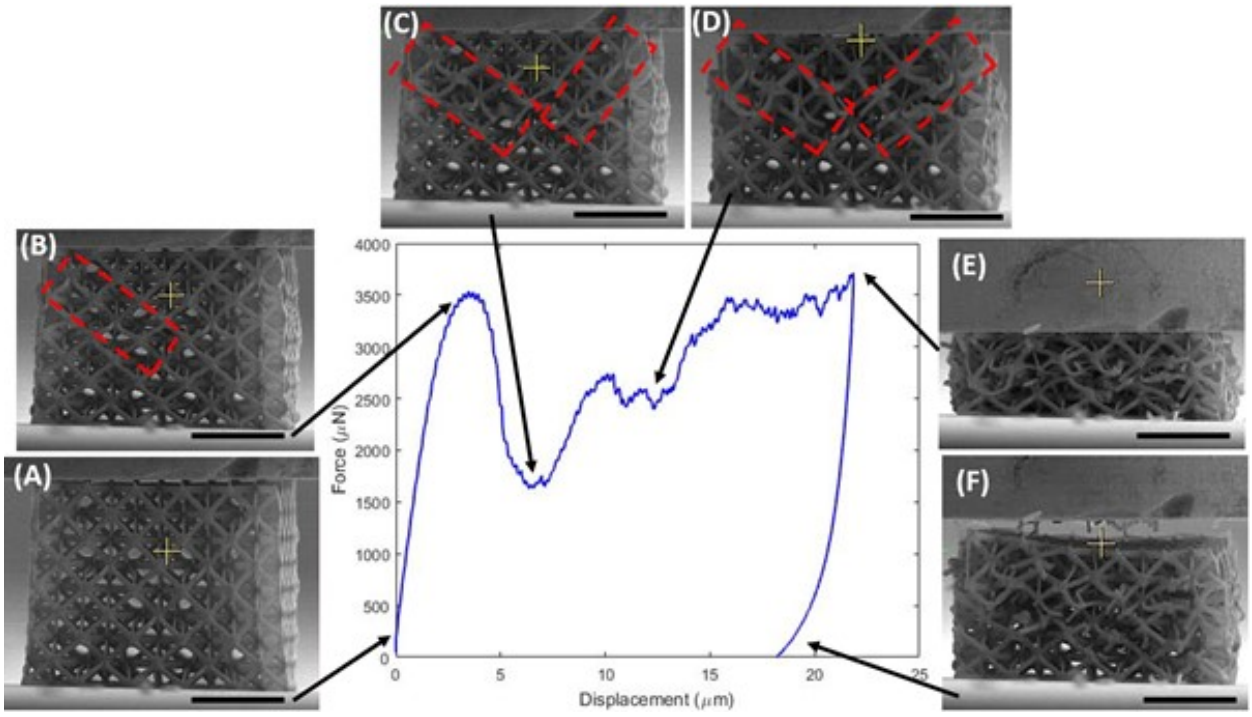

Figure 5.19: Force versus displacement response of the SB2 metamaterial structure. Characteristic deformation stages (A–F) were determined from SEM images and Video S2 of the full load/unload cycle. After the engagement of the flat tip with the top face of the structure (A) and the gradual increase of the load, excessive deformation of microlattice members (enclosed by dashed red lines) occurred in the -45^o diagonal plane, resulting in beam buckling (B). With the further increase of the load, large deformations were instigated in the mirror $+45^o$ diagonal plane of the structure (C), afterwards leading to the collapse and fracture of both diagonal planes (D). Further loading propelled the collapse of several layers of the structure (E). Unloading revealed the global collapse of the structure. The scale bar in all the SEM images is equal to $16\mu m$.

of instability and plastic deformation resulted in an average stress drop of $\sim 0.16MPa$ before the first stress peak, and after exhibiting softening, it reached a steady state of $\sim 0.51MPa$ through the whole loading at high repetition rate. Instead of the abrupt changes in force slope of the SP3 and SB2 structures observed after the first buckling event, the evolution of structural damage in the OT structure densified the regions with fractured members (Figs. 5.20(C)–5.20(E)), resembling a ductile behavior, with the structure exhibiting a catastrophic collapse characterized by distributed damage [140]. A uniform collapse of the layers of the lower half of the structure was observed upon full unloading (Fig. 5.20(F)). The FEA results shown in Fig. 5.14(G) demonstrate high stresses at the bottom layer correlating to the subsequent collapse of the bottom layer.

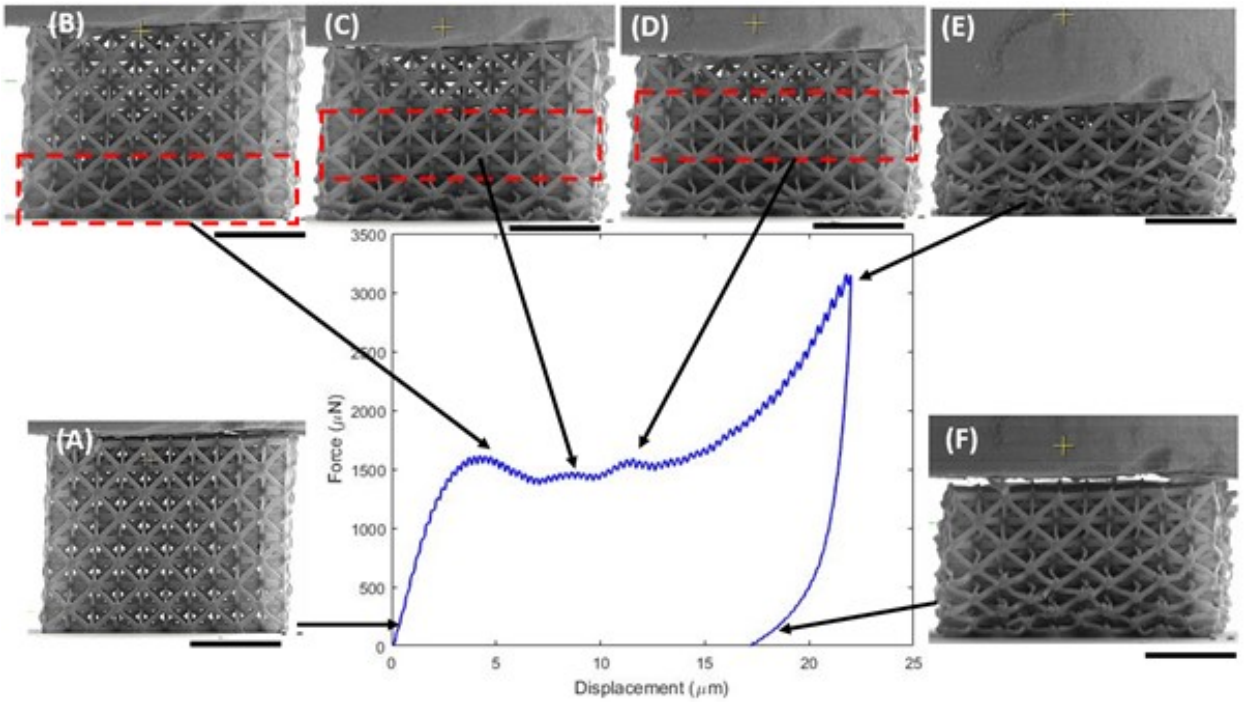

Figure 5.20: Force versus displacement response of the OT metamaterial structure. Characteristic deformation stages (A–F) were determined from SEM images and Video S3 of the full load/unload cycle. After the engagement of the flat tip with the top face of the structure (A) and the gradual increase of the load, buckling of microlattice members (enclosed by dashed red lines) was instigated at the bottom layer of the structure leading to its collapse (B). The further increase of the load resulted in the catastrophic collapse of subsequent layers (enclosed by dashed red lines) of the structure (C–E). Unloading revealed the total collapse of the bottom layers (F). The scale bar in all the SEM images is equal to $10\mu m$.

Characteristic force-displacement responses of other metamaterial structures are shown in Figs. 5.21–5.24. The mechanical behaviors of these structures reveal similar characteristics with those shown in Figs. 5.18–5.20. Statistical experimental and FEA results of the structural stiffness, S_{exp} and S_{FEA}, respectively, critical buckling load, P_{cr}, and elastic strain energy density, u_e, are given in Table 5.7. The stiffness and strain energy density were calculated from the initial elastic response of the structures, i.e., before the instigation of the first buckling event. The results show that the stiffness, critical buckling load, and strain energy density of all structures are higher than those of the OT structure, with the only exception of the stiffness of the SP3 structure attributed to its fewer microlattice members. However, despite the higher critical buckling load of the structures, not all of them embrace the design objective of localized failure, because the collapse of subsequent layers in some of the structures resembled the deformation mode of the OT structure; nevertheless, the stress-strain

Structure	$S_{exp}(MPa)$	$S_{FEA}(MPa)$	$S_{cr}(\mu N)$	$u_e(J/cm^3)$
SP1	113.070 ± 5.36	108.164	3385 ± 32	2.04 ± 0.18
SP2	172.040 ± 7.56	162.064	4241 ± 130	2.07 ± 0.28
SP3	85.650 ± 5.13	91.436	2230 ± 57	1.60 ± 0.15
SB1	125.040 ± 8.32	128.770	4375 ± 63	4.67 ± 0.33
SB2	182.970 ± 8.24	172.508	3527 ± 108	2.14 ± 0.21
SB3	139.020 ± 46.67	202.552	3649 ± 45	2.65 ± 0.05
OT	98.720 ± 3.05	95.648	1607 ± 98	0.69 ± 0.08

Table 5.7: Components of the stiffness tensor (Eq. and 5.8 5.9).

responses shown in Fig. 5.25 reveal a remarkably improved mechanical behavior even for these designs. All of the structures demonstrate significantly higher strain energy density than the OT structure, indicated by the larger hysteresis area of the corresponding stress-strain response. To compare the mechanical performance of each structure, the experimental data are contrasted in Fig. 5.26. The numerical values of the statistical data of all structures are given in Table 5.7.

Figure 5.26(A) shows that the critical buckling load of all structures is higher than that of the OT structure by as much as 172% (SB1 structure). The SP3 structure shows the lowest increase in critical buckling load, i.e., 38% higher than that of the OT structure. Nonetheless, this is still a notable improvement considering the significantly fewer microlattice members of the SP3 structure, which intuitively would suggest a lower buckling load. This shows that tactical and concinnated placement of defects and substitutional unit cells can increase the structure resilience to collapse. For post contact of microlattice members to effectively increase the energy dissipation and stiffness of structures with intertwined geometries, buckling must commence in the early stage of deformation [393, 395]. However, for structures that lack intertwined microlattices, buckling promotes fracture of the beam members. Hence, for structures with microlattice members that do not exhibit post contact during deformation, buckling must be forestalled to enhance the structure's resilience to catastrophic failure. Figure 5.26(B) shows the elastic stain energy density of each structure calculated as the area under the stress-strain response up to the instigation of buckling. The elastic strain energy density increased with the buckling load. Most notably, the SB1 structure demonstrated a strain energy density 577% higher than that of the OT structure. The main reason for this result is that the neighboring IE and OT unit cells do not share the same faces; consequently, at large deformations, they come into contact, stiffening the structure and preventing collapse during the initial stage of deformation. The strain energy density of the SP3 structure is 132% higher than that of the OT structure, which is counterintuitive considering its lower relative density. Figure 5.26(C) shows a comparison between the structure stiffness measured in the [001] direction during the initial stage of elastic deformation with the structural

stiffness obtained from the FEA simulations also for the [001] direction. The close agreement between experimental and simulation results validates the effective stiffness maps (Fig. 5.13). The only structure showing a significant difference between experimental and FEA effective stiffness in the [001] direction is the SB3 structure. This disagreement is most likely due to imperfections in contact between the flat tip and the top face of the SB3 structure, as indicated by the large standard deviation of the measurements of this structure alone. The SB2 and SP3 structures showed the highest and lowest experimental stiffness, i.e., higher by 85.65% and 13% than that of the OT structure, respectively. It is noted that in addition to a higher stiffness, the SP3 structure demonstrated a better structural integrity and higher strain energy dissipation capacity than the OT structure, despite its lower relative density.

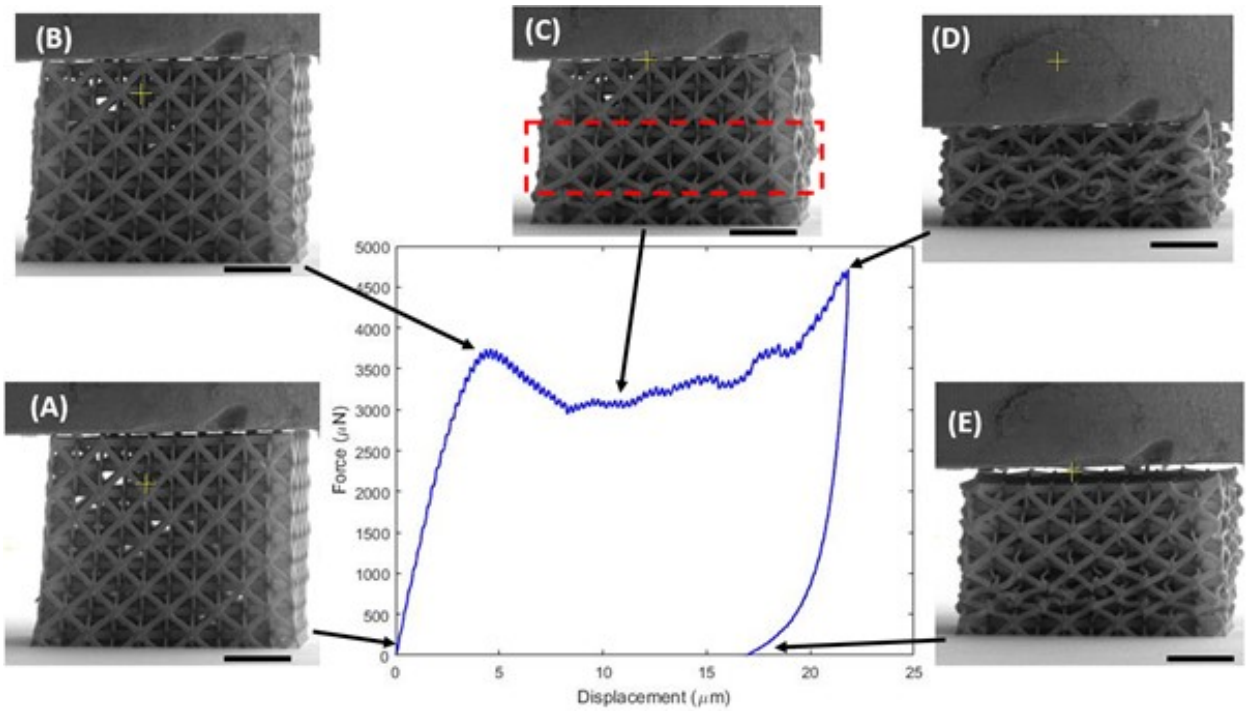

Figure 5.21: Force versus displacement response of the SP1 metamaterial structure. Characteristic deformation stages (A–E) were determined from SEM images and Video S4 of the full load/unload cycle. After the flat tip was brought into contact with the top face of the structure (A), buckling commenced at the bottom layer of the structure, resulting in the collapse of the whole structure (B). This event prompted the catastrophic collapse of subsequent layers of the structure (C–D). Unloading revealed the total collapse of the bottom layers of the structure (E). The scale bar in all the SEM images is equal to $8\mu m$.

Further insight into the mechanical behavior of the designed microlattice structures was provided by fractography results of fractured microlattice members. Despite the large deformations caused by buckling and the macroscopic mechanical behavior resembling ductile

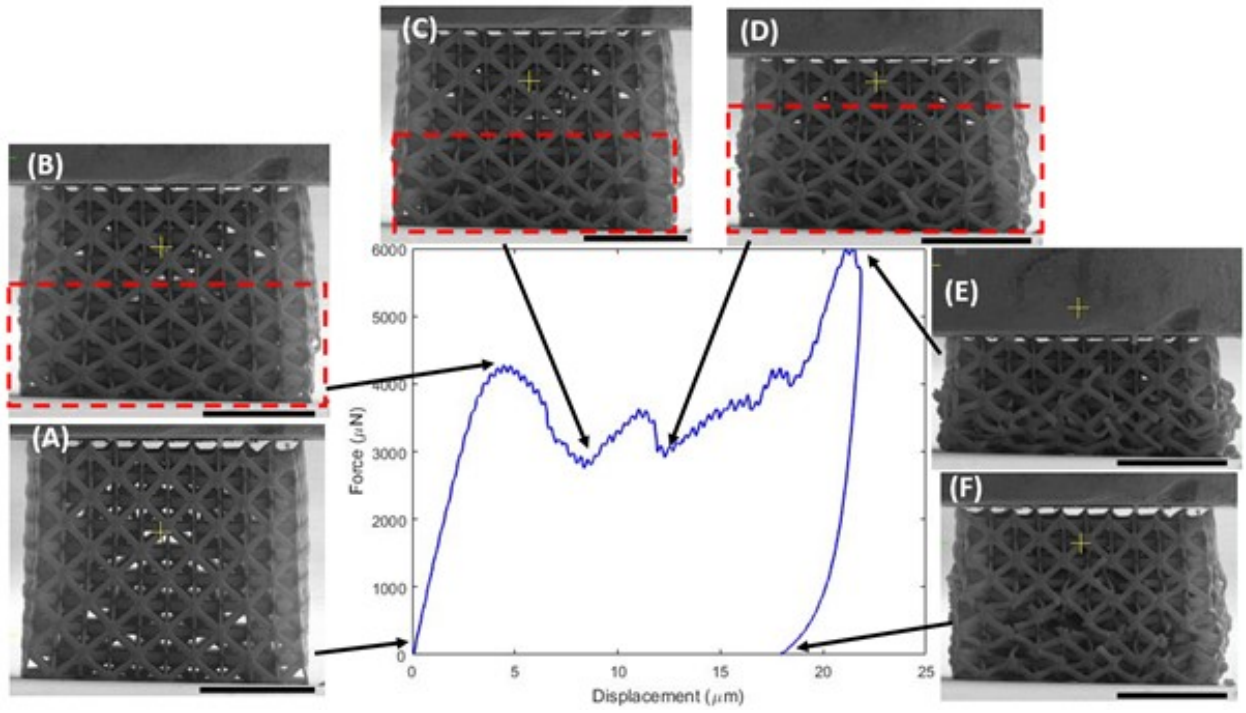

Figure 5.22: Force versus displacement response of the SP2 metamaterial structure. Characteristic deformation stages (A–F) were determined from SEM images and Video S5 of the full load/unload cycle. After the flat tip was brought into contact with the top face of the structure (A), buckling commenced at the bottom layer of the structure, resulting in the collapse of the whole structure (B). This event prompted the catastrophic collapse of subsequent layers of the structure (C–E). Unloading revealed the total collapse of the bottom layers of the structure (F). The scale bar in all the SEM images is equal to $16\mu m$.

behavior, the microlattice beams incurred sudden fracture. Because the beam diameter was equal to $\sim 125nm$ in all structures, a significantly higher imaging resolution was necessary for capturing the morphological features on fracture cross sections. In addition, it was riveting to reveal the internal failure of the structures to further elucidate the 3D deformation of failed microlattice members. This was accomplished by HIM imaging. This technique does not require the deposition of a conductive surface layer, which may alter the surface micro/nanomorphology, and provides high depth of focus that enables the observation of the internal layers of the structure and features as small as a few nanometers. Characteristic HIM images of deformed, buckled, and fractured microlattice members located in the interior of the SP1 and SB3 structures are shown in Fig. 5.27. Figures 10A and 10B show that buckling of microlattice members contributed to excessive deformation and twisting of the unit cells. The twisting mode of deformation was not captured in the linear FEA of the struc-

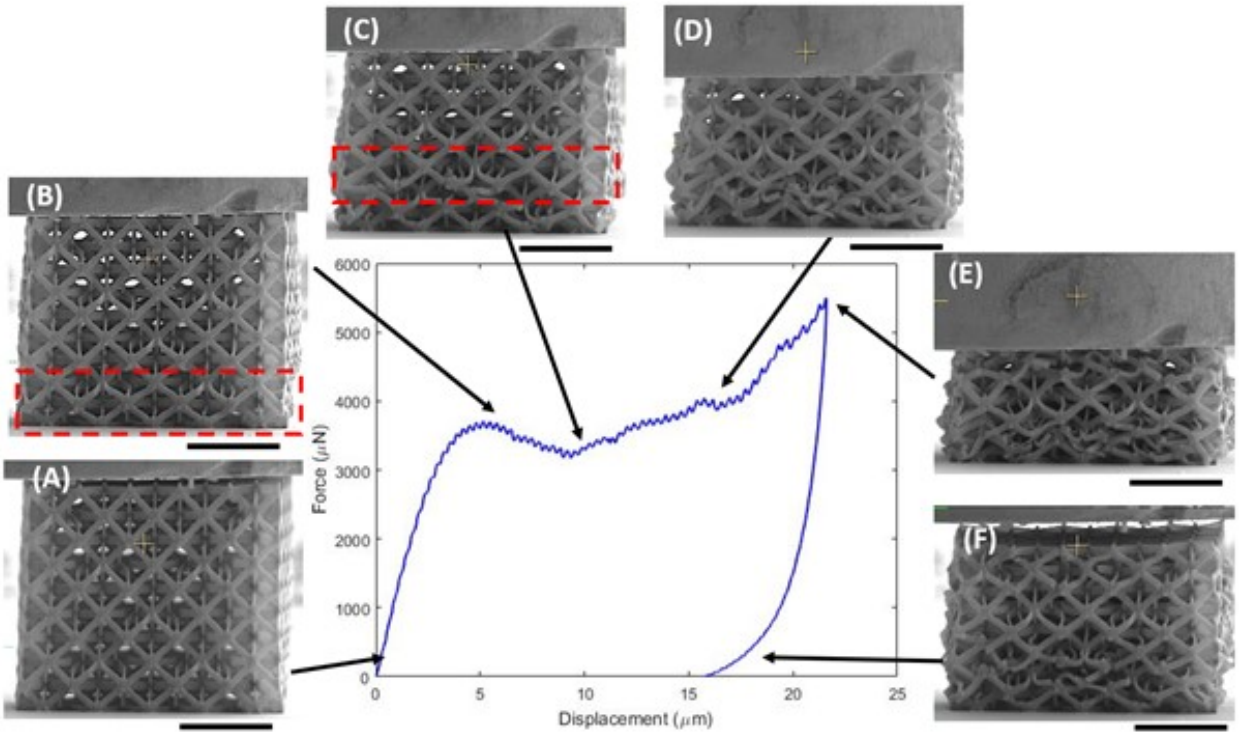

Figure 5.23: Force versus displacement response of the SB1 metamaterial structure. Characteristic deformation stages (A–F) were determined from SEM images and Video S6 of the full load/unload cycle. After the flat tip was brought into contact with the top face of the structure (A), buckling was instigated at the intersection of the two bottom layers of the structure (B), leading to the collapse of the whole structure (C). This event prompted the catastrophic collapse of subsequent layers of the structure (D–E). Unloading revealed the total collapse of the bottom layers of the structure (F). The scale bar in all the SEM images is equal to $16\mu m$.

tures, presumably because of the manifestation of effects encountered at micrometer length scales that are associated with higher order deformation gradient terms in the constitutive relation [444]. While these models may capture the observed mechanical response, they have not been used to analyze 3D microlattice structures because of their high complexity. In addition, the twisting deformation suggests that the microlattice members reached the post yield regime and the structure evolved to exhibit a ductile behavior. Nevertheless, the occurrence of fracture in a few hundred microseconds (captured in the video recordings) resembles brittle behavior and is supported by the high-resolution fractography images shown in Figs. 5.27(C) and 5.27(D), which illuminate the absence of discernible roughness (texture) and dimple formation. These features together with the fibril formation observed in Fig. 5.28 indicate the commencement of brittle fracture caused by crazing [81]. Crazing occurs when

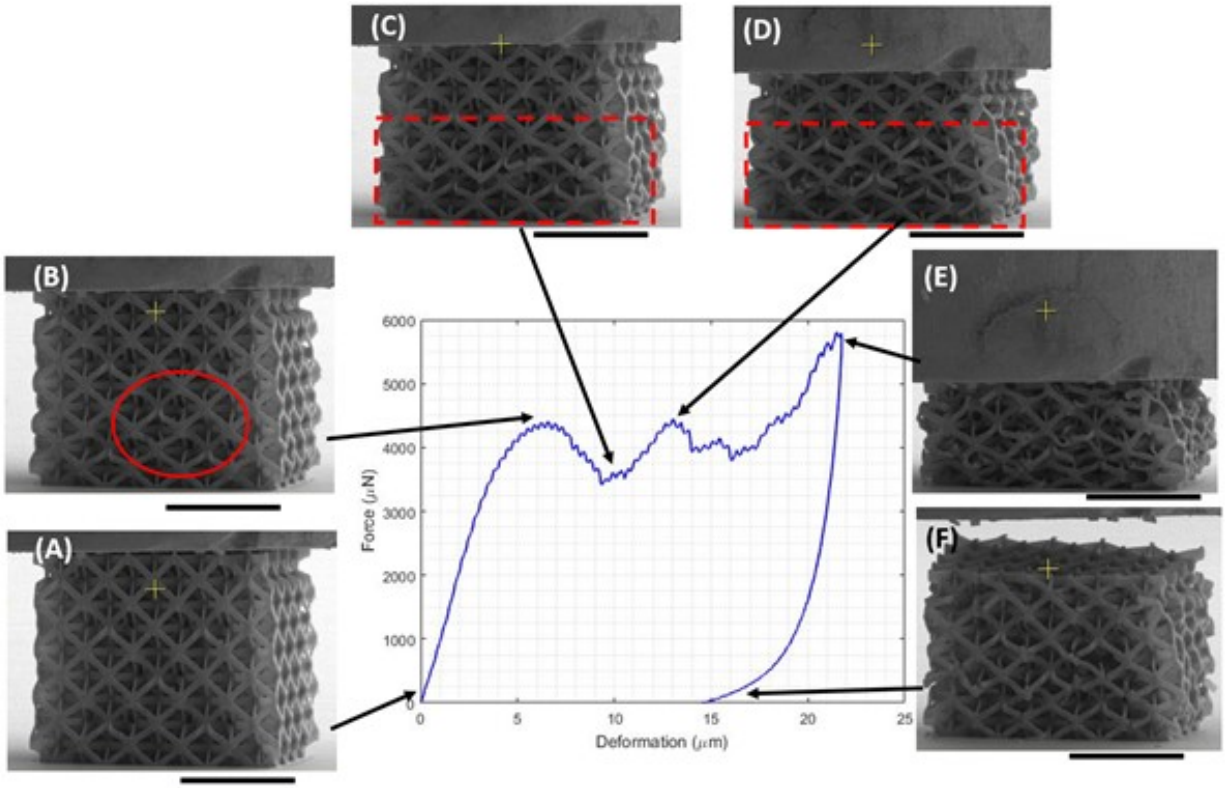

Figure 5.24: Force versus displacement response of the SB3 metamaterial structure. Characteristic deformation stages (A–F) were determined from SEM images and Video S7 of the full load/unload cycle. After the flat tip was brought into contact with the top face of the structure (A), buckling commenced at the bottom layer of the structure, resulting in the collapse of the whole structure (B). This event prompted the catastrophic collapse of subsequent layers of the structure (C–E). Unloading revealed the total collapse of the bottom layers of the structure (F). The scale bar in all the SEM images is equal to $10\mu m$.

an excessive tensile stress is exerted to a polymer, leading to microvoid nucleation and fibril formation at the crack front. Buckling of microlattice members led to the development of tensile stresses at one side of the beams that caused microcracking, as seen in Figs. 5.27(C) and 5.27(D) and Fig. 5.28. Considering the photoresist used to fabricate the metamaterial structures is classified as polymeric-ceramic hybrid, this failure mode matches the evidence derived from the HIM images.

Discussion

The increased stiffness, critical buckling load, and elastic strain energy density demonstrated by the architected microlattice structures are attributed to the tailored defects and substi-

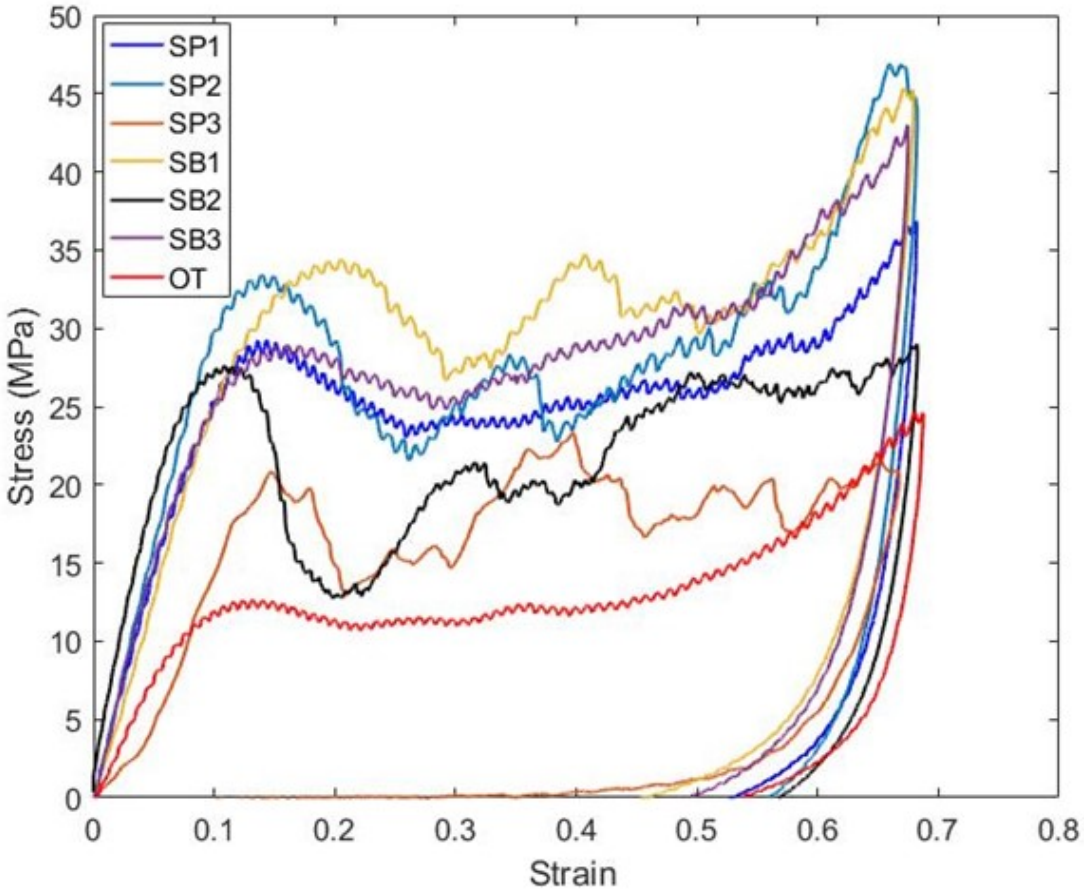

Figure 5.25: Stress-strain responses of metamaterial structures. The results indicate commensurate augmentation of the stiffness and strain energy density of all architected structures compared to the OT structure. The stress-strain responses of all structures are characterized by multiple regions of structural instability and post yield stress fluctuations, whereas the densification of the collapsed OT structure resembles macroscopic hardening, mitigating the buckling instabilities observed with the collapse of subsequent layers in the architected structures.

tutional unit cells introduced in the OT unit cells. The uniqueness of these enhancing mechanisms is that they lead to localized deformation at predetermined locations of the structure, promoting either post contact that leads to stiffening or inherent stiffening, as shown by the stiffness maps obtained by the FEA. In addition, the directional stiffness of the OT structure obtained with an analytical approach [2] was found to be in fair agreement with the FEA results of this study.

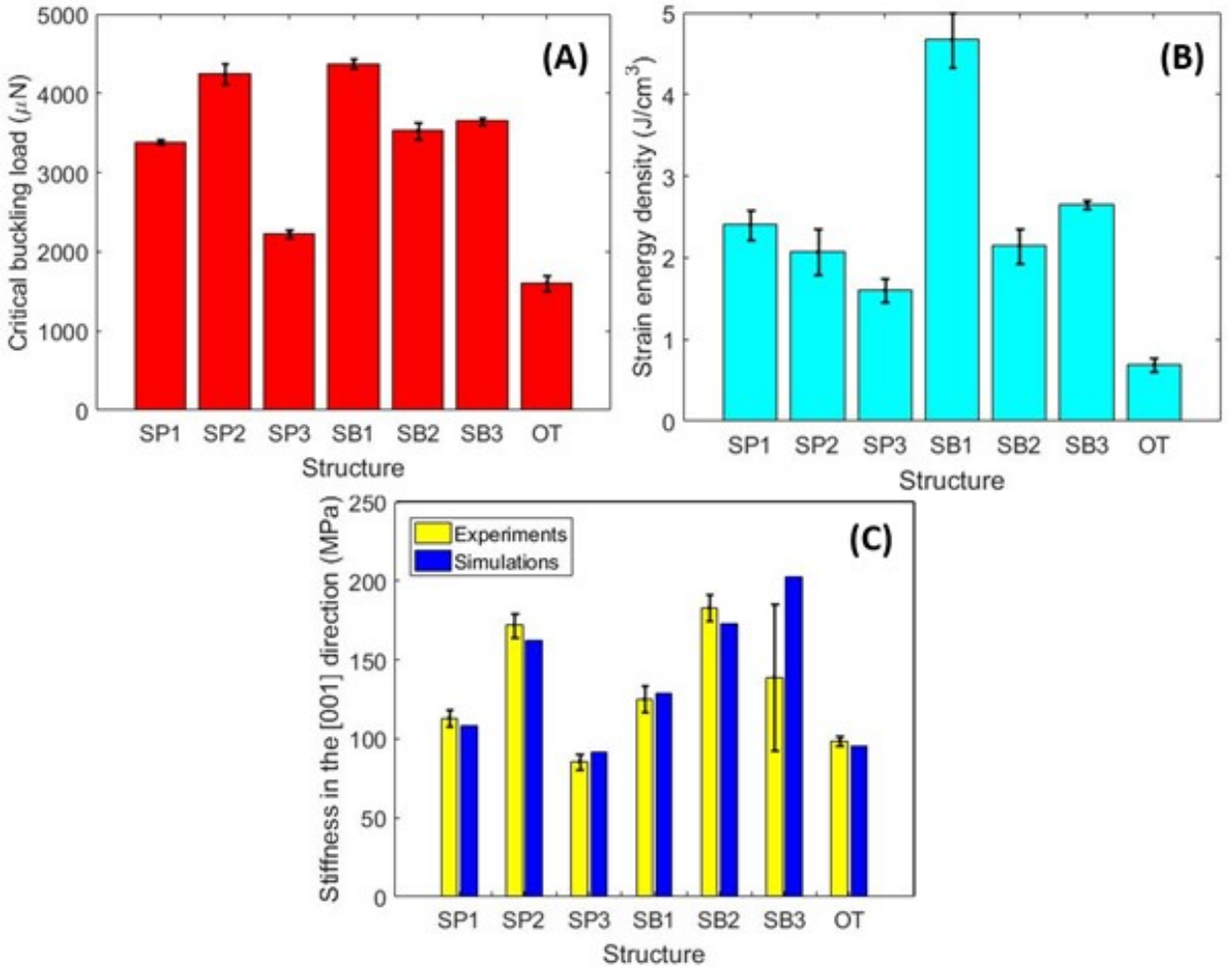

Figure 5.26: Experimental and FEA simulation results of the mechanical performance of metamaterial structures with fixed relative density ($\bar{\rho} = 0.025$). (A) Critical buckling load at the instigation of the first buckling event. All structures show a higher buckling load than the OT structure, indicating a significant enhancement of their structural integrity. (B) Strain energy density of each structure computed as the area under the stress-strain curve up to the first instant of buckling. The significant increase in elastic strain energy density exhibited by all architected structures is attributed to the increase of the critical buckling load and the post contact behavior of proximal microlattice members in some of the designs. (C) Comparison of experimental and simulation results of the structure stiffness in the [001] direction. Apart from the SP3 structure which, despite having fewer beam members, showed approximately the same stiffness with the OT structure, all other structures demonstrated significantly higher stiffness.

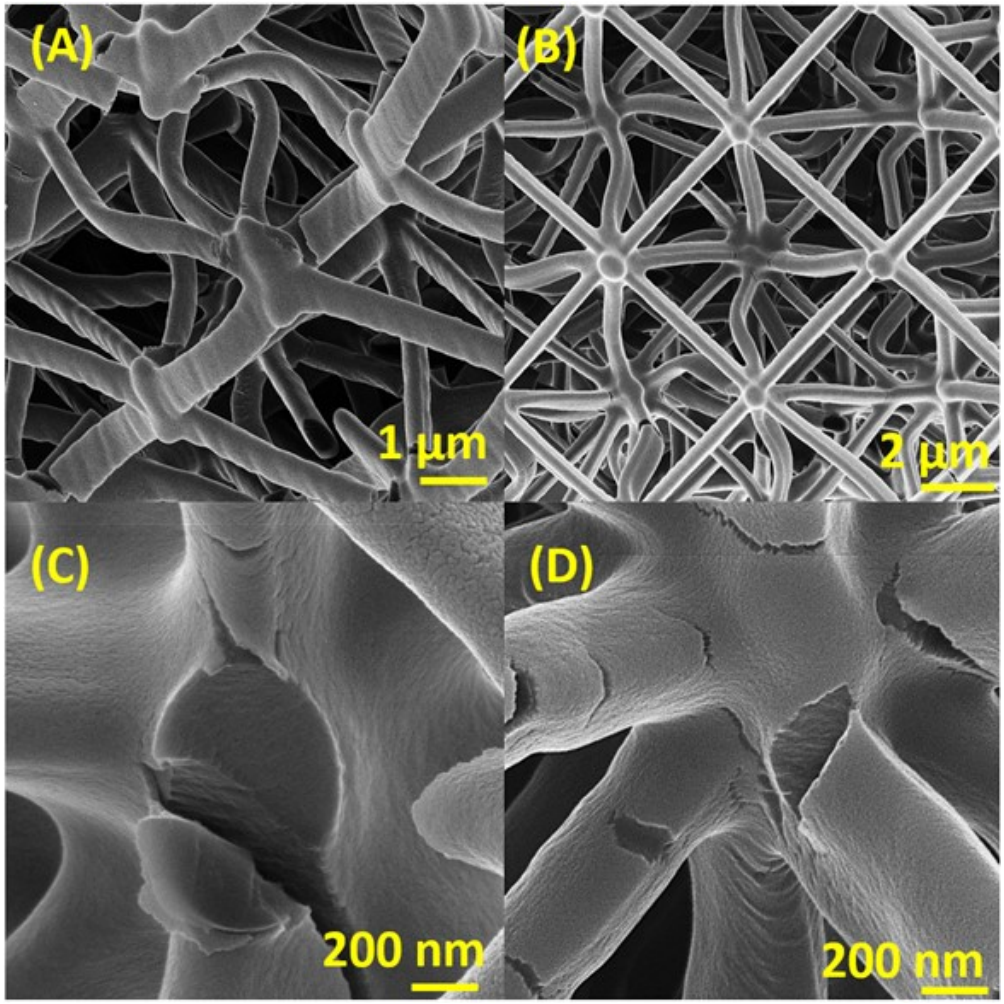

Figure 5.27: High-magnification images of fractured regions in SP1 and SB3 metamaterial structures obtained with a helium ion microscope. (A) Tilted view of fractured beam members in the SP1 structure revealing excessive deformation propelled by localized buckling. (B) Top view of a tested SB3 structure showing torsional deformation of the beams of internal layers and localized microcracking activated after buckling. (C) Characteristic fracture cross section of the SP1 structure. Despite the large deformation induced by buckling resembling ductile behavior, the lack of dimple formation on the fractured cross-sectional area and the extensive microcracking indicate brittle fracture due to crazing. (D) High-magnification image of the intersection of several microlattice members in the SB3 structure. Microcracking and the lack of texture (roughness) in the fractured cross sections indicate the dominance of brittle fracture.

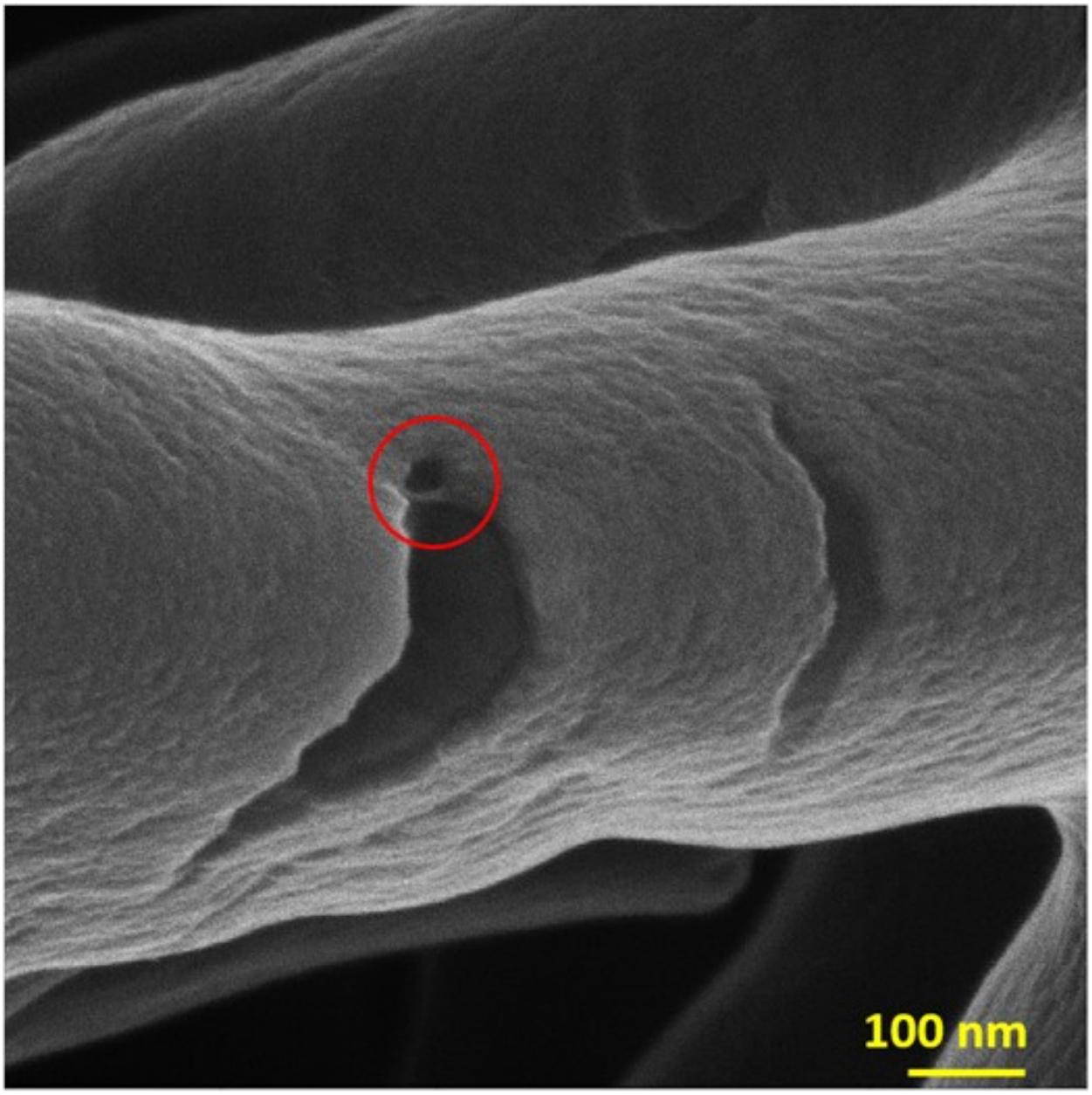

Figure 5.28: High-magnification HIM image of a fracture cross section of the tested SB2 metamaterial structure. The formation of fibrils (circled) and the lack of texture in the cross section indicate the occurrence of brittle fracture.

Although the present designs enhanced the mechanical performance in the [001] direction, other modifications can be employed to improve the performance in other directions. The intriguing result observed with the SEM is that localized buckling leads to a collapse

avalanche or uniform layer-by-layer failure. These mechanical behaviors have been inspired by and aimed to resemble mechanisms that strengthen and control failure in bulk materials [323, 12]. It is well established that defects affect the dislocation mobility and substitutional atoms cause hardening. The present study shows that their microscale equivalents can accomplish similar effects. While localized failure mimics dislocation movement or grain boundary failure, hardening is reflected by the higher stain energy density of the material and the increased resilience to buckling and fracture. Despite the fact that the deformation mode of the examined microlattice structures illuminates ductile behavior, the HIM images and video recordings revealed that the fracture behavior was actually brittle. Considering the previous work with intertwined metamaterial structures that provided insight into brittle-to-ductile transition [402], it may be inferred that utilizing these types of unit cells can potentially enhance the mechanical performance even more. Consequently, different unit cells or defects may further improve the performance of microlattice structures. For example, plate structures demonstrate the same stiffness in all directions [377].

Another interesting finding of this study is the different characteristics of the serrated force-displacement (stress-strain) profiles of the SP3, SB2, and OT structures. (The SP1, SP2, SB1, and SB3 structures demonstrated serrated stress profiles similar to that of the OT structure.). The SP3, SB2, and OT structures showed significantly different serrated stress profiles. Despite the fact that this mechanical trait was precipitated by means different from those of bulk materials, the stress patterns resemble bulk material behavior due to Portevin-Le Chatelier bands resulting from nonuniform plastic flow [65]. The regular stress fluctuations and high stress drops resembling type C bands [65] demonstrated by the SP3 structure are attributed to an avalanche mechanism. The initially small number of collapsing microlattice members activated an abrupt collapse of beams at the -45^o diagonal plane of the SP3 structure. Conversely, the SB2 structure yielded irregular stress fluctuations and smaller stress drops than the SP3 structure. The stress irregularity displayed by the SB2 structure was instigated by a change in collapse direction, evidenced by the uniform collapse of the -45^o diagonal plane, the sequential collapse of the 45^o diagonal plane, and, finally, the collapse of the bottom layer. The small stress fluctuations are attributed to the cumulative effect of buckling instabilities and beam microcracking events at both diagonal planes before the instigation of uniform beam failure at the diagonal planes. In a bulk material, such stress drops are classified as type A [65]. The OT structure demonstrated regular stress fluctuations and fixed stress drops resembling type B [65]. This behavior may be associated with a steady layer-by-layer collapse without changing direction. Again, the small stress drops may be ascribed to the agglomeration of instabilities and beam microcracking in each collapsing layer. It is noted that the SP3 structure did not collapse because of the concurrent instigation of microcracks along the diagonal planes but because of the increase of microfracturing events during deformation. While these mechanisms commence in bulk materials at different strain rates [65], the underlying reason for the incidence of these mechanisms in the tested structures was the structure architecture. Therefore, it may be argued that introducing architected defects in metamaterial structures provides an effective means for controlling the development of plasticity.

Although more complex polyhedral structures can be designed, increasing the array of structures also increases the complexity of the design. To overcome this difficulty, optimization tools, such as deep learning [245] and topology optimization [60, 56], can be instrumental in the design of metamaterial structures exhibiting a specific performance and even isotropic behavior. Nevertheless, topology optimization requires the use of continuous quantitative design variables and thus far has led to the design of monolithic lattice structures [60, 56]. Importantly, such optimization techniques are sensitive to the size of the design space. In previous studies of architected materials that utilized optimization methods, such as deep learning [245], machine learning [77, 458, 212], and Bayesian optimization [458], it was reported that using either qualitative or quantitative variables requires tens of thousands of initial random data to explore and exploit the design space and obtain the optimum structure, even for design spaces smaller than those of the present study [77, 458]. Therefore, such optimization methods can be effective when the simulations can be automated and performed expeditiously. However, the selective removal or alteration of microlattice beam members and the connectivity of different neighboring unit cells requires high computational time to design arrays of structures. Furthermore, if the cost functions that need to be minimized are related to a post yield or fracture material parameter, the computational cost to solve the boundary value problem or such complex arrays will be unaccountably high. The present study promulgates the necessity to develop optimization techniques necessitating a small number of data points that can be achieved with considerably lower computational cost. These tools are essential for optimizing complex 3D structure problems involving discrete non-monolithic lattices of large arrays. To further elucidate the intriguing complex deformation and fracture mechanisms of architected structures, more advanced modeling tools [122], such as the Kirchhoff rod theory [80], may be incorporated in the design methodology. The FEA simulations of this study revealed the initial evolution of stresses in the structures, illuminating the most likely locations of plastic deformation and microfracture. The simulation results qualitatively portrayed where failure may commence and did not require prohibitively expensive computation. To elucidate the post yield mechanical response, FEA elastic-plastic FEA analyses accounting for the evolution of localized fracture must be performed, significantly increasing the computational cost of the design analysis. Therefore, elastic material parameters should be used as proxy functions to improve the performance of the structure beyond the elastic regime and evaluate these intuitive results through experiments. Nevertheless, predicting instabilities due to localized buckling and microfracture from FEA simulations will provide further insight into their contribution to the stress drops observed in the post yield regime and avalanche and collapse mechanisms. Therefore, future work should also focus on minimizing the computational cost of such simulations.

Considering that scale effects that reveal brittle-to-ductile transitions have been reported [271, 402], performing fractography studies of architected structures designed at different length scales may yield invaluable insight into the scale-dependent deformation of mechanical metamaterials, providing impetus for the development of sophisticated FEA models. Because the observed localized failure mechanisms occurred in a few hundred nanometers and within a few hundred microseconds, high-resolution SEM imaging was critical to char-

acterizing the deforming structures. This investigation has shown that combining in situ SEM-nanoindentation, fast video recording, and high-resolution HIM imaging provides an effective methodology for studying deformation and microcracking processes at length scales of a few nanometers. Moreover, considering the significant enhancement of the mechanical performance of the microlattice structures examined in this study, it is imperative to extend the applicability of the MPL process to larger structure dimensions. Rapid fabrication of such architected structures on surfaces extending to several centimeters, while preserving nanometer-scale features, may facilitate metamaterial developments spanning a wide range of applications, such as structural materials, bio-implants, and even 3D tissue scaffoldings. Recent advances in mesoscale printing and 3D focal-field engineering are important steps toward this goal and the design of metamaterial structures with superior and controllable mechanical properties.

Section Conclusions

A new design strategy was developed in this study by introducing hybrid microlattice structures augmented with strengthening mechanisms that resemble those of crystal materials. The novelty of the designed architected structures is rooted in two principles. First, the tactical removal or alteration of microlattice members, inspired by defects observed in slip planes, aimed to control localized deformation at predetermined positions and, ultimately, enhance the structure properties. Second, the incorporation of substitutional unit cells that distort the symmetry of the microlattice structure in proximal regions, precipitating the same effects as the first design principle.

FEA simulations revealed how the directional stiffness of the structure can be increased in predetermined locations and directions, whereas in situ SEM-nanoindentation experiments with structures fabricated by a modified MPL process revealed how the microscopic (localized) mechanical response manifests itself into the significant increase of the stiffness, strain energy density and overall mechanical integrity of the structure. Thus, a noteworthy finding of this study is how the mechanical behavior of microlattice structures consisting of stiff and strong metamaterial structures can be significantly improved compared to their monolithic counterparts. Another valuable contribution of this work is the insight into the complex deformation modes of internal unit cells accomplished by HIM imaging, particularly the illumination of large deformations that resemble ductile behavior and fracture mechanisms associated with crazing. From a more general perspective, the present investigation introduced a new methodology for modifying the mechanical behavior of 3D microlattices, furnishing 3D artificial defects and unit cells in strategic locations of the array of the architected structure.

5.3 Strength through Defects: A Novel Bayesian Approach for the Optimization of Architected Materials

Section Summary

In this section a novel Bayesian optimization (BO) to systematically design the arrangement of defects in an architected microlattice to maximize its strain energy density prior to undergoing catastrophic failure is employed. The BO searches a design space with more than four billion 4x4x5 3D lattices, yet it finds the global optimum with only 250 cost function evaluations. This optimum has a normalized strain energy density four orders of magnitude greater than its commonly studied defect-free counterpart. Traditional optimization is not possible for this microlattice because (1) the design space has discrete, qualitative parameter states as input variables, (2) the cost function is computationally expensive, and (3) the design space is large.

Problem Setup

Design of the Problem

Fig. 5.29 illustrates the design scheme used to obtain and validate the optimum structure. The objective is to design an optimal, non-monolithic microlattice consisting of discrete unit cells. In this study, we use 4 different unit cells, henceforth described as states. Each of these 4 possible states, shown in Fig. 5.29(a), is labeled by a letter A, B, C, or D. The octet truss unit cell [91] without any defects is labelled with A, and hereafter is referred to as the unblemished structure. Unit cells B, C, and D have missing members. We selected them as inputs because a lattice made up with any combination of them has sufficient rigidity and will not collapse under its own weight [153, 393, 392]. Furthermore, lattices made of these 4 cells will not have a disproportional reduction in structural stiffness [153, 393, 392]. These unit cells, or states, are positioned in a $4 \times 4 \times 5$ array. Note that there are 5 layers in the "extruded" direction of the microlattice. That is, whatever 4×4 array of cells is selected (e.g., the structure shown at the bottom of Fig. 5.29(a)) is exactly repeated in all 5 layers of the extruded direction. The reason that our array is this size is due to computational cost, which is addressed in the next section. The 16 qualitative design variables (i.e., the lattice sites of the 16 unit cells) can each have four possible states. However, there is one additional important design variable: the relative orientation of the unit cells. Adjacent cells can be connected either at their faces (labelled as state F in Fig. 5.29) or their edges (state E). This two-valued state is the 17^{th} variable of the problem. The reason for selecting only these two orientations is that other orientations would lead to a non-cuboid distortion of the lattice, and allowing that distortion in the design space would significantly increase the complexity of our search. Fig. 5.29(a) shows a compact way to symbolically represent the 17 inputs of

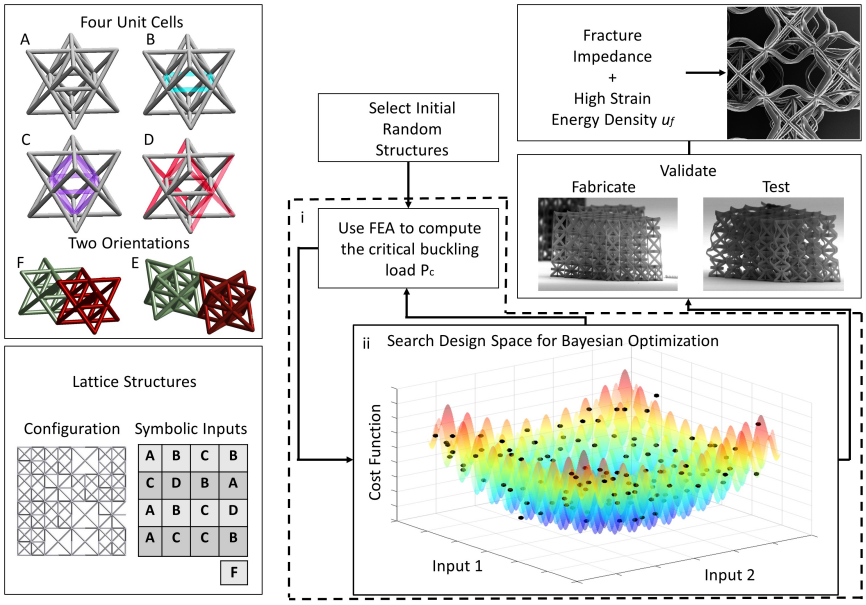

Figure 5.29: (a) Classification of inputs. *Top*: Four types of unit cells: (A) unblemished (no missing members); (B) defected (4 missing members shown in cyan); (C) defected (12 missing members shown in purple); and (D) defected (16 missing members shown in red); *Middle*: Schematic of orientations; *Bottom left*: Schematic of the 2D cross section of the 3D lattice in the plane perpendicular to the extrusion, showing 4×4 unit cells; *Bottom right*: Symbolic representation of the lattice, where a letter F or E in the right-most box indicates that all the unit cells are either aligned or rotated by 45°. In both orientations the structure is perpendicular to the load (vertical) direction. Thus, the input has 16 dimensions with 4 possible values and 1 dimension with 2 possible values. (b) Flow chart beginning with the selection of 50 initial random microlattices (and 5 "intuitive solutions" – see text). The two-step iteration loop, shown within the box with broken lines, consists of (i) FEA evaluation of the critical buckling load P_c, of a microlattice structure, i.e., the proxy cost function minimized by the BO algorithm, and (ii) the BO search algorithm that produces the 17 input values of the next microlattice to be evaluated. The search space of the BO for the *cost function* is illustrated with a schematic showing 2 of the 17 dimensions of one of the test functions on which we tested our BO algorithm. The solid black circles represent the true values sampled from the black-box function and the continuous surface represents the Gaussian process fitted to the data, which is detailed in the EM section. Like the actual design surface of the lattice, this function has many false minima. After the two-step iteration loop is exited, the optimal design is fabricated and tested as illustrated with SEM images of the microlattice structure *before* loading and *after* the instigation of buckling. Our objective is optimizing the impedance of fracture due to the early commencement of buckling modes, illustrated in the HIM image, and consequently the increase of the strain energy density.

a design: the unit cells in the $4\sim \times \sim 4$ array and their orientation.

Fig. 5.29(b) shows the optimization scheme of the problem. Ideally as a load is applied to a lattice, our optimization goal would be to maximize the strain energy density of the lattice, while maintaining the lattice's structural integrity and stiffness before fracturing. To achieve this goal, a numerical code would be required to compute the static behavior of the lattice in its elastic domain and its elastic-plastic domain (where post contact of lattice members induces densification) at the instigation of fracture-induced collapse. For the optimization of a 3D lattice with thousands of beam members, this analysis would need to be repeatedly carried out, which would be prohibitively costly with any search method. Furthermore, this optimization goal presents difficulties with respect to experimental fabrication and verification. Since the MPL polymerization process is a near-threshold phenomenon [468, 343, 299], we have observed that small variations in the process can affect the plastic performance [393, 392]. Hence, the strain energy density at fracture collapse u_f and other post-yield constitutive parameters of the fabricated lattices, such as the back stress modulus, yield function, tensile flow resistance, and rate of strain-hardening, are likely to be too sensitive for a valid comparison between experimental and numerical results.

To mitigate the problems of the high computational cost of numerically optimizing u_f and the inherent sensitivities in the mechanical properties of the fabricated materials, we conceived another metric to optimize the structure: the structure's critical buckling load P_c. Our motivation for choosing P_c as the proxy cost function to be *minimized* is that the large deformation of lattice members instigated by buckling instability leads to the densification and stiffening of the structure by the post contact of the deformed lattice members. The consequence of densification is that fracture is impeded despite excessive plastic deformation. Using P_c as the proxy performance function to be minimized is advantageous because the calculation of P_c does not require excessive computation since P_c can be determined by solving an eigenvalue problem in the elastic domain. Moreover, P_c depends on parameters that characterize the deformation of the structure in the easier-to-compute elastic domain. Not only is the optimization with this proxy less expensive to compute, but the laboratory measurement of P_c is not overly sensitive to fabrication variations. In previous sections, it was found that the elastic modulus and Poisson's ratio are relatively more insensitive to variations of the fabrication conditions [393, 392]. Although the effect of buckling deformation on densification is well established [140], there is not a succinct, closed expression that relates the critical buckling load P_c to the strain energy density at fracture-induced collapse u_f. In part this is due to the fact that u_f depends on properties in the elastoplastic contact and fracture regime, while P_c depends on those in the elastic regime. However, we show below that laboratory experiments demonstrate that minimizing the critical buckling load leads to an exponential increase of the structure's strain energy density; therefore, a small P_c is a very good proxy for large u_f.

The flow chart in Fig. 5.29(b) shows that our optimization method is initialized with 50 randomly chosen lattice structures. The main work needed to achieve optimization is carried out in a two-step *iterative loop* (shown by the steps within the dashed lines). The first (and most computationally expensive) step (i) is the FEA calculation of the P_c of *either* the 50

random structures (but only for the first iteration of the loop) *or* the calculation of the P_c of the new lattice design that was selected by the BO algorithm (step (ii)) in the previous iteration. The algorithm exits the iterative loop with an "optimally designed" lattice, i.e., with the *globally* minimized P_c. As shown in Fig. 5.29(b), step (ii), our 17-dimensional search space has many *local* minima. A key strength of our BO search is that it does not become "stuck" at a local minimum, but moves on to find the global minimum. Once found, that optimum lattice is then fabricated and tested.

The Bayesian optimization algorithm

Optimization techniques, in general, are used for optimizing functions with *ordered* continuous, input states. If an input is a real number or an integer, it is an ordered input state. In our problem, an input state is a unit cell or an orientation with no inherent numerical value i.e. a *qualitative* variable. Even non-convex optimization problems in which all of the inputs are quantitative variables can often be efficiently solved with gradient and other standard methods, but for our optimization problem the qualitative inputs rule out these methods. A defining property of our optimization problem is that step (i) of the iterative loop, where the cost function (i.e., P_c) is computed, is much more costly to evaluate than step (ii), where the search algorithm determines the next set of input values (i.e., the 17 values in Fig. 5.29(a)) to be evaluated. In optimizations like ours, it is highly advantageous to choose a search algorithm that converges to the optimal solution *with the fewest possible iterations of the two-step loop*, even if it requires a slight increase in the cost of step (ii).

The novel BO used in step (ii) is a powerful sequential optimization technique that we adapted for use with input variables that are discrete parameter states and that uses all of the information about the cost function that was obtained from the random initial structures *and* from all the materials tested in the previous iterations of the two-step loop. The task of the BO search is to find the lattice with the globally minimum P_c in a 17-dimensional design space where 16 inputs have 4 input states (i.e., the 4 unit cells) and 1 input with 2 states (i.e., the 2 orientations). Because the lattice is reflection-symmetric about the middle plane, which is orthogonal to the load and transverse directions (see Fig. 5.29(a)), the number of possible, physically independent, inputs, or structural configurations is $(4^{16}\times 2)/2 \simeq 4.3\times 10^9$. Running our BO algorithm with optimization searches on test problems with known values of their global minima (see the next section) and with complexities and dimensions similar to our microlattice optimization problem, we determined that our BO would find the global minimum of P_c in the $4\sim \times \sim 4$ lattice with 4 units cells and 2 orientations within 250 evaluations of the cost function. Choosing a bigger microlattice or a microlattice with more than 4 different types of unit cells would increase the number of possible configurations as well as the number of FEA evaluations of P_c needed to find the optimum and therefore become significantly more costly. For example, increasing the number of possible unit cells from 4 to 5 would increase the design space by a factor of 35.5; increasing the lattice to $4\sim \times \sim 5$ from $4\sim \times \sim 4$ sites increases the space by a factor of 256. However based on our

experience in optimizing the test functions, it is granted that the microlattice design selected by the BO after 250 evaluations (Fig. 5.29(b)) is a global optimum.

Compared to other optimization techniques, 250 evaluations for this 17-dimensional problem is very small. For example, our numerical experiments on searches with our test functions showed that GAs require an order of magnitude more evaluations of the cost functions to find the global minimum than our BO required. Unlike the tests of the BO described in the next section, the search used in the actual optimization of the lattice was initiated not only with the P_c values of 50 random lattices, but also with the P_c values of 5 lattices that we refer to as "intuitive solutions" that were selected, fabricated, and tested, because studies by others (or our own intuition) suggested they might be near optimal. In fact, as discussed in the next section, they were not even close to optimal. If this study were focused on the mathematical analysis of the BO, we would not have included the five "intuitive solutions" in the initial data of the BO; however, we included them here because the focus is to find an optimal design.

Testing the robustness of the Bayesian optimization algorithm

Our BO algorithm was tested using five functions, including the Rastringin, Syblinski-Tang, and spherical functions that are often used in optimization studies. In addition, we tested our BO with the *amalgamated function*, which we created to have features of several standard test functions. However, unlike many standard functions that are isotropic (i.e., each of the 17 inputs affects the test functions in the same manner), with independent dimensions, the amalgamated function, like the lattice, is anisotropic and some of its input dimensions are dependent upon others. The values of these four functions, which *are* the cost functions that we seek to minimize, are defined with respect to continuous ordered inputs. We show how we discretize the 17 inputs, so they have 4 possible discrete states, like our lattice optimization. The fifth test function we used is the *encrypted* amalgamated function, designed to simulate qualitative, rather than ordered, inputs. This is done by randomly encrypting the input values. For ease of the analyses, we shift the output values (i.e., the cost function) of the test functions so that the global minima are all zero.

The test results in Fig. 5.30(a) show the value of each cost function as a function of its evaluation number n. (Note that the iteration number of the BO is equal to the evaluation number n minus 50 because there are 50 initial, random configurations that need to have their cost functions evaluated.) The plotted value of the cost function at n is not the cost function of the n^{th} evaluation, rather it is the minimum value of the cost function for all evaluations with evaluation number less than or equal to n. Therefore, the first cost function value plotted, and labeled as $n = 50$, is the smallest value of the cost function of the 50 random initial configurations. We have scaled, or normalized, each of the test functions such that the value of its cost function at $n = 50$ is unity. Therefore, each optimization of a test function in Fig. 5.30(a) begins with unity and monotonically decreases. If the BO reaches the global minimum, the cost function will be zero. We ran each of the five test functions 10 times, each time with a different set of 50 random configurations (and for the encrypted amalgamated

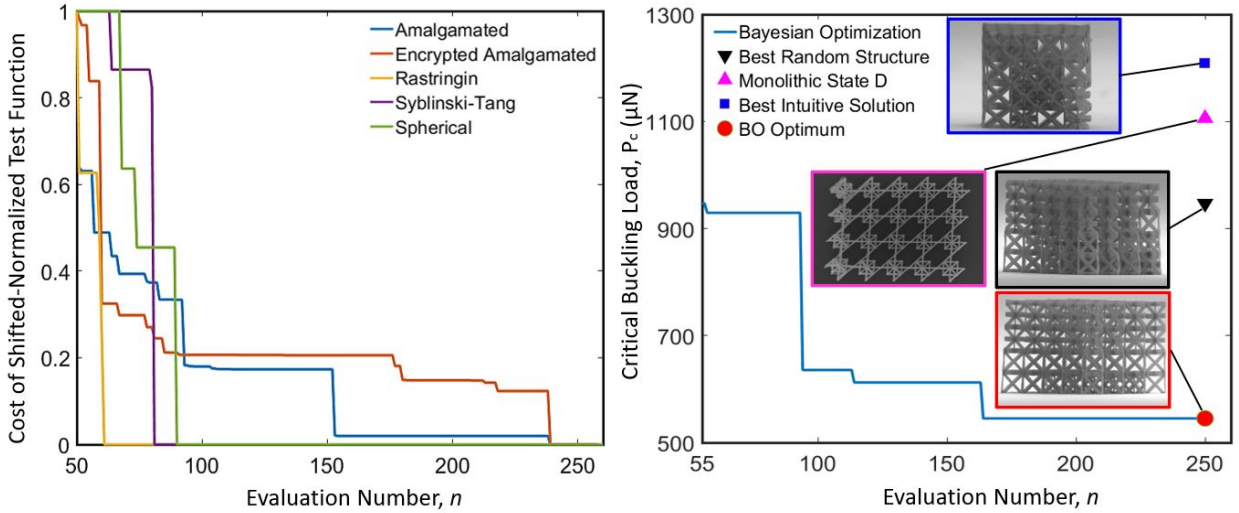

Figure 5.30: (a) Convergence tests of our BO algorithm with the normalized and shifted amalgamated, *encrypted* amalgamated, Rastringin, Syblinski-Tang, and spherical test functions in 17 dimensions, each dimension with 4 discrete inputs. Each of the test functions was "shifted" by adding a constant to it so that its global minimum in the discrete search space of input values is zero. The shifted test functions were then evaluated with 50 random configurations, and the minimum cost function value was defined as the norm. Each test function's value was divided by its norm so its shifted and normalized "cost" was unity after the 50^{th} evaluation. The cost function of the optimized configuration is zero. (b) Convergence of the BO algorithm for the FEA-computed critical buckling load P_c of the microlattice plotted as in Fig. 5.30(a) but for the lattice the cost function is not shifted or normalized. Evaluations 1-50 are for random configurations, 51-55 for our initial intuitive solutions (see text), and 56-250 for the 195 configurations determined by the BO algorithm. The insets in panel (b) show SEM images of the structures with 4 fabricated states: the random structure with the lowest P_c, the monolithic state D made of only D unit cells; the intuitive solution with the lowest P_c; and the BO optimum, or optimal lattice found with the BO algorithm (see text for details of these structures). The colored symbols at evaluation 250 show the respective P_c values of these configurations. Our five intuitive solutions turned out to have very non-optimal P_c, which is one of the reasons we believe that systematic BO searches are needed to design optimal materials.

test function case, different random encryptions). All 50 tests reached the global minimum (fully optimized), with little variation among the 10 runs of each test function. Fig. 5.30(a) shows one BO search for each of our test functions.

Results of the Bayesian Optimization

Applying the BO algorithm to optimize architected microlattice structures

Fig. 5.30(b) shows the results of using the BO algorithm to optimize the lattice problem initialized with 50 random lattices. In addition, 5 microlattice structures that we call the "intuitive solutions" were also used in the initialization. These lattices were based on the proposed design principles for the strain energy density [393, 392].

These 5 structures have defected states in their $\pm 45^{\circ}$ planes, leading to localized collapse that imitates the failure of bulk materials at the planes of maximum shear [393]. From those 5 structures, the one with the lowest P_c, referred to as the "best intuitive solution", was fabricated and tested, along with 8 structures that were randomly generated. These structures were fabricated by the MPL process. The 17 inputs of the fabricated materials and the numerical values of their P_c are given in Tables 5.8 and 5.9. These structures were tested and the average difference between experiments and simulations with respect to P_c was found to be equal to 7.4%, indicating a good match between experiments and simulations. Fig. 2b shows results of the optimization algorithm. After 160 evaluations of the P_c (or $105 \equiv (160 - 55)$ BO iterations), our search found a structure with a critical buckling load 42.4% less than that of the best random structure. Since the algorithm did not find any better solution for the remaining 90 BO iterations, we defined this lattice to be the "BO optimum". The P_c of the BO optimum is 85.7% less than that of the defect-free unblemished structure.

However, there are 4 other microlattice structures that we deemed important to evaluate. We anticipated that the lattice with the lowest P_c should be a configuration consisting of only one of the four units cells. The logic being that if one unit cell is better than all of the others, then a lattice made up of only those superior unit cells would be the optimal lattice. Therefore, we evaluated the P_c values of the A, B, C, and D unit cells. Thus, we found an *ordering* of the P_c values of the unit cells. The P_c values of the A, B, C, and D unit cells are 338.23, 290.72, 131.68, and 32.59 μN, respectively. Moreover, a lattice structure comprised only with monolithic state D has a critical buckling load equal to 964.68 and 1130.32 μN, for connection at the edges (E) or at the faces (F), respectively. [1] In addition, the P_c values of $4\sim \times \sim 4$ monolithic microlattices made up exclusively of unit cells A, B, C, or D, have the same ordering as the P_c values of the unit cells. Moreover, the $4\sim \times \sim 4$ microlattice with only D unit cells connected at their edges (17^{th} design variable = E), has lower critical

[1] We had originally believed that we could quantitatively order the state inputs A, B, C, and D to reflect the relative ordering of their P_c values. By doing so, we could have then used a search method or a BO with ordered, rather than qualitative, inputs. However, tests with our BO using encrypted amalgamated function showed that the ordering of inputs did not affect the performance of search.

Structure	1	2	3	4	5	6	7	8	9	10	11	12	13	14	15	16	17
1	B	D	D	D	C	D	D	D	B	C	D	C	A	C	C	C	E
2	C	D	D	D	C	C	D	D	C	C	D	C	D	D	D	C	E
3	D	C	D	D	D	D	C	D	C	C	C	C	C	C	B	C	E
4	D	D	D	A	D	D	C	C	D	D	D	C	D	D	D	D	F
5	D	D	D	D	D	D	D	D	D	D	D	D	D	D	D	D	E
6	D	D	D	D	D	D	D	D	D	D	D	D	D	D	D	D	F
7	A	D	D	D	D	C	D	C	D	C	D	D	C	D	C	D	F
8	A	A	A	C	C	B	C	D	C	C	C	D	C	C	D	D	F
9	C	C	C	D	C	D	D	C	C	D	D	C	D	C	C	B	F
10	D	D	D	A	A	A	C	D	D	D	C	D	D	C	D	C	F
11	A	A	C	C	C	A	A	C	C	A	A	D	C	A	C	D	F
12	C	C	B	C	B	C	C	B	B	C	C	B	C	B	B	C	F
13	B	B	C	C	B	C	B	B	C	C	B	C	B	B	C	C	F
14	A	A	A	A	A	A	A	A	A	A	A	A	A	A	A	A	F

Table 5.8: Tested microlattice structures. Each row of letters corresponds to the 17 values of the input variables as defined in Fig. 5.29(a) of the main text. Row 1: BO optimum structure. Row 2: BO penultimate optimum structure. Row 3: BO antepenultimate optimum structure. Row 4: example of the 50 initial random structures. Row 5: monolithic state D. Row 7: example of the 50 initial random structures. Row 8: best intuitive solution. Rows 9-13: examples of the 50 initial random structures. Row 14: unblemished structure.

buckling load compared to the microlattice with D unit cells connected at their faces (F). Hence, we speculated that the optimum lattice had only D cells connected at their edges. We call this the "monolithic state D." However, Fig. 5.30(b) shows that the P_c of the BO optimum is 43.4% less than that of the monolithic state D, which is opposed to our initial expectation based on mechanics principles only.

The 17 input values of the BO optimum lattice that uniquely determine its structure along with its P_c are listed in the first row of Table 5.8. Fig. 5.30(b) shows SEM images of the fabricated best random structure, the monolithic state D, and the BO optimum. Note that 17 input states of the BO optimum have no discernible pattern that would have led to its design by intuition. The reduced P_c and the unexpected structure of the BO optimum not only support the efficiency of BO, but also, more generally, the argument against the use of intuition in designing materials.

Structure	$P_{c_{num}}(\mu N)$	$P_{c_{exp}}(\mu N)$	$u_f(MJ/m^3)$	$S(MPa)$	$\frac{(u_{f1}/u_{b1})}{(u_{fi}/u_{bi})}$
1	545.1	547.1 ± 30.5	14.71 ± 0.23	460.35 ± 2.25	1
2	592.4	669.9 ± 29.9	13.82 ± 0.35	351.04 ± 4.18	2.09
3	610.1	685.4 ± 47.4	8.79 ± 0.14	248.18 ± 3.27	4.87
4	996.2	938.6 ± 33.7	2.85 ± 0.17	347.19 ± 5.62	20.12
5	964.7	1106.0 ± 54.1	2.51 ± 0.28	208.53 ± 1.98	52.80
6	1130.3	1378.2 ± 127.4	2.99 ± 0.31	267.19 ± 7.76	53.75
7	1140.9	1182.5 ± 45.3	2.99 ± 0.41	303.65 ± 6.51	34.80
8	1135.6	1209.1 ± 80.3	3.08 ± 0.05	295.87 ± 2.89	36.22
9	1079.2	1147.9 ± 77.8	1.95 ± 0.11	275.19 ± 6.41	87.90
10	1141.5	1317.6 ± 101.2	3.95 ± 0.23	379.66 ± 1.12	26.15
11	1483.1	1409.7 ± 75.6	1.63 ± 0.51	363.28 ± 5.52	75.70
12	1471.6	1460.4 ± 55.2	1.29 ± 0.07	385.93 ± 4.38	96.7
13	1764.5	1837.0 ± 78.6	0.52 ± 0.19	342.13 ± 10.05	429.1
14	3814.5	3905.8 ± 67.7	0.071 ± 0.005	388.21 ± 5.43	12464

Table 5.9: Numerically and experimentally obtained values of the critical buckling load $P_{c_{num}}$ and $P_{c_{exp}}$, respectively, the experimentally measured value of the strain energy density at fracture u_f, and the elastic stiffness S of the tested microlattice structures. The numbering is the same as in Table 5.8. Uncertainties are the rms values of the experimentally measurements of the fabricated structures. The last column is the ratio of the normalized strain energy density for the BO-optimum structure compared with the other structures.

Properties of the BO-optimized microlattice structures

To assess the effect of the critical buckling load on the mechanical response and strain energy density of the microlattice structures, additional specimens were fabricated (14 in total). Apart from the structures mentioned in the previous section, i.e., the three best solutions determined by the BO algorithm, the unblemished structure comprised only of state A and the monolithic structure with state D were also fabricated. The arrays of the 14 different geometries are given in Table 5.8. The results of the measured buckling load P_c, strain energy density at fracture-induced collapse u_f, and measured stiffness S are summarized in Table 5.9. As shown in Table 5.9, the BO optimum possesses substantially lower critical buckling load compared to the other geometries and there is close match between the experiments and simulations.

Fig. 5.31 shows illustrative results revealing the mechanical performance of microlattice structures. The stress-strain curves shown in Fig. 5.31(a) and Fig. 5.32 indicate that the design determined by the BO algorithm sustained fracture at significantly larger deformation compared to the unblemished structure, the best intuitive structure, and the monolithic

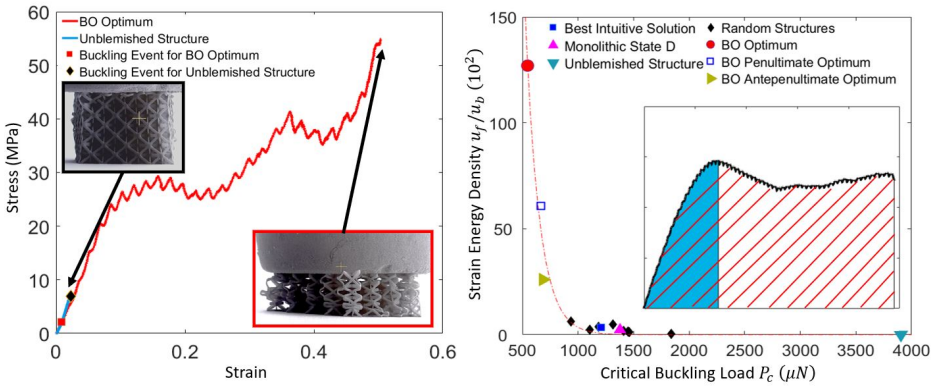

Figure 5.31: Mechanical performance of microlattice structures. The commencement of buckling is indicated by a square for the BO optimum (red) and a diamond for the unblemished structure (black)). (a) The prematurely instigated buckling in the optimum structure found by the BO algorithm precipitated an "avalanche" of buckling events, leading to densification of the structure and the impedance of fracture (shown in the SEM image). Because buckling occurred at a later deformation stage of the unblemished structure, fracture was not obstructed, resulting in early collapse of the first layer (shown in the SEM image) and lower strain energy density before fracture. (b) Experimentally determined critical buckling load P_c versus strain energy density at the instant of fracture collapse u_f normalized by the strain energy density at the onset of buckling u_b. The results show that $1/P_c$ is a good proxy function for u_f; as P_c decreases, u_f increases. With only 14 non-randomly selected points, this figure should *not* be used to infer to *correlations* between u_f/u_b and P_c. The strain energy density of the optimum structures is 12,464 times that of the unblemished structure. *Inset*: schematic to determine the onset of buckling. The critical buckling load P_c at (B) is calculated upon the commencement of an instability and is consistent with the onset of deformation in the videos (published in the near future). With the progression of deformation, fracture of the layers or conglomeration of beam members occurred, leading to the collapse of the structure (F). The blue, black-lined (red-lined) shaded area represents the strain energy density u_b at the onset of buckling (at fracture u_f). In the schematic, u_f and u_b are commensurate for illustrative purposes.

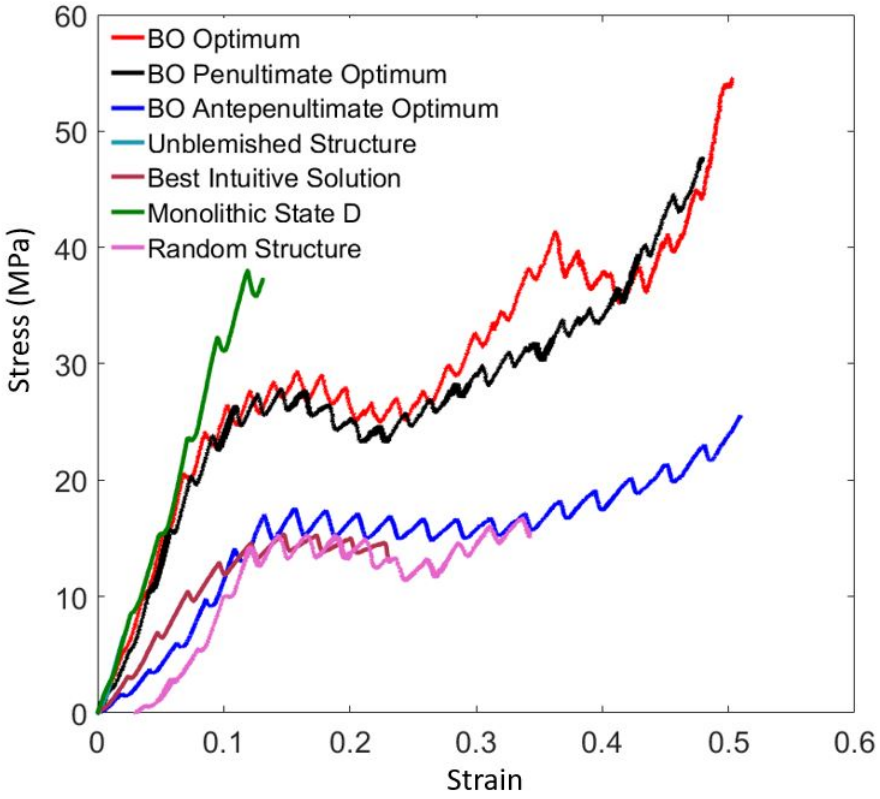

Figure 5.32: Mechanical performance of the BO optimum (# 1 on Table 1), BO penultimate optimum (# 2), BO antepenultimate optimum (# 3), unblemished structure (# 14), best intuitive solution (# 8), monolithic state D, (# 5) and representative random structure (# 11).

structure with state D. To evaluate the delaying of fracture-induced collapse, the deformation of the unblemished and the BO optimum structures were recorded and are presented in Video 1 and Video 2, respectively. For the case of the unblemished structure (Video 1), shortly after the beginning of the loading, the first layer begun to undergo buckling and almost instantly collapsed, resulting in the fracture-induced collapse event shown in the SEM image of the inset of Fig. 5.31(a) and indicated by the diamond symbol. As the indenter continued to load the structure, the next layer that carried the load also sustained fracture-induced collapse and the same mechanism occurred in the subsequent layer. Nevertheless, it is shown in Video 2 that the unblemished structure sustained buckling almost instantly after the initiation of loading (marked by the red box in Fig. 5.31(a)), resulting in contact of the beam members. This mechanism obstructed fracture-induced collapse of the layers due to the densification of the structure. The stress-strain curves of the optimum structures

show serrated profiles, indicating the conglomeration of buckling and post-contact events prompted by densification, which is the same mechanism that has been investigated in our previous work [392]. In the light of Video 2, the layers of the structure sustained plastic deformation and fracture commenced only at 50% of deformation, which is verified by the video recording. The deformed structure just before the instigation of fracture is shown in the inset of Fig. 5.31(a) . As it will be shown later, this was also verified by high-depth-of-focus imaging of the tested specimens. While such responses can be efficiently characterized for a limited number of experiments, such a complex 3D mechanical response beyond the plastic domain is extremely computationally expensive to be attained with FEA simulations and then compared with experimental results obtained at the microscale for the reasons interpreted earlier. The effectiveness of the choice of the proxy cost function is illustrated in Fig. 5.31(b), where the normalized strain energy density u_f/u_b is plotted against the critical buckling load P_c, where u_b is the stain energy density at the instigation of buckling. This normalization is used to enable focusing on the effect of the critical buckling load on the mechanical response after the occurrence of buckling. The normalized strain energy density of the optimum structure is 12,464 times higher than that of the unblemished structure. The ratio of the normalized strain energy density of the other structures with respect to the BO optimum is given in Table 5.9. Even without normalization the strain energy density of the optimum structure is 203 times higher than that of the unblemished structure, one of the most thoroughly investigated and utilized architected geometries [456, 25, 466, 264, 377, 91, 265, 63, 363, 153, 393, 392, 306, 140, 344]. The strain energy density corresponding to the three best solutions determined by the BO algorithm shows a high sensitivity to the critical buckling load. While the mechanics responsible for the observed direct correlation between u_f/u_b and P_c with respect to the selected states requires further investigation, Fig. 3b shows that the selected cost function yields a solution that is orders of magnitude better than that of the unblemished structure. It is noted that in previously reported results relying solely on mechanics principles, the best result was inferior by just one or two orders of magnitude [393, 392]. Moreover, although the random structures and the rest of the defined designs also exhibit one or two orders of magnitude higher u_f/u_b than the unblemished structure, they do not approach the optimum structure because they do not posses such a low P_c. In comparison with previous studies that did not employ optimization [312, 153, 393, 392], this result illuminates the unique effectiveness of our BO algorithm. Nevertheless, it is also important to elucidate these results in the light of the perspective deformation profiles of the tested specimens.

Fig. 5.33 shows high-resolution images of undeformed and deformed microlattice structures obtained with helium ion microscopy (HIM). HIM was selected since it provides high resolution and high depth of focus that cannot be accomplished by other imaging techniques, enabling the effective characterization of the internal members of the structure. The unblemished structure (Fig. 5.33(a)) sustained excessive collapse of the top layer (Fig. 5.33(b)), which propagated and proliferated in the next layers and the internal beam members (Fig. 5.33(c)). However, the optimum structure (Fig. 5.33(d)) demonstrated excessive buckling rather than catastrophic collapse and almost no fracture (Fig. 5.33(e)). The deformed buck-

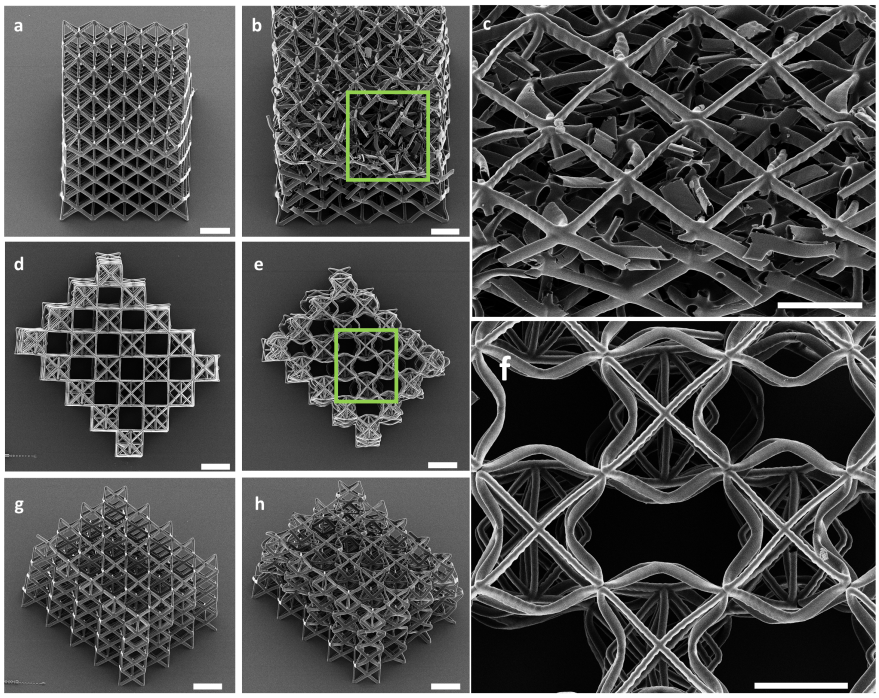

Figure 5.33: HIM images of the loaded and unloaded unblemished and optimum structures. (a) Image of the unblemished structure consisting only of units cells of type A as in Fig. 5.29. (b) Same as (a) but after loading, showing severe fracture and collapse of many beam members. (c) High-depth-of-focus image of the region inside the square box shown in (b) revealing several fractured beams and the internal collapse of the upper layer that subsequently instigated the accumulation of damage in the underlying layers. (d) Same as in (a) but for the unloaded optimum structure. (e) Same as in (b) but after the structure was subjected to the same maximum compressive load as the structure shown in (b). Unloading of the optimum structure showed only excessive plastic deformation without catastrophic collapse and the manifestation of the buckling mode. (f) High-depth-of-focus image of the region inside the square box shown in (e) revealing the effect of buckling that led to deformation but no fracture due to the occurrence of densification. (g) Side view of the unloaded optimum structure shown from an isometric view. (h) Side view of the unloaded optimum structure shown from an isometric view revealing that fracture was inhibited throughout the structure due to the densification precipitated by the low critical buckling load. Each scale bar is equal to $10\mu m$.

ling mode shows the out-of-plane buckling mechanism of beam members that was observed in Video 1 (Fig. 5.33(f)), without the total collapse of the layers, conversely to the unblemished structure. Fig. 5.33(g) shows a side view of the optimum structure before testing. The large deformation of the array induced structure densification, which, in turn, inhibited fracture, leading to partial deformation recovery of the array upon unloading (Fig. 5.33(h)). A comparison of the mechanical responses of the unblemished and optimum structures reveals the remarkably improved mechanical performance determined by the BO algorithm based on the minimum critical buckling load. It was observed that the monolithic structure with state D also sustained premature fracture due to the delay of the instigation of buckling (Fig. 5.34). A random orientation of defected states does not provide the same response as the optimum structure *a priori* because specimens with random geometries, such as that shown in Video 3, sustained catastrophic collapse at the early stage of deformation. Finally, the best intuitive structure (Video 4) exhibited localized failure (Fig. 5.35), in agreement with our previously reported results [393, 392]. However, this localized mechanism did not lead to uniform densification as in the BO optimum structure and fracture could not be impeded. It is also noted that the stiffness of the optimum structure is 18% larger than that of the unblemished structure (Table 5.9). The stiffness enhancement is attributed to the design of the states, as dictated by the previous work that guided the incorporation of the architected defects in the present study [393, 392].

Section Conclusions

A novel Bayesian optimization (BO) scheme has been employed that can be used for problems with discrete, qualitative design variables and a large input design space comprised of billions of possible combinations. Utilizing different test functions, we showed that our BO algorithm would lead to the global optimum design of our 3D geometrically defected microlattice with only 250 function calls (i.e., FEA calculations of the critical buckling load). Based on experiments for the optimization of test functions, the required number of function calls to obtain the global optimum of our microlattice would have been an order of magnitude larger than the number required by a genetic algorithm (GA) and two orders of magnitude greater than the number that would have been required in previously reported optimizations of architected materials [28, 460, 244, 57]. To apply BO to discrete and qualitative variables, three novel modifications were made: introducing a new acquisition function which we call 'stochastic Monte Carlo sampling', using a GA to optimize the acquisition function and restrict it to discrete states, and introducing a new metric for covariance to work with qualitative variables which we term 'capped norm'. Rather than trying to directly maximize the normalized critical strain energy density u_f/u_b to obtain our optimal design, we chose to minimize the critical buckling load P_c as a less expensive and easier to experimentally validate proxy cost function. The optimal microlattice that we obtained using this proxy, has a normalized strain energy density that is four orders of magnitude greater than the unblemished microlattice structure.The use of the critical buckling load P_c as a proxy during the optimization revealed an unexpected strong inverse correlation between P_c and u_f/u_b.

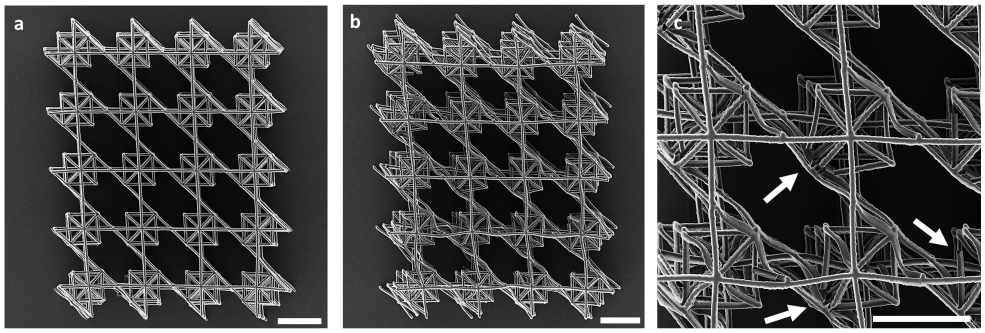

Figure 5.34: HIM images of the microlattice structure with a monolithic state D: (a) unloaded structure, (b) loaded structure, and (c) high magnification of part of the panel shown in (b) revealing fracture at the nodes of beam members (shown by white arrows). In all panels, the length of the horizontal white bar is equal to $10\mu m$.

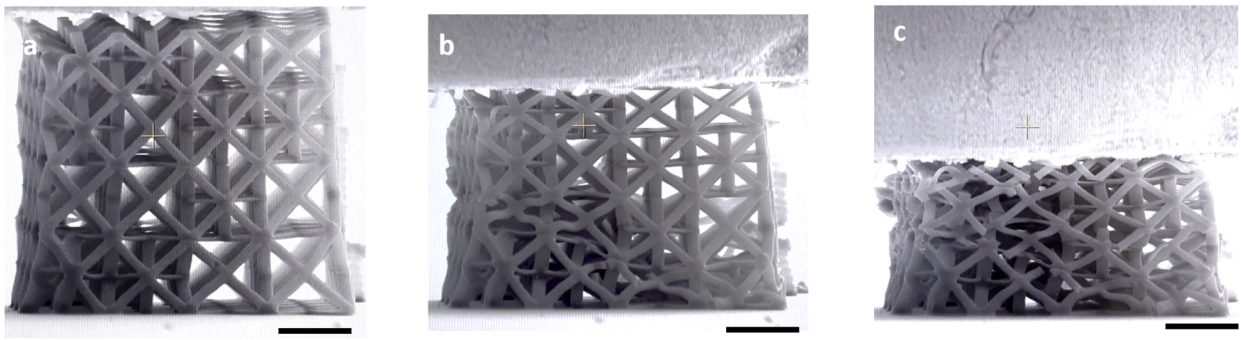

Figure 5.35: SEM images of the microlattice structure with the best intuitive solution obtained (a) before loading, (b) after loading showing excessive deformation in a slopped plane that eventually led to the collapse of the beam members on that plane, and (c) at maximum deformation showing sustained global collapse in the proximal region of the sloped plane. In all panels, the length of the horizontal black bar is equal to $10\mu m$.

While a qualitative inverse relation has been previously established [140, 264, 312, 393, 392], it was shown that near the maximum value of u_f/u_b, it increases much faster than $1/P_c$ increases.

These results illuminate a mathematical methodology to design optimal architected materials with exceptional mechanical properties and they pave the way on how the BO can be critical for inexpensive, low budget optimization of large, multi-variable problems. The BO technique presented here is suitable for use not only in other architected materials but also a wide range of problems in science and engineering where other optimization techniques either fail or are too costly. Future work will include a new, parallelized acquisition function and modifying our BO algorithm for multi-objective, mixed variable (continuous and discrete) optimization.

Chapter 6

Applications in Tissue Engineering

6.1 Remodeling of Architected Mesenchymal Microtissues Generated on Mechanical Metamaterials

Section Summary

In this work, an in vitro tissue model based on different designs of mechanical metamaterials was developed to study how the metamaterial architecture would affect the tissue formation. Two types of thoroughly investigated metamaterials (octet truss and auxetic bowtie structures) were fabricated using multi-photon lithography (MPL). The microtissues were generated by growing mesenchymal stromal cells (MSCs) on the metamaterial scaffolds. We found that both overall tissue morphology and local cell behaviors were highly dependent on the microarchitecture of metamaterials. Furthermore, mechanical force generated from the microtissues induced unique deformation patterns on the metamaterial scaffolds, leading to structural instability due to buckling. This in vitro model provides the avenue to obtain a fundamental understanding of biomechanical interactions between living microtissues and metamaterial scaffolds, which will potentially be utilized to formulate new design principles to guide the generation of artificial tissues for various applications.

Results and Discussion

Two types of unit structure designs were employed, namely the octet truss and the auxetic bowtie structures, to create metamaterial scaffolds. The octet truss, furnishing ultra-stiff and ultra-light material properties, has been used as the building block of load-bearing biomaterials for hard tissue implants [466, 11]. The bowtie structure, on the other hand, is heralded macroscopically negative Poisson's ratios, fracture resistance and high energy absorption performance [250, 339] (Figure 6.1(A)). Previously reported dimensions of structural units were used in our designs (Octet truss: beam thickness: $1.5\mu m$, base length: $50\mu m$;

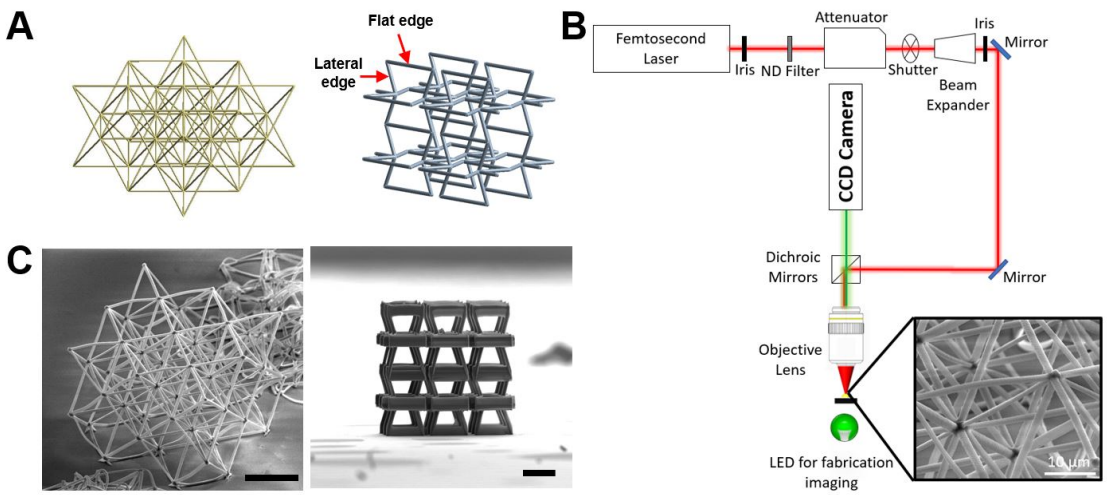

Figure 6.1: Demonstration of octet truss and auxetic metamaterials. (A) Diagrams of designs for two different metamaterials. The unit of octet truss was composed of eight tetrahedra surrounding an octahedron core. The unit of auxetic structures was made of two orthogonal re-entrant honeycombs and two short arms.(B) Set up of the laser fabrication process using MPL. Two-photon polymerization enabled the production of complex beam-based structures at a high resolution. (C) Laser-fabricated scaffolds showed a great consistency with the design files and excellent mechanical integrity. The black scale bar is $50\mu m$.

Bowtie structures: beam thickness: $8\mu m$, base length: $50\mu m$) [91, 119], which ensure that the scaffolds possess the minimum volume possible, while simultaneously have the structural integrity to hinder collapse. The bowtie structures had beam members of larger diameter to obstruct collapse during the fabrication process. The 3D metamaterial scaffolds was fabricated using the apparatus used in the previous sections (power: $1mW$, scanning speed: $10\mu m/s$) to achieve sub-micron resolution on scaffold printing (Figure 6.1(B)) [119]. An organic-inorganic hybrid resin, SZ2080TM, was used as the basal material for fabricating all scaffolds [299].

Fabricated scaffolds were imaged using scanning electron microscopy (SEM), showing precise microstructures and great mechanical integrity (Figure 6.1(C)). The length scale of metamaterial structural units was similar to the size of individual biological cells, which would provide direct associations between biomechanical responses of cells and structural geometry of metamaterial unit. MSCs were differentiated from human induced pluripotent stem cells (hiPSC-MSCs) using a serum-free protocol [426], and seeded onto Geltrex-coated metamaterial scaffolds with a density of $1.5 * 10^7/ml$. The high cell-seeding density resulted in the formation of a 3D thick tissue on the metamaterial scaffolds. We estimated around four hiPSC-MSCs surrounding each structural unit of metamaterials.

On the octet truss metamaterial scaffolds, we observed efficient penetration of hiPSC-

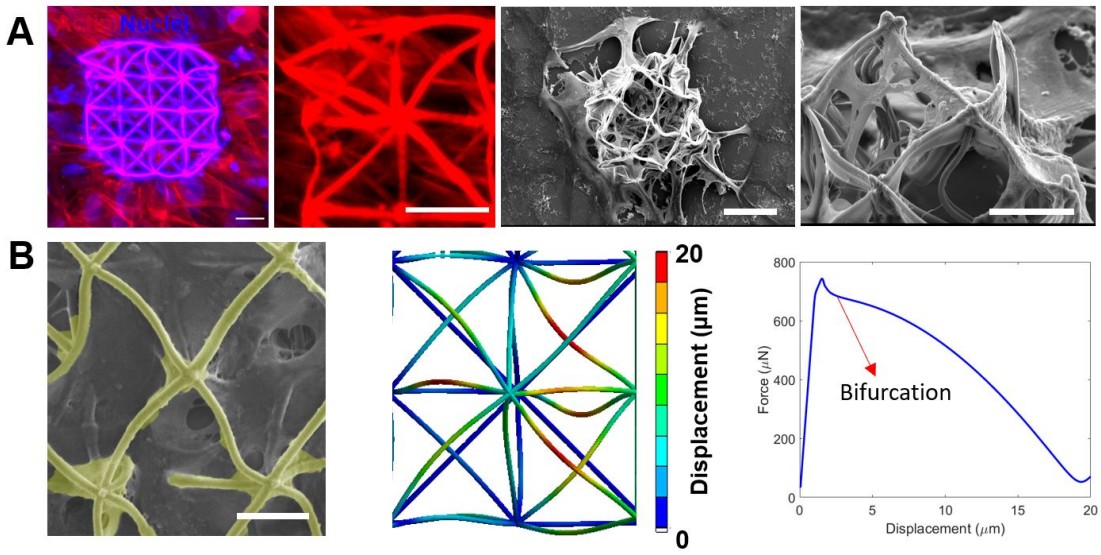

Figure 6.2: Characterization of mesenchymal microtissue morphology on octet truss metamaterials and their deformation mode under mechanical stress. (A) Fluorescent and SEM images showing the microtissues formed on octet truss. hiPSC-MSCs efficiently penetrated the entire scaffold and exhibited elongated morphology. Scale bars: $20\mu m$. (B) FEA simulation results indicates octet truss had a bifurcation buckling mode under biological mechanical stress generated by microtissues. Scale bar: $20\mu m$.

MSCs throughout the 3D scaffolds based on the immunostaining of actin filaments and cell nuclei (Figure 6.2(A)). Though many structural branches were present in the octet truss structure, cells were able to traverse the struts, invaded into the pores within the scaffolds and exhibited an elongated morphology. Compared to standard SEM imaging, helium ion microscopy (HIM) enhances the contrast, resolution and depth of field, which enable the visualization of tissue-material interactions under microscopic levels [190]. In order to maximize the attachment to the metamaterials with a low material density, hiPSC-MSCs grew and elongated following the longitudinal orientation of the beams, which is a common phenomenon for cells on most architected scaffolds (Figure 6.3(A)) [311, 240, 310]. To further facilitate the cell adhesion, thin branches of plasma membranes were extended from cell bodies to attach to the adjacent beams (Figure 6.3(B)). In addition, micropores were present on cell bodies, which might be created under high mechanical tension when hiPSC-MSCs spanned over different beams (Figure 6.3(C)).

The mechanical load generated by the microtissues led to a large deformation of entire octet truss metamaterial scaffold, manifested as the decrease of its height and the inward buckling of struts at the corners (Figure 6.2(A)). The stability of center posts maintained an isotropic stress distribution across octet truss structure, in order to keep the overall

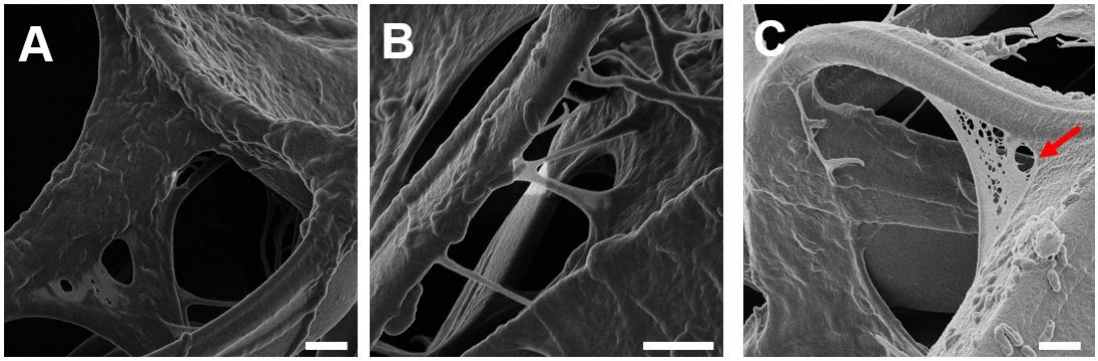

Figure 6.3: Microscopic behaviors of hiPSC-MSCs on octet truss metamaterials resolved using HIM. (A) hiPSC-MSCs grew along the direction of beam members within octet truss. (B) Ultrathin branches of plasma membranes were generated to maximize the adhesion of cells on octet truss. (C) Micropores (red arrows) formed on the cell bodies to release their interior tension. Scale bar: $2\mu m$.

integrity of metamaterial scaffold. To define the deformation modes of metamaterials, finite element analysis (FEA) simulations were performed using the Multiphysics Software ANSYS R18.1. Both the bowtie and the octet truss were discretised by 3D-10-node tetrahedral solid elements. Specifically, the Octet truss was discretized with 173018 nodes and 84558 elements, while the Bowties was discretized with 32301 nodes and 16648 elements. The mechanical properties were set with the same values that have been reported previously [119]. Based on the microscope images, for the case of the bowtie the cells tend to distribute at the edges of the beam members, while for the case for the octet truss, they occupy the sides of the lattice. For this reason, a quasi-static displacement field was applied at these specific members of both lattices for large, nonlinear deformations. Specifically, for the bowtie, the distributed displacement was set at the nodes of the beam members at the edges of the unit cell, applying compression, while the beam members at the top were subject to a distributed displacement that would cause them to bend inwards, similar with the profiles from the helium ion microscopy imaging. For the Octet truss, the beam members at the sides were subject to a distributed displacement that will cause compression of the array. Since the structures were fixed at the glass substrate, the bottom beam members were defined as fixed supports. The force-displacement curves were obtained by the reaction force at the fixed supports. We first simulated the mechanical behaviors of octet truss structure under uniform mechanical load. The octet truss structure can sustain high mechanical force without fracture with a linear relationship between force and displacement (Figure 6.4), which confirmed the ultra-stiff property of this structure.

To recapitulate the deformation characteristics of octet truss metamaterial scaffolds under the mechanical loading from microtissues, the beam members at the top part of octet

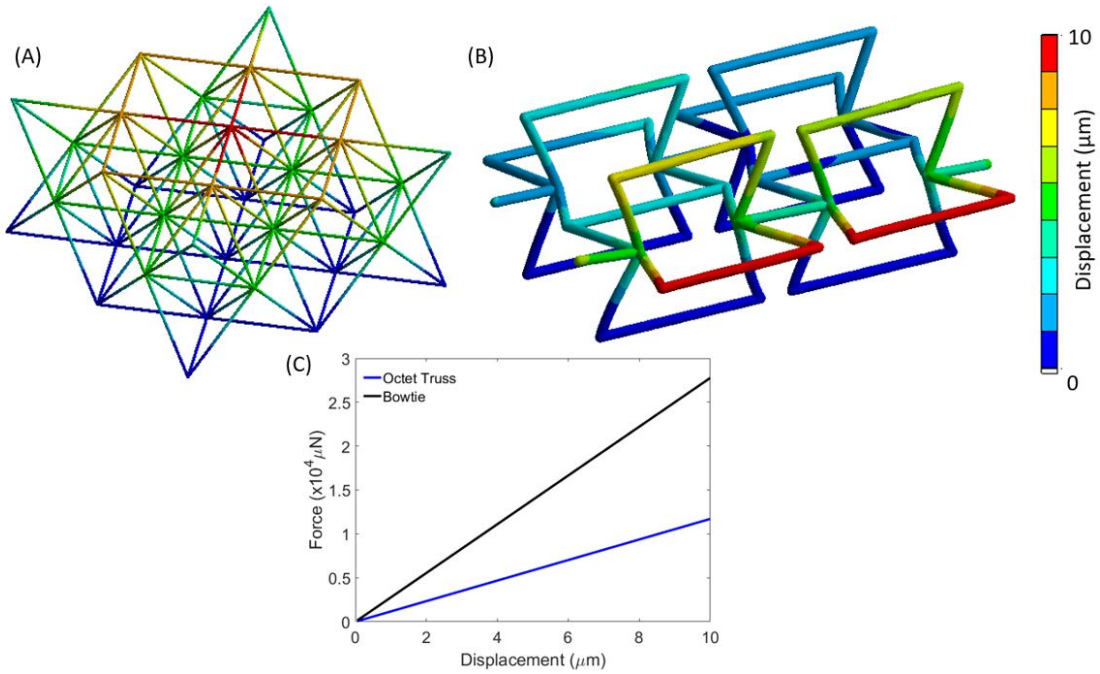

Figure 6.4: FEA simulations of metamaterial deformations under uniform mechanical load. Displacement heatmaps of octet truss (A) and auxetic structures (B) under uniform load. (C) The force-displacement curves when applying uniform load. There is a linear relationship between the force and displacement for both designs.

truss structure were subjected to a distributed displacement, which caused a compression of the array (Figure 6.2(B)). The force-displacement relationship showed that the octet truss structure experienced a bifurcation buckling mode evidenced by the positive-negative-positive transition of the slope [116]. This distinct deformation mode indicated a unique way of mechanical loading from living biological tissues on metamaterial scaffolds. The mesenchymal tissues growing on the scaffolds formed tight connections with monolayer tissues grown on the surface of the coverslip, which applied a dominant compressive force transmitted through the main axis of beam members of the metamaterial scaffolds. Since octet truss is a stretch-dominated meta-structure, the compression-induced displacement was limited by the interior hardness of materials [341]. However, the top part of octet truss had a better compliance, showing that most of beams buckled under the biological force from mesenchymal microtissues. The buckling of individual beams disrupted the integrity of unit structure, and then modulated the loading bearing mode of the octet truss metamaterial scaffolds. Once the force was applied in perpendicular to the beam axis, it was possible to deform the scaffold to a large extent with less mechanical loading.

On the auxetic bowtie metamaterial scaffolds, a thicker tissue formed with a bulky morphology that had a clear tissue boundary following the contour of the scaffolds (Figure 6.6A).

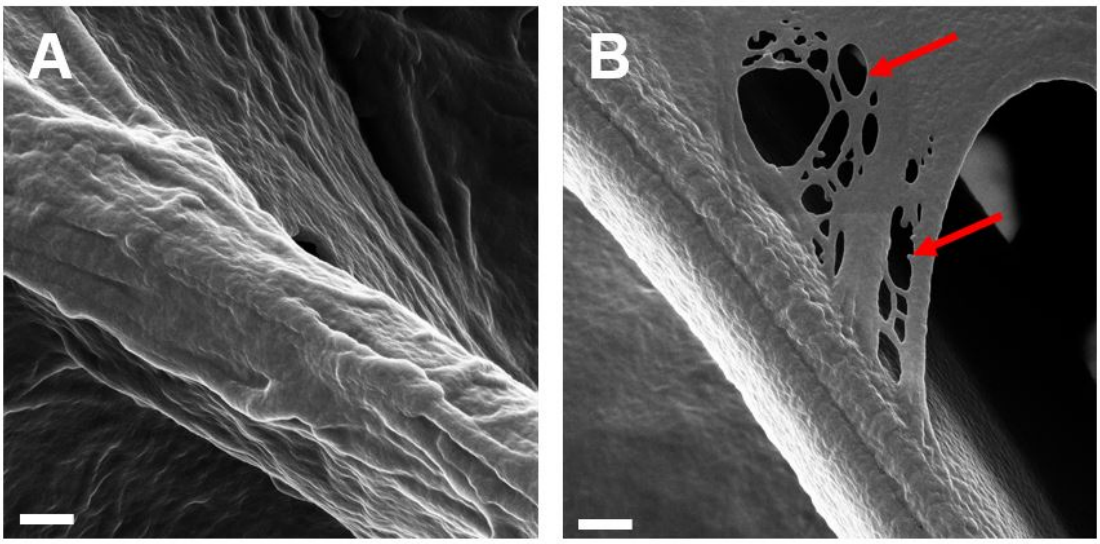

Figure 6.5: Microscopic behaviors of hiPSC-MSCs on auxetic metamaterials resolved using HIM. (A) Wrapping of cells around the beams and (B) the formation of membrane micropores (red arrows) on auxetic structures. Scale bar: $500nm$.

The cells tended to aggregate around the bowtie structures with dense tissue formation, instead of extending cell bodies with thin plasma membrane branches that were observed on the octet truss metamaterial scaffolds. When imaging with HIM, we observed that cell wrapped around the beams and micropores formed on the cell membrane (Figure 6.5(A)- 6.5(B)). The flat edges of bowtie structures were significantly deformed inwards by the microtissues, leading to the shrinkage of their diagonal ribs and the closing of the pores (Figure 6.6(A)). In addition, the vertical parts flipped 90 degrees and met their neighbors due to the high compression force.

To simulate the deformation characteristics of bowtie metamaterial scaffolds under the mechanical loading from microtissues, the distributed displacement was set at the nodes of beam members at the flat edges, while the top beams were subjected to a displacement that would cause them to bend inwards (Figure 6.6(B)). The mechanical force of the microtissue caused a snap through buckling mode on the bowtie structure demonstrated as a plateau on the force-displacement curve [330]. Compared to the octet truss, composed of multidirectional beam members that provide a homogeneous mechanical behavior, high anisotropy degree of the bowtie structure based on its beam arrangement assured sufficient area for cell attachment without stretching cell membrane to form thin branches. Due to the disruption of structural units, the metamaterial scaffold became more compliant. However, the bowtie structure had less stress relaxation comparing to the octet truss, since bowtie structures contained less buckled beams under the mechanical loading. More importantly, the nega-

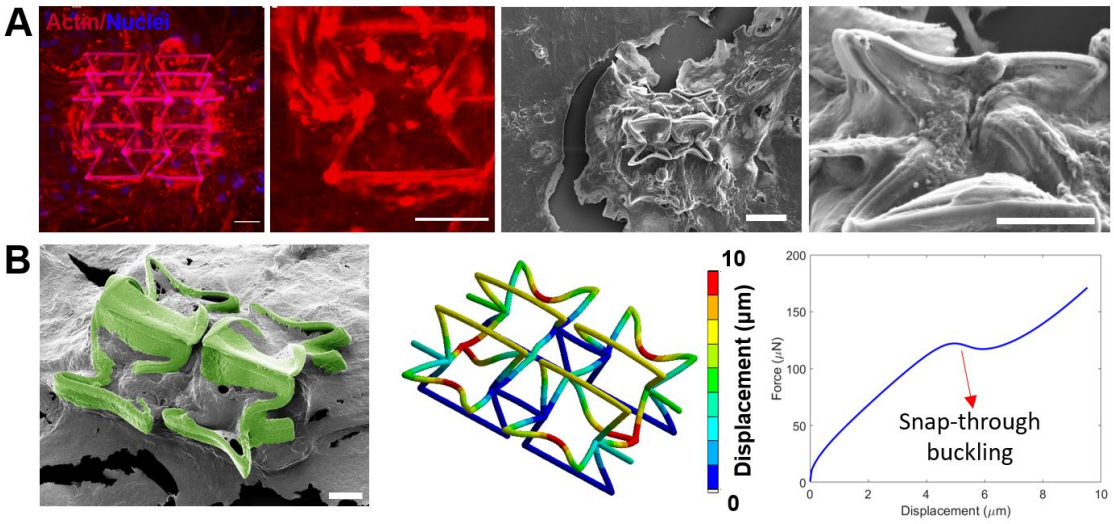

Figure 6.6: Characterization of mesenchymal microtissue morphology on auxetic metamaterials and their deformation mode under mechanical stress. (A) Fluorescent and SEM images showing the microtissues formed on auxetic structures. hiPSC-MSCs efficiently penetrated the entire scaffold and exhibited bulky morphology. Scale bars: $20\mu m$. (B) FEA simulation results indicates auxetic structures had a snap-through buckling mode under biological mechanical stress generated by microtissues. Scale bar: $20\mu m$.

tive Poisson's ratio of bowtie structure allowed the tissues to aggregate in a natural way, which brought the cells in close contact with strong intercellular connections. Hence, the entire scaffold was dramatically compressed, shown as inward buckling of individual beams at scaffold edges, flipping of vertical flat beams and closing up the unit pores.

Results described above evidenced the fact that mechanical load from biological tissues was prone to cause the buckling of individual fibers and trigger the instability of metamaterials. However, the metamaterial scaffolds could sustain a significant distortion without fracture, which was possibly resulted from efficient tissue-scaffold integration as a single "living composite". The active remodeling of mesenchymal microtissues made it possible to establish an equilibrium state of the composite under minimal mechanical force and energy potential. In comparison, uniform mechanical loading was passive and externally exerted to the metamaterial scaffolds, thus it was not able to create the buckling forms that generated internally from the living composite. The concept of living tissue-scaffold composite should be taken into consideration for future mechanistic analysis on tissue-material mechanical interaction and evolution of tissue instability.

Section Conclusions

In summary, the first 3D human microtissue model on metamaterial scaffolds fabricated using MPL technology was generated. hiPSC-MSCs could assemble into 3D microtissues on different metamaterial scaffolds, but tissue morphology and scaffold deformation mode were significantly different between octet truss and bowtie structures. On microscopic level, we observed the microtissue remodeling adapting to the complex scaffold geometry. FEA simulations unraveled that mesenchymal microtissues induced different deformation modes on the metamaterial scaffolds and caused a large transformation of their geometries. Further quantification of cell surface tension, immunostaining of other cell markers and simulation of force distribution within the meta-structures would benefit a deeper understanding of how unit geometries of metamaterials affect tissue phenotypes.

Chapter 7

Epilogue

In ilation, the design principles that predicate the structural and mechanical properties of mechanical metamaterials were delineated. The main topic of this work was initiated by a demonstration of these results in auxetic, tensegrity and pantographic structures, fabricated and tested in microscale. Next, intertwined members were arranged such that the anisotropy and post elastic behavior of the structure can be tailored through fastigiate members that cause indissoluble plastic deformation instead of proliferation of fracture. It was found that a random arrangement of beam members does not provide the same mechanical performance, but both elastic and nonelastic properties are highly sensitive to the different arrangements of the unit cells. These principles were the crux to define the control parameters that can be used: Geometrical defects as design variables and the critical buckling load and buckling modes to control the nonlinear behavior. Next, it was shown how this quandary, suffering from excessive profligacy which required a surfeit of computational power, can be circumvented using Bayesian Optimization. Even ceteris paribus, this strategy can find the global optimum of the design space using a few hundred simulations without deluging the problem with an exorbitant number of experiments or simulations. Its was proven that the global optimum is inimitable, since it did not have any specific pattern to distinguish it. However, it was thousands times better than the defect free fracture with respect to its strain energy density. Despite the fact that this can be considered the lucida of this thesis and the most novel finding regarding mechanical metamaterials, the true translunary result was its reverberation in tissue engineering. It was shown that controlled stiffness of specific beam members can align the tissue at specific positions, precipitating buckling on the scaffold and densifcation of the tissue and higher loading on the cells. These contorted scaffolds can be employed for biocomposite structures that are malleable and be an intriguing pathway for the development of architected materials. The principles that have been elucidated in this thesis can be applied for the whole rang of length scales, providing an avenue in macroscale with conventional 3D printing or with multiphoton lithography at the microscale.

Bibliography

[1] Mohamed Abdelhamid and Aleksander Czekanski. "Impact of the lattice angle on the effective properties of the octet-truss lattice structure". In: *Journal of Engineering Materials and Technology* 140.4 (2018).

[2] Mohamed Abdelaziz Abdelrahma Abdelhamid. "Effective Mechanical Properties of 3D Structural Metamaterials". In: (2017).

[3] Sandra V Abramson et al. "Pulmonary hypertension predicts mortality and morbidity in patients with dilated cardiomyopathy". In: *Annals of internal medicine* 116.11 (1992), pp. 888–895.

[4] N Adan, I Sheinman, and E Altus. "Post-buckling behavior of beams under contact constraints". In: (1994).

[5] Alderson Alderson and KL Alderson. "Auxetic materials". In: *Proceedings of the Institution of Mechanical Engineers, Part G: Journal of Aerospace Engineering* 221.4 (2007), pp. 565–575.

[6] Jean-Jacques Alibert, Pierre Seppecher, and Francesco dell'Isola. "Truss modular beams with deformation energy depending on higher displacement gradients". In: *Mathematics and Mechanics of Solids* 8.1 (2003), pp. 51–73.

[7] Maen Alkhader, Mohammad Nazzal, and Karim Louca. "Design of bending dominated lattice architectures with improved stiffness using hierarchy". In: *Proceedings of the Institution of Mechanical Engineers, Part C: Journal of Mechanical Engineering Science* 233.11 (2019), pp. 3976–3993.

[8] Holm Altenbach and Victor A Eremeyev. "On the bending of viscoelastic plates made of polymer foams". In: *Acta Mechanica* 204.3 (2009), pp. 137–154.

[9] Ada Amendola, Antonino Favata, and Andrea Micheletti. "On the mechanical modeling of tensegrity columns subject to impact loading". In: *Frontiers in Materials* 5 (2018), p. 22.

[10] Ugo Andreaus et al. "A Ritz approach for the static analysis of planar pantographic structures modeled with nonlinear Euler–Bernoulli beams". In: *Continuum Mechanics and Thermodynamics* 30.5 (2018), pp. 1103–1123.

[11] Sajad Arabnejad et al. "High-strength porous biomaterials for bone replacement: A strategy to assess the interplay between cell morphology, mechanical properties, bone ingrowth and manufacturing constraints". In: *Acta biomaterialia* 30 (2016), pp. 345–356.

[12] Ali Argon. *Strengthening mechanisms in crystal plasticity*. Vol. 4. Oxford University Press on Demand, 2008.

[13] Michael F Ashby. "The properties of foams and lattices". In: *Philosophical Transactions of the Royal Society A: Mathematical, Physical and Engineering Sciences* 364.1838 (2006), pp. 15–30.

[14] Michael F Ashby and Kara Johnson. *Materials and design: the art and science of material selection in product design*. Butterworth-Heinemann, 2013.

[15] Daphne Attard et al. "On the properties of auxetic rotating stretching squares". In: *physica status solidi (b)* 246.9 (2009), pp. 2045–2054.

[16] Sahab Babaee et al. "3D soft metamaterials with negative Poisson's ratio". In: *Advanced Materials* 25.36 (2013), pp. 5044–5049.

[17] Lidia Badarnah and Usama Kadri. "A methodology for the generation of biomimetic design concepts". In: *Architectural Science Review* 58.2 (2015), pp. 120–133.

[18] M Bakarezos et al. "Ultrafast laser pulse chirp effects on laser-generated nanoacoustic strains in Silicon". In: *Ultrasonics* 86 (2018), pp. 14–19.

[19] David P Banks et al. "Nanodroplets deposited in microarrays by femtosecond Ti: sapphire laser-induced forward transfer". In: *Applied physics letters* 89.19 (2006), p. 193107.

[20] Emilio Barchiesi, Mario Spagnuolo, and Luca Placidi. "Mechanical metamaterials: a state of the art". In: *Mathematics and Mechanics of Solids* 24.1 (2019), pp. 212–234.

[21] Emilio Barchiesi et al. "Pantographic beam: A complete second gradient 1D-continuum in plane". In: *Zeitschrift für angewandte Mathematik und Physik* 70.5 (2019), p. 135.

[22] F Barthelat et al. "On the mechanics of mother-of-pearl: a key feature in the material hierarchical structure". In: *Journal of the Mechanics and Physics of Solids* 55.2 (2007), pp. 306–337.

[23] Jens Bauer et al. "Approaching theoretical strength in glassy carbon nanolattices". In: *Nature materials* 15.4 (2016), pp. 438–443.

[24] Jens Bauer et al. "Push-to-pull tensile testing of ultra-strong nanoscale ceramic–polymer composites made by additive manufacturing". In: *Extreme Mechanics Letters* 3 (2015), pp. 105–112.

[25] JB Berger, HNG Wadley, and RM McMeeking. "Mechanical metamaterials at the theoretical limit of isotropic elastic stiffness". In: *Nature* 543.7646 (2017), pp. 533–537.

[26] K Berkache et al. "Construction of second gradient continuum models for random fibrous networks and analysis of size effects". In: *Composite Structures* 181 (2017), pp. 347–357.

[27] Katia Bertoldi et al. "Flexible mechanical metamaterials". In: *Nature Reviews Materials* 2.11 (2017), pp. 1–11.

[28] Miguel A Bessa, Piotr Glowacki, and Michael Houlder. "Bayesian machine learning in metamaterial design: fragile becomes supercompressible". In: *Advanced Materials* 31.48 (2019), p. 1904845.

[29] Christopher J Bettinger, Robert Langer, and Jeffrey T Borenstein. "Engineering substrate topography at the micro-and nanoscale to control cell function". In: *Angewandte Chemie International Edition* 48.30 (2009), pp. 5406–5415.

[30] Sukhwinder K Bhullar et al. "Design and fabrication of auxetic PCL nanofiber membranes for biomedical applications". In: *Materials Science and Engineering: C* 81 (2017), pp. 334–340.

[31] Z Bhumgara. "Polyhipe foam materials as filtration media". In: *Filtration & separation* 32.3 (1995), pp. 245–251.

[32] Sherrill B Biggers and Stephane S Pageau. "Shear buckling response of tailored composite plates". In: *AIAA journal* 32.5 (1994), pp. 1100–1103.

[33] Sherrill B Biggers and Sundar Srinivasan. "Compression buckling response of tailored rectangular composite plates". In: *AIAA journal* 31.3 (1993), pp. 590–596.

[34] Sherrill B Biggers and Sundar Srinivasan. "Postbuckling response of piece-wise uniform tailored composite plates in compression". In: *Journal of Reinforced Plastics and Composites* 13.9 (1994), pp. 803–821.

[35] Sherrill B Biggers Jr and Thomas M Browder Jr. "Buckling-load interaction in tailored composite plates". In: *Composites Engineering* 4.7 (1994), pp. 745–761.

[36] FSL Bobbert, S Janbaz, and AA Zadpoor. "Towards deployable meta-implants". In: *Journal of Materials Chemistry B* 6.21 (2018), pp. 3449–3455.

[37] FSL Bobbert et al. "Russian doll deployable meta-implants: Fusion of kirigami, origami, and multi-stability". In: *Materials & Design* 191 (2020), p. 108624.

[38] Colin Bonatti and Dirk Mohr. "Large deformation response of additively-manufactured FCC metamaterials: From octet truss lattices towards continuous shell mesostructures". In: *International Journal of Plasticity* 92 (2017), pp. 122–147.

[39] Arthur Peter Boresi, Richard Joseph Schmidt, Omar M Sidebottom, et al. *Advanced mechanics of materials*. Vol. 6. Wiley New York, 1993.

[40] Thomas Boudou et al. "A microfabricated platform to measure and manipulate the mechanics of engineered cardiac microtissues". In: *Tissue Engineering Part A* 18.9-10 (2012), pp. 910–919.

[41] Claude Boutin. "Microstructural effects in elastic composites". In: *International Journal of Solids and Structures* 33.7 (1996), pp. 1023–1051.

[42] Christos Boutopoulos et al. "Sticking of droplets on slippery superhydrophobic surfaces by laser induced forward transfer". In: *Applied Physics Letters* 103.2 (2013), p. 024104.

[43] Christopher Bradley and Arthur Cracknell. *The mathematical theory of symmetry in solids: representation theory for point groups and space groups*. Oxford University Press, 2009.

[44] Stefan Bronder, Stefan Diebels, and Anne Jung. "Neural Networks for Structural Optimisation of Mechanical Metamaterials". In: *PAMM* 20.1 (2021), e202000238.

[45] TE Bruns, O Sigmund, and Daniel A Tortorelli. "Numerical methods for the topology optimization of structures that exhibit snap-through". In: *International Journal for Numerical Methods in Engineering* 55.10 (2002), pp. 1215–1237.

[46] Tiemo Bückmann et al. "An elasto-mechanical unfeelability cloak made of pentamode metamaterials". In: *Nature communications* 5.1 (2014), pp. 1–6.

[47] Keith Burridge and Magdalena Chrzanowska-Wodnicka. "Focal adhesions, contractility, and signaling". In: *Annual review of cell and developmental biology* 12.1 (1996), pp. 463–519.

[48] Michael Burt. "Infinite polyhedra lattice (IPL) space trusses: morphology, analysis and application". In: *International Journal of Space Structures* 11.1-2 (1996), pp. 115–126.

[49] CR Calladine and S Pellegrino. "First-order infinitesimal mechanisms". In: *International Journal of Solids and Structures* 27.4 (1991), pp. 505–515.

[50] Christophe Caloz and Tatsuo Itoh. *Electromagnetic metamaterials: transmission line theory and microwave applications*. John Wiley & Sons, 2005.

[51] MTHRGDM Campbell et al. "Fabrication of photonic crystals for the visible spectrum by holographic lithography". In: *Nature* 404.6773 (2000), pp. 53–56.

[52] Antonio Carcaterra et al. "Macroscopic description of microscopically strongly inhomogenous systems: A mathematical basis for the synthesis of higher gradients metamaterials". In: *Archive for Rational Mechanics and Analysis* 218.3 (2015), pp. 1239–1262.

[53] Antonio Cazzani et al. "Constitutive models for strongly curved beams in the frame of isogeometric analysis". In: *Mathematics and Mechanics of Solids* 21.2 (2016), pp. 182–209.

[54] Marianneza Chatzipetrou et al. "Direct creation of biopatterns via a combination of laser-based techniques and click chemistry". In: *Langmuir* 33.4 (2017), pp. 848–853.

[55] Chun-Teh Chen and Grace X Gu. "Effect of constituent materials on composite performance: exploring design strategies via machine learning". In: *Advanced Theory and Simulations* 2.6 (2019), p. 1900056.

[56] Chun-Teh Chen and Grace X Gu. "Machine learning for composite materials". In: *MRS Communications* 9.2 (2019), pp. 556–566.

[57] Desai Chen et al. "Computational discovery of extremal microstructure families". In: *Science advances* 4.1 (2018), eaao7005.

[58] Kang Chen and Kenneth S Schweizer. "Theory of yielding, strain softening, and steady plastic flow in polymer glasses under constant strain rate deformation". In: *Macromolecules* 44.10 (2011), pp. 3988–4000.

[59] Qi Chen, Xianmin Zhang, and Benliang Zhu. "Design of buckling-induced mechanical metamaterials for energy absorption using topology optimization". In: *Structural and Multidisciplinary Optimization* 58.4 (2018), pp. 1395–1410.

[60] Qiyi Chen et al. "3D printed multifunctional, hyperelastic silicone rubber foam". In: *Advanced Functional Materials* 29.23 (2019), p. 1900469.

[61] Tian Chen et al. "Harnessing bistability for directional propulsion of soft, untethered robots". In: *Proceedings of the National Academy of Sciences* 115.22 (2018), pp. 5698–5702.

[62] Wai-Fah Chen. *Limit analysis and soil plasticity*. Elsevier, 2013.

[63] Wen Chen et al. "Stiff isotropic lattices beyond the Maxwell criterion". In: *Science advances* 5.9 (2019), eaaw1937.

[64] Xueyan Chen et al. "Optimal isotropic, reusable truss lattice material with near-zero Poisson's ratio". In: *arXiv preprint arXiv:2003.07973* (2020).

[65] K Chihab et al. "The kinetics of the Portevin-Le Chatelier bands in an Al-5at% Mg alloy". In: *Scripta metallurgica* 21.2 (1987), pp. 203–208.

[66] Jaewon Choi et al. "Guided assembly of block copolymers in three-dimensional woodpile scaffolds". In: *ACS applied materials & interfaces* 10.49 (2018), pp. 42933–42940.

[67] Johan Christensen et al. "Vibrant times for mechanical metamaterials". In: *Mrs Communications* 5.3 (2015), pp. 453–462.

[68] M Colina et al. "Laser-induced forward transfer of liquids: Study of the droplet ejection process". In: *Journal of applied physics* 99.8 (2006), p. 084909.

[69] Corentin Coulais et al. "Multi-step self-guided pathways for shape-changing metamaterials". In: *Nature* 561.7724 (2018), pp. 512–515.

[70] Harold Scott Macdonald Coxeter, HT Flather, and JF Petrie. *The fifty-nine icosahedra*. Springer Science & Business Media, 2012.

[71] Nicholas B Cramer et al. "Elastic shape morphing of ultralight structures by programmable assembly". In: *Smart Materials and Structures* 28.5 (2019), p. 055006.

[72] Peter R Cromwell. *Polyhedra*. Cambridge University Press, 1999.

[73] Cameron Crook et al. "Plate-nanolattices at the theoretical limit of stiffness and strength". In: *Nature communications* 11.1 (2020), pp. 1–11.

[74] Ferenc F Csikor et al. "Dislocation avalanches, strain bursts, and the problem of plastic forming at the micrometer scale". In: *Science* 318.5848 (2007), pp. 251–254.

[75] Huachen Cui et al. "Additive Manufacturing and size-dependent mechanical properties of three-dimensional microarchitected, high-temperature ceramic metamaterials". In: *Journal of Materials Research* 33.3 (2018), pp. 360–371.

[76] Steven A Cummer, Johan Christensen, and Andrea Alù. "Controlling sound with acoustic metamaterials". In: *Nature Reviews Materials* 1.3 (2016), pp. 1–13.

[77] Vahid Daghigh et al. "Machine learning predictions on fracture toughness of multiscale bio-nano-composites". In: *Journal of Reinforced Plastics and Composites* 39.15-16 (2020), pp. 587–598.

[78] Chiara Daraio and Fernando Fraternali. *Method and apparatus for wave generation and detection using tensegrity structures*. US Patent 8,616,328. 2013.

[79] Cesare Davini, Andrea Micheletti, and Paolo Podio-Guidugli. "On the impulsive dynamics of T3 tensegrity chains". In: *Meccanica* 51.11 (2016), pp. 2763–2776.

[80] Fabrizio Davı. "The theory of Kirchhoff rods as an exact consequence of three-dimensional elasticity". In: *Journal of elasticity* 29.3 (1992), pp. 243–262.

[81] Rudy AC Deblieck et al. "Failure mechanisms in polyolefines: The role of crazing, shear yielding and the entanglement network". In: *Polymer* 52.14 (2011), pp. 2979–2990.

[82] Marc Defossez. "Shape memory effect in tensegrity structures". In: *Mechanics Research Communications* 30.4 (2003), pp. 311–316.

[83] Francesco Dell'Isola and David J Steigmann. *Discrete and Continuum Models for Complex Metamaterials*. Cambridge University Press, 2020.

[84] Francesco Dell'Isola et al. "Force–displacement relationship in micro-metric pantographs: Experiments and numerical simulations". In: *Comptes Rendus Mécanique* 347.5 (2019), pp. 397–405.

[85] Francesco Dell'Isola et al. "Designing a light fabric metamaterial being highly macroscopically tough under directional extension: first experimental evidence". In: *Zeitschrift für angewandte Mathematik und Physik* 66.6 (2015), pp. 3473–3498.

[86] Francesco dell'Isola et al. "Large deformations of planar extensible beams and pantographic lattices: heuristic homogenization, experimental and numerical examples of equilibrium". In: *Proceedings of the Royal Society A: Mathematical, Physical and Engineering Sciences* 472.2185 (2016), p. 20150790.

[87] A Della Corte et al. "Large deformations of Timoshenko and Euler beams under distributed load". In: *Zeitschrift für angewandte Mathematik und Physik* 70.2 (2019), pp. 1–19.

[88] Dhananjay Dendukuri et al. "Continuous-flow lithography for high-throughput microparticle synthesis". In: *Nature materials* 5.5 (2006), pp. 365–369.

[89] Bolei Deng et al. "Focusing and mode separation of elastic vector solitons in a 2D soft mechanical metamaterial". In: *Physical review letters* 123.2 (2019), p. 024101.

[90] Hao Deng et al. "Topology optimization for energy dissipation design of lattice structures through snap-through behavior". In: *Computer Methods in Applied Mechanics and Engineering* 358 (2020), p. 112641.

[91] Vikram S Deshpande, Norman A Fleck, and Michael F Ashby. "Effective properties of the octet-truss lattice material". In: *Journal of the Mechanics and Physics of Solids* 49.8 (2001), pp. 1747–1769.

[92] Vikram S Deshpande, Robert M McMeeking, and Anthony G Evans. "A bio-chemo-mechanical model for cell contractility". In: *Proceedings of the National Academy of Sciences* 103.38 (2006), pp. 14015–14020.

[93] VS Deshpande, MF Ashby, and NA Fleck. "Foam topology: bending versus stretching dominated architectures". In: *Acta materialia* 49.6 (2001), pp. 1035–1040.

[94] Boris Desmorat, Mario Spagnuolo, and Emilio Turco. "Stiffness optimization in nonlinear pantographic structures". In: *Mathematics and Mechanics of Solids* 25.12 (2020), pp. 2252–2262.

[95] Vasilis Dimitriou et al. "The thermo-mechanical behavior of thin metal films under nanosecond laser pulse excitation above the thermoelastic regime". In: *Applied Physics A* 118.2 (2015), pp. 739–748.

[96] Dennis E Discher, Paul Janmey, and Yu-li Wang. "Tissue cells feel and respond to the stiffness of their substrate". In: *Science* 310.5751 (2005), pp. 1139–1143.

[97] Liang Dong, Vikram Deshpande, and Haydn Wadley. "Mechanical response of Ti–6Al–4V octet-truss lattice structures". In: *International Journal of Solids and Structures* 60 (2015), pp. 107–124.

[98] Liang Dong and Haydn Wadley. "Shear response of carbon fiber composite octet-truss lattice structures". In: *Composites Part A: Applied Science and Manufacturing* 81 (2016), pp. 182–192.

[99] Kokou D Honorat Dorkenoo et al. *Monitoring the Contractile Properties of Optically Patterned Liquid Crystal Based Elastomers*. InTech, 2012.

[100] Nicholas G Dou et al. "Ultralow thermal conductivity and mechanical resilience of architected nanolattices". In: *Nano Letters* 18.8 (2018), pp. 4755–4761.

[101] B Druyanov and R Nepershin. *Problems of technological plasticity*. Elsevier, 2013.

[102] Shengyu Duan, Weibin Wen, and Daining Fang. "Additively-manufactured anisotropic and isotropic 3D plate-lattice materials for enhanced mechanical performance: Simulations & experiments". In: *Acta Materialia* 199 (2020), pp. 397–412.

[103] Patric Eberle et al. "Single entity resolution valving of nanoscopic species in liquids". In: *Nature Nanotechnology* 13.7 (2018), pp. 578–582.

[104] John Edmiston et al. "A model for elastic–viscoplastic deformations of crystalline solids based on material symmetry: Theory and plane-strain simulations". In: *International Journal of Engineering Science* 63 (2013), pp. 10–22.

[105] Nader Engheta and Richard W Ziolkowski. *Metamaterials: physics and engineering explorations*. John Wiley & Sons, 2006.

[106] Victor A Eremeyev et al. "Linear pantographic sheets: existence and uniqueness of weak solutions". In: *Journal of Elasticity* 132.2 (2018), pp. 175–196.

[107] Tolga Ergin et al. "Three-dimensional invisibility cloak at optical wavelengths". In: *science* 328.5976 (2010), pp. 337–339.

[108] Jeroen Eyckmans et al. "A hitchhiker's guide to mechanobiology". In: *Developmental cell* 21.1 (2011), pp. 35–47.

[109] Francesco Fabbrocino et al. "Seismic application of pentamode lattices". In: *Ing. Sismica* 33.1-2 (2016), pp. 62–70.

[110] Hualin Fan et al. "Approaching perfect energy absorption through structural hierarchy". In: *International Journal of Engineering Science* 130 (2018), pp. 12–32.

[111] Xin Fang et al. "Ultra-low and ultra-broad-band nonlinear acoustic metamaterials". In: *Nature communications* 8.1 (2017), pp. 1–11.

[112] Antonino Favata, Andrea Micheletti, and Paolo Podio-Guidugli. "A nonlinear theory of prestressed elastic stick-and-spring structures". In: *International Journal of Engineering Science* 80 (2014), pp. 4–20.

[113] Antonino Favata et al. "How graphene flexes and stretches under concomitant bending couples and tractions". In: *Meccanica* 52.7 (2017), pp. 1601–1624.

[114] Cornelius Fendler et al. "Microscaffolds by Direct Laser Writing for Neurite Guidance Leading to Tailor-Made Neuronal Networks". In: *Advanced Biosystems* 3.5 (2019), p. 1800329.

[115] T Fiedler, IV Belova, and GE Murch. "μ-CT-based finite element analysis on imperfections in open-celled metal foam: Mechanical properties". In: *Scripta Materialia* 67.5 (2012), pp. 455–458.

[116] Claudio Findeisen et al. "Characteristics of mechanical metamaterials based on buckling elements". In: *Journal of the Mechanics and Physics of Solids* 102 (2017), pp. 151–164.

[117] William Nichols Findley et al. "Creep and relaxation of nonlinear viscoelastic materials with an introduction to linear viscoelasticity". In: (1977).

[118] Joachim Fischer and Martin Wegener. "Three-dimensional direct laser writing inspired by stimulated-emission-depletion microscopy". In: *Optical Materials Express* 1.4 (2011), pp. 614–624.

[119] George Flamourakis et al. "Laser-made 3D Auxetic Metamaterial Scaffolds for Tissue Engineering Applications". In: *Macromolecular Materials and Engineering* 305.7 (2020), p. 2000238.

[120] Norman A Fleck, Vikram S Deshpande, and Michael F Ashby. "Micro-architectured materials: past, present and future". In: *Proceedings of the Royal Society A: Mathematical, Physical and Engineering Sciences* 466.2121 (2010), pp. 2495–2516.

[121] Samuel Forest et al. "Continuum modeling of strain localization phenomena in metallic foams". In: *Journal of materials science* 40.22 (2005), pp. 5903–5910.

[122] F Fraternali and A Amendola. "Mechanical modeling of innovative metamaterials alternating pentamode lattices and confinement plates". In: *Journal of the Mechanics and Physics of Solids* 99 (2017), pp. 259–271.

[123] F Fraternali, L Senatore, and C Daraio. "Solitary waves on tensegrity lattices". In: *Journal of the Mechanics and Physics of Solids* 60.6 (2012), pp. 1137–1144.

[124] Fernando Fraternali et al. "Multiscale tunability of solitary wave dynamics in tensegrity metamaterials". In: *Applied Physics Letters* 105.20 (2014), p. 201903.

[125] Tobias Frenzel, Muamer Kadic, and Martin Wegener. "Three-dimensional mechanical metamaterials with a twist". In: *Science* 358.6366 (2017), pp. 1072–1074.

[126] Tobias Frenzel et al. "Tailored buckling microlattices as reusable light-weight shock absorbers". In: *Advanced Materials* 28.28 (2016), pp. 5865–5870.

[127] Jianping Fu et al. "Mechanical regulation of cell function with geometrically modulated elastomeric substrates". In: *Nature methods* 7.9 (2010), pp. 733–736.

[128] Darius Gailevičius et al. "Additive-manufacturing of 3D glass-ceramics down to nanoscale resolution". In: *Nanoscale Horizons* 4.3 (2019), pp. 647–651.

[129] Stavros Gaitanaros and Stelios Kyriakides. "On the effect of relative density on the crushing and energy absorption of open-cell foams under impact". In: *International Journal of Impact Engineering* 82 (2015), pp. 3–13.

[130] Stavros Gaitanaros, Stelios Kyriakides, and Andrew M Kraynik. "On the crushing response of random open-cell foams". In: *International Journal of Solids and Structures* 49.19-20 (2012), pp. 2733–2743.

[131] Huajian Gao et al. "Materials become insensitive to flaws at nanoscale: lessons from nature". In: *Proceedings of the national Academy of Sciences* 100.10 (2003), pp. 5597–5600.

[132] Libo Gao et al. "High-entropy alloy (HEA)-coated nanolattice structures and their mechanical properties". In: *Advanced Engineering Materials* 20.1 (2018), p. 1700625.

[133] Emmanuel E Gdoutos. *Fracture mechanics: an introduction*. Vol. 263. Springer Nature, 2020.

[134] Paul Germain. "The method of virtual power in the mechanics of continuous media, I: Second-gradient theory". In: *Mathematics and Mechanics of Complex Systems* 8.2 (2020), pp. 153–190.

[135] Giuseppe Geymonat, Stefan Müller, and Nicolas Triantafyllidis. "Homogenization of nonlinearly elastic materials, microscopic bifurcation and macroscopic loss of rank-one convexity". In: *Archive for rational mechanics and analysis* 122.3 (1993), pp. 231–290.

[136] SK Ghaswala. "Aluminium Structures General Aspects of Design". In: (1961).

[137] Mergen H Ghayesh and Ali Farajpour. "A review on the mechanics of functionally graded nanoscale and microscale structures". In: *International Journal of Engineering Science* 137 (2019), pp. 8–36.

[138] SM Giannitelli et al. "Graded porous polyurethane foam: A potential scaffold for oro-maxillary bone regeneration". In: *Materials Science and Engineering: C* 51 (2015), pp. 329–335.

[139] Lorna J Gibson, MF Ashby, and Kenneth E Easterling. "Structure and mechanics of the iris leaf". In: *Journal of Materials Science* 23.9 (1988), pp. 3041–3048.

[140] Lorna J Gibson and Michael F Ashby. *Cellular solids: structure and properties*. Cambridge university press, 1999.

[141] Lorna J Gibson et al. "The mechanics of two-dimensional cellular materials". In: *Proceedings of the Royal Society of London. A. Mathematical and Physical Sciences* 382.1782 (1982), pp. 25–42.

[142] Lorna Jane Gibson. "The elastic and plastic behaviour of cellular materials". PhD thesis. University of Cambridge, 1981.

[143] Erik van der Giessen et al. "Roadmap on multiscale materials modeling". In: *Modelling and Simulation in Materials Science and Engineering* 28.4 (2020), p. 043001.

[144] Ivan Giorgio et al. "Buckling modes in pantographic lattices". In: *Comptes Rendus Mecanique* 344.7 (2016), pp. 487–501.

[145] Raphaël N Glaesener et al. "Continuum representation of nonlinear three-dimensional periodic truss networks by on-the-fly homogenization". In: *International Journal of Solids and Structures* 206 (2020), pp. 101–113.

[146] MAF Gomes et al. "Mechanically deformed crumpled surfaces". In: *Journal of Physics D: Applied Physics* 22.8 (1989), p. 1217.

[147] L Gong, S Kyriakides, and N Triantafyllidis. "On the stability of Kelvin cell foams under compressive loads". In: *Journal of the Mechanics and Physics of Solids* 53.4 (2005), pp. 771–794.

[148] L Gong and St Kyriakides. "Compressive response of open cell foams Part II: Initiation and evolution of crushing". In: *International Journal of Solids and Structures* 42.5-6 (2005), pp. 1381–1399.

[149] Aldair E Gongora et al. "A Bayesian experimental autonomous researcher for mechanical design". In: *Science Advances* 6.15 (2020), eaaz1708.

[150] Ryan Gosselin and Denis Rodrigue. "Cell morphology analysis of high density polymer foams". In: *Polymer testing* 24.8 (2005), pp. 1027–1035.

[151] M Goto et al. "Micro-patterning of multiple organic molecules by laser implantation". In: *Applied Physics A* 79.1 (2004), pp. 157–160.

[152] Joseph N Grima and Kenneth E Evans. "Auxetic behavior from rotating squares". In: (2000).

[153] Andrew Gross et al. "Correlation between topology and elastic properties of imperfect truss-lattice materials". In: *Journal of the Mechanics and Physics of Solids* 124 (2019), pp. 577–598.

[154] Dietmar Gross and Thomas Seelig. *Fracture mechanics: with an introduction to micromechanics*. Springer, 2017.

[155] Grace X Gu et al. "Printing nature: Unraveling the role of nacre's mineral bridges". In: *Journal of the mechanical behavior of biomedical materials* 76 (2017), pp. 135–144.

[156] Xiang-Dong E Guo et al. "Finite element modeling of damage accumulation in trabecular bone under cyclic loading". In: *Journal of biomechanics* 27.2 (1994), pp. 145–155.

[157] Chan Soo Ha, Roderic S Lakes, and Michael E Plesha. "Design, fabrication, and analysis of lattice exhibiting energy absorption via snap-through behavior". In: *Materials & Design* 141 (2018), pp. 426–437.

[158] Babak Haghpanah et al. "Buckling of regular, chiral and hierarchical honeycombs under a general macroscopic stress state". In: *Proceedings of the Royal Society A: Mathematical, Physical and Engineering Sciences* 470.2167 (2014), p. 20130856.

[159] Babak Haghpanah et al. "Multistable shape-reconfigurable architected materials". In: *Advanced Materials* 28.36 (2016), pp. 7915–7920.

[160] Ian W Hamley and Ian W Hamley. *The physics of block copolymers*. Vol. 19. Oxford University Press Oxford, 1998.

[161] Fusheng Han et al. "Acoustic absorption behaviour of an open-celled aluminium foam". In: *Journal of Physics D: Applied Physics* 36.3 (2003), p. 294.

[162] Adam F Hannon et al. "Optimizing topographical templates for directed self-assembly of block copolymers via inverse design simulations". In: *Nano letters* 14.1 (2014), pp. 318–325.

[163] Ryan L Harne and KW Wang. "A review of the recent research on vibration energy harvesting via bistable systems". In: *Smart materials and structures* 22.2 (2013), p. 023001.

[164] R Hedayati et al. "Effect of mass multiple counting on the elastic properties of open-cell regular porous biomaterials". In: *Materials & Design* 89 (2016), pp. 9–20.

[165] Hirofumi Hidai et al. "Self-standing aligned fiber scaffold fabrication by two photon photopolymerization". In: *Biomedical microdevices* 11.3 (2009), pp. 643–652.

[166] Archibald Vivian Hill. "The heat of shortening and the dynamic constants of muscle". In: *Proceedings of the Royal Society of London. Series B-Biological Sciences* 126.843 (1938), pp. 136–195.

[167] Rodney Hill. *The mathematical theory of plasticity*. Vol. 11. Oxford university press, 1998.

[168] Scott J Hollister. "Porous scaffold design for tissue engineering". In: *Nature materials* 4.7 (2005), pp. 518–524.

[169] Yang Hu et al. "Dislocation avalanche mechanism in slowly compressed high entropy alloy nanopillars". In: *Communications Physics* 1.1 (2018), pp. 1–8.

[170] Peter Hyman, Adelaja I Osofero, and Srinivas Sriramula. "Buckling behaviour of three-dimensional prestressed stayed columns". In: *IOP Conference Series: Materials Science and Engineering*. Vol. 413. 1. IOP Publishing. 2018, p. 012007.

[171] Donata Iandolo et al. "Electron microscopy for 3D scaffolds–cell biointerface characterization". In: *Advanced biosystems* 3.2 (2019), p. 1800103.

[172] Maria Iannone et al. "Nanoengineered surfaces for focal adhesion guidance trigger mesenchymal stem cell self-organization and tenogenesis". In: *Nano letters* 15.3 (2015), pp. 1517–1525.

[173] Aniket Ingrole, Ayou Hao, and Richard Liang. "Design and modeling of auxetic and hybrid honeycomb structures for in-plane property enhancement". In: *Materials & Design* 117 (2017), pp. 72–83.

[174] Nobuo Inoue. "A new method of solution of the two-dimensional isostatical problem in the mathematical theory of plasticity". In: *Journal of the Physical Society of Japan* 7.5 (1952), pp. 518–523.

[175] Alexandra Ion et al. "Digital mechanical metamaterials". In: *Proceedings of the 2017 CHI Conference on Human Factors in Computing Systems*. 2017, pp. 977–988.

[176] Dongchan Jang et al. "Deformation mechanisms in nanotwinned metal nanopillars". In: *Nature nanotechnology* 7.9 (2012), p. 594.

[177] Dongchan Jang et al. "Fabrication and deformation of three-dimensional hollow ceramic nanostructures". In: *Nature materials* 12.10 (2013), pp. 893–898.

[178] Wen-Yea Jang, Andrew M Kraynik, and Stelios Kyriakides. "On the microstructure of open-cell foams and its effect on elastic properties". In: *International Journal of Solids and Structures* 45.7-8 (2008), pp. 1845–1875.

[179] Wen-Yea Jang and Stelios Kyriakides. "On the crushing of aluminum open-cell foams: Part II analysis". In: *International Journal of Solids and Structures* 46.3-4 (2009), pp. 635–650.

[180] Wen-Yea Jang, Stelios Kyriakides, and Andrew M Kraynik. "On the compressive strength of open-cell metal foams with Kelvin and random cell structures". In: *International Journal of Solids and Structures* 47.21 (2010), pp. 2872–2883.

[181] Farhad Javid et al. "Architected materials with ultra-low porosity for vibration control". In: *Advanced materials* 28.28 (2016), pp. 5943–5948.

[182] Rachael K Jayne et al. "Dynamic Actuation of Soft 3D Micromechanical Structures Using Micro-Electromechanical Systems (MEMS)". In: *Advanced Materials Technologies* 3.3 (2018), p. 1700293.

[183] Benjamin Jenett et al. "Discretely assembled mechanical metamaterials". In: *Science advances* 6.47 (2020), eabc9943.

[184] Hojeong Jeon, Eunpa Kim, and Costas P Grigoropoulos. "Measurement of contractile forces generated by individual fibroblasts on self-standing fiber scaffolds". In: *Biomedical microdevices* 13.1 (2011), pp. 107–115.

[185] Hojeong Jeon et al. "Directing cell migration and organization via nanocrater-patterned cell-repellent interfaces". In: *Nature materials* 14.9 (2015), pp. 918–923.

[186] Hojeong Jeon et al. "Fabrication of arbitrary polymer patterns for cell study by two-photon polymerization process". In: *Journal of Biomedical Materials Research Part A: An Official Journal of The Society for Biomaterials, The Japanese Society for Biomaterials, and The Australian Society for Biomaterials and the Korean Society for Biomaterials* 93.1 (2010), pp. 56–66.

[187] Hojeong Jeon et al. "The effect of micronscale anisotropic cross patterns on fibroblast migration". In: *Biomaterials* 31.15 (2010), pp. 4286–4295.

[188] Yanhui Jiang and Qiming Wang. "Highly-stretchable 3D-architected mechanical metamaterials". In: *Scientific reports* 6.1 (2016), pp. 1–11.

[189] F López Jiménez and N Triantafyllidis. "Buckling of rectangular and hexagonal honeycomb under combined axial compression and transverse shear". In: *International Journal of Solids and Structures* 50.24 (2013), pp. 3934–3946.

[190] Matthew S Joens et al. "Helium Ion Microscopy (HIM) for the imaging of biological samples at sub-nanometer resolution". In: *Scientific reports* 3.1 (2013), pp. 1–7.

[191] Knud Winstrup Johansen. *Yield-line formulae for slabs*. CRC Press, 1972.

[192] Chris G Johnson et al. "On the buckling of an elastic holey column". In: *Proceedings of the Royal Society A: mathematical, physical and engineering sciences* 473.2207 (2017), p. 20170477.

[193] Scott R Johnston et al. "Analysis of mesostructure unit cells comprised of octet-truss structures". In: (2006).

[194] Christa P de Jonge, Helena Kolken, and Amir A Zadpoor. "Non-auxetic mechanical metamaterials". In: *Materials* 12.4 (2019), p. 635.

[195] Linas Jonušauskas et al. "Mesoscale laser 3D printing". In: *Optics express* 27.11 (2019), pp. 15205–15221.

[196] Makarand G Joshi and Sherrill B Biggers Jr. "Thickness optimization for maximum buckling loads in composite laminated plates". In: *Composites Part B: Engineering* 27.2 (1996), pp. 105–114.

[197] Muamer Kadic et al. "On the practicability of pentamode mechanical metamaterials". In: *Applied Physics Letters* 100.19 (2012), p. 191901.

[198] Muamer Kadic et al. "Pentamode metamaterials with independently tailored bulk modulus and mass density". In: *Physical Review Applied* 2.5 (2014), p. 054007.

[199] A Kalaitzis et al. "Jetting dynamics of Newtonian and non-Newtonian fluids via laser-induced forward transfer: Experimental and simulation studies". In: *Applied Surface Science* 465 (2019), pp. 136–142.

[200] Yoshihiro Kanno. "Exploring new tensegrity structures via mixed integer programming". In: *Structural and Multidisciplinary Optimization* 48.1 (2013), pp. 95–114.

[201] Z Kantor, Z Toth, and T Szörényi. "Metal pattern deposition by laser-induced forward transfer". In: *Applied surface science* 86.1-4 (1995), pp. 196–201.

[202] Z Kántor and T Szörényi. "Dynamics of long-pulse laser transfer of micrometer-sized metal patterns as followed by time-resolved measurements of reflectivity and transmittance". In: *Journal of applied physics* 78.4 (1995), pp. 2775–2781.

[203] Elli Käpylä et al. "Direct laser writing and geometrical analysis of scaffolds with designed pore architecture for three-dimensional cell culturing". In: *Journal of Micromechanics and Microengineering* 22.11 (2012), p. 115016.

[204] E Kaselouris et al. "Elastoplastic study of nanosecond-pulsed laser interaction with metallic films using 3D multiphysics fem modeling". In: *International Journal of Damage Mechanics* 25.1 (2016), pp. 42–55.

[205] Nicholas T Kattamis et al. "Laser direct write printing of sensitive and robust light emitting organic molecules". In: *Applied Physics Letters* 94.10 (2009), p. 80.

[206] S Graham Kelly. *Mechanical vibrations: theory and applications*. Cengage learning Stamford, CT, 2012.

[207] Oraib Al-Ketan and Rashid K Abu Al-Rub. "Multifunctional mechanical metamaterials based on triply periodic minimal surface lattices". In: *Advanced Engineering Materials* 21.10 (2019), p. 1900524.

[208] Oraib Al-Ketan et al. "Microarchitected stretching-dominated mechanical metamaterials with minimal surface topologies". In: *Advanced Engineering Materials* 20.9 (2018), p. 1800029.

[209] Helmut Keupp and Joachim Reitner. *Fossil and Recent Sponges*. Springer-Verlag, 1991.

[210] Romik Khajehtourian and Dennis M Kochmann. "A continuum description of substrate-free dissipative reconfigurable metamaterials". In: *Journal of the Mechanics and Physics of Solids* 147 (2021), p. 104217.

[211] Sooho Kim and Chang-Woo Lee. "A review on manufacturing and application of open-cell metal foam". In: *Procedia Mater. Sci* 4.305 (2014), pp. 10–1016.

[212] Yongtae Kim et al. "Designing an adhesive pillar shape with deep learning-based optimization". In: *ACS applied materials & interfaces* 12.21 (2020), pp. 24458–24465.

[213] Hagen Kleinert. "Gravity as a theory of defects in a crystal with only second gradient elasticity". In: *Annalen der Physik* 499.2 (1987), pp. 117–119.

[214] Hideo Kodama. "Automatic method for fabricating a three-dimensional plastic model with photo-hardening polymer". In: *Review of scientific instruments* 52.11 (1981), pp. 1770–1773.

[215] Warner Tjardus Koiter and AMA Van Der Heijden. *WT Koiter's elastic stability of solids and structures*. Cambridge University Press Cambridge, UK; New York, NY, USA, 2009.

[216] Hunter T Kollmann et al. "Deep learning for topology optimization of 2D metamaterials". In: *Materials & Design* 196 (2020), p. 109098.

[217] AM Kraynik, DA Reinelt, et al. "Elastic-plastic behavior of a Kelvin foam". In: *The Kelvin Problem. Foam Structures of Minimal Surface Area* (1996), pp. 93–1085.

[218] Steen Krenk. *Non-linear modeling and analysis of solids and structures*. Cambridge University Press, 2009.

[219] Anastasiia O Krushynska, Varvara G Kouznetsova, and Marc GD Geers. "Towards optimal design of locally resonant acoustic metamaterials". In: *Journal of the Mechanics and Physics of Solids* 71 (2014), pp. 179–196.

[220] Leonid Kucherov and Michael Ryvkin. "Fracture toughness of open-cell Kelvin foam". In: *International Journal of Solids and Structures* 51.2 (2014), pp. 440–448.

[221] Akira Kudo et al. "Compressive response of non-slender octet carbon microlattices". In: *Frontiers in Materials* 6 (2019), p. 169.

[222] Chil-Chyuan Kuo. "Micro-Raman spectroscopy characterization of polycrystalline silicon films fabricated by excimer laser crystallization". In: *Optics and lasers in engineering* 47.5 (2009), pp. 612–616.

[223] Haresh Lalvani. "Non-periodic space structures". In: *International Journal of Space Structures* 2.2 (1987), pp. 93–108.

[224] Haresh Lalvani. "Structures on hyper-structures". In: *Structural Topology, 1982, núm. 6* (1982).

[225] Ilaresh Lalvani. "TRUSS CONFIGURATIONS". In: (1990).

[226] David CC Lam et al. "Experiments and theory in strain gradient elasticity". In: *Journal of the Mechanics and Physics of Solids* 51.8 (2003), pp. 1477–1508.

[227] Sander Leeflang, Shahram Janbaz, and Amir A Zadpoor. "Metallic clay". In: *Additive Manufacturing* 28 (2019), pp. 528–534.

[228] Enrico Domenico Lemma et al. "Mechanical properties tunability of three-dimensional polymeric structures in two-photon lithography". In: *IEEE transactions on nanotechnology* 16.1 (2016), pp. 23–31.

[229] Jin Li et al. "Nanoscale stacking fault–assisted room temperature plasticity in flash-sintered TiO2". In: *Science advances* 5.9 (2019), eaaw5519.

[230] Linqing Li, Jeroen Eyckmans, and Christopher S Chen. "Designer biomaterials for mechanobiology". In: *Nature materials* 16.12 (2017), pp. 1164–1168.

[231] Shuaifeng Li et al. "Observation of elastic topological states in soft materials". In: *Nature communications* 9.1 (2018), pp. 1–9.

[232] Xiaoyan Li and Huajian Gao. "Smaller and stronger". In: *Nature materials* 15.4 (2016), pp. 373–374.

[233] Tim Liedl et al. "Self-assembly of three-dimensional prestressed tensegrity structures from DNA". In: *Nature nanotechnology* 5.7 (2010), pp. 520–524.

[234] Esben Lindgaard and Jonas Dahl. "On compliance and buckling objective functions in topology optimization of snap-through problems". In: *Structural and Multidisciplinary Optimization* 47.3 (2013), pp. 409–421.

[235] Yun Ling et al. "Mechanically assembled, three-dimensional hierarchical structures of cellular graphene with programmed geometries and outstanding electromechanical properties". In: *ACS nano* 12.12 (2018), pp. 12456–12463.

[236] Fan Liu et al. "Machine learning-based design and optimization of curved beams for multistable structures and metamaterials". In: *Extreme Mechanics Letters* 41 (2020), p. 101002.

[237] Tongwei Liu et al. "A predictive deep-learning approach for homogenization of auxetic kirigami metamaterials with randomly oriented cuts". In: *Modern Physics Letters B* 35.01 (2021), p. 2150033.

[238] Yanping Liu and Hong Hu. "A review on auxetic structures and polymeric materials". In: *Scientific Research and Essays* 5.10 (2010), pp. 1052–1063.

[239] Zengqian Liu, Zhefeng Zhang, and Robert O Ritchie. "On the materials science of nature's arms race". In: *Advanced Materials* 30.32 (2018), p. 1705220.

[240] Zhiqiang Liu et al. "The influence of chitosan hydrogel on stem cell engraftment, survival and homing in the ischemic myocardial microenvironment". In: *Biomaterials* 33.11 (2012), pp. 3093–3106.

[241] Arthur L Loeb and William Varney. "A Stabilized Cuboctahedron Frame". In: *International Journal of Space Structures* 7.2 (1992), pp. 85–90.

[242] Shi Luo and Julia R Greer. "Bio-mimicked silica architectures capture geometry, microstructure, and mechanical properties of marine diatoms". In: *Advanced Engineering Materials* 20.9 (2018), p. 1800301.

[243] Weitao Lv, Dong Li, and Liang Dong. "Study on mechanical properties of a hierarchical octet-truss structure". In: *Composite Structures* 249 (2020), p. 112640.

[244] Wei Ma, Feng Cheng, and Yongmin Liu. "Deep-learning-enabled on-demand design of chiral metamaterials". In: *ACS nano* 12.6 (2018), pp. 6326–6334.

[245] Zhen Ma et al. "Contractile deficits in engineered cardiac microtissues as a result of MYBPC3 deficiency and mechanical overload". In: *Nature biomedical engineering* 2.12 (2018), pp. 955–967.

[246] Alessandro Maggi, Hanqing Li, and Julia R Greer. "Three-dimensional nano-architected scaffolds with tunable stiffness for efficient bone tissue growth". In: *Acta biomaterialia* 63 (2017), pp. 294–305.

[247] E Magnucka-Blandzi and K Magnucki. "Effective design of a sandwich beam with a metal foam core". In: *Thin-Walled Structures* 45.4 (2007), pp. 432–438.

[248] Gillian Dumsile Mahumane et al. "3D scaffolds for brain tissue regeneration: architectural challenges". In: *Biomaterials science* 6.11 (2018), pp. 2812–2837.

[249] M Marder and Xiangming Liu. "Instability in lattice fracture". In: *Physical Review Letters* 71.15 (1993), p. 2417.

[250] Paul Mardling et al. "The use of auxetic materials in tissue engineering". In: *Biomaterials science* 8.8 (2020), pp. 2074–2083.

[251] Jerrold E Marsden and Thomas JR Hughes. *Mathematical foundations of elasticity*. Courier Corporation, 1994.

[252] Shoji Maruo and John T Fourkas. "Recent progress in multiphoton microfabrication". In: *Laser & Photonics Reviews* 2.1-2 (2008), pp. 100–111.

[253] Shoji Maruo and Koji Ikuta. "Submicron stereolithography for the production of freely movable mechanisms by using single-photon polymerization". In: *Sensors and Actuators A: Physical* 100.1 (2002), pp. 70–76.

[254] I Maskery and IA Ashcroft. "The deformation and elastic anisotropy of a new gyroid-based honeycomb made by laser sintering". In: *Additive Manufacturing* 36 (2020), p. 101548.

[255] Arturo J Mateos et al. "Discrete-continuum duality of architected materials: failure, flaws, and fracture". In: *Advanced Functional Materials* 29.5 (2019), p. 1806772.

[256] Takashi Matsushima, René Chambon, and Denis Caillerie. "Second gradient models as a particular case of microstructured models: a large strain finite elements analysis". In: *Comptes Rendus de l'Académie des Sciences-Series IIB-Mechanics-Physics-Astronomy* 328.2 (2000), pp. 179–186.

[257] Frank L Matthews and Rees D Rawlings. *Composite materials: engineering and science*. CRC press, 1999.

[258] David Brian McCallen and KM Romstad. "A continuum model for the nonlinear analysis of beam-like lattice structures". In: *Computers & structures* 29.2 (1988), pp. 177–197.

[259] William H Meeks III. "The theory of triply periodic minimal surfaces". In: *Indiana University Mathematics Journal* (1990), pp. 877–936.

[260] Leonard Meirovitch. "Analytical methods in vibrations." In: (1967).

[261] Liang Meng et al. "An emerging class of hyperbolic lattice exhibiting tunable elastic properties and impact absorption through chiral twisting". In: *Extreme Mechanics Letters* 40 (2020), p. 100869.

[262] AM Merzer and R Freund. "Buckling of strike-slip faults—in a model and in nature". In: *Geophysical Journal International* 43.2 (1975), pp. 517–530.

[263] Mark C Messner. "Optimal lattice-structured materials". In: *Journal of the Mechanics and Physics of Solids* 96 (2016), pp. 162–183.

[264] Lucas R Meza, Satyajit Das, and Julia R Greer. "Strong, lightweight, and recoverable three-dimensional ceramic nanolattices". In: *Science* 345.6202 (2014), pp. 1322–1326.

[265] Lucas R Meza et al. "Reexamining the mechanical property space of three-dimensional lattice architectures". In: *Acta Materialia* 140 (2017), pp. 424–432.

[266] Lucas R Meza et al. "Resilient 3D hierarchical architected metamaterials". In: *Proceedings of the National Academy of Sciences* 112.37 (2015), pp. 11502–11507.

[267] Andrea Micheletti. "Modular Tensegrity Structures: The" Tor Vergata" Footbridge". In: *Mechanics, models and methods in civil engineering*. Springer, 2012, pp. 375–384.

[268] Andrea Micheletti. "The indeterminacy condition for tensegrity towers: A kinematic approach". In: *Revue française de génie civil* 7.3 (2003), pp. 329–342.

[269] Andrea Micheletti, Giuseppe Ruscica, and Fernando Fraternali. "On the compact wave dynamics of tensegrity beams in multiple dimensions". In: *Nonlinear Dynamics* 98.4 (2019), pp. 2737–2753.

[270] Andrea Micheletti and William Williams. "A marching procedure for form-finding for tensegrity structures". In: *Journal of mechanics of materials and structures* 2.5 (2007), pp. 857–882.

[271] Maxime Mieszala et al. "Micromechanics of amorphous metal/polymer hybrid structures with 3D cellular architectures: size effects, buckling behavior, and energy absorption capability". In: *Small* 13.8 (2017), p. 1602514.

[272] JCP Miller. *The Fifty-Nine Icosahedra*. 1939.

[273] NJ Mills. "The high strain mechanical response of the wet Kelvin model for open-cell foams". In: *International Journal of Solids and Structures* 44.1 (2007), pp. 51–65.

[274] Graeme W Milton and Andrej V Cherkaev. "Which elasticity tensors are realizable?" In: (1995).

[275] Raymond David Mindlin. "Second gradient of strain and surface-tension in linear elasticity". In: *International Journal of Solids and Structures* 1.4 (1965), pp. 417–438.

[276] Seyed M Mirvakili and Ian W Hunter. "Artificial muscles: Mechanisms, applications, and challenges". In: *Advanced Materials* 30.6 (2018), p. 1704407.

[277] ES Mistakidis, KT Thomopoulos, and M Ap Tzaferopoulos. "Effective methods for the analysis of steel structures with strain-softening behaviour". In: *Journal of Constructional Steel Research* 44.1-2 (1997), pp. 3–21.

[278] Widianto P Moestopo et al. "Pushing and Pulling on Ropes: Hierarchical Woven Materials". In: *Advanced Science* 7.20 (2020), p. 2001271.

[279] Amir Mohammadipour and Kaspar Willam. "Lattice approach in continuum and fracture mechanics". In: *Journal of Applied Mechanics* 83.7 (2016).

[280] Camilla Mohrdieck et al. "A theoretical description of elastic pillar substrates in biophysical experiments". In: *ChemPhysChem* 6.8 (2005), pp. 1492–1498.

[281] Mehrdad Mohsenizadeh et al. "Additively-manufactured lightweight Metamaterials for energy absorption". In: *Materials & Design* 139 (2018), pp. 521–530.

[282] M Morales et al. "Laser-Induced Forward Transfer Techniques and Applications". In: *Advances in Laser Materials Processing* (2018), pp. 339–379.

[283] Davood Mousanezhad et al. "Hierarchical honeycomb auxetic metamaterials". In: *Scientific reports* 5.1 (2015), pp. 1–8.

[284] SF Mu
ller de Almeida and Jorn S Hansen. "Enhanced elastic buckling loads of composite plates with tailored thermal residual stresses". In: (1997).

[285] T Mukhopadhyay and S Adhikari. "Stochastic mechanics of metamaterials". In: *Composite Structures* 162 (2017), pp. 85–97.

[286] Christian C Nadell et al. "Deep learning for accelerated all-dielectric metasurface design". In: *Optics express* 27.20 (2019), pp. 27523–27535.

[287] Kai Narita et al. "3D Architected Carbon Electrodes for Energy Storage". In: *Advanced Energy Materials* (2020), p. 2002637.

[288] Adnan H Nayfeh and Mohamed S Hefzy. "Continuum modeling of three-dimensional truss-like space structures". In: *AIAA Journal* 16.8 (1978), pp. 779–787.

[289] Michael P Nemeth. "A treatise on equivalent-plate stiffnesses for stiffened laminated-composite plates and plate-like lattices". In: (2011).

[290] Rebecca L Noad, Colm G Hanratty, and Simon J Walsh. "Clinical impact of stent design". In: *Interventional Cardiology Review* 9.2 (2014), p. 89.

[291] Andrew N Norris. "Mechanics of elastic networks". In: *Proceedings of the Royal Society A: Mathematical, Physical and Engineering Sciences* 470.2172 (2014), p. 20140522.

[292] Mark Randall O'Masta et al. "The fracture toughness of octet-truss lattices". In: *Journal of the Mechanics and Physics of Solids* 98 (2017), pp. 271–289.

[293] Kotaro Obata et al. "High-aspect 3D two-photon polymerization structuring with widened objective working range (WOW-2PP)". In: *Light: Science & Applications* 2.12 (2013), e116–e116.

[294] Kotaro Obata et al. "Multi-focus two-photon polymerization technique based on individually controlled phase modulation". In: *Optics express* 18.16 (2010), pp. 17193–17200.

[295] Dai Okumura, Atsushi Okada, and Nobutada Ohno. "Long Wavelength Buckling of Cubic Open-Cell Foams Subjected to Uniaxial Compression". In: *Key Engineering Materials*. Vol. 353. Trans Tech Publ. 2007, pp. 583–586.

[296] Anita Orlowska, Cezary Graczykowski, and Adam Galezia. "The effect of prestress force magnitude on the natural bending frequencies of the eccentrically prestressed glass fibre reinforced polymer composite beams". In: *Journal of Composite Materials* 52.15 (2018), pp. 2115–2128.

[297] Yannis Orphanos et al. "An integrated method for material properties characterization based on pulsed laser generated surface acoustic waves". In: *Microelectronic engineering* 112 (2013), pp. 249–254.

[298] Martin Ostoja-Starzewski. "Lattice models in micromechanics". In: *Appl. Mech. Rev.* 55.1 (2002), pp. 35–60.

[299] Aleksandr Ovsianikov et al. "Ultra-low shrinkage hybrid photosensitive material for two-photon polymerization microfabrication". In: *ACS nano* 2.11 (2008), pp. 2257–2262.

[300] Stefano Palagi, Dhruv P Singh, and Peer Fischer. "Light-Controlled Micromotors and Soft Microrobots". In: *Advanced Optical Materials* 7.16 (2019), p. 1900370.

[301] Panayiotis Papadopoulos. "Introduction to continuum mechanics". In: *Berkeley, California* (2008).

[302] P Papakonstantinou, NA Vainos, and C Fotakis. "Microfabrication by UV femtosecond laser ablation of Pt, Cr and indium oxide thin films". In: *Applied surface science* 151.3-4 (1999), pp. 159–170.

[303] Om Prakash Parida and N. Bhat. "CHARACTERIZATION OF OPTICAL PROPERTIES OF SU-8 AND FABRICATION OF OPTICAL COMPONENETS". In: 2009.

[304] Sang Hu Park et al. "Improvement of spatial resolution in nano-stereolithography using radical quencher". In: *Macromolecular research* 14.5 (2006), pp. 559–564.

[305] William J Parnell. "Nonlinear pre-stress for cloaking from antiplane elastic waves". In: *Proceedings of the Royal Society A: Mathematical, Physical and Engineering Sciences* 468.2138 (2012), pp. 563–580.

[306] Damiano Pasini and James K Guest. "Imperfect architected materials: mechanics and topology optimization". In: *MRS Bulletin* 44.10 (2019), pp. 766–772.

[307] JB Patel et al. "Rheo-processing of an alloy specifically designed for semi-solid metal processing based on the Al–Mg–Si system". In: *Materials Science and Engineering: A* 476.1-2 (2008), pp. 341–349.

[308] Amit Pathak et al. "The simulation of stress fibre and focal adhesion development in cells on patterned substrates". In: *Journal of The Royal Society Interface* 5.22 (2008), pp. 507–524.

[309] Jayson Paulose, Anne S Meeussen, and Vincenzo Vitelli. "Selective buckling via states of self-stress in topological metamaterials". In: *Proceedings of the National Academy of Sciences* 112.25 (2015), pp. 7639–7644.

[310] Fei Peng, Xiaohua Yu, and Mei Wei. "In vitro cell performance on hydroxyapatite particles/poly (L-lactic acid) nanofibrous scaffolds with an excellent particle along nanofiber orientation". In: *Acta Biomaterialia* 7.6 (2011), pp. 2585–2592.

[311] Fabrizio A Pennacchio et al. "Three-dimensionally patterned scaffolds modulate the biointerface at the nanoscale". In: *Nano letters* 19.8 (2019), pp. 5118–5123.

[312] Minh-Son Pham et al. "Damage-tolerant architected materials inspired by crystal microstructure". In: *Nature* 565.7739 (2019), pp. 305–311.

[313] Nico Pietroni et al. "Position-based tensegrity design". In: *ACM Transactions on Graphics* 36.6 (2017).

[314] A Piqué et al. "A novel laser transfer process for direct writing of electronic and sensor materials". In: *Applied Physics A* 69.1 (1999), S279–S284.

[315] Alberto Piqué and Pere Serra. *Laser printing of functional materials: 3D microfabrication, electronics and biomedicine*. John Wiley & Sons, 2018.

[316] Alberto Piqué et al. "Laser 3D micro-manufacturing". In: *Journal of Physics D: Applied Physics* 49.22 (2016), p. 223001.

[317] Luca Placidi. "A variational approach for a nonlinear one-dimensional damage-elasto-plastic second-gradient continuum model". In: *Continuum Mechanics and Thermodynamics* 28.1-2 (2016), pp. 119–137.

[318] Luca Placidi et al. "Variational methods in continuum damage and fracture mechanics". In: *Encyclopedia of continuum mechanics* (2020), pp. 2634–2643.

[319] William J Polacheck and Christopher S Chen. "Measuring cell-generated forces: a guide to the available tools". In: *Nature methods* 13.5 (2016), pp. 415–423.

[320] William J Polacheck et al. "Microfabricated blood vessels for modeling the vascular transport barrier". In: *Nature protocols* 14.5 (2019), pp. 1425–1454.

[321] Bogdan-Ioan Popa and Steven A Cummer. "Non-reciprocal and highly nonlinear active acoustic metamaterials". In: *Nature communications* 5.1 (2014), pp. 1–5.

[322] Carlos M Portela et al. "Extreme mechanical resilience of self-assembled nanolabyrinthine materials". In: *Proceedings of the National Academy of Sciences* 117.11 (2020), pp. 5686–5693.

[323] David A Porter and Kenneth E Easterling. *Phase transformations in metals and alloys (revised reprint)*. CRC press, 2009.

[324] Maura Power et al. "A monolithic force-sensitive 3D microgripper fabricated on the tip of an optical fiber using 2-photon polymerization". In: *Small* 14.16 (2018), p. 1703964.

[325] O Prakash et al. "A note on the deformation behaviour of two-dimensional model cellular structures". In: *Philosophical Magazine A* 73.3 (1996), pp. 739–751.

[326] Phanisri P Pratapa, Phanish Suryanarayana, and Glaucio H Paulino. "Bloch wave framework for structures with nonlocal interactions: Application to the design of origami acoustic metamaterials". In: *Journal of the Mechanics and Physics of Solids* 118 (2018), pp. 115–132.

[327] Yunan Prawoto. "Seeing auxetic materials from the mechanics point of view: a structural review on the negative Poisson's ratio". In: *Computational Materials Science* 58 (2012), pp. 140–153.

[328] Andrew Pressley. "Gauss' Theorema Egregium". In: *Elementary differential geometry*. Springer, 2010, pp. 247–268.

[329] Chunlei Qiu et al. "Influence of processing conditions on strut structure and compressive properties of cellular lattice structures fabricated by selective laser melting". In: *Materials Science and Engineering: A* 628 (2015), pp. 188–197.

[330] Ahmad Rafsanjani, Abdolhamid Akbarzadeh, and Damiano Pasini. "Snapping mechanical metamaterials under tension". In: *Advanced Materials* 27.39 (2015), pp. 5931–5935.

[331] Ahmad Rafsanjani, Katia Bertoldi, and André R Studart. "Programming soft robots with flexible mechanical metamaterials". In: *arXiv preprint arXiv:1906.00306* (2019).

[332] Ahmad Rafsanjani and Damiano Pasini. "Bistable auxetic mechanical metamaterials inspired by ancient geometric motifs". In: *Extreme Mechanics Letters* 9 (2016), pp. 291–296.

[333] K Kanaka Raju and G Venkateswara Rao. "Free vibration behavior of prestressed beams". In: *Journal of Structural Engineering* 112.2 (1986), pp. 433–437.

[334] U Ramamurty and A Paul. "Variability in mechanical properties of a metal foam". In: *Acta materialia* 52.4 (2004), pp. 869–876.

[335] Jordan R Raney et al. "Stable propagation of mechanical signals in soft media using stored elastic energy". In: *Proceedings of the National Academy of Sciences* 113.35 (2016), pp. 9722–9727.

[336] Shivakumar I Ranganathan and Martin Ostoja-Starzewski. "Universal elastic anisotropy index". In: *Physical Review Letters* 101.5 (2008), p. 055504.

[337] Ludovic Rapp et al. "Pulsed-laser printing of silver nanoparticles ink: control of morphological properties". In: *Optics express* 19.22 (2011), pp. 21563–21574.

[338] Janet Reinbold et al. "The rise of (chiral) 3D mechanical metamaterials". In: *Materials* 12.21 (2019), p. 3527.

[339] Xin Ren et al. "Auxetic metamaterials and structures: a review". In: *Smart materials and structures* 27.2 (2018), p. 023001.

[340] Kelvin Roovers and Niels De Temmerman. "Deployable scissor grids consisting of translational units". In: *International Journal of Solids and Structures* 121 (2017), pp. 45–61.

[341] Carlos J Ruestes et al. "Hardening under compression in Au foams". In: *Acta Materialia* 108 (2016), pp. 1–7.

[342] Amir Hossein Sadeghi et al. "Engineered 3D cardiac fibrotic tissue to study fibrotic remodeling". In: *Advanced healthcare materials* 6.11 (2017), p. 1601434.

[343] Ioanna Sakellari et al. "Diffusion-assisted high-resolution direct femtosecond laser writing". In: *ACS nano* 6.3 (2012), pp. 2302–2311.

[344] Brian Salazar et al. "Polymer lattice-reinforcement for enhancing ductility of concrete". In: *Materials & Design* 196 (2020), p. 109184.

[345] Talal Salem et al. "Maneuverable postbuckling of extensible mechanical metamaterials using functionally graded materials and carbon nanotubes". In: *Thin-Walled Structures* (2020), p. 107264.

[346] Francesca Santoro et al. "Revealing the cell–material interface with nanometer resolution by focused ion beam/scanning electron microscopy". In: *ACS nano* 11.8 (2017), pp. 8320–8328.

[347] Robert L Satcher Jr and C Forbes Dewey Jr. "Theoretical estimates of mechanical properties of the endothelial cell cytoskeleton". In: *Biophysical journal* 71.1 (1996), pp. 109–118.

[348] Daria Scerrato and Ivan Giorgio. "Equilibrium of Two-Dimensional Cycloidal Pantographic Metamaterials in Three-Dimensional Deformations". In: *Symmetry* 11.12 (2019), p. 1523.

[349] Tobias A Schaedler et al. "Ultralight metallic microlattices". In: *Science* 334.6058 (2011), pp. 962–965.

[350] Robert Schittny et al. "Elastic measurements on macroscopic three-dimensional pentamode metamaterials". In: *Applied Physics Letters* 103.23 (2013), p. 231905.

[351] MW Schraad and N Triantafyllidis. "Scale effects in media with periodic and nearly periodic microstructures, Part I: Macroscopic properties". In: (1997).

[352] MW Schraad and N Triantafyllidis. "Scale effects in media with periodic and nearly periodic microstructures, Part II: failure mechanisms". In: (1997).

[353] Almut Schroer, Jeffrey M Wheeler, and Ruth Schwaiger. "Deformation behavior and energy absorption capability of polymer and ceramic-polymer composite microlattices under cyclic loading". In: *Journal of Materials Research* 33.3 (2018), pp. 274–289.

[354] Sicong Shan et al. "Multistable architected materials for trapping elastic strain energy". In: *Advanced Materials* 27.29 (2015), pp. 4296–4301.

[355] Lucas A Shaw et al. "Computationally efficient design of directionally compliant metamaterials". In: *Nature communications* 10.1 (2019), pp. 1–13.

[356] GC Shephard. "Isohedral deltahedra". In: *Periodica Mathematica Hungarica* 39.1-3 (2000), pp. 83–106.

[357] VPW Shim, BY Tay, and WJ Stronge. "Dynamic crushing of strain-softening cellular structures—a one-dimensional analysis". In: (1990).

[358] Matthew J Silva and Lorna J Gibson. "The effects of non-periodic microstructure and defects on the compressive strength of two-dimensional cellular solids". In: *International Journal of Mechanical Sciences* 39.5 (1997), pp. 549–563.

[359] Siddharth Sivankutty et al. "Supercritical angle fluorescence for enhanced axial sectioning in sted microscopy". In: *Methods* 174 (2020), pp. 20–26.

[360] Mark A Skylar-Scott et al. "Guided Homing of Cells in Multi-Photon Microfabricated Bioscaffolds". In: *Advanced healthcare materials* 5.10 (2016), pp. 1233–1243.

[361] Pranav Soman et al. "A three-dimensional polymer scaffolding material exhibiting a zero Poisson's ratio". In: *Soft Matter* 8.18 (2012), pp. 4946–4951.

[362] Jian Song et al. "Metal-coated hybrid meso-lattice composites and their mechanical characterizations". In: *Composite Structures* 203 (2018), pp. 750–763.

[363] Jian Song et al. "Octet-truss cellular materials for improved mechanical properties and specific energy absorption". In: *Materials & Design* 173 (2019), p. 107773.

[364] Mario Spagnuolo et al. "Are higher-gradient models also capable of predicting mechanical behavior in the case of wide-knit pantographic structures?" In: *Mathematics and Mechanics of Solids* (), p. 1081286520937339.

[365] Ioannis Spanos et al. "Design and Characterization of Microscale Auxetic and Anisotropic Structures Fabricated by Multiphoton Lithography". In: *Nanomaterials* 11.2 (2021), p. 446.

[366] David J Steigmann. "Applications of polyconvexity and strong ellipticity to nonlinear elasticity and elastic plate theory". In: *Poly-, Quasi-and rank-one convexity in applied mechanics*. Springer, 2010, pp. 265–299.

[367] Johan van der Stok et al. "Enhanced bone regeneration of cortical segmental bone defects using porous titanium scaffolds incorporated with colloidal gelatin gels for time-and dose-controlled delivery of dual growth factors". In: *Tissue Engineering Part A* 19.23-24 (2013), pp. 2605–2614.

[368] Harold T Stokes and Dorian M Hatch. *Isotropy subgroups of the 230 crystallographic space groups*. World Scientific, 1988.

[369] Cornelis Storm et al. "Nonlinear elasticity in biological gels". In: *Nature* 435.7039 (2005), pp. 191–194.

[370] Ziqi Sun et al. "Fly-eye inspired superhydrophobic anti-fogging inorganic nanostructures". In: *Small* 10.15 (2014), pp. 3001–3006.

[371] James Utama Surjadi et al. "Mechanical metamaterials and their engineering applications". In: *Advanced Engineering Materials* 21.3 (2019), p. 1800864.

[372] Joe Swift et al. "Nuclear lamin-A scales with tissue stiffness and enhances matrix-directed differentiation". In: *Science* 341.6149 (2013).

[373] DM Sykes. "Lattice frames in turbulent airflow". In: *Journal of Wind Engineering and Industrial Aerodynamics* 7.2 (1981), pp. 203–214.

[374] Barna Szabó and Ivo Babuška. *Finite element analysis*. John Wiley & Sons, 1991.

[375] Ping Tan, Liyong Tong, and GP Steven. "Behavior of 3D orthogonal woven CFRP composites. Part II. FEA and analytical modeling approaches". In: *Composites Part A: applied science and manufacturing* 31.3 (2000), pp. 273–281.

[376] Thomas Tancogne-Dejean, Adriaan B Spierings, and Dirk Mohr. "Additively-manufactured metallic micro-lattice materials for high specific energy absorption under static and dynamic loading". In: *Acta Materialia* 116 (2016), pp. 14–28.

[377] Thomas Tancogne-Dejean et al. "3D Plate-Lattices: An Emerging Class of Low-Density Metamaterial Exhibiting Optimal Isotropic Stiffness". In: *Advanced Materials* 30.45 (2018), p. 1803334.

[378] Michael Taylor et al. "Low porosity metallic periodic structures with negative Poisson's ratio". In: *Advanced Materials* 26.15 (2014), pp. 2365–2370.

[379] Nimalan Thavandiran et al. "Design and formulation of functional pluripotent stem cell-derived cardiac microtissues". In: *Proceedings of the National Academy of Sciences* 110.49 (2013), E4698–E4707.

[380] Christian Rye Thomsen, Fengwen Wang, and Ole Sigmund. "Buckling strength topology optimization of 2D periodic materials based on linearized bifurcation analysis". In: *Computer Methods in Applied Mechanics and Engineering* 339 (2018), pp. 115–136.

[381] Robb Thomson, C Hsieh, and V Rana. "Lattice trapping of fracture cracks". In: *Journal of Applied Physics* 42.8 (1971), pp. 3154–3160.

[382] William Thomson et al. "On the division of space with minimum partitional area". In: *Acta mathematica* 11 (1887), pp. 121–134.

[383] Richard JD Tilley. *Defects in solids*. Vol. 4. John Wiley & Sons, 2008.

[384] Stephen P Timoshenko and James M Gere. *Theory of elastic stability*. Courier Corporation, 2009.

[385] M Touratier. "An efficient standard plate theory". In: *International journal of engineering science* 29.8 (1991), pp. 901–916.

[386] Nicolas Triantafyllidis and BN Maker. "On the comparison between microscopic and macroscopic instability mechanisms in a class of fiber-reinforced composites". In: (1985).

[387] Naoto Tsutsumi et al. "Direct laser writing for micro-optical devices using a negative photoresist". In: *Optics express* 25.25 (2017), pp. 31539–31551.

[388] ZH Tu, VPW Shim, and CT Lim. "Plastic deformation modes in rigid polyurethane foam under static loading". In: *International Journal of Solids and Structures* 38.50-51 (2001), pp. 9267–9279.

[389] Alessandro Tuniz et al. "Weaving the invisible thread: design of an optically invisible metamaterial fibre". In: *Optics express* 18.17 (2010), pp. 18095–18105.

[390] Sanna Turunen et al. "Direct laser writing of tubular microtowers for 3D culture of human pluripotent stem cell-derived neuronal cells". In: *ACS applied materials & interfaces* 9.31 (2017), pp. 25717–25730.

[391] Lucas Van Belle et al. "On the impact of damping on the dispersion curves of a locally resonant metamaterial: Modelling and experimental validation". In: *Journal of Sound and Vibration* 409 (2017), pp. 1–23.

[392] Z Vangelatos, K Komvopoulos, and CP Grigoropoulos. "Regulating the mechanical behavior of metamaterial microlattices by tactical structure modification". In: *Journal of the Mechanics and Physics of Solids* 144 (2020), p. 104112.

[393] Z Vangelatos, K Komvopoulos, and CP Grigoropoulos. "Vacancies for controlling the behavior of microstructured three-dimensional mechanical metamaterials". In: *Mathematics and Mechanics of Solids* 24.2 (2019), pp. 511–524.

[394] Z Vangelatos et al. "Anisotropic and curved lattice members enhance the structural integrity and mechanical performance of architected metamaterials". In: *International Journal of Solids and Structures* 193 (2020), pp. 287–301.

[395] Zacharias Vangelatos, Grace X Gu, and Costas P Grigoropoulos. "Architected metamaterials with tailored 3D buckling mechanisms at the microscale". In: *Extreme Mechanics Letters* 33 (2019), p. 100580.

[396] Zacharias Vangelatos, Kyriakos Komvopoulos, and Costas P Grigoropoulos. "Tailoring 3D Buckling and Post Contact in Microlattice Metamaterials". In: *Developments and Novel Approaches in Biomechanics and Metamaterials*. Springer, 2020, pp. 471–484.

[397] Zacharias Vangelatos, Letian Wang, and Costas P Grigoropoulos. "Laser pyrolysis for controlled morphing and chemical modification on 3D microlattices". In: *Journal of Micromechanics and Microengineering* 30.5 (2020), p. 055008.

[398] Zacharias Vangelatos et al. "Architected mechanical designs in tissue engineering". In: *MRS Communications* 10.3 (2020), pp. 379–390.

[399] Zacharias Vangelatos et al. "Biomechanical metamaterials fabricated through multiphoton lithography by tailoring 3D buckling". In: *Laser-based Micro-and Nanoprocessing XIV*. Vol. 11268. International Society for Optics and Photonics. 2020, p. 1126812.

[400] Zacharias Vangelatos et al. "Comparison of the mechanical performance of architected three-dimensional intertwined lattices at the macro/microscale". In: *Extreme Mechanics Letters* 40 (2020), p. 100930.

[401] Zacharias Vangelatos et al. "Design and Testing of Bistable Lattices with Tensegrity Architecture and Nanoscale Features Fabricated by Multiphoton Lithography". In: *Nanomaterials* 10.4 (2020), p. 652.

[402] Zacharias Vangelatos et al. "Intertwined microlattices greatly enhance the performance of mechanical metamaterials". In: *Mathematics and Mechanics of Solids* 24.8 (2019), pp. 2636–2648.

[403] Zacharias Vangelatos et al. "Investigating the mechanical response of microscale pantographic structures fabricated by multiphoton lithography". In: *Extreme Mechanics Letters* (2021), p. 101202.

[404] Zacharias Vangelatos et al. "Tailoring the Dynamic Actuation of 3D-Printed Mechanical Metamaterials through Inherent and Extrinsic Instabilities". In: *Advanced Engineering Materials* (), p. 1901586.

[405] Fernando Guevara Vasquez, Graeme W Milton, and Daniel Onofrei. "Complete characterization and synthesis of the response function of elastodynamic networks". In: *Journal of Elasticity* 102.1 (2011), pp. 31–54.

[406] Giuseppe Vicidomini, Paolo Bianchini, and Alberto Diaspro. "STED super-resolved microscopy". In: *Nature methods* 15.3 (2018), p. 173.

[407] Lawrence Virgin. "Tailored buckling constrained by adjacent members". In: *Structures*. Vol. 16. Elsevier. 2018, pp. 20–26.

[408] Gaszton Vizsnyiczai, Lóránd Kelemen, and Pál Ormos. "Holographic multi-focus 3D two-photon polymerization with real-time calculated holograms". In: *Optics express* 22.20 (2014), pp. 24217–24223.

[409] Viola Vogel and Michael Sheetz. "Local force and geometry sensing regulate cell functions". In: *Nature reviews Molecular cell biology* 7.4 (2006), pp. 265–275.

[410] Marius A Wagner et al. "Programmable, active lattice structures: Unifying stretch-dominated and bending-dominated topologies". In: *Extreme Mechanics Letters* 29 (2019), p. 100461.

[411] TJ Wallin, J Pikul, and RF Shepherd. "3D printing of soft robotic systems". In: *Nature Reviews Materials* 3.6 (2018), pp. 84–100.

[412] Rodger M Walser. "Electromagnetic metamaterials". In: *Complex Mediums II: Beyond Linear Isotropic Dielectrics*. Vol. 4467. International Society for Optics and Photonics. 2001, pp. 1–15.

[413] Chenyan Wang et al. "Maladaptive contractility of 3D human cardiac microtissues to mechanical nonuniformity". In: *Advanced healthcare materials* 9.8 (2020), p. 1901373.

[414] Guoli Wang et al. "Large deformation shape optimization of cut-mediated soft mechanical metamaterials". In: *Materials Research Express* 6.5 (2019), p. 055802.

[415] Qiming Wang et al. "Lightweight mechanical metamaterials with tunable negative thermal expansion". In: *Physical review letters* 117.17 (2016), p. 175901.

[416] Yu Wang et al. "Level-set topology optimization for multimaterial and multifunctional mechanical metamaterials". In: *Engineering Optimization* 49.1 (2017), pp. 22–42.

[417] Ian M Ward and Dennis W Hadley. *An introduction to the mechanical properties of solid polymers*. 1993.

[418] John J Warner et al. "3D-printed biomaterials with regional auxetic properties". In: *Journal of the mechanical behavior of biomedical materials* 76 (2017), pp. 145–152.

[419] WE Warren and AM Kraynik. "Linear elastic behavior of a low-density Kelvin foam with open cells". In: (1997).

[420] J Peter Watt. "Hashin-Shtrikman bounds on the effective elastic moduli of polycrystals with orthorhombic symmetry". In: *Journal of Applied Physics* 50.10 (1979), pp. 6290–6295.

[421] Denis Weaire. *The Kelvin Problem*. CRC Press, 1997.

[422] James C Weaver et al. "Hierarchical assembly of the siliceous skeletal lattice of the hexactinellid sponge Euplectella aspergillum". In: *Journal of structural biology* 158.1 (2007), pp. 93–106.

[423] Lulu Wei et al. "A novel star auxetic honeycomb with enhanced in-plane crushing strength". In: *Thin-Walled Structures* 149 (2020), p. 106623.

[424] Magnus J Wenninger. *Polyhedron models*. Cambridge University Press, 1974.

[425] Jackson K Wilt, Charles Yang, and Grace X Gu. "Accelerating Auxetic Metamaterial Design with Deep Learning". In: *Advanced Engineering Materials* (2020), p. 1901266.

[426] Tackla S Winston et al. "Serum-Free Manufacturing of Mesenchymal Stem Cell Tissue Rings Using Human-Induced Pluripotent Stem Cells". In: *Stem cells international* 2019 (2019).

[427] Richard Wollhofen et al. "120 nm resolution and 55 nm structure size in STED-lithography". In: *Optics express* 21.9 (2013), pp. 10831–10840.

[428] Jinglai Wu et al. "Level-set topology optimization for mechanical metamaterials under hybrid uncertainties". In: *Computer Methods in Applied Mechanics and Engineering* 319 (2017), pp. 414–441.

[429] Lingling Wu et al. "A machine learning-based method to design modular metamaterials". In: *Extreme Mechanics Letters* 36 (2020), p. 100657.

[430] Lingling Wu et al. "Mechanical metamaterials for full-band mechanical wave shielding". In: *Applied Materials Today* 20 (2020), p. 100671.

[431] Wenwang Wu et al. "Mechanical design and multifunctional applications of chiral mechanical metamaterials: A review". In: *Materials & Design* 180 (2019), p. 107950.

[432] Shanqing Xu et al. "Design of lattice structures with controlled anisotropy". In: *Materials & Design* 93 (2016), pp. 443–447.

[433] Rui Xue et al. "Mechanical design and energy absorption performances of novel dual scale hybrid plate-lattice mechanical metamaterials". In: *Extreme Mechanics Letters* 40 (2020), p. 100918.

[434] Tianju Xue et al. "A data-driven computational scheme for the nonlinear mechanical properties of cellular mechanical metamaterials under large deformation". In: *Soft matter* 16.32 (2020), pp. 7524–7534.

[435] Hang Yang and Li Ma. "Multi-stable mechanical metamaterials by elastic buckling instability". In: *Journal of materials science* 54.4 (2019), pp. 3509–3526.

[436] Hang Yang and Li Ma. "Multi-stable mechanical metamaterials with shape-reconfiguration and zero Poisson's ratio". In: *Materials & Design* 152 (2018), pp. 181–190.

[437] Hua Yang et al. "Material characterization and computations of a polymeric metamaterial with a pantographic substructure". In: *Zeitschrift für angewandte Mathematik und Physik* 69.4 (2018), p. 105.

[438] Li Yang et al. "Mechanical properties of 3D re-entrant honeycomb auxetic structures realized via additive manufacturing". In: *International Journal of Solids and Structures* 69 (2015), pp. 475–490.

[439] Yang Yang et al. "Recent progress in biomimetic additive manufacturing technology: from materials to functional structures". In: *Advanced Materials* 30.36 (2018), p. 1706539.

[440] Yan Yao et al. "A novel auxetic structure based bone screw design: Tensile mechanical characterization and pullout fixation strength evaluation". In: *Materials & Design* 188 (2020), p. 108424.

[441] Hiromi Yasuda et al. "Origami-based impact mitigation via rarefaction solitary wave creation". In: *Science advances* 5.5 (2019), eaau2835.

[442] Tony Yeung et al. "Effects of substrate stiffness on cell morphology, cytoskeletal structure, and adhesion". In: *Cell motility and the cytoskeleton* 60.1 (2005), pp. 24–34.

[443] M Erden Yildizdag, Emilio Barchiesi, and Francesco dell'Isola. "Three-point bending test of pantographic blocks: numerical and experimental investigation". In: *Mathematics and Mechanics of Solids* (), p. 1081286520916911.

[444] Mustafa Erden Yildizdag et al. "A multi-disciplinary approach for mechanical metamaterial synthesis: a hierarchical modular multiscale cellular structure paradigm". In: *State of the art and future trends in material modeling*. Springer, 2019, pp. 485–505.

[445] Hang Yin et al. "Orthogonal programming of heterogeneous micro-mechano-environments and geometries in three-dimensional bio-stereolithography". In: *Nature communications* 9.1 (2018), pp. 1–7.

[446] Xianglong Yu et al. "Mechanical metamaterials associated with stiffness, rigidity and compressibility: A brief review". In: *Progress in Materials Science* 94 (2018), pp. 114–173.

[447] Shangqin Yuan, Chee Kai Chua, and Kun Zhou. "3D-Printed Mechanical Metamaterials with High Energy Absorption". In: *Advanced Materials Technologies* 4.3 (2019), p. 1800419.

[448] Amir A Zadpoor. "Mechanical meta-materials". In: *Materials Horizons* 3.5 (2016), pp. 371–381.

[449] Amir A Zadpoor. "Meta-biomaterials". In: *Biomaterials science* 8.1 (2020), pp. 18–38.

[450] Amir Abbas Zadpoor and Reza Hedayati. "Analytical relationships for prediction of the mechanical properties of additively manufactured porous biomaterials". In: *Journal of Biomedical Materials Research Part A* 104.12 (2016), pp. 3164–3174.

[451] Ioanna Zergioti et al. "Microdeposition of metal and oxide structures using ultrashort laser pulses". In: *Applied Physics A: Materials Science & Processing* 66 (1998), pp. 579–582.

[452] Huikai Zhang, Yangjun Luo, and Zhan Kang. "Bi-material microstructural design of chiral auxetic metamaterials using topology optimization". In: *Composite Structures* 195 (2018), pp. 232–248.

[453] Wenqiang Zhang et al. "Liquid Metal-Polymer Microlattice Metamaterials with High Fracture Toughness and Damage Recoverability". In: *Small* 16.46 (2020), p. 2004190.

[454] Xu Zhang et al. "Kirigami Engineering—Nanoscale Structures Exhibiting a Range of Controllable 3D Configurations". In: *Advanced Materials* (2020), p. 2005275.

[455] Xuan Zhang et al. "Design, fabrication, and mechanics of 3D micro-/nanolattices". In: *Small* 16.15 (2020), p. 1902842.

[456] Xuan Zhang et al. "Lightweight, flaw-tolerant, and ultrastrong nanoarchitected carbon". In: *Proceedings of the National Academy of Sciences* 116.14 (2019), pp. 6665–6672.

[457] Xuan Zhang et al. "Three-dimensional high-entropy alloy–polymer composite nanolattices that overcome the strength–recoverability trade-off". In: *Nano letters* 18.7 (2018), pp. 4247–4256.

[458] Yichi Zhang, Daniel W Apley, and Wei Chen. "Bayesian Optimization for Materials Design with Mixed Quantitative and Qualitative Variables". In: *Scientific reports* 10.1 (2020), pp. 1–13.

[459] Yuan-Fang Zhang et al. "Fast-response, stiffness-tunable soft actuator by hybrid multimaterial 3D printing". In: *Advanced Functional Materials* 29.15 (2019), p. 1806698.

[460] Zhizhou Zhang and Grace X Gu. "Finite-Element-Based Deep-Learning Model for Deformation Behavior of Digital Materials". In: *Advanced Theory and Simulations* (2020), p. 2000031.

[461] Zuhua Zhang et al. "Mechanical, thermal insulation, thermal resistance and acoustic absorption properties of geopolymer foam concrete". In: *Cement and Concrete Composites* 62 (2015), pp. 97–105.

[462] Wenting Zhao et al. "Nanoscale manipulation of membrane curvature for probing endocytosis in live cells". In: *Nature nanotechnology* 12.8 (2017), p. 750.

[463] Yushun Zhao et al. "Carbon nanotubes kirigami mechanical metamaterials". In: *Physical Chemistry Chemical Physics* 19.18 (2017), pp. 11032–11042.

[464] Nina A Zharova et al. "Nonlinear control of invisibility cloaking". In: *Optics express* 20.14 (2012), pp. 14954–14959.

[465] Li Zheng, Siddhant Kumar, and Dennis M Kochmann. "Data-driven topology optimization of spinodoid metamaterials with seamlessly tunable anisotropy". In: *Computer Methods in Applied Mechanics and Engineering* 383 (2021), p. 113894.

[466] Xiaoyu Zheng et al. "Ultralight, ultrastiff mechanical metamaterials". In: *Science* 344.6190 (2014), pp. 1373–1377.

[467] Yongfeng Zheng et al. "Evolutionary topology optimization for mechanical metamaterials with auxetic property". In: *International Journal of Mechanical Sciences* 179 (2020), p. 105638.

[468] Xiaoqin Zhou, Yihong Hou, and Jieqiong Lin. "A review on the processing accuracy of two-photon polymerization". In: *AIP Advances* 5.3 (2015), p. 030701.